ALMA MATER STUDIORUM
UNIVERSITÀ DI BOLOGNA

DOTTORATO DI RICERCA IN

SCIENZE E TECNOLOGIE AGRARIE, AMBIENTALI E ALIMENTARI

Ciclo 37

Settore Concorsuale: 07/E1 - CHIMICA AGRARIA, GENETICA AGRARIA E PEDOLOGIA

Settore Scientifico Disciplinare: AGR/07 - GENETICA AGRARIA

UNCOVERING GENETIC DETERMINANTS OF DISEASE RESISTANCE IN DURUM WHEAT AGAINST CAUSATIVE AGENTS OF YELLOW RUST AND SEPTORIA TRITICI BLOTCH AND, ENVIRONMENTAL ADAPTATION OF ZYMOSEPTORIA TRITICI: INSIGHTS FROM MULTI-ENVIRONMENT GWAS AND PATHOGEN THERMAL ADAPTATION

Presentata da: Francesco De Sario

Coordinatore Dottorato

Diana Di Gioia

Supervisore

Marco Maccaferri

Co-supervisore

Roberto Tuberosa

Esame finale anno 2025

SUMMARY

Abstract 5
1. Introduction 6
1.1 Challenges in Sustainable Agriculture in the Middle of Global Population Growth and Climate Change 6
1.2 The Dual Threat of Climate Change: Impacts of Biotic and Abiotic Stresses on Crop Yields and Food Security 6
1.3 Leveraging Genetic Resistance: A Sustainable Agricultural Approach for Biotic Pressures Management 7
1.4 Climate Change and Its Impact on Fungal Pathogens Affecting Wheat 8
1.5 Origin and Evolution of tetraploid wheat (Triticum turgidum ssp. durum) 8
1.6 Global Wheat Production Overview: Economic and Nutritional Relevance of Durum Wheat in Italy and Across the World 9
1.7 Evolution of Durum Wheat Breeding in Italy: From Traditional Practices to Modern Innovations 10
1.8 General overview of Plant-Pathogens Interaction: The “Disease Triangle” and Induced-priming agents 12
1.9 Fungal Pathogens Overview: Plant Recognition and defence mechanisms towards plant-infecting fungal pathogens 12
1.10 Qualitative (Single R genes) and Quantitative Disease Resistance (QTLs): Integration into Pyramiding Strategies for Durable Resistance 14
1.11 Major Foliar and Spike Wheat Diseases 15
1.12 Quantitative Traits Locus (QTL) Definition and Analysis 16
1.13 QTL mapping methods 16
1.13.1 Experimental populations for QTL mapping 16
1.13.2 Genome-Wide Assoication Study (GWAS) 18
1.13.3 Meta-QTL Analysis and Projection of QTLs onto Physical Maps: Integrating Linkage Mapping and GWAS in Wheat 19
1.14 Genotyping Technologies 20
1.14.1 SNPs-Based Genotyping Chips 20
1.14.2 SNPs Genotyping Arrays in Wheat 20
1.14.3 Genomic Selection, MAS and KASP Technologies in wheat 21

2 Genome-Wide Association Study (GWAS) conducted in a panel of tetraploid wheat durum wheat landraces to map MTAs associated to Yellow rust (Yr) resistance 22
2.1 Introduction 22
2.1.1 Yellow rust: the disease and current state-of-the-art 22
2.1.2 Life cycle and biology 23
2.1.3 Triticum turgidum subspecies landraces, a valuable pool gene to uncover resistance genes in Tetraploid Wheat 23
2.2 Materials and methods 24
2.2.1 Plant materials, Experimental Design and Environments 24
2.2.2 Phenotypic Data Analysis 25
2.2.3 Phenotypic Data Analysis 27
2.2.4 SNP Genotyping 28
2.2.5 LD decay analysis, SNPs Pruning, population structure analysis and Identity By State (IBS) genetic similarity matrix 29
2.2.6 Genome-Wide Association Study for TGC panels 30
2.2.7 Genome-Wide Association Study within TGC subpopulations 30
2.2.8 Downstream analysis: General Linear model and Stepwise regression 31
2.2.9 LD-Blocks detection and Haplotype Analysis 31
2.2.10 Projection of Yr Loci and QTLs onto the cv Svevo reference genome 31
2.3 RESULTS 33
2.3.1 Multi-environmental clustering and correlations 33
2.3.2 Environments 36
2.3.3 Population structure, Clustering and Identiy By State (IBS) Kinship Matrix 40
2.3.4 LD decay estimation for Tetraploid Global Collection (TGC) 43
2.3.5 Yr Loci and QTL projection onto the Svevo reference genome physical map 44
2.3.6 GWAS RESULTS 48
2.4 DISCUSSION 71
2.5 CONCLUSION CHAPTER II 77
3 Genome-Wide Association Study (GWAS) conducted in a panel of tetraploid wheat durum wheat landraces to map MTAs associated to Septoria Tritici Blotch Resistance (Stb) 77
3.1 Introduction 77
3.1.1 Life cycle and biology 77
3.1.2 Host-pathogen interaction in Zymoseptoria tritici pathosystem 78
3.1.3 Septoria Tritici Blotch: Current State-Of-The-Art and QTLs mapping 79
3.2 Materials and methods 80
3.2.1 Plant material, Experimental Design and Environment 80
3.2.2 Inoculation and disease assesment 81
3.2.3 Phenotypic Data Analysis 83

3.2.4 SNP Genotyping, LD decay analysis, SNPs Pruning, population structure analysis and Identity By State (IBS) genetic similarity matrix 84
3.2.5 Genome-Wide Association Study for CEREALMED panel 84
3.2.6 Genome-Wide Association Study within TGC subpopulations 84
3.2.7 Downstream analysis, LD-Blocks detection and Haplotype Analysis 85
3.2.8 Projection of Stb Loci and QTLs onto the cv Svevo reference genome 85
3.3 RESULTS 85
3.3.1 Descriptive statistic, phenotypic data distribution and correlation 85
3.3.2 Stb Loci and QTLs projection onto the Svevo reference genome physical map 89
3.3.3 GWAS RESULTS 92
3.4 DISCUSSION 107
3.5 Conclusion chapter 3 110
4 Chapter IV: Genome-Wide Association Study (GWAS) conducted on an European panel of Zymoseptoria tritici to map regions associated with thermal adaptation and plastic response 111
4.1 Introduction 111
4.1.1 Zymoseptoria tritici, fungal genome and insight from the pathogen side 111
4.1.2 Thermal adaptation and response in Zymoseptoria tritici and other plant pathogenic fungi 112
4.1.3 Phenotypic plasticity in relation to a climate shift 113
4.2 Material and Methods 113
4.2.1 Fungal Material 113
4.2.2 Thermal Response Phenotypes 114
4.2.3 Whole-genome sequencing and variants calling 114
4.2.4 Pathogenicity assay 116
4.2.5 Statistical analysis of phenotypic data 118
4.2.6 Population Structure and Linkage Disequilibrium 119
4.2.7 Genome-Wide Association and Local Score Analyses 119
4.2.8 Downstream Analyses: Linear Model and Stepwise Regression 120
4.2.9 Identification of Candidate Genes 120
4.3 RESULTS 120
4.3.1 Genetic structuration of the population 120
4.3.2 Estimation of LD decay 123
4.3.3 Response to temperature within geographic populations and subpopulations 124
4.3.4 Avrstb6 phylogenetic analysis 126
4.3.5 Influence of temperature on pathogenic variability and plasticity 130
4.3.6 GWAS and resolution increase through Local Score approach 137
4.3.7 Candidate genes annotation within the QTLs Lindley region 145
4.4 Discussion 149

4.5 Conclusion chapter IV 151
5 Conclusions and future perspectives 152
6 Contributions 152
7 References 153
8 Supplementary Materials 184

Abstract

This thesis explores the genetic factors underpinning disease resistance against the causative agents of *Yellow rust* (Yr) and *Septoria tritici blotch (Stb)* in durum wheat and environmental adaptation in durum wheat and *Zymoseptoria tritici*, aiming to develop a sustainable crop management strategy. Chapter 1 focuses on identifying genetic regions associated with *Yellow rust* (Yr) resistance in durum wheat, assessing a panel of 1324 *Triticum turgidum* landraces and related subspecies in the Mediterranean region (Italy, Turkey, Tunisia, and Lebanon). This panel represents a subset of the Tetraploid wheat Global Collection (TGC, Maccaferri et al. 2019), which has been genotyped through Illumina 90K SNP array and, subpopulations have been identified through ADMIXTURE analysis. Using a multi-year, multi-environment approach, Genome-Wide Association Studies (GWAS) with four models (MLM, MLMM, FarmCPU, and BLINK) revealed 11 QTLs significantly associated with Yr resistance, located on chromosomes 1B, 2A, 2B, 5B, 7A, and 7B. Haplotype analysis provided insights into allelic diversity, origin, and phenotypic effects, increasing our understanding of resistant genetic variants within the *Triticum turgidum* global gene pool. Additionally, GWAS was also conducted within the single identified subpopulation for each environment, to either detect rare resistant allele variants deeply conserved in the single subpopulations or track the origin of the QTLs detected from the global GWAS. Chapter 2 investigates genetic resistance to *Septoria tritici blotch* (*Stb*) within a second panel of 510 durum wheat landraces and related subspecies from the CEREALMED collection, assessed in Cadriano (Bologna). Artificial inoculation and subsequent disease scoring of *Stb* symptoms was performed in the flag leaf and the rest of the canopy at two timepoints in order to assess Area Under the Disease Progression Curve (AUDPC). Global GWAS and subpopulation GWAS enabled detection of eight QTLs across the entire panel and 16 within specific subpopulations. These QTLs include novel loci not overlapping known *Stb* loci, thus expanding potential breeding targets for *Stb* resistance. Chapter 3 shifts focus to *Zymoseptoria tritici*, exploring genetic determinants underlying thermal adaptation and responses in a collection of 238 isolates from 8 different Euro-Mediterranean countries with heterogeneous climatic regions. Using data on optimal temperature (Topt) and thermal performance breadth (TPB80), along with pathogenicity metrics (PLACL and PycLes) assessed via high-throughput phenotyping, GWAS identified candidate genes associated with thermal adaptation and temperature-dependent plastic responses. Most candidate genes include heat shock proteins, chaperones, and zinc finger proteins, known for roles in thermal adaptation and response. Taken Together, these findings reveal essential genetic targets for crop breeding programs focused on disease resistance and climate resilience. By enhancing understanding of host-pathogen interactions and adaptation, this study contributes to the development of integrated crop management strategies, supporting Green Deal objectives to lessen the use of chemical inputs while improving resilience to environmental stresses.

1. Introduction

1.1 Challenges in Sustainable Agriculture in the Middle of Global Population Growth and Climate Change

The global population is expected to grow substantially in the coming decades, with estimates suggesting it could reach between 9.7 and 10.4 billion people by 2050 (United Nations, 2022; Gerland et al., 2023). This substantial increase in population will result in considerable pressure on agricultural systems, requiring a significant increase in food production, an expected 60-70% increase compared to current levels, to meet the rising demand (FAO, 2017). At the same time, it is mandatory to mitigate the adverse impacts of agriculture on key natural resources such as land, water, and the climate (FAO, 2017). Furthermore, improving food quality, particularly in terms of nutrient content, is essential to ensure the health and well-being of future populations (FAO, 2020; Myers et al., 2014). Achieving all these important missions implies the development of sustainable agricultural practices, the adoption of innovative technologies, and policies that prioritize both food security and environmental sustainability. The challenge of increasing food production is paired with climate change, which is expected to provoke rising temperatures, more frequent extreme weather events, and shifts in rainfall patterns, all of which could negatively affect agricultural productivity (IPCC, 2022). Higher concentrations of atmospheric CO2 may increase yields in certain crops, such as wheat but the overall benefits remain uncertain and context-dependent (Leakey, 2019). Additionally, any potential gains from CO2 fertilization are likely to be counterbalanced by the detrimental effects of elevated temperatures, droughts, and the increased occurrence of pests and diseases outbreaks (Lobell et al., 2011; Zhang et al., 2021). Notably, rising temperatures are widely known to reduce crop yields, with many crops evidencing considerable declines in production when temperatures exceed critical thresholds (Challinor et al., 2014). Major crops, including wheat, maize, and rice, display yield reductions as temperatures rise beyond these thresholds, ranging from 30°C to 35°C, particularly in regions already vulnerable to heat stress (Challinor et al., 2014). Moreover, climate change is expected to maximise other environmental stresses such as salinity, drought, and ozone pollution, while also increasing the risk of invasive species and pathogens that can further damage crops (Myers et al., 2017). For instance, elevated temperatures can accelerate plant growth rates, reducing the time available for the accumulation of key nutrients, including proteins, fats, and carbohydrates (Chandio et al., 2023). Rising CO2 levels have also been associated with diminished nutritional quality in crops, particularly reductions in mineral and protein content (Myers et al., 2014). Given these challenges, simply expanding agricultural land will not be a durable solution. The degradation of arable land due to desertification, salinity, and erosion, combined with competition from urbanization and industrial use, limits the availability of new land for agriculture (Foley et al., 2011). Furthermore, converting natural ecosystems into farmland can have other environmental consequences, such as biodiversity loss, soil degradation, and increased carbon emissions due to the release of stored carbon in vegetation and soils (IPCC, 2022). These interconnected challenges underscore the need for a comprehensive approach that balances productivity with resilience and environmental stewardship (FAO, 2020).

1.2 The Dual Threat of Climate Change: Impacts of Biotic and Abiotic Stresses on Crop Yields and Food Security

Climate change represents a critical threat to global food security, primarily by exacerbating both biotic and abiotic stresses that affect crop yields. Rising global temperatures, shifting precipitation patterns, and an increase in the frequency of extreme weather events create unfavourable conditions

for agricultural production (IPCC, 2022). Biotic stresses, such as the spread of pests and diseases, are expected to worsen, contributing to significant yield reductions. Warmer temperatures enable agricultural pests and pathogens to expand their geographic range, reproduce more rapidly, and cause more frequent and severe outbreaks (Deutsch et al., 2018). For example, the proliferation of cereal aphids and pathogens like *Fusarium* and *Puccinia* species is likely to worsen, threatening key crops such as wheat and maize (Lobell et al., 2011; Chakraborty & Newton, 2011). Climate change may also influence host-pathogen interactions, as elevated CO2 levels and warmer temperatures can affect plant defences and nutritional quality, potentially increasing susceptibility to infections (Zhang et al., 2021). In addition to these biotic stresses, climate change intensifies abiotic stresses such as drought, salinity, and extreme temperatures, further reducing crop resilience. Droughts are projected to become more frequent and severe due to altered precipitation patterns, leading to considerable yield losses, particularly in water-sensitive crops like maize (FAO, 2017). The Intergovernmental Panel on Climate Change (IPCC) estimates that for each degree Celsius increase in temperature, yields of major crops such as wheat and maize could decline by at least 5-10% (IPCC, 2014). Similarly, rising sea levels and reduced freshwater availability are expected to increase soil salinity, particularly in coastal agricultural regions, further constraining crop growth and productivity (Jagadeesh, G. S., & Sampath, P. V. (2022). These abiotic stresses can also increase crop vulnerability to biotic factors, thereby jeopardizing food production and security (FAO, 2017). The combined impact of biotic and abiotic stresses not only threatens agricultural output but also poses socio-economic challenges, particularly for farmers in developing countries who lack the resources and technology to adapt to these rapid changes (Thornton et al., 2018). The continued reliance on conventional farming practices in these vulnerable regions often favours environmental degradation, making it increasingly difficult to maintain soil health and fertility (Pretty, 2018). Conventional practices, which frequently depend on synthetic inputs such as fertilizers and pesticides, can have long-term ecological consequences. The extensive use of chemical fertilizers, for example, can degrade soil organic matter and biodiversity over time, while also contributing to water pollution through runoff (Tilman et al., 2002). Similarly, excessive pesticide use can be detrimental to the ecosystems by harming beneficial organisms and favour the development of pesticide-resistant pest populations (Goulson, 2013). In response to these challenges, there is an urgent need for sustainable agricultural practices that reduce chemical inputs and promote ecological resilience. Integrated pest management (IPM), the development of genetically resistant crop varieties, and organic farming are promising strategies for enhancing the sustainability of agricultural systems while maintaining productivity (Pretty et al., 2018).

1.3 Leveraging Genetic Resistance: A Sustainable Agricultural Approach for Biotic Pressures Management

Plant breeding is a key component in enhancing genetic resistance to both biotic stresses (e.g., pests and diseases) and abiotic stresses (e.g., drought, salinity, and extreme temperatures), playing a vital role in the development of sustainable agricultural systems. By creating crop varieties that are resilient to these stresses, plant breeding reduces reliance on conventional agricultural practices, including the heavy use of chemical pesticides and fertilizers, which often have negative environmental consequences (Tester & Langridge, 2010). Developing disease-resistant varieties, for instance, can significantly reduce crop losses, thereby minimizing the need for chemical interventions and lowering the environmental footprint of agriculture (Singh et al., 2018). Breeding for abiotic stress tolerance also plays an essential role in improving water-use efficiency, which is particularly crucial in the context of increasing water scarcity driven by climate change. By producing varieties that are more tolerant to drought, breeders help stabilize food production in regions affected by fluctuating and unpredictable environmental conditions (Bhaduri et al., 2020). Additionally, these improvements in water efficiency contribute to more energy-efficient farming systems by reducing the need for irrigation and other resource-intensive practices. Incorporating stress-tolerant and resilient crop

varieties into sustainable agricultural practices thus offers a valuable method to secure food production while conserving essential natural resources. As a result, plant breeding serves as a cornerstone for sustainable agriculture, addressing the interconnected challenges of food security, water conservation, and climate resilience for future generations (Tuberosa et al., 2010).

1.4 Climate Change and Its Impact on Fungal Pathogens Affecting Wheat

As global temperatures rise and climatic variability intensifies, conditions favoring the proliferation of fungal pathogens are becoming more frequent, thereby increasing the vulnerability of wheat, one of the world's key staple crops. Elevated temperatures and increased humidity create optimal environments for the growth of fungi such as *Fusarium graminearum*, *Puccinia triticina*, and *Zymoseptoria tritici*, which are respectively, the causative agents of Fusarium head blight, wheat rust, and Septoria tritici blotch, respectively (Masih, 2024; Fabre et al., 2022). These diseases lead to significant yield losses and deteriorate wheat quality, resulting in economic repercussions and food security challenges (Chai et al., 2022). Furthermore, climate change is projected to alter precipitation patterns, leading to intense rainfall followed by dry periods. These fluctuations can stress wheat plants, weakening their natural defenses and making them more susceptible to fungal attacks (Williams SL et al., 2024). The phenomenon of "climate-induced incompatibility," where rising temperatures and shifting growing seasons create mismatches between plant life cycles and pathogen development, poses a major concern. Accelerated pathogen life cycles due to warmer conditions can lead to earlier and more severe infections, limiting effective management windows for disease control (Chai et al., 2022). The rising prevalence of these diseases due to climate change underscores the urgent need for robust crop management strategies. Breeding wheat varieties with enhanced genetic resistance to both abiotic and biotic stresses is vital. Sustainable agricultural practices, including crop rotation, intercropping, and biological control, have been considered to mitigate the effects of climate change on wheat diseases while maintaining productivity and protecting ecosystems (Chai et al., 2022). However, the emergence of new pathogen strains adapted to shifting climates requires continuous research and monitoring to understand the dynamic interactions between pathogens and climate variables. As predictive models for climate change improve, they provide crucial insights for designing effective strategies to safeguard plant health in a changing climate. Addressing the growing threat of fungal pathogens in wheat due to climate change is not only an agricultural challenge but also a global issue concerning food security and environmental sustainability. In view of this, it is mandatory to outline proactive strategies that entail interdisciplinary collaboration among researchers, policymakers, and agricultural stakeholders (Fabre et al., 2022; Chai et al., 2022).

1.5 Origin and Evolution of tetraploid wheat (Triticum turgidum ssp. durum)

The wheat genus (*Triticum ssp.*) belongs to the Graminaceae family (also referred to as Poaceae), specifically within the Triticeae tribe and Triticinae subtribe. Among the multitude of wheat species, two main crops hold immense dietary value: bread wheat (*Triticum aestivum*) and durum wheat (*Triticum turgidum*, commonly known as *Triticum durum Desf.*). Despite their similarities, these species are genetically and agronomically distinct. Bread wheat is classified as an allohexaploid, whereas durum wheat is an allotetraploid, and both are characterized by large and complex genomes (Ganal and Röder, 2007). The genome of durum wheat has been assembled after extensive research, utilizing state-of-the-art sequencing technologies that allow for rapid DNA sequencing. The assembly of the durum wheat cultivar Svevo, comprising 10.45 Gbs, serves as a critical tool for studying the plant's domestication, evolution, and breeding while enhancing our understanding of gene function and the organization of quantitative trait loci (QTLs) associated with important agronomic traits (Maccaferri et al., 2019). Genetically, wheat species exist within an allopolyploid series (x = 7) based on genomes A, B, D, and G, resulting from a succession of interspecific hybridizations (Blanco et al.,

1990; Monneveux et al., 2000). This series includes diploid species (2n = 2x = 14 chromosomes) with the genomic formula AA; allotetraploid species (2n = 4x = 28 chromosomes) with the genomic formulas AABB (*Triticum dicoccoides*, *Triticum dicoccum*, and *Triticum turgidum* ssp. durum) and AAGG (*Triticum timopheevi*); and allohexaploid species (2n = 6x = 42 chromosomes) with the genomic formula AABBDD (*Triticum aestivum* ssp. spelta and *Triticum aestivum* ssp. aestivum). The evolutionary journey of cultivated wheat species began around 10,000 to 8,500 years ago during the Neolithic Revolution, which marked the transition from a nomadic hunter-gatherer lifestyle to an agrarian society. This pivotal change took root in the Levantine Corridor and spread through the Fertile Crescent, a region in the Middle East that includes parts of modern-day Jordan, Israel, Lebanon, Syria, southeastern Turkey, and stretches along the Tigris and Euphrates rivers through Iraq and western Iran (Tuberosa, Graner, & Frison, 2014). Domestication, the genetic selection process that transforms wild forms into domesticated varieties of crops, significantly altered key traits to make the crop easier to harvest, notably seed size, ear rachis stiffness, and threshability (Salamini et al., 2002). Durum wheat has a tetraploid genome (AABB) resulting from the cross between *Triticum urartu* (AA) and *Aegilops speltoides* (BB genome) (Akhunov et al., 2005), which produced the ancestral wild wheat (*Triticum turgidum* ssp. *dicoccoides*). From this ancestral form, emmer wheat (*Triticum turgidum* ssp. *dicoccum*) and subsequently durum wheat were derived, a process that began around 10,000 years ago (Özkan et al., 2002). Diploid species have played a fundamental role in interspecific hybridization by serving as potential sources of beneficial alleles and genomes for cultivated varieties, offering critical insights into their phylogenetic relationships (Blanco et al., 1990; Monneveux et al., 2000). Reliable phylogenetic reconstructions indicate that the A genome is the common foundation for all wheat species, derived from an ancestor of wild wheat, *Triticum urartu* (AA genome, 2n = 14) (Dvorak et al., 2006). Conversely, the origin of the B genome remains more complex, possibly tracing back to an *Aegilops* species from the Sitopsis section, akin to the present *Aegilops speltoides* (Sarkar and Stebbins, 1956; van Slageren, 1994). The D genome, integral to the bread wheat genome (AABBDD), is absent in durum wheat (AABB) and is derived from a second hybridization with an ancestor of diploid *Aegilops tauschii* var. strangulate (DD genome, McFadden and Sears, 1946).

1.6 Global Wheat Production Overview: Economic and Nutritional Relevance of Durum Wheat in Italy and Across the World

the Food and Agriculture Organization (FAO) has predicted global wheat production to reach approximately 791 million tonnes. This comprehensive estimate takes into account all types of wheat, such as bread wheat and durum wheat. In this extensive network of agricultural output, approximately 8-10% is attributed to durum wheat, which means the production of durum wheat is estimated to fall within the range of approximately 63 to 79 million tonnes globally, depending on various factors such as climatic conditions and agricultural practices.

Economic Relevance

Durum wheat (*Triticum turgidum* subsp. *durum*) plays a crucial economic role both globally and particularly within Italy. While it represents a smaller portion of total wheat production compared to bread wheat, durum wheat is a key crop for many Mediterranean and North African countries, where it is predominantly used for pasta and semolina production. In Italy, the cultivation of durum wheat is concentrated in regions such as Puglia, Sicily, and Campania, where the climate is favorable for its growth. Italy is undoubtedly recognised as the largest producer of durum wheat in Europe, significantly contributing to the country's agricultural economy. The Italian pasta industry, highly recognized for its quality, extensively utilizes durum wheat semolina; in 2020, pasta production contributed over €2.7 billion to Italian exports. This industry not only impacts local farmers and

producers but also creates substantial employment opportunities across the supply chain from agriculture to food processing and international trade (Italian Ministry of Agricultural Food and Forest Policies, 2021). Furthermore, the economic impact of durum wheat extends to international markets. Countries that produce durum wheat benefit from export opportunities, capitalizing on the growing global demand for pasta and related food products.

Nutritional Relevance

Nutritionally, durum wheat is valued for its composition, which generally includes 12-16% protein, predominantly gluten, making it ideal for pasta production. In addition, durum wheat is rich in dietary fiber, essential minerals such as iron, magnesium, and zinc, and vitamins like B vitamins and vitamin E (Marcos-Barbero et al., 2032). The benefits of durum wheat extend into dietary habits, especially within the context of the Mediterranean diet. Foods derived from durum wheat, such as pasta and couscous, are central to this diet, providing complex carbohydrates, proteins, and essential nutrients while promoting health and well-being. Many studies have evidence that diets rich in whole grain products, including those made from durum wheat, are associated with a reduced risk of chronic diseases such as obesity, type 2 diabetes, and cardiovascular diseases (Thompson et al., 2017). The low glycemic index of durum wheat products presents a favorable option for managing blood glucose levels, making it a preferred choice for health-conscious consumers seeking nutritious food options (Thompson et al., 2017).

1.7 Evolution of Durum Wheat Breeding in Italy: From Traditional Practices to Modern Innovations

The evolution of durum wheat breeding in Italy is an interesting narrative that reflects both the deep-rooted agricultural traditions and the scientific advancements that have shaped this vital crop over the decades. In19th century and early 20th century, durum wheat cultivation in Italy was predominantly based on a wide variety of landraces, which represented the primary source of germplasm for farmers at that time (Motzo et al., 2001). By definition, these landraces are defined as genetically diversified cultivated varieties that are adapted to specific ecological and geographic environments. Additionally, landraces are normally cultivated based on traditional management practices and local needs, which contribute to their considerable adaptability and resilience (Casañas et al., 2017). The use of these landraces not only ensured a high degree of genetic diversity within durum wheat but also allowed farmers to maintain stable yields despite fluctuating environmental conditions and market requirements. The formal breeding of durum wheat in Italy began in the early 20th century, driven by the need to improve local varieties, to meet growing agricultural demands and resist diseases (Maccaferri et al., 2019). The first-ever breeding program in Italy was launched in the early 1900s, focusing on tapping the genetic diversity within a select number of landraces primarily grown in Southern Italy, North Africa, and West Asia (D'Amato, 1989; Scarascia Mugnozza, 2005). This pioneering effort marked a significant shift in durum wheat cultivation practices, as it sought to improve the performance of these local landraces through selective breeding. By tapping into the existing genetic diversity, breeders aimed to improve key traits such as yield, disease resistance, and adaptability to the specific agro-climatic conditions of the region. In this context, the durum wheat variety SENATORE CAPPELLI is recognized as a significant variety, which is believed to have been selected from the North African landrace JEAN RHETIFAH (Taranto et al., 2020). Released in 1915 by the esteemed breeder Nazareno Strampelli, CAPPELLI became the most widely used variety in breeding programs throughout Italy for over 30 years, until the end of the 1960s (Scarascia Mugnozza, 2005). Its widespread cultivation accounted for more than 60% of Italy's durum wheat area for several decades (Bozzini, 1989). Until today, CAPPELLI has left a lasting legacy in durum wheat breeding; since it appears in the pedigree of almost all durum wheat varieties developed in Italy as well as in many other countries (Laidò et al., 2013). The post-World War II era gave rise to the beginning of

the Green Revolution in Italy, which saw the introduction of semi-dwarf varieties, resulting in significant yield increases, particularly in the 1960s and 1970s (Royo et al., 2021).
In the specific case of wheat breeding, a pivotal event during the "Green Revolution" was the introduction and widespread use of the semi-dwarf gene Rht-B1b, originally derived from the Japanese bread wheat variety "Norin 10" (Autrique et al., 1996). This gene contributed to earlier maturation and was responsible for a reduced plant height phenotype without affecting total plant dry weight, while also massively enhancing the harvest index (McCaig and Clarke, 1995; De Vita et al., 2007; Royo et al., 2007). As a result, the architecture of the wheat plant was transformed, allowing for greater grain production per unit of biomass. This alteration not only increased competitiveness in modern agricultural systems but also made the wheat plant less prone to lodging, thus improving overall stability. Additionally, the shorter stature and increased responsiveness to agricultural inputs like water and fertilizers provided unique opportunities for crop intensification, particularly in irrigated or high rainfall environments, significantly optimizing production efficiency. Currently, the genetic diversity available in wheat has significantly diminished following the dramatic displacement of traditional landraces by modern cultivars (Royo et al., 2021). A study examining 51 cultivars developed through the CIMMYT/ICARDA (International Maize and Wheat Improvement Center/International Center for Agricultural Research in the Dry Areas) breeding programs revealed that 15 ancestors accounted for 72% of the genetic makeup of these improved cultivars (Autrique et al., 1996).
Additionally, nowadays the cultivation of modern wheat varieties derived from contemporary breeding programs must meet specific criteria, including distinctiveness, uniformity, stability, and superior agronomic value. While these qualities are essential for ensuring high yields and performance in agricultural systems, the excessive uniformity among elite germplasm also brings significant drawbacks. Such excessive dependence on a small pool of genetic resources raises concerns about the long-term sustainability of wheat production, as a restricted genetic variability may not provide the necessary traits and variability to withstand emerging challenges such as climate change, pest pressures, and diseases (Motzo et al., 2001). To ensure the continued success and resilience of wheat cultivars, it is crucial for breeding programs to tackle genetic erosion and therefore, broaden their genetic foundation by incorporating traits from a wider range of genetic resources, including traditional landraces and wild relatives, thereby enhancing the diversity and sustainability of future wheat varieties (Maccaferri et.; al 2019). there is a pressing need to identify and conserve new sources of genetic variability within wheat, and germplasm conservation is essential for achieving this goal. Recognized as the most effective strategy for preserving the genetic traits of endangered and commercially valuable species, germplasm conservation acts as a living repository of genetic information. It allows for the long-term storage of diverse genes present in various plants, which can be regenerated as needed. Germplasm conservation can be implemented through two primary strategies: in-situ and ex-situ conservation. In-situ conservation involves maintaining genetic resources within their natural habitats, often through the establishment of biosphere reserves and national parks, which help sustain the ecological integrity of these species. In contrast, ex-situ conservation focuses on safeguarding genetic material outside its natural environment. This approach includes preserving cultivated and wild plant species in the form of in vitro cultures and seeds, which are stored in gene banks for long-term availability and usage. Such efforts create a valuable bank of genes, DNA, seeds, and germplasm, functioning as a genetic information library (Bhatia, 2015). The resources stored in these gene banks can be strategically utilized in breeding programs, facilitating the introduction of new genetic variability into modern wheat varieties.
In summary, the ongoing evolution of durum wheat breeding in Italy thus represents a dynamic interplay between tradition, innovation, and sustainability in agricultural practices.

1.8 General overview of Plant-Pathogens Interaction: The "Disease Triangle" and Induced-priming agents

Plant disease is defined as any impairment of a plant's normal state that disrupts its vital functions due to specific causal agents, which may be biotic (pathogens) or abiotic (environmental factors). The term "disease" stems from "dis" and "ease," signifying a state of uneasiness (Ravichandra, 2013). Pathogens, which can induce disease in particular hosts, typically act as parasites by deriving nutrients from living plants, unlike saprophytes that derive nutrients from decayed and dead organic matter (Mehrotra, 1980). Plants coexist with many microorganisms, including bacteria, fungi, and nematodes, remaining exposed throughout their lifespan. For successful infection, pathogens must penetrate plant tissues, acquire necessary nutrients, and evade defence mechanisms, with virulent pathogens inducing disease while avirulent pathogens do not. The "disease triangle" concept highlights that for a disease to occur, three components must interact: a susceptible host, a virulent pathogen, and a conducive environment (Sauban Musa Jibril et al., 2016). The elimination of any of these elements can prevent disease (Ravichandra, 2013).

Plants potential pathogens as 'non-self' and respond by employing a range of signals derived from microorganisms and their environment to trigger defense mechanisms. This recognition enables them to activate various defense strategies, including the production of antimicrobial compounds, reinforcement of cell walls, and systemic acquired resistance (David and John, 1997). These stimuli, which enhance plant responsiveness, are known as priming agents (Desmedt et al., 2021). While many chemical priming agents exist, only a few are commonly used commercially, categorized into five main classes. The first class includes small molecules produced by plants, such as β-aminobutyric acid (BABA) (Cohen et al., 2016), pipecolic acid (Bernsdorff et al., 2016; Návarová et al., 2012), azelaic acid (Cecchini et al., 2015), hexanoic acid (Cecchini et al., 2015), and thiamine (Camañes et al., 2015). The second class consists of chemical analogs of plant defence hormones like salicylic acid (SA) and jasmonic acid (JA), including SA analogs such as acibenzolar-S-methyl (ASM, also known as BTH), probenazole (Ishii et al., 2007), and isotianil (Ogawa et al., 2011), alongside JA derivatives like methyl jasmonate (Okada et al., 2015; Kępczyńska et al., 2012) and cis-jasmone (Oluwafemi et al., 2013; Bruce et al., 2003; Farmer et al., 1990). The third class comprises phosphite salts, such as potassium phosphite and fosetyl-Al, which act as both fertilizers and crop protection products (Machinandiarena et al., 2012; Massoud et al., 2012; Eshraghi et al., 2011; Thao et al., 2009). The fourth class consists of volatile organic compounds (VOCs), which are produced in response to herbivory or wounding (Meyer et al., 2018; Frost et al., 2008). Despite their potential, VOCs are not frequently used in field studies because of the complexity in using highly volatile substances. Finally, the fifth category features biological macromolecules and their oligomers, including chitin and chitosan (El Hadrami et al., 2010), laminarin (Aziz et al., 2003), lipopolysaccharides (Newman et al., 2007), and pectin oligomers (Ferrari et al., 2013). Additionally, proteins like harpin proteins—from *Erwinia* spp. also act as macromolecular priming agents (Dong et al., 1999).

1.9 Fungal Pathogens Overview: Plant Recognition and defence mechanisms towards plant-infecting fungal pathogens

Based on nutritional strategies, plant pathogenic fungi are classified into three main categories: biotrophs, necrotrophs, and hemibiotrophs. Biotrophic fungi typically form haustoria, which are specialized, nutrient-absorbing appendages that penetrate the host's cells without causing immediate cell death. These structures facilitate the exchange of nutrients and signals between the fungus and the host plant, allowing biotrophs to maintain the viability of the living tissue they infect. In contrast, necrotrophic fungi acquire nutrients from dead or decaying tissue, functioning as saprophytes that feed on the remains of living organisms following their death. On the other hand, hemibiotrophic

fungi initially produce haustoria during the biotrophic phase to extract nutrients from living plant cells. However, as the infection progresses, these fungi transition to a necrotrophic phase, where they develop intracellular hyphae that invade and kill host cells, allowing the fungus to utilize the nutrients from the decaying tissue (Fei and Liu., 2023). It has been reported for decades that components generated from fungi must be recognized by plant hosts in order to trigger specific host response, during fungal infection, which hinders or sometimes even fully arrests the fungal proliferation (Kogel et al., 1988; De Wit and Roseboom, 1980). These components, commonly referred to as elicitors, are generally categorized into two classes. The first class includes pathogen-associated molecular patterns (PAMPs), which are molecules released by a broad spectrum of microbes, encompassing both pathogens and non-pathogens. PAMPs serve as general signals recognized by plant immune systems, triggering innate immune responses. The second class consists of effectors, which are specific to particular pathogen species or races. Effectors are used by pathogens to manipulate host cellular processes, allowing them to promote virulence and facilitate successful infection (Jones and Dangl, 2006). PAMPs include several diversified molecules, like peptides and polysaccharides. These PAMPs are typically recognized by plant hosts in the apoplastic space through transmembrane proteins that face the extracellular environment, specifically receptor kinases (RLKs) and receptor-like proteins (RLPs), collectively known as pattern recognition receptors (PRRs) (Couto and Zipfel, 2016). A noteworthy example of a fungal PAMP is chitin, a structural component of the fungal cell wall, which triggers immune responses upon recognition by the plant's PRRs (Kombrink et al., 2011). Additionally, fungal attempts to penetrate host cells can also trigger the release of the so-called damage-associated molecular patterns (DAMPs). DAMPs consist of host components that are either released or produced in response to cell or cell wall damage and are subsequently secreted into the extracellular space. These DAMPs are recognised by pattern recognition receptor (PRR)-like proteins, which recognize the signals and trigger signaling outputs similar to those observed in pattern-triggered immunity (PTI) (Choi and Klessig, 2016). Subsequently, the effectors, also referred to as fungal virulence factors, are components secreted by pathogens that promote fungal proliferation in specific host plants. Most effectors are also called toxins due to their ability to manipulate host cellular processes. During infection by obligate biotrophic pathogens or upon the introduction of biotrophic elicitors into host tissues, localized host cell death. This type of reaction is commonly called hypersensitive response (HR). This response is typically initiated when host immune receptors, encoded by Resistance (R) genes, recognize these effectors (Cui et al., 2015; Dodds and Rathjen, 2010; Greenberg and Yao, 2004). The HR plays a critical role in arresting the invasion of biotrophic pathogens because these organisms rely exclusively on living host cells for their proliferation. Many Resistance (R) genes have been described to encode nucleotide-binding leucine-rich repeat receptors (NB-LRRs or NLRs), leading to the common use of the terms ‘R protein’ and ‘effector-triggered immunity (ETI)’, which are able to recognize intracellular effectors encoded by pathogen avirulence (Avr) genes. However, recent researches on the interactions between fungal pathogens and cereal crops, as well as other plants, have revealed the variability of R gene products. Additionally, R proteins may possess enzymatic activities that can disable the virulence functions of fungal effectors, through the detoxification of fungal toxins (Saur and Hückelhoven., 2021). By definition, resistance in plants can also be categorized into two main types: vertical resistance and horizontal resistance (Kou & Wang, 2012). Qualitative (vertical) resistance is conferred by specific R-genes, which trigger a gene-for-gene interaction with pathogen proteins, leading to a high level of resistance (Poland et al., 2009). This type of resistance is effective against specific strains of pathogens; however, it is likely to get overcome very easily overtime due to its reliance on single genes, making it vulnerable to rapid fluctuations in pathogen populations. In contrast, quantitative (horizontal) resistance is derived from the cumulative effect of multiple genes with small-to-medium effect. This form of resistance offers greater flexibility concerning pathogen variability, as it is effective against a wider range of pathogen races and is generally more durable (Poland et al., 2009). A critical aspect of resistance is its durability, since it should remain effective in cultivars even after extensive cultivation in particular environments (Johnson, 1983). To achieve durable resistance, it may be essential to

pyramid multiple resistance factors, deriving from different genetic backgrounds, resulting in broad-spectrum resistance (Fuchs, 2017).

1.10 Qualitative (Single R genes) and Quantitative Disease Resistance (QTLs): Integration into Pyramiding Strategies for Durable Resistance

Resistance durability is essential for sustaining long-term control of plant diseases, reducing the need for chemical inputs, and supporting agricultural sustainability (Brown 2015). Improving resistance durability involves understanding the mechanisms behind both qualitative and quantitative resistance. Qualitative resistance, controlled by a few major genes, often provides complete resistance but can be easily overcome by pathogens due to strong selection pressure for virulent strains. In contrast, quantitative resistance, controlled by multiple genes with smaller effects, tends to be more durable because it imposes a more gradual selection pressure on pathogens, making it harder for them to adapt (Johnson 1984). These genes are typically found in specific genomic regions called quantitative trait loci (QTL). Quantitative resistance usually offers partial protection, meaning it does not entirely prevent pathogen infection. Instead, it limits critical factors such as pathogen reproduction, spread within the plant, and the intensity of symptoms (Niks et al., 2015). Due to its polygenic nature, this type of resistance tends to be more durable and harder for pathogens to be circumvent. Although quantitative resistance is often incomplete and may require additional management strategies, its polygenic nature contributes to long-term effectiveness and lower risks of resistance breakdown (Johnson 1984). Gene pyramiding, also known as gene stacking, is a genetic strategy used to enhance the durability and effectiveness of resistance in crops against diseases. This approach involves the introduction and combination of multiple resistance genes into a single plant variety. By stacking genes that confer resistance to different strains or pathogens, gene pyramiding helps prevent the rapid evolution of resistant pathogens, which can often occur when a crop relies on a single resistance gene (Christopher C. Mund 2018). The simultaneous expression of multiple genes enhances the robustness of the plant's defense mechanisms, thereby mitigating the risk of the pathogen overcoming the plant's resistance (Christopher C. Mund 2018). Different Breeding schemes have been implemented for adequately stacking major R genes and resistance QTLs, with the purpose of increasing the durability of crop resistance to pathogens. Breeding strategies for pyramiding major resistance (R) genes have been extemsively tested (Ordon & Kühne, 2014), resulting in the development of resistant crop varieties that are now commonly grown (Ellis et al., 2014). Combining major genes, each targeting resistance against specific pathogen isolates, has been suggested as a way to increase the durability of resistance (Miedaner, T. (2016)). However, the success of these gene pyramids can be undermined by the emergence of multi-virulent pathogen populations. Three major conditions have been suggested: (i) when virulence mutations are linked and impose minimal fitness penalties on the pathogen, (ii) when virulence factors are already present in pathogen populations, or (iii) when resistance mechanisms overlap or function redundantly (Brown, 2015). Moreover, because resistance genes are often used independently in breeding programs without coordinated management, it is likely that pathogens will eventually overcome the resistance provided by these pyramids. Breeding schemes for pyramiding resistance QTL were also designed to improve resistance levels in some of the economically relevant cultivated crops, such as in barley, wheat, bean, and pepper (St. Clair, 2010). There are few studies focused on integrating disease resistance QTL into breeding strategies, unlike the widespread use of major R genes. Most efforts target major-effect QTL, with minor-effect QTL receiving little attention. Pyramiding resistance QTL with varying pathogen specificities may exert conflicting selection pressures on pathogen evolution (Pilet-Nayel M-L et al., 2017). However, combining QTL with different gene-for-gene interaction or broad-spectrum resistance is expected to extend durability. Breeding schemes for pyramiding QTL and major genes were developed to improve disease resistance by diversifying the combined mechanisms (Baumgartner et al., 2015).

These schemes also aim to preserve the effectiveness of major genes by (i) reducing pathogen population size, (ii) limiting the effective population that reproduces, potentially increasing genetic drift, (iii) lowering selection pressure on pathogen variants, and (iv) applying diversifying selection pressures (Quenouille et al., 2014).

1.11 Major Foliar and Spike Wheat Diseases

Wheat is significantly affected by several major fungal diseases, particularly rusts, Fusarium, and Septoria which impact yield and grain quality worldwide. Among foliar diseases, wheat rusts have posed significant challenges to global wheat production since the crop's domestication and continue to threaten the world's wheat supply (Roelfs et al., 1992). These diseases, primarily caused by species such as *Puccinia triticina* (leaf rust), *Puccinia striiformis* (stripe rust), and *Puccinia graminis* (stem rust), can lead to severe yield reductions and affect grain quality. It is estimated that global annual losses due to wheat rust pathogens range between US$ 4.3 to 5.0 billion (Figueroa et al., 2018)**.** Yellow rust is particularly aggressive, capable of causing yield reductions of up to 100% during severe epidemics, although typical losses range from 10% to 70% (Chen, 2005). Alarmingly, approximately 88% of global wheat varieties have been reported to be vulnerable to *Puccinia striiformis* f. sp. *tritici* (Pst), the causal agent of stripe rust, leading to substantial economic implications **(**Figueroa et al., 2018**)**. *Puccinia triticina* (Ptt), the causative agent of Brown rust is a critical concern for durum wheat production in the Mediterranean, where it is endemic and can lead to extensive epidemics, causing yield losses that can exceed 50% under favorable environmental conditions (El-Orabey, 2018). Additionally, due to the high genetic diversity of the pathogen, it has been observed a continuous emergence of new virulence profiles, making it difficult to maintain effective resistance in wheat cultivars. Additionally, the pathogen's adaptability to various climatic conditions enables it to thrive in a wide range of environments, complicating control measures (McCallum et al., 2016). *Puccinia graminis f. sp. tritici* (Pgt), the agent of wheat stem (black) rust, is found globally but is less prevalent than other wheat rusts. This pathogen thrives in warm, moist conditions and has historically caused significant epidemics in major wheat-producing regions, prompting the development of semi-dwarf, stem rust-resistant varieties during the Green Revolution (Singh et al., 2015; Figueroa et al., 2016). While stem rust is controlled in many areas, forecasts indicate potential global losses averaging 6.2 million metric tons annually under severe outbreaks, especially with the emergence of new virulence traits in Pgt populations (Pardey et al., 2013). The Ug99 race, identified in Uganda in 1998, and its variants represent a significant threat, with estimates suggesting that 90% of wheat varieties are susceptible, raising food security concerns (Singh et al., 2015). Recent epidemics, such as the 'Digalu' race in Ethiopia in 2014 and a virulent race in Sicily in 2016, further highlight the urgent need for effective management strategies (Olivera Firpo et al., 2015, 2017; Bhattacharya, 2017). Fusarium Head Blight (FHB) is a devastating floral disease affecting wheat worldwide, with significant outbreaks reported in major wheat-producing regions, including the USA, China, the EU, the UK, Africa, and Brazil. Epidemics typically occur every four to five years, particularly under weather conditions conducive to fungal growth, such as heavy rain during crop flowering (anthesis). In the USA, FHB caused an estimated US$ 3 billion in yield losses between the early 1990s and 2008 (Figueroa et al., 2018**)**. The disease reduces both yield and grain quality, leading to compromised marketability and contamination of wheat with harmful mycotoxins like deoxynivalenol (DON), a type B trichothecene that poses significant health risks to humans and animals. Beyond economic and food safety concerns, FHB also has broader ecological implications, affecting natural ecosystems through mycotoxin accumulation. Despite its severity, resistance to FHB in wheat remains limited. The most significant resistance source identified so far is the PFT gene, though no wheat cultivars have demonstrated complete resistance, making breeding efforts to combat FHB an ongoing challenge (Jia et al., 2019). Moreover, the disease has become a critical issue in regions like China and Brazil, where climate conditions favor the spread of Fusarium species, further emphasizing the global threat posed by FHB (Mesterházy et al., 2020). Septoria tritici blotch (*Stb*),

caused by the hemi-biotrophic fungus *Zymoseptoria tritici* is one of the most damaging foliar diseases of wheat, especially in temperate regions like Europe. It is considered the most serious wheat disease in the European Union, where annual losses, including management costs, range from €280 million to €1.2 billion (Fones & Gurr, 2015). *Stb* thrives in cool, moist environments, leading to extensive damage to wheat leaves and significantly reducing yields. On the other hand, its impact is less severe in other wheat-growing regions, the disease is still a concern. In Australia, for instance, *Stb* has historically been responsible for around 20 million in losses per year, and its prevalence has been increasing over time (Murray & Brennan, 2009; Figueroa et al., 2018). This rise in *Stb* cases highlights the ongoing challenge of managing the disease, particularly given the pathogen's ability to adapt to fungicides and resistant wheat varieties.

1.12 Quantitative Traits Locus (QTL) Definition and Analysis

Traits of interest in high-yield vegetable crops often exhibit wide variation and intricate inheritance patterns that typically deviate from Mendelian segregation principles. These quantitative traits are influenced by the additive effect of multiple genes, along with environmental factors and gene interactions such as epistasis (Falconer & Mackay, 1996; Lynch & Walsh, 1998). By definition, a quantitative trait locus (QTL) is defined as a specific genomic region associated with the genetic variation of these complex traits (Miles & Wayne, 2008). QTL analysis is a statistical approach that combines phenotypic data, such as trait measurements or scoring in case of diseases, with genotypic data, usually in the form of molecular markers, to uncover and dissect the genetic basis of these traits (Falconer & Mackay, 1996; Kearsey, 1998). The primary goal of QTL analysis is to link specific complex traits to regions of chromosomes, providing insights into the number, location, effect, and interactions of these regions. Molecular markers are used in QTL analysis to identify regions of the genome that statistically correlate with variations in phenotypes, which aids in unraveling quantitative traits (Lynch & Walsh, 1998). Given that, the genetic variation of quantitative traits can arise from the cumulative effect of numerous loci, QTL analysis must have a high trait heritability to ensure reliable results (Kearsey, 1998). A key objective of QTL analysis is to gain insight whether phenotypic differences are predominantly influenced by a small number of loci with significant effects, or by many loci with minimal effects. It appears that a substantial portion of the phenotypic variation in many quantitative traits can be attributed mainly to a few loci with large effects, while the rest is linked to a multitude of loci with small effects (Mackay, 2009). This approach facilitates the identification of genes responsible for complex traits, essential for enhancing crop yield, disease resistance, and quality traits through breeding techniques. By accurately locating these genomic regions, scientists can create more focused breeding programs designed to improve desirable traits in crops.

1.13 QTL mapping methods

1.13.1 Experimental populations for QTL mapping

Over the years, advancements in high-throughput genetic marker systems, the creation of high-density linkage maps, and the development of specialized analytical software have significantly enhanced the application of QTL analysis for the detailed study of complex traits in crop genetics (Doerge et al., 1997; Mackay, 2009). Constructing a linkage map for QTL mapping with experimental populations like Recombinant Inbred Lines (RILs), F2 generations, and Backcross populations is crucial for understanding and dissecting complex quantitative traits. This process begins by creating populations that segregate for the trait of interest deriving from a biparental cross between two pure lines carrying contrasting phenotypes at target traits, which is essential for QTL mapping (Darvasi & Soller, 1997). RILs result from multiple cycles of self-fertilization of F1 hybrids, producing stable

homozygous lines with higher mapping resolution compared to F2 and backcross populations, which are temporary genetic resources based on single plants (Kearsey & Pooni, 1996; Darvasi & Soller, 1997). The development of molecular markers, such as SNPs, SSRs, and RFLPs, is vital for genotyping and identifying polymorphisms across the genome (Gupta et al., 2013). The segregation and recombination frequency (recombinant gametes produced in meiosis) of these markers are essential for constructing a comprehensive linkage map, which is crucial for locating QTL associated with specific phenotypic traits, allowing researchers to determine the position and number of loci influencing these traits based on the association between the recombination rate and a statistically significant variation of the investigated phenotype (Lander & Botstein, 1989). While double haploid (DH) strategies provide complete homozygous inbred lines in one generation at all genomic loci (Bao et al., 2002; Xu & Crouch, 2008), Near-isogenic lines (NILs) and introgression lines (ILs) are important tools in genetic mapping, sharing an isogenic background except for the QTL region being studied. These lines are developed through backcrossing to a recurrent parent over multiple generations, allowing researchers to assess the phenotypic effects of specific QTL (Pumphrey et al., 2007; Xu & Crouch, 2008). However, a common limitation of these segregating experimental populations is that the confidence intervals for many identified QTL often span several centimorgans and may encompass hundreds of genes (Doerge, 2002; Holland, 2007). To maximise mapping resolution, new segregating populations are being developed and implemented in recent times, which increase both the size of the population and the opportunities for effective meiosis. One such approach is the use of advanced intercross lines (AILs), which are created through random intercrossing before fixation via selfing (Darvasi & Soller, 1995). This method, also referred to as intermated recombinant inbred lines (iRILs), improves the precision of QTL detection while still originating from bi-parental lines. However, the inherent limitation of bi-parental mapping populations is their restricted statistical inference space, which is confined to just the two parental lines, making QTL analysis highly specific to those populations (Xu, 1995). In this context, QTLs mapping using multi-parental populations (MPPs) offers a promising alternative to the limitations associated with traditional biparental linkage mapping populations. In contrast to biparental populations, MPPs exhibit significantly higher recombination rates and mapping accuracy, enabling the incorporation of a greater diversity of alleles, including rare variants, at the same locus. MPPs strategies have been implemented in plant genetics via multiparent advanced generation intercrosses (MAGIC) (Mackay and Powell, 2007; Cavanagh et al., 2008;) and Nested Association Mapping (NAM) (Kitony, J.K et al., 2023). Specifically, the MAGIC (Multi-parent Advanced Generation Intercross) strategy entails crossing a variable number of highly diversified founder lines (minimum 4 up to 12) through a prearranged breeding scheme (4-way crosses, 6-way-crosses and so forth) designed to produce intermediate lines. These intermediate lines are then randomly intercrossed for a varying number of generations before fixation, allowing the founder genomes to be thoroughly shuffled. As a result, each fixed recombinant inbred line (RIL) is a unique mosaic of the original parental lines. Although the development of MAGIC populations is certainly a time-consuming endeavour, it has been effectively applied to several crops, such as wheat, and rice (Huang et al. 2012; Bandillo et al. 2013, Mackay et al. 2014). This method plays a crucial role in increasing genetic variability by incorporating multiple genetic backgrounds and alleles within the same mapping study (Rebai & Goffinet, 2000). On the other hand, A NAM population typically is made of independent families, including inbred lines originating from crosses between "diversity donor" parents (founders) and a common parent. Besides RILs, NAM populations can also be established using backcross-derived RILs and double haploids (DH) (Kitony, J.K et al., 2023). The first effective example of NAM population was documented in maize, which included 5,000 RILs organized into 25 families, with the maize inbred line 'B73' serving as the common parent in its development (Yu et al., 2008).

1.13.2 Genome-Wide Assoication Study (GWAS)

Association mapping (AM) is considered a more advanced technique than traditional QTL linkage mapping. The primary goal of GWAS is to detect associations between genetic markers and traits (phenotype) within a panel (germplasm collections) using linkage disequilibrium (LD), a phenomenon where alleles at different loci are non-randomly associated (Breseghello et al., 2006, Santure & Garant, 2018). This approach has been widely evidenced in crop genetics and it relies on LD to explore the genetic basis of quantitative traits (Breseghello and Sorrells, 2006; Gupta et al. 2005; Rafalski, 2010, Santure & Garant, 2018). In GWAS, historical recombination events within a highly diversified panel are analysed to identify statistical links between markers and phenotypes (Santure & Garant, 2018). The major advantage of GWAS is related to its higher resolution for mapping compared to traditional QTL mapping methods, which are limited to meiotic information deriving from experimental inbreeding (Morgante and Salamini, 2003, Santure & Garant, 2018). However, the effectiveness of GWAS in terms of resolution and power depends on the extent of LD across the genome and specifically within the target region which affects the SNPs density (Santure & Garant, 2018). Moreover, genetic bottlenecks resulting from domestication, selection and breeding practices have led to a significant identity-by-descent among chromosomes, increasing genetic similarities among individuals (Remington et al., 2001), which might reduce the genetic resolution potential of association mapping.

GWAS can be carried out by employing two main strategies (Rafalski, 2002): Genome-wide scanning**,** which implies the use of markers evenly distributed across the genome to comprehensively capture the extent of linkage disequilibrium (LD). Otherwise, association for candidate gene targeting and discovery which implies focusing specific genes in genomic regions with rapid LD decay to identify polymorphisms that may be responsible for variations in traits of interest. Despite the recognised advantages of GWAS in the QTL mapping process, it presents certain limitations. One major issue is an increased risk of Type I error (false positives), which can occur due to unrecognized subpopulations within the sample, leading to erroneous estimations of allele effects and leading to spurious associations (Flint-Garcia et al., 2005, Santure & Garant, 2018). Additionally, GWAS may fail to detect rare variants at loci that exhibit significant variability between populations but are largely fixed within subpopulations (Breseghello and Sorrells, 2006; Flint-Garcia et al., 2005). This challenge is further compounded by an increased risk of Type II error (lack of statistical power) due to a weak correlation between markers and genes. This weak correlation power is mainly caused by three factors: LD decay, uneven marker distribution across the genome due to varying allele frequencies, and issues with multiple testing, which lead to high thresholds for genome-wide significance (Gordon and Finch, 2005). Furthermore, GWAS can be affected by inferential issues related to the presence of major sub-populations within the whole germplasm collection or varying degrees of relatedness among the lines. To address these challenges, various methods have been proposed to better understand population substructure in GWAS studies. The most commonly employed method for assessing population structure in association studies is the likelihood-based approach was introduced by Pritchard et al. (2000), known as the "Bayesian modeling method." This approach uses unlinked genetic markers to infer details about population structure (Q) and to estimate the relative kinship among individuals (K), which are then utilized for association mapping within subpopulations. Kinship matrix refers to individual pairwise-comparisons among genotypes, in order to estimate the genetic similarity, also called Identity-By-State (IBS), with an index ranging from 0 (no similarity at all) up to 1 (full identity). On the other hand, population structure analysis aims at subdividing the panel into a number of highly representative subpopulations based on selected unlinked markers or markers representative of a certain linkage block. This approach is commonly referred to as SNPs pruning (Calus, & Vandenplas (2018).

Upon the identification of a number of informative subpopulations (Qs), a membership score is given to each Q, ranging from 0 up to 1 for each individual, allowing the assignment to a specific subpopulation based on the highest membership score (Santure & Garant, 2018). Conducting a Genome-Wide Association Study (GWAS) within single subpopulations can enhance the detection of rare alleles that might be overlooked in larger, more heterogeneous population analyses. This approach minimizes population stratification, which can lead to spurious associations, by focusing on genetically similar individuals. Within these subpopulations, the genetic background is more uniform, thereby increasing the power to detect rare variants that have significant effects on traits (Kang et al., 2010). Moreover, by reducing noise from population substructure, researchers can achieve more accurate estimations of allele frequencies and effect sizes, which is crucial for identifying rare alleles that contribute to complex traits (Edwards AO et al., 2008). This refined approach also facilitates the exploration of gene-environment interactions and the study of genetic architecture in specific populations (Mathieson et al., 2012).

1.13.3 Meta-QTL Analysis and Projection of QTLs onto Physical Maps: Integrating Linkage Mapping and GWAS in Wheat

Meta-QTL (mQTL) analysis plays a crucial role in refining quantitative trait loci (QTLs) by integrating data from multiple independent studies, thereby improving the accuracy of QTL mapping and their projection onto a reference genome. In wheat, mQTL analysis is normally used for the identification of Meta-QTLs (QTLs clusters), by reducing the QTL confidence interval (CI) and aligning these intervals onto physical maps. This approach leads to a more precise understanding of the genetic architecture of quantitative (multifactorial) traits such as yield, disease resistance, and abiotic stress tolerance (Kaur et al., 2023). The process entails compiling QTL data from various populations and environments, projecting them onto a common reference genome to detect the most stable QTLs, and prioritizing regions for candidate gene identification (Soriano et al., 2021). To estimate the confidence intervals (CIs) of QTLs derived from traditional linkage mapping populations**,** Darvasi and Soller's empirical formulas are widely used. According to these formulas, the confidence interval for a certain QTL is inversely proportional to the population size and the proportion of phenotypic variance explained by the QTL (Darvasi & Soller, 1997). The K value (numerator) changes based on the population type, reflecting differences in recombination frequency and genetic structure. Specifically, a different formula is adopted for the type of linkage mapping population:

- ***CI=163/(N·R2)*** for RILs
- ***CI=287/(N·R2)*** for Double Haploid (DH)
- ***CI=530/(N·R2)*** for F2 and Backcrossing (BC)

where N represents the population size and R2 refers to phenotypic variance explained by that QTL. Larger populations and higher R2 result in a narrower CIs, increasing the precision of QTL localization. This is particularly useful when projecting QTLs onto the physical map, as it ensures that the meta-QTLs (mQTLs) have tighter confidence intervals, thereby increasing their utility for fine mapping and candidate gene discovery (Soriano et al., 2021). On the other hand, the projection and estimation of Marker Trait Associated (MTAs)'s CI deriving from independent Genome-Wide Association Studies (GWAS) onto the physical map relies on Linkage Disequilibrium (LD) values in correspondence of R2 equal to 0.3 or 0.2 maximum. In genome-wide association studies (GWAS), linkage disequilibrium (LD) decays with increasing physical distance, and the extent of LD directly impacts the resolution of marker-trait associations (MTAs) (Gautier et al., 2019). In wheat, which has a complex polyploid genome, the rate of LD decay varies across different genomic regions, subspecies, and populations, thereby influencing the accuracy of MTA projections (Desiderio et al.,

2019). Specifically, centromeric regions of chromosomes often exhibit higher SNP density, with many being monomorphic in modern cultivars due to selective breeding, while telomeric regions tend to have lower SNP density but higher recombination rates. This results in varying rates of recombination and LD decay across the chromosome regions (Akhunov et al., 2003). For GWAS, confidence intervals (CIs) are typically estimated by considering the average or local LD decay of the panel, based on the physical position of the projected MTA. Alternatively, as suggested by Maccaferri et al. (2019), a standard LD decay value specific to the crop or species can be used. In the case of tetraploid wheat (AABB), Maccaferri et al. (2019) proposed using a typical LD decay value of 3 Mb (1.5 Mb on either side of the projected MTA) to estimate the CI.

1.14 Genotyping Technologies

1.14.1 SNPs-Based Genotyping Chips

Single Nucleotide Polymorphisms (SNPs) are widely recognized as one of the most valuable sources of genomic variation within populations. Their importance lies in their high frequency across genomes and their relatively low mutation rate, making them reliable genetic markers (Vignal et al., 2002). SNPs offer a unique advantage due to their stability and the ability to be turned into highly informative genetic markers. These markers are easily integrated into high-throughput genotyping platforms, enabling multiplexed, cost-effective, and automated analyses (Rafalski, 2002; Mammadov et al., 2012). Today, several advanced SNP-genotyping platforms are capable of scanning hundreds of thousands to over a million SNPs in parallel, such as the Illumina Infinium and Axiom platforms (Wang et al., 2014, Thompson et al., 2014; Winfield et al., 2015). SNP technology has become the preferred marker system, replacing older methods like Simple Sequence Repeats (SSRs) and Diversity Arrays Technology (DArT) markers, particularly in plant species where high-throughput and precise genotyping are crucial (Ganal et al., 2011; Rasheed et al., 2017). Applications of SNP markers are widespread, ranging from constructing high-resolution genetic maps and assessing linkage disequilibrium to analyzing genetic diversity, discovering marker-trait associations. Additionally, SNPs play a central role in marker-assisted breeding (Rasheed et al., 2017) and genomic selection (Hickey et al., 2017), revolutionizing the ability to map complex phenotypes and accelerate crop improvement programs.

1.14.2 SNPs Genotyping Arrays in Wheat

Single Nucleotide Polymorphism (SNP) genotyping arrays are crucial tools for studying genetic variation within plant populations. These arrays allow the simultaneous identification and analysis of hundreds of thousands of SNPs in a single assay, providing a high-throughput, cost-effective method for assessing genetic diversity (Bassil et al., 2015). SNP arrays have been widely applied in constructing genetic linkage maps, studying evolutionary relationships, and exploring functional genomics (Burridge et al., 2024). In breeding programs, SNP arrays are indispensable, particularly in Genomic Selection (GS), where they enable the prediction and evaluation of quantitative traits (Kang et al., 2023; Hickey et al., 2017). They are also integral to Marker-Assisted Selection (MAS) (Arruda et al., 2016), Genome-Wide Association Studies (GWAS) (Balagué-Dobón et al., 2022; Negro *et al*., 2019, Yu et al., 2023), and Quantitative Trait Loci (QTL) mapping (Xu et al., 2017). These approaches have significantly accelerated crop improvement by allowing breeders to rapidly screen for key genetic variants associated with important traits. SNP genotyping arrays have been particularly valuable in tetraploid durum wheat (AABB) and hexaploid bread wheat (AABBDD) research, enabling efficient and accurate screening of varieties, identification of genetic variants

linked to agronomic traits, and the development of diagnostic markers for breeding programs. Numerous SNP arrays have been developed for wheat, including:

- Wheat Breeders' Array (Allen et al., 2017),
- TaBW280K high-throughput genotyping array (Rimbert et al., 2018),
- 15K wheat Infinium array (Sun et al., 2020),
- 90K SNPs array (Wang et al., 2014),
- Ultra-high-density Axiom (®) genotyping array (Winfield et al., 2016),
- Triticum aestivum Next Generation (TaNG) array (Burridge et al., 2024).

These arrays, containing large numbers of SNPs, have proven to be effective tools for various genomic applications, including linkage analysis, QTL mapping, and GWAS (Allen et al., 2017; Bourke et al., 2018).

1.14.3 Genomic Selection, MAS and KASP Technologies in wheat

Genomic Selection (GS), Marker-Assisted Selection (MAS), and KASP Technology are powerful tools in the modern breeding of wheat, facilitating the rapid development of improved varieties that can meet the challenges posed by climate change and increasing global food demands. Genomic Selection (GS) leverages dense marker information across the genome to predict the breeding value of genotypes based on their genotypic data. This predictive power allows for more accurate selection of individuals with desirable traits, such as drought tolerance, disease resistance, and improved grain quality, significantly reducing the breeding cycle time and maximizing the breeding decision-making process (Heslot et al., 2015). Recent studies have demonstrated that GS can remarkably increase genetic gains by integrating phenomic and genomic data, allowing for more accurate selection strategies that consider quantitative (multifactorial) traits (Anilkumar et al., 2022, Kumar et al., 2021). Marker-Assisted Selection (MAS) serves as a complementary approach, facilitating the introgression of specific traits through the use of molecular markers tightly linked to loci underlying important agronomic traits. This method not only accelerates the selection process but also enhances the precision of breeding programs by allowing breeders to monitor specific alleles associated with traits of interest (Kumar et al., 2021). MAS is also used in back-crossing, so-called Marker-Assisted-Backcrossing (MABC), to recover the portion of the recurrent parent genome following the introgression of the desired allele. Molecular markers, tightly linked to beneficial allele variants of target traits and used for breeding programs are normally denominated diagnostic markers. For instance, MAS has been successfully applied in the development of wheat varieties resistant to various diseases, such as wheat rusts and Fusarium head blight or, quality traits (Rafalski, 2010**).** KASP (Kompetitive Allele Specific PCR) Technology has emerged as a highly efficient and versatile tool for genotyping in wheat breeding. This technology enables the rapid and cost-effective detection of SNPs, providing breeders with the ability to perform high-throughput screening of large populations (Rahman, M.Z. et al., 2023). Recent applications of KASP technology in wheat research include the identification of genetic variants linked to key traits such as yield potential, quality attributes, and abiotic stress tolerance (Kumar S et al., 2021, Rahman, M.Z. et al., 2023). The adaptability of KASP assays makes them suitable for various applications, including population structure analysis, QTL mapping, and the validation of genomic selection predictions. KASP (Kompetitive Allele Specific PCR) Technology has emerged as a highly efficient and versatile tool for genotyping in wheat breeding by designing a set a of competitive forward primers for a single tag-SNPs (one primer designed for each allele variant) and common reverse primer. This technology enables the rapid and cost-effective detection of SNPs, providing breeders with the ability to perform high-throughput screening of large populations (He et al., 2014). Recent applications of KASP

technology in wheat research include the identification of genetic variants linked to key traits such as yield potential, quality attributes, and abiotic stress tolerance (Rahman, M.Z. et al., 2023).

The integration of GS, MAS, and KASP technology has significantly advanced wheat breeding programs, facilitating the development of high-yielding and resilient wheat varieties.

2 Genome-Wide Association Study (GWAS) conducted in a panel of tetraploid wheat durum wheat landraces to map MTAs associated to Yellow rust (Yr) resistance

2.1 Introduction

2.1.1 Yellow rust: the disease and current state-of-the-art

Yellow rust (YR), caused by *Puccinia striiformis f. sp. tritici* (Pst), is a highly destructive fungal disease that significantly threatens global wheat production (Chen 2005; Milus et al., 2009). Production losses due to Pst typically range from 0.1% to 5%, but in severe cases, they can reach up to 25%, amounting to 5.47 million tons of durum and common wheat annually (Wellings et al., 2011; Lin et al., 2018). While chemical treatments can control stripe rust, the most sustainable, cost-effective, and environmentally friendly solution is to develop and promote disease-resistant wheat varieties. Wheat resistance to yellow rust falls into two main categories: all-stage resistance (ASR), also known as race-specific seedling resistance, and adult plant resistance (APR), which is race-nonspecific (Chen et al., 2013). ASR is governed by major genes that provide strong, specific resistance from the seedling to adult stages against certain Pst races. In contrast, APR is a quantitative trait controlled by multiple minor genes, offering a broader, non-race-specific resistance that typically becomes effective at the adult plant stage, resulting in varying degrees of resistance (Chen et al., 2013). APR is also commonly termed as high-temperature adult-plant (HTAP) resistance (Chen 2005). However, race-specific genes tend to lose their effectiveness over time due to the high variability of Pst. For instance, a Pst virulence survey in Ethiopia during 2013-2014 identified 18 races, 14 of which represented new virulence combinations (Wan et al., 2016). Since race-nonspecific resistance tends to be more durable, combining race-specific and race-nonspecific resistance genes is critical for effective long-term control of yellow rust (Chen, 2005, 2007). Additionally, over the past 60 years, recurrent *Puccinia striiformis* (Pst) epidemics have affected most wheat-growing regions, leading to significant yield losses and declines in grain quality (Wellings, 2011). In the last two decades, more aggressive and genetically diverse Pst populations have rapidly emerged on a global scale, showing increased adaptation to warmer temperatures (Bouvet et al., 2022, Hovmøller et al., 2016). To date, 86 yellow rust (YR) resistance genes have been identified and cataloged in wheat, and more than 300 quantitative trait loci (QTLs) associated with yellow rust resistance have been reported in various wheat varieties and breeding lines (McIntosh et al., 2020; Zhu et al., 2023; Chen and Kang, 2017; McIntosh et al., 2018; Saleem et al., 2022). Among these, eight YR resistance genes have been successfully cloned, with five of them being all-stage resistance (ASR) genes and the remaining three being adult plant resistance (APR) genes. The cloned ASR genes include *Yr5*, *YrSP* (allelic to *Yr5*), *Yr7*, *Yr15*, *Yr28*, and *YrU1*, four of which encode nucleotide-binding domain and leucine-rich repeat (NLR) proteins that play a key role in pathogen recognition and defense activation (Marchal et al., 2018; Klymiuk et al., 2018; Zhang et al., 2019; Wang et al., 2020). Notably, *Yr15* is distinct from the others as it encodes a tandem kinase-pseudokinase, which offers a unique mode of action against yellow rust (Klymiuk et al., 2018). The three cloned APR genes include *Yr18*, *Yr36*,

and *Yr46*. *Yr18* encodes an ATP-binding cassette (ABC) transporter that confers partial resistance by slowing pathogen growth (Krattinger et al., 2009), *Yr36* encodes a wheat kinase start 1 (WKS1) protein that contributes to heat and drought-tolerant rust resistance (Fu et al., 2009), and *Yr46* encodes a hexose transporter, which plays a role in regulating sugar transport during infection (Moore et al., 2015). Despite these advancements, the resistance conferred by single genes is often insufficient under high disease pressure due to the ability of *Puccinia striiformis* to evolve and overcome single-gene defenses (Zhang et al., 2019). To ensure durable and sustainable protection, it is essential to combine APR genes with one or more ASR genes. This gene stacking strategy helps provide stable resistance over the long term by reducing the risk of pathogen adaptation (Ellis et al., 2014; Liu et al., 2018). When ASR is functional, wheat cultivars that carry both types of resistance will be fully protected from specific *Puccinia striiformis* races. However, if new pathotypes (strains) overcome the race-specific ASR, the plant can still rely on HTAP resistance to maintain a degree of protection, although this resistance may be less complete (Chen et al., 2013). Wheat rust resistance genes, whether they provide all-stage resistance (ASR) or adult plant resistance (APR), are denoted with specific abbreviations (McIntosh et al., 2020). These include *Lr* for leaf rust (also known as brown rust), *Sr* for stem rust (black rust), and *Yr* for yellow rust (stripe rust). There is no distinction between ASR and APR in these naming conventions, and the number following the abbreviation increases as new resistance genes are discovered and characterized (Ellis et al., 2014).

2.1.2 Life cycle and biology

Puccinia striiformis f. sp. tritici (Pst), the pathogen responsible for yellow rust in wheat, has a complex lifecycle that involves both sexual and asexual reproduction, allowing it to generate genetic diversity and adapt to changing environments (Bouvet et al., 2022). The primary hosts for Pst are wheat and other grasses, where the fungus undergoes its asexual phase, producing urediniospores that spread the disease rapidly through wind dispersal. Urediniospores can infect wheat at various growth stages, creating repeating cycles of infection and spore production throughout the growing season (Chen, 2005). Pst also has a sexual stage that occurs on alternate hosts, primarily *Berberis* species (barberry), where the fungus produces basidiospores after undergoing meiosis (Bouvet et al., 2022). This sexual cycle allows for genetic recombination, which contributes to the pathogen's ability to generate new virulent strains. While the sexual phase was historically thought to be rare, it has been observed more frequently in recent years, particularly in regions where barberry is present (Bouvet et al., 2022; Zhao et al., 2013). The combination of asexual and sexual reproduction enhances the evolutionary potential of Pst, contributing to its ability to overcome resistance genes in wheat and making the development of durable resistant varieties a significant challenge (Bouvet et al., 2022; Hovmøller et al., 2016).

2.1.3 Triticum turgidum subspecies landraces, a valuable pool gene to uncover resistance genes in Tetraploid Wheat

Exploring the genetic diversity within highly informative collections of tetraploid wheat accessions is an effective strategy for identifying novel and uncharacterized resistance genes, as well as for dissecting the genetic reservoir of this important crop (Maccaferri et al., 2019). Currently, many cultivated durum wheat varieties exhibit a high degree of genetic similarity, which, when combined with ongoing climate change and the emergence of novel aggressive *Puccinia striiformis* (Pst) races, significantly increases the risk of vulnerability and potential yield losses. In this context, *Triticum turgidum* landraces serve as a valuable source of beneficial resistant alleles that can be harnessed to enhance wheat resilience (Maccaferri et al., 2019). Bi-parental mapping populations have often been utilized to map multiple yellow rust resistance (Yr) genes and quantitative trait loci

(QTLs) in both durum and bread wheat, revealing important genetic variants among various parental lines (Zhou et al., 2021; Firdissa E. Bokore et al., 2021, Lin X et al., 2018). In recent years, genome-wide association studies (GWAS) have also been conducted to detect loci underlying Yr resistance by using panels composed of elite durum wheat cultivars, durum wheat landraces or triticum dicoccum (Liu et al., 2017b; Liu et al., 2017c; Liu et al., 2017d; Aoun M., et al 2021; Mehrabi et al., 2022; Sela et al., 2014; Miedaner et al., 2019; Alemu et al., 2021; Marone et al., 2024). In this study, a highly diversified panel composed of 1324 Triticum turgidum landraces and other related subspecies belonging to the Tetraploid wheat Global Collection (TGC, Maccaferri et al. 2019) were selected to assess the diversity of yellow rust resistance and identify promising region underlying genetic resistance towards Pst in durum wheat genome. A multi-year and multi-environmental survey were conducted to detect promising genomic regions underlying genetic resistance towards yellow rust (Yr).

2.2 Materials and methods

2.2.1 Plant materials, Experimental Design and Environments

The Tetraploid Wheat Global Collection (TGC) is a diverse panel comprising approximately 1,800 genotypes, developed using a reverse approach to encompass the full genetic variability of tetraploid wheat. This collection includes the four primary germplasm groups pivotal in wheat breeding and domestication: wild emmer wheat, domesticated emmer wheat, durum wheat landraces, and durum wheat cultivars (Maccaferri et al., 2019). From this comprehensive assembly, 1,324 *Triticum turgidum* landraces were selected for a multi-year and multi-environment survey. The environments included in this assessment are representative of the Mediterranean basin, the main production area for durum wheat. 4 different countries were considered Italy (4), Turkey (1), Lebanon (1) and Tunisia (2) with a timeline of 4 years, from 2018 until 2021. In Italy, the considered environment was the same but for 4 years in a row. The multi-environment trial was specifically designed to identify potential differences in responses to various pathogenic races, enabling the detection of robust and consistent loci of resistance against the primary races affecting this region. The environments considered for the study are:

- Grosseto 2018, (42° 45' 48.69" N ,11° 6' 44.507" E), Italy
- Grosseto 2019, (42° 45' 48.69" N ,11° 6' 44.507" E), Italy
- Izmir 2019, (38° 25' 25.4388" N, 27° 8' 34.1736" E), Turkey
- Tel Amara (LARI Institute) 2019, (33º 17 ‘ 00” N, 35 º 12 ‘ 00” E), Lebanon
- Grosseto 2020, (42° 45' 48.69" N ,11° 6' 44.507" E), Italy
- Beja 2020, (36°43′30″N, 9°10′55.2″E), Tunisia
- Kodia 2020, (36°32′51.89 N, 9°0′40.73 E), Tunisia,
- Grosseto 2021, (42° 45' 48.69" N ,11° 6' 44.507" E), Italy

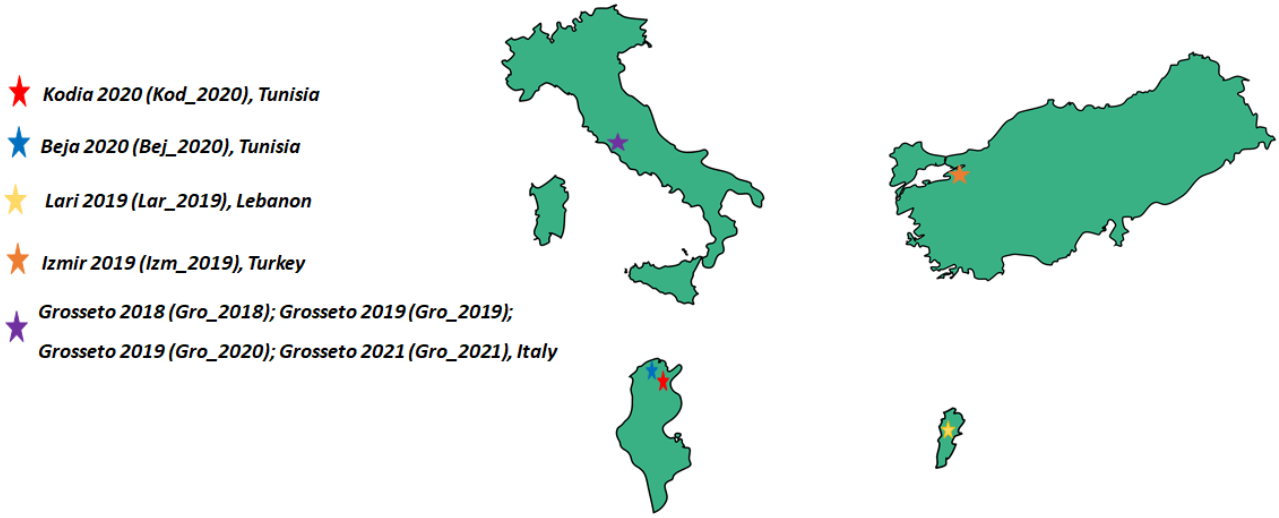

Figure 1: Simplified map highlighting the position of the considered environments for multi-year and multi-environmental assay

For a visual representation of the environments, see figure 1.

This highly diversified panel of durum wheat landraces and related subspecies was assembled with the purpose of being a valuable genetic resource (gene pool) to dissect and investigate thoroughly for agronomic traits of interest, not only disease resistances but also abiotic stress resistances, grain yield-related traits, root and spike architecture (Maccaferri et al., 2019). In addition to *Triticum durum* landraces (Tdl), this panel is also composed of other related subspecies, such as:

- *Triticum turgidum* subsp *aethiopicum, commonly known as Ethiophian wheat*
- *Triticum turgidum* subsp *carthlicum*
- *Triticum turgidum* subsp *polonicum, commonly known as Polish wheat*
- *Triticum turgidum* subsp. *turgidum*

The experimental design followed an augmented randomized block design across all environments, with the panel of genotypes subdivided into blocks, each containing an equal number of accessions and common checks. Unlike the accessions, the checks were the only genotypes repeated in every block, serving as controls to ensure consistency across the different environments. Each accession was assigned a specific plot within the experimental field, and the layout was further organized into rows and columns to precisely indicate the location of each genotype. This design allows for efficient comparison of genotypes while accounting for environmental variability.

2.2.2 Phenotypic Data Analysis

The Tetraploid Wheat Global Collection (TGC) panel was evaluated for both infection type (IT) and severity (SEV) across all environments. Infection type refers to the nature of the plant's response to yellow rust infection, recorded on a numerical scale from 0 to 9 (Line and Qayoum, 1992). In contrast, severity represents the percentage of the plot affected by symptoms, measured on a scale ranging from 0% (no symptoms) to 100% (entire plot covered by symptoms).

The IT scale can be divided into three broad categories:

- **Values 0-3**: Indicate no or slight symptoms, signifying resistance.

- **Values 4-6**: Reflect partial resistance.
- **Values 7-9**: Indicate susceptibility.

Detailed Infection Type (IT) Scale:

1. **0**: No visible signs or symptoms.
2. **1**: Hypersensitive necrotic and/or chlorotic reactions, with flecks.
3. **2**: Necrotic/chlorotic reactions with blotches or stripes; no sporulation.
4. **3**: Necrotic/chlorotic reactions with blotches or stripes; trace sporulation.
5. **4**: Necrotic/chlorotic reactions with blotches or stripes; light sporulation.
6. **5**: Necrotic/chlorotic reactions with blotches or stripes; intermediate sporulation.
7. **6**: Necrotic/chlorotic reactions with blotches or stripes; moderate sporulation.
8. **7**: Necrotic/chlorotic reactions with blotches or stripes; abundant sporulation.
9. **8**: Chlorosis behind sporulation areas, with abundant sporulation.
10. **9**: No necrosis or chlorosis; intense sporulation, representing full susceptibility.

This evaluation method, combining IT and SEV scores, provides a comprehensive assessment of the resistance levels across genotypes, aiding in the identification of resistant wheat accessions.

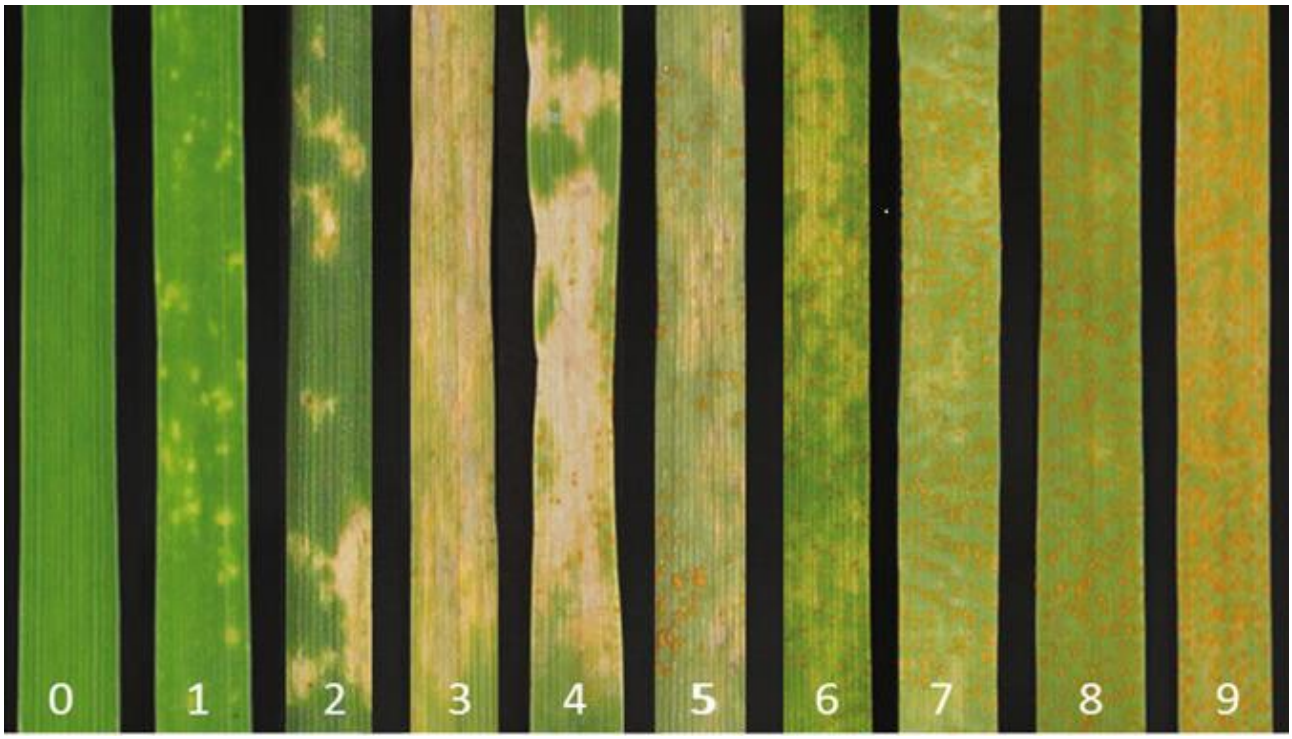

Figure 2: Infection Type (IT) scale used to assess the Yr symptoms.

Symptoms were evaluated at a late stage of wheat development, specifically during the milk (ZS: 73-77) or dough (ZS: 83-87) stages of the Zadoks growth scale (Zadoks et al., 1974). Since the assessments were conducted at a single timepoint, it was not possible to calculate the Area Under the Disease Progress Curve (AUDPC), which requires multiple evaluations over time to estimate the overall disease progression. Consequently, this limits the ability to monitor disease dynamics over the course of the season but provides a snapshot of disease severity at a critical stage of wheat development.

2.2.3 Phenotypic Data Analysis

A series of statistical analyses were conducted on the phenotypic data using R and RStudio (RStudio Team, 2020). Multiple normalizing functions were tested via the bestNormalize package in R, which evaluates several transformation functions and selects the most appropriate one based on the Estimated Normality Statistics (Pearson's P/df, where lower values indicate greater normality). After normalization, all transformed data were standardized using the scale() function to obtain a distribution with a mean of 0 and a standard deviation of 1.

Four primary transformation methods were applied to normalize all the data frames:

1. **Order-Normal Transformation:** $g(x)= f^{-1}(\text{rank}(x)-0.5/\text{length}(x))$
2. **Yeo-Johnson Normalization:**
$$\Psi(\lambda,y) = \begin{cases} ((y+1)^{\lambda} -1)/\ \lambda & \text{if } \lambda \neq 0,\ y \geq 0 \\ \log\ (y+1) & \text{if } \lambda = 0,\ y \geq 0 \\ -[(-y+1)^{2-\lambda} -1)]/(2-\lambda) & \text{if } \lambda \neq 2,\ y < 0 \\ -\log(-\ y\ +1) & \text{if } \lambda = 2,\ y < 0 \end{cases}$$
3. **Square Root Transformation:** $\sqrt{x}$
4. **Center Scaling (CS):** scale(x,center=TRUE,scale=TRUE)

Overall, the normality of the raw phenotypic data was improved. The improvement in normality following transformation was confirmed using the Shapiro-Wilk normality test (Beasley et al., 2009). An analysis of variance (ANOVA) was conducted on the transformed data using a mixed linear model procedure. This model included genotypes, environments, and genotype-environment interaction as random factors. The formula for estimating broad-sense heritability (H^2) was:

$$h^2 = \sigma^2_G / [\sigma^2_G + (\sigma^2_E + \sigma^2_{EXG} + \sigma^2_e)/n]$$

Where:

- σ^2_G = Genotypic variance
- σ^2_E = Environmental variance
- σ^2_{GE} = Genotype × Environment interaction variance
- σ^2_e = Residual variance
- n = Number of environments

Pearson's correlation coefficients were calculated among all environments to identify potential environmental clusters exhibiting high correlation. This was performed using the cor() function in R. Additionally, a three-dimensional principal component analysis (PCA) was conducted for the TGC panels using only IT phenotypic data. The analysis helped identify distinct environmental clusters for further analysis of highly correlated environments. The PCA3D package in R was used for this. Best Linear Unbiased Estimates (BLUEs) were calculated using the lme4 package in R via mixed model analysis (lmer). The model parameters differed based on the specific environments and multi-environmental clusters. The transformed and standardized phenotypic data served as the dependent variable, while the genotype was treated as a fixed effect, with all other variables treated as random effects.

For BLUEs estimation across environmental clusters, the following model was applied:

Phenotype ~ Genotype + Block + Genotype:Block + Environment + Genotype:Environment

This model allowed for evaluating genotype-environment interaction (G × E) and environmental effects, which were considered during the standardization of phenotypic values for BLUEs calculation. The significant interactions between environment (E) and G × E were identified using ANOVA, with a significance threshold of $p < 0.05$.

For individual environments, the same analysis was performed using the following model to obtain BLUEs:

Phenotype ~ Genotype + Row+ Columns+ Block + Genotype: Block

2.2.4 SNP Genotyping

The NucleoSpin Plant II kit was used to extract DNA from leaves of each genotype at 10-day seedlings stage according to the instructions and Illumina iSelect 90K wheat SNP array was used to carry out genotyping (Wang et al., 2014). Raw data (Theta/R) from single genotyping experiments were jointly examined for genotype calling and cluster assignment after export from the GenomeStudio software. Polymorphic SNPs markers were selected by using following steps: First, select markers with unique map positions in available genetic maps and align the marker sequences to a single position on the Svevo reference genome RefSeq V1.0 (Maccaferri et al., 2015, 2019); second, samples with a high proportion of missing data (>0.2, with the threshold defined as the third quartile + 1.5*inter-quartile range) were deleted; third, similarly markers with minor alleles presents in less than 5 genotypes and with a high proportion of missing calls were also removed. SNP imputation was performed using Beagle 5 software using default parameters (Browning et al., 2018). The imputation accuracy was measured at 98.6% by running 1,000 replicates of randomly masked 1% of the called genotypes (Hancock et al., 2012). As a result of these preliminary steps, a final SNP-based genotyping matrix was generated for all the accessions in both VCF (Variant Call Format) and Hapmap formats. The final genotyping matrix contained 20235 biallelic SNPs in total covering the whole genome (See table 1 for a summary description).

Table 1: Summary table displaying the total number of SNPs, starting position (Bps), ending position (Bps), physical distance (Bps).

Chr	N°SNPs	Start_Pos (Bps)	End_Pos (Bps)	Distance (Bps)
1A	1315	940814	585260682	584319868
1B	1953	1544472	681099570	679555098
2A	1387	25912	775254290	775228378
2B	2181	957589	789417865	788460276
3A	1159	72927	746462554	746389627
3B	1597	304289	836443563	836139274
4A	948	262144	735878684	735616540
4B	986	43001	674637583	674594582
5A	1212	4115	668643224	668639109
5B	1751	1751452	701170690	699419238
6A	1301	319202	615259428	614940226
6B	1465	2064455	697515419	695450964
7A	1525	156512	727023042	726866530
7B	1455	114117	721752470	721638353

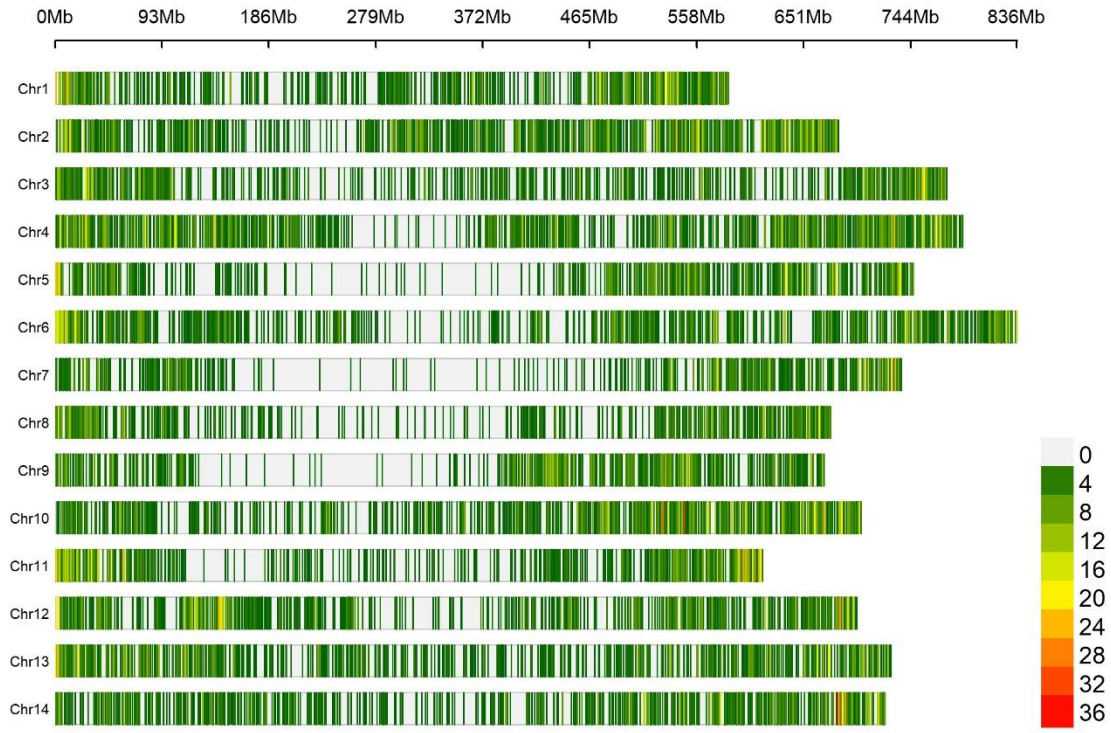

Figure 3: Visual representation of TGC Hapmap, showing the chromosome physical distance in Megabases (Mb) scale and the marker density on the right. R Package (CMplot).

2.2.5 LD decay analysis, SNPs Pruning, population structure analysis and Identity By State (IBS) genetic similarity matrix

The extent of pairwise linkage disequilibrium (LD) was estimated across all chromosomes in the TGC panel of 1,324 landraces by calculating squared correlation coefficients (r^2) using Tassel 5.0. The genome-wide LD pattern was graphically represented through a nonlinear regression model, plotting r^2 values over physical distance based on the Illumina 90K SNP physical map. To monitor LD decay, three thresholds of r^2 were considered: high LD ($r^2 = 0.8$), medium LD ($r^2 = 0.5$), and low LD ($r^2 = 0.3$). PLINK software (Chang et al., 2015) was used to prune redundant markers based on genome-wide LD, where SNPs with an $r^2 \geq 0.99$ were merged into unique SNP calls. Additionally, three further pruned HapMap datasets were produced by selecting a single SNP from those with r^2 values of 0.8, 0.5, and 0.3 to conduct population structure analyses. The population structure was analyzed using ADMIXTURE, a model-based likelihood method optimized with the block relaxation algorithm, quasi-Newton convergence acceleration method, and q = 3 secants (Alexander et al., 2009). Sub-population memberships were determined for k-values ranging from 2 to 20. The optimal number of subpopulations was selected based on the cross-validated error rate, delta cv error, minimum group size, maximum percentage of admixed lines in a group, and the overall percentage of admixed lines. In the reported dataset, k = 8 and an r^2 threshold of 0.5 were identified as the most suitable parameters for analysis. To further investigate genetic relationships, the TASSEL 5 software was used to convert the imputed HapMap file into a distance matrix based on the Identity By State (IBS) index, where values ranged from 0 (complete diversity) to 1 (full identity), yielding a kinship data frame. A heatmap and Ward clustering (using the Ward.D2 algorithm) were performed on the kinship matrix, utilizing the R packages *pheatmap* v1.0.12 and *dendextend* v1.15.2 (R Core Team, 2020).

2.2.6 Genome-Wide Association Study for TGC panels

The full genotyping matrix, consisting of 20,235 polymorphic SNPs and 1,324 landraces, was used for a genome-wide association study (GWAS). GWAS was conducted using the linear mixed model implemented in the GAPIT v.3.0 package in R (Wang et al., 2021). Four different models provided by GAPIT v.3.0 were tested: the Mixed Linear Model (MLM) (Yu et al., 2006), the Multi-Locus Mixed Model (MLMM) (Segura et al., 2012), the Fixed and Random Model Circulating Probability Unification (FarmCPU) (Liu et al., 2016), and the Bayesian Information and Linkage Disequilibrium Iteratively Nested Keyway (BLINK) (Huang et al., 2018). Due to differences in the number of accessions with phenotypic data across environments, and the removal of those with missing values, SNP allele frequencies varied between environments. As a result, Minor Allele Frequency (MAF) filtering (< 5%) was applied separately for each environment and environmental cluster to generate distinct genotyping matrices. The association analysis was performed on the transformed Best Linear Unbiased Estimates (BLUEs) for datasets from individual environments (IT and SEV), as well as for the multi-environment datasets, selected based on correlation tests and PCA analysis. To minimize the risk of spurious associations, a kinship matrix based on Identity By State (IBS) was generated for each environment using TASSEL 5.0 (Bradbury et al., 2007). The population structure membership scores from ADMIXTURE v1.3 were not included in the GWAS models to avoid overfitting but were later used as covariates in downstream linear model analysis. On average, the Bonferroni significance threshold calculated through permutation testing ranged between 4 and 5, indicating that SNPs with p-values below this threshold had an increased probability (approximately 10^{-4} to 10^{-5}) of being associated with the traits. The final cut-off for significant associations was set at 10^{-4} (equivalent to a LOD score of 4). However, SNPs were considered as marker-trait associations (MTAs) only when their LOD score was ≥ 3 in at least two models and detected in at least two environments. This criterion was designed to include loci with small-to-moderate effects and mitigate issues such as linkage disequilibrium (LD) decay or uneven marker distribution across the genome (Gordon & Finch, 2005). Manhattan plots (see supplementary files) and QQ plots were generated using GAPIT v.3.0 to visualize the association results.

2.2.7 Genome-Wide Association Study within TGC subpopulations

Based on the results of population structure analysis using ADMIXTURE v1.3, the entire TGC panel was divided into eight highly structured and diversified subpopulations, each representative of the different tetraploid subspecies of Triticum turgidum and the regions where these landraces are still locally cultivated. This detailed subdivision was crucial for conducting association studies within individual subpopulations. The goal was to either identify rare beneficial alleles conserved within specific subpopulations—alleles that may have been missed in the global GWAS—or to trace the origin of resistant alleles detected across both the GDP and TGC panels. Due to the limited resolution of GWAS within each subpopulation, which was attributed to the smaller number of accessions and the high genetic similarity within subpopulations, more markers were filtered using a Minor Allele Frequency (MAF) threshold of 5%. As a result, GWAS was only performed within subpopulations that included more than 50 individuals across both individual environments and multi-environmental clusters (see supplementary files). Like the global GWAS, the four models implemented in GAPIT—MLM, MLMM, FarmCPU, and BLINK—were used to detect associations, with the kinship matrix generated by TASSEL 5.0 serving as a covariate. As with the global GWAS, the significance threshold was set at LOD ≥ 4, and MTAs were considered significant when their LOD score exceeded 3 and the association was detected in at least two environments. Additionally, admixed genotypes identified from the ADMIXTURE analysis were excluded from these subpopulation-based analyses.

2.2.8 *Downstream analysis: General Linear model and Stepwise regression*

SNPs were considered Marker-Trait Associations (MTAs) only when their LOD score for either IT or SEV was ≥ 3 in at least two models and detected in at least two environments. A general linear model using the lmer4 package in R was employed to estimate the phenotypic variance (R^2) explained by each MTA for both IT and SEV. In this linear model (lm()), the phenotype(s) were treated as the dependent variable, with each SNP serving as the fixed-effect predictor and the population structure membership scores (Qs) used as covariates. The linear model was followed by an ANOVA test using the car package in R to assess the significance of the associations. A p-value < 0.05 was used as the threshold for significance. Only the significant MTAs were then included in a stepwise-regression general linear model using the stepAIC function from the MASS package in R, which combined all SNPs and Qs to estimate the global phenotypic variance explained (R^2) for both IT and SEV within a specific environment or environmental cluster. The Akaike Information Criterion (AIC) and Bayesian Information Criterion (BIC) were used in the stepwise-regression model to select the final MTAs to be retained (see supplementary files). The selected SNPs, with the strongest association based on p-values, were designated as QTL-representative markers (referred to as QTL-tagging SNPs). The *lm*() and stepAIC functions were also used to estimate the phenotypic variance explained by each Q and all Qs collectively. In contrast to the global GWAS, the subpopulation-specific GWAS did not use Qs as covariates in the linear model. For these subpopulation analyses, the model included only the phenotypes as the dependent variable and the selected MTAs as predictors.

2.2.9 *LD-Blocks detection and Haplotype Analysis*

Once the target MTAs were selected, QTL confidence intervals (CIs) were defined by identifying the corresponding LD-blocks around the MTAs. The complete genotyping matrix, consisting of 20,235 polymorphic SNPs across all genotypes in the GDP and TGC panels, as well as specific TGC subpopulations, was used for this analysis. HAPLOVIEW 4.2 software (Barrett et al., 2005) was employed to calculate the squared allele frequency correlation (r^2) for all pairwise comparisons between intrachromosomal SNPs and to visualize local LD patterns. These LD patterns were used to define haploblocks around the QTL-tagging SNPs. The map distance at which LD decay fell below an r^2 threshold of 0.5 was used to establish the QTL confidence intervals, a commonly applied threshold for QTL detection (Ardlie et al., 2002; Shifman et al., 2003; Khatkar et al., 2008; Lawrence et al., 2009). Singleton MTAs that showed no linkage with surrounding markers were discarded. After defining the haploblocks for the selected MTAs, HAPLOVIEW was further used to estimate the total number of haplotype variants for each detected LD-block within the respective panel or subpopulation. A phylogenetic analysis of these haploblock variants was performed to cluster similar haploblocks. For each QTL, the phenotypic performance of all haploblock variants was assessed to distinguish resistant haploblocks from susceptible ones. Additionally, the frequency of each haploblock variant within individual TGC subpopulations was estimated in order to reconstruct the origin.

2.2.10 *Projection of Yr Loci and QTLs onto the cv Svevo reference genome*

To compare our results with previously mapped Yr loci and QTLs reported in independent studies, a comprehensive QTL projection analysis was conducted. This was achieved by leveraging the previously published tetraploid wheat consensus map (Maccaferri et al., 2015) and the 10.45 Gb genome assembly of the durum wheat cultivar Svevo (Maccaferri et al., 2019). As suggested by Goffinet and Gerber (2000), QTL projection, or better still, meta-analysis, is crucial for (i) identifying genomic regions repeatedly involved in trait variation, (ii) narrowing down QTL confidence intervals, and (iii) facilitating the identification of candidate genes for positional cloning. In this study, three types of QTLs or Yr loci were projected onto the consensus and physical maps:

- Yr QTLs mapped from linkage mapping populations,
- Yr QTLs detected through GWAS using panels of DWC, TDL, DEW, and WEW,
- Previously mapped or cloned Yr resistance loci.

A thorough literature review was conducted using Web of Science, Scopus, and Google Scholar, employing keywords such as "wheat yellow rust resistance QTL". Additional information was retrieved from databases such as GrainGenes, KOMUGI, and the Catalogue of Gene Symbols for Wheat (McIntosh et al., 2012–2020). The QTL dataset was created using data available from 2000 to 2023, focusing on QTLs associated with Infection Type (IT) and Disease Severity (SEV) in bread wheat (Triticum aestivum L.), durum wheat cultivars, durum wheat landraces, and domesticated emmer wheat (See supplementary file). For linkage mapping studies, data such as parental cross type, number of progenies, QTL name, chromosome location, LOD score, phenotypic variance explained (PVE), QTL position, and original confidence interval (CI) were collected. For GWAS studies, information such as collection size, local LD estimates, chromosome location, LOD score, PVE, MTA positions, and CIs were documented. For previously mapped Yr loci, the Yr acronym, physical and genetic interval, and FASTA sequences (for cloned genes) were noted. Different criteria were used to project QTLs onto the consensus and physical maps. In linkage mapping studies, the Darvasi formulas were used to estimate the QTL CI based on the population type:

- F2: $CI = 530 / (\text{Number of lines} \times R^2)$
- Backcross: $CI = 530 / (\text{Number of lines} \times R^2)$
- RILs: $CI = 163 / (\text{Number of lines} \times R^2)$
- DH: $CI = 287 / (\text{Number of lines} \times R^2)$

The start and end of the CI were calculated as follows:

- CI start: Peak marker position (cM) − CI/2
- CI stop: Peak marker position (cM) + CI/2

Using these boundaries, the closest markers to the left and right ends of the CI were identified on both the original linkage map and the consensus map (Maccaferri et al., 2015). If no marker was located exactly at the defined position, the interval was expanded until a marker was found. The ratio between the original map and the consensus map was calculated to maintain consistency, allowing for the estimation of the final CI:

- CI left on consensus map = ((CI start − left marker on original map) / ratio) + left marker on consensus map
- CI right on consensus map = ((CI stop − right marker on original map) / ratio) + right marker on consensus map
- QTL peak on consensus map = (CI left + CI right) / 2

After defining the CI in cM on the consensus map, the closest markers to the CI boundaries and peak were projected onto the Svevo genome to determine the physical positions and intervals. If the peak marker on the original map was not present on the consensus map, its sequence was BLASTED onto the Svevo reference genome to find its physical position, and the closest marker on the consensus map was chosen as the peak. For GWAS-derived QTLs, the reported peak markers were located on the consensus and Svevo maps to determine their position in both cM and bp. When available, local LD values from the study were used to define the CI; otherwise, general LD decay estimates were applied based on tetraploid wheat subspecies:

- 0.5 Mb for wild and domesticated emmer),

- 0.7 Mb for landraces,
- 1.5 Mb for cultivars and elite lines,

The consensus map positions were calculated as:

- Left marker: Peak marker position (cM) − LD interval
- Right marker: Peak marker position (cM) + LD interval

The corresponding markers were then projected onto the Svevo genome to determine the physical interval. For Yr loci, many were initially mapped using older molecular markers (e.g., SSR and DArT) in bread wheat or related species like *Triticum urartu* or *Triticum timopheevii*. These markers were blasted onto the Svevo genome to find the closest 90K SNP markers and refine the CI. If the peak marker was unavailable, it was chosen as the midpoint of the estimated CI. Similarly, markers were projected onto the consensus map to translate physical positions (bp) into genetic positions (cM). Cloned Yr genes were annotated, while Yr loci mapped with 90K SNPs were projected following the same method used for independent GWAS studies.

2.3 RESULTS

2.3.1 Multi-environmental clustering and correlations

A total of 1,324 landraces were assessed for yellow rust resistance through a multi-environment experimental survey conducted over three years, from 2018 to 2021. Overall, the phenotypic evaluation demonstrated diverse mean values for infection type (IT) and severity (SEV) across the TGC panel in all environments, with IT values ranging from 3.15 to 6.89 and SEV percentages between 16.46% and 59.63%. Analysis of variance indicated that broad-sense heritability exceeded 0.60 in every environment, suggesting that genetic factors played a dominant role compared to environmental influences (Table 2). Correlation plots for non-transformed data indicated strong correlations between certain environments, specifically between Grosseto (2019-2021) and Izmir (2019), as well as Grosseto (2018) and Lari (2019) (Fig). These findings were further supported by a three-dimensional principal component analysis (PCA) plot, which utilized only the IT phenotypic data from the respective environments (figure 4). Ultimately, we identified two distinct minor multi-environmental clusters within the TGC: the first cluster comprising Grosseto (2019-2021) and Izmir (2019), and the second cluster including Grosseto (2018) and Lari (2019). Descriptive statistics and heritability (h^2) for each single environment and the two detected multi-environmental clusters is shown below (see table 2). the correlation plot among the environments for both IT and SEV confirms the environmental clusters observed in 3D-PCA (figure 5).

Table 2*:* Table displaying descriptive statistic for both IT and SEV: Max (Maximum), Min (Minimum), Grand Mean (mean), Genetic Variance, Residual Variance, Phenotypic Variance, h2 (Broad-Sense Heritability), SD (Standard Deviation), SE (Standard Error)

Environments	**Grosseto_2018**	**Izmir_2019**	**Grosseto_2020**	**Lari_2019**	**Kodia_2020**	**Beja_2020**	**Grosseto_2019**	**Grosseto_2021**	**Multi_Environment_1**	**Multi_Environments_2**
IT										
Max	9	9	9	9	9	9	9	9	9	9
Min	0	0	0	0	0	0	1	1	0	0
Grand mean	4.2	3.2	3.2	6.9	3.6	5.3	5.4	6.3	4.91	5.35
Genetic Variance	2.9	8.9	1.6	6.5	2.6	2	2.4	2.5	2.3	1.49
Residual Variance	1.6	0.2	0.8	0	2.3	1.7	0.3	0.3	2.24	4.12
Phenotypic Variance	4.9	9.1	2.5	6.7	5.7	3.8	3	2.7	3.83	6.19
h^2	65	98	66	97	63	53	89	89	70.62	58.32
SD	2.2	3	1.6	2.6	2.4	1.9	1.7	1.6	1.96	2.49
SE	0.1	0.1	0.1	0.1	0.1	0.1	0.3	0.1	0.08	0.1
Environments	**Grosseto_2018**	**Izmir_2019**	**Grosseto_2020**	**Lari_2019**	**Kodia_2020**	**Beja_2020**	**Grosseto_2019**	**Grosseto_2021**	**Multi_Environment_1**	**Multi_Environments_2**
SEV										
Max	100	100	100	100	90	90	100	100	100	100
Min	0	0	0	5	0	0	0	5	0	2
Grand Mean	44	24	16	44	24	46	68	60	50.47	41.2
Genetic Variance	568	577	221	635	252	265	609	472	100.63	373.21
Residual Variance	77	14	67	32	167	220	118	130	468.47	206.79
Phenotypic Variance	674	615	296	694	469	538	766	595	502.8	628.65
h^2	88	98	77	95	70	55	84	78	64.83	64.34
SD	26	25	17	26	22	23	28	24	22.42	25.07
SE	1.5	1.2	0.6	1.3	0.7	0.8	1.3	1.6	0.92	1.05

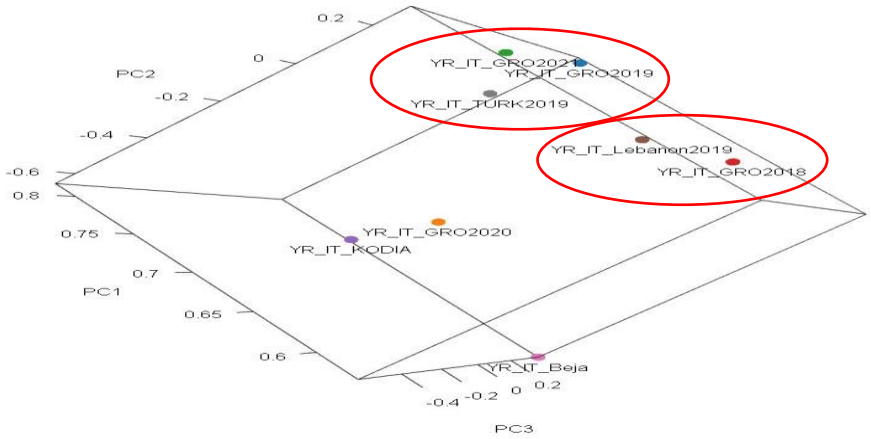

Figure 4: 3D Principal Component Analysis (PCA) among the considered environments. 3D Principal Component Analysis (PCA) by using IT data only, where two 2 independent environmental clusters are detected and encircled in red. 1st cluster: Grosseto 2019 (YR_IT_GRO2019), Grosseto 2021 (YR_IT_GRO2021) and Izmir 2019 (YR_TURK2019). 2nd cluster: Lari 2019 (YR_IT_Lebanon2019) and Grosseto 2018 (YR_IT_GRO2018). The remaining three environments were independent and did not cluster with any, namely, Grosseto 2020 (YR_IT_GRO2020) and Kodia 2020 (YR_IT_KOD2020).

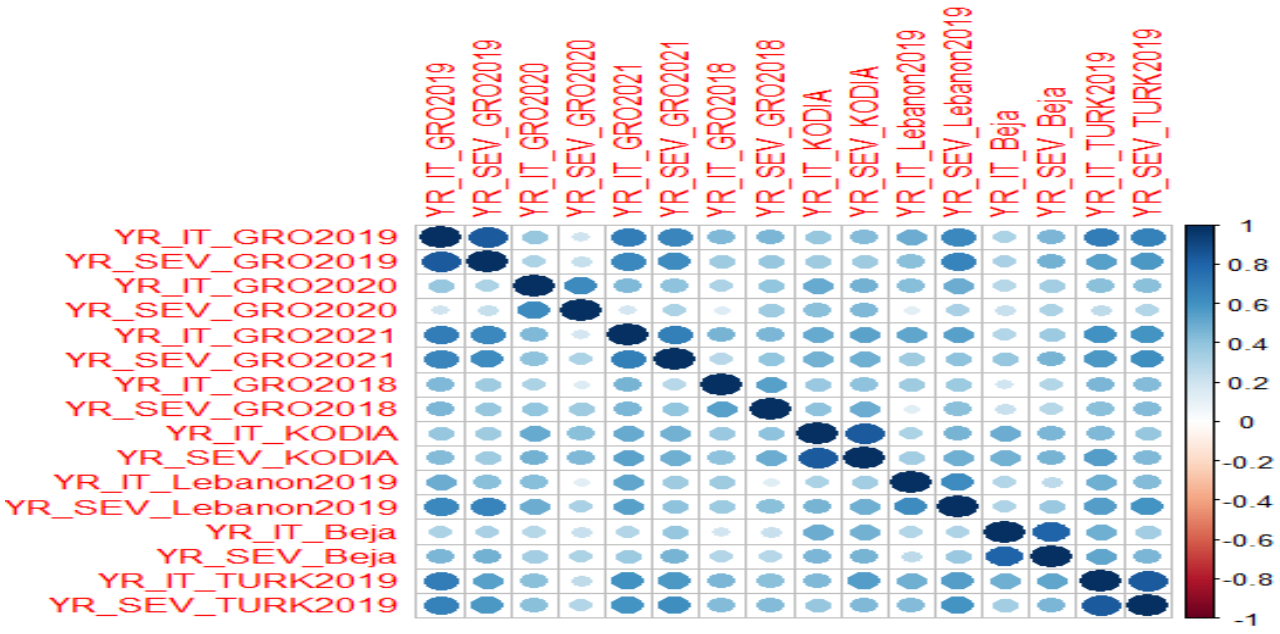

Figure 5: Correlation plot among the all the considered environments for both IT and SEV. On the whole, there is a positive correlation among all environments (Blue colour).

2.3.2 Environments

- 1st Multi-environmental cluster (Grosseto 2019, Grosseto 2021 and Izmir 2019)

IT and SEV distribution data were respectively transformed through Yeo-Johnson Normalization and Order-Normal Transformation. Upon normalization, the distribution of data meets the normality criteria (figure 6).

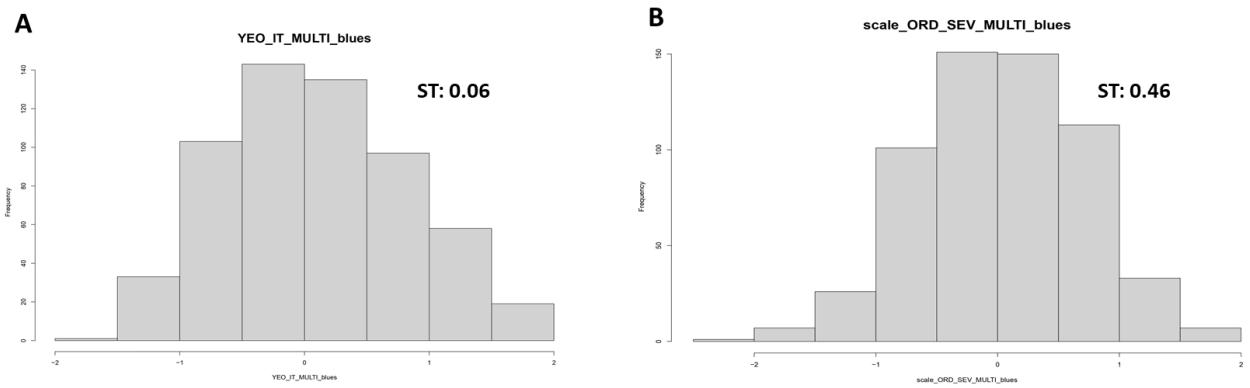

Figure 6: Transformed data histogram for BLUES deriving from 1st multi-environmental cluster for IT (A) and SEV (B). The result of Shapiro Test (ST) is reported.

- 2nd Multi-environmental cluster (Grosseto 2018, Lari 2019)

  IT and SEV distribution data were both transformed through Yeo-Johnson Normalization. Upon normalization with the best transforming function according to BestNormalize R package, the distribution of data are almost normal (figure 7).

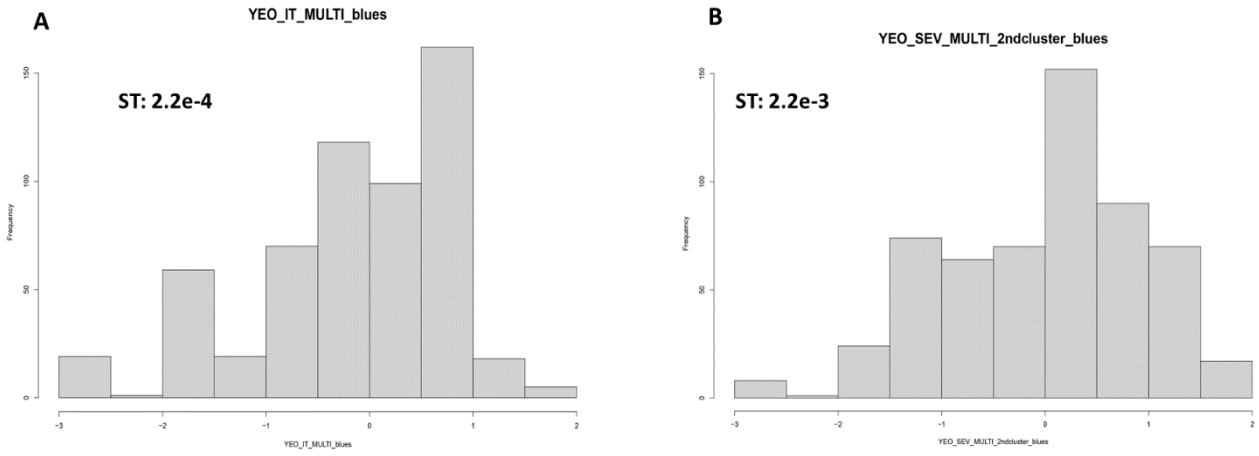

Figure 7: Transformed data histogram for BLUES deriving from 2nd multi-environmental cluster for IT (A) and SEV (B). The result of Shapiro Test (ST) is reported.

- Grosseto 2018

  IT and SEV distribution data were both transformed through Order-Normal Transformation. Upon normalization with the best transforming function according to BestNormalize R package,

the distribution of data are very close to normality. IT shows a slight bimodal distribution (figure 8).

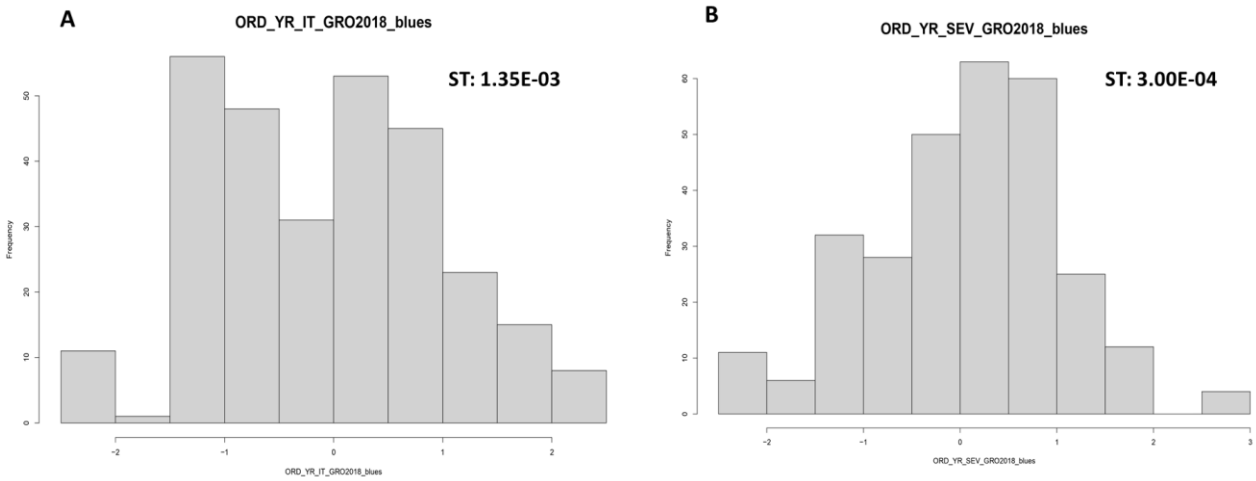

Figure 8: Transformed data histogram for BLUES deriving single environment Grosseto 2018 for IT (A) and SEV (B). The result of Shapiro Test (ST) is reported.

- Grosseto 2019

IT and SEV distribution data were both transformed through Yeo-Johnson Normalization and Order-Normal Transformation. Upon normalization with the best transforming function according to BestNormalize R package, the distribution of data are almost normal. In particular, SEV shows a medium-high level of disease (figure 9).

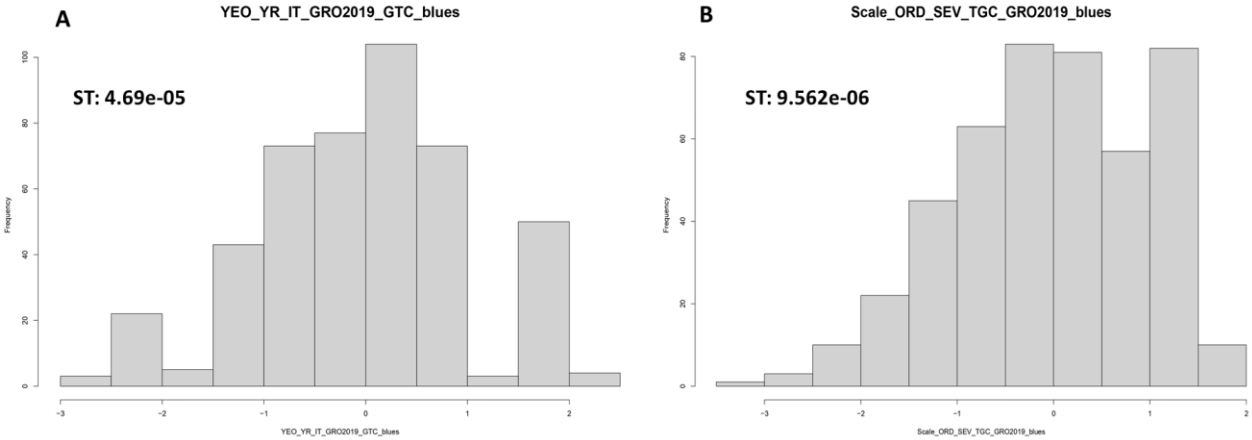

Figure 9: Transformed data histogram for BLUES deriving single environment Grosseto 2019 for IT (A) and SEV (B). The result of Shapiro Test (ST) is reported.

- Lari 2019 (Rola Amil)

IT and SEV distribution data were both transformed through through Order-Normal Transformation. Upon normalization with the best transforming function according to

BestNormalize R package, , the distribution of data are still not normal. In particular, IT shows a considerably high level of disease, whereas SEV is more leveled (figure 10).

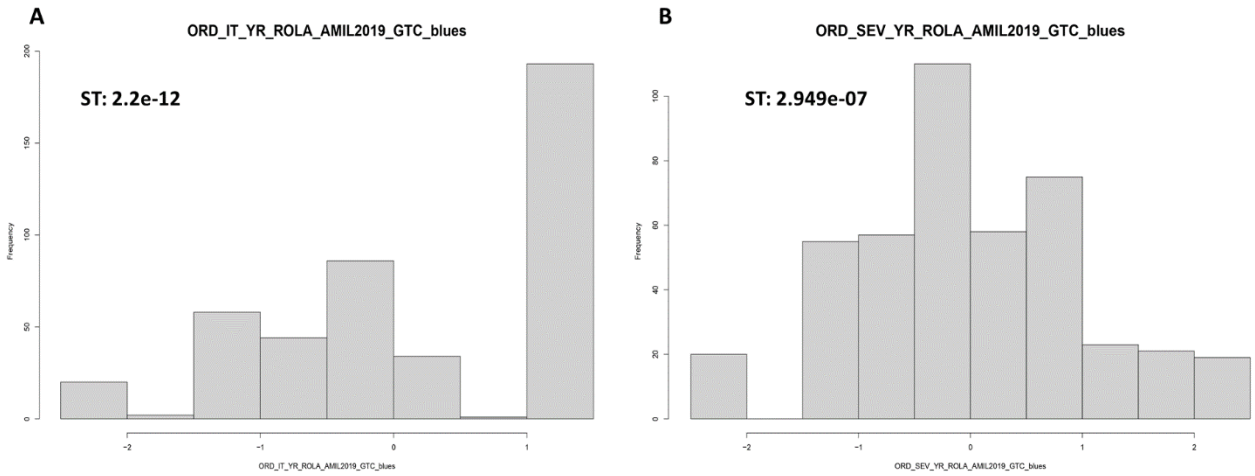

Figure 10: Transformed data histogram for BLUES deriving single environment Lari 2019 (Rola Amil) for IT (A) and SEV (B). The result of Shapiro Test (ST) is reported.

- Izmir 2019

IT and SEV distribution data were both transformed through through Order-Normal Transformation. Upon normalization with the best transforming function according to BestNormalize R package, the distribution of data are still not normal. In particular, IT shows a medium-low level of disease with a bimodal distribution, whereas SEV is more leveled (figure 11).

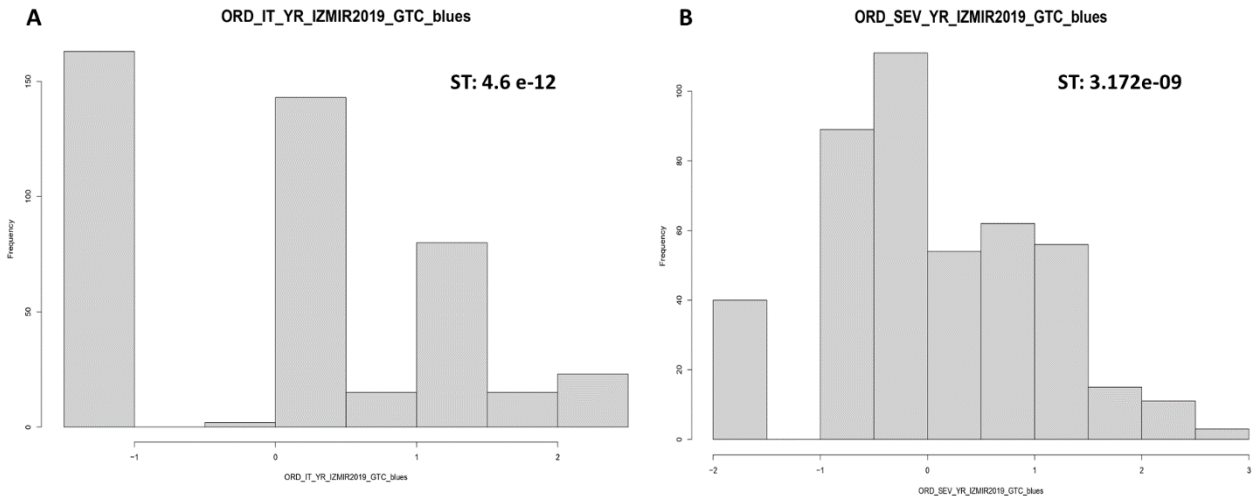

Figure 11: Transformed data histogram for BLUES deriving single environment Izmir 2019 for IT (A) and SEV (B). The result of Shapiro Test (ST) is reported.

- Beja 2020

IT and SEV distribution data were respectively transformed through Square-root function (SQRT) and Order-Normal Transformation. Upon normalization with the best transforming function according to BestNormalize R package, the distribution of data are still not normal for IT, whereas very close to normality for SEV. In particular, IT shows a L-shape distribution with high level of disease (figure 12).

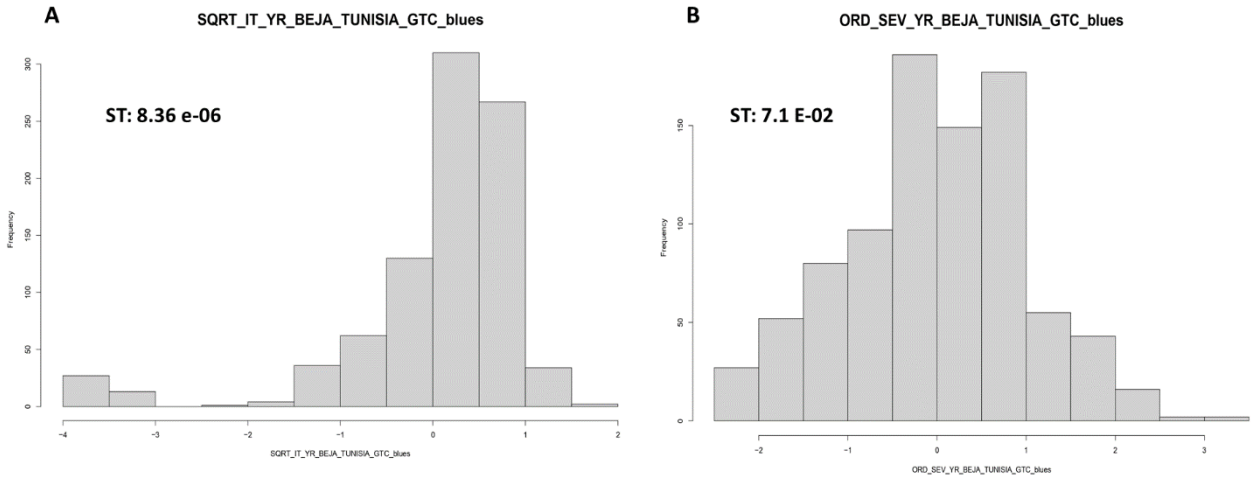

Figure 12: Transformed data histogram for BLUES deriving single environment Beja 2020 for IT (A) and SEV (B). The result of Shapiro Test (ST) is reported.

- Kodia 2020

IT and SEV distribution data were respectively transformed through Center Scaling function (CS) and Order-Normal Transformation. Upon normalization with the best transforming function according to BestNormalize R package, the distribution of data are still not normal for both IT and SEV. Both traits show a bimodal distribution overall (figure 13).

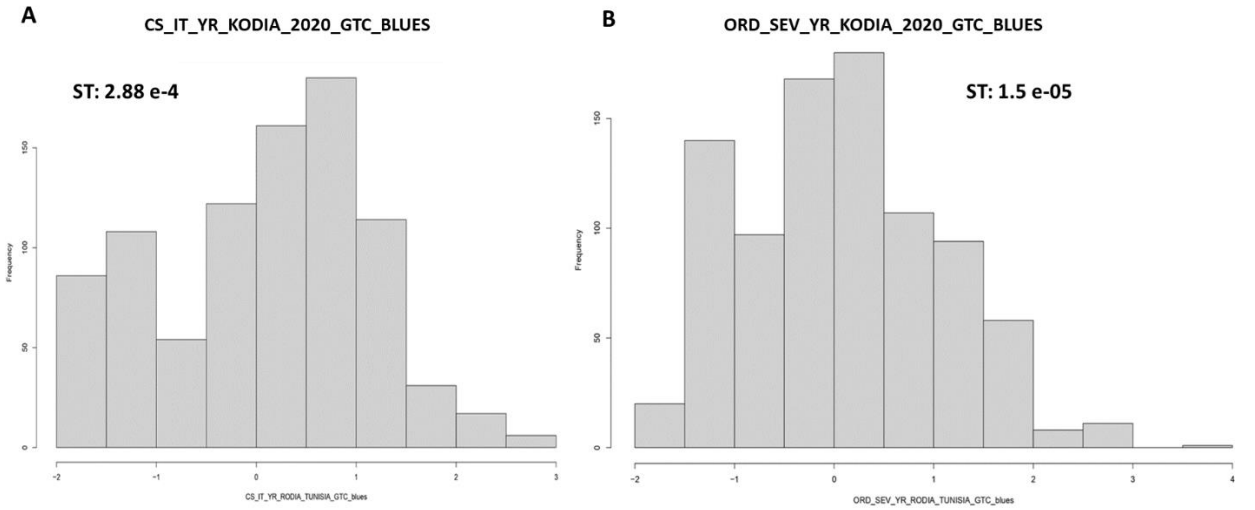

Figure 13: Transformed data histogram for BLUES deriving single environment Kodia 2020 for IT (A) and SEV (B). The result of Shapiro Test (ST) is reported.

- Grosseto 2020

IT and SEV distribution data were respectively transformed through Center Scaling function (CS) and Square Root (SQRT) transformation. Upon normalization with the best transforming function according to BestNormalize R package, the distribution of data are close to normality for both IT and SEV. IT shows a bimodal distribution, whereas SEV shows a slight skewness (figure 14).

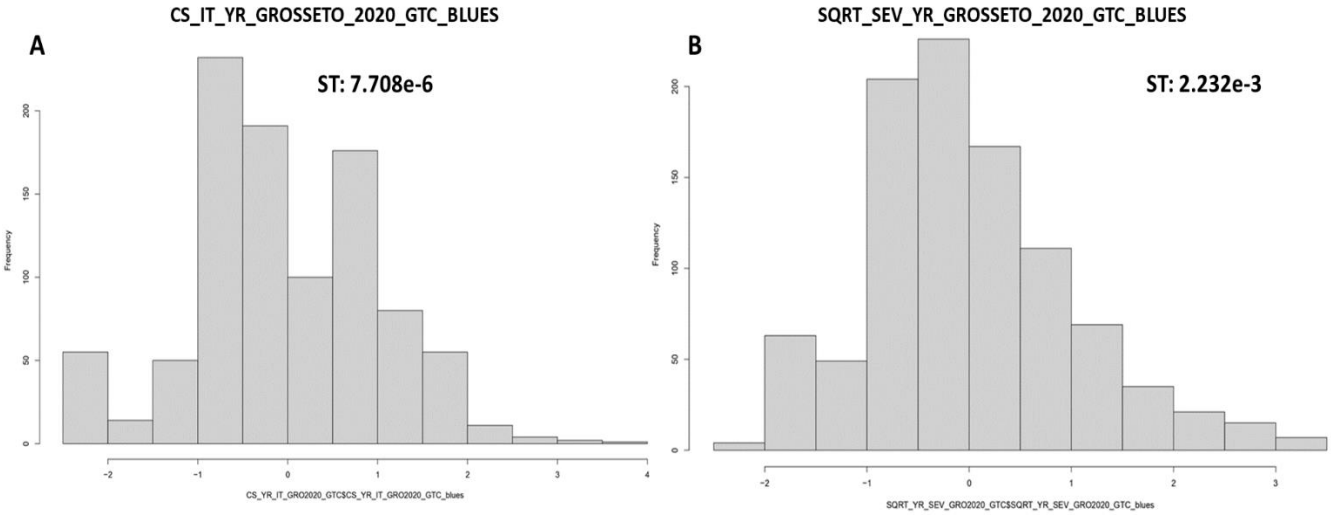

Figure 14: Transformed data histogram for BLUES deriving single environment Grosseto 2020 for IT (A) and SEV (B). The result of Shapiro Test (ST) is reported.

- Grosseto 2021

IT and SEV distribution data were respectively both transformed through through Order-Normal Transformation. Upon normalization with the best transforming function according to BestNormalize R package, the distribution of data are very close to normality normal (figure 15).

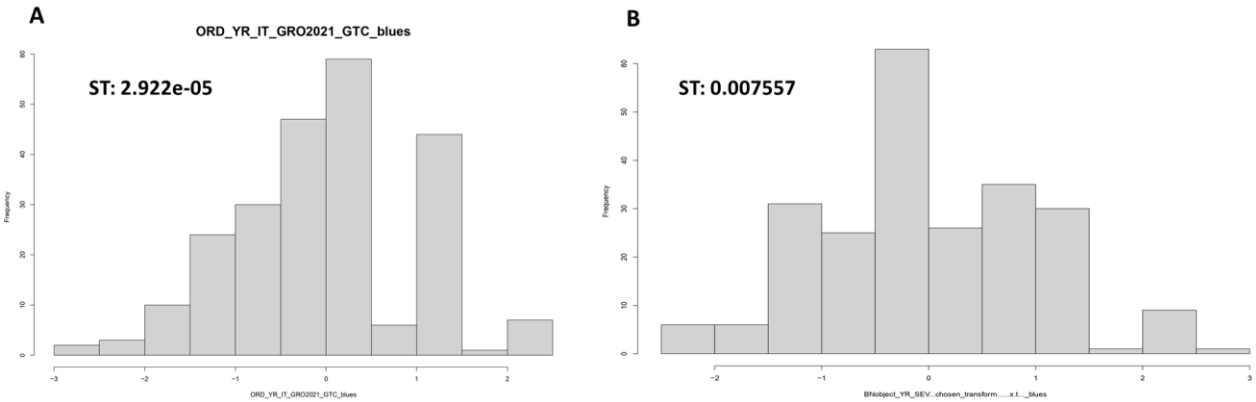

Figure 15: Transformed data histogram for BLUES deriving single environment Grosseto 2021 for IT (A) and SEV (B). The result of Shapiro Test (ST) is reported.

2.3.3 Population structure, Clustering and Identiy By State (IBS) Kinship Matrix

Population structure was analyzed using the Illumina iSelect 90K SNP array, focusing on non-redundant genotypes with less than 10% missing data across the genomes of 1,324 Triticum turgidum landraces and related subspecies from the Tetraploid Wheat Global Collection (TGC) (Maccaferri et al., 2019). A combination of Bayesian model clustering and Hierarchical Ward clustering identified eight primary genetic clusters, which corresponded to different geographic regions and, in some cases, durum-related subspecies within the TGC collection. These clusters

represent the original regions where tetraploid wheat domestication and selection occurred, primarily in the Middle East and specific areas in the Mediterranean and North and Central Africa (See figure 16 and 17).

- The first (Q1) and second (Q2) genetic clusters were primarily composed of landraces from East Africa, particularly from the Horn of Africa and Ethiopia. Q1 included Ethiopian germplasm, while Q2 represented a more restricted cluster of Triticum turgidum subsp. carthlicum genotypes.
- The third cluster (Q3) comprised landraces from the Middle East, including Iran, Iraq, and Syria, where original domestication and selection processes occurred or where these landraces are still cultivated.
- The fourth cluster (Q4) was dominated by Triticum turanicum landraces from Southwest Asia, particularly within Iran.
- The fifth cluster (Q5) was primarily composed of ancient Triticum turgidum subsp. turgidum landraces from the Mediterranean region, particularly the Balkans.
- The sixth (Q6), the second largest, represented landraces from the Caucasus region (including Russia and Kazakhstan) and Western Asia.
- The seventh cluster (Q7) was the largest, representing landraces from multiple Mediterranean areas and North Africa, including Cyprus, Egypt, and the Iberian region (Georgia).
- The eighth cluster (Q8) was a smaller but diverse group, consisting of Central African and Western Asian Triticum turgidum landraces.

Accessions with population membership scores lower than 50% were classified as admixed and not assigned to any of the eight identified genetic clusters. In total, 123 accessions were categorized as admixed. The results from Ward clustering, genotypic similarities, and subgroup structure coefficients revealed a high degree of genetic mixing among landraces from relatively close regions, especially within the Q6, Q7, and Q8 subpopulations in the TGC assembly. In contrast, the remaining genetic clusters were more clearly defined by specific Triticum turgidum subspecies. For example, Q3, Q4, and Q5 primarily represented Triticum turgidum subsp. carthlicum, Triticum turanicum, and Triticum turgidum subsp. turgidum, respectively, while Q1 and Q2 encompassed landraces from the Ethiopian Panel (EP) and Triticum polonicum. These findings underscore the completeness of the TGC assembly in terms of its comprehensive representation of available genetic resources, covering diverse geographic regions where Triticum turgidum subspecies landraces originated. It is important to note, however, that the subpopulation proportions shown in the figure reflect the composition of the germplasm resources described above and do not necessarily represent the current genetic composition of varieties within specific countries or breeding programs.

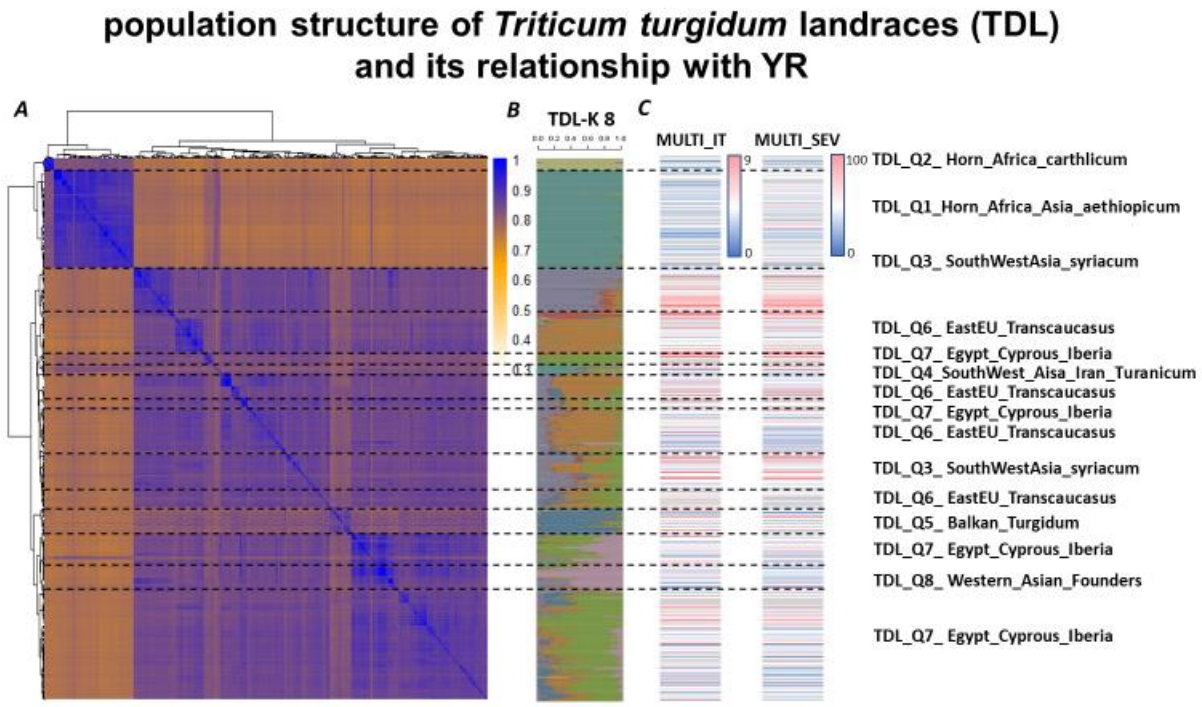

Figure 16: This Figure displays all the genotypes belonging to the TGC panel clustered based on Ward Clustering Algoritm. A: 1324 x 1324 kinship matrix based on simple matching genetic similarities (IBS, identity by state). B: Barplots showing the results of Admixtire analysis with each colour corresponding to a certain Q and the final score resulting from the cumulation of the single membership score of each subpopulation (eight in total). C: Phenotypic barplot for both IT and SEV referring to the BLUES of the 1st environmental cluster (Gro2019, Gro2021, Izmir 2019). Red colour indicates susceptibility, white indicates partial resistance and blue indicates resistance. Black dashed lines define a single cluster with the corresponding subpopulation identification name and Qs on the right.

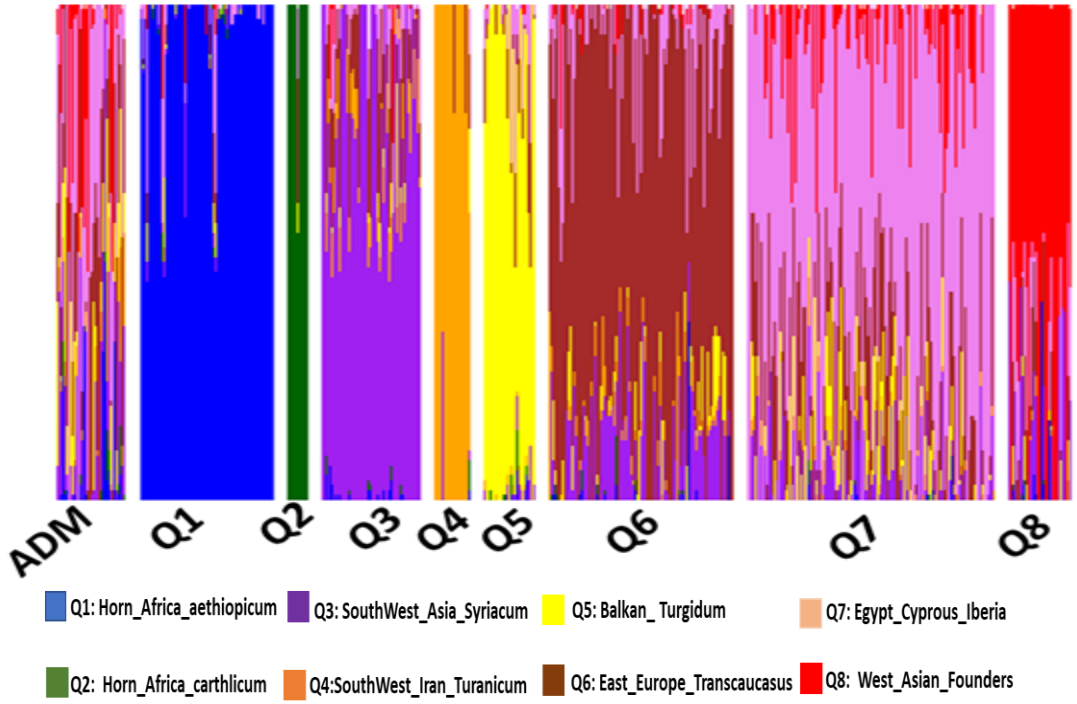

Figure 17: This figure displays a more accurate subdivision of genotypes based on their Population structure membership score deriving from Admixture analyss. In this case, Genotype are grouped based on the same belonging Q. This is also confirmed by the colours. ADM stands for Admixed.

Table 3: Summary table displaying the total number of accessions in each considered environment (highlighted in yellow) and the total number of subpopulations representative. Highlighted in grey, the subpopulations containing more than 50 individuals, namely, selection criterion used to conduct GWAS within the single subpopulations.

SUBPOPULATIONS	3.3.3 **Gro_2018**	**Gro_2019**	**Lar_2019**	**Izmir_2019**	**Bej_2020**	**Kod_2020**	**Gro_2020**	**Gro_2021**	**1st_CLUSTER**	**2nd_CLUSTER**
Q1	10	100	89	89	171	185	198	23	113	92
Q2	0	0	0	0	12	15	15	0	10	0
Q3	39	75	61	61	108	116	129	43	81	68
Q4	2	4	3	3	4	9	11	2	11	3
Q5	4	8	5	5	34	39	42	20	35	6
Q6	54	117	92	94	157	193	222	111	165	99
Q7	72	112	83	83	209	225	268	126	175	95
Q8	24	54	35	37	36	39	67	51	67	37
ADM	19	43	31	31	57	68	82	46	65	35
Total	224	513	399	403	788	889	1034	422	722	435

2.3.4 LD decay estimation for Tetraploid Global Collection (TGC)

All 20,235 SNP markers from Illumina 90K SNP Array (Wang et al., 2014) were utilized to estimate the pairwise linkage disequilibrium (LD) squared correlation coefficients (r^2) across all chromosomes in both the GDP and TGC panels. The genome-wide LD patterns for the 1,324 landraces were analyzed using Tassel 5.0, and the results were graphically represented through a nonlinear regression model of the pairwise LD r^2 against physical distance in the genotyping matrix (hapmap) (See Figure 18). As anticipated, LD decay was notably high in the TGC collection due to its significant genetic variability, underscored by subpopulation subdivision. High LD values ($r^2 = 0.8$) and medium LD values ($r^2 = 0.5$) were observed at distances of 0.0696 Mb and 0.277 Mb, respectively, while lower LD values of $r^2 = 0.3$, $r^2 = 0.2$ and $r^2 = 0.1$ reached at distances of 0.648 Mb, 1.11 Mb and 2.5 Mb (See Figure 20).

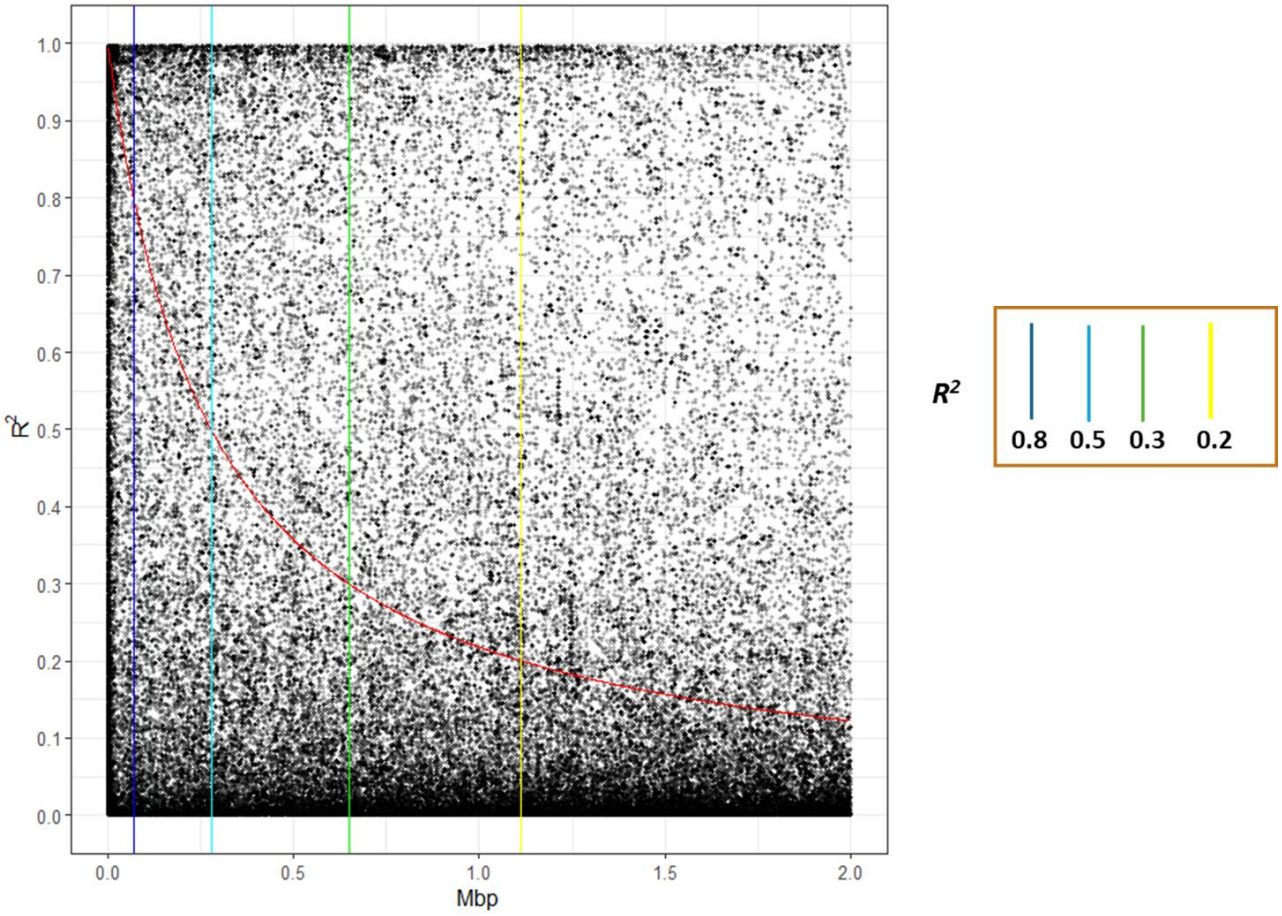

Figure 18: Plot of pair-wise single-nucleotide polymorphism LD r^2 values. X axis represents the progressive physical distance in Mbp and the y axis refers to the LD R^2 ranging from 0 up to 1. The red curve represents the model fit to LD decay. The blue, light-blue, green, yellow vertical lines indicate the physical position in correspondence of R2, 0.8 (high linkage), 0.5 (medium linkage), 0.3 (low linkage), 0.2 (low linkage

2.3.5 Yr Loci and QTL projection onto the Svevo reference genome physical map

All previously mapped or cloned Yr and YRqtl were mapped onto Svevo reference based on the criteria described previously. The high level of synteny between the Chinese Spring hexaploid wheat reference genome and the Svevo tetraploid wheat reference genome provides a valuable framework for projecting quantitative trait loci (QTLs) identified in one species onto the other. This genomic conservation facilitates the comparison and transfer of genetic information across different wheat types, particularly in the context of yellow rust resistance (Yr loci). Numerous previously mapped Yr loci have been characterized in bread wheat, and leveraging the conserved synteny allows for these loci to be accurately projected onto the Svevo reference genome. As for Yr loci, only the ones detected in A and B subgenomes were projected, whereas different projection criteria were used for linkage mapping and association studies. Herein, you find a summary table with the CI of the projected Yr loci in A and B subgenomes and another table summarising the independent QTL mapping studies used for QTLs projection, subdivided by Linkage mapping populations and GWAS:

Table 4: Summary table showing the CI of the projected Yr loci onto the Svevo reference genome. In addition to the locating chromosome, the table displas also the starting, middle and end point of the projected CI. The type of resistance is also reported, namely, ASR (All-Stage-resistance) or APR (Adult-Plant Resistance). Reference(s) for each Yr loci is reported.

Yr Loci	Chr	START(Mbp)	END (Mbp)	midpoint (Mbp)	Type of Resistance	PUBBLICATION(S)
Yr10	1B	1.54	7.14	3.82	ASR	Yuan C et al. (2018); Maccaferri M et al. (2015);Liu W et al. (2014) ;Ma JX et al. (2001)
Yr9	1B	3.84	19.46	4.93	ASR	Maccaferri M et al. (2015) ; Weng DX et al. (2005)
Yr84	1B	4.92	8.22	6.66	ASR	Klymiuk, V et al.(2022)
Yr85	1B	25.66	50.95	35.21	ASR	Feng J et al. (2024)
YrAlp	1B	27.19	268.18	41.68	ASR	Maccaferri M et al. (2015); Lin F and Chen XM (2007)
Yr15	1B	47.63	66.91	51.85	ASR	Qie YM et al. (2019), Maccaferri M et al. (2015)
YrH52	1B	52.51	90.03	62.54	ASR	Maccaferri M et al. (2015); Cheng P et al. (2014)
Yr64	1B	53.33	140.38	100.22	ASR	Qie YM et al. (2019); Maccaferri M et al. (2015) ;Maccaferri M et al. (2015)
Yr65	1B	294.39	341.56	315.75	ASR	Cheng P et al. (2014)
Yr24	1B	341.56	411.21	362.82	ASR	Huerta-Espino J and Singh RP (2017); Li GQ et al. (2006)
Yr26	1B	341.56	411.21	362.82	ASR	Cheng P et al. (2014); Zhang X et al. (2013)
YrExp1	1B	618.30	635.05	626.96	APR	Lin F and Chen XM (2008); Maccaferri M et al. (2015)
Yr29/Lr46	1B	661.20	678.52	670.27	APR	Cobo N et al. (2019); William M et al. (2003); Hou L et al. (2015)
Yr21	1B	NP	NP	NP	ASR	Chen XM et al., (1995)
Yr69	2A	0.03	10.99	10.21	ASR	Hou, L. Y.,(2016); Yufan Wang et al. (2022)
Yr17	2A	0.03	46.87	21.50	ASR	Juliana P et al. (2018); Sthapit J et al. (2012) ; Bariana HS and McIntosh RA (1993)
Yr56	2A	2.14	15.70	9.31	ASR	Maccaferri M et al. (2015);
Yrxy2	2A	463.18	598.09	560.74	APR	Maccaferri M et al. (2015); Zhou XL et al. (2011)
Yr32	2A	677.34	716.90	686.14	ASR	Maccaferri M et al. (2015); Eriksen L et al. (2004);
Yr86	2A	707.33	707.33	707.33	APR	Cao et al., (2024)
Yr1	2A	757.72	767.22	766.29	ASR	Maccaferri M et al. (2015); Lupton FCH and Macer RCF (1962);Bansal UK et al. (2009)
YrP81	2B	68.32	97.94	88.89	ASR	Pu ZJ et al. (2009); Maccaferri M et al. (2015)

YrC51	2B	69.89	101.95	88.89	ASR	Maccaferri M et al. (2015);Zheng J et al. (2014)
Yr41	2B	92.44	210.33	148.21	ASR	Maccaferri M et al. (2015); Luo PG et al. (2008); Luo PG et al. (2005)
YrKK	2B	101.24	170.65	143.62	APR	Maccaferri M et al. (2015); Li Z et al. (2013)
Yr31	2B	101.95	121.06	106.92	ASR	Singh RP et al., (2003); Rosewarne et al., (2012)
YrH9014	2B	120.78	135.33	122.16	ASR	Maccaferri M et al. (2015); Ma DF et al. (2013)
Yr27	2B	146.29	158.32	152.20	APR	Athiyannan N et al. (2022); McDonald DB et al. (2004)
Yr5	2B	647.19	677.24	668.91	APR	Maccaferri M et al. (2015); Zhang P et al. (2009); Sun Q et al. (2002); Macer RCF (1966)
Yr44	2B	647.95	677.24	649.45	ASR	Maccaferri M et al. (2015); Xu LS et al. (2013); Cheng P and Chen XM (2010); Sui XX et al. (2009)
Yr7	2B	672.75	705.44	673.74	ASR	Gardiner L-J et al., (2020); Marchal, C. et al., (2018)
Yr53	2B	677.24	731.93	701.10	ASR	Maccaferri M et al. (2015); Xu LS et al. (2013)
Yr43	2B	731.93	746.73	741.30	ASR	Maccaferri M et al. (2015); Xu LS et al. (2013); Cheng P and Chen XM (2010)
Yr72	2B	752.08	761.24	754.99	ASR	Chhetri M, et al. 2015
Yr3	2B	769.23	778.03	773.21	ASR	Maccaferri M et al. (2015) ;Lupton FCH and Macer RCF (1962)
Yr76	3A	12.89	18.36	15.84	ASR	Xiang, C. et al., (2016.)
Yr4	3B	0.30	3.66	1.54	ASR	Maccaferri M et al. (2015); Lupton FCH and Macer RCF (1962)
Yr57	3B	0.30	17.44	3.42	ASR	Randhawa MS et al. (2015); Maccaferri M et al. (2015)
Yr30_ICARDA	3B	0.51	6.23	1.10	APR	Singh RP (2005);Basnet BR et al., (2012); Wang X et al. (2024)
Yr58	3B	1.40	2.64	2.03	APR	Bansal et al., (2013)
Yrns-B1	3B	15.23	17.85	16.39	ASR	Boerner A et al. (2000); Maccaferri M et al. (2015)
Yr80	3B	550.82	609.40	552.75	APR	Nsabiyera V et al. (2018); Li H et al. (2020)
Yr82	3B	752.56	755.22	754.48	ASR	Pakeerathan, (2019)
Yr51	4A	675.51	710.65	697.05	ASR	Randhawa M et al. (2014)
Yr60	4A	720.85	722.90	722.88	ASR	Herrera-Foessel SA et al. (2015); Maccaferri M et al. (2015)
Yr50	4B	396.24	646.42	530.54	ASR	Maccaferri M et al. (2015); Liu J et al. (2013)
Yr62	4B	504.88	574.12	557.36	APR	Maccaferri M et al. (2015); Lu Y et al. (2014)

Yr68	4B	579.49	604.53	583.43	APR	Ellis, J. G et al.,(2014)
Yr48	5A	651.23	668.64	667.29	APR	Maccaferri M et al. (2015); Lowe I et al. (2011)
Yr34	5A	665.73	668.64	667.29	APR	Maccaferri M et al. (2015); Bariana HS et al. (2006)
Yr47	5B	7.73	19.50	9.79	ASR	Maccaferri M et al. (2015); Bansal UK et al. (2011);Qureshi N et al., (2017)
Yr74	5B	526.58	#VALORE!	528.31	ASR	Dracatos et al.(2016)
YrExp2	5B	531.35	540.71	533.65	ASR	Maccaferri M et al. (2015); Lin F and Chen XM (2008)
Yr19	5B	NP	NP	NP	ASR	Chen XM et al., (1995)
Yr81	6A	1.03	4.92	2.38	ASR	Gessese M et al. (2019)
YrLM168	6A	586.90	598.71	591.44	ASR	Maccaferri M et al. (2015); Feng J et al. (2014)
Yr38	6A	NP	NP	NP	ASR	Marais GF at al., 2010
Yr35	6B	1.65	47.75	19.10	ASR	Marais GF et al., (2005); Dadkhodaie NA et al., (2011)
Yr78	6B	67.34	115.75	88.88	APR	Dong ZZ et al., (2017)
Yr36	6B	121.50	139.71	129.28	APR	Uauy C et al. (2005); Segovia, V., et al., (2014)
Yr61	7A	81.34	257.75	131.53	ASR	Maccaferri M et al. (2015) ; Zhou XL et al. (2014)
Yrxy1	7A	606.72	654.56	638.76	APR	Maccaferri M et al. (2015);Zhou XL et al. (2011)
Yr75	7A	704.96	713.25	711.85	ASR	Kanwal, M., et al.,(2021).
Yr63	7B	1.03	5.95	3.74	ASR	Maccaferri M et al. (2015)
Yr79	7B	222.95	243.59	227.04	APR	Feng J et al. (2018)
Yr39	7B	247.27	620.99	552.99	APR	Maccaferri M et al. (2015); Lin F and Chen XM (2007)
yrMY37	7B	247.27	369.39	302.28	ASR	Ren, Y. (2015).
Yr6	7B	691.59	693.58	692.27	ASR	Ma J, et al., (2015); Gardiner L-J et al., (2016)
Yr67	7B	696.33	709.15	700.02	APR	Bariana, H et . Al (2022) ;Bansal U (2014)
YrZH84	7B	700.01	707.95	703.38	ASR	Maccaferri M et al. (2015); Li ZF et al. (2006)
Yr59	7B	703.84	711.76	707.95	ASR	Maccaferri M et al. (2015); Zhou XL et al. (2014)
Yr52	7B	706.92	711.31	707.95	APR	Maccaferri M et al. (2015); Ren RS et al. (2012)
Yr2	7B	NP	NP	NP	ASR	Mcintosh RaA et al., (1995)

Yr11	ND	NP	NP	NP	APR	Mcintosh RaA et al., (1995)
Yr12	ND	NP	NP	NP	APR	Mcintosh RaA et al., (1995)
Yr13	ND	NP	NP	NP	APR	Mcintosh RaA et al., (1995)
Yr14	ND	NP	NP	NP	APR	Mcintosh RaA et al., (1995)

Table 5: Summary table listing alle the independent QTL mapping studies considered for the Yrqtl projection.

LINKAGE MAPPING POPULATION			
Reference	**Population Type**	**Population Size**	**QTLs Number**
Zhou et al., (2021)	RILs	137	48
Firdissa E. Bokore et al., (2021)	DH	87	14
Lin X et al., (2018)	DH	155	5
GWAS			
Liu et al., (2017b)	elite durum cultivars	250	16
Liu et al., (2017c)	Dicoccum panel	176	37
Liu et al., (2017d)	Ethiopian durum wheat landraces	182	80
Mehrabi et al., (2022)	durum wheat landraces	123	186
Aoun et al., (2021)	durum wheat cultivars	248	4
Miedaner et al., (2019)	durum wheat cultivars	328	6
Alemu et al., (2021)	durum wheat cultivars and landraces	300	4
Marone et al (2024)	durum wheat cultivar	230	12

All the projected QTLs are listed in Summary table S1 (See summary files).

2.3.6 GWAS RESULTS

2.3.6.1 Global GWAS

GTC panel was used to perform GWAS for each of the eight single environments separately and the 2 detected multi-environmental clusters. SNPs were picked as MTAs only when LOD score for either IT or SEV was ≥ 3 in at least two models and detected in at least two environments. As a whole, eleven QTLs were identified as significantly associated with either infection type (IT) or severity (SEV) of yellow rust resistance on several chromosomes: 1B (QYr.ubo-1B.1, QYr.ubo-1B.2), 2A (QYr.ubo-2A.1, QYr.ubo-2A.2), 2B (QYr.ubo-2B.1, QYr.ubo-2B.2), 5B (QYr.ubo-5B.1, QYr.ubo-5B.2), 7A (QYr.ubo-7A.1), and 7B (QYr.ubo-7B.1, QYr.ubo-7B.2) (see Summary Table 4 for Global GWAS). QYr.ubo-1B.1 demonstrated significant results in Grosseto 2019 and Grosseto 2020 but was not significant in Grosseto 2021, as well as in Izmir 2019 (IT) and Lari 2019. Conversely, it exhibited high significance in Beja 2020 (p-value < 0.00001) and low significance in the first and second SEV multi-environmental clusters for landraces, Kodia 2020 (IT) and Izmir 2019 (SEV). The additional QTL on chromosome 1B, QYr.ubo-1B.2, had the highest number of significant associations, being significant across nearly all environments except

Grosseto 2018, with an individual percentage of variation explained (PVE) ranging from 0.77% to 3%. Although QYr.ubo-2A.1 was not significant in the first environmental cluster, it was significantly associated in both Izmir 2019 and Grosseto 2019, which are part of that cluster. In contrast, QYr.ubo-2A.1 was also significant in the second environmental cluster and Lari 2019, with global PVEs for IT and SEV ranging from 3% to 6%. Additionally, QYr.ubo-2A.2, QYr.ubo-2B.1, and QYr.ubo-7A.1 were significant in both environmental clusters and the corresponding individual environments included in them. QYr.ubo-5B.2 showed an interesting case of environmental specificity, being significant only in Lari 2019, with estimated PVEs of 1.42% for IT and 4.21% for SEV, and also in the second environmental cluster stemming from Lari 2019 and Grosseto 2018. Another notable example of environmental specificity was QYr.ubo-7B.2, which was significant only in Lari 2019, the first environmental cluster, Izmir 2019, and Grosseto 2019 within the same cluster. QYr.ubo-7B.1 was significant across all TGC environments except in the second cluster (SEV), Grosseto 2020, Kodia 2020 (SEV), and Lari 2019 (IT). This QTL exhibited the highest PVE for both IT and SEV in TGC, ranging from 3% to 9%. Overall, the eleven detected QTLs explained a considerable range of multiple R-squared values across all environments, from 18.52% to 53.66% for IT and from 14.30% to 49.94% for SEV. The confidence interval of each QTL was defined as the haploblock containing the peak marker, as determined by LD-based analysis using Haploview. For each QTL, the start and end points correspond to the physical positions of the linked markers (see figures). The phenotypic variance explained by each QTL in the evaluated environments was estimated using a linear model (lm). ANOVA test was performed to estimate the significance. All Manhattan Plots are available in supplementary files.

Table 6: Summary table showing the results of the global GWAS and subsequent Linear Model and Anova Test for each selected MTAs. This table comprises several information, from top to bottom: QTL acronym, MTA (SNP), alleles (major/mino), chromosome, position (Mbs), Block start position (Mbp), Block end postion (Mbp), overlapping projected Yr confidence intervals, overlapping QTL detected also in the single subpopulation, maximum LOD for that MTA across all the environments, maximum single R2 across all the environments, Adjusted R-squared for alle the environments and multi-environmental clusters (%) and results of the statistically significant ANOVA test within each environment or environmental cluster: NS stands for non-significant, NA stands for Not applicable (removed by MAF), * 0.05 – 0.01, ** 0.01-0.001, *** 0.0001-0.00001, **** < 0.00001

QTL name	***QYr.ubo-1B.1***	***QYr.ubo-1B.2***	***QYr.ubo-2A.1***	***QYr.ubo-2A.2***	***QYr.ubo-2B.1***	***QYr.ubo-2B.2***	***QYr.ubo-5B.1***	***QYr.ubo-5B.2***	***QYr.ubo-7A.1***	***QYr.ubo-7B.1***	***QYr.ubo-7B.2***
SNP	**IWB31756**	**IWB30252**	**IWB24147**	**IWA1579**	**IWB32197**	**IWB32488**	**IWB32919**	**IWB23006**	**IWB8440**	**IWB71291**	**IWA1436**
Alleles	G/T	T/C	G/A	A/G	A/G	C/T	T/C	A/G	T/C	C/T	C/T
Chromosome	1B	1B	2A	2A	2B	2B	5B	5B	7A	7B	7B
Position (Mbs)	318.23	548.16	13.06	392.89	16.96	647.25	682.18	465.85	535.85	696.94	41.73
Block_start position (Mbo)	318.23	548.15	10.21	392.89	16.95	642.90	681.25	463.87	535.85	696.94	41.72
Block_end position (Mbo)	318.41	548.28	13.73	407.33	16.96	647.95	682.58	467.80	536.64	699.08	41.73
Overlapping_Yr_Loci	*Yr65*		*Yr17*, *Yr56*, *Yr69*			*Yr5*, *Yr44*					*Yr67*
Subpopulations_landraces	Q1						Q3, Q6		Q1	Q7	Q7
Projected_QTL			Zhou X L et al., 2021	Liu et al., 2017b	Liu et al., 2017d; Firdissa E. Bokore et al., 2021		Liu et al., 2017d	Mehrabi et al., 2022; Liu et al., 2017d		Xue Lin et al., 2018	
LOD (max)	4.2	6.44	3.54	9.13	7.24	3.23	4.74	6.68	7.72	9.79	7.32
R^2 (%) (max)	2.57	2.72	6.03	4.75	3.81	6.86	2.74	4.21	5.6	9.37	3.69
IT/SEV Adjusted R-	**Anova Test**										

		squared (%)											
Across Environments_ landraces_ 1	IT	35.5	*	*	NA	****	**	NS	***	NA	***	****	**
	SEV	30.5	**	***	NA	****	*	*	***	NA	***	****	*
Across Environments_ landraces_ 2	IT	47.9	NS	*	****	NS	***	NS	*	**	****	NS	NS
	SEV	44.7	*	**	****	***	****	NS	**	**	****	****	NS
Grosseto (GRO)_2018	IT	17.1	NS	NS	NA	**	NS	**	NS	NS	NS	*	NS
	SEV	28.6	NS	NS	NA	*	NS	****	NS	NS	NS	***	NS
Grosseto (GRO)_2019	IT	38.2	*	***	****	****	***	NS	**	NS	*	****	*
	SEV	29.5	*	***	****	****	**	NS	*	NS	**	***	NS
Grosseto (GRO)_2020	IT	17.2	*	***	NA	*	NS	NS	NS	NS	NS	NS	NS
	SEV	13.9	**	**	NA	***	NS	***	NS	NS	NS	NS	NS
Grosseto (GRO)_2021	IT	17.5	NS	NS	NA	****	NS	NS	**	NS	NS	****	NS
	SEV	23.7	NS	*	NA	****	NS	*	***	NS	NS	****	NS
Beja (BEJ)_2020	IT	13.8	****	**	NA	NA	NS	*	NS	NS	NS	*	NS
	SEV	14.7	****	***	NA	NA	NS	NS	**	NS	NS	***	NS
Kodia (KOD)_2020	IT	28	NS	****	NA	NA	*	NS	***	NS	**	*	NS
	SEV	12.6	*	***	NA	NA	NS	NS	*	NS	NS	NS	NS
Lari (LAR)_2019	IT	51.2	NS	**	***	NS	**	NS	NS	*	****	NS	NS
	SEV	47.5	NS	**	****	***	***	NS	*	****	****	***	*
Izmir (IZM)_2019	IT	38.4	NS	**	***	**	NS	NS	*	NS	**	****	***
	SEV	43.7	**	*	****	**	NS	NS	*	NS	***	****	***

Table 7: Summary table presenting the results of the linear model for Qs. This table outlines the total phenotypic variance attributed to Qs in each environment, along with the ANOVA test results for each Q across all examined environments for both IT and SEV.

		Qs	**Q1**	**Q2**	**Q3**	**Q4**	**Q5**	**Q6**	**Q7**	**Q8**
Environments	IT/SEV	Adjusted R-squared (%)	**Anova Test**							
Across Environments_landraces_1	IT	20.15	****	***	****	****	NS	***	***	***
	SEV	11.58	****	*	****	****	NS	NS	NS	***
Across Environments_landraces_2	IT	35.56	****	NS	****	****	NS	****	****	*
	SEV	28.7	****	**	****	****	NS	****	****	**
Grosseto (GRO)_2018	IT	13.16	NS	NS	NS	***	NS	NS	NS	*
	SEV	10.09	NS	*	NS	****	NS	NS	NS	**
Grosseto (GRO)_2019	IT	19.59	****	***	****	****	NS	*	***	****
	SEV	13.43	NS	**	****	****	NS	NS	NS	****
Grosseto (GRO)_2020	IT	12.15	****	*	****	****	NS	NS	*	****
	SEV	8.2	**	NS	****	****	NS	**	NS	NS
Grosseto (GRO)_2021	IT	6.17	NS	NS	**	****	NS	NS	NS	***
	SEV	9.58	*	*	***	****	NS	NS	NS	*
Beja (BEJ)_2020	IT	7.28	*	NS	*	*	*	**	****	NS
	SEV	5.34	****	NS	****	**	NS	**	NS	NS
Kodia (KOD)_2020	IT	22.29	****	NS	***	****	****	****	****	***
	SEV	8.08	****	NS	NS	**	**	***	***	****
Lari (LAR)_2019	IT	39.56	****	NS	****	****	*	****	****	****
	SEV	29.72	****	**	****	****	NS	**	****	**
Izmir (IZM)_2019	IT	19.36	****	**	****	****	NS	*	**	NS
	SEV	22.03	****	**	****	****	NS	NS	**	NS

- ***QYr.ubo-1B.1***

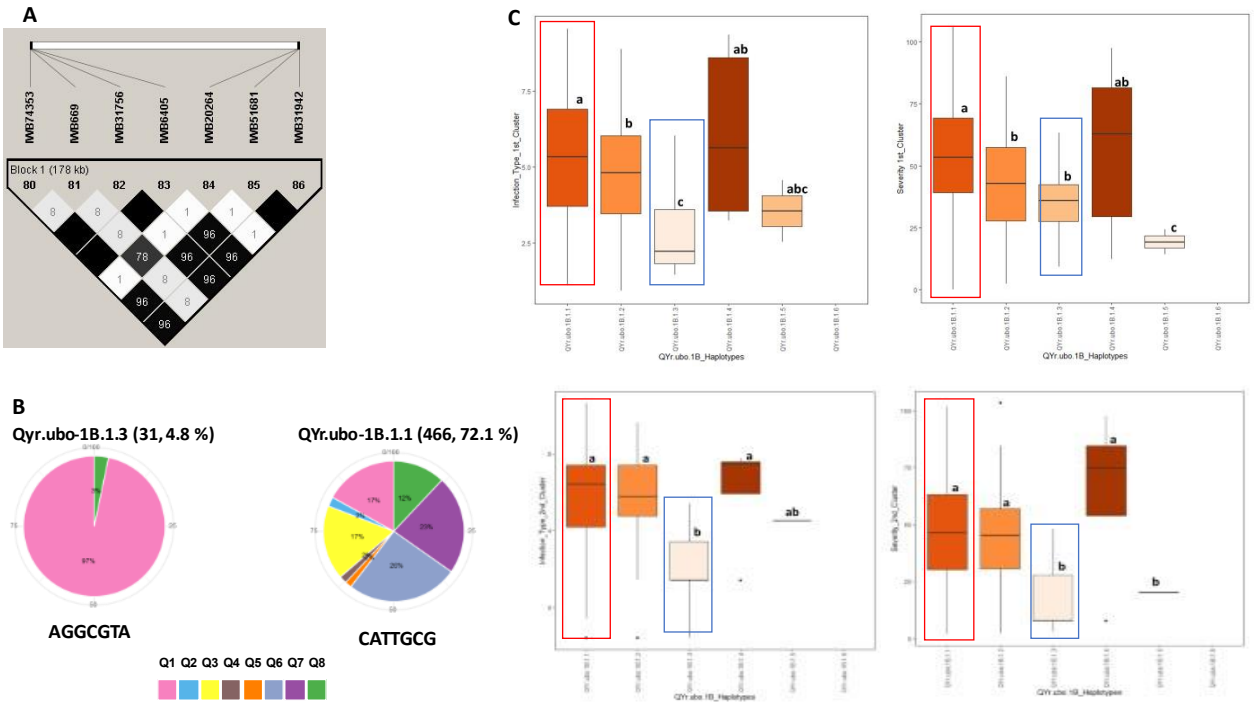

Figure 19: This figure displays the *QYr.ubo-1B.1* haploblock. A: *QYr.ubo-1B.1* LD-block. IWB31756 (82) highlighted in red is the peak marker of the QTL. B: The frequency of the most resistant (*QYr.ubo-1B.1.3*) and most susceptible (*QYr.ubo-1B.1.1*) haplotypes within the single subpopulations is displayed C: Comparison of the phenotypic performance of all identified haploblock variants of *QYr.ubo-1B.1* in terms of infection type (IT) and severity (SEV) within the first and second environmental clusters. Resistant haplotypes is encircled with a blue rectangle, whereas chosen susceptible haplotype is in red.

A clear distinction between resistant and susceptible haplotypes was observed for *QYr.ubo-1B.1* (figure 19). *QYr.ubo-1B.1.3* was the most resistant haplotype overall and was deeply conserved in Q1 (Horn_Africa_Asia_aethiopicum) and partially in Q8 (West_Asian_Founders) with a frequency of 4%. *QYr.ubo-1B.1.5* gave evidence to be a resistant haplotype but was very rare and present in 3 subpopulations (DWL_East_Europe_Transcaucasus, Egypt_Cyprous _Iberia and West_Asian_Founders*).* *QYr.ubo-1B.1.1* was the most frequent haplotype with a long range and was widely spread across all the TGC subpopulations with different frequency. Similarly, QYr.ubo-1B.1.2 and *QYr.ubo-1B.1.3* were susceptible haplotypes with a frequency highly diversified across the subpopulations. A summary table displaying the frequency within each subpopulation, the total count and mean value for IT and SEV is reported below (Table 8):

Table 8: A summary table displaying the frequency of *QYr.ubo-1B.1* haplotype variants within each subpopulation, the total count and mean value for IT and SEV.

Haplotype Acronym	Haplotype Variant	Global Count	1st_cluster		2nd_cluster		adm	Q1	Q2	Q3	Q4	Q5	Q6	Q7	Q8
			IT	SEV	IT	SEV									
QYr.ubo.1B.1.1	AGGCGTA	1122	5.30	53.87	5.56	46.36	78	190	35	162	59	24	223	266	85
QYr.ubo.1B.1.2	AAGCATA	380	4.75	43.11	5.71	45.14	45	3	1	4	0	64	96	153	14
QYr.ubo.1B.1.3	CATTGCG	51	2.84	35.77	2.13	16.97	0	50	0	0	0	0	0	0	1
QYr.ubo.1B.1.4	AAGCGTA	13	6.04	56.93	6.01	63.63	0	2	0	2	0	0	3	6	0
QYr.ubo.1B.1.5	AGGCATA	6	3.54	19.27	4.50	20.19	0	0	0	0	0	0	2	3	1

- ***QYr.ubo-1B.2***

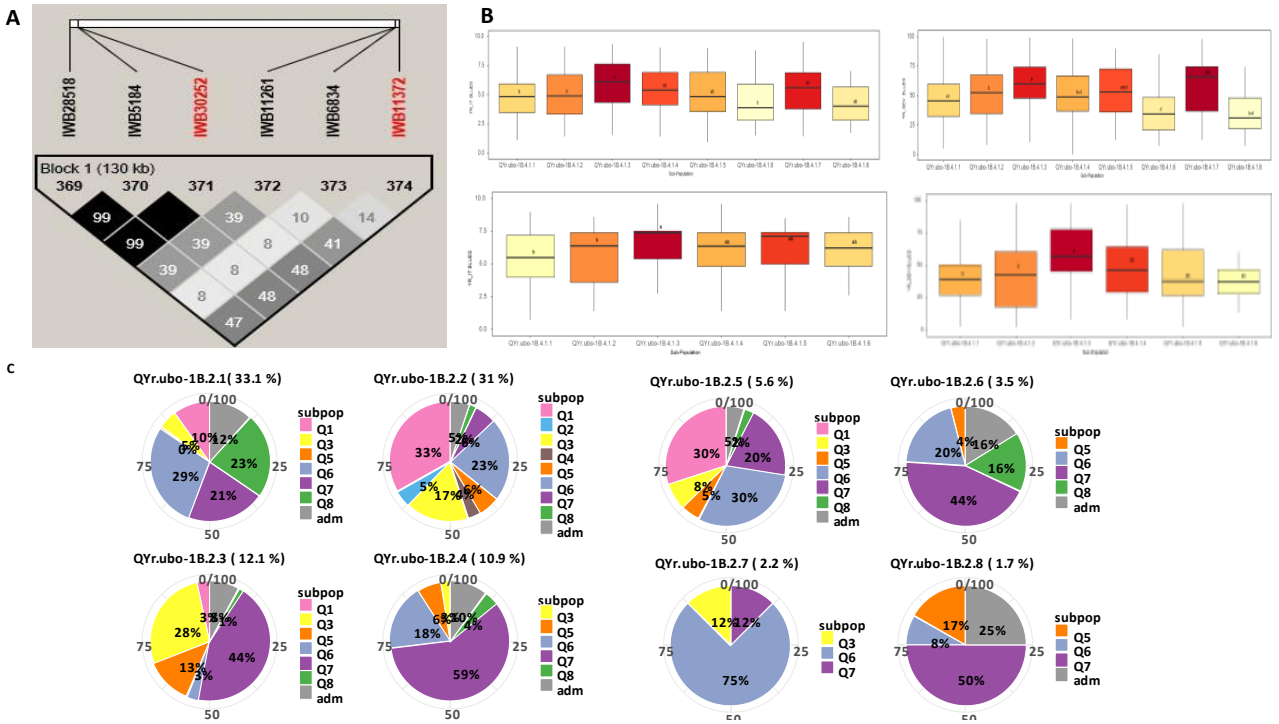

Figure 20: This figure displays the *QYr.ubo-1B.2* haploblock. A: *QYr.ubo-1B.2* LD-block. IWB30252 (371) and IWB11372 (374) highlighted in red is the peak marker of the QTL. B: Comparison of the phenotypic performance of all identified haploblock variants of *QYr.ubo-1B.2* in terms of infection type (IT) and severity (SEV) within the first and second environmental clusters. C: The frequency of *all QYr.ubo-1B.2* haplotypes variants within the single subpopulations is displayed.

In contrast to *QYr.ubo-1B.1.1*, *QYr.ubo-1B.2* did not show a clear differentiation between resistant and susceptible haplotypes (figure 20). A total of eight haplotypes were identified for this QTL, but

with the exception of *QYr.ubo-1B.2.7*, all haplotype variants were widely distributed across more than four subpopulations (refer to summary table 9).

Table 9: A summary table displaying the frequency of *QYr.ubo-1B.2* within each subpopulation, the total count and mean value for IT and SEV.

Haplotype_Acronym	Haplotype_Variant	Count	1st_cluster		2nd_cluster		adm	Q1	Q2	Q3	Q4	Q5	Q6	Q7	Q8
			IT	SEV	IT	SEV									
QYr.ubo-1B.2.1	CGCCCC	237	4.76	45.99	5.19	39.74	28	24	0	12	0	1	68	50	54
QYr.ubo-1B.2.2	AATTCT	222	4.97	52.49	5.11	44.07	12	74	10	38	8	13	50	13	4
QYr.ubo-1B.2.3	AATCCT	87	5.93	60.57	6.63	58.30	7	3	0	24	0	11	3	38	1
QYr.ubo-1B.2.4	CGCCTC	78	5.46	50.08	5.72	48.76	8	0	0	2	0	5	14	46	3
QYr.ubo-1B.2.5	AATCCC	40	4.96	52.03	5.08	43.01	2	12	0	3	0	2	12	8	1
QYr.ubo-1B.2.6	AATCTC	25	4.51	37.39	5.88	35.90	4	0	0	0	0	1	5	11	4
QYr.ubo-1B.2.7	AATTCC	16	5.53	59.44	6.86	70.41	0	0	0	2	0	0	12	2	0
QYr.ubo-1B.2.8	CGCCCT	12	4.24	35.95	6.00	40.73	3	0	0	0	0	2	1	6	0

- ***QYr.ubo-2A.1***

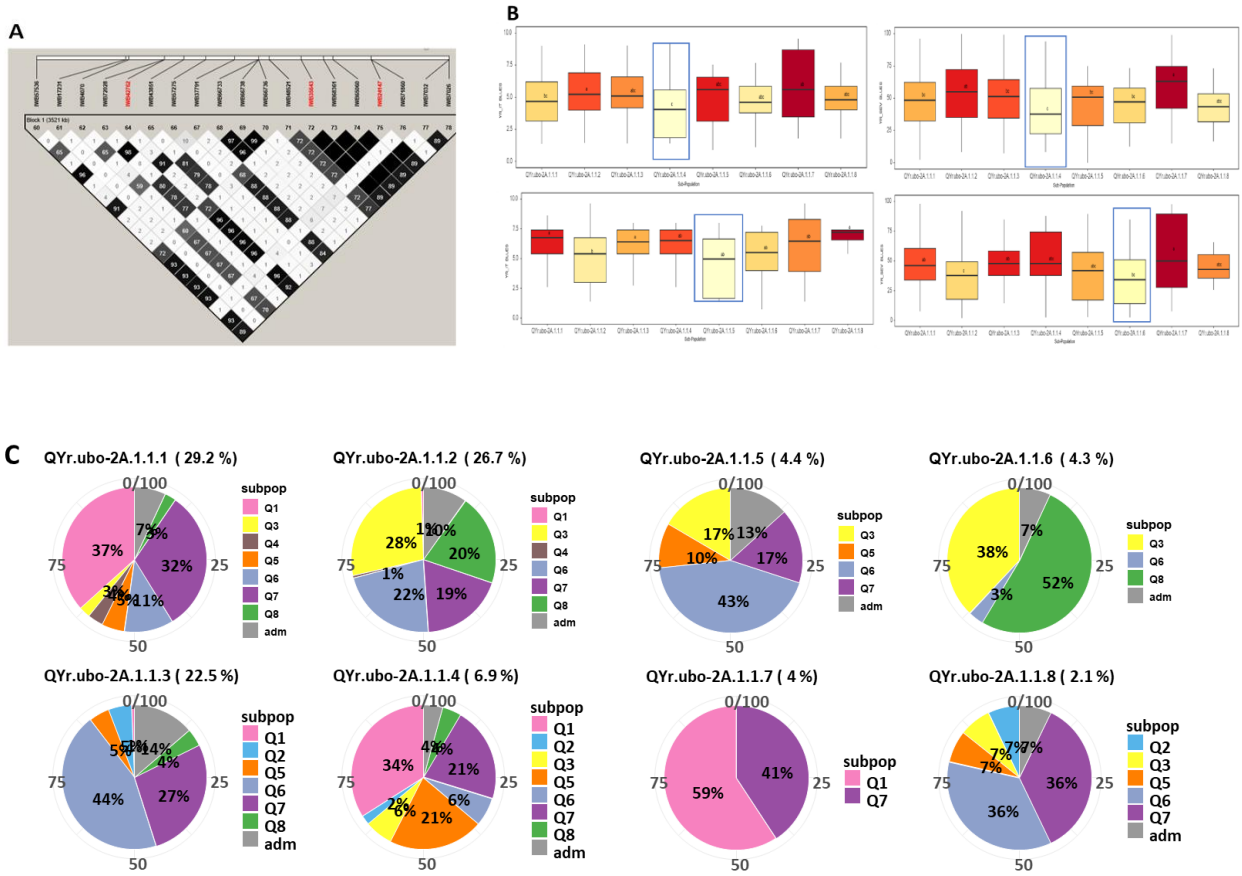

Figure 21: This figure displays the QYr.ubo-2A.1 haploblock. A: QYr.ubo-2A.1 LD-block. IWB42762 (64), IWB35643 (72) and IWB24147 (75) highlighted in red is the peak marker of the QTL. B: Comparison of the phenotypic performance of all identified haploblock variants of QYr.ubo-2A.1in terms of infection type (IT) and severity (SEV) within the first and second environmental clusters. C: The frequency of all QYr.ubo-2A.1 haplotypes variants within the single subpopulations is displayed.

QYr.ubo-2A.1 exhibited 24 haplotypes variants in total but for the sake of clarity, only the first 8 haploblock variants have been displayed and *QYr.ubo-2A.1.4* was the only haplotype showing a slight resistant haplotype as compared to the all the other haplotypes which are all leveled (figure 21)**.** Except for QYr.ubo-2A.1.7, all haplotype variants were widely distributed across several subpopulations (See summary table 10).

Table 10: A summary table displaying the frequency of QYr.ubo-2A.1 within each subpopulation, the total count and mean value for IT and SEV.

Haplotype_Acronym	Haplotype_Variant	Count	1st_cluster		2nd_cluster		adm	Q1	Q2	Q3	Q4	Q5	Q6	Q7	Q8
			IT	SEV	IT	SEV									
QYr.ubo-2A.1.1	GGACCGGCACATAGTGGTC	199	4.76	48.20	6.16	48.58	14	73	0	5	7	10	22	63	5
QYr.ubo-2A.1.2	GGATCAGCGTGTAGTGGTC	182	5.40	54.50	4.15	36.92	18	1	0	51	1	0	40	34	37
QYr.ubo-2A.1.3	GGACCGGCACATAGTGATC	153	5.22	49.78	5.98	48.89	21	1	8	0	0	7	68	42	6
QYr.ubo-2A.1.4	GAACCGGCACATAGTGGTC	47	4.24	42.91	5.71	51.53	2	16	1	3	0	10	3	10	2
QYr.ubo-2A.1.5	GAATCAGCGTGTAGTGGTC	30	4.87	44.18	4.53	40.86	4	0	0	5	0	3	13	5	0
QYr.ubo-2A.1.6	GAACCGGCGTGTAGTGGTC	29	4.48	44.28	5.25	34.42	2	0	0	11	0	0	1	0	15
QYr.ubo-2A.1.7	AGGCAGGTACACGAGAGCT	27	5.70	64.28	5.88	58.19	0	16	0	0	0	0	0	11	0
QYr.ubo-2A.1.8	GAACCGGCACATAGTGATC	14	4.99	44.84	7.04	44.01	1	0	1	1	0	1	5	5	0

- ***QYr.ubo-2A.2***

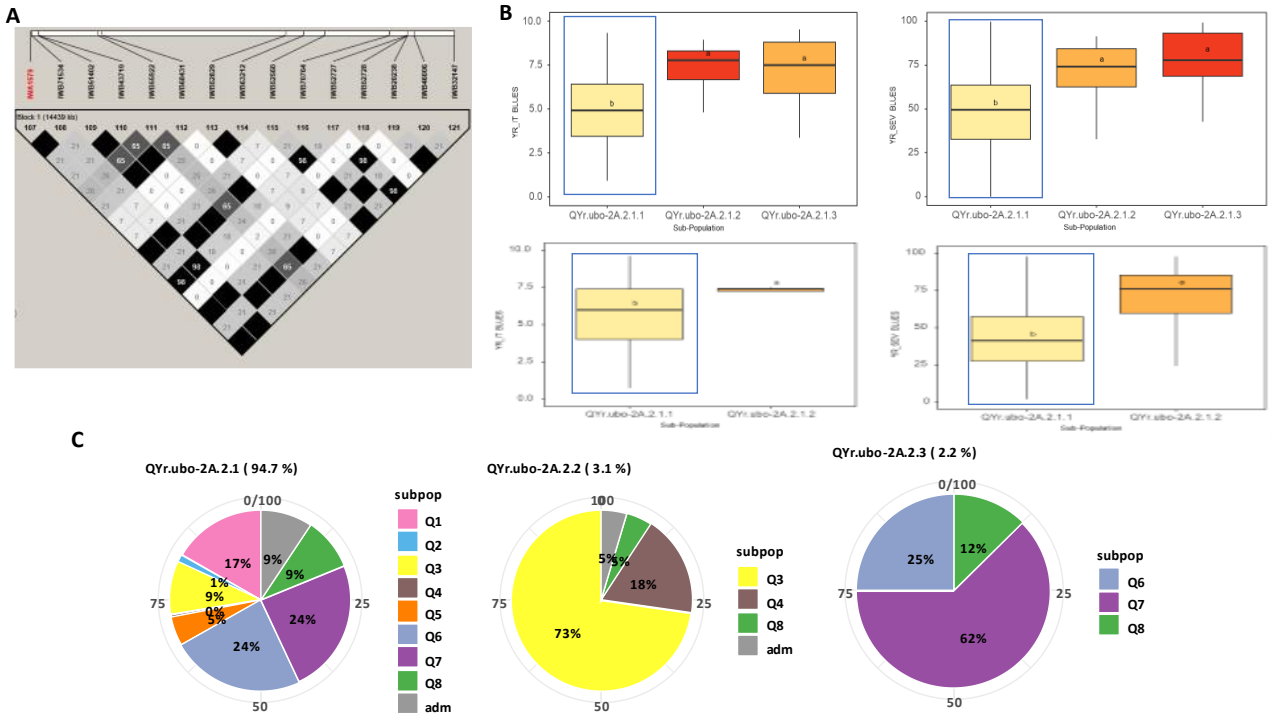

Figure 22: This figure displays the *QYr.ubo-2A.2* haploblock. A: *QYr.ubo-2A.2* LD-block. IWA1579 (107) highlighted in red is the peak marker of the QTL. B: Comparison of the phenotypic performance of all identified haploblock variants of QYr.ubo-2A.1in terms of infection type (IT) and severity (SEV) within the first and second environmental clusters. C: The frequency of all *QYr.ubo-2A.2* haplotypes variants within the single subpopulations is displayed.

QYr.ubo-2A.2 displayed a total of seven haplotype variants, with only three identified as major haplotypes (figure 22). *QYr.ubo-2A.2.1*, despite being the most frequent haplotype and exhibiting a wide distribution, is the only variant that demonstrates a resistant phenotype. In contrast, both *QYr.ubo-2A.2.2* and *QYr.ubo-2A.2.3* exhibit a highly susceptible phenotype and are also found in

multiple subpopulations. The remaining 4 *QYr.ubo-2A.2* haplotypes are extremely rare, present in less than 10 genotypes (see summary table 11).

Table 11: A summary table displaying the frequency of QYr.ubo-2A.2 within each subpopulation, the total count and mean value for IT and SEV.

Haplotype_Acronym	Haplotype_Variant	Count	1st_cluster		2nd_cluster		adm	Q1	Q2	Q3	Q4	Q5	Q6	Q7	Q8
			IT	SEV	IT	SEV									
QYr.ubo-2A.2.1	ATAGGCGATTAAAAC	674	4.93	48.85	5.30	42.68	63	112	10	64	3	35	160	163	64
QYr.ubo-2A.2.2	GCAGGCGACTGAGAT	22	7.43	71.34	6.99	72.31	1	0	0	16	4	0	0	0	1
QYr.ubo-2A.2.3	GCGTTAGACCGAGCT	16	7.11	78.96	7.24	79.35	0	0	0	0	0	0	4	10	2
QYr.ubo-2A.2.4	GCAGTCTGCTGAGAT	4	5.71	66.71	7.50	69.42	1	0	0	1	1	0	0	1	0
QYr.ubo-2A.2.5	ATAGTCGATTAAAAC	1	1.80	14.94	9.60	92.72	0	1	0	0	0	0	0	0	0
QYr.ubo-2A.2.6	GCAGTCTGCTGGGAT	1	6.62	66.46	0.00	0.00	0	0	0	0	0	0	1	0	0
QYr.ubo-2A.2.7	GCGTTAGACCAAGCT	1	8.77	99.04	0.00	0.00	0	0	0	0	0	0	0	1	0

- ***QYr.ubo-2B.1***

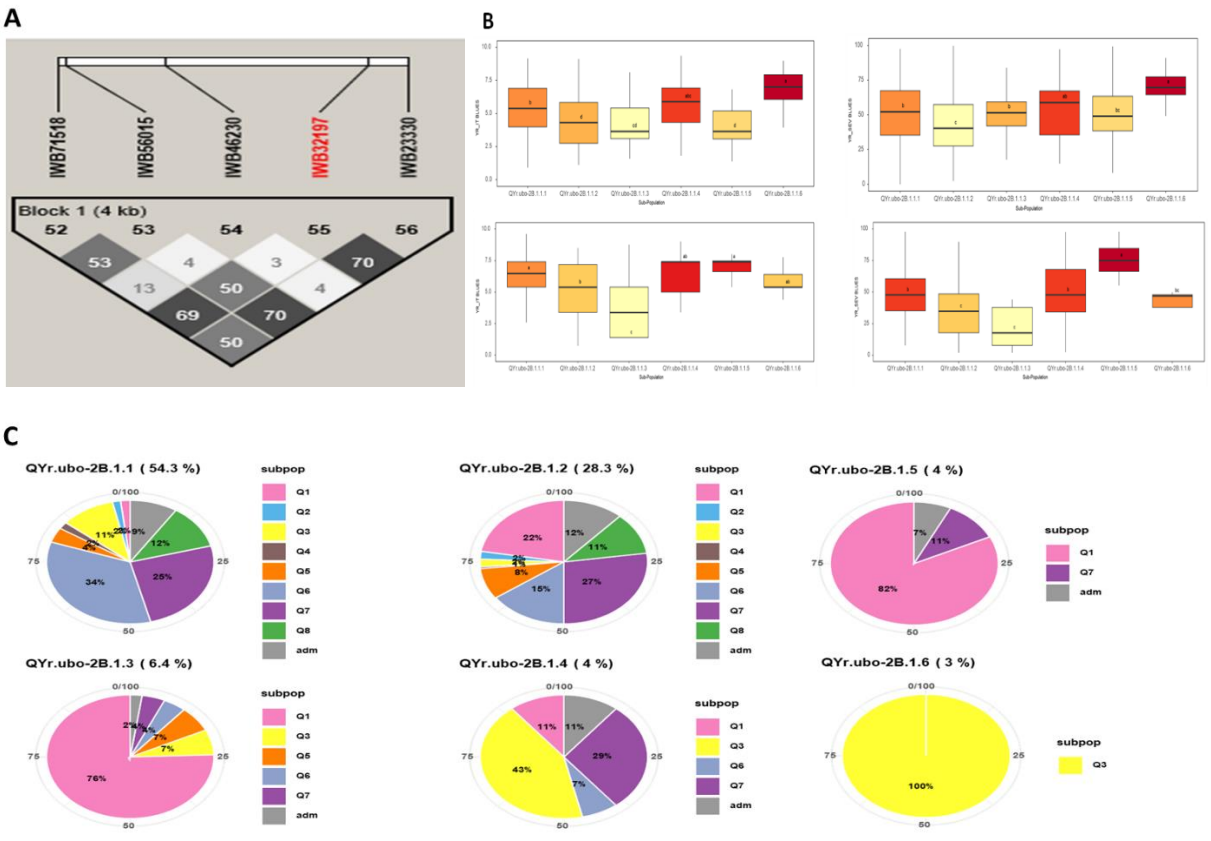

Figure 23: This figure displays the *QYr.ubo-2B.1* haploblock. A: *QYr.ubo-2B.1* LD-block. IWB32197 (55) highlighted in red is the peak marker of the QTL B: Comparison of the phenotypic performance of all identified haploblock variants of *QYr.ubo-2B.1* in terms of infection type (IT) and severity (SEV) within the first and second environmental clusters. C: The frequency of all *QYr.ubo-2B.1* haplotypes variants within the single subpopulations is displayed.

A total of 12 different haplotypes were identified for *QYr.ubo-2B.1*, which includes six major haplotypes (figure 23) and six minor ones. Among these, *QYr.ubo-2B.1.3* exhibited the highest

level of resistance, displaying low phenotypic values for both infection type (IT) and severity (SEV), particularly in the second cluster (Grosseto 2018 and Lari 2019). Additionally, *QYr.ubo-2B.1.2* showed partial resistance compared to the other haplotypes, as well as a wide distribution range. Overall, all haplotypes are dispersed across several subpopulations, but *QYr.ubo-2B.1.3* is predominantly found in Q1. Notably, the susceptible haplotype *QYr.ubo-2B.1.6* is also present in Q3 (see summary table 12).

Table 12: A summary table displaying the frequency of QYr.ubo-2B.1 haplotypes within each subpopulation, the total count and mean value for IT and SEV.

Haplotype_Acronym	Haplotype_Variant	Count	1st_cluster		2nd_cluster		adm	Q1	Q2	Q3	Q4	Q5	Q6	Q7	Q8
			IT	SEV	IT	SEV									
QYr.ubo-2B.1.1	AGAAA	380	5.35	51.31	6.11	49.12	35	7	6	40	7	15	130	96	44
QYr.ubo-2B.1.2	GAAGG	198	4.36	43.22	4.57	34.69	23	44	4	4	1	16	30	54	22
QYr.ubo-2B.1.3	GGGGA	45	4.36	53.21	2.77	26.53	1	34	0	3	0	3	2	2	0
QYr.ubo-2B.1.4	GAAAA	28	5.64	56.84	6.06	50.60	3	3	0	12	0	0	2	8	0
QYr.ubo-2B.1.5	GGGAA	28	4.18	49.76	6.93	73.93	2	23	0	0	0	0	0	3	0
QYr.ubo-2B.1.6	AAAAA	21	6.85	71.52	5.66	45.30	0	0	0	21	0	0	0	0	0
QYr.ubo-2B.1.7	GGAAA	6	5.99	52.41	6.34	56.35	1	0	0	0	0	0	0	4	1
QYr.ubo-2B.1.8	GAGGA	5	7.47	79.03	6.92	89.83	0	0	0	0	0	0	0	5	0
QYr.ubo-2B..9	GAAGA	3	5.40	61.84	6.05	67.78	0	0	0	0	0	0	1	2	0
QYr.ubo-2B.1.10	GAGAA	2	8.37	98.73	7.40	62.79	0	0	0	1	0	0	0	1	0
QYr.ubo2B.1.11	GGAAG	2	6.09	69.09	9.60	92.72	0	2	0	0	0	0	0	0	0
QYr.ubo-2B.1.12	GGAGA	1	7.15	35.83	0.00	0.00	0	0	0	0	0	1	0	0	0

- ***QYr.ubo-2B.2***

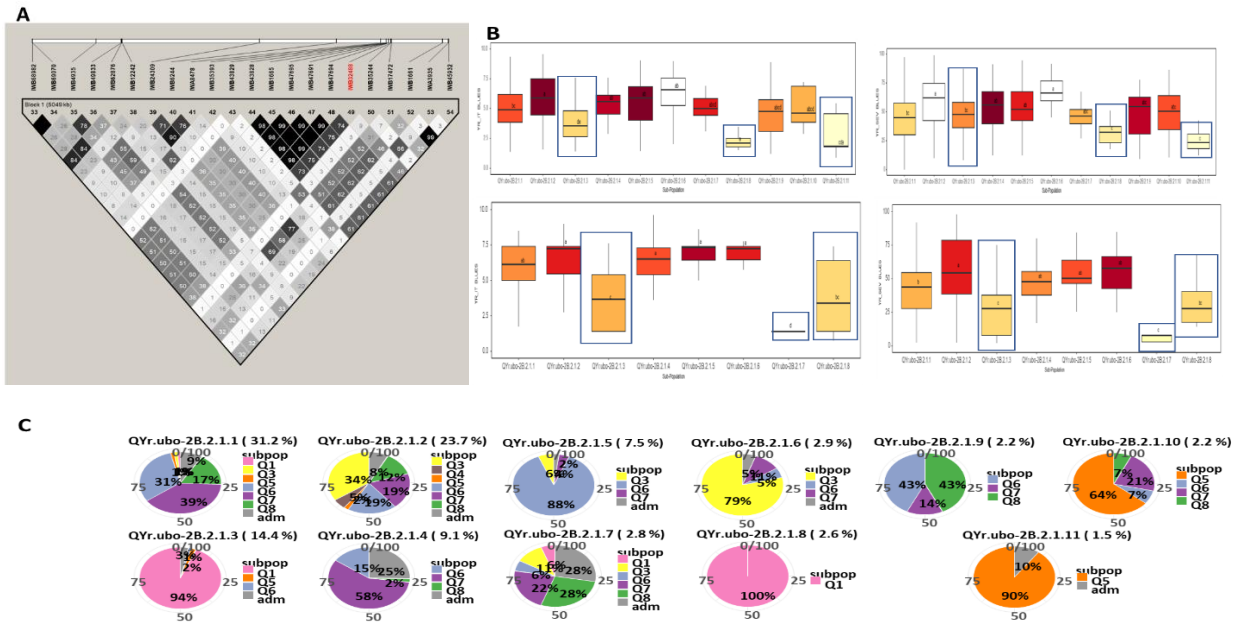

Figure 24: This figure displays the *QYr.ubo-2B.2* haploblock. A*: QYr.ubo-2B.2* LD-block. IWB32488 (40) highlighted in red is the peak marker of the QTL. B : Comparison of the phenotypic performance of all identified haploblock variants of *QYr.ubo-2B.2* in terms of infection type (IT) and severity (SEV) within the first and second environmental clusters. C: The frequency of all *QYr.ubo-2B.2* haplotypes variants within the single subpopulations is displayed.

A total of 11 different haplotypes were identified for *QYr.ubo-2B.2*, which includes 5 minor haplotypes (figure 24) and 7 minor ones. Unike the other QTLs, three haplotypes showed high resistance towards Yr in both environmental clusters, namely, *QYr.ubo-2B.2.8*, *QYr.ubo-2B.3*,

QYr.ubo-2B.9. Interestingly, both *QYr.ubo-2B.2.8* was only found in Q1 (Horn_Africa_Asia_aethiopicum), whereas *QYr.ubo-2B.2.8* was also mainly conserved in Q1 and partially in Q5 and Q6. As a whole, many haplotypes are mainly present in certain subpopulations with Q3, Q5 and Q6 being important reservoir of haplotypes (See summary table 13).

Table 13: A summary table displaying the frequency of *QYr.ubo-2B.2* haplotypes within each subpopulation, the total count and mean value for IT and SEV.

Haplotype_Acronym	Haplotype_Variant	Count	1st_cluster		2nd_cluster		adm	Q1	Q2	Q3	Q4	Q5	Q6	Q7	Q8
			IT	SEV	IT	SEV									
QYr.ubo-2B.2.1	CCGACCGTCACGATTGCTAGTG	203	4.98	45.41	5.78	42.89	18	2	0	3	0	3	63	80	34
QYr.ubo-2B.2.2	ATTCACACTACTGCCATTGATA	154	5.86	59.58	6.44	56.89	12	0	0	53	8	3	30	29	19
QYr.ubo-2B.2.3	CCTCCTACTGCGATTGCTGGTG	94	3.90	46.47	3.11	27.65	3	88	0	0	0	2	1	0	0
QYr.ubo-2B.2.4	ATTCACACTACTGCCATTGGTG	59	5.46	53.74	6.25	49.48	15	0	0	0	0	0	9	34	1
QYr.ubo-2B.2.5	ATTCACGTCACGATTGCTAGTG	49	5.48	53.38	6.64	53.89	1	0	0	3	0	0	43	2	0
QYr.ubo-2B.2.6	ATTCACGCCACGATTGCTAGTG	19	6.18	63.86	6.65	54.80	1	0	0	15	0	0	1	2	0
QYr.ubo-2B.2.7	CCTCACGCCACGATTGCTAGTG	18	4.89	45.49	0.81	9.88	5	1	0	2	0	0	1	4	5
QYr.ubo-2B.2.8	CCGCCTACTGCGATTGCTGGTG	17	2.53	34.70	4.03	34.10	0	17	0	0	0	0	0	0	0
QYr.ubo-2B.2.9	ATGACCGTCAAGATTGTCAGGG	14	4.67	46.99	3.87	33.07	0	0	0	0	0	0	6	2	6
QYr.ubo-2B.2.10	CCTCCTACTAAGATTGTCAGGG	14	5.03	49.87	8.07	63.01	0	0	0	0	0	9	1	3	1
QYr.ubo-2B.2.11	CCTCCTACTACGATTGCTAGTG	10	3.29	27.64	7.40	83.54	1	0	0	0	0	9	0	0	0

- ***QYr.ubo-5B.1***

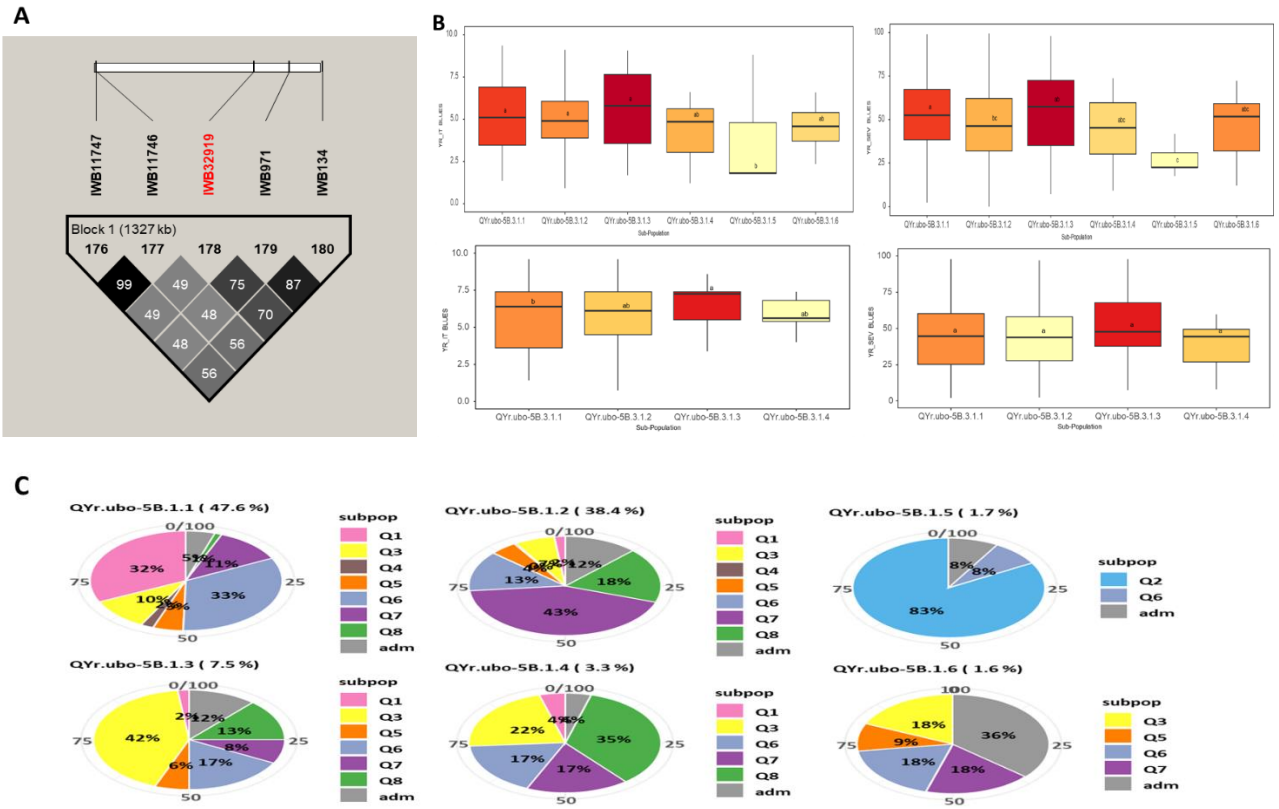

Figure 25: This figure displays the *QYr.ubo-5B.1* haploblock. A: *QYr.ubo-5B.1* LD-block. IWB32919 (178) highlighted in red is the peak marker of the QTL. B: Comparison of the phenotypic performance of all identified haploblock variants of *QYr.ubo-5B.1* in terms of infection type (IT) and severity (SEV) within the first and second environmental clusters. C: The frequency of all *QYr.ubo-5B.1* haplotypes variants within the single subpopulations is displayed.

A total of 10 different haplotypes were identified for *QYr.ubo-5B.1* (figure 25). Among them, *QYr.ubo-5B.1.5* was the only haplotype exhibiting resistance in the first cluster, yet it was

surprisingly absent in the second cluster. The remaining haplotypes predominantly displayed a susceptible phenotype. Notably, the resistant haplotype *QYr.ubo-5B.1.5* was primarily conserved in Q2 and partially in Q6 and admixed genotypes, while all the other susceptible haplotypes were widely distributed across several subpopulations (see summary table 14).

Table 14: A summary table displaying the frequency of *QYr.ubo-5B.1* haplotypes within each subpopulation, the total count and mean value for IT and SEV.

Haplotype_Acronym	Haplotype_Variant	Count	1st_cluster		2nd_cluster		adm	Q1	Q2	Q3	Q4	Q5	Q6	Q7	Q8
			IT	SEV	IT	SEV									
QYr.ubo-5B.1.1	GCAGT	331	5.19	53.56	5.09	43.92	16	106	0	34	7	17	109	38	4
QYr.ubo-5B.1.2	ATGAC	267	4.99	47.44	5.68	44.74	33	5	0	18	1	12	35	115	48
QYr.ubo-5B.1.3	ATAGT	52	5.66	55.72	6.54	53.63	6	1	0	22	0	3	9	4	7
QYr.ubo-5B.1.4	GCGAC	23	4.35	43.45	5.18	37.94	1	1	0	5	0	0	4	4	8
QYr.ubo-5B.1.5	ATAGC	12	3.28	33.07	4.38	47.35	1	0	10	0	0	0	1	0	0
QYr.ubo-5B.1.6	ATGGT	11	4.56	45.87	4.96	42.59	4	0	0	2	0	1	2	2	0
QYr.ubo5B.1.7	GCGGT	8	5.49	51.21	5.24	24.32	0	0	0	0	0	0	4	4	0
QYr.ubo-5B.1.8	GCAAT	7	4.70	44.22	5.40	37.79	2	0	0	0	0	2	1	2	0
QYr.ubo-5B.1.9	ATAAC	6	3.21	34.90	0.00	0.00	2	0	0	0	0	0	0	4	0
QYr.ubo5B.1.10	GCAAC	2	4.90	40.64	0.00	0.00	0	0	0	0	0	0	0	2	0

- ***QYr.ubo-5B.2***

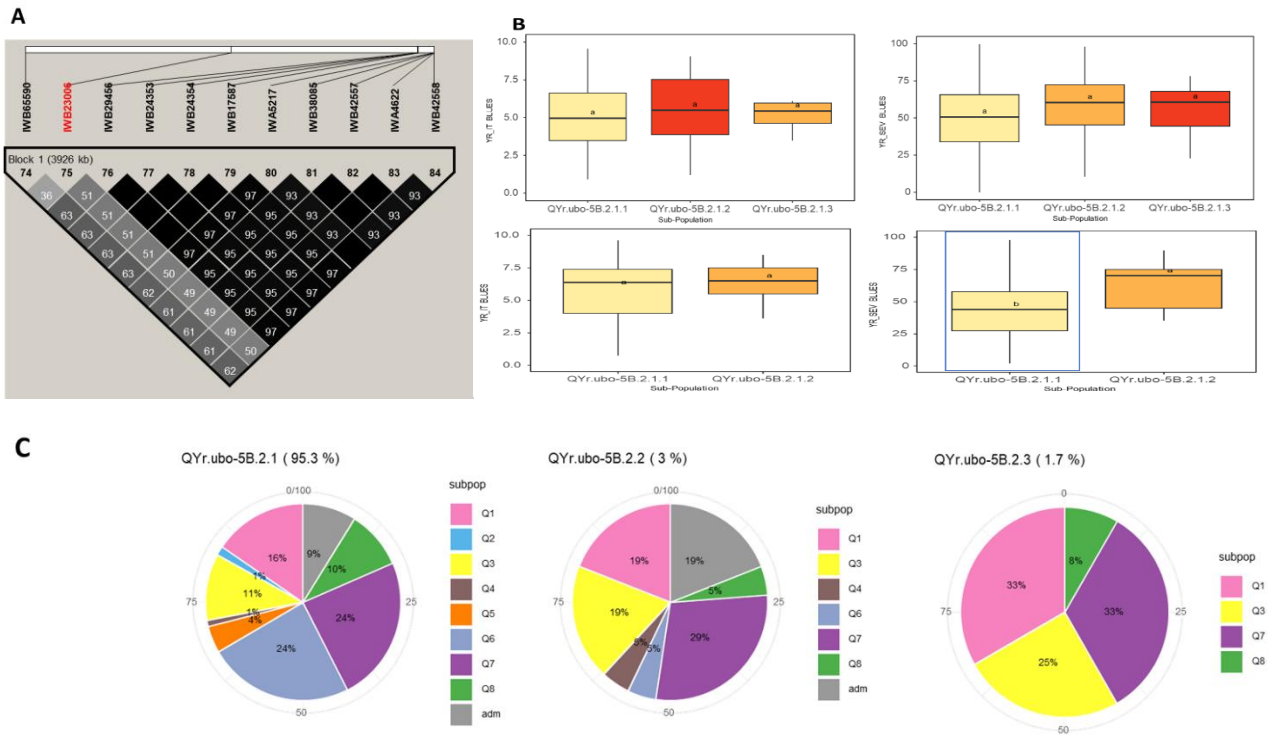

Figure 26: This figure displays the *QYr.ubo-5B.2* haploblock. A: *QYr.ubo-5B.2* LD-block. IWB23006 (76) highlighted in red is the peak marker of the QTL. B: Comparison of the phenotypic performance of all identified haploblock variants of *QYr.ubo-5B.2* in terms of infection type (IT) and severity (SEV) within the first and second environmental clusters. C: The frequency of all QYr.ubo-5B.2 haplotypes variants within the single subpopulations is displayed.

A total of 7 different haplotypes were identified for *QYr.ubo-5B.2* (figure 26). As a whole, three haplotype variants were major and the remaining four minor. *QYr.ubo-5B.2.1* was the only one showing a slight resistant phenotype, with a significant difference recorded only for SEV in the 2nd

cluster. All the three major haplotypes are widely spread across several subpopulations. Seven distinct haplotypes were identified for *QYr.ubo-5B.2*. Among these, three haplotype variants were classified as major, while the remaining four were considered minor. *QYr.ubo-5B.2.1* was the sole variant exhibiting a slight resistant phenotype, with a significant difference observed only in SEV within the second cluster. All three major haplotypes are widely distributed across multiple subpopulations (See summary table 15).

Table 15: A summary table displaying the frequency of *QYr.ubo-5B.2* within each subpopulation, the total count and mean value for IT and SEV.

Haplotype_Acronym	Haplotype_Variant	Count	1st_cluster		2nd_cluster		adm	Q1	Q2	Q3	Q4	Q5	Q6	Q7	Q8
			IT	SEV	IT	SEV									
QYr.ubo-5B.2.1	GAACAGCAGGG	676	5.04	50.05	5.36	43.95	60	105	10	74	7	30	163	162	65
QYr.ubo-5B.2.2	GGACAGCAGGG	21	5.41	57.79	6.53	62.92	4	4	0	4	1	0	1	6	1
QYr.ubo-5B.2.3	AGCTGATGAAA	12	5.37	55.79	6.71	55.21	0	4	0	3	0	0	0	4	1
QYr.ubo-5B.2.4	AAACAGCAGGG	6	5.41	53.00	5.40	56.95	0	0	0	0	0	5	1	0	0
QYr.ubo-5B.2.5	GAACAGCGAAG	2	5.44	41.72	5.40	16.95	0	0	0	0	0	0	0	2	0
QYr.ubo-5B.2.6	AGCTGACGAAG	1	3.98	28.48	0.00	0.00	1	0	0	0	0	0	0	0	0
QYr.ubo-5B.2.7	GGCTGATGAAA	1	4.30	57.48	0.00	0.00	0	0	0	0	0	0	0	1	0

- ***QYr.ubo-7A.1***

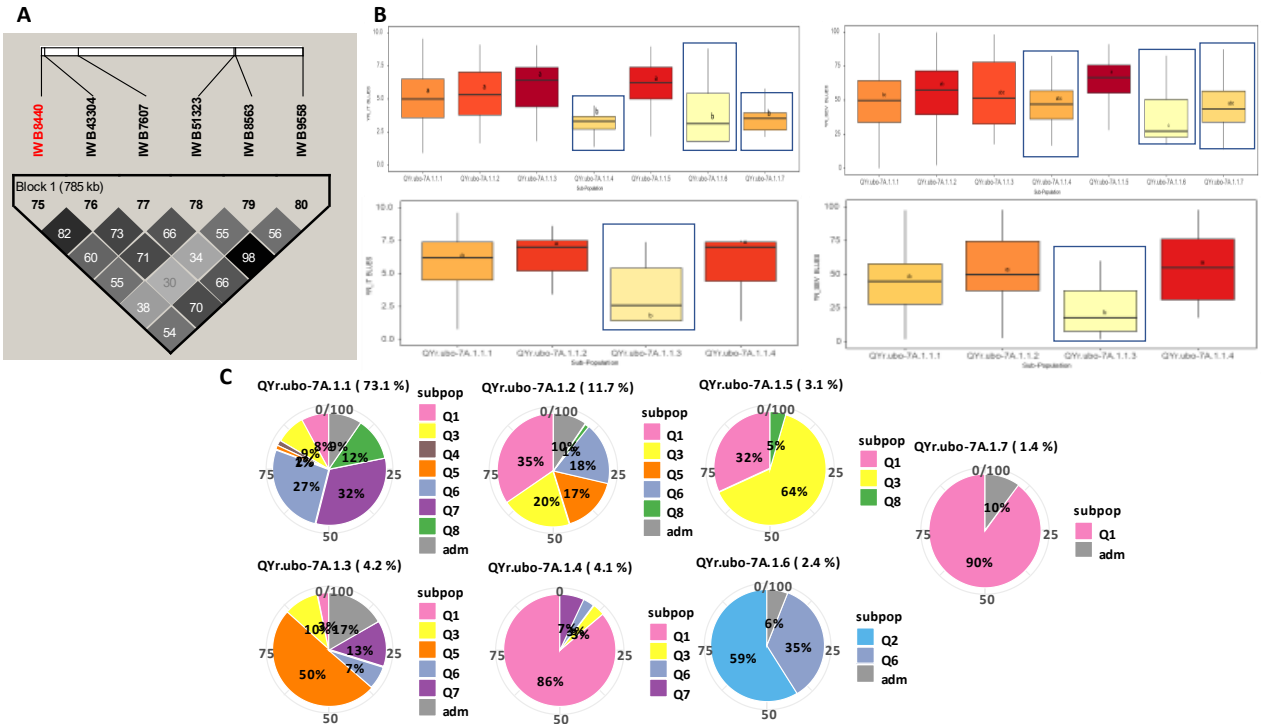

Figure 27: This figure displays the *QYr.ubo-7A.1* haploblock. A: *QYr.ubo-7A.1* LD-block. IWB8440 (75) highlighted in red is the peak marker of the QTL. B: Comparison of the phenotypic performance of all identified haploblock variants of *QYr.ubo-7A.1* in terms of infection type (IT) and severity (SEV) within the first and second environmental clusters. C: The frequency of all *QYr.ubo-7A.1* haplotypes variants within the single subpopulations is displayed.

QYr.ubo-7A.1 displayed a total of 9 haplotypes, with 6 identified as major haplotypes (figure 27). Interestingly, three haplotypes showed a clear resistant phenotype, namely, *QYr.ubo-7A.1.4*, *QYr.ubo-7A.1.5*, *QYr.ubo-7A.1.6. QYr.ubo-7A.4* showed a resistant phenotype in both environmental clusters, whereas the other two were detected in the second one. Both *QYr.ubo-7A.1.4* and *QYr.ubo-7A.1.6* were mainly conserved in Q1, whereas *QYr.ubo-7A.1.5* was mainly present in Q2. All the other susceptible haplotypes are widely spread across several subpopulations (See summary table 16).

Table 16: A summary table displaying the frequency of *QYr.ubo-7A.1* within each subpopulation, the total count and mean value for IT and SEV.

Haplotype_Acronym	Haplotype_Variant	Count	1st_cluster		2nd_cluster		adm	Q1	Q2	Q3	Q4	Q5	Q6	Q7	Q8
			IT	SEV	IT	SEV									
QYr.ubo-7A.1.1	TGACCA	523	5.1	49.4	5.6	44.5	49	42	0	45	8	6	140	168	65
QYr.ubo-7A.1.2	CACTTC	84	5.3	55.0	5.9	52.6	8	29	0	17	0	14	15	0	1
QYr.ubo-7A.1.3	CACTCC	30	5.9	54.2	5.6	53.3	5	1	0	3	0	15	2	4	0
QYr.ubo-7A.1.4	TGCCCA	29	3.5	46.7	2.3	26.0	0	25	0	1	0	0	1	2	0
QYr.ubo-7A.1.5	CACCCA	22	6.0	63.2	7.3	55.3	0	7	0	14	0	0	0	0	1
QYr.ubo-7A.1.6	TACTCC	17	3.9	38.0	0.0	13.3	1	0	10	0	0	0	6	0	0
QYr.ubo-7A.1.7	TGCTTC	10	3.7	45.7	7.2	45.6	1	9	0	0	0	0	0	0	0
QYr.ubo-7A.1.8	TGATTC	3	5.5	61.7	5.3	59.8	0	0	0	1	0	0	1	1	0
QYr.ubo-7A.1.9	TGACTC	1	7.1	84.8	5.4	47.8	1	0	0	0	0	0	0	0	0

- ***QYr.ubo-7B.1***

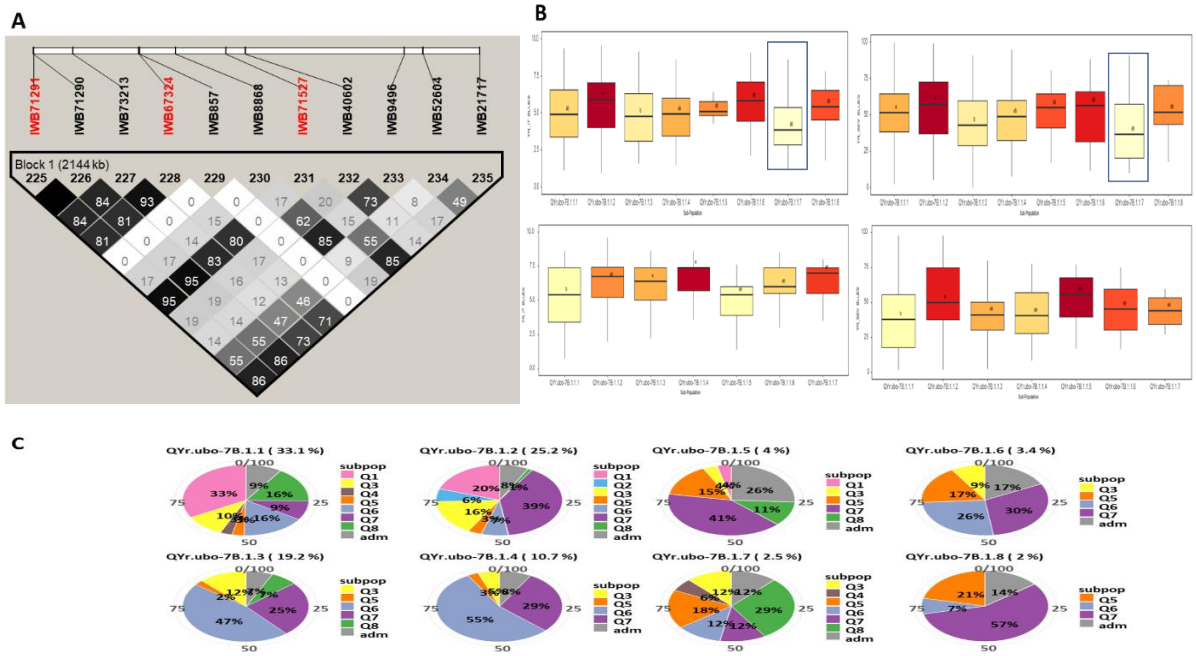

Figure 28: This figure displays the *QYr.ubo-7B.1* haploblock. A*: QYr.ubo-7B.1* LD-block. IWB71281 (225), IWB67234 and IWB71257 (231) highlighted in red is the peak marker of the QTL. B: Comparison of the phenotypic performance of all identified haploblock variants of *QYr.ubo-7B.1* in terms of infection type (IT) and severity (SEV) within the first and second environmental clusters. C: The frequency of all *QYr.ubo-7B.1* haplotypes variants within the single subpopulations is displayed.

A total of 10 different haplotypes were identified for *QYr.ubo-7B.1* (figure 28). Overall, there was no clear distinction between resistant and susceptible haplotypes, except for *QYr.ubo-7B.1.7*, which exhibited a slight resistant phenotype compared to the other haplotypes in the first environmental cluster. Additionally, all haplotypes of *QYr.ubo-7B.1* do not clearly belong to a specific subpopulation; rather, they are distributed widely across all subpopulations (see summary table 17).

Table 17: A summary table displaying the frequency of *QYr.ubo-7B.1*within each subpopulation, the total count and mean value for IT and SEV.

Haplotype_Acronym	Haplotype_Variant	Count	1st_cluster		2nd_cluster		adm	Q1	Q2	Q3	Q4	Q5	Q6	Q7	Q8
			IT	SEV	IT	SEV									
QYr.ubo-7B.1.1	CGAGAGCCACC	226	5.00	52.15	4.66	40.35	21	75	0	23	7	7	37	20	36
QYr.ubo-7B.1.2	CGAGAACTCCC	172	5.53	55.32	5.54	52.30	13	34	10	28	0	6	12	67	2
QYr.ubo-7B.1.3	TTGAAGTCATT	131	4.72	44.40	5.92	41.70	9	0	0	16	0	3	61	33	9
QYr.ubo-7B.1.4	TTGAAGTCACT	73	4.90	47.03	6.62	42.04	6	0	0	4	0	2	40	21	0
QYr.ubo-7B.1.5	CGAGAACCACC	27	5.00	51.28	4.97	52.74	7	1	0	1	0	4	0	11	3
QYr.ubo-7B.1.6	CGAGAGCTACC	23	5.92	52.24	6.11	44.98	4	0	0	2	0	4	6	7	0
QYr.ubo-7B.1.7	TTAGAGTCATT	17	4.43	40.59	6.37	46.12	2	0	0	2	1	3	2	2	5
QYr.ubo-7B.1.8	CGAGAGCTACT	14	5.36	53.24	4.76	33.66	2	0	0	0	0	3	1	8	0
QYr.ubo-7B.1.9	CGAAAGCCACC	9	3.68	39.04	6.48	47.96	0	0	0	0	0	0	0	0	9
QYr.ubo-7B.1.10	TTAGAGTCACT	6	4.38	40.78	7.02	63.23	0	0	0	3	0	0	2	0	1

- ***QYr.ubo-7B.2***

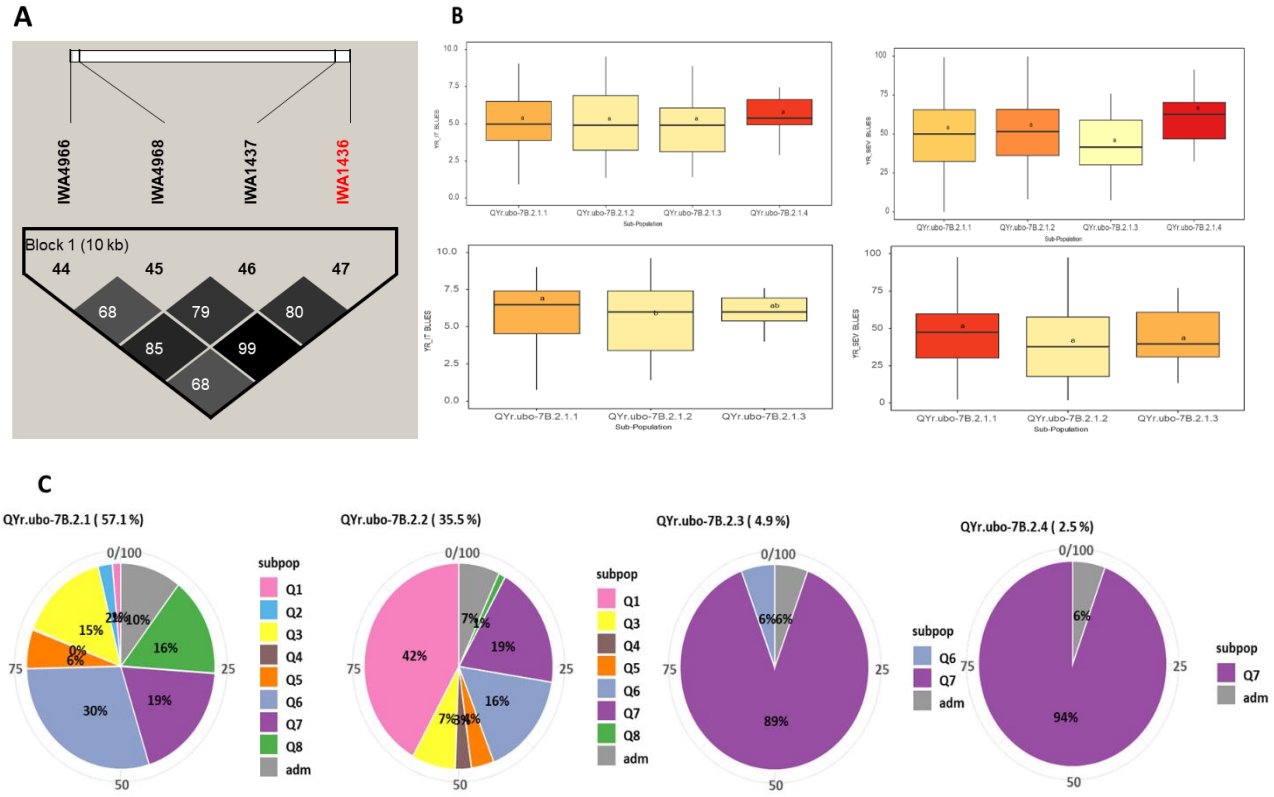

Figure 29: This figure displays the *QYr.ubo-7B.2* haploblock. A: *QYr.ubo-7B.2* LD-block. IWB1436 (47) highlighted in red is the peak marker of the QTL. B: Comparison of the phenotypic performance of all identified haploblock variants of *QYr.ubo-7B.2* in terms of infection type (IT) and severity (SEV) within the first and second environmental clusters. C: The frequency of all *QYr.ubo-7B.2* haplotypes variants within the single subpopulations is displayed.

QYr.ubo-7B.2 was the last QTL detected from the global GWAS. Only 4 haplotypes were detected for *QYr.ubo-7B.2* but none of them showed a clear resistant phenotype across the two multi-environmental clusters (figure 29). *QYr.ubo-7B.2.1* and *QYr.ubo-7B.2.2* were widely spread across several subpopulations, whereas *QYr.ubo-7B.2.3* and *QYr.ubo-7B.2.4* were both mainly conserved in Q7 (Egypt_Cyprous _Iberia). See summary table 18.

Table 18: A summary table displaying the frequency of *QYr.ubo-7B.2* within each subpopulation, the total count and mean value for IT and SEV.

Haplotype_Acronym	Haplotype_Variant	Count	1st_cluster		2nd_cluster		adm	Q1	Q2	Q3	Q4	Q5	Q6	Q7	Q8
			IT	SEV	IT	SEV									
QYr.ubo_7B.2.1	TGGC	410	5.1	49.0	5.9	46.8	43	6	10	62	1	25	121	78	64
QYr.ubo_7B.2.2	CAAT	255	5.0	52.7	4.7	41.8	18	107	0	19	7	10	42	49	3
QYr.ubo_7B.2.3	CGAC	35	4.7	43.5	5.8	45.3	2	0	0	0	0	0	2	31	0
QYr.ubo_7B.2.4	CGGC	18	5.5	58.8	6.0	47.8	1	0	0	0	0	0	0	17	0
QYr.ubo_7B.2.5	CAGC	1	6.9	87.3	0.0	0.0	1	0	0	0	0	0	0	0	0

After identifying the resistant haplotypes and distinguishing them from the susceptible ones for each QTL, a general correlation plot was created combining the IT phenotypic values from the first cluster with the cumulative scores of all haplotypes. Haplotype scoring with an average phenotypic value below the environmental average was classified as resistant and assigned a score of 1, while those above the average were classified as susceptible and given a score of 0. The final score for each genotype was derived from the cumulative sum of the haplotype scores at each QTL. Overall, a strong statistically significant negative correlation was observed between the decrease in infection type (IT) and the accumulation of resistant haplotypes, with an R^2 value of -0.62, confirming the reliability of these findings and indicating that the infection type (IT) decreases progressively as resistant haplotypes accumulate (figure 30).

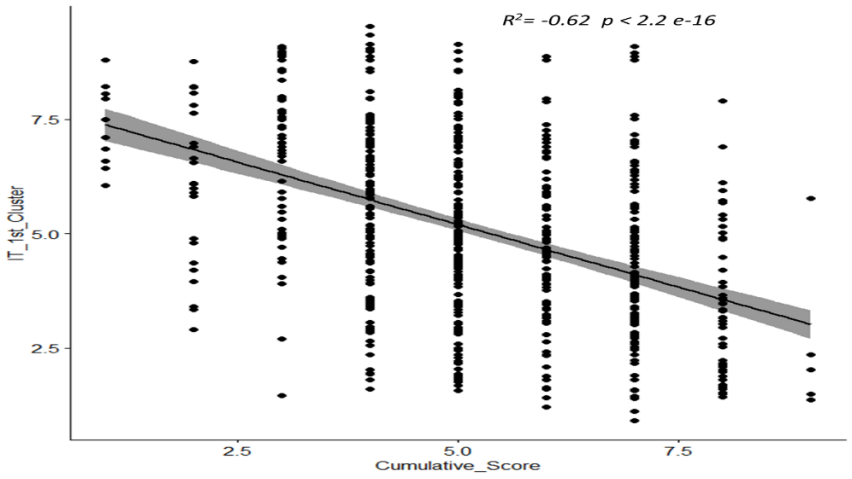

Figure 30: Correlation plot between the IT in the 1st environmental cluster and the cumulative score of all the haplotype variants for each QTL. Correlation coefficient (R^2) and p-values are reported on top

2.3.6.2 GWAS Within Subpopulations

Furthermore, GWAS was conducted within TGC subpopulations when the number of accessions in a particular subpopulation exceeded 50 individuals. This approach aimed to identify either novel marker-trait associations (MTAs) not detected in the global GWAS or to confirm previously identified MTAs to trace the origins of resistant alleles. Five subpopulations met this criterion for the association study: (Q1) DWL_Horn_Africa_Asia_aethiopicum, analyzed in six environments plus both environmental clusters; (Q3) DWL _SouthWestAsia_ Syriacum, also assessed in six environments plus both environmental clusters; (Q6) DWL_East_Europe_Transcaucasus, evaluated in all environments and both environmental clusters; (Q7) DWL_ Egypt_Cyprous _Iberia, examined in all environments and both environmental clusters; and (Q8) DWL_ West_Asian_Founders, studied in three environments plus one environmental cluster (see Table 3). All Manhattan Plots are available in supplementary files. Overall, 12 QTL were detected in Q1 on chromosome 1B (QYr_ubo_Q1_1B, QYr_ubo_Q1_1B.2), 2A (QYr_ubo_Q1_2A),), 3A (QYr_ubo_Q1_3A), 3B (QYr_ubo_Q1_3B), 3B (QYr_ubo_Q1_4B, QYr_ubo_Q1_4B.2), 5B (QYr_ubo_Q1_5B), 6A (QYr_ubo_Q1_6A), 6B (QYr_ubo_Q1_6B), 7A (QYr_ubo_Q1_7A), 7B (QYr_ubo_Q1_7B). QYr_ubo_Q1_1B and QYr_ubo_Q1_7A overlapped with the CI of two QTLs detected from the global GWAS, respectively, QYr.ubo-1B.1 and QYr.ubo-7A.1. Additionally, QYr_ubo_Q1_2A, QYr_ubo_Q1_3B, QYr_ubo_Q1_6A, QYr_ubo_Q1_7B overlapped respectively, Yr32, Yr80, YrLM168, YrZH84, Yr52, Yr59. Whereas, all the remaining QTL did not overlap with any known or detected region (see table 7).

Table 19: Summary table showing the results of the GWAS within Q1 (DWL_Horn_Africa_Asia_aethiopicum). This table comprises several information, from top to bottom: QTL acronym, MTA (SNP), alleles (major/mino), chromosome, position (Mbs), Block start position (Mbp), Block end postion (Mbp), overlapping QYr.ubo detected in the global GWAS, overlapping projected Yr confidence intervals and the results of the statistically significant ANOVA test within each environment or environmental cluster: NS stands for non-significant, NA stands for Not applicable (removed by MAF), * 0.05 – 0.01, ** 0.01-0.001, *** 0.0001-0.00001, **** < 0.00001. Environments containing fewer than 50 accesions belonging to that subpopulation are not reported.

	QTL name	***QYr_ubo_Q1_1B***	***QYr_ubo_Q1_1B.2***	***QYr_ubo_Q1_2A***	***QYr_ubo_Q1_3A***	***QYr_ubo_Q1_3B***	***QYr_ubo_Q1_4B***	***QYr_ubo_Q1_4B.2***	***QYr_ubo_Q1_5B***	***QYr_ubo_Q1_6A***	***QYr_ubo_Q1_6B***	***QYr_ubo_Q1_7A***	***QYr_ubo_Q1_7B***
	SNP	**IWB59567**	**IWB50261**	**IWB59335**	**IWB12392**	**IWB40192**	**IWB73835**	**IWB7508**	**IWB40361**	**IWB57893**	**IWB54452**	**IWA7600**	**IWB30479**
	Alleles	**T/C**	**G/A**	**A/G**	**C/T**	**G/A**	**T/C**	**G/A**	**G/A**	**A/C**	**G/A**	**C/T**	**G/A**
	Chromosomes	1B	1B	2A	3A	3B	4B	4B	5B	6A	6B	7A	7B
	Position (Mb)	317.10	426.38	709.52	726.87	595.63	26.39	30.28	614.68	603.80	669.78	535.28	715.51
	Block_start position (SVEVO)	317.10	426.38	700.04	726.87	584.46	26.35	30.28	614.68	603.77	669.74	535.27	715.26
	Block_end position (SVEVO)	320.21	426.38	709.52	728.96	595.63	27.18	35.03	614.69	603.80	669.78	535.28	715.76
	Overlapping_QYr.ubo	QYr.ubo-1B.1										QYr.ubo-7A.1	
	Overlapping_Yr_Loci			Yr32, Yr86		Yr80							YrZH84; Yr52; Yr59
	Projected_QTL			Mehrabi et al., 2022	Liu et al., 2017d	Liu et al., 2017c	Mehrabi et al., 2022	Liu et al., 2017c		Mehrabi et al., 2022			Liu et al., 2017b; Liu et al., 2017d
	IT/SEV	**Anova Test**											
Across Environments_landraces_1	IT	NS	*	**	***	***	****	***	**	**	**	**	*
	SEV	***	**	****	**	**	***	***	***	*	**	***	***
Across Environments_landraces_2	IT	NS	*	**	***	***	****	***	**	**	**	**	*
	SEV	*	***	*	*	***	****	***	****	NS	**	**	NS
Grosseto (GRO)_2019	IT	NS	*	*	NS	****	NS	**	**	**	NS	NS	****
	SEV	*	NS	NS	NS	***	NS	NS	**	*	*	*	****
Grosseto (GRO)_2020	IT	**	NS	NS	NS	***	**	***	*	NS	*	NS	NS
	SEV	***	NS	*	NS	NS	NS	NS	NS	**	NS	NS	*
Beja (BEJ)_2020	IT	***	NS	NS	**	NS	*	NS	**	*	**	NS	NS
	SEV	****	NS	NS	*	NS	*	*	**	NS	**	NS	NS
Kodia (KOD)_2020	IT	NS	*	**	****	**	****	****	***	****	****	*	NS
	SEV	NS	NS	NS	****	NS	*	NS	NS	****	NS	NS	NS
Lari (LAR)_2019	IT	NS	**	**	***	****	****	***	**	*	****	***	*
	SEV	NS	****	*	*	****	***	**	****	NS	**	***	NS
Izmir (IZM)_2019	IT	NS	*	**	NS	**	*	NS	**	NS	***	***	NS
	SEV	***	**	****	*	*	*	NS	**	NS	*	***	NS

In Q3, other 12 QTLs were detected on chromose 1A (*QYr_ubo_Q3_1A), 1B (QYr_ubo_Q3_1B), 2B (QYr_ubo_Q3_2B), 3A (QYr_ubo_Q3_3A),* 3B *(QYr_ubo_Q3_3B, QYr_ubo_Q3_3B.2), 4A (QYr_ubo_Q3_4A, QYr_ubo_Q3_4A.2),* 5B *(QYr_ubo_Q3_5B, QYr_ubo_Q3_5B.2), 7A (QYr_ubo_Q3_7A), 7B (QYr_ubo_Q3_7B). QYr_ubo_Q3_5B.2* overlapped with the CI of one QTL detected from the global GWAS, respectively, QYr.ubo-5B.2. QYr_ubo_Q3_1B, QYr_ubo_Q3_2B, QYr_ubo_Q3_3B, QYr_ubo_Q3_5B, QYr_ubo_Q3_7A, QYr_ubo_Q3_7B overlapped with *Yr29, YrC51, YrP81, Yr57, Yr30, Yr50, Yrxy1 and YrZH84; Yr52; Yr59*. Whereas, all the remaining QTL did not overlap with any known or detected region (see table 8).

Table 20: Summary table showing the results of the GWAS within Q3 (DWL _SouthWestAsia_ Syriacum). This table comprises several information, from top to bottom: QTL acronym, MTA (SNP), alleles (major/mino), chromosome, position (Mbs), Block start position (Mbp), Block end postion (Mbp), overlapping QYr.ubo detected in the global GWAS, overlapping projected Yr confidence intervals and the results of the statistically significant ANOVA test within each environment or environmental cluster: NS stands for non-significant, NA stands for Not applicable (removed by MAF), * 0.05 – 0.01, ** 0.01-0.001, *** 0.0001-0.00001, **** < 0.00001. Environments containing fewer than 50 accesions belonging to that subpopulation are not reported.

	QTL name	***QYr_ubo_Q3_1A***	***QYr_ubo_Q3_1B***	***QYr_ubo_Q3_2B***	***QYr_ubo_Q3_3A***	***QYr_ubo_Q3_3B***	***QYr_ubo_Q3_3B.2***	***QYr_ubo_Q3_4A***	***QYr_ubo_Q3_4A.2***	***QYr_ubo_Q3_5B***	***QYr_ubo_Q3_5B.2***	***QYr_ubo_Q3_7A***	***QYr_ubo_Q3_7B***
	SNP	**IWB73557**	**IWB9772**	**IWB71896**	**IWB58656**	**IWB67376**	**IWB12218**	**IWB27643**	**IWB42118**	**IWB33379**	**IWB23973**	**IWB11000**	**IWB75238**
	Alleles	A/G	T/C	C/T	G/A	A/G	G/A	C/A	G/A	G/A	C/T	G/T	C/A
	Chromosomes	1A	1B	2B	3A	3B	3B	4A	4A	5B	5B	7A	7B
	Position (Mb)	539.88	666.65	75.00	598.39	10.86	827.14	641.39	735.48	487.00	682.87	612.34	717.79
	Block_start position (SVEVO)	539.13	666.40	75.00	598.39	10.86	827.14	641.39	734.71	484.38	682.18	612.33	716.46
	Block_end position (SVEVO)	540.18	666.65	79.62	602.57	10.91	827.89	641.39	735.88	487.74	683.00	612.34	721.75
	Overlapping_QYr.ubo										QYr.ubo-5B.1		
	Overlapping_Yr_Loci		Yr29/Lr46	YrC51, YrP81		Yr57; Yr30				Yr50		Yrxy1	YrZH84; Yr52; Yr59
	Projected_QTL	Zhou X L et al., 2021	Zhou X L et al., 2021			Miedaner et al., (2019)	Liu et al., 2017c; Liu et al., 2017d	Zhou X L et al., 2021			Liu et al., 2017d		Liu et al., 2017b; Liu et al., 2017d ; Aoun et al., (2021)
	IT/SEV	**Anova Test**											
Across Environments_landraces_1	IT	**	****	****	****	****	****	*	****	***	***	**	****
	SEV	**	****	****	****	****	****	****	****	****	***	***	***
Across Environments_landraces_2	IT	NS	*	**	*	***	NS	NS	***	NS	NS	NS	NS
	SEV	NS	***	***	**	****	***	NS	****	**	*	****	NS
Grosseto (GRO)_2019	IT	**	****	***	****	****	**	*	***	***	**	**	**
	SEV	*	****	***	**	****	**	****	**	***	**	**	*
Grosseto (GRO)_2020	IT	*	*	*	**	NS	NS	NS	*	*	****	NS	**
	SEV	NS	**	*	**	NS	**	NS	NS	NS	*	NS	***
	IT	NS	NS	NS	NS	NS	NS	**	NS	NS	*	NS	NS

Beja (BEJ)_2020	SEV	*	NS	*	NS	NS	***	**	NS	NS	**	NS	*
Kodia (KOD)_2020	IT	****	*	*	**	NS	***	**	NS	*	*	**	***
	SEV	***	*	*	*	NS	***	*	NS	NS	*	*	***
Lari (LAR)_2019	IT	NS	*	*	NS	**	NS	**	**	NS	NS	NS	NS
	SEV	NS	***	**	*	****	*	NS	***	*	NS	***	NS
Izmir (IZM)_2019	IT	*	****	**	****	**	**	NS	**	**	**	**	****
	SEV	**	****	***	****	**	***	*	****	**	**	***	***

In Q6, 11 QTLs were detected in total. 4 QTLs were detected on Chromosome 1B (QYr_ubo_Q6_1B, QYr_ubo_Q6_1B.2, QYr_ubo_Q6_1B.3, QYr_ubo_Q6_1B.4) but only QYr_ubo_Q6_1B and QYr_ubo_Q6_1B-4 overlapped with projected Yr loci, namely, Yr10, Yr 84 and Yr29. Whereas, QYr_ubo_Q6_5B.2 overlapped with QYr.ubo-5B.1. The other QTLs were detected on chromose 1A (QYr_ubo_Q6_1A), 2A (QYr_ubo_Q6_2A), 5A (QYr_ubo_Q6_5A), 5B (QYr_ubo_Q6_5B, QYr_ubo_Q6_5B.2), 7A (QYr_ubo_Q6_7A), 7B (QYr_ubo_Q6_7B). QYr_ubo_Q6_2A and QYr_ubo_Q6_7B overlapped with the CI of Yr32 and Yr39(see table 8).

Table 21: Summary table showing the results of the GWAS within Q6 (DWL_East_Europe_Transcaucasus). This table comprises several information, from top to bottom: QTL acronym, MTA (SNP), alleles (major/mino), chromosome, position (Mbs), Block start position (Mbp), Block end postion (Mbp), overlapping QYr.ubo detected in the global GWAS, overlapping projected Yr confidence intervals and the results of the statistically significant ANOVA test within each environment or environmental cluster: NS stands for non-significant, NA stands for Not applicable (removed by MAF), * 0.05 – 0.01, ** 0.01-0.001, *** 0.0001-0.00001, **** < 0.00001. Environments containing fewer than 50 accesions belonging to that subpopulation are not reported.

	QTL name	***QYr_ubo_Q6_1A***	***QYr_ubo_Q6_1B***	***QYr_ubo_Q6_1B.2***	***QYr_ubo_Q6_1B.3***	***QYr_ubo_Q6_1B.4***	***QYr_ubo_Q6_2A***	***QYr_ubo_Q6_5A***	***QYr_ubo_Q6_5B***	***QYr_ubo_Q6_5B.2***	***QYr_ubo_Q6_7A***	***QYr_ubo_Q6_7B***
	SNP	**IWB2429**	**IWB11788**	**IWB47697**	**IWB19967**	**IWB71547**	**IWB48026**	**IWB28350**	**IWB66660**	**IWB32919**	**IWB72818**	**IWB55750**
	Alleles	T/G	T/C	T/C	A/G	A/G	T/C	T/C	C/A	A/G	G/A	A/G
	Chromosomes	1A	1B	1B	1B	1B	2A	5A	5B	5B	7A	7B
	Position (Mb)	285.71	2.09	367.62	379.47	674.75	715.52	398.12	588.13	682.18	113.94	569.37
	Block_start position (SVEVO)	270.19	2.09	360.71	379.47	674.74	714.62	398.11	588.13	681.25	113.94	569.22
	Block_end position (SVEVO)	331.25	4.04	373.46	381.49	674.75	716.04	399.05	588.42	684.44	113.94	572.33
	Overlapping_QYr.ubo									QYr.ubo-5B.1		
	Overlapping_Yr_Loci		Yr10; Yr84			Yr29/Lr46	Yr32		Yr68			Yr39
	Projected_QTL	Mehrabi et al., 2022		Liu et al., 2017b		Mehrabi et al., 2022; Liu et al., 2017d			Firdissa E. Bokore et al.,2021	Liu et al., 2017d	Mehrabi et al., 2022	Liu et al., 2017b
	IT/SEV	**Anova Test**										
Across Environments_landraces_1	IT	****	*	***	***	***	NS	***	****	***	**	****
	SEV	***	NS	**	**	****	NS	***	****	**	****	**
Across Environments_landraces_2	IT	NS	NS	**	**	*	**	NS	*	**	NS	**
	SEV	****	NS	NS	NS	**	*	**	*	NS	*	NS
Grosseto (GRO)_2018	IT	NS	NS	NS	NS	NS	***	NS	*	NS	NS	NS
	SEV	NS	NS	NS	NS	NS	NS	NS	NS	NS	NS	NS
Grosseto (GRO)_2019	IT	*	*	****	****	*	**	**	**	****	**	***
	SEV	*	NS	***	***	***	NS	NS	*	**	**	***
Lari (LAR)_2019	IT	NS	NS	*	NS	NS	NS	NS	NS	**	NS	****
	SEV	***	NS	**	**	NS	NS	**	NS	**	*	****
Izmir (IZM)_2019	IT	**	NS	NS	NS	*	NS	**	***	***	***	*
	SEV	**	NS	NS	NS	**	NS	**	**	****	****	*
Grosseto (GRO)_2020	IT	*	*	NS	NS	NS	NS	NS	***	NS	NS	NS
	SEV	NS	*	NS	NS	NS	NS	NS	NS	NS	*	NS
Beja (BEJ)_2020	IT	**	***	NS	NS	NS	NS	**	NS	NS	NS	NS
	SEV	***	**	**	**	NS	*	***	NS	NS	NS	NS
Kodia (KOD)_2020	IT	NS	**	NS	*	NS	**	NS	NS	NS	NS	NS
	SEV	NS	***	NS	*	NS	***	NS	NS	NS	NS	NS

Grosseto (GRO)_2021	IT	*	**	*	*	*	NS	NS	NS	**	NS	*
	SEV	NS	NS	NS	NS	**	NS	NS	NS	*	NS	NS

Q7 was the subpopulation showing the largest number (14) of significant markers with strong effect. 5 QTLs were detected on chromose 3B (QYr_ubo_Q7_3B, QYr_ubo_Q7_3B.2, QYr_ubo_Q7_3B.3, QYr_ubo_Q7_3B.4, QYr_ubo_Q7_3B.5), 4 on chromosome 7A ( ) and two on chromosome 7B (QYr_ubo_Q7_7B, QYr_ubo_Q7_7B.2). whereas the others on chromosome 1A (QYr_ubo_Q7_1A), 5A (QYr_ubo_Q7_5A), 6B (QYr_ubo_Q7_6B). QYr_ubo_Q7_7B.2 overlapped with QYr.ubo-7B.1 and two Yr loci, Yr67 and Yr6). The other QTL on chromosome 7B, QYr_ubo_Q7_7B overlapped with another QTL, QYr.ubo-7B.2. QYr_ubo_Q7_3B, QYr_ubo_Q7_3B.4 and QYr_ubo_Q7_7A.4 overlapped with some Yr loci, namely, Yr57, Yrns-B1, Yr80 and Yr75 (see figure 8).

Table 22: Summary table showing the results of the GWAS within Q7 (DWL_ Egypt_Cyprous _Iberia). This table comprises several information, from top to bottom: QTL acronym, MTA (SNP), alleles (major/mino), chromosome, position (Mbs), Block start position (Mbp), Block end postion (Mbp), overlapping QYr.ubo detected in the global GWAS, overlapping projected Yr confidence intervals and the results of the statistically significant ANOVA test within each environment or environmental cluster: NS stands for non-significant, NA stands for Not applicable (removed by MAF), * 0.05 – 0.01, ** 0.01-0.001, *** 0.0001-0.00001, **** < 0.00001. Environments containing fewer than 50 accesions belonging to that subpopulation are not reported.

	QTL name	***QYr_ubo_Q7_1A***	***QYr_ubo_Q7_3B***	***QYr_ubo_Q7_3B.2***	***QYr_ubo_Q7_3B.3***	***QYr_ubo_Q7_3B.4***	***QYr_ubo_Q7_3B.5***	***QYr_ubo_Q7_5A***	***QYr_ubo_Q7_6B***	***QYr_ubo_Q7_7A***	***QYr_ubo_Q7_7A.2***	***QYr_ubo_Q7_7A.3***	***QYr_ubo_Q7_7A.4***	***QYr_ubo_Q7_7B***	***QYr_ubo_Q7_7B.2***
	SNP	**IWB36084**	**IWB73813**	**IWB9145**	**IWB27206**	**IWB34451**	**IWB72215**	**IWB7371**	**IWB45723**	**IWB71799**	**IWB59468**	**IWB67145**	**IWB38551**	**IWA4968**	**IWB71291**
	Alleles	G/T	C/A	A/C	T/C	A/C	C/T	C/T	C/T	C/T	A/G	C/T	T/C	G/A	C/T
	Chromosomes	1A	3B	3B	3B	3B	3B	5A	6B	7A	7A	7A	7A	7B	7B
	Position (Mb)	47.14	23.10	129.98	343.84	596.04	626.88	535.01	682.08	115.04	198.72	420.17	715.96	41.72	696.94
	Block_start position (SVEVO)	47.14	23.10	125.80	291.20	596.04	626.14	535.01	681.67	114.91	198.72	306.56	715.96	41.72	696.94
	Block_end position (SVEVO)	47.56	23.85	140.05	343.84	602.04	627.59	536.10	682.08	119.10	201.35	439.37	715.98	41.73	699.08
	Overlapping_QYr.ubo													QYr.ubo-7B.2	QYr.ubo-7B.1
	Overlapping_Yr_Loci		Yr57; Yrns-B1			Yr80							Yr75		Yr67 ; Yr6
	Projected_QTL						Liu et al., 2017c								Xue Lin et al., 2018
	IT/SEV	**Anova Test**													
Across Environments_landraces_1	IT	**	****	****	*	****	****	****	****	****	****	**	****	****	****
	SEV	***	****	****	***	****	****	****	****	****	****	****	****	**	****
Across Environments_	IT	*	***	**	*	NS	*	*	*	NS	***	NS	**	*	NS
	SEV	***	****	****	**	**	****	****	****	**	****	****	****	**	***

landraces_2															
Grosseto (GRO)_2018	IT	**	**	*	NS	NS	NS	*	*	NS	**	*	**	*	NS
	SEV	NS	****	****	*	***	***	****	****	**	****	****	****	*	**
Grosseto (GRO)_2019	IT	**	****	****	***	****	****	****	****	****	****	****	****	***	****
	SEV	**	****	****	**	****	****	****	****	**	****	****	****	*	**
Lari (LAR)_2019	IT	NS	*	NS	*	NS	NS	NS	NS	NS	*	NS	NS	NS	NS
	SEV	***	****	***	NS	*	****	****	****	*	****	****	****	***	***
Izmir (IZM)_2019	IT	*	****	***	*	NS	**	***	****	*	**	***	***	****	***
	SEV	*	****	***	*	*	**	***	****	**	****	****	****	****	****
Grosseto (GRO)_2020	IT	*	****	NS	*	****	****	**	***	*	****	**	**	*	*
	SEV	NS	****	*	****	****	****	****	****	NS	****	***	****	**	NS
Beja (BEJ)_2020	IT	NS	***	NS	*	**	***	***	***	NS	#N/D	**	*	NS	***
	SEV	NS	****	NS	**	****	****	****	****	NS	#N/D	****	****	*	*
Kodia (KOD)_2020	IT	NS	****	NS	NS	****	****	****	****	NS	****	*	****	NS	***
	SEV	NS	****	*	NS	****	****	****	****	*	***	*	***	NS	***
Grosseto (GRO)_2021	IT	**	****	****	*	****	****	*	****	****	****	*	****	*	***
	SEV	**	****	****	**	****	****	**	****	****	****	***	****	NS	***

Q8 was the subpopulation with the fewest number of accession and GWAS was possible only in 3 environments (Grosseto 2019, Grosseto 2020, Grosseto 2021) and the 1st environmental cluster. 9 QTLs were detected in total on chromosome 1A (QYr_ubo_Q8_1A, QYr_ubo_Q8_1A.2), 1B (QYr_ubo_Q8_1B), 3 on chromosome 2B (QYr_ubo_Q8_2B, QYr_ubo_Q8_2B.2, QYr_ubo_Q8_2B.3), 1 on chromosome 3A (QYr_ubo_Q8_3A), 1 on chromosome 4B (QYr_ubo_Q8_4B) and 6A (QYr_ubo_Q8_6A). Three Yr loci overlapped QTLs detected in Q8 (Yr41m Yr39 and YrMY37). No overlap was observed with the QTL detected from global GWAS.

Table 23: Summary table showing the results of the GWAS within Q8 (DWL_ West_Asian_Founders). This table comprises several information, from top to bottom: QTL acronym, MTA (SNP), alleles (major/mino), chromosome, position (Mbs), Block start position (Mbp), Block end postion (Mbp), overlapping QYr.ubo detected in the global GWAS, overlapping projected Yr confidence intervals and the results of the statistically significant ANOVA test within each environment or environmental cluster: NS stands for non-significant, NA stands for Not applicable (removed by MAF), * 0.05 – 0.01, ** 0.01-0.001, *** 0.0001-0.00001, **** < 0.00001. Environments containing fewer than 50 accesions belonging to that subpopulation are not reported.

	QTL name	***QYr_ubo_Q8_1A***	***QYr_ubo_Q8_1A.2***	***QYr_ubo_Q8_1B***	***QYr_ubo_Q8_2B***	***QYr_ubo_Q8_2B.2***	***QYr_ubo_Q8_2B.3***	***QYr_ubo_Q8_3A***	***QYr_ubo_Q8_4B***	***QYr_ubo_Q8_6A***
	SNP	**IWB72042**	**IWB28824**	**IWA3588**	**IWB69976**	**IWB2427**	**IWB58269**	**IWB66838**	**IWB25024**	**IWB64744**
	Alleles	C/T	C/T	G/A	A/G	T/C	A/C	A/G	A/G	G/A
	Chromosomes	1A	1A	1B	2B	2B	2B	3A	4B	6A
	Position (Mb)	45.81	47.24	450.00	28.55	69.87	204.32	447.01	21.01	353.70
	Block_start position (SVEVO)	43.72	47.14	449.30	28.54	52.36	204.18	436.22	21.01	305.09
	Block_end position (SVEVO)	46.94	47.56	462.85	28.60	69.87	205.79	454.80	22.11	399.74
	Overlapping_QYr.ubo									
	Overlapping_Yr_Loci						Yr41			
	Projected_QTL				Liu et al., 2017d; Firdissa E. Bokore et al.,2021			Firdissa E. Bokore et al.,2021	Mehrabi et al., 2022	
	IT/SEV	**Anova Test**								
Across Environments_landraces_1	IT	**	*	****	****	***	**	****	**	****
	SEV	**	*	****	***	****	**	****	*	****
Grosseto (GRO)_2019	IT	**	NS	****	*	NS	**	****	*	*
	SEV	****	NS	****	NS	NS	***	****	**	**
Grosseto (GRO)_2020	IT	NS	NS	NS	NS	NS	*	NS	NS	*
	SEV	*	NS	***	*	NS	****	***	**	NS
Grosseto (GRO)_2021	IT	*	NS	***	****	**	*	*	**	**
	SEV	**	***	**	***	*	NS	**	***	**

2.4 DISCUSSION

The results of this multi-year and multi-environmental GWAS provide valuable insights into the genetic architecture underlying yellow rust resistance in tetraploid wheat, particularly among landraces. The identification of multiple significant marker-trait associations (MTAs) across diverse environments underscores the importance of leveraging the genetic diversity found in these traditional landraces for breeding programs. The study identified multiple marker-trait associations (MTAs) that remained consistent across various environments, confirming the robustness of the loci despite fluctuating environmental conditions. The strong correlations observed between certain environments, particularly between Grosseto (2019–2021) and Izmir (2019), as well as Grosseto (2018) and Lari (2019), suggest that these locations may be subject to similar pathogen pressures, thus facilitating the detection of stable resistance loci. These findings were corroborated by the principal component analysis (PCA), which highlighted two distinct environmental clusters. Broad-

sense heritability estimates, which exceeded 0.60 across all environments, emphasize the genetic control of resistance in the landraces, making them valuable resources for breeding programs aimed at improving resistance. Additionally, correlation plot suggests a strong significant negative correlation (0.62%) between the cumulation of resistant haplotypes for the detected QTLs and a subsequent decrease of infection type. Notably, the study's reliance on a comprehensive tetraploid wheat global collection ensured the inclusion of diverse alleles, which may not be present in elite wheat lines. This diversity enhances the potential for developing new wheat cultivars with durable resistance to yellow rust.

Chromosome 1A

In the global GWAS, no significant QTLs were identified on chromosome 1A. However, the subpopulation GWAS revealed five QTLs across four subpopulations: *QYr_ubo_Q3_1A***,** *QYr_ubo_Q6_1A***,** *QYr_ubo_Q7_1A***,** *QYr_ubo_Q8_1A***,** and *QYr_ubo_Q8_1A.2***.** While none of these QTLs overlapped with the confidence intervals (CIs) of mapped Yr loci, *QYr_ubo_Q3_1A* did overlap with a QTL identified in a linkage mapping study by Zhou et al. (2021), and *QYr_ubo_Q6_1A* overlapped with a QTL reported by Mehrabi et al. (2022). Notably, *QYr_ubo_Q8_1A* and *QYr_ubo_Q8_1A.2* represent two closely situated but independent QTLs at 45.81 Mb and 47.24 Mb, respectively, with *QYr_ubo_Q8_1A* perfectly overlapping with *QYr_ubo_Q8_1A.2*. Although these QTLs do not coincide with any known Yr loci, they may represent subpopulation-specific resistance loci that are less prevalent or less effective across broader germplasm. The overlaps with QTLs from Zhou et al. (2021), which involved a linkage mapping population of the durum wheat cultivar Svevo and wild emmer wheat Zavitian, and from Mehrabi et al. (2022), which used a diversified panel of durum wheat landraces, support the hypothesis that these regions could be novel sources of yellow rust resistance. Further validation is required to confirm their effectiveness and assess their potential utility in breeding programs.

Chromosome 1B

Chromosome 1B played a significant role in both global and subpopulation GWAS for yellow rust resistance. In the global GWAS, two key loci**,** *QYr.ubo-1B.1* and *QYr.ubo-1B.2*, demonstrated consistent associations across multiple environments. Notably, *QYr.ubo-1B.1* overlapped with the confidence interval (CI) of Yr65 and aligned with *QYr.ubo-Q1-1B*, identified in the Q1 subpopulation (Horn_Africa_Asia_aethiopicum), suggesting a possible origin of the resistant allele from this subpopulation. This hypothesis is further supported by haplotype analysis, which shows that the resistant haplotype *QYr.ubo-1B.1.3* is highly conserved within Q1. In contrast**,** *QYr.ubo-1B.2* did not overlap with any known Yr loci or projected QTLs, making it a potentially novel locus for yellow rust resistance, especially given its consistency across multiple environments. Chromosome 1B stands out as a major reservoir of resistance loci, with a total of 14 Yr loci identified. Beyond the global GWAS, subpopulation analyses revealed several other significant associations on this chromosome. In addition to *QYr.ubo-Q1-1B*, another QTL, *QYr.ubo-Q1-1B.2*, was detected in the Q1 subpopulation, although it did not overlap with any known Yr loci or projected QTLs, highlighting its potential as a novel locus. In subpopulation Q3, QYr_ubo_Q3_1B overlapped with a QTL from the linkage mapping study by Zhou et al. (2021) and the APR locus *Yr29/Lr46*, which is known for contributing durable resistance (Cobo N et al. 2019). Subpopulation Q6 (DWL_West_Asian_Founders) yielded four distinct QTLs on chromosome 1B (*QYr_ubo_Q6_1B.1*, *QYr_ubo_Q6_1B.2***,** *QYr_ubo_Q6_1B.3*, and *QYr_ubo_Q6_1B.4*). *QYr_ubo_Q6_1B.1* overlapped with both Yr10 and Yr84, while QYr_ubo_Q6_1B.4 aligned with Yr29/Lr46 and two QTLs identified in previous GWAS studies on durum wheat landraces (Mehrabi et al., 2022; Liu et al., 2017d). *QYr_ubo_Q6_1B.2*, while not overlapping with any known Yr loci, overlapped with a QTL detected by Liu et al. (2017b) in a study on elite durum wheat cultivars. In subpopulation Q8, the only QTL detected on chromosome 1B was *QYr_ubo_Q8_1B.1*, which did not overlap with any known Yr loci or projected QTLs, but may represent a subpopulation-specific resistance locus. In conclusion,

chromosome 1B serves as a critical hotspot for yellow rust resistance, harboring both known resistance genes and potential novel loci identified in subpopulation GWAS. The combination of overlapping known loci and novel QTLs across different subpopulations highlights its importance as a valuable resource for breeding programs aimed at improving yellow rust resistance in durum wheat. Further validation and exploration of these loci will be essential for harnessing their full potential.

Chromosome 2A

In the global GWAS, *QYr.ubo-2A.1* was consistently detected, particularly in environments like Izmir 2019 and Grosseto 2019. It was aligned with previously known loci such as *Yr17, Yr56* and *Yr69* and a QTL deriving from a linkage mapping study conducted by Zhou X L et al., 2021. Another QTL was detected from global GWAS on distal region of chromosome 2A, namely, *QYr.ubo-2A.2* which did not overlap with any know Yr loci and QTLs. *QYr.ubo-Q1-2A* was detected in the Q1 subpopulation (Horn_Africa_Asia_aethiopicum), this QTL overlaps with the CI of two ASR Yr loci *Yr32* and *Yr86*. This QTL overlaps also with CI of a QTL deriving from the association study conducted by Mehrabi et al., 2022. *QYr.ubo-Q6-2A* was found in subpopulation Q6, this QTL also overlapped with *Yr32* and was very close to *QYr.ubo-Q1-2A*, 6 Mbs apart only. These findings suggest that chromosome 2A harbors significant QTLs for yellow rust resistance, both in the global context and within specific subpopulations. The overlap of certain QTLs with previously identified Yr loci further emphasizes its role in providing durable resistance, while the unique QTLs, *QYr.ubo-2A.2*, identified in the global GWAS highlight the potential for discovering new resistance genes.

Chromosome 2B

On chromosome 2B, two QTLs were identified in the global GWAS*: QYr.ubo-2B.1* and *QYr.ubo-2B.2. QYr.ubo-2B.1* showed significant associations across environmental clusters and related single environments. While this QTL did not overlap with any known Yr loci, it coincided with the confidence intervals (CIs) of QTLs detected in two independent studies: an association study on Ethiopian durum landraces and a double haploid (DH) population derived from a cross between 'Strongfield' and 'Blackbird' (Firdissa E. Bokore et al., 2021). Conversely, *QYr.ubo-2B.2* overlapped with the CIs of two known resistance genes, *Yr5* and *Yr44* (an APR and ASR gene, respectively), but did not coincide with any projected QTLs.In the subpopulation GWAS, *QYr.ubo-Q3-2B* was detected in subpopulation Q3, showing strong significance in all considered environments. This QTL overlapped with two known ASR Yr loci, namely *YrC51* and *YrP81*. Additionally, three QTLs were found in subpopulation Q8**:** *QYr.ubo-Q8-2B, QYr.ubo-Q8-2B.2*, and *QYr.ubo-Q8-2B.3*. Among these, only *QYr.ubo-Q8-2B.3* overlapped with a known Yr locus, Yr41, while *QYr.ubo-Q8-2B.1* and *QYr.ubo-Q8-2B.2* were detected in novel regions. These findings suggest that chromosome 2B is an important region for yellow rust resistance, exhibiting significant QTLs in both the global context and within specific subpopulations. The overlap of *QYr.ubo-2B.2* with *Yr5* and *Yr44*, along with the overlaps of subpopulation-specific QTLs with known Yr loci like *YrC51*, *YrP81* and *Yr41*, further emphasizes the chromosome's role in providing durable resistance. Additionally, the unique QTLs identified in specific subpopulations indicate the potential for discovering new resistance genes that can enhance yellow rust management strategies in breeding programs.

Chromosome 3A

Chromosome 3A is known to have the fewest mapped Yr loci, with only *Yr76* reported. While it was not prominent in the global GWAS, three QTLs were detected in three subpopulations. In subpopulation Q1 (DWL_Horn_Africa_Asia_aethiopicum), *QYr.ubo-Q1-3A*, located in the distal region, did not overlap with *Yr76* but notably overlapped with the confidence interval (CI) of a QTL identified in an association study on an Ethiopian durum panel by Liu et al. (2017d). Similarly, *QYr.ubo-Q8-3A* did not overlap with *Yr76*, but aligned with the CI of a QTL from a double haploid (DH) population study (Firdissa E. Bokore et al., 2021). Finally, *QYr.ubo-Q3-3A* did not overlap with

any previously identified regions, suggesting it may represent a novel source of yellow rust resistance. The QTLs identified on chromosome 3A, particularly in subpopulations, could be novel sources of yellow rust resistance. While these regions did not overlap with known Yr loci, two of them have already been mapped from QTLs mapping studies and their consistent detection across different environments and subpopulations suggests that chromosome 3A holds promise for contributing new resistance genes. Further validation studies will be crucial to confirm their effectiveness and potential for incorporation into breeding programs.

Chromosome 3B

Despite being an important reservoir of Yr loci, no QTLs were identified on chromosome 3B in the global GWAS. However, subpopulation-specific analyses revealed several QTLs. In subpopulation Q7 (DWL_Egypt_Cyprous_Iberia), five QTLs were detected, including *QYr.ubo-Q7-3B.1*, which overlapped with two ASR loci, *Yr57* and *Yrns-B1*. Additionally, *QYr.ubo-Q7-3B.4* overlapped with the APR locus *Yr80*, known for conferring resistance to multiple *Puccinia striiformis* races (Li H et al., 2020). *QYr.ubo-Q7-3B.5* did not overlap with any Yr loci, but coincided with the confidence interval (CI) of a QTL identified in an association study on domesticated emmer wheat (W. Liu et al., 2021b). Meanwhile, *QYr.ubo-Q7-3B.2* and *QYr.ubo-Q7-3B.3* did not overlap with any known regions, suggesting they may represent new sources of resistance. Other subpopulations also identified unique QTLs on chromosome 3B. In subpopulation Q1 (DWL_Horn_Africa_Asia_aethiopicum), *QYr.ubo-Q1-3B* was detected in the same region as *QYr.ubo-Q7-3B.4*, overlapping with *Yr80* and a QTL from a dicoccum panel (W. Liu et al., 2021b). In subpopulation Q3, two QTLs, *QYr.ubo-Q3-3B.1* and *QYr.ubo-Q3-3B.2*, were identified. *QYr.ubo-Q3-3B.1* was localized near the beginning of chromosome 3B in a region rich in Yr loci. This QTL overlapped with *Yr57*, *Yr30*, and a QTL from an association study on a durum wheat panel (Miedaner et al., 2019), and was proximal to several other Yr loci, including *Yr4*, *Yr58*, and *Yrns-B1*. Finally, *QYr.ubo-Q3-3B.2*, located in the distal region of chromosome 3B, did not overlap with any Yr loci, but aligned with two QTLs from separate association studies conducted on dicoccum (Liu et al., 2021c) and durum wheat landrace panels (Liu et al., 2021d).

Chromosome 4A

Similar to chromosome 3A, chromosome 4A is also considered a poor reservoir for Yr loci, with only two detected on this chromosome to date. No significant QTLs were identified on chromosome 4A in the global GWAS, suggesting that it may not play a major role in yellow rust resistance on a broader scale. However, two QTLs, *QYr.ubo-Q3-4A.1* and *QYr.ubo-Q3-4A.2*, were detected in subpopulation Q3. Neither of these QTLs overlapped with known Yr loci, but their presence across multiple environments indicates that they may represent important subpopulation-specific loci for yellow rust resistance. Unlike other chromosomes, chromosome 4A showed no clear overlap with previously mapped Yr loci, implying that the QTLs identified in the subpopulation GWAS may be novel regions of resistance. These findings suggest that chromosome 4A could harbor untapped genetic sources of yellow rust resistance, potentially valuable for future breeding programs focused on uncovering new resistance genes.

Chromosome 4B

No significant QTLs were detected on chromosome 4B in the global GWAS. However, two QTLs were identified in subpopulation Q1 (DWL_Horn_Africa_Asia_aethiopicum), namely, *QYr.ubo-Q1-4B.1* and *QYr.ubo-Q1-4B.2*. Both QTLs were located in the distal region of chromosome 4B, just 4 Mbp apart, but overlapped with two different QTLs from independent association studies conducted on panels of durum wheat landraces (Mehrabi et al., 2022) and domesticated emmer wheat (Liu et

al., 2017c). Additionally, another QTL, *QYr.ubo-Q8-4B*, was detected in subpopulation Q8. This QTL did not coincide with any previously reported Yr loci but overlapped with the same QTL identified by Mehrabi et al., 2022. Although no QTLs were found on chromosome 4B in the global GWAS, subpopulation-specific analyses uncovered potentially novel QTLs in subpopulations Q1 and Q8. The absence of overlap with known Yr loci suggests that chromosome 4B may harbor unique resistance alleles, particularly in specific regions or germplasm. These findings underscore the potential of chromosome 4B as a source of new resistance genes for yellow rust, making it a promising target for future breeding programs.

Chromosome 5A

In the global GWAS, no significant QTLs were detected on chromosome 5A, suggesting that this chromosome may not have a major influence on yellow rust resistance across broad environments. Only two QTLs were detected in single subpopulations: one in Q6, *QYr.ubo-Q6-5A*, and another in Q7**,** *QYr.ubo-Q7-5A*. Both QTLs overlapped with neither known Yr loci or projected QTLs, thereby representing new potential regions underlying resistance towards Puccinia striiformis. This suggests that these QTLs identified in the subpopulations may represent novel regions for yellow rust resistance, with unique alleles that have not been previously documented.

Chromosome 5B

The global GWAS identified two significant QTLs on chromosome 5B, specifically *QYr.ubo-5B.1* and *QYr.ubo-5B.2*. *QYr.ubo-5B.1* demonstrated strong associations with yellow rust resistance across multiple environments, while *QYr.ubo-5B.2* exhibited environmental specificity, showing significant associations only in Lari 2019 and the second environmental cluster. Neither of these QTLs overlapped with any known Yr loci; however, both coincided with reported QTLs from previous studies. In particular, *QYr.ubo-5B.2* overlapped with the confidence interval (CI) of two QTLs identified in independent association studies on different panels of durum wheat landraces (Mehrabi et al., 2022; Liu et al., 2017d), whereas *QYr.ubo-5B.1* also overlapped with a QTL reported by Liu et al. (2017d). Additionally, *QYr.ubo-5B.1* was detected in two subpopulations: *QYr_ubo_Q3_5B.2* and *QYr_ubo_Q6_5B.2*. Other QTLs were identified in subpopulations Q1 (*QYr_ubo_Q1_5B*), Q3 (*QYr_ubo_Q3_5B.2*), and Q6 (*QYr_ubo_Q6_5B*). Notably, *QYr_ubo_Q3_5B.2* overlapped with *Yr50*, while *QYr_ubo_Q6_5B* overlapped with *Yr68***,** was proximal to *Yr62*, and coincided with the CI of a projected QTL from a linkage mapping study (Firdissa E. Bokore et al., 2021). Overall, chromosome 5B emerges as a crucial region for yellow rust resistance, with significant QTLs identified in both global and subpopulation GWAS analyses. The overlaps with established Yr loci in multiple studies highlight its importance for durable resistance, while the unique QTLs found in subpopulations Q1 and Q6 indicate the potential for discovering new resistance genes that could improve yellow rust management strategies in breeding programs. Notably, *QYr_ubo_Q6_5B.2* represents an interesting case of a QTL detected in multiple subpopulations, overlapping with projected QTLs, and could serve as an important target for future breeding validations.

Chromosome 6A

In the global GWAS, no significant QTLs were identified on chromosome 6A. This absence suggests that chromosome 6A may not play a major role in yellow rust resistance across a broad range of environments, or that important QTLs may be more prevalent in specific subpopulations. The QTL *QYr.ubo-Q1-6A*, detected in subpopulation Q1, was located near *YrLM168* and overlapped with the confidence interval of a QTL identified by Mehrabi et al. (2022). The identification of this QTL within a specific subpopulation highlights the potential for unique resistance alleles that may not be represented in the broader germplasm. In contrast, *QYr.ubo-Q8-6A*, found in subpopulation Q6, showed significant associations with yellow rust resistance but did not overlap with any known Yr

loci or projected QTLs. Its presence across multiple environments suggests that it could confer important resistance traits specific to this population. The absence of overlaps with established Yr loci for the QTLs detected on chromosome 6A indicates that this chromosome may harbor previously unidentified resistance genes, potentially conserved within specific subpopulations, making it a promising source for new alleles.

Chromosome 6B

In the global GWAS, no significant QTLs were detected on chromosome 6B. However, two QTLs were detected in Q1, *QYr.ubo-Q1-6B* and Q7, *QYr.ubo-Q7-6B***.** Both QTL did not overlap with any known Yr loci or projected QTL, and therefore, could represent a novel source of resistance specific deeply conserved within specific subpopulations, making chromosome 6B a potential source for discovering new alleles.

Chromosome 7A

The global GWAS identified one significant QTL on chromosome 7A, specifically *QYr.ubo-7A.1*, which demonstrated consistent associations with yellow rust resistance across multiple environments. Although this QTL did not overlap with any known Yr loci or previously mapped QTLs, it was also detected in subpopulation Q1 as *QYr_ubo_Q1_7A*, suggesting a possible origin and conservation of the resistant haplotype within Q1. Interestingly, four independent QTLs were identified in subpopulation Q7, namely *QYr_ubo_Q7_7A.1*, *QYr_ubo_Q7_7A.2*, *QYr_ubo_Q7_7A.3*, and *QYr_ubo_Q7_7A.4*. Among these, *QYr_ubo_Q7_7A.4* was the only one that overlapped with a known Yr locus, specifically *Yr75*, while the others were detected in novel regions. Additional QTLs were found in subpopulations Q3 and Q6, designated as *QYr_ubo_Q3_7A* and *QYr_ubo_Q6_7A*, respectively. *QYr_ubo_Q3_7A* overlapped with the confidence interval of the APR gene *Yrxy1*, while *QYr_ubo_Q6_7A* coincided with a projected QTL reported by Mehrabi et al. (2022). Overall, chromosome 7A emerges as a crucial region for yellow rust resistance, with significant QTLs identified in both the global GWAS and subpopulation-specific analyses. The overlap with established Yr loci such as *Yr75* and *Yrxy1* highlights their importance for durable resistance, while the unique QTLs found in subpopulation Q7 indicate the potential for discovering new resistance genes.

Chromosome 7B

The global GWAS identified two significant QTLs on chromosome 7B: *QYr.ubo-7B.1*, which showed strong associations with yellow rust resistance across various environments, and *QYr.ubo-7B.2*, which was mainly significant in the 1st cluster and related single environments. *QYr.ubo-7B.1* overlapped with the established APR and ASR genes *Yr67* and *Yr6*. Additionally, *QYr.ubo-7B.1* was also detected in subpopulation Q7 as *QYr_ubo_Q7_7B.2*. Interestingly, *QYr.ubo-7B.2* was also found in Q7 as *QYr_ubo_Q7_7B.1*. Furthermore, the same QTL located in the distal region of chromosome 7B was detected in subpopulations Q1 (*QYr_ubo_Q1_7B.1*) and Q3 (*QYr_ubo_Q3_7B.1*). This QTL overlapped with three Yr loci: YrZH84**,** Yr52, and Yr59, as well as two projected QTLs identified in independent association studies (Liu et al., 2017b; Liu et al., 2017d). Chromosome 7B emerges as a vital region for yellow rust resistance, showcasing significant QTLs in both the global GWAS and subpopulation-specific analyses. Its overlaps with established Yr loci emphasize its role as a key reservoir of resistance genes, similar to chromosome 1B. The potential for discovering new resistance genes in the distal region of chromosome 7B makes it a promising target for future breeding efforts aimed at improving yellow rust resistance in wheat.

2.5 CONCLUSION CHAPTER II

In conclusion, this multi-year and multi-environment association study has successfully uncovered significant QTLs associated with yellow rust resistance across various chromosomes of the durum wheat genome. Notable findings include the identification of QTLs in both global and subpopulation-specific GWAS, with many regions overlapping known Yr loci such as *Yr65* on chromosome 1B and *Yr67* on chromosome. These results emphasize the role of chromosomes like 1B and 7B as critical reservoirs of yellow rust resistance genes which harbor multiple overlapping QTLs and Yr loci. The discovery of novel QTLs in specific subpopulations, often without overlap with known resistance genes, suggests the presence of new, subpopulation-specific resistance alleles that could be of great value for future breeding programs. These regions warrant further investigation, and the next logical steps should focus on the fine-mapping of these QTLs. This can be achieved by constructing an ad-hoc population of congenic lines to precisely map the regions and identify potential candidate genes responsible for yellow rust resistance. Additionally, the development of KASP (Kompetitive Allele Specific PCR) diagnostic markers for the most promising QTLs could accelerate marker-assisted selection in breeding programs. These markers will enable high-throughput, cost-effective screening of durum wheat populations for yellow rust resistance, thus enhancing the efficiency of breeding strategies aimed at improving resistance durability. By integrating these findings into practical breeding tools, the study paves the way for more resilient wheat varieties that can better withstand the threat of yellow rust in various environments.

3 Genome-Wide Association Study (GWAS) conducted in a panel of tetraploid wheat durum wheat landraces to map MTAs associated to Septoria Tritici Blotch Resistance (Stb)

3.1 Introduction

3.1.1 Life cycle and biology

Zymoseptoria tritici, the causal agent of Septoria Tritici Blotch (*Stb*), follows a hemibiotrophic life cycle, meaning it alternates between an initial biotrophic phase, where it feeds on living host tissue without immediately causing visible damage, and a subsequent necrotrophic phase, where it kills host cells and absorbs nutrients from the dead tissue (Kema et al., 1996). The pathogen's life cycle and infection success are tightly linked to environmental conditions, particularly temperature and humidity, which influence spore dispersal, germination, and disease progression. The infection begins when ascospores, released from sexual fruiting bodies called pseudothecia, or asexual pycnidiospores land on the wheat leaf. The ascospores are typically wind-dispersed over long distances, while pycnidiospores are disseminated locally by rain splash (Eyal, 1999; McDonald & Mundt, 2019). The pathogen gets into the host through natural openings like stomata, without the aid of any haustoria, making the initial penetration of the leaf tissue passive. After entering the leaf, *Z. tritici* colonizes the apoplastic space (the intercellular space between plant cells), where it remains symptomless during the latent biotrophic phase, which can last between 7 and 14 days, depending on environmental conditions (Keon et al., 2007; Orton et al., 2011). During this asymptomatic phase, the fungus grows extensively in the leaf without causing immediate tissue damage, thereby evading the plant's defense mechanisms (Sanchez-Vallet et al., 2015). This biotrophic phase is followed by the necrotrophic phase, where the pathogen switches to an aggressive lifestyle, killing host cells and forming necrotic

lesions on the leaf surface (Kettles & Kanyuka, 2016). The lesions are typically recognised as dotted with black pycnidia, the asexual fruiting bodies, which produce pycnidiospores. These spores are released into the environment, especially during rain events, and can infect new leaves, provoking additional disease cycles (Palma-Guerrero et al., 2016). *Zymoseptoria tritici* 's life cycle is highly dependent on environmental conditions, particularly leaf wetness, which is crucial for both spore germination and infection. Optimal infection occurs under cool temperatures (10-20°C) and prolonged periods of leaf wetness, typically from rainfalls (Fones & Gurr, 2015). These conditions favour the dispersal of pycnidiospores and ascospores, and subsequent germination and infection of wheat leaves (Shaw & Royle, 1993). This dependency on moisture is a key factor in the pathogen's prevalence in temperate regions with frequent rainfall, such as Europe and parts of North America (McDonald & Mundt, 2019). Sexual reproduction in *Zymoseptoria tritici* occurs on wheat debris left in the field after harvesting. The pathogen survives on this debris in the form of pseudothecia, which produce ascospores during wet conditions in the following growing season (Kema et al., 1996). The sexual cycle generates genetic diversity in the *Zymoseptoria tritici* population, facilitating the arise of new virulent strains and contributing to fungicide resistance (Stukenbrock et al., 2011). This genetic diversity is a major challenge for disease control, as it enables rapid adaptation to resistant wheat varieties and fungicide treatments (McDonald & Mundt, 2019). The pathogen's ability to alternate a biotrophic and necrotrophic lifestyle, coupled with its dependence on specific environmental conditions and its sexual reproductive capacity, makes *Zymoseptoria tritici* a considerable threat for wheat security and yield production, due to its complex and not durable management (Kettles & Kanyuka, 2016).

3.1.2 Host-pathogen interaction in Zymoseptoria tritici pathosystem

The interaction between wheat and *Zymoseptoria tritici* involves a complex interplay between the host's defense mechanisms and the pathogen's strategies to evade and suppress them. *Zymoseptoria tritici* is a hemibiotrophic pathogen, initially adopting a biotrophic lifestyle, where it grows between host cells in the apoplast without causing visible symptoms, actively suppressing immune responses (Keon et al., 2007). During this phase, *Zymoseptoria tritici* secretes effector proteins that inhibit the plant's immune pathways, such as pattern-triggered immunity (PTI), which is activated by the recognition of pathogen-associated molecular patterns (PAMPs) like chitin, a key component of fungal cell walls (Rudd et al., 2015). To evade chitin detection, *Zymoseptoria tritici* produces LysM domain-containing proteins (e.g., Mg1LysM, Mg3LysM, and MgxLysM), which bind to chitin and prevent the host's immune system from recognizing it. This mechanism allows the pathogen to remain undetected during its biotrophic phase, avoiding immune activation and start the symptomless phase (Kettles & Kanyuka, 2016). Of these LysM proteins, it has been suggested that Mg1LysM and Mg3LysM are upregulated during the symptomless colonization of wheat, with peak expression of Mg3LysM at day 4 and Mg1LysM at day 9 post-infection. Both proteins bind chitin, but only Mg3LysM can block chitin-induced immune responses. In addition to immune suppression, Mg1LysM and Mg3LysM protect *Zymoseptoria tritici* by shielding its cell walls from degradation by plant chitinases, further aiding in immune evasion (Kettles & Kanyuka, 2016). This dual function implying immune evasion and protection from chitin-induced PTI, enables the pathogen to maintain its biotrophic phase and avoid hypersensitive responses (HR), which could lead to cell death and hinder pathogen growth. After approximately 7-14 days, *Zymoseptoria tritici* transitions to the necrotrophic phase, characterized by visible necrotic lesions on leaves surface, as the pathogen kills host cells and absorbs nutrients from the dead tissue (Palma-Guerrero et al., 2016). During this phase, *Zymoseptoria tritici* upregulates necrosis-inducing effectors, such as NEP1 (Necrosis and Ethylene-inducing Peptide 1), which facilitate host cell death, contributing to the pathogen's aggressive colonization (Duba et al., 2018). This switch from a biotrophic symptomless colonizer to a destructive necrotroph underscores the pathogen's dual life style and its ability to evade plant's recognition system first and secondly, manipulate the host's immune pathways. The *Zymoseptoria tritici* -wheat

interaction also highlights the importance of both qualitative (R genes) and quantitative resistance. While R genes can provide race-specific resistance, the high genetic variability of *Zymoseptoria tritici* allows it to rapidly overcome these defences based on gene-for-gene interaction. On the other hand, quantitative resistance, controlled by multiple small-effect genes, offers more durable protection by slowing the pathogen's development without completely preventing infection (Brown et al., 2015).

3.1.3 Septoria Tritici Blotch: Current State-Of-The-Art and QTLs mapping

Septoria Tritici Blotch (*Stb*), caused by the fungal pathogen *Zymoseptoria tritici*, is one of the most devastating foliar diseases of wheat, particularly in temperate regions with high humidity and frequent rainfall. It has become a serious threat to global wheat production, especially in Europe, where yield losses can range from 10% to 50% in severe epidemics (Fones & Gurr, 2015). In the European Union, annual yield losses combined with the cost of fungicides for controlling Stb have been estimated to reach up to €1.2 billion (Fones & Gurr, 2015). Similar impacts have been observed in other wheat-producing regions, including parts of North America, where losses of around 20-30% have been reported under favorable conditions for the pathogen (Torriani et al., 2015). The economic burden of *Stb* also extends to reduced grain quality, which affects marketability and results in lower prices for infected crops (Heick, T. M et al., 2017). One of the key challenges in managing *Stb* is the high genetic diversity of *Z. tritici* populations. This diversity is driven by frequent sexual recombination, which occurs primarily on wheat debris during the winter, and contributes to the rapid evolution of new virulent strains. Studies have shown that *Zymoseptoria tritici* populations exhibit significant genetic diversity across regions, which allows the pathogen to adapt quickly to environmental changes, overcome host resistance, and develop fungicide resistance (Stukenbrock et al., 2008; Hartmann et al., 2017). Genomic analyses have revealed extensive genetic variation within and between populations of *Zymoseptoria tritici*, with high levels of recombination and gene flow facilitating the emergence of new pathotypes (McDonald et al., 2019). This genetic plasticity is particularly concerning because it enables the pathogen to evade control measures, necessitating continuous development of new resistant wheat varieties and updated fungicide formulations (Chedli et al.,2022; Mekonnen, T. et al., 2020). In recent years, significant progress has been made in identifying the genetic basis of resistance to *Stb* through quantitative trait loci (QTL) mapping using both genome-wide association studies (GWAS) and traditional linkage mapping populations. Nowadays, 23 *Stb* genes have been mapped and published (Brown et al. 2015; Goodwin et al., (2015); Liu et al. (2013); Tabib Ghaffary et al. (2012); Tabib Ghaffary et al. (2011) Cuthbert et al., (2011); Chartrain et al. (2009); Raman et al., (2009); Arraiano et al. (2007b); Cowling (2006) ; Chartrain et al., (2005a); Chartrain et al.(2005c); Adhikari et al. (2004abc)). Among all of these 22 have been mapped in haxaploid wheat (AABBDD), whereas only one in *Triticum monococcum* (AA), *TmStb1* (Jing et al., 2008). So far, no *Stb* resistance genes have been mapped in tetraploid wheat (AABB), and the situation is similar for QTL mapping studies. Most QTL mapping studies have focused on bread wheat, with a larger number of studies identifying resistance loci in this species (Patial et al., 2024; Radecka-Janusik et al., 2024; Mikaberidze, A., et al., 2024; Stapley, J et al., 2024; Zakieh, M., et al 2023; Mahboubi et al., 2022; Yang et al., 2022; Langlands et al., 2022; Mahboubi et al., 2021; Riaz et al., 2020; Stewart et al., 2016). In contrast, QTL mapping efforts in durum wheat remain limited, with only a few studies reported (Ferjaoui et al., 2022; Ouaja, M et al., 2022; Ballini et al., 2020; Kidane et al., 2017). The QTLs identified in both species are often race-specific, providing resistance against particular strains of the pathogen. However, these race-specific QTLs are susceptible to breakdown over time due to the rapid evolution of *Zymoseptoria tritici* populations (Orton et al., 2011). These loci are often associated with quantitative, partial resistance, which is generally more durable than race-specific resistance, as it slows the evolution of virulence in the pathogen (Kettles et al., 2018). GWAS has proven particularly effective in capturing the complex genetic architecture of *Stb* resistance. For instance, Kettles et al. (2018) identified several marker-

trait associations, highlighting the role of minor-effect loci that together contribute to the overall resistance phenotype. Despite these advances, the durability of *Stb* resistance remains a significant challenge. The quantitative nature of *Stb* resistance, influenced by environmental interactions, genetic backgrounds, and the high adaptability of the pathogen, complicates breeding efforts. To address this, breeding programs are increasingly focusing on stacking multiple resistance genes (pyramiding) by combining major QTLs with minor-effect loci to enhance durability (Chartrain et al., 2009). Furthermore, the integration of modern breeding tools such as genomic selection (GS) and high-throughput phenotyping is expected to accelerate the development of wheat varieties with more robust resistance to *Stb* (Jighly et al., 2016). In addition to genetic resistance, it has been suggested that several physiological traits also play an important role in wheat's response to *Zymoseptoria tritici*. Heading date and flowering time, in particular, are critical factors that influence the timing of wheat's exposure to *Zymoseptoria tritici* spores. Epidemics typically peak during certain periods of the growing season when moisture and temperature conditions are optimal for spore dispersal and infection (Kollers et al., 2013). In contrast, late-heading varieties may avoid infection if environmental conditions become less favourable for pathogen development later in the season (Croll et al., 2013). Flowering time is another physiological trait that affects the interaction between *Zymoseptoria tritici* and the host plant. Wheat is generally more vulnerable to infection during key developmental stages, particularly during early grain filling, when leaf area and photosynthetic activity are essential for yield (Glazebrook, 2005). Synchronizing plant development with periods of lower pathogen pressure can help minimize disease impact. Genotypes that flower earlier or later than the peak infection period can exploit this natural variation to avoid severe infection (Chartrain et al., 2009). In conclusion, while fungicide application remains an essential tool in *Stb* management, the increasing resistance of *Zymoseptoria tritici* to fungicides emphasizes the need for more durable genetic resistance discovery. Especially, in durum wheat, there is an urgent need for exploring and characterizing novel reservoir and sources of genetic resistance towards *Stb*. This study utilized a highly diverse subpanel of 501 *Triticum turgidum* landraces and related subspecies, also called CEREALMED, extracted from the Tetraploid Wheat Global Collection, to evaluate the diversity of resistance to Septoria tritici blotch (*Stb*). The goal was to identify genomic regions associated with genetic resistance to *Stb* in durum wheat through genome-wide association studies (GWAS).

3.2 Materials and methods

3.2.1 Plant material, Experimental Design and Environment

Table 24: Summary of the total number of individuals from each of the 8 subpopulations identified in the TGC panel, which make up the CEREALMED panel.

Qs	Subpopulation	Count
Q1	DWL_Horn_Africa_Aethiopicum	74
Q2	DWL_Horn_Africa_Carthlicum	5
Q3	DWL_SouthWestAsia_Syriacum	71
Q4	DWL_SouthWestAsia_Turanicum	2
Q5	DWL_Balkan_Turgidum	19
Q6	DWL_East_Europe_Trancaucasus	126
Q7	DWL_Egypt_Cyprous_Iberia	124
Q8	DWL_West_Asian_Founders	52
ADM	Admixed	37

The panel used for this association study comprises 501 durum wheat landraces and related subspecies, representative of all the 8 subpopulations, previously described in chapter 1. The total count of individuals for each subpopulation is reported in table 24. The experimental trial was conducted at the University of Bologna's experimental fields in Cadriano (44°33′00.09″N 11°23′37.81″E, figure 31). The layout consisted of two randomized macro blocks, with nine checks repeated eight times in each replicate. These checks, representing either durum wheat cultivars or landraces, were carefully selected to cover a broad range of susceptibility and resistance to Septoria tritici blotch. This experiment has already been described partially by (Novi J.B, doctoral dissertation., 2023)

The selected cultivars were:

- Cappelli (susceptible),
- Iran1 (resistant),
- Karim (susceptible),
- Kirmizi (resistant),
- Kunduru (resistant),
- Meridiano (susceptible),
- Svevo (susceptible),
- Trinakria (resistant),
- Valnova (susceptible).

Each plot, containing a single genotype, measured 1.50 meters in length and 30 centimeters in width.

Figure 31: A simplified map indicating the location of the experimental field in Cadriano (44°33′00.09″N 11°23′37.81″E), where *Stb* symptom scoring was conducted.

3.2.2 Inoculation and disease assesment

Before inoculation, the plants were kept wet for two consecutive days to ensure optimal humidity levels. A sprinkler system was then installed across the experimental field to provide effective irrigation, facilitating the spread of the pathogen. The inoculum, consisting of a selected *Zymoseptoria tritici* strain sampled from the same location the previous year and provided by UNIBO, was evenly distributed across the plants using a spray bar. The inoculation was carried out twice, with a 4-day interval, during the onset of the booting stage, corresponding to ZS43–ZS47 on the Zadoks growth scale (Zadoks et al., 1974). Following inoculation, the plants were monitored for 20 days, during which time the Symptomless Latent Phase (biotrophic phase) occurred. Heading date (ZS59)

was recorded during this phase. After 20 days, symptoms were assessed for the first time using a disease assessment scoring scale for *Zymoseptoria tritici* provided by INRAE BIOGER, a French research institute. The scoring focused on infection type symptoms on the flag leaf (IT_FL) and the canopy below the flag leaf (IT_CANO). A second disease assessment was conducted 7 days later to evaluate disease progression, allowing for the calculation of the Area Under the Disease Progression Curve (AUDPC).

The first three traits were recorded on a scale of 0 to 9. The scoring scale was divided into two levels, each corresponding to a specific range:

- **0 to 5**: This range indicates the detection of necrotic regions, referred to as sporulating lesions, across the canopy or flag leaf, signaling Hypersensitive Responses (HR). The scale further distinguishes between single isolated lesions (1-3) and merged lesions (4-5).
- **6 to 9**: This range indicates merged irregular necrotic lesions, with the percentage of sporulation covering the leaf area. The percentages are categorized as low (6, 10% to 25%), medium-low (7, 25% to 50%), medium-high (8, 50% to 75%), and complete coverage (9, over 75%).

This assessment method provides a comprehensive evaluation of disease symptoms and progression over time. For a more detailed representation of the used scoring scale provided by INRAE BIOGER, see figure 32.

Figure 32: Example of the scoring scale used to evaluate *Stb* infection type symptoms.

Hence, as follow:

- **0**: No visible symptoms.
- **1:** One single necrotic spot
- **2**: two to five single isolated necrotic spots
- **3:** More than five necrotic spots
- **4**: Mix of single and merging necrotic spots
- **5:** Only merging necrotic lesions without sporulations
- **6**: 10% to 25% of sporulating area across leaf surface
- **7:** 25% to 50% of sporulating area across leaf surface
- **8**: 50% to 75% of sporulating area across leaf surface
- **9**: Over 75% of sporulating area across leaf surface

3.2.3 Phenotypic Data Analysis

Like for chapter 2, a series of statistical analyses were conducted on the phenotypic data using R and RStudio (RStudio Team, 2020). The Area Under the Disease Progression Curve (AUDPC) was calculated to quantify the progression of Septoria tritici blotch (*Stb*) over time based on two disease assessments conducted 7 days apart. The AUDPC provides a summary measure of disease progression over a specified time period.

The formula used for calculating AUDPC is as follows:

$$AUDPC = \sum_{i=1}^{n-1} \left(\frac{y_i + y_{i+1}}{2} \right) (t_{i+1} - t_i)$$

Where:

- y_i = infection type score at the i-th time point (ranging from 0 to 9).
- y_i+1 = infection type score at the (i+1)-th time point.
- t_i = time (in days) at the iii-th assessment.
- t_i+1 = time (in days) at the (i+1)(i+1)(i+1)-th assessment.
- n = total number of time points assessed (in this case, n=2n).

In this study, the first assessment was performed at t_1 (day 0 in accordance with AUDPC formula but 20 days post-inoculation) and the second assessment at t_2 (day 7, 27 days post-inoculation). The AUDPC was thus calculated based on the infection types scores obtained at these two time points, which allowed for the evaluation of disease progression over the 7-day interval. For the analysis of IT_FL and IT_CANO, only the final score was considered. All traits, including heading date, were normalized and standardized using the Yeo-Johnson normalization function from the bestNormalize package in R. The improvement in normality after transformation was assessed using the Shapiro-Wilk normality test. The Pearson correlation coefficient and statistical significance among traits were also evaluated. An analysis of variance (ANOVA) was performed on the transformed data using a mixed linear model to estimate broad-sense heritability (h^2), following the procedures described in Chapter 2. Best Linear Unbiased Estimates (BLUES) were obtained through mixed model analysis (lmer) using the lme4 package in R. In this model, the transformed and standardized phenotypic data served as the dependent variable, with genotype (ID) treated as a fixed effect and heading date (HD)

included as a covariate. Other factors, including row, column, and replicates, were treated as random effects. The model is exemplified below:

Phenotype ~ Genotype +HD + 1|Row+ 1|Column+ 1|Block

3.2.4 SNP Genotyping, LD decay analysis, SNPs Pruning, population structure analysis and Identity By State (IBS) genetic similarity matrix

The same SNP-based genotyping matrix, which includes 20,235 biallelic SNPs and is detailed in Section 2.2.4, was utilized for the association study. For the analysis of LD decay, SNP pruning, population structure, and IBS, please refer to Chapter 2. It is important to note that the CEREAL panel is a subset of the core TGC panel used in the multi-year and multi-environmental assessment of yellow rust.

3.2.5 Genome-Wide Association Study for CEREALMED panel

Unlike the multi-year and multi-environmental association study described in chapter 2, in this case, phenotypic data were available for only one environment. In this context, GWAS was also conducted using the linear mixed model implemented in the GAPIT v.3.0 package in R (Wang et al., 2021). The same four different models provided by GAPIT v.3.0 were tested: the Mixed Linear Model (MLM) (Yu et al., 2006), the Multi-Locus Mixed Model (MLMM) (Segura et al., 2012), the Fixed and Random Model Circulating Probability Unification (FarmCPU) (Liu et al., 2016), and the Bayesian Information and Linkage Disequilibrium Iteratively Nested Keyway (BLINK) (Huang et al., 2018). Minor Allele Frequency (MAF) filtering (< 5%) was applied only once, resulting in 15708 SNP markers. The association analysis was performed on the transformed Best Linear Unbiased Estimates (BLUEs) for the four traits IT_Fl, IT_CANO, AUDPC_Fl and AUDPC_CANO. In the same way, kinship matrix was generated using TASSEL 5.0 (Bradbury et al., 2007). The population structure membership scores from ADMIXTURE v1.3 were not included in the GWAS models to avoid overfitting but were later used as covariates in downstream linear model analysis. Considering the Bonferroni significance threshold calculated through permutation testing ranged between 4 and 5, in this case the final cut-off for significant associations was set for 5 in order to prioritize only QTLs with strong effect and high LOD. MTAs were only selected provided that they were detected in more than one model and in at least two traits. Manhattan plots (see supplementary files) and QQ plots were generated using GAPIT v.3.0 to visualize the association results.

3.2.6 Genome-Wide Association Study within TGC subpopulations

Similar to approach described in chapter 2, GWAS was also conducted within the single subpopulations, provided that number of members was superior to 50 individuals.

As reported in table 24, 5 subpopulations met this criterion:

- Q1: DWL_Horn_Africa_Aethiopicum – 74 individuals
- Q3: DWL_SouthWestAsia_Syriacum – 71 individuals
- Q6: DWL_East_Europe_Trancaucasus – 126 individuals
- Q7: DWL_Egypt_Cyprous_Iberia – 124 individuals
- Q8: DWL_West_Asian_Founders – 52 individuals

GWAS was conducted by following the same criteria described in section 2.2.6.

SNP-based genotyping was generated for each subpopulation following MAF (5%) filtering as well as kinship matrix.

Considering the high genetic similarity characterizing the single subpopulation in comparison with the whole panel, cut-off significance threshold was lower to 4 (p-vluae = 0.0001).

3.2.7 Downstream analysis, LD-Blocks detection and Haplotype Analysis

Downstream analysis and Haplotype detection were both performed by following the same procedure thoroughly described in chapter 2 at the sections 2.2.7 and 2.2.8.

3.2.8 Projection of Stb Loci and QTLs onto the cv Svevo reference genome

Following the approach and projection criteria outlined in Section 2.2.9 of Chapter 2, *Stb* loci and QTLs identified through independent linkage mapping and GWAS studies on tetraploid wheat were projected onto the Svevo reference genome. This projection was conducted to enhance the accuracy and conclusiveness of result interpretation. Since many known *Stb* loci were originally mapped using older molecular markers (such as SSR, DArT, and RAPD), the projected positions (in Mbp) correspond to the physical locations of the closest SNP markers on the Svevo reference genome, unless the *Stb* gene has been cloned. Given the documented influence of physiological traits like heading date and flowering time on wheat susceptibility to *Zymoseptoria tritici*, the identified QTLs were also compared with the physical positions of known loci associated with these important traits in wheat.

- Locus Q
- Flowering time loci (FL)
- Vernalization (Vrn) loci
- Photoperiod response (Ppd)

The information regarding these selected genes were extracted from Ensembl plant database (https://www.ensemblgenomes.org) and Graingenes (https://wheat.pw.usda.gov).

3.3 RESULTS

3.3.1 Descriptive statistic, phenotypic data distribution and correlation

A preliminary GWAS was conducted on a panel of 501 accessions of durum wheat landraces and related subspecies, evaluated in a single environment (Cadriano) and year (2022). All accessions were assessed for Septoria tritici blotch (*Stb*) symptoms, focusing on infection type (IT) on the flag leaf (IT_FL) and the rest of the canopy (IT_CANO). The phenotypic evaluation revealed a wide range of symptom severity for both IT_FL and IT_CANO, with scores spanning the full scale from 0 to 9. For AUDPC_FL and AUDPC_CANO, which measure disease progression, the results showed consistent patterns, with some genotypes exhibiting no change in symptoms over the 7-day interval, leading to an AUDPC value of 0, while others demonstrated significant disease progression, with AUDPC values reaching up to 70. The average change (delta) in IT_FL and IT_CANO between the two time

points was 1.26 and 1.23, respectively, indicating a slight overall increase in infection symptoms. However, there were five instances where the IT delta reached 9, reflecting a severe disease outbreak in certain genotypes. Heading date (HD) varied by 16 days across the panel, with early genotypes reaching heading 30 days after germination and late genotypes reaching heading 46 days after germination. Analysis of variance showed that broad-sense heritability (h^2) exceeded 60% for all disease-related traits, indicating that genetic factors played a more significant role than environmental effects. As expected, HD exhibited even higher heritability at 87%, confirming its strong genetic basis. A summary table displaying statistic for the 4 *Stb* traits and HD is reported below. Overall, a strong and significant correlation was observed among the four *Stb* phenotypes, with correlation coefficients consistently above 0.70 (figure 33). Regarding heading date (HD), significant correlations were found in all pairwise comparisons, though the correlation coefficients ranged from -0.20 to -0.31. This statistically significant negative correlation aligns with documented theories suggesting that wheat genotypes with earlier heading dates can escape peak infection periods, thereby reducing disease severity (Arraiano et al., 2009). Based on these findings, HD was included as a fixed-effect variable in the BLUES models for the four *Stb* traits

Table 25: Table displaying descriptive statistic for IT_FL, IT_CANO, AUDPC_FL, AUDPC_CANO and HD: Max (Maximum), Min (Minimum), Grand Mean (mean), Genetic Variance, Residual Variance, Phenotypic Variance, h2 (Broad-Sense Heritability), SD (Standard Deviation), SE (Standard Error).

Grosseto_2020	IT_FL	IT_CANO	AUDPC_FL	AUDPC_Cano	HD
max	9.2	9.29	61.26	63	46
min	0	0		0	30
Grand mean	4.2	5.48	24.96	33.85	39.75
Genetic Variance	2.07	1.98	93.03	111.63	8.96
Residual Variance	3.78	2.88	130.77	101.79	1.32
Phenotypic Variance	0.86	0.89	0.88	0.93	10.60
h^2	61	67	66	69	87
SD	2.53	2.28	15.61	15.36	3.26
SE	0.1	0.09	0.64	0.63	0.12

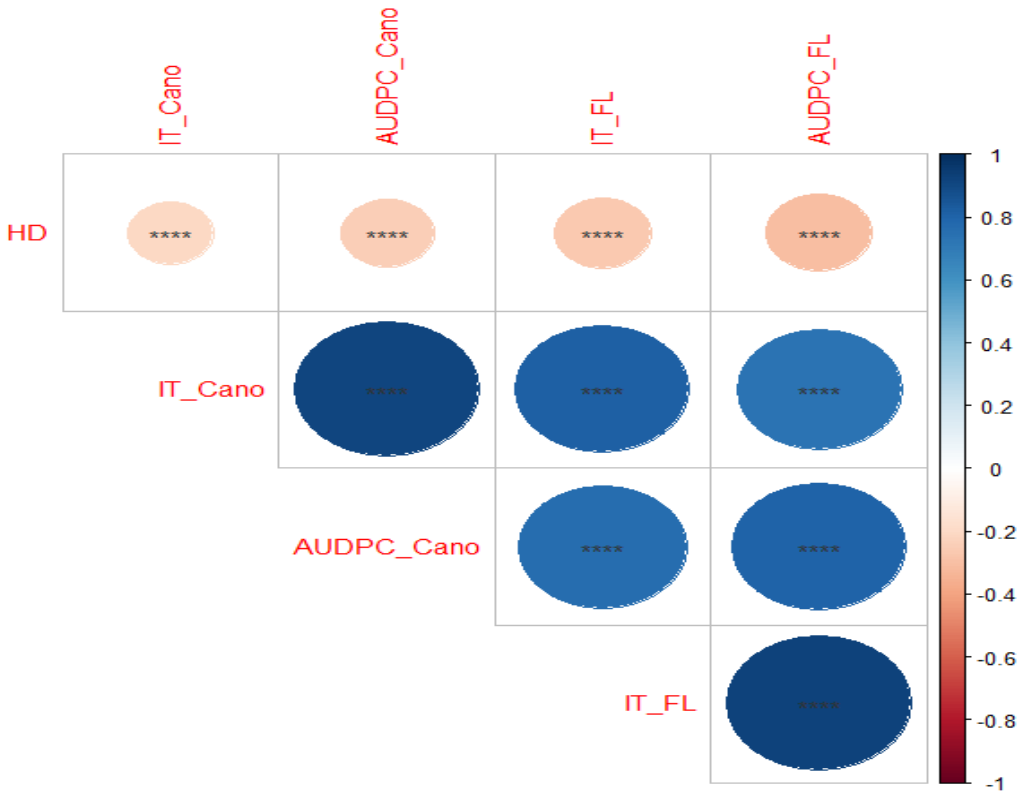

Figure 33: **This figure presents a correlation plot of the four *Stb* phenotypes: infection type on the flag leaf (IT_FL), infection type on the canopy (IT_CANO), AUDPC for the flag leaf (AUDPC_FL), and AUDPC for the canopy (AUDPC_CANO). Heading Date (HD) isalso included. Correlation values range from -1 (red) to 1 (blue), with asterisks indicating significance levels: * (0.05-0.01), ** (0.01-0.001), *** (0.001-0.0001), **** (< 0.00001).**

Table 26: Table displaying the numeric result of correlation plot also displayed in figure 34.

	IT_FL	IT_CANO	AUDPC_FL	AUDPC_Cano	HD
IT_FL	1	0.81	0.92	0.77	-0.26
IT_CANO	0.81	1	0.74	0.91	-0.2
AUDPC_FL	0.92	0.74	1	0.81	-0.31
AUDPC_Cano	0.77	0.91	0.81	1	-0.24
HD	-0.26	-0.2	-0.31	-0.24	1

.

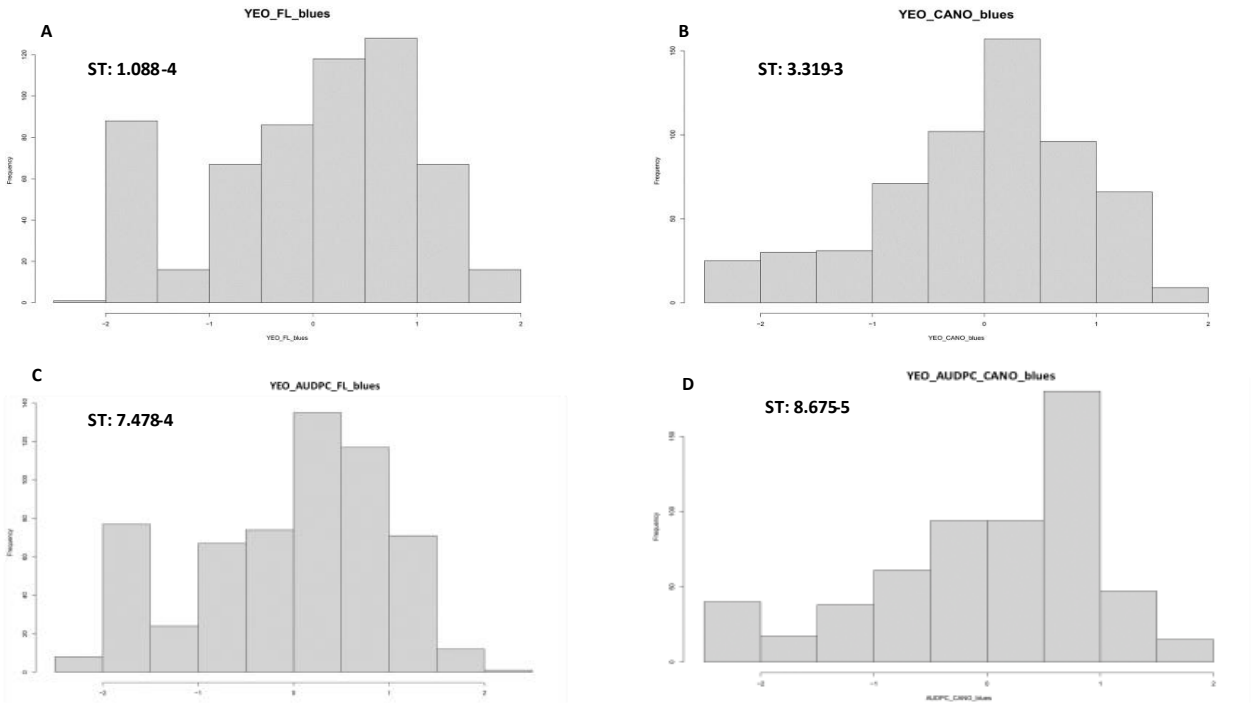

Figure 34: Transformed data histogram for BLUES deriving single environment Cadriano (BO) 2022 for IT_FL (A), IT_CANO(B), (C) AUDPC_FL and (D) AUDPC_CANO. The result of Shapiro Test (ST) is reported.

After normalization using the best transforming function provided by the bestNormalize R package, the four phenotypic traits did not meet the normality assumption (Shapiro-Wilk test, p-value < 0.05). Both YEO_FL_blues and YEO_AUDPC_FL_blues exhibited a bimodal distribution, while YEO_CANO_BLUES and YEO_AUDPC_CANO_BLUES displayed a more uniform distribution overall (figure 34).

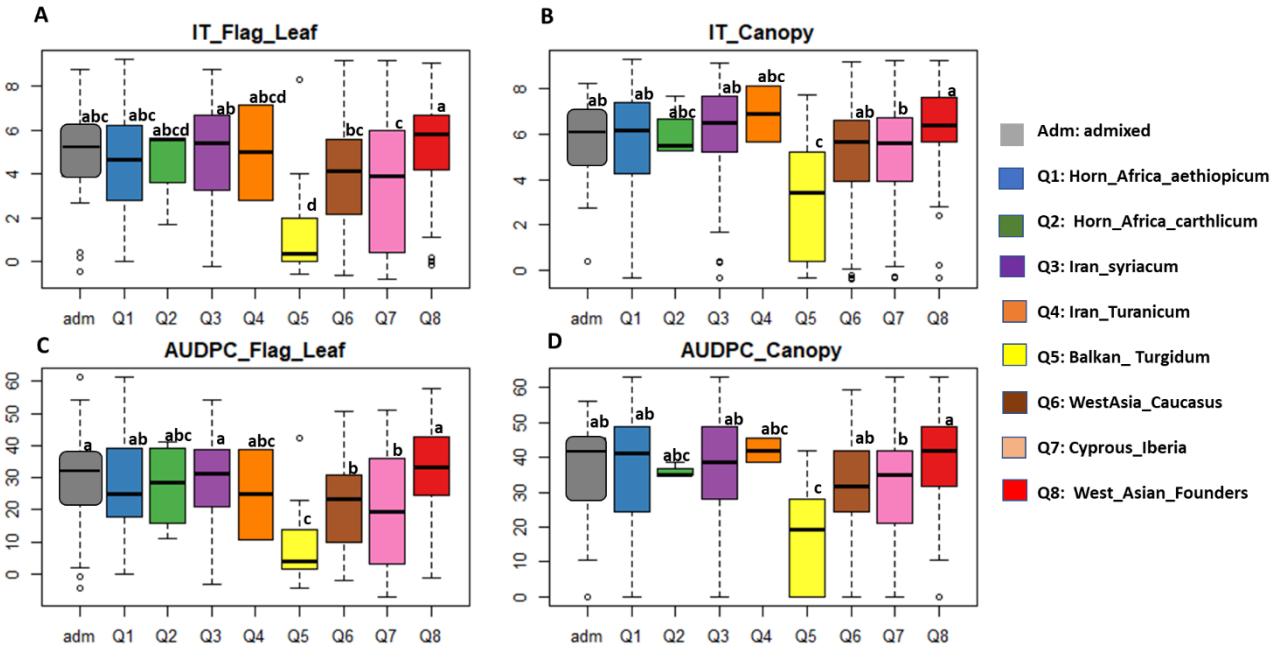

Figure 35: Boxplots displaying the phenotypic performance comparison for the 4 *Stb* traits among all the 8 subpopulations composing the CEREALMED panel plus admixed accessions. Compact letters refer to the result of post-hoc Tukey test. IT_FL (A), IT_CANO (B), AUDPC_FL (C) and (D) AUDPC_CANO.

The phenotypic comparison revealed considerable variability across all eight subpopulations for the four *Stb* traits, with both resistant and susceptible genotypes identified in each group. Notably, subpopulation Q5 (Balkan_Turgidum) consistently displayed values significantly below the population average for all four *Stb* traits, suggesting the presence of genotypes carrying resistant alleles within this group (figure 35).

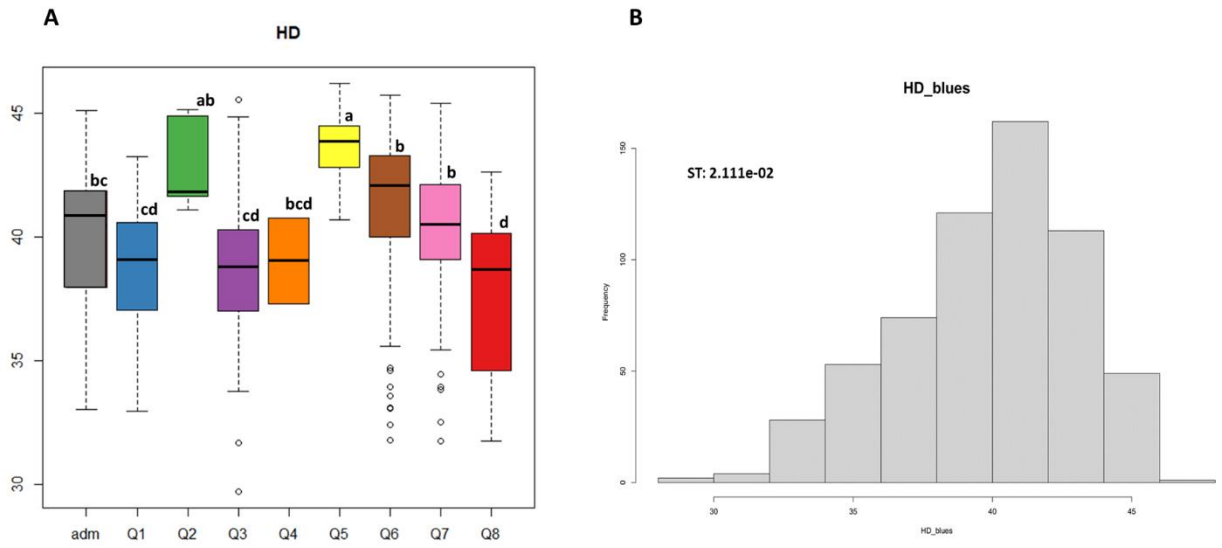

Figure 36: (A) Boxplots displaying the difference phenotypic performance comparison for Heading date among all the 8 subpopulations composing the CEREALMED panel plus admixed accessions. Compact letters refer to the result of post-hoc Tukey test. (B) Hisogram of frequency of HD. Shapiro-Test (ST) is reported.

Similar to the phenotypic comparison for *Stb* traits, the CEREALMED panel displayed significant variability in heading date within the individual subpopulations. Subpopulations Q1, Q3, Q6, Q7, and Q8 exhibited a wide range of heading dates, indicating the presence of both early- and late-heading accessions. In contrast, Q4 was primarily composed of mid-heading genotypes. Interestingly, both Q2 and Q5 were predominantly late-heading. However, this similarity in heading date between Q2 and Q5 did not align with their performance in *Stb* traits, as Q5 showed a predominantly resistant phenotype, while Q2 was more medium-susceptible (figure 36).

3.3.2 Stb Loci and QTLs projection onto the Svevo reference genome physical map

Similar to the projection of *Yr* loci described in Chapter 2, all known *Stb* loci and QTLs were mapped onto the Svevo reference genome following the previously established criteria. As no *Stb* locus has been mapped or cloned in durum wheat—most being identified in bread wheat—the high level of synteny between the Chinese Spring hexaploid wheat reference genome and the Svevo tetraploid wheat reference genome provided a reliable framework for projecting quantitative trait loci (QTLs) identified in hexaploid wheat. Like the yellow rust loci, all 23 *Stb* loci have been characterized in bread wheat, and the conserved synteny allows these loci to be accurately projected onto the Svevo genome. Below, you will find a summary table detailing the projected *Stb* loci on the A and B subgenomes, along with another table summarizing independent QTL mapping studies conducted on tetraploid wheat, categorized by linkage mapping populations and GWAS:

Table 27: Summary table showing the projected physical position of known Stb loci, mapped on the A and B subegenomes, onto the Svevo reference genome. In addition to the locating chromosome, the table displays also the physical position of the projection, the chromosome and reference(s) for each Stb loci.

***Stb* Locus**	**Pos (Mbp)**	**Chr**	**References**
Stb2	35.387	1B	Adhikari et al. (2004b); Liuet al. (2013)
Stb11	37.821	1B	Chartrain et al., (2005c)
StbWW	47.631	1B	Raman et al. (2009)
Stb9	650.00	2B	Brown et al., (2015)
StbSm3	15.398	3A	Cuthbert (2011)
Stb6	22.465	3A	Brading et al., (2002)
Stb14	33.559	3B	Cowling et al., (2006)
Stb7	720.000	4A	McCartney et al., (2003)
Stb12	736.475	4AL	Chartrain et al., (2005a)
Stb17	350.00	5A	Brown et al., (2015)
Stb1	401.530	5B	Adhikari et., Al 2004, Graingenes
Stb15	300.00	6A	Brown et al., (2015)
TmStb1	112.626	7A	Jing et al. (2008)
Stb3	87.182	7A	Brown et al., (2015), Goodwin and Thompson (2011)
Stb13	537.588	7B	Cowling et al., (2006)
Stb8	716.216	7B	Adhikari et al., (2003)

Table 28: Summary table listing all the independent QTL mapping studies considered for the projection onto the Svevo reference genome.

LINKAGE MAPPING POPULATION			
Reference	**Population Type**	**Population Size**	**QTLs Number**
Ferjaoui et al., (2022)	RILs	200	19
GWAS			
Y. G. Kidane et al., (2017)	Ethiopian durum wheat landraces and modern varieties	318	5
Ballini et al., (2020)	Evolutionary Pre-breeding pOpulation (EPO)	190	3

All projected QTLs are listed in Suppmentary table 2 available in supplementary file. Additonally, given the known influences of physiological traits on *Stb* reaction and susceptibility, all known genes underlying physiological traits such as photoperiod response, vernalization, heading date and flowering time were extracted from ensembl plant database and Graingenes. Herein, you find the summary table of all the considered physiological genes considered:

Table 29: Summary table listing all the annotated physiological genes considered for the QTL projection onto the Svevo reference genome.

Gene	Function	TRITD_Acronym	Physical position	Chromosome
Ppd-2A	Response to photoperiod	TRITD2Av1G019250	36567124-36570283	2A
Ppd-2B	Response to photoperiod		64958972-64962982	2B
Vrn-A1	Response to vernalization	TRITD5Av1G204680	549152139-549156384	5A
Vrn-B1	Response to vernalization	TRITD5Bv1G200510	570831391-570844281	5B
fcp650(Q)	Ethylene-responsive transcription factor	TRITD5Av1G231510	608,793,004-608,796,079	5A
FL-1A	Flowering Locus	TRITD1Av1G197270	519559220-519560818	1A
FL-1B	Flowering Locus	TRITD1Bv1G186910	575313190-575314760	1B
FL-2A	Flowering Locus	TRITD2Av1G037370	78480126-78482035	2A
FL-2A.2	Flowering Locus	TRITD2Av1G209010	578379733-578381694	2A
FL-2A.3	Flowering Locus	TRITD2Av1G281520	747434066-747434505	2A
FL-2A.3	Flowering Locus	TRITD2Av1G006520	10971928-10987767	2A
FL-2A.4	Flowering Locus	TRITD2Av1G266170	717396105-717397239	2A
FL-2A.5	Flowering Locus	TRITD2Av1G281530	747469264-747469703	2A
FL-2A.4	Flowering Locus	TRITD2Av1G281510	747421722-747422161	2A
FL-2A.5	Flowering Locus	TRITD2Av1G281490	747387400-747388428	2A
FL-2B	Flowering Locus	TRITD2Bv1G048450	122153813-122155703	2B
FL-2B.2	Flowering Locus	TRITD2Bv1G172950	511050164-511052127	2B
FL-2B.3	Flowering Locus	TRITD2Bv1G229600	694602854-694603741	2B
FL-2B.4	Flowering Locus	TRITD2Bv1G247690	743783888-743784892	2B
FL-3A	Flowering Locus	TRITD3Av1G056840	130022895-130026548	3A
FL-3A.2	Flowering Locus	TRITD3Av1G002080	3552839-3553814	3A
FL-3A.3	Flowering Locus	TRITD3Av1G002110	3609569-3611085	3A
FL-3B	Flowering Locus	TRITD3Bv1G003270	5939674-5940628	3B
FL-3B.2	Flowering Locus	TRITD3Bv1G003320	6014032-6015577	3B
FL-3B.3	Flowering Locus	TRITD3Bv1G003340	6081293-6082393	3B
FL-3B	Flowering Locus	TRITD3Bv1G060120	165364878-165367905	3B
FL-4A	Flowering Locus	TRITD4Av1G179660	543668582-543670425	4A
FL-4B	Flowering Locus	TRITD4Bv1G203310	664511606-664530639	4B
FL-4B.2	Flowering Locus	TRITD4Bv1G203490	664696012-664697386	4B
FL-4B.3	Flowering Locus	TRITD4Bv1G024800	67434393-67436205	4B
FL-5A	Flowering Locus	TRITD5Av1G115320	325235853-325236928	5A
FL-5A.2	Flowering Locus	TRITD5Av1G172070	468247346-468252005	5A
FL-5A.3	Flowering Locus	TRITD5Av1G254740	659472125-659473571	5A
FL-5A.3	Flowering Locus	TRITD5Av1G254690	659408839-659410240	5A
FL-5B.2	Flowering Locus	TRITD5Bv1G097410	286164879-286166027	5B
FL-5B	Flowering Locus	TRITD5Bv1G163060	481518028-481523125	5B
FL-6A	Flowering Locus	TRITD6Av1G063310	151632836-151633982	6A
FL-6A.2	Flowering Locus	TRITD6Av1G134310	389530499-389531709	6A
FL-7A	Flowering Locus	TRITD7Av1G033560	69366080-69366904	7A
FL-7A.2	Flowering Locus	TRITD7Av1G190760	515288430-515290196	7A
FL-7B	Flowering Locus	TRITD7Bv1G003900	9126441-9126704	7B
FL-7B.2	Flowering Locus	TRITD7Bv1G057630	162519251-162520668	7B
FL-7B.3	Flowering Locus	TRITD7Bv1G153470	484290062-484292286	7B

3.3.3 GWAS RESULTS

3.3.3.1 Global GWAS

As a whole, 8 QTL were detected from global GWAS on different chromosomes: Chromosome 1A (*Qstb.ubo.1A*), Chromosome 1B (*Qstb.ubo.1B*), Chromosome 4A (*Qstb.ubo.4A*), Chromosome 4B (*Qstb.ubo.4B*), Chromosome 5A (*Qstb.ubo.5A*), Chromosome 5B (*Qstb.ubo.5B*), Chromosome 6A (*Qstb.ubo.6A*), Chromosome 7A (*Qstb.ubo.7A*). *Qstb.ubo.4B* was the only QTL overlapping known projected Stb genes, namely, Stb7 and Stb12. None of these QTLs overlapped with the CI of projected QTLs, suggesting the detection of new regions underlying Stb resistance. The phenotypic variance explained by the 8 QTLs for the 4 Stb traits, ranges from 21.78% to 27.44%, including the effect of Qs which does not exceed the 10% overall (see summary tables 30 and 31). Furthermore, except for *Qstb.ubo.6A and Qstb.ubo.7A,* all the other QTLs are consistently significant for Stb traits. In particular, *Qstb.ubo.5A* and *Qstb.ubo.5B* show strong significance for all the traits (see summary tables 30 and 31). Despite being a subpopulation with a number of members lower than 50, Q5 showed strong significance for the 4 Stb traits, confirming a "structured" resistance phenotype. Additionally, Q3 and Q8 are also significant for all Stb traits, whereas Q1, Q6, Q7 for some of them. Q2 and Q4 are not significant for all of them. The correlation plot combining the cumulative effect of resistant or susceptible haplotypes and IT_FL and IT_CANO, showed a negative trend, suggesting a decrease of IT for both traits in correspondence of an accumulation of resistant haplotypes. The estimated person correlation coefficient was -0.60 for IT_FL and -0.63 for IT_CANO, with a very significant p-value for both (p-value < 2.2 e-16) (See figure 36). All Manhattan Plots are available in supplementary files.

Table 30: Summary table showing the results of the global GWAS and subsequent Linear Model and Anova Test for each selected MTAs. This table comprises several information, from top to bottom: QTL acronym, MTA (SNP), alleles (major/mino), chromosome, position (Mbs), Block start position (Mbp), Block end postion (Mbp), overlapping projected Stb confidence intervals, overlapping QTL detected also in the single subpopulation, maximum LOD for that MTA across all the environments, maximum single R2 across all the environments, Adjusted R-squared for alle the environments and multi-environmental clusters (%) and results of the statistically significant ANOVA test within each environment or environmental cluster: NS stands for non-significant, NA stands for Not applicable (removed by MAF), * 0.05 – 0.01, ** 0.01-0.001, *** 0.0001-0.00001, **** < 0.0000.

	QTL_name		***QStb.ubo.1A***	***QStb.ubo.1B***	***QStb.ubo.4A***	***QStb.ubo.4B***	***QStb.ubo.5A***	***QStb.ubo.5B***	***QStb.ubo.6A***	***QStb.ubo.7A***
	SNP		**IWB12695**	**IWB65512**	**IWB71695**	**IWB72366**	**IWB11636**	**IWB68790**	**IWB71886**	**IWB9749**
	Alleles		C/T	A/G	C/T	G/A	A/C	G/A	C/T	T/C
	Chromosomes		1A	1B	4A	4B	5A	5B	6A	7A
	Position (Mb)		573.76	659.4	730.46	492.75	411.50	528.74	561.88	564.51
	Block_start position (SVEVO)		572.97	659.06	730.42	489.66	411.48	527.27	560.27	564.25
	Block_end position (SVEVO)		574.02	659.40	730.55	492.76	411.50	530.56	563.92	564.51
	Subpopulations_landraces									
	Overlapping_Stb_Loci				*Stb7, Stb12*					
	Projected_QTL									
	LOD (max)		5	6.68	5.85	5.52	8.55	5.2	8.39	5.02
	R^2 (%) (max)		2.36	2.83	4.64	4.59	8.58	7.71	2.1	1.2
Environment	Stb_trait	Adjusted R-squared (%)	**Anova Test**							
CADRIANO(CAD)_2022	IT_Fl	26.64	**	**	***	***	****	****	NS	NS
	IT_CANO	20.38	*	**	**	**	****	***	*	*
	AUDPC_Fl	27.44	*	*	***	***	****	****	*	NS
	AUDPC_CANO	21.78	*	*	***	*	****	***	**	*

Table 31: Summary table presenting the results of the linear model for Qs. This table outlines the total phenotypic variance attributed to Qs in each environment, along with the ANOVA test results for each Q across all examined environments for both IT and SEV.

	Qs		**Q1**	**Q2**	**Q3**	**Q4**	**Q5**	**Q6**	**Q7**	**Q8**
Environment	*Stb*_trait	Adjusted R-squared (%)	**Anova Test**							
CADRIANO(CAD)_ 2022	IT_Fl	9.00	*	NS	***	NS	****	NS	**	**
	IT_CANO	5.8	NS	NS	**	NS	****	NS	NS	*
	AUDPC_Fl	9.75	*	NS	**	NS	****	*	**	**
	AUDPC_CANO	6.05	NS	NS	**	NS	****	NS	NS	*

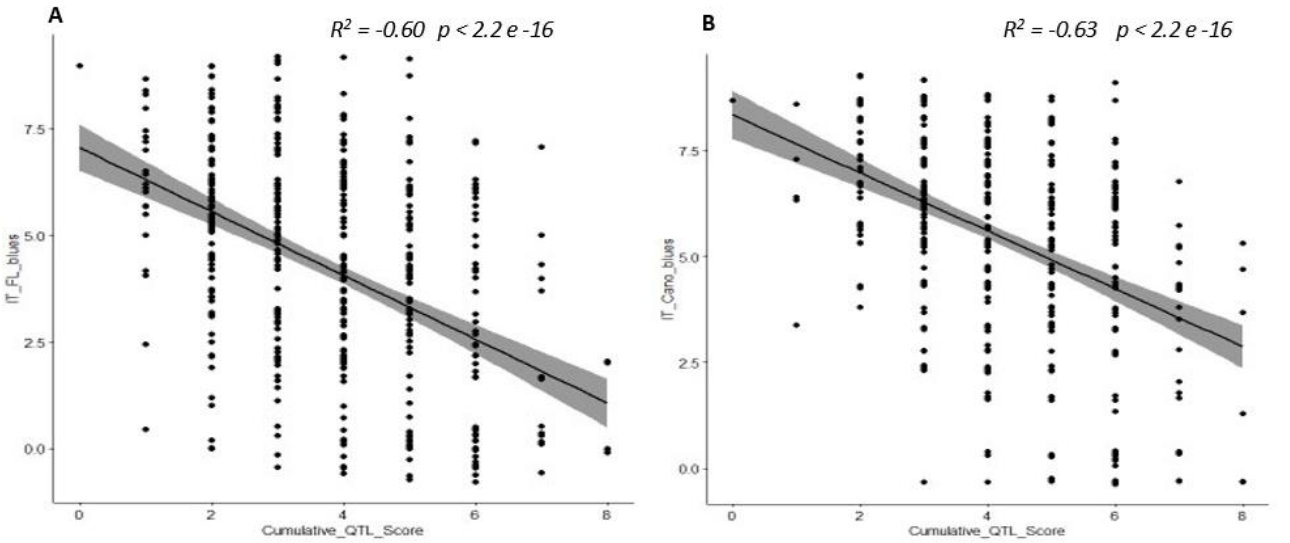

Figure 36: Correlation plot between the (A) IT_FL and (B) IT_CANO in and the cumulative score of all the haplotype variants for each QTL. Correlation coefficient (R^2) and p-values are reported on top.

- *QStb.ubo.1A*

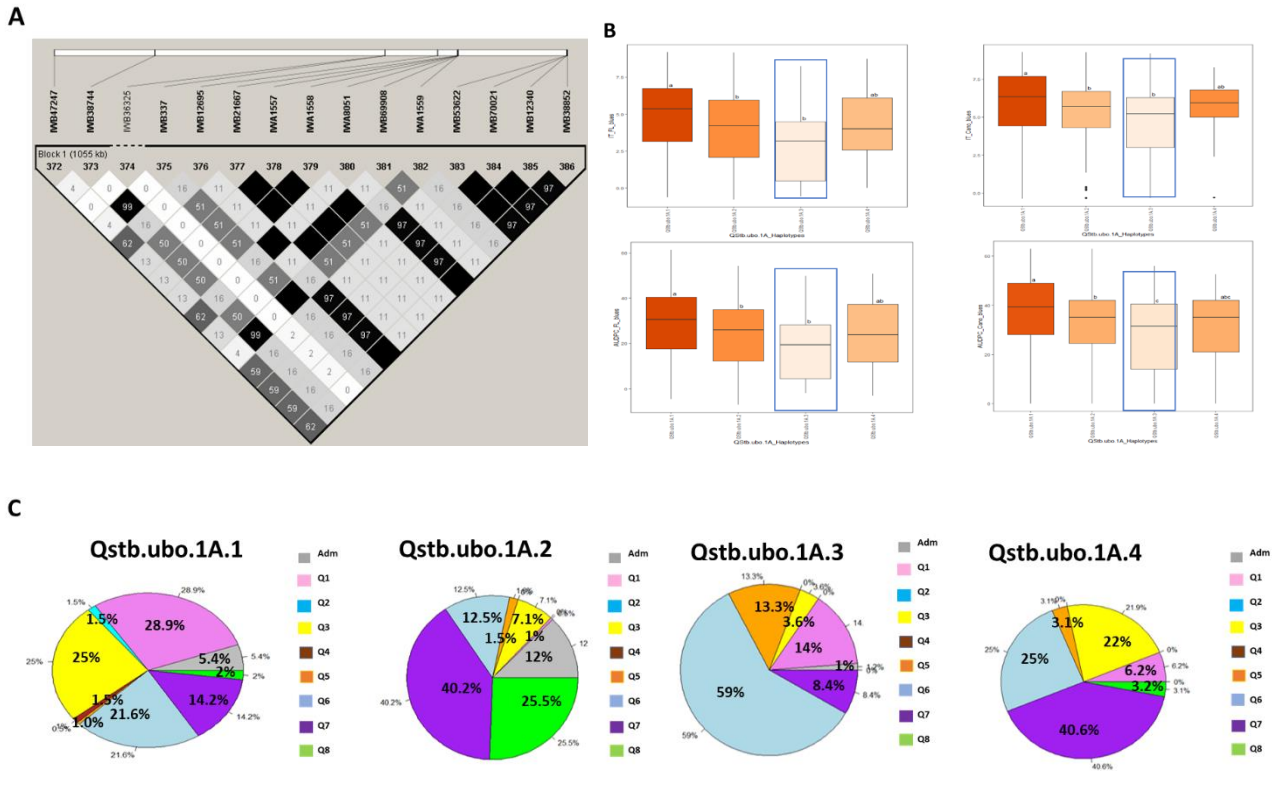

Figure 37: This figure displays the *QStb.ubo.1A* haploblock. A: *QStb.ubo.1A* LD-block B: Comparison of the phenotypic performance of all identified haploblock variants of QStb.ubo.1A for the 4 Stb traits, IT_FL (Topright), IT_Cano (Topleft), AUDPC_FL (Bottomright) and AUDPC_Cano (Bottomleft) C: The frequency of the major *QStb.ubo.1A* haplotypes variants within the single subpopulations is displayed.

A total of 7 different haplotypes were identified for *QStb.ubo.1A*, including 4 major haplotypes and 3 minor haplotypes. Among these, haplotype QStb.ubo.1A.3 exhibited the highest level of resistance,

displaying low phenotypic values for the 4 *Stb* traits. Additionally, *QStb.ubo.1A.2* also showed partial resistance compared to the other haplotypes. Overall, all haplotypes are dispersed across several subpopulations, but resistant haplotype *QStb.ubo.1A.3* is predominantly found in Q6 (see summary table 32 for a complete overview of all *QStb.ubo.1A* distribution and average phenotype). In figure 37, only the major haplotypes are displayed.

Table 32: A summary table displaying the frequency of *QStb.ubo.1A* within each subpopulation, the total count and mean value for IT_FL, IT_CANO, AUDPC_FL, AUDPC_Cano.

QStb.ubo.1A	**Haplotype variant**	**Count**	**IT_FL_blues**	**IT_Cano_blues**	**AUDPC_FL_blues**	**AUDPC_Cano_blues**	**adm**	**Q1**	**Q2**	**Q3**	**Q4**	**Q5**	**Q6**	**Q7**	**Q8**
QStb.ubo.1A.1	CCGTCATGGTTAGTG	204	4.89	5.92	29.07	36.97	11	59	3	51	2	1	44	29	4
QStb.ubo.1A.2	CTGCCGCAGCCAGTG	184	3.88	5.28	23.27	32.67	23	1	0	13	0	3	23	74	47
QStb.ubo.1A.3	TTGCTATGATCGTGA	81	3.1	4.54	18.11	27.41	1	12	0	3	0	11	49	7	0
QStb.ubo.1A.4	TCGTCATGGTTAGTG	32	4.2	5.57	23.74	31.75	0	2	0	7	0	1	8	13	1
QStb.ubo.1A.5	TTGCCGCAGCCAGTG	6	2.47	5.13	13.11	32.08	1	0	0	0	0	3	1	1	0
QStb.ubo.1A.6	CTACCATGGTCGTGG	2	5.64	5.66	41.22	35.00	0	0	2	0	0	0	0	0	0
QStb.ubo.1A.7	CCGCCGCAGCCAGTG	1	4.45	4.40	29.77	28.00	0	0	0	0	0	0	1	0	0

- *QStb.ubo.1B*

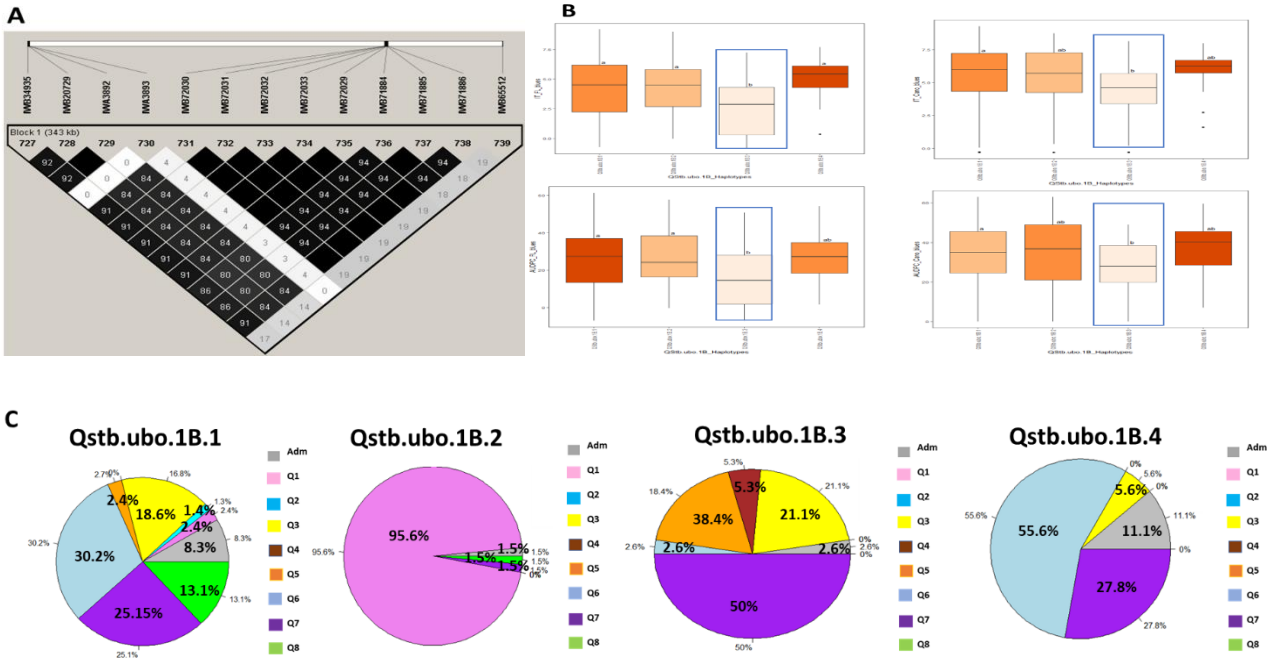

Figure 38: This figure displays the *QStb.ubo.1B* haploblock. A: *QStb.ubo.1B* LD-block B: Comparison of the phenotypic performance of all identified haploblock variants of *QStb.ubo.1B* for the 4 Stb traits, IT_FL (Topright), IT_Cano (Topleft), AUDPC_FL (Bottomright) and AUDPC_Cano (Bottomleft) C: The frequency of the major *QStb.ubo.1B* haplotypes variants within the single subpopulations is displayed.

A total of 9 different haplotypes were identified for *QStb.ubo.1B*, including 4 major haplotypes and 5 minor haplotypes. Among these, haplotype *QStb.ubo.1B.3* stood out for resistant phenotype among all the major haplotypes for the 4 Stb traits. Notably, *QStb.ubo.1B.2* was highly conserved in Q1 (95.6%) and minimally in Q7 and Q8. Resistant haplotype *QStb.ubo.1B.3* was highly found in Q7 (50%) and 4 other subpopulations, *QStb.ubo.1B.3* was highly present in Q6 and partially in Q3 and Q7. The most frequent haplotype, *QStb.ubo.1B.2*, was widely spread across all subpopulations (See summary table 33). In figure 38, only the major haplotypes are displayed.

Table 33: A summary table displaying the frequency of *QStb.ubo.1B* within each subpopulation, the total count and mean value for IT_FL, IT_CANO, AUDPC_FL, AUDPC_Cano.

QStb.ubo.1B	**Haplotype variant**	**Count**	**IT_FL_blues**	**IT_Cano_blues**	**AUDPC_FL_blues**	**AUDPC_Cano_blues**	**adm**	**Q1**	**Q2**	**Q3**	**Q4**	**Q5**	**Q6**	**Q7**	**Q8**
QStb.ubo.1B.1	AATAAGTGAGGAA	374	4.26	5.56	25.31	34.15	31	9	5	63	0	10	113	94	49
QStb.ubo.1B.2	AATAAGTGAGGAG	68	4.3	5.32	25.84	33.79	1	65	0	0	0	0	0	1	1
QStb.ubo.1B.3	GGCACTCACAACG	38	2.74	4.31	16.2	26.27	1	0	0	8	2	7	1	19	0
QStb.ubo.1B.4	GGCACTCACAACA	18	4.99	5.98	27.17	36.65	2	0	0	1	0	0	10	5	0
QStb.ubo.1B.5	GATACTCACAACG	4	1.86	2.57	13.78	18.67	0	0	0	0	0	0	2	2	0
QStb.ubo.1B.6	AATAAGTGAAAAA	3	5.29	6.74	27.03	35	0	0	0	0	0	0	0	3	0
QStb.ubo.1B.7	AATACTCACAACG	2	1.19	3.55	7.85	21	0	0	0	0	0	2	0	0	0
QStb.ubo.1B.8	AATGCTCACAACG	2	4.85	5.51	37.11	38.5	0	0	0	0	0	0	0	0	2
QStb.ubo.1B.9	AATGCTCACAACA	1	3.20	2.77	13.85	10.50	1	0	0	0	0	0	0	0	0

- QStb.ubo.4A

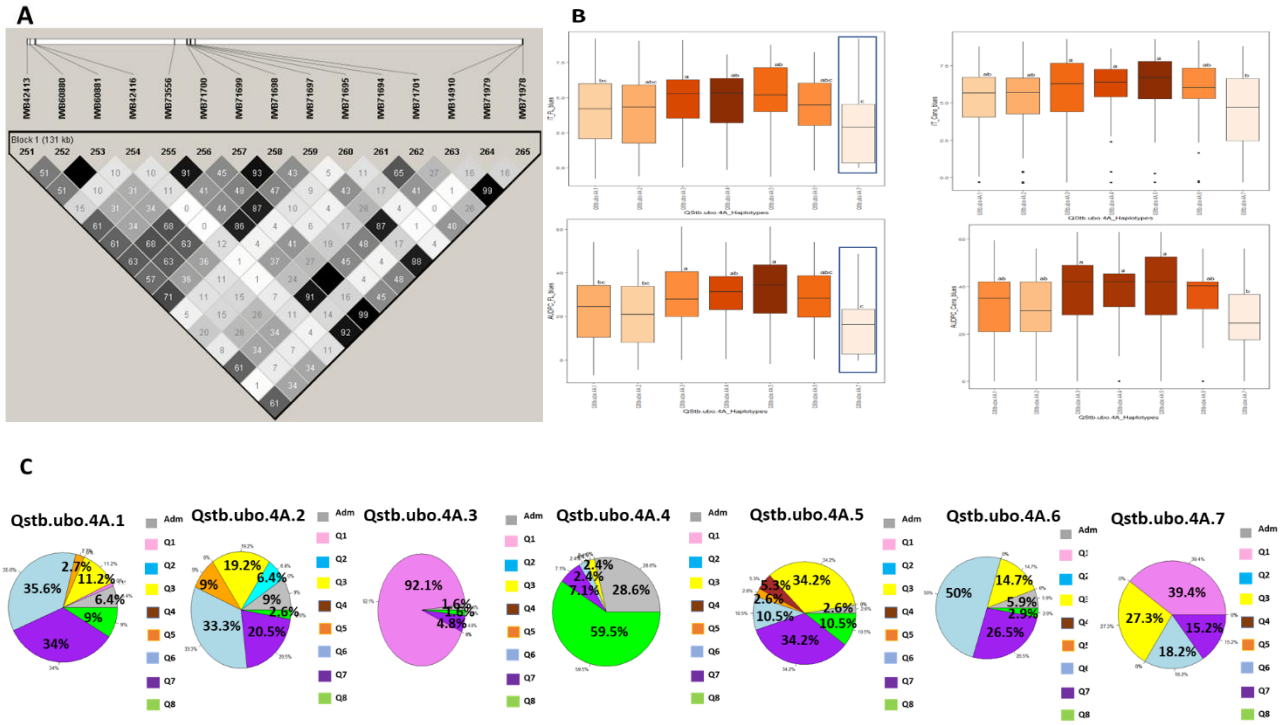

Figure 39: This figure displays the *QStb.ubo.4A* haploblock. A: *QStb.ubo.4A* LD-block B: Comparison of the phenotypic performance of all identified haploblock variants of *QStb.ubo.4A* for the 4 Stb traits, IT_FL (Topright), IT_Cano (Topleft), AUDPC_FL (Bottomright) and AUDPC_Cano (Bottomleft) C: The frequency of the major *QStb.ubo.4A* haplotypes variants within the single subpopulations is displayed.

A total of 16 different haplotypes were identified for *QStb.ubo.4A*, including 7 major haplotypes and 9 minor haplotypes. Among these, haplotype, *QStb.ubo.4A.7* stood out for resistant phenotype among all the major haplotypes for IT_FL and AUDPC_FL and only partially for IT_Cano and AUDPC_CANO. Notably, *QStb.ubo.4A.7* was spread across 4 subpopulations, mainly in Q1. Susceptible haplotype *QStb.ubo.4A.3* was highly found in Q1 (92%) and 4 other subpopulations, whereas *QStb.ubo.4A.4* was mainly conserved in Q8 (60%). All others were widely spread across several subpopulations (See summary table 34). In figure 39, only the major haplotypes are displayed.

Table 34: A summary table displaying the frequency of *QStb.ubo.4A* within each subpopulation, the total count and mean value for IT_FL, IT_CANO, AUDPC_FL, AUDPC_Cano.

QStb.ubo.4A	Haplotype variant	Count	IT_FL_blues	IT_Cano_blues	AUDPC_FL_blues	AUDPC_Cano_blues	adm	Q1	Q2	Q3	Q4	Q5	Q6	Q7	Q8
QStb.ubo.4A.1	CAAAAGCAACGGACA	188	3.9	5.18	22.85	31.86	12	2	0	21	0	5	67	64	17
QStb.ubo.4A.2	TGGAGATGGCAACCC	78	3.93	5.27	21.6	30.2	7	0	5	15	0	7	26	16	2
QStb.ubo.4A.3	TGGAGATGGCGGCTC	63	5.05	5.93	30.33	37.94	1	58	0	0	0	0	0	3	1
QStb.ubo.4A.4	TAAGGACAGCAGCCC	42	4.83	5.94	29.33	37.43	12	0	0	1	0	0	1	3	25
QStb.ubo.4A.5	CAAAGACAGCAACTC	38	5.1	6.11	31.51	38.95	1	0	0	13	2	1	4	13	4
QStb.ubo.4A.6	TAAGGATGGCGGCCC	34	4.36	5.76	27.30	35.98	2	0	0	5	0	0	17	9	1
QStb.ubo.4A.7	TGGAGATGGTAACCC	33	2.82	4.33	16.96	25.15	0	13	0	9	0	0	6	5	0
QStb.ubo.4A.8	CAAAGACGACGGCCC	7	6.18	7.1	37.23	48.02	1	0	0	0	0	0	6	0	0
QStb.ubo.4A.9	CAAAGGCAACGGACA	6	2.48	5.55	12.04	30.33	0	0	0	1	0	3	1	1	0
QStb.ubo.4A.10	CAAAGGCAACAGACA	6	2.33	5.77	24.14	37.90	0	0	0	0	0	0	2	4	0
QStb.ubo.4A.11	CAAAGACAACGGCCC	4	1.17	3.66	9.55	27.13	0	0	0	1	0	3	0	0	0
QStb.ubo.4A.12	TAAAGGCAGCGGACA	4	4.91	6.19	28.17	35	0	0	0	0	0	0	1	2	1
QStb.ubo.4A.13	CAAAGATGGTAACTC	2	3.7	4.74	24.35	21.00	0	1	0	0	0	0	0	0	1
QStb.ubo.4A.14	CAAGGACGGCGGCCC	2	5.1	7.48	35.56	52.5	0	0	0	0	0	0	0	2	0
QStb.ubo.4A.15	CAAAGATGGCAACCC	1	-0.31	0.23	-2.99	0.00	0	0	0	0	0	0	0	1	0
QStb.ubo.4A.16	TAAAGGCAGCGGACC	1	4.02	6.27	23.40	42.00	0	0	0	0	0	0	1	0	0

- *QStb.ubo.4B*

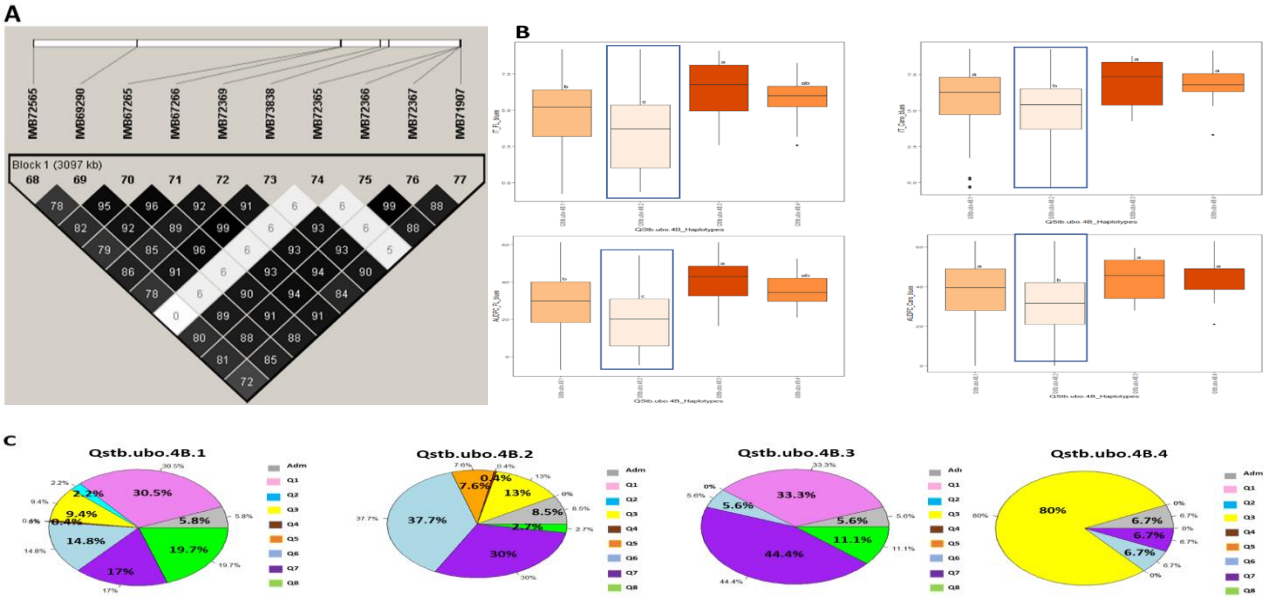

Figure 40: This figure displays the *QStb.ubo.4B* haploblock. A: *QStb.ubo.4B* LD-block B: Comparison of the phenotypic performance of all identified haploblock variants of *QStb.ubo.4B* for the 4 Stb traits, IT_FL (Topright), IT_Cano (Topleft), AUDPC_FL (Bottomright) and AUDPC_Cano (Bottomleft) C: The frequency of the major *QStb.ubo.4B* haplotypes variants within the single subpopulations is displayed.

A total of 13 different haplotypes were identified for *QStb.ubo.4B*, including 4 major haplotypes and 9 minor haplotypes. Among these major haplotypes, *QStb.ubo.4B.1* and *QStb.ubo.4B.2* were the most frequent haplotypes and both present in equal number (223 individuals each). *QStb.ubo.4B.2* stood out for a resistant phenotype for all the Stb traits (see figure 42). Except for *QStb.ubo.4B.4*, which was mainly conserved in Q3, all the other major haplotypes were widely spread across multiple subpopulations (see summary table 35). In figure 40 only the major haplotypes are displayed.

Table 35: A summary table displaying the frequency of *QStb.ubo.4B* within each subpopulation, the total count and mean value for IT_FL, IT_CANO, AUDPC_FL, AUDPC_Cano.

QStb.ubo.4B	Haplotype variant	Count	IT_FL_blues	IT_Cano_blues	AUDPC_FL_blues	AUDPC_Cano_blues	adm	Q1	Q2	Q3	Q4	Q5	Q6	Q7	Q8
QStb.ubo.4B.1	AACCTCAAAG	223	4.72	5.8	28.25	36.06	13	68	5	21	1	0	33	38	44
QStb.ubo.4B.2	GGATCTAGCA	223	3.05	4.66	18.16	28.24	19	0	0	29	1	17	84	67	6
QStb.ubo.4B.3	AACCTCGAAG	18	6.46	6.9	39.94	44.19	1	6	0	0	0	0	1	8	2
QStb.ubo.4B.4	GACCTCGAAG	15	5.71	6.83	35.37	45.03	1	0	0	12	0	0	1	1	0
QStb.ubo.4B.5	GGATCTAGCG	8	4.13	5.16	25.24	33.91	1	0	0	0	0	1	4	2	0
QStb.ubo.4B.6	GACCCCAAAG	5	3.8	4.02	17.45	17.37	0	0	0	0	4	0	0	1	0
QStb.ubo.4B.7	GACCCCAGCG	5	2.97	4.53	16.74	27.30	1	0	0	0	0	0	2	2	0
QStb.ubo.4B.8	GAATCTAGCA	4	2.58	5.06	14.41	33.25	0	0	0	1	0	1	1	1	0
QStb.ubo.4B.9	GGACTCAAAG	4	4.48	5.06	29.25	32.71	0	0	0	4	0	0	0	0	0
QStb.ubo.4B.10	AACCTCAGCA	1	0.16	3.80	2.78	21.00	0	0	0	0	0	0	0	1	0
QStb.ubo.4B.11	AACCTTAAAG	1	7.73	7.27	43.68	45.50	0	0	0	0	0	0	0	1	0
QStb.ubo.4B.12	GAATCTAAAA	1	6.12	7.11	28.41	35.00	0	0	0	1	0	0	0	0	0
QStb.ubo.4B.13	GAATCTAACG	1	4.30	4.39	27.71	28.00	0	0	0	0	0	0	0	1	0

- *QStb.ubo.5A*

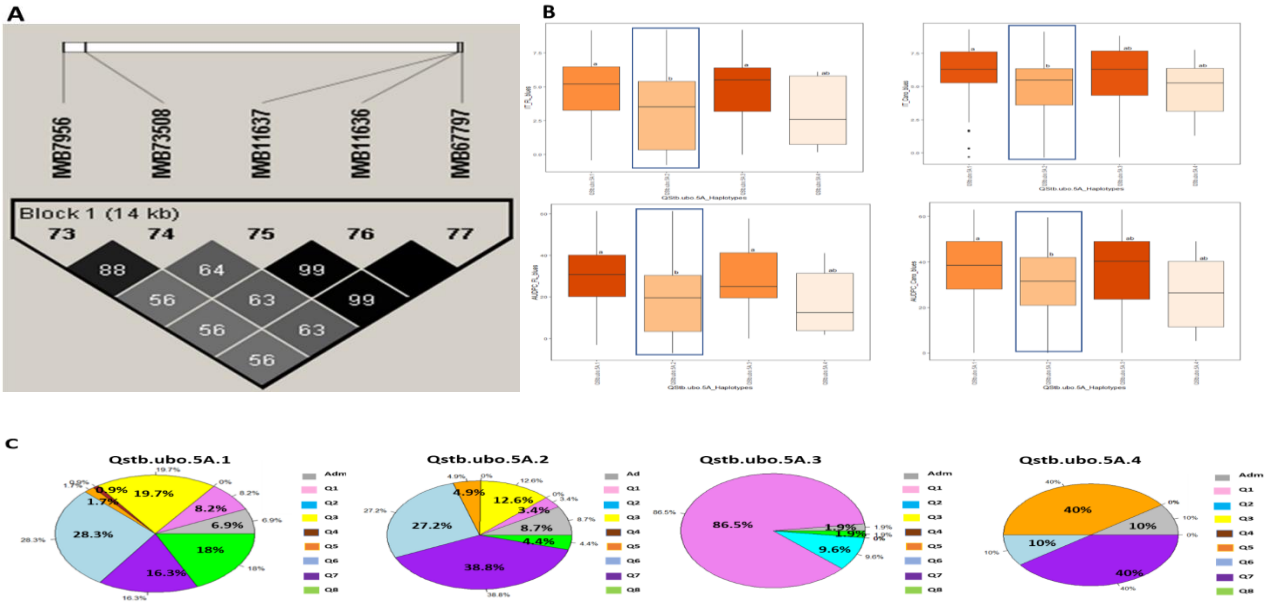

Figure 41: This figure displays the *QStb.ubo.5A* haploblock. A: *QStb.ubo.5A* LD-block B: Comparison of the phenotypic performance of all identified haploblock variants of *QStb.ubo.5A* for the 4 Stb traits, IT_FL (Topright), IT_Cano (Topleft), AUDPC_FL (Bottomright) and AUDPC_Cano (Bottomleft) C: The frequency of the major *QStb.ubo.5A* haplotypes variants within the single subpopulations is displayed.

A total of 8 different haplotypes were identified for *QStb.ubo.5A*, including 4 major haplotypes and 4 minor haplotypes. Among these major haplotypes, *QStb.ubo.5A.1* and *QStb.ubo.5B.2* were the prevalently present, respectively, in 233 and 203, individuals. However, *QStb.ubo.5A.3* was the only one showing a clear resistant phenotype for all the Stb traits (see figure 4e). Except for *QStb.ubo.5A.3*, which was mainly conserved in Q1, all the other major haplotypes were widely spread across multiple subpopulations (see summary table 36). In figure 41, only the major haplotypes are displayed.

Table 36: A summary table displaying the frequency of *QStb.ubo.5A* within each subpopulation, the total count and mean value for IT_FL, IT_CANO, AUDPC_FL, AUDPC_Cano.

QStb.ubo.5A	Haplotype variant	Count	IT_FL_blues	IT_Cano_blues	AUDPC_FL_blues	AUDPC_Cano_blues	adm	Q1	Q2	Q3	Q4	Q5	Q6	Q7	Q8
QStb.ubo.5A.1	TGGAA	233	4.96	6.08	29.64	37.73	16	19	0	46	2	4	66	38	42
QStb.ubo.5A.2	GAACC	206	3.25	4.77	19.03	29.17	18	7	0	26	0	10	56	80	9
QStb.ubo.5A.3	GAGAA	52	4.76	5.61	28.43	35.36	1	45	5	0	0	0	0	0	1
QStb.ubo.5A.4	TAACC	10	3.12	4.77	17.52	26.08	1	0	0	0	0	4	1	4	0
QStb.ubo.5A.5	GGGAA	3	5.35	7.02	29.32	37.33	0	0	0	0	0	0	2	1	0
QStb.ubo.5A.6	TAGAA	3	2.04	2.98	12.43	18.67	0	3	0	0	0	0	0	0	0
QStb.ubo.5A.7	GAAAA	1	4.23	4.36	27.89	28.00	0	0	0	0	0	0	1	0	0
QStb.ubo.5A.8	TGACC	1	-0.01	-0.30	1.68	0.00	0	0	0	0	0	1	0	0	0

- *QStb.ubo.5B*

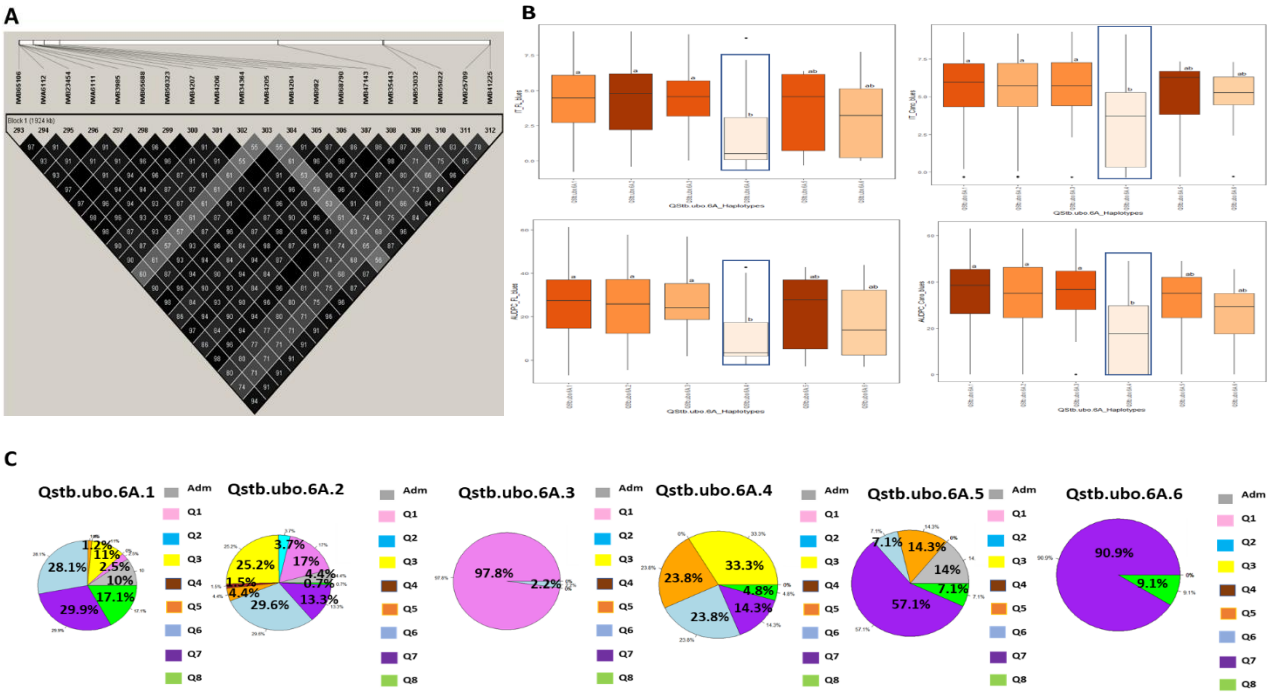

Figure 42: This figure displays the QStb.ubo.5B haploblock. A: *QStb.ubo.5B* LD-block B: Comparison of the phenotypic performance of all identified haploblock variants *QStb.ubo.5B* the 4 Stb traits, IT_FL (Topright), IT_Cano (Topleft), AUDPC_FL (Bottomright) and AUDPC_Cano (Bottomleft) C: The frequency of the major *QStb.ubo.5B* haplotypes variants within the single subpopulations is displayed.

A total of 17 different haplotypes were identified for *QStb.ubo.5B* However, among all these, only three can be considered as major haplotypes and most importantly, *QStb.ubo.5B.1* was largely frequent (408) as compared to the other two major haplotypes, respectively, present in 52 and 14 individuals. None of the major haplotype stood out for the resistant phenotype in all 4 Stb traits and they were widely spread across several subpopulations (see summary table 37). In figure 42, only the major haplotypes are displayed.

Table 37: A summary table displaying the frequency of *QStb.ubo.5B* within each subpopulation, the total count and mean value for IT_FL, IT_CANO, AUDPC_FL, AUDPC_Cano.

QStb.ubo.5B	Haplotype variant	Count	IT_FL_blues	IT_Cano_blues	AUDPC_FL_blues	AUDPC_Cano_blues	adm	Q1	Q2	Q3	Q4	Q5	Q6	Q7	Q8
QStb.ubo.5B.1	CCGGTTGCAGCGCGCTACGA	408	4.09	5.38	24.08	33.05	25	59	5	61	0	0	119	88	51
QStb.ubo.5B.2	TTAACCAAGATATATCGTAG	52	3.85	4.22	17.89	22.38	7	0	0	3	2	16	3	21	0
QStb.ubo.5B.3	TTAACCAAGACATATCGTAG	14	5.55	6.69	33.86	43.02	2	9	0	0	0	0	0	2	1
QStb.ubo.5B.4	TTAACCAAGACATATCGCGG	8	6.82	7.52	42.77	48.56	1	0	0	0	0	0	1	6	0
QStb.ubo.5B.5	TTAACCAAGACATATCGTGG	6	4.63	5.29	29.71	34.62	0	0	0	1	0	0	0	5	0
QStb.ubo.5B.6	CCGGTTGCGACACACCACGA	4	6.66	7.09	43.66	49.00	0	0	0	4	0	0	0	0	0
QStb.ubo.5B.7	CCAATTGCGACACACCACGA	3	1.84	4.26	8.46	22.75	0	0	0	0	0	1	1	1	0
QStb.ubo.5B.8	CCGGTTGCAGCGCACCACGA	3	5.20	6.54	34.33	44.33	0	0	0	1	0	0	2	0	0
QStb.ubo.5B.9	TTAACCAAGATATATCGCGA	3	5.31	5.13	36.81	33.83	0	3	0	0	0	0	0	0	0
QStb.ubo.5B.10	TTAACCAAGATATATCGTGG	2	5.44	5.88	25.18	0.06	0	0	0	2	0	0	0	0	0
QStb.ubo.5B.11	CCAATTGCAGCGCGCTACGA	1	3.88	5.69	27.29	42.00	0	0	0	0	0	0	0	1	0
QStb.ubo.5B.12	TCAATTAAGACATATCGCAG	1	0.52	2.30	1.99	14.00	0	1	0	0	0	0	0	0	0
QStb.ubo.5B.13	TCAATTAAGACATATCGTAG	1	5.44	5.40	36.77	35.00	0	1	0	0	0	0	0	0	0
QStb.ubo.5B.14	TTAACCAAGACATATCGCAG	1	6.21	7.17	41.89	49.00	0	1	0	0	0	0	0	0	0
QStb.ubo.5B.15	TTAACCAAGATATATCCGTAG	1	0.30	0.39	-0.29	0.00	0	0	0	0	0	1	0	0	0
QStb.ubo.5B.16	TTAACCAAGATATATCGCAG	1	-0.56	-0.32	-1.95	0.00	0	0	0	0	0	1	0	0	0
QStb.ubo.5B.17	TTGGCCGCAGCGCGCTACGA	1	3.20	2.77	13.85	10.50	1	0	0	0	0	0	0	0	0

- *Qstb.ubo.6A*

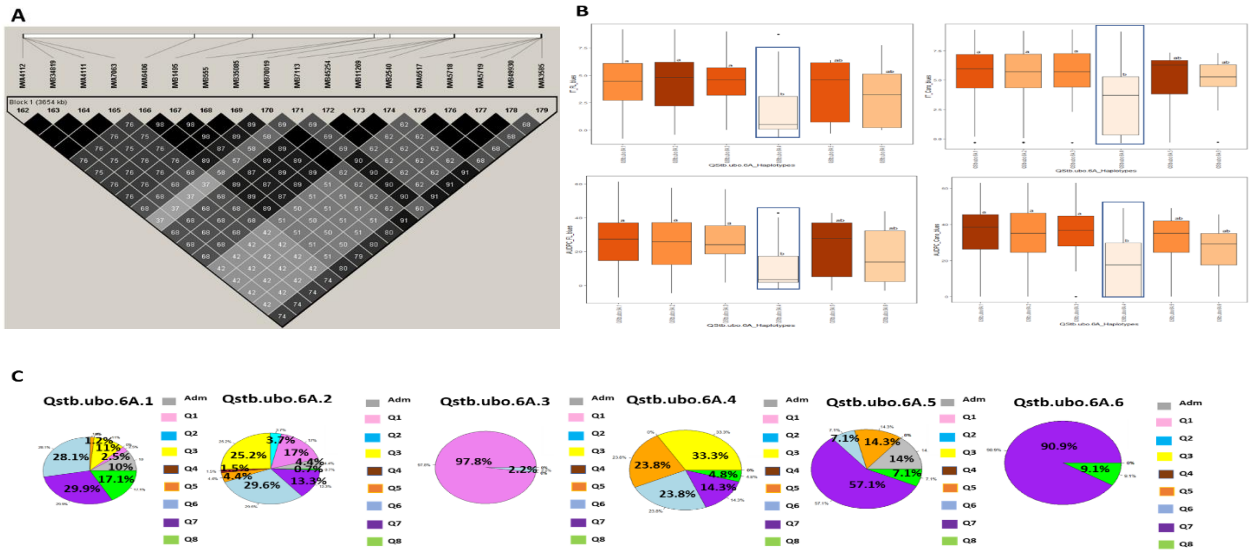

Figure 43: This figure displays the *QStb.ubo.6A* haploblock. A: *QStb.ubo.6A* LD-block B: Comparison of the phenotypic performance of all identified haploblock variants QStb.ubo.6A the 4 Stb traits, IT_FL (Topright), IT_Cano (Topleft), AUDPC_FL (Bottomright) and AUDPC_Cano (Bottomleft) C: The frequency of the major *QStb.ubo.6A* haplotypes variants within the single subpopulations is displayed.

A total of 7 different haplotypes were detected for *QStb.ubo.6A*. Among all these, 6 were considered as major, due to their frequency in more than 10 individuals (figure 43). However, *QStb.ubo.6A.4* was the only haplotype standing out for the resistant phenotype in all Stb traits. Excpet for *QStb.ubo.6A.3* and *QStb.ubo.6A.6*, mainly conserved respectively, in Q1 and Q7, all the other haplotypes were differently scattered across several subpopulations (see summary table 38).

Table 38: A summary table displaying the frequency of *QStb.ubo.6A* within each subpopulation, the total count and mean value for IT_FL, IT_CANO, AUDPC_FL, AUDPC_Cano.

QStb.ubo.6A	Haplotype variant	Count	IT_FL_blues	IT_Cano_blues	AUDPC_FL_blues	AUDPC_Cano_blues	adm	Q1	Q2	Q3	Q4	Q5	Q6	Q7	Q8
QStb.ubo.6A.1	AGGGGCCCCTTCATCCTG	281	4.27	5.63	25.76	35.09	28	7	0	31	0	4	79	84	48
QStb.ubo.6A.2	GAAATTATACCTGGTTCA	135	4.34	5.41	25.09	32.97	6	23	5	34	2	6	40	18	1
QStb.ubo.6A.3	GAAATTATATCTGTCCTA	45	4.56	5.63	26.64	35.53	0	44	0	0	0	0	1	0	0
QStb.ubo.6A.4	AGGGTTATACCTGGTTCA	21	2.04	3.34	11.18	18.14	0	0	0	7	0	5	5	3	1
QStb.ubo.6A.5	AGGGGCCCACCTGGTTCA	14	3.65	4.91	22.52	30.83	2	0	0	0	0	2	1	8	1
QStb.ubo.6A.6	AGGGTTATACCTGTCCTG	11	3.17	4.87	17.45	26.2	0	0	0	0	0	0	0	10	1
QStb.ubo.6A.7	AGGGGTCCCTTCATCCTG	2	0.11	2.21	1.52	8.75	0	0	0	0	0	2	0	0	0

- *QStb.ubo.7A*

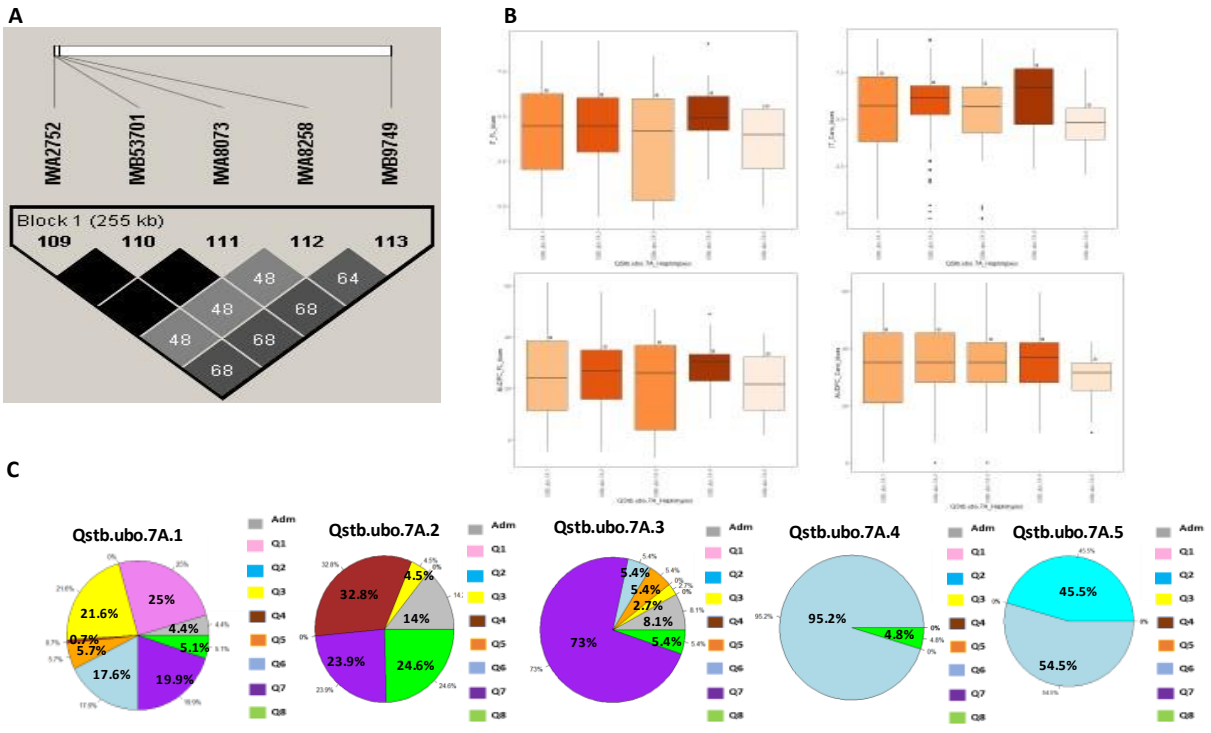

Figure 44: This figure displays the QStb.ubo.7A haploblock. A: *QStb.ubo.7A* LD-block B: Comparison of the phenotypic performance of all identified haploblock variants *QStb.ubo.7A* the 4 Stb traits, IT_FL (Topright), IT_Cano (Topleft), AUDPC_FL (Bottomright) and AUDPC_Cano (Bottomleft) C: The frequency of the major QStb.ubo.7A haplotypes variants within the single subpopulations is displayed.

A total of eight distinct haplotypes were identified for *QStb.ubo.7A*. Of these, five were classified as major haplotypes, each occurring in more than 10 individuals. Overall, no clear separation between resistant and susceptible haplotypes was evident for this QTL (figure 44). Haplotypes *QStb.ubo.7A*.4

and *QStb.ubo.7A.5* were predominantly found in subpopulation Q6, while the remaining haplotypes were distributed across other subpopulations at varying frequencies (see summary table 39).

Table 39: A summary table displaying the frequency of *QStb.ubo.7A* within each subpopulation, the total count and mean value for IT_FL, IT_CANO, AUDPC_FL, AUDPC_Cano.

QStb.ubo.7A	Haplotype variant	Count	IT_FL_blues	IT_Cano_blues	AUDPC_FL_blues	AUDPC_Cano_blues	adm	Q1	Q2	Q3	Q4	Q5	Q6	Q7	Q8
QStb.ubo.7A.1	AAAGT	296	4.14	5.31	24.57	32.54	13	74	0	64	2	17	52	59	15
QStb.ubo.7A.2	GGGAC	134	4.22	5.74	25.12	35.61	19	0	0	6	44	0	0	32	33
QStb.ubo.7A.3	GGGGC	37	3.73	5.05	22.07	31.88	3	0	0	1	0	2	2	27	2
QStb.ubo.7A.4	AAAAC	21	5.03	6.1	27.87	35.92	0	0	0	0	0	0	20	0	1
QStb.ubo.7A.5	GGGGT	11	3.49	4.74	21.25	29.05	0	0	5	0	0	0	6	0	0
QStb.ubo.7A.6	GGGAT	7	4.28	5.64	27.08	36.5	0	0	0	1	0	0	1	4	1
QStb.ubo.7A.7	AAAGC	2	7.23	7.78	45.43	52.5	1	0	0	0	0	0	0	1	0
QStb.ubo.7A.8	AAAAT	1	3.19	3.79	24.35	28.00	0	0	0	0	0	0	1	0	0

3.3.3.2 GWAS Within Subpopulations

A total of 16 QTLs were identified from the subpopulation GWAS analysis. Five subpopulations met the required criterion of having more than 50 individuals: Q1 (Horn_Africa_aethiopicum), Q3 (SouthWest_Asia_Syriacum), Q6 (East_Europe_Transcaucasus), Q7 (Egypt_Cyprus_Iberia), and Q8 (West_Asian_Founders).

- Three QTLs were detected in Q1 on chromosomes 2B, 3A, and 5B: *QStb.ubo.Q1.2B*, *QStb.ubo.Q1.3A*, and *QStb.ubo.Q1.5B*.
- Three QTLs were identified in Q3 on chromosomes 4A, 4B, and 6A*: QStb.ubo.Q3.4A*, *QStb.ubo.Q3.4B*, and *QStb.ubo.Q3.6A*.
- Two QTLs were found in Q6 on chromosomes 1B and 3B*: QStb.ubo.Q6.1B* and *QStb.ubo.Q6.3B*.
- Two QTLs were observed in Q7, both on chromosome 4A: *QStb.ubo.Q7.4A* and *QStb.ubo.Q7.4A.2*.
- Six QTLs were detected in Q8 on chromosomes 1A, 2A, 2B, 3A, 4A, and 6A: *QStb.ubo.Q8.1A, QStb.ubo.Q8.2A, QStb.ubo.Q8.2B, QStb.ubo.Q8.3A, QStb.ubo.Q8.4A*, and *QStb.ubo.Q8.6A*.

Despite having the smallest number of individuals among the subpopulations meeting the criterion, Q8 contributed the largest number of QTLs compared to the other four subpopulations (see summary table 40). All detected QTLs were consistently significant for the Stb traits examined. As anticipated, due to the limited genetic variability within each subpopulation compared to the entire panel, the resulting R^2 values were notably high, ranging from 5% to 39% (see summary table 40). No overlap was observed between the QTLs detected here and those identified in the global GWAS, projected Stb loci, or independent studies, suggesting the potential discovery of previously unknown resistance alleles for Stb (see summary table 40). However, overlaps were found between subpopulations. For instance, *QStb.ubo.Q3.6A* and *QStb.ubo.Q8.6A* were both located in the telomeric region of chromosome 6A (590 Mbp). On chromosome 4A, two QTLs were detected in subpopulations Q7 and Q8, positioned 10 Mbp apart, indicating the possible presence of an important hotspot for Stb

resistance genes in this region of chromosome 4A (see figure table 45). All Manhattan Plots are available in supplementary files.

Table 40: Summary table showing the results of the GWAS within the 5 subpopulations matching required criteria for the association study: Q1 (Horn_Africa_aethiopicum), Q3 (SouthWest_Asia_Syriacum), Q6 (East_Europe_Transcaucasus), Q7 (Egypt_Cyprous_Iberia) and Q8 (West_Asian_Founders). This table comprises several information, from top to bottom: QTL acronym, MTA (SNP), alleles (major/mino), chromosome, position (Mbs), Block start position (Mbp), Block end postion (Mbp), overlapping QYr.ubo detected in the global GWAS, overlapping projected Yr confidence intervals and the results of the statistically significant ANOVA test within each environment or environmental cluster: NS stands for non-significant, NA stands for Not applicable (removed by MAF), * 0.05 – 0.01, ** 0.01-0.001, *** 0.0001-0.00001, **** < 0.00001. Environments containing fewer than 50 accesions belonging to that subpopulation are not reported.

QTL name	***QStb.ubo.Q1.2B***	***QStb.ubo.Q1.3A***	***QStb.ubo.Q1.5B***	***QStb.ubo.Q3.4A***	***QStb.ubo.Q3.4B***	***QStb.ubo.Q3.6A***	***QStb.ubo.Q6.1B***	***Qstb.ubo.Q6.3B***	***QStb.ubo.Q7.4A***	***QStb.ubo.Q7.4A.2***	***Qstb.ubo.Q8.1A***	***QStb.ubo.Q8.2A***	***Qstb.ubo.Q8.2B***	***QStb.ubo.Q8.3A***	***QStb.ubo.Q8.4A***	***QStb.ubo.Q8.6A***
SNP	IWB18835	IWB62796	IWB26978	IWB42813	IWB23940	IWB72907	IWB13057	IWB21844	IWB10389	IWB26090	IWA3799	IWB51951	IWB2227	IWB28136	IWB73881	IWB67847
Alleles	***Q1***	***Q1***	***Q1***	***Q3***	***Q3***	***Q3***	***Q6***	***Q6***	***Q7***	***Q7***	***Q8***	***Q8***	***Q8***	***Q8***	***Q8***	***Q8***
Chromosomes	**2B**	**3A**	**5B**	**4A**	**4B**	**6A**	**1B**	**3B**	**4A**	**4A**	**1A**	**2A**	**2B**	**3A**	**4A**	**6A**
Position (Mb)	718.60	541.12	356.16	537.34	37.52	588.26	668.93	243.42	4.53	655.23	584.67	57.94	770.41	48.96	665.31	590.11
Block_start position (SVEVO)	718.53	540.92	355.30	534.12	37.52	586.62	666.70	209.13	4.53	655.23	584.67	57.94	769.41	48.96	662.43	589.84
Block_end position (SVEVO)	718.60	541.54	371.59	548.27	37.64	588.26	668.93	243.42	4.56	655.23	585.26	60.23	770.79	48.96	666.00	590.11
Overlapping_QYr.ubo																
Overlapping_Yr_Loci																
Projected_QTL																
LOD (max)	4.42	4.47	4.16	6.71	6.23	10.07	4.00	7.17	7.00	4.90	5.15	4.21	8.25	4.47	8.36	4.74
R^2 (%) (max)	28.97	15.54	18.67	18	5.04	22.54	20.17	7.17	20	12.21	31.33	15.84	39	28.8	22.95	27.36
Stb Traits	**Anova Test**															
IT_FL	****	***	****	***	*	**	*	****	****	****	***	**	****	****	**	***
IT_Cano	****	****	***	***	**	**	**	****	****	****	****	***	****	****	****	****
AUDPC_FL	****	***	***	***	*	****	***	**	****	****	****	**	****	****	***	****
AUDPC_Cano	****	****	****	**	**	****	**	***	***	****	****	***	****	****	****	****

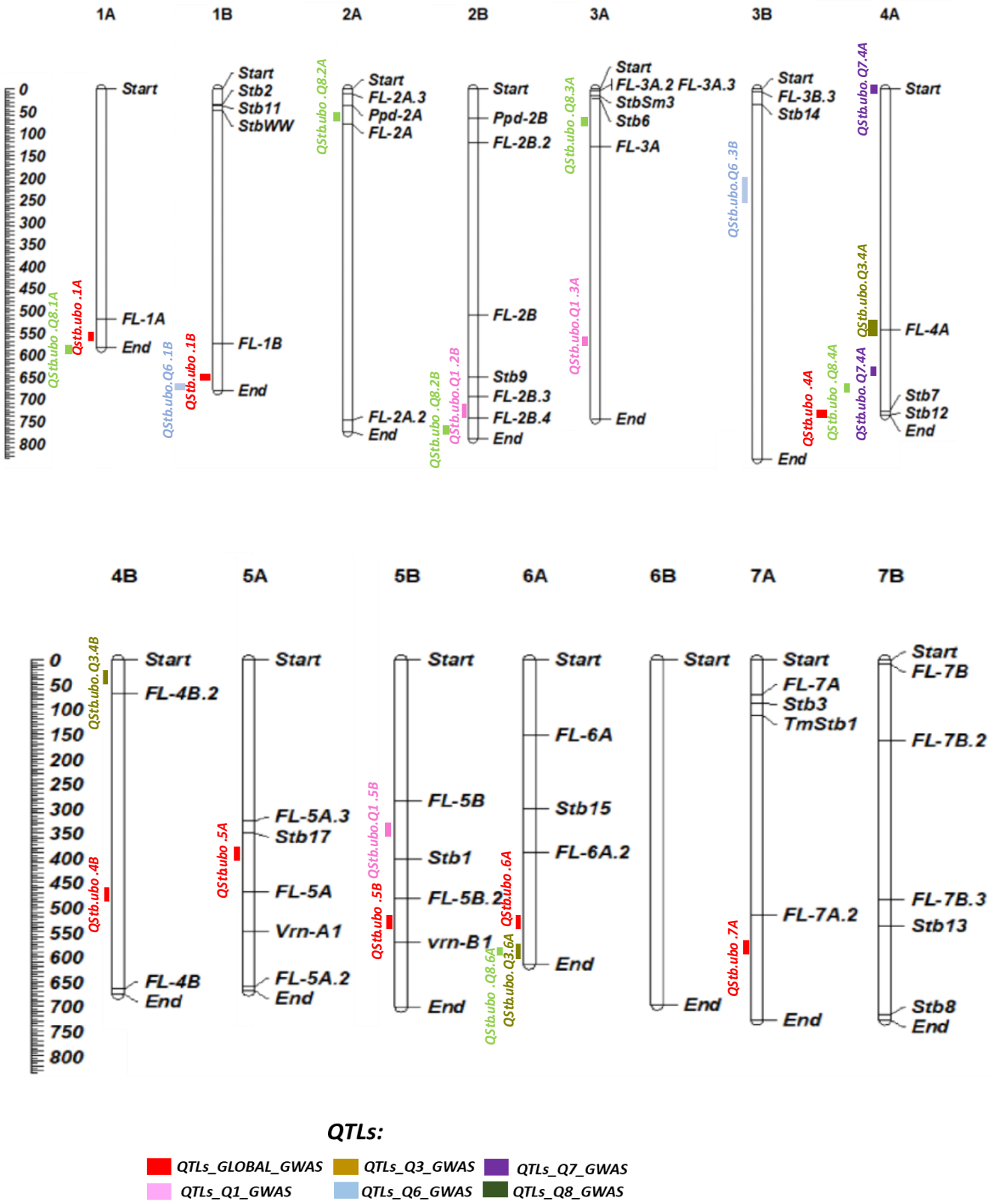

Figure 45: This figure shows all the detected QTLs onto the Svevo reference genome. A different color is assigned to a specific subpopulation or the global GWAS (see legend). Projected *Stb* loci are also reported as well as annotated genes underlying physiological traits such as *Ppd*, *Vrn* and *Fl*.

3.4 DISCUSSION

The genetic potential of a highly diverse panel, including *Triticum turgidum* landraces and related durum subspecies, offers a valuable resource for uncovering resistance to both biotic and abiotic stresses. In the context of Septoria tritici blotch (STB) disease, however, only a few QTL mapping studies have been conducted on tetraploid wheat. Additionally, Most known STB resistance loci have been mapped in bread wheat, with the exception of TmStb1, identified in *Triticum monococcum*. This lack of documented STB resistance loci in durum wheat has resulted in a widespread susceptibility in the most cultivated elite durum cultivars globally, where STB is typically managed through fungicide applications (Heick, T. M et al., 2017). Moreover, numerous studies have highlighted the extensive genetic variation and plasticity of *Zymoseptoria tritici* populations, where high levels of recombination and gene flow contribute to the emergence of new virulent pathotypes that evade current control strategies (Chedli et al., 2022; Mekonnen, T. et al., 2020). This highlights the urgent need to explore and exploit novel sources of genetic diversity within tetraploid wheat to establish durable resistance against STB. A genome-wide association study (GWAS) was conducted in a single environment, Cadriano 2022, on a panel of 501 *Triticum durum* landraces and related subspecies, known as CEREALMED, to identify genetic resistance to STB. The panel comprised genotypes from eight subpopulations, as thoroughly described in Chapter 2. GWAS analysis was performed both on the entire panel and within five subpopulations that included more than 50 individuals. The identified QTLs showed strong significance across all assessed STB traits, with broad-sense heritability exceeding 60% for each trait, emphasizing the importance of genetic factors in explaining phenotypic variance. Furthermore, correlation analysis revealed a strong negative correlation, greater than 60%, between the accumulation of resistant haplotypes for the detected QTLs and a subsequent reduction in infection levels, both in the flag leaf and across the rest of the canopy. The identified QTLs were then compared with previously projected STB loci, QTLs from independent studies, and annotated genes associated with key physiological traits in wheat, such as flowering time, vernalization, and photoperiod response.

Chromosome 1A

In the global GWAS analysis, a QTL, *QStb.ubo.1A*, was identified in the distal region of chromosome 1A, around 573.76 Mb. In the same distal region, another QTL, *QStb.ubo.Q8.1A*, was detected within subpopulation Q8, but located 10 Mb away (at 584.67 Mb). Although no previously documented STB loci have been mapped on chromosome 1A, both QTLs are situated near a flowering locus (FL-1A). The only QTL previously reported on chromosome 1A comes from a GWAS conducted on a diverse panel of Ethiopian durum wheat landraces and modern varieties by Kidane et al.2017, and was positioned 100 Mb away (at 477 Mb) from the locations of the two QTLs identified in this study. One haplotype in *QStb.ubo.1A*, named *QStb.ubo.1A.3*, exhibited a resistant phenotype and was predominantly present in subpopulation Q6 (60%) and, to a lesser extent, in four other subpopulations, except for Q8. This distribution suggests a potential distinction between the QTLs detected in the global GWAS and in subpopulation Q8, despite their close physical proximity.

Chromosome 1B

Chromosome 1B is well-known as a significant source of resistance genes against various pathogenic fungi, including those conferring resistance to both yellow rust (Yr) and *Septoria tritici blotch* (*Stb*). Specifically, three *Stb* resistance loci—*Stb2*, *Stb11*, and *StbWW*—have been mapped to the proximal region of chromosome 1B, spanning from 35 Mb to 47 Mb, a range of approximately 12 Mb. However, no QTLs identified in this study overlapped with that region on chromosome 1B. Similar to chromosome 1A, two QTLs were detected in the distal region of chromosome 1B: *QStb.ubo.1B* from the global GWAS and *QStb.ubo.Q6.1B* from subpopulation Q6, positioned 7 Mb apart. Within

QStb.ubo.1B, the haplotype *QStb.ubo.1B.3* showed a resistant phenotype and was present in five different subpopulations, with a higher frequency in Q7 (50%) and a lower frequency in Q6 (2.6%). Meanwhile, haplotype *QStb.ubo.1B.4* was primarily found in Q6 but did not display a resistant phenotype. These findings suggest that *QStb.ubo.1B* and *QStb.ubo.Q6.1B* represent distinct genetic regions on chromosome 1B.

Chromosome 2A

No QTL was identified on chromosome 2A in the global GWAS, and no STB resistance loci have been previously mapped to this chromosome. However, chromosome 2A is a key region for genes controlling physiological traits, such as the Flowering locus (Fl) and, more notably, *Ppd-2A*. A QTL, *QStb.ubo.Q6.2A*, was detected within subpopulation Q8 in the proximal region of chromosome 2A, at 57.94 Mb, positioned midway between *Ppd-2A* and *Fl-2A*, approximately 20 Mb away from both. Given the significant distance between *QStb.ubo.Q6.2A* and these two annotated physiological genes, it is likely that *QStb.ubo.Q6.2A* represents an independent locus conferring resistance to Stb.

Chromosome 2B

Like chromosome 2A, chromosome 2B is a key reservoir for loci related to physiological traits, including the flowering locus (Fl) and *Ppd-2B*, the homeologous gene to *Ppd-2A*. Additionally, the *Stb9* locus, associated with STB resistance, has been mapped to chromosome 2B. Although no QTLs were identified on this chromosome in the global GWAS, two QTLs were detected in different subpopulations: *QStb.ubo.Q1.2B* in subpopulation Q1, and *QStb.ubo.Q8.2B* in subpopulation Q6, both located in the distal region of chromosome 2B. These QTLs are approximately 50 Mb apart, with *QStb.ubo.Q1.2B* positioned at 718 Mb and *QStb.ubo.Q8.2B* at 770.41 Mb. Both are located far from *Stb9* (650 Mb) and another QTL reported by Kidane et al. (2017) at 476.70 Mb. While the two QTLs are proximal to distinct flowering loci, *Fl-2B.3* and *Fl-2B.4*, they do not overlap with them. This suggests that the two QTLs, detected in separate subpopulations, may represent independent loci conferring resistance to Stb.

Chromosome 3A

Chromosome 3A contains three flowering loci and two STB resistance loci, *StbSm3* and *Stb6*, located within a proximal region spanning 23 Mb. No QTLs were identified on chromosome 3A from the global GWAS. However, two QTLs were detected in different subpopulations: *QStb.ubo.Q1.3A* in Q1 and *QStb.ubo.Q8.3A* in Q8. *QStb.ubo.Q8.3A* was the closest QTL to the gene hotspot in the proximal region of chromosome 3A, positioned at 48.96 Mb, approximately 25 Mb away from the nearest STB locus. In contrast, *QStb.ubo.Q1.3A* was located much farther away, at 541.12 Mb, in a region isolated from known STB loci or annotated physiological genes. Two additional QTLs, from independent mapping studies, have been projected onto the *Svevo* reference genome. One QTL from an association study on an Evolutionary Pre-breeding Population (EPO) panel by Ballini et al. (2020) overlapped with the physical position of *Stb6*, while another QTL identified by Kidane et al. (2017) was positioned 40 Mb away from *QStb.ubo.Q1.3A*. Given the distance of the detected QTLs from the known Stb loci, these two QTLs may represent independent loci conferring resistance to Stb placed on chromosome 3A.

Chromosome 3B

No QTL was identified on chromosome 3B in the global GWAS; however, one QTL, *QStb.ubo.Q6.3B*, was detected in subpopulation Q6. The only known STB resistance gene on chromosome 3B, *Stb14*, is located at 33.5 Mb, while *QStb.ubo.Q6.3B* is positioned much farther away

at 243.42 Mb. Given this significant distance, *QStb.ubo.Q6.3B* is likely an independent locus conferring resistance to Stb on chromosome 3B.

Chromosome 4A

Chromosome 4A had the highest number of detected QTLs, with a total of five. Additionally, two known STB loci, *Stb7* and *Stb12*, were projected onto the Svevo reference genome in the distal region, just 16 Mb apart. One QTL from the global GWAS, *QStb.ubo.4A*, overlapped with these two Stb loci. The other four QTLs were identified in three different subpopulations: two in Q7, *QStb.ubo.Q7.4A.1* and *QStb.ubo.Q7.4A.2*, located at a significant distance from each other; one in Q3, *QStb.ubo.Q3.4A*, which overlapped with an annotated flowering locus (FL-4A); and the last in Q8, *QStb.ubo.Q8.4A*, situated in the distal region of chromosome 4A, just 7 Mb away from *QStb.ubo.Q7.4A.2*. Both *QStb.ubo.Q7.4A.2* and *QStb.ubo.Q8.4A* were far from *QStb.ubo.4A*, which was located at 740.46 Mb, suggesting that these are independent loci. Since *QStb.ubo.4A* overlapped with both *Stb7* and *Stb12*, it is likely one of these loci. Overall, chromosome 4A proved to be a crucial reservoir of resistance loci from distinct subpopulations, which should be investigated further.

Chromosome 4B

In contrast to chromosome 4A, no known Stb loci have been mapped to chromosome 4B. However, one QTL, *QStb.ubo.4B*, was identified in the global GWAS, located in a relatively isolated region at 492.75 Mb. Another QTL, *QStb.ubo.Q3.4B*, was detected in subpopulation Q3, positioned much closer to the proximal end at 37.52 Mb. Notably, one haplotype from *QStb.ubo.4B, QStb.ubo.4B.2*, exhibited a strong resistant phenotype and was distributed widely across several subpopulations. Given the absence of previously known Stb loci on chromosome 4B, these two detected QTLs represent novel candidate loci for Stb resistance.

Chromosome 5A

Chromosome 5A is critical for physiological responses in wheat, housing three key genes associated with flowering time (*Fl-5A.1*, *Fl-5A.2*, and *Fl-5A.3*) and one related to vernalization (*Vrn-5A*). Additionally, the known Stb resistance locus *Stb17* is located on this chromosome. Despite this, only one significant QTL, *QStb.ubo.5A*, was identified on chromosome 5A in the global GWAS. This QTL is positioned at 411.5 Mb, situated between a flowering locus (*Fl-5A*) at 468 Mb and *Stb17* at 350 Mb. The substantial distance between *QStb.ubo.5A* and *Stb17* suggests that *QStb.ubo.5A* may represent an independent QTL conferring Stb resistance on chromosome 5A. Notably, the haplotype *QStb.ubo.5A.2* showed a distinct resistant phenotype and was widely distributed across several subpopulations, albeit to varying degrees. None of these known loci or *QStb.ubo.5A* overlapped with any of the projected QTLs identified by Ballini et al. (2020) and Kidane et al. (2017), detected respectively at 652.45 Mbp and 577.98 Mbp.

Chromosome 5B

Like chromosome 5A, chromosome 5B is crucial for wheat's physiological responses, housing the homeologous *Vrn-5B* gene and two flowering loci. Additionally, the known Stb resistance gene *Stb1* is located at 401.53 Mb. Two QTLs were identified on chromosome 5B. The first, *QStb.ubo.5B*, was detected in the global GWAS at 528.74 Mb, positioned between the flowering locus *Fl-5B.2* (481.5 Mb) and *Vrn-5B* (570.8 Mb). The second QTL, *QStb.ubo.Q1.5B*, was found in subpopulation Q1 at 356.16 Mb, situated between another flowering locus (*Fl-5B.1* at 286.16 Mb) and *Stb1* (401.53 Mb). Given the significant distance between these QTLs and the known loci, both *QStb.ubo.5B* and *QStb.ubo.Q1.5B* can be considered independent regions conferring resistance to Stb.

Chromosome 6A

A total of three QTLs were identified in the distal region of chromosome 6A, all located in close proximity. One QTL, *QStb.ubo.6A*, was detected in the global GWAS at 561.88 Mb, while the other two, *QStb.ubo.Q3.6A* and *QStb.ubo.Q6.6A*, were identified in subpopulations Q3 and Q6, respectively. These two subpopulation QTLs were nearly overlapping, being less than 1 Mb apart and positioned between 588 Mb and 590 Mb. Due to the approximately 30 Mb distance between *QStb.ubo.6A* and the other two QTLs, they are considered independent loci. Additionally, *Stb15* and two flowering loci (*Fl-6A* and *Fl-6A.2*) are also located on chromosome 6A, but are positioned far from the detected QTLs. *QStb.ubo.6A.4* stood out for the resistant phenotype overall, but was widely spread across several subpopulations.

Chromosome 6B

Chromosome 6B does not play any role in Stb resistance or physiological response, since neither Stb genes nor Fl, Vrn and Ppd genes have been documented. Additionally, no QTL was detected confirming this initial assumption.

Chromosome 7A

Chromosome 7A is another chromosome which plays an important role for both Stb resistance and physiological response. In addition to Stb3, the TmStb1 loci, detected in *Triticum monococcum*, was also projected on chromosome 7A. These two Stb loci as well as a Flowering locus (FL-7A) are located in the proximal region of chromosome 7A. Apart from this, only one QTL was found on chromosome 7A, *QStb.ubo.7A*, positioned at 564.51 Mbp and therefore, very distant from the hotspot detected in the proximal region of chromosome 7A. None of the identified *QStb.ubo.7A* haplotype in the CEREALMED panel, stood out for a resistant phenotype and consequently, this QTL should be considered as putative.

Chromosome 7B

Chromosome 7B plays a critical role in conferring resistance against Stb and regulating physiological responses, since it houses 2 Stb loci, Stb8 and Stb13 plus 3 Flowering loci (Fl-7B.1, Fl-7B.2, Fl-7B.3). However, No QTL was detected on chromosome 7B from both global and subpopulation specific GWAS.

3.5 Conclusion chapter 3

Overall, the results from both the global and subpopulation-specific GWAS, along with the projection of QTL and *Stb* loci, confirm the identification of numerous novel regions conferring resistance to *Stb*, with the exception of *QStb.ubo.4A*, which overlapped with *Stb7* and *Stb12*. Haplotype comparisons within individual QTLs revealed statistically significant differences between resistant and susceptible haplotypes, supporting the robustness and reliability of these findings. However, unlike the case observed for *Yr*, none of the resistant haplotypes were exclusively or predominantly conserved within a single subpopulation; instead, they were distributed across at least three or four subpopulations. This could explain the lack of overlap between QTLs detected in the global GWAS and those identified in specific subpopulations, complicating the understanding of the origin of resistant haplotypes. Nonetheless, 16 subpopulation-specific QTLs were detected across five subpopulations, highlighting the rich pool of untapped resistant alleles that individual subpopulations may harbor. The Q5 (Balkan_Turgidum) subpopulation, in particular, exhibited a strong resistant phenotype in the subpopulation comparison (figure 35). However, due to the limited number of

individuals, GWAS could not be performed for this group, underscoring the unexploited genetic diversity present not only in the entire TGC/CEREALMED panel but also within individual subpopulations. In conclusion, further studies should aim to validate these detected QTLs, identify potential causative genes, and develop diagnostic KASP markers for use in Marker-Assisted Selection (MAS) and Genomic Selection (GS). Moreover, these results from a single environment should be supplemented with multi-year and multi-environmental studies to confirm or identify additional effective resistance loci across different environments and years and associate environmental clusters with similar disease rate and severity.

4 Chapter IV: Genome-Wide Association Study (GWAS) conducted on an European panel of *Zymoseptoria tritici* to map regions associated with thermal adaptation and plastic response

4.1 Introduction

4.1.1 *Zymoseptoria tritici*, fungal genome and insight from the pathogen side

The filamentous ascomycete *Zymoseptoria tritici* is the causal agent of Septoria tritici blotch disease and recognised devastating foliar disease of wheat (Fones and Gurr 2015). *Zymoseptoria tritici* represents a major threat to global food security, with estimated yield losses around 10%. Disease management practices primarily relies on chemical products and resistant wheat cultivars to a lesser extent (Fones and Gurr 2015). It has been reported that 70% of fungicides used in Europe target this single disease. This intense and specific use of fungicides favours the arise of resistant strains towards the fungicides with same mode of action (Triazoles) making the control strategy more complicated overtime (Chowdhary et al. 2013). Understanding the molecular interactions and interplay between pathogens and host plants is crucial for developing long-lasting and effective control strategies (Amezrou et al., 2023). A central component in the disease-causing ability of fungal pathogens is their capability of producing effectors—proteins that are secreted into the plant apoplast or transferred directly into host cells to alter plant physiology and suppress immune responses, thereby inducing infection (Marina et al., 2022). On the other side, in response to pathogen invasion, plants activate defense mechanisms through receptors located on cell surfaces and within cells, which recognize pathogen effectors. The discovery of resistance (R) genes encoding these receptors has been instrumental in developing breeding disease-resistant crops (lo Presti et al., 2015). However, pathogen strains are able to overcome these defence strategies from host overtime by either avoiding detection or by suppressing the plant's immune responses (Amezrou et al., 2023). This ability result from genetic variation in effector loci and continuous genome evolution (Amezrou et al., 2023). The most common approached underlying gene diversification and resulting in permanent changes in effector-encoding regions are: gene deletions (macrostructural variations) and horizontal gene transfer (Amezrou et al., 2023). Furthermore, transposable elements, along with elevated mutation and recombination rates, contribute significantly to the extensive genetic diversity seen in many fungal genomes, allowing these pathogens to be highly diversified within the single populations and therefore circumvent plant defenses effectively (Möller & Stukenbrock, 2017; Raffaele & Kamoun, 2012; Rouxel et al., 2011; Stukenbrock & Dutheil, 2018, Goodwin et al., 2011). These control challenges are further emphasized by the high genome plasticity and strong gene flow rates between *Zymoseptoria tritici* populations (Möller et al. 2018). Nowadays, the sequenced genome of the *Zymoseptoria tritici* isolate IP0323 is available (Goodwin et al., 2011). The total assembly of genome comprehends all 21-chromosomes with a total extension of 39.7 Mb (Goodwin et al., 2011). It has to be mentioned that in *Zymoseptoria tritici*, the genome can be subdivided into two distinct sets. The core-set including the first 13 chromosomes that are essential for vitally important biological function

in the pathogen such as reproduction, pathogen effectors production, thermal adaptation and so forth (Goodwin et al., 2011). Whereas, the remaining 8 chromosomes are part of the so-called dispensable chromosomes, which are extremely variable among the single isolates and whose function has to be investigated further (Goodwin et al., 2011). However, recent studies have revealed that certain dispensable chromosomes are essential for host specificity and contribute to the pathogen's high levels of genome plasticity, including frequent chromosome loss (Möller et al., 2018). Additionally, a *Zymoseptoria tritici* pangenome revealed a conserved core of approximately 9,149 genes (Plissonneau et al., 2018). Thanks to these two important assemblies, in recent years, there has been a considerable boost to gain insight into *Zymoseptoria tritici* molecular and biological mechanisms underlying infection infection strategy, secondary metabolite production and function, and its full and varied arsenal of secreted effectors (King et al., 2018; Steinberg 2015; Cairns & Meyer 2017; Rudd et al., 2015; Kettles et al., 201; Zhong et al., 2017). However, the majority of *Zymoseptoria tritici* genes and their resulting protein functions remain unknown and uncharacterized.

4.1.2 Thermal adaptation and response in Zymoseptoria tritici and other plant pathogenic fungi

The constant climate change has influenced the distribution of many plant pathogens (Ramotowski, and Gurr, 2013). Rising temperatures favours the frequency and severity of disease outbreaks, as well as the emergence of aggressive pathogen strains (McDonald and Stukenbrock 2016). For instance, in recent decades, many examples of heat-adapted aggressive strains of the fungal wheat pathogen have been documented (de Vallavieille-Pope et al., 2018; Milus, Walter et al., 2016; Onaga et al., 2017). In view of this, understanding the molecular and biological patterns behind fungal pathogens adaptation to temperature is crucial for predicting and deal with their responses to climate change (Minana-Posada, S et al., 2024). It has been observed in many cases that fungal pathogen adaptation to a small scale is the result of interactions and combination between natural selection, gene flow, and events like founder effects (Boixel et al., 2022; Mboup et al., 2012; Stefansson, McDonald, and Willi 2013; Zhan and McDonald 2011). Nevertheless, the genetic basis of thermal adaptation in fungal plant pathogens are still poorly understood because of the multifactorial and polygenic nature of this trait, involving numerous genes that affect a wide range of morphological, cellular, and molecular processes. However, some specific molecular and biological functions and mechanism have been attributed to fungi response to temperature input such as morphological changes, alterations in membrane composition, the production of stress-related metabolites like pyruvate, and protein stabilization through heat shock proteins (Blasi et al., 2015; Feurtey et al., 2023; Maclean et al., 2017; Lendenmann et al., 2016; Tralamazza et al., 2024; Weiss et al., 2018; Keuenhof et al., 2021; Masser et al., 2019; Covino et al. 2016; Leach and Cowen 2014; Zhang et al., 2018). Additionally, it has been reported that the response to temperature stress in fungi is also associated with oxidative and osmotic stress responses, resulting in the production of antioxidants and subsequent activation of the high osmolarity glycerol (HOG) pathway (Minana-Posada, S et al., 2024; Stapley et al., 2024). This pathway is essential for managing cold stress and heat stress respectively in Antarctic fungi and heat stress in species like *Saccharomyces cerevisiae* and *Aspergillus nidulans* (Kubicek and Druzhinina 2007; Yaakoub et al., 2022; Panadero et al., 2006). Additionally, Mitogen-activated protein kinase (MAPK) pathways also play a pivotal role in regulating fungal responses to temperature, oxidative, and osmotic stresses (Stapley et al., 2024). Transcription factors also play a pivotal role in regulating temperature-related responses, especially, the so-called heat shock transcription factors (Hsfs), which regulate the expression of temperature-responsive genes (Veri, Robbins, and Cowen 2018). In this study, an association study was conducted on panel of 238 *Zymoseptoria tritici* isolates representative of heterogenous wheat growing areas in 8 different Euro-Mediterranean countries to detect genetic regions associated with thermal adaptation traits such as optimal temperature (Topt), temperature performance breadth (TPB80).

4.1.3 Phenotypic plasticity in relation to a climate shift

Phenotypes can show a wide range of variability, which can be affected by the combination of genetic and environmental inputs. However, not all the individuals are capable of adapting themselves to environmental shifts, thereby reshaping their phenotype. The ability of a single individual to reshape the phenotypes based on environmental changes is commonly referred to as phenotypic plasticity (Bradshaw, 2006). In view of the ongoing climate change and global temperature rise**,** phenotypic plasticity (plastic response) and its genetic basis has become a critical topic to address, as researchers aims at understanding its potential contribution to population persistence and adaptation (Chevin & Hoffmann., 2017). Reaction norms showcase the direction and magnitude of phenotypic plasticity and changes induced by environmental factors and can be used to make comparisons among single individuals, populations, or species (Arnold et al., 2018). Reaction norms in plants and other species are generally evaluated by comparing trait variation (reshaping) at two or more distinct temperatures or by assuming a linear relation to temperature. Despite having considerable advantages from a statistical standpoint, a simple linear relation may not provide a complete representation of the phenotype reshaping in response to environmental changes, thus limiting a full understanding of plasticity (Chevin & Lande, 2011). Consequently, nonlinear models such as Random Regression Mixed Model can be more instrumental and accurate than a simple linear model in describing the type of shape (reaction norm) and obtaining the corresponding slope coefficient referring to the magnitude of the plastic response (Arnold et al., 2018). In plants, a good number of studies on plant plasticity to environmental inputs are available (Stotz et al., 2021; Valladares et al., 2014; Dostál et al., 2016; Gianoli & Valladares, 2012). In fungi, plasticity has also been investigated (Ferguson et al., 2020; Slepecky et al.,2009). In *Zymoseptoria tritici*, two studies have been conducted on thermal adaptation and plasticity (Jallet et al., 2020; Zhan & McDonald, 2011). In this study, the same panel described in 4.1.2 has been used for a pathogenicity assay at seedling stage to investigate the plastic response of isolates in terms of necrotic area and pycnidia production in response to 3 temperature regimes T18°C, T°20 and T°22. Association study was performed to identify genetic determinants underlying the plastic response of these two pathogenic traits in response to temperature.

4.2 Material and Methods

4.2.1 Fungal Material

238 *Zymoseptoria tritici* isolates have been sampled from 8 countries representing the existing heterogeneity of climatic conditions in the Euro-Mediterranean area. From each country, 25 to 30 isolates were selected and sampled from the same field. This number is necessary and sufficient to investigate the variability of thermal response, or other adaptative traits, in a local population, with sufficient power, accuracy, and precision (Dale & Fortin, 2014). The sampling design and subculturing methods have been described by Boixel *et al.* (2022).

Table.41: Geographic Origin of all the geographic populations with indications regarding the sampling site and total number of isolates.

Scale	ID	Sampling site	Coordinates	Total Number of Isolates
Geographic	RU	Russia, Moscow	55.649,36.958	26
	KZ	Kazakhistan, Penkovo	54.975,69.226	30
	LV	Latvia, Jelgava	56.542,23.726	31
	DK	Denmark, Flakkebjerg	55.308,11.388	30
	FR	France, Grignon	48.843, 1.946	30
	IR	Ireland, Carlow	52.860,6.909	31
	TN	Tunisia, Manouba	36.923, 9.839	30
	IS	Israel, Kiryat Tiv'on	32.696,35.125	30

4.2.2 Thermal Response Phenotypes

The thermal performance curves (TPCs) for each isolate were previously determined by Boixel et al. (2022), following the procedure outlined in Boixel et al. (2019). TPCs describe the relationship between the in vitro growth rate of each isolate and temperature, illustrating how growth varies across different temperatures. These curves were constructed by fitting a quadratic model to temperature-dependent growth data for each isolate. This approach allowed for the identification of optimal growth temperatures and the evaluation of performance across a range of thermal conditions.

$P(T) = P\text{max} + Curv(T - T\text{opt})2$

P = Performance (temperature–growth rate)
Pmax = Maximum Performance
$Curv$ = shape parameters
Topt = Thermal Optimum

Three key parameters were used to characterize the shape of the thermal performance curves (TPCs): maximum performance (Pmax), which represents the peak growth rate (μ) of each strain, referred to as the "vertical shift"; thermal optimum (Topt), the temperature at which the highest performance is achieved, denoting the "horizontal shift"; and thermal performance breadth (TPB80), the temperature range where performance remains above 80% of Pmax, providing insight into the sensitivity of growth rate to temperature fluctuations around Topt (the "width shift"). Among these 3 key traits composing the thermal performance curves (TPCs), only the two parameters directly referring to the temperature, namely, optimal temperature (Topt) and thermal performance breadth (TPB80) were considered for the Association Study, Pmax was not considered. The thermal response data were retrieved from the Supplementary Material of Boixel et al. (2022; "dataset_S1_Ecology_and_Evolution").

4.2.3 Whole-genome sequencing and variants calling

For the 238 *Zymoseptoria tritici* isolates, spores were collected after 7 days of growth in liquid yeast extract-peptone-dextrose broth (Difco YPD Broth). The spores were then freeze-dried for 24 hours. High molecular weight DNA was extracted using a phenol-chloroform method, adapted from Fagundes et al. (2020). Whole-genome sequencing data were generated using 150 bp paired-end reads on the Illumina HiSeq6000 platform at IntegraGen (Évry-Courcouronnes, France). Raw sequencing

reads were subjected to quality control, trimming, and alignment against the *Z. tritici* reference genome, following the method described by Amezrou et al. (2023). Reads from each isolate were trimmed using Trimmomatic v0.32, then aligned to the reference genome IPO323 (Goodwin et al., 2011) using the BWA-MEM algorithm v0.7.7 with default parameters. SAMtools v0.1.19 and Picard tools v1.106 were used to filter out optical duplicates, secondary alignments, and reads with a mapping quality below 30, retaining only pairs where both reads met quality standards. High-confidence single nucleotide polymorphisms (SNPs) were called using FreeBayes. Regions identified as highly repetitive or containing indels and transposable elements were excluded using RepeatMasker 4.0 and REPET. Depth of coverage (DP) at each genomic position was normally distributed around a central peak, and multi-allelic SNPs were retained in the final genotype file. The 8 dispensable chromosomes (Chr14 to Chr21) were excluded due to excessive missing data and instability across the isolates, leaving the core 13 chromosomes. The resulting SNP matrix was filtered to exclude loci with >20% missing data and <5% minor allele frequency (MAF) using PLINK v1.9 (Chang et al., 2015). SNP imputation was performed with Beagle 5.4 (Browning et al., 2018), and the final matrix contained 345,288 genomic sites (see figure 46). This SNP matrix was further divided into haploblocks and singletons using PLINK, resulting in 54,173 haploblocks and 71,644 singletons (a total of 125,817 blocks). A second genotypic matrix was generated for association analyses involving temperature-related plasticity of aggressiveness on the wheat variety Chinese Spring. Isolates carrying the avirulent allele at *AvrStb6* gene or producing no symptoms on Chinese Spring were excluded, leaving 219 isolates. After applying the 5% MAF filter, this second matrix contained 342,939 variants.

Table.42: Summary table displaying some features of the 238 *Zymoseptoria tritici* genotyping matrix used for genetic analysis including the total number of SNPs, the starting and ending positions (in base pairs, Bps), and the physical distances between these positions (Bps).

Chr	N°SNPs	Start_Pos (Bps)	End_Pos (Bps)	Distance (Bps)
1	66062	110766	6006500	5895734
2	35382	31417	3792292	3760875
3	35422	21149	3498560	3477411
4	24578	15709	2857539	2841830
5	26110	69160	2799815	2730655
6	20190	105227	2659152	2553925
7	23856	9059	2608081	2599022
8	26761	28184	2374601	2346417
9	22001	20050	2118215	2098165
10	21438	20318	1662144	1641826
11	16598	47941	1589185	1541244
12	14914	29287	1418493	1389206
13	11976	65012	1150167	1085155

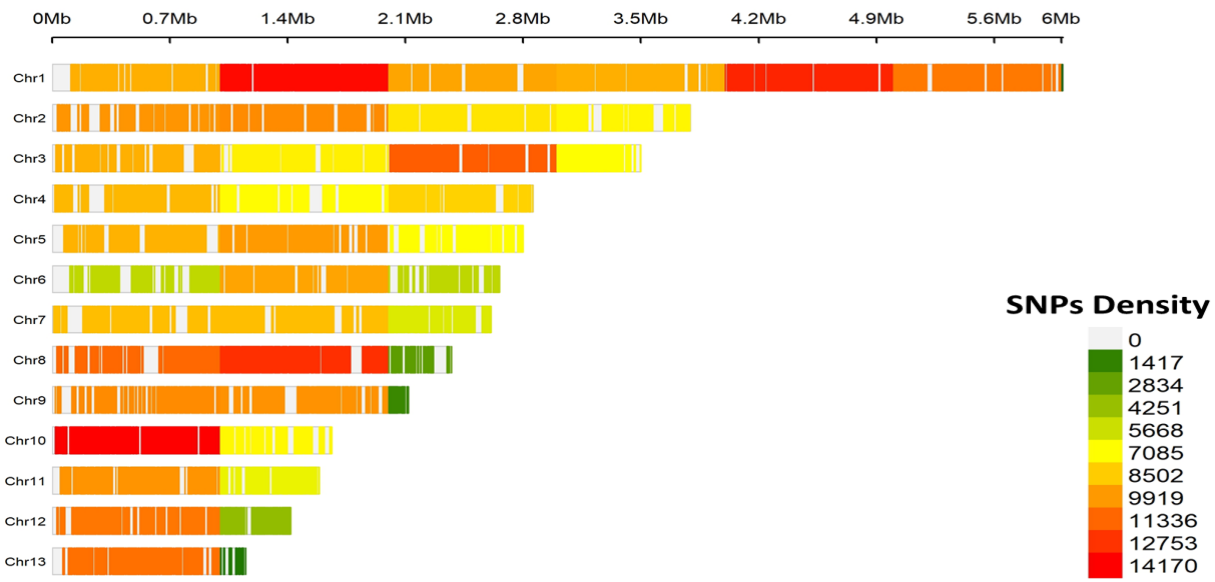

Figure 46: Visual representation of the 238 *Zymoseptoria tritici* showing the chromosome physical distance in Megabases (Mb) scale and the marker density on the right. R Package (CMplot).

4.2.4 Pathogenicity assay

4.2.4.1 Phylogenetic analysis for AvrStb6 gene

The bread wheat cultivar Chinese Spring (CS), reference genome for hexaploid wheat (AABBDD), was selected as host in pathogenicity assays due to its known genetic composition. CS carries the *Stb6* resistance gene, making it resistant to *Zymoseptoria tritici* isolates that express corresponding avirulence gene *AvrStb6*, such as the reference strain IPO323. Utilizing whole-genome resequencing data available for each isolate, a phylogenetic analysis was performed on the *AvrStb6* isoforms across the whole panel in addition to IPO323. The aim of this analysis was to determine the diversity of *AvrStb6* isoforms and to quantify the proportion of isolates carrying the avirulent *AvrStb6* protein compared to those with virulent versions.

4.2.4.2 Inoculation and Experimental Design

Inoculum was prepared from stock tubes of *Z. tritici* spores suspension conserved at -80°C in a 1:1 glycerol–water mixture. The subcultures were grown on PDA (potato dextrose agar, 39 g L−1) in a Petri dish and kept at 18 °C in the dark for 4 days. To homogenize the concentrations of the resulting suspensions, spores were scraped from the agar surface and suspended in water. For each *Z. tritici* strain, six inoculation tubes at a final concentration of 20×10^5 spores mL^{-1} were prepared in a 70% water / 30% glycerol mix. A Malassez counting chamber was used to adjust the concentrations.
Pathogenicity assays were conducted following the method of Langlands-Perry *et al.* (2022) and Amezrou *et al.* (2023).
The virulence and aggressivity of the 238 isolates were assessed on the bread wheat variety Chinese Spring at three different temperature regimes: 22°C day/18°C night, 20°C day/16°C night, and 18°C day/14°C night, in duplicated trials. This setup was designed to explore the potential influence of temperature on the pathogenicity of the isolates and to evaluate the plasticity of aggressiveness related to temperature variation. Beside temperatures, before and after inoculation, the plants were placed in a growth chamber with a 16-hour photoperiod (300 $\mu mol.m^{-2}.s^{-1}$) and 80% relative humidity. Three seeds per pot were sown, and 16 days after sowing, the first true leaf was marked with black lines to

delimit a 75 mm area. This delimited section was inoculated with six strokes (three passes in each direction) using a paintbrush dipped in an inoculum solution containing a drop of Tween20 to enhance spore cohesion across the leaf surface. After inoculation, the plants were watered and enclosed in transparent polyethylene bags for 72 hours to create a water-saturated atmosphere, promoting infection (Amezrou *et al.* (2023). Symptoms were scored at about 413 degree-days, which corresponds more or less to 20, 22 and 25 days after inoculation for the three temperature regimes (from warmest to coolest, respectively).

4.2.4.3 Scanning and Image Analysis

The procedure adopted followed the protocol designed by Stewart and McDonald (2014) and subsequently improved by Stewart *et al.* (2016). Firstly, for sample identification, A4 pages are produced using a Linux supported macro. The page is divided into eight sections, each carrying a QR code which recognizes a sample. For each isolate, the three leaves are mounted inside the corresponding section. Pages are then scanned using a conventional flatbed scanner (resolution = 1200 dpi, luminosity = contrast = 0) and the resulting images are saved as .tiff files. After scanning, the resulting images were processed using ImageJ via a batch-processing macro. This macro allows to quantify several traits associated with the virulence symptoms: the percentage of the leaf surface covered by lesions or by necrosis only (PLACL or PLACN, respectively), the total number of pycnidia per sample, the size of the pycnidia and the grey value of the pycnidia, pycnidia density per leaf area (total number of pycnidia/ leaf area), and pycnidia per square centimeter of lesion leaf area (PycLes). Color threshold settings were ad-hoc designed to analyse the images and recognise the symptoms. In our study, we only used the two traits PLACL and PycLes.

4.2.4.4 Phenotypic plasticity of aggressiveness in response to temperature

The phenotypic plasticity of traits related to aggressiveness in response to the three temperature regimes was estimated following the methods proposed by Arnold *et al.* (2018), with a tutorial available in the supplementary files. Reaction norms and phenotypic plasticity for PLACL and PycLes were assessed as average responses at the population level and as individual responses across the three tested temperatures (18°C, 20°C, 22°C). A simple linear mixed model and a more complex random regression mixed model (RRMM) were developed to identify the best model that describes the overall population-level average effects of temperature. Additionally, we aimed to quantify the variation around these average responses in the form of reaction norms for individual genotypes related to the two selected aggressiveness traits. Temperature was included as a fixed effect variable in both models. Standard model selection approaches, including Akaike Information Criterion (AIC) and likelihood ratio tests, were employed to determine the best-fitting model, whether linear or nonlinear, relating temperature to phenotypic variation. Before model testing, the environmental variable was mean-centred to ensure that intercepts reflected average values for both the population and individuals. The tested models were:

A basic mixed model: $y_{ij} = a + \beta x_j + a_i + e_{ij}$

A random regression mixed model (RRMM): $y_{ij} = a + \beta x_j + a_i + b_i x_j + e_{ij}$

Where y_{ij} refers to the phenotypic trait value of an individual i on occasion j; a and b correspond to the fixed effects of the overall intercept (the population mean phenotype if x is mean-centred) and slope regression coefficients, respectively; x_j is the environment (e.g. temperature) experienced on occasion j (mean-centred for convenience); and the random effects in the model are a_i, the random

intercept coefficient for individual i (representing the difference in means between individuals), and e_{ij}, the residual for individual i on occasion j.
The RRMM model includes an additional component b_i for the random slope of individual i in response to environment x. The fixed components of the model, the intercept (a) and slope (b), are as above and describe the population mean reaction norm. The right-hand side of the equation contains the random regression component and fits individual-level intercepts (a) and slopes (b). It is important to note that these are relative to the population-level fixed effects. Nonlinear fixed effect of temperature was used in the model by fitting a polynomial fixed-effect function. The degree of polynomial was set by the *poly()* function (*lme4* package in R) where degree 2 is a quadratic. *poly(ctemperature, 2, raw = T)1* is the slope coefficient of the quadratic function and *poly(ctemperature, 2, raw = T)2* is the quadratic coefficient of the quadratic function that reflects the curvature of the regression. Unlike the basic mixed model, from RRMM, an absolute and relative coefficient was extracted for two random regression coefficients, namely, the slope for each individual. BLUPs were extracted from the mixed-effects models by using the function *ranef()* in R. Here, BLUPs reproduces the response of a given genotype to the fixed effect of temperature in terms of difference between that genotype's predicted response and the population-level average predicted response. BLUPs were used to compare the intercepts (elevation as starting point of the reaction norm) and rank individuals based on relative slope (relative steepness of change). Whereas absolute random regression coefficient was extracted as the individual's predicted response and used as a phenotypic data referring to plasticity in the GWAS and to compare the phenotypic performance within and among the 8 geographic populations and 4 detected subpopulations.

4.2.5 Statistical analysis of phenotypic data

The original phenotypic data were analysed with R software. For the two "thermal response traits", Topt and TPB80, bestNormalize R package was used for data normalization and standardization. Boxcox transforming function was picked as best normalization for Topt, whereas square root was picked for TPB80. For the two aggressivity traits obtained from pathogenicity assay PLACL and PycLes, phenotypic the data were normalized using the *transformTukey* function (rcompanion package in R), which performs iterative Shapiro–Wilk tests, and finds the *lambda* value that maximizes the W statistic from those tests. This finds the power transformation that makes the data fit the normal distribution as closely as possible. Following normalization, standardization of transformed dataset was performed. The Shapiro-Wilk normality test confirmed the improved normality of the transformed data in comparison with the original data. No normalization was needed for the two phenotypic plasticity indexes. Descriptive statistic indexes were estimated for each trait: Minimum (Min), Maximum (Max), Mean, Median, Standard Deviation (std.dev), Variance (Var), Range, Coefficient of Variation (Coef.Var), 1st Quantile and 3rd Quantile.
Broad sense heritability was calculated using the following formula:

$$h^2 = \sigma^2_G / [\sigma^2_G + (\sigma^2_E + \sigma^2_{EXG} + \sigma^2_e)]$$

Where:

- σ^2_G = Genotypic variance
- σ^2_E = Environmental variance
- σ^2_{GE} = Genotype × Environment interaction variance
- σ^2_e = Residual variance

Pearson correlation coefficients among phenotypic traits were estimated by using corrplot () function in R.

4.2.6 Population Structure and Linkage Disequilibrium

The average linkage disequilibrium (LD) decay across the entire population (Figure 5) and for each geographic population (Figure 6) was computed with the software TASSEL Version 5.0 (Bradbury *et al.*, 2007) and subsequently plotted using an internally developed R script pipeline. The four most common LD decay levels (R^2 = 0.8, 0.5, 0.3, 0.2) were drawn to observe the progressive LD decay while physical distance between markers increases. The genetic structuration of the panel of 238 *Z. tritici* strains was analyzed using the software Admixture 1.3 (Alexander *et al.*, 2011). For this analysis, a new genotyping matrix was generated containing a subset of the filtered bi-allelic SNPs using PLINK v.1.9 (Chang *et al.*, 2015). Considering the ~~high~~ LD-decay observed within our panel, only one marker per windows of 1 kbp was kept in the new genotyping matrix. Following this procedure, we obtained a new matrix with 54715 markers. A range of subpopulations from 2 up to 8 were included into the analysis with three LD decay levels tested, respectively 0.8, 0.5 and 0.3, to identify the number of subpopulations which fits best the collection and to employ as a covariate in the downstream linear model analysis. To identify the best number of subpopulations (K), we evaluated the cross-validation error rate, the smallest cluster size and the number of isolates assigned to any cluster with a coefficient higher than 0.75 (considered as non-admixed). Finally, a principal component analysis (PCA) was carried out with the complete matrix using PLINK v.1.9 (Chang *et al.*, 2015). The first two PC were plotted, which explain the highest percentage of variance, respectively 22.6% and 14.6%.

4.2.7 Genome-Wide Association and Local Score Analyses

Genome-Wide Association study (GWAS) was performed using the linear mixed models MLMM and BLINK, implemented in the R package 'GAPIT v.3.0' (Segura *et al.*, 2012; Huang *et al.*, 2019; Wang *et al.*, 2021). To mitigate the risk of spurious associations, a kinship matrix was estimated using the VanRaden algorithm and added to the GWAS models (VanRaden *et al.*, 2008). Population structure membership score was not included into the GWAS models in order to avoid overfitting issues, but was subsequently used as a covariate in the downstream linear model analysis to detect spurious associations (false positives). An initial threshold to detect associations was set at 4 (*p*-value = 0.0001). Additionally, GWAS resolution was increased through local score approach was integrated to the association study because of the polygenic nature of the investigated traits (Bonhomme *et al.*, 2019; Fariello *et al.*, 2017). The local score approach is specifically designed to improve the resolution of GWAS and enhance the detection of minor quantitative trait loci (QTLs), particularly when marker density is high and p-values are moderate, as observed in our study. This method builds on cumulative association signals, or p-values, derived from linkage disequilibrium (LD) between SNPs within a defined genomic region, including those housing a causal variant with a small-to-moderate effect. The approach converts p-values from consecutive single-marker tests along the chromosome into scores, with the local score defined as the maximum of a Lindley process applied to the sequence of scores. One key advantage of this method is that it leverages the fixed LD patterns across the genome, removing the need for a fixed window size, which is often a limitation of sliding window methods that rely on predetermined criteria based on general features like average LD decay. The local score identifies regions starting from the first non-null score in an excursion, continuing until the highest peak of the excursion is reached. The formula used in this local score approach is as follows:

$$X_m = -\log_{10}(p_m) - \xi$$

- X_m is the *p*-value turned into score
- p_m is the *p*-value of a statistical test at position *m*

- ξ is a tuning parameter (the *p*-value threshold on single-marker tests, in $\log_{10}$ scale), ranging from 1 up to 4. For large values of ξ (3 or 4), the local score approach is quite similar to the single-marker approach, as only the most significant markers contribute to the Lindley process. For lower values of ξ (1 or 2), excursions of the Lindley process above zero become more common, and the associated intervals become wider.

The local score approach was applied on *p*-values obtained with both MLMM and BLINK models. For each test, ξ was set at 2 to be less exclusive and obtain wider regions of associated markers. This allowed us to identify other regions, which were not detected by GWAS with a cut-off set at 4. Markers with the highest LOD scores from one or both GWAS models, and located within regions identified by the local score approach, were selected as peak markers for further testing in the downstream linear model analysis.

4.2.8 Downstream Analyses: Linear Model and Stepwise Regression

Following the Local Score Approach, phenotypic variance explained (PVE) and significance (ANOVA) of the most associated markers (highest LOD) were obtained, using the *lm()* and *Anova(lm())* functions from the *lme4* and *car* packages in R. All significant markers and the detected Qs were reassessed using a general linear model to estimate the global adjusted R^2. Stepwise regression model from the *MASS* and *lme4* packages in R, to derive the global adjusted R^2 based solely on a restricted number of significant markers. Both Bayesian Information Criterion (BIC) and Akaike Information Criterion (AIC) were used in this analysis. The stepwise regression approach enhanced our confidence in selecting the detected associations, differentiating suggested associations (identified by one or both AIC and BIC) from putative associations (significant but not selected by both criteria).

4.2.9 Identification of Candidate Genes

The intervals defined by the Lindley process were used as confidence intervals to assist in annotating candidate genes. The gene annotations were sourced from the reference genome of *Zymoseptoria tritici* strain IPO323. This genomic information, including detailed annotations, was accessed through the JGI MycoCosm web portal (https://mycocosm.jgi.doe.gov/Zymtr1/Zymtr1.home.html), which provides comprehensive genomic data for *Z. tritici*.

4.3 RESULTS

4.3.1 Genetic structuration of the population

Based on genetic profiles present in the final SNP-based genotyping matrix covering the core-chromosomes assembly, the *Z.tritici* panel was subject to a population structure analysis in order to gain insight into genetic smilarity and individual ancestries. The characterization of these 238 isolates was conducted using a combination of hierarchical Ward clustering, Principal Component Analysis and population structure model through Admixture, and revealed the presence of four main groups. The results of these three grouping methods are consistent, since they clearly identify 4 clusters which showed a strong association with the geographic origin of the isolates present in this panel. PCA was conducted by using the first two PCs, respectively, accounting for 22.6% and 14.6% and the full matrix (See figure 47). Group A and B were mainly represented by individuals from the same geographic origin and clearly distanced from the remaining clusters. Group A was entirely composed of individuals from Israel (28/30). Whereas, group B was predominant in isolates from Tunisia (30/30) and a restricted number from other geographic countries, Russia (2/26), Ireland (1/30) and

Kazakhstan (1/31). Unlike A and B, Group C is the largest and most diversified cluster and massively represented by isolates from Western European countries: France (30/30), Denmark (30/30), Latvia (30/31), Ireland (29/30) and, all the other geographic countries excluding Tunisia to a minimal extent: Russia (8/ 26), Kazakhstan (2 /31) and, Israel (2/30). Analogously, cluster D was entirely by Eastern European countries, with a strong predominance of isolates from Kazakhstan (27/30) and a large to a minimal presence of individuals from Russia (7/26) and Latvia (1/31). PCA clustering subdivision was clearly confirmed by an analysis of the genetic ancestry through Admixture (figure 48). The three LD-decay levels showed the same trend after being tested from 2 up to 8 subpopulations and the Cross-Validation Error Rate reaches the flat point (the least error rate) in correspondence of 4 tested subpopulations before a new increase (figure 48, image A). The other selection criterion, namely, Minimum Group Size, Admixed lines percentage in Total and maximum admixed lines in a group (%) underpins the goodness of the choice, since the flat point is reached in correspondence of 4 subpopulations before decreasing massively under 25 individuals in the smallest group when augmented the subpopulations. Analogously, 4 was also the fairest choice in terms of Admixed lines percentage in Total and maximum admixed lines in a group (%), since it resulted in a restrained number of admixed individuals before observing an increase over 20% when augmented the subpopulations (See figure 50, image A). Q1 and Q2 were equivalent to Group A and Group B, since they were composed entirely of individuals from Israel and Tunisia plus a few isolates from Russia, Ireland and Kazakhstan (See figure 47, image B). As expected, Q3 subgroup membership score is prevalent in the isolates belonging to the Western European countries and is equivalent to group C. Analogously, Q4 corresponds to group D (Figure 7, image C). The Russian population is the only ones showing a restricted number of admixed individuals with the highest subgroup membership lower than 50%. All isolates were also separated based on Ward's based clustering and single-pairwise comparisons were used to estimate the genetic similarity (Identity by state) and plot the Kinship matrix (See figure 47, image A). This result is consistent with a geographic subdivision of individuals on a large scale, but it is important to specify that the proportions of subgroups presented in Figure 5, represent a restricted number of isolates deriving from the same sampling and therefore, is unlikely to represent the exact current composition of isolates in a specific country or group.

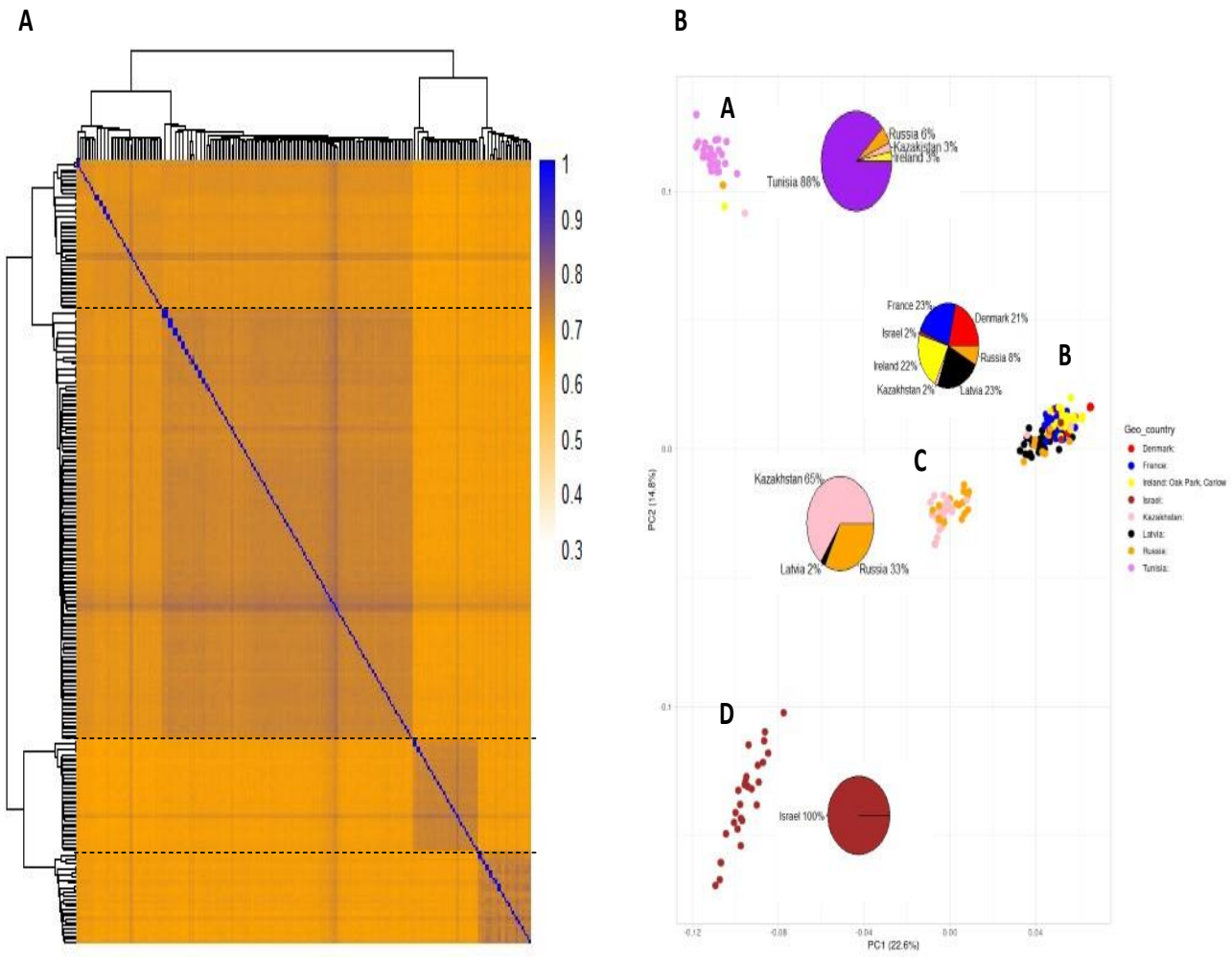

Figure 47: Population genetic structure analysis. (A): clustering of 238 individuals from the population panel. 238 × 238 kinship matrix based on simple matching genetic similarities (IBS, identity by state). (B) Principal Component Analysis (PCA) with the first two PCs by using the full genotyping matrix. A, B, C, D indicate the detected clusters. Different colours are assigned to each geographic population. Pie charts indicate the corresponding frequency of each geographic population in the 4 detected clusters.

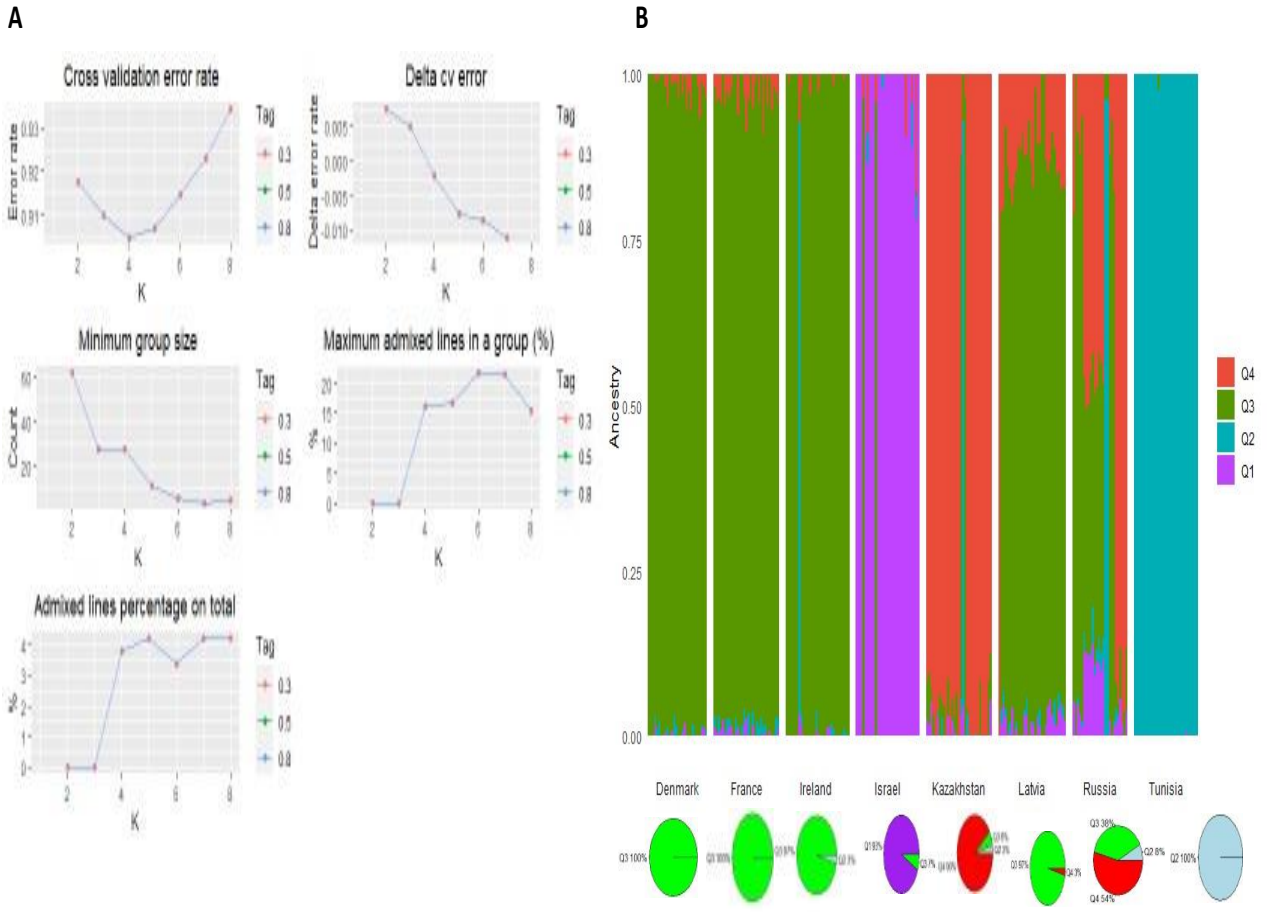

Figure 48: Population genetic structure analysis. (A) Plots showing the 5 cosnidered parameters used for the selection of the proper number of subpopulations resulting from the Admixture analysis. The five plots refer to the Cross Validation Error Rate, Delta Cv Error, Minimum Group Size, Maximum Admixed lines in a group (%) and admixed line percentage in total (%). (B) Barplot chart subdivided by Geographic populations displaying the admixture-derived population structure membership coefficient by considering 4 subpopulations. Pie charts below the barplots indicate the frequency of every subpopulation within every geographic population.

4.3.2 Estimation of LD decay

The LD extension and the average trend of LD decay rate of core chromosomes only within the whole *Z.tritici* association panel and each geographic population singularly were estimated based on pairwise LD squared correlation coefficients (r2) at 4 LD levels, namely, 0.8 (high linkage), 0.5 (medium linkage), 0.3 (low linkage) and 0.2 (low linkage) for all intrachromosomal SNP loci (See figure 51). The average trend of LD decay was estimated through a nonlinear regression of the pairwise r2 values on the corresponding physical distance (bp) based on the genetic information present in the final SNP-based genotyping matrix, containing 345,288 molecular markers, deriving from the whole-resequencing data. The average trend shows a rapid LD decay, as the least LD levels (0.3 and 0.2) are reached sooner than 1 kbp, respectively, after 0.260 kpb and 0.440 kbp (see figure 49). Even the LD decay analysis within each geographic population confirms the same trend with 7 geographic populations out of 8 reaching the least LD-decay level extremely fast and with the same trend except for the Israeli population whose LD decay is less rapid (see figure 51). This analysis justifies the resulting high-density genotyping matrix used for the association study. In accordance with the structural features of *Z. tritici* core karyotype, from chromosome 1 onward there is a

progressive descending extension, which conversely is not directly proportional to the SNPs density (see figure 46). Each chromosome presents several blank spots not only located in the telomeric regions but approximately everywhere (See figure 48).

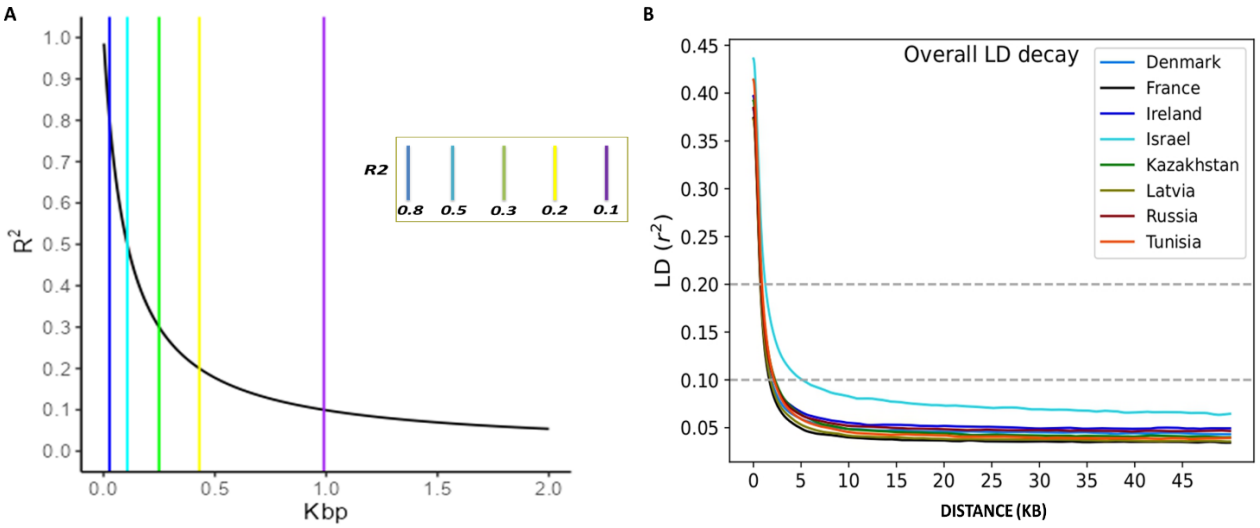

Figure 49: Genome-wide average linkage disequilibrium (LD) decay over physical distance. Image A : Plot of pair-wise single-nucleotide polymorphism LD r^2 values. X axis represents the progressive physical distance in kb and the y axis refers to the LD R2 ranging from 0 up to 1. The red curve represents the model fit to LD decay. The blue, light-blue, green, yellow and purple vertical lines indicate the physical position in correspondence of R2, 0.8 (high linkage), 0.5 (medium linkage), 0.3 (low linkage), 0.2 (low linkage), 0.1 (low linkage). Image B: LD-decay plot within each geographic population, highlighted with an assigned colour. Horizontal dashed line indcates the physical position in correspondence of R2 equal to 0.3, 0.2, 0.1.

4.3.3 Response to temperature within geographic populations and subpopulations

The Boxcox and square root transformations used in this study fulfilled the normality of the data after testing with Shapiro Test and qqplots (Figure 50, image A, B). Pearson correlation coefficient for Topt and TPB80 was positive (R2 = 0.38) with a highly significant p-value = 2.735e-09, reflecting a medium-low positive correlation between the two thermal traits (figure 50, image C). Thermal responses were compared among the 8 geographic and the 4 detected Admixture-derived subpopulations (figure 51, images A, B, C, D). As for Topt, in the comparison among geographic populations, unlike all the others, Israel average is clearly above the population mean (indicated by a dashed horizontal line), and the Post-hoc Analysis with Tukey's Test shows statistically significant differences when Israel is compared with Denmark, Kazhakistan, Latvia and Russia and not significant with France, Ireland and Tunisia. Whereas no significant differences were detected from all the other comparisons among geographic populations, excluding Israel. The situation is analogous when Topt performance is compared among Admixture-derived subpopulations, since Q1 average (Cluster A, including only isolates from Israel) is way above the population mean and shows statistically significant differences with Q3 (the largest Cluster C, including all isolates from Western Europe) and Q4 (Isolates from Eastern Europe) but not with Q2 (Isolates from Tunisia and a few other geographic areas). Like the previous comparisons, no significant differences were detected among the remaining three Admixture-derived subpopulations (Q2, Q3 and Q4), excluding Q1. As for TPB80, Israel and Q1 still stood out above the population mean and shows significant differences with all the other geographic populations and Qs, except for Latvia. Whereas all the other comparisons among geographic populations and Qs showed no significant differences.

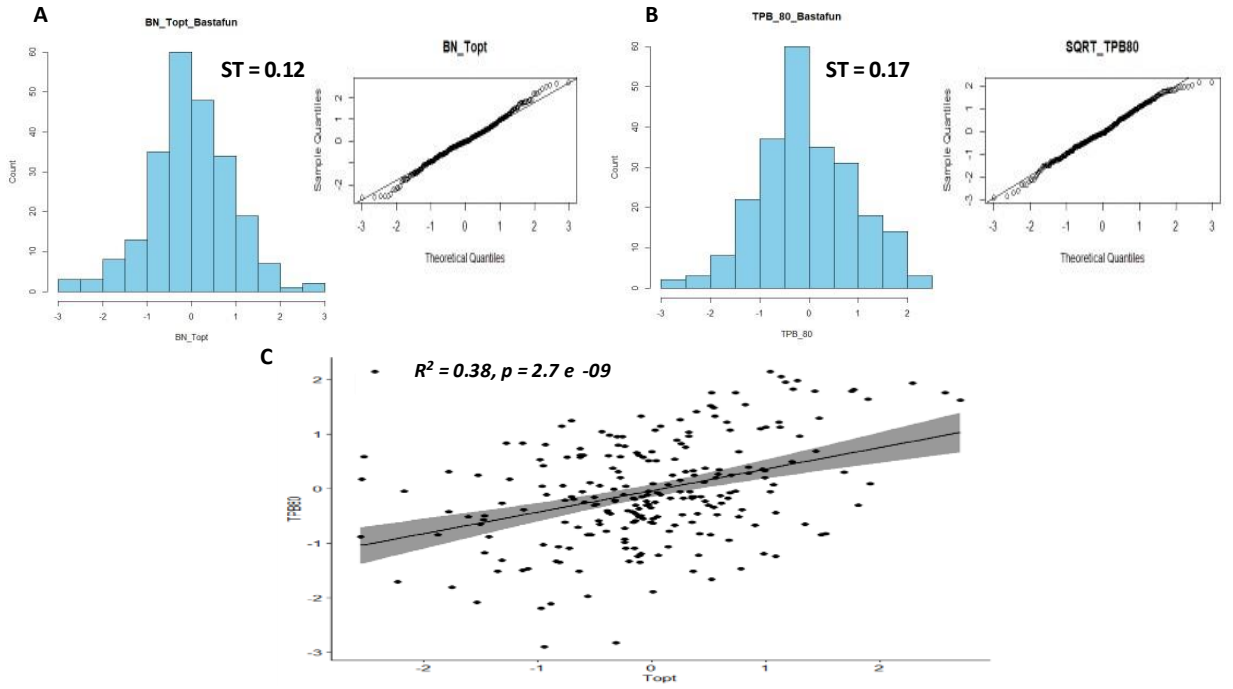

Figure 50: Image A: Histogram of frequency of the transformed data for Topt and corresponding Shapiro Test (ST), besides qqplot with comparison between Theoretical quantiles versus Sample quantiles. Image B: Histogram of frequency of the transformed data for TPB80 and corresponding Shapiro Test (ST), besides qqplot with comparison between Theoretical quantiles versus Sample quantiles. Image C: Correlation plot between Topt and TPB80 with Pearson Correlation Coefficient above and statistical p-value.

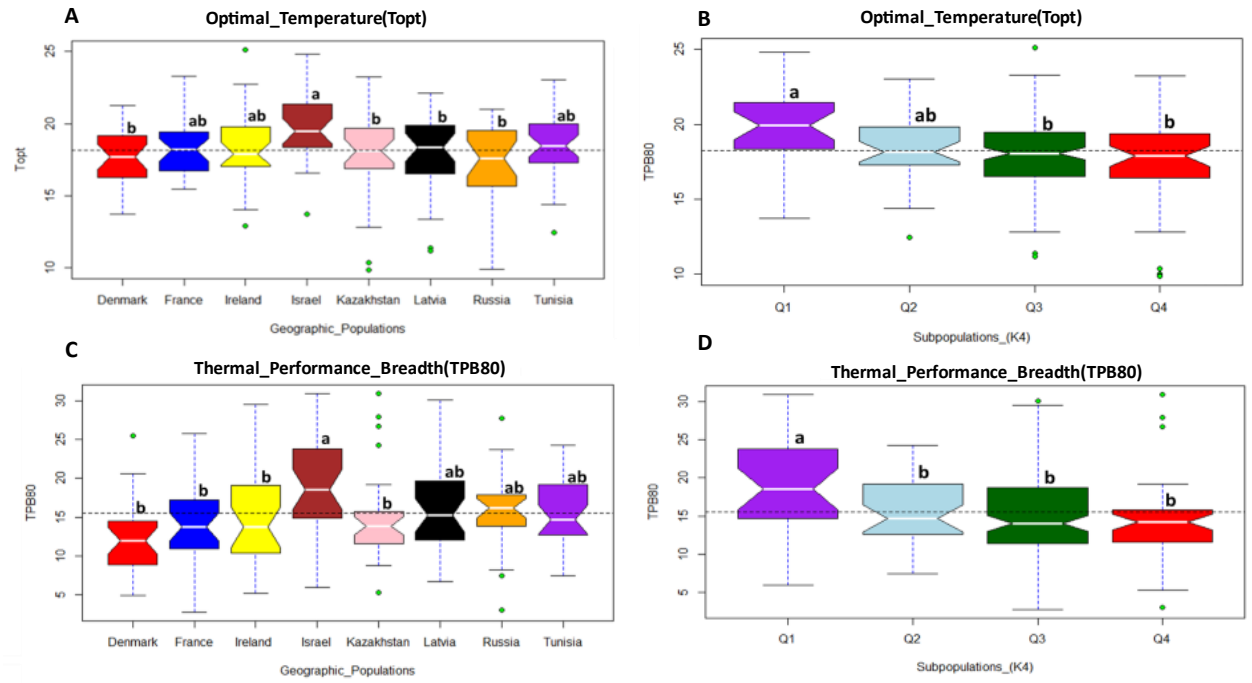

Figure 51: Phenotypic performance comparison among geographic populations and subpopulations for Topt and TPB80: Image A: Boxplots plotting phenotypic performance of all the isolates subdivided by geographic populations for Topt with compact letters indicating the results of the Post-Hoc analysis with Tukey's Test. Image B: Boxplots plotting phenotypic performance of all the isolates subdivided by the 4 admixture-derived subpopulations for Topt with compact letters indicating the results of the Post-Hoc Analysis with Tukey's Test. Image C: Boxplots plotting phenotypic performance of all the isolates subdivided by geographic populations for TPB80 with compact letters indicating the results of the Post-Hoc Analysis with Tukey's Test. Image D: Boxplots plotting phenotypic performance of all the isolates subdivided by the 4 admixture-derived subpopulations for TPB80 with compact letters indicating the results of the Post-Hoc Analysis with Tukey's Test.

Table.43: Table displaying the Minimum (Min), 1st Quantile, Median, Mean, 3rd Quantile, Range, Variance, Standard Deviation (std.dev), Coefficient of Variation (coef.var), and Maximum (Max) for Topt and TPB80 in the whole *Z. trtitici* population, in each geographic population and admixture-derived subpopulations.

		Min	Median	Mean	Range	var	std.dev	coef.var	Max
Entire panel	Topt	9.87	18.24	18.16	15.25	6.94	2.63	0.15	25.12
	TPB80	2.8	14.4	15.54	28.1	33.38	5.78	0.37	30.9
GEOGRAPHIC POPULATIONS									
DK	Topt	13.74	17.69	17.62	7.49	3.8	1.95	0.11	21.23
	TPB80	4.9	12	12.61	20.6	22.2	4.71	0.37	25.5
FR	Topt	15.46	18.18	18.14	7.81	3.56	1.89	0.1	23.27
	TPB80	2.8	13.75	14.08	23	25.2	5.02	0.36	25.8
IR	Topt	12.89	17.92	18.11	12.23	6.91	2.63	0.15	25.12
	TPB80	5.2	13.7	14.98	24.3	39.8	6.31	0.42	29.5
ISR	Topt	13.7	19.49	19.95	11.12	5.41	2.33	0.12	24.82
	TPB80	6	18.55	19.53	24.9	41.12	6.41	0.33	30.9
KZ	Topt	9.87	18.1	17.83	13.36	10.18	3.19	0.18	23.23
	TPB80	5.3	13.85	14.93	25.6	34.54	5.88	0.39	30.9
LV	Topt	11.16	18.33	17.83	10.96	8	2.83	0.16	22.12
	TPB80	6.7	15.25	16.42	23.4	34.05	5.84	0.36	30.1
RU	Topt	9.9	17.59	17.13	11.09	9.11	3.02	0.18	20.99
	TPB80	3	16.15	15.91	24.7	27.15	5.21	0.33	27.7
TU	Topt	12.45	18.47	18.47	10.57	5.42	2.33	0.13	23.02
	TPB80	7.5	14.7	15.69	16.8	21.04	4.59	0.29	24.3
ADMIXTURE-DERIVED SUBPOPULATIONS									
Q1	Topt	13.7	19.91	20.01	11.12	5.76	2.4	0.12	24.82
	TPB80	6	18.55	19.48	24.9	43.21	6.57	0.34	30.9
Q2	Topt	12.45	18.15	18.33	10.57	5.05	2.25	0.12	23.02
	TPB80	7.5	14.7	15.51	16.8	21.91	4.68	0.3	30
Q3	Topt	11.16	18.05	17.95	13.96	5.6	2.37	0.13	25.12
	TPB80	2.8	14.05	15.12	27.3	32.77	5.73	0.38	2.8
Q4	Topt	9.87	17.87	17.46	13.36	10.8	3.29	0.19	23.23
	TPB80	3	14.2	14.26	27.9	27.76	5.27	0.37	30.9

4.3.4 Avrstb6 phylogenetic analysis

Bread wheat cv. Chinese Spring (CS), known to carry *Stb6* resistance gene on Chromosome 3A was chosen as host variety to use for the pathogenicity assay and therefore, was expected to be highly susceptible towards all the isolates carrying a different isoform from *Avrstb6* present in *Z. tritici* reference strain IPO323. Thanks to the available whole-genome resequencing libraries for the 238 isolates and by comparing the sequences with IPO323 in the *Avrstb6* region (Chromosome 5: 68701…69530), for most of the isolates the complete sequences were extracted (167/ 240) and therefore, translated into the corresponding protein products. Phylogeny analysis was conducted to identify branching clusters based on the *Avrstb6* isoforms similarity (see table 45). In total, 20 different isoforms for *Avrstb6* plus the avirulent one carried by IPO323 were detected across the entire panel and renamed based on their arrangement in the phylogenic analysis (see table 45). The total

number of isoforms and their frequency within each geographic population are listed in table 6. *IPO323 Avrstb6* isoform is highly present in the French population (19/30) and in a few Isolates from Israel (2/30) (see table 44 and figure 53). Like the population structure clustering, some alternative *Avrstb6* isoforms are mainly conserved either in the same geographic population or geographic area, but there are still a few cases of isoforms present in countries very distant from each other (see table 44 and 45). Except for Kazakhstan carrying only two isoforms, all the others are highly diversified with a number ranging from 3 up to 8 in total and showing a prevalent one and many minors. Analyzing the output of the phylogenetic analysis on a large scale, it aligned with the geographic distribution of the countries to a great extent: from branch 1 (*Avrstb6-Iso_1)* up to 10 (*Avrstb6-Iso_10)* including *IPO323 Avrstb6* isoform, all Eastern-Middle European countries with the addition of a few isolates from Isolates are represented, whereas from 11 ((*Avrstb6-Iso_11)* to 14 (*Avrstb6-Iso_14)*, there was a prevalence of isolates from Middle-Eastern Europe. *Avrstb6-Iso 15* was the most diversified in terms of European area of origin, including individuals from Israel, Tunisia, Russia and France. An analogous situation was observed for *Avrstb6-Iso_19* with isolates from Middle Eastern countries (Latvia and Kazakhstan) and Mediterranean Area (Tunisia). *Avrstb6-Iso_16 and Avrstb6-Iso_18* was deeply conserved in the Mediterranean countries, respectively, Tunisia and Israel. Overall, *Avrstb6-Iso_21* was the most frequent Isoform and collocated at the opposite end compared to *IPO323 Avrstb6* isoform. *Avrstb6-Iso_21* was also highly diversified, including individuals from West-Middle Europe in prevalence and East to a minimal extent (see figure 52). Overall, there were several rare isoforms, that were uniquely carried by one individual but aligning with the global arrangement in the phylogenic tree analysis in respect to the geographic area (See table 44).

Table.44: Table showing the total numbe5 of *Avrstb6* detected in the *Zymoseptoria tritici* population subdivided by Geographic country and isoforms.

Geographic Population	Total Number of Isoforms	Isoforms
Denmark	6	*IsoAvrstb6_2, IsoAvrstb6_5, IsoAvrstb6_7, IsoAvrstb6_7, IsoAvrstb6_8, IsoAvrstb6_2*
France	3 plus *Avrstb6*	*Avrstb6*, IsoAvrstb6_3, IsoAvrstb6_15, IsoAvrstb6_21
Ireland	4	IsoAvrstb6_4, IsoAvrstb6_7, IsoAvrstb6_16, IsoAvrstb6_21
Israel	3 plus *Avrstb6*	Avrstb6, IsoAvrstb6_15, IsoAvrstb6_17, IsoAvrstb6_18
Kazakhstan	2	IsoAvrstb6_16, IsoAvrstb6_19
Latvia	8	IsoAvrstb6_2, IsoAvrstb6_7, IsoAvrstb6_9, IsoAvrstb6_10, IsoAvrstb6_11, IsoAvrstb6_14, IsoAvrstb6_19, IsoAvrstb6_21
Russia	6	IsoAvrstb6_11, IsoAvrstb6_12, IsoAvrstb6_13, IsoAvrstb6_15, IsoAvrstb6_20, IsoAvrstb6_21
Tunisia	3	IsoAvrstb6_15, IsoAvrstb6_16, IsoAvrstb6_19

Table.45: Table displaying all the Avrst6 isoforms and protein products arranged based on phylogenetic analysis

Isoforms_Acronym	Protein Product
IsoAvrstb6_1	MRSVLQGFLAFALAVGVQAKAKCGSVGDLCARGQSCCNYPEYDCFQDGQYPRCHTACGNWNFGFCHDGKQCDCQ-LWGCRCV
Avrstb6	MRSILQGLLAFALAVGVQARVSCGGIGDLCKAGDSCCNYPGTDCFQDGQYPRCHTACGHFQFGFCHDGKQCNCQVILGCGCV
IsoAvrstb6_2	MRSILQGLLAFALAVGVQARVSCGGIGDLCKAGASCCNYPGTDCFQDGQYPRCHTACGHYNFGFCHDGKLCNCQHIPGCGCV
IsoAvrstb6_3	MRSILQGLLAFALAVGVQARVSCGGIGDLCKAGPSCCNYPGTDCFQDGQYPRCHTACGHYNFGFCHDGKQCNCQVIPGCGCV
IsoAvrstb6_4	MRSILQGLLAFALAVGVQARVSCGGIGDLCKAGDSCCNYPITDCFQDGQYPRCHTACGHFHFGFCHDGKRCNCQVIRGCGCV
IsoAvrstb6_5	MRSILQGLLAFALAVGVQARVSCGGIGDLCKAGDSCCNYPITNCFQDGQYPRCHTACGHFHFGFCHDGKRCNCQVIRGCGCV
IsoAvrstb6_6	MRSILQGLLAFALAVGVQARVSCGGIGDLCKAGDSCCNYPITNCFQDGQYPRCHTACGHFHFGFCPDGKRCNCQVIRGCGCV
IsoAvrstb6_7	MRSILQGLLAFALAVGVQARVSCGGIGDLCKAGDSCCNYPINNCFQDGQYPRCHTACGHFHFGFCPDGKQCNCQVIPGCGCV
IsoAvrstb6_8	MRSILQGLLAFALAVGVQARVSCGGIGDLCKAGDSCCNYPITNCFQDGQYPRCHTACGHFHFGFCPDGKQCNCQVVRGCGCV
IsoAvrstb6_9	MRSIL-GLLAFALAVGV-ARVSCGGIGDLCKAGASCYNYPLTGCF-DGQYLRCHTTYGHYHFGFCYDGKQCNC-TVPSCSCV
IsoAvrstb6_10	MRSILQGLLAFALAVGVQARVSCGGIGDLCKAGASCCNYPLTGCFQDGQYPRCHTACGHYHFGFCHDGKQCNCQTIPGCGCV
IsoAvrstb6_11	MRSILQGLLAFALAVGVQARVSCGGIGDLCKAGNSCCNYPITNCFQDGQYPRCHTACGHYHFGFCHDGKQCNCQTVPGCGCV
IsoAvrstb6_12	MRSILQGLLAFALAVGVQARVSCGGIGDLCKAGDSCCNYPITNCFQDGQYPRCHTACGHYKFGFCHDGKQCNCQTVPGCGCV
IsoAvrstb6_13	MRSILQGLLAFALAVGVQARVTCGGIGDLCKAGPSCCNYPITNCFQDGQYPRCHTACGNWNFGFCHDGKQCNCQTVTGCGCV
IsoAvrstb6_14	MRSILQGLLAFALAVGVQARVVCGGIGDLCKAGPSCCNYPITNCFQDGQYPRCHTACGNWNFGFCHDGKQCNCQTIPGCGCV
IsoAvrstb6_15	MRSILQGLLAFALAVGVQARVVCGGIGDLCKAGPSCCNYPITNCFQDGQYPRCHTACGNWNFGFCHDGKQCNCQTVPGCGCV
IsoAvrstb6_16	MRSIL-GLLAFALAVGVQARVVYGGIGDLCKAGPSCCNYPITNCFQDGQYPRCYTACGN-NFGFCYDGKQCNC-TIPGCSYV
IsoAvrstb6_17	MRSILQGLLAFALAVGVQARVTCGGIGDLCKAGPSCCNYPITNCIQDGQYPRCHTACGNWNFGLCPDGKQCNCQVVPGCGCV
IsoAvrstb6_18	MRSILQGLLAFALAVGVQARVVCGGIGDLCKAGPSCCNYPITNCFQDGQYPRCHTACGNWNFGFCPDGKQCNCQVIPGCGCV
IsoAvrstb6_19	MRSILQGLLAFALAVGVQARVVCGGIGDLCKAGPSCCNYPITNCF-DGQYLRCHTACGNWNFGFCPDGKQCNCQVIPGCGCV
IsoAvrstb6_20	MRSILQGLLAFALAVGVQARVVCGGIGDLCKAGPSCCNYPITNCFQDGQYPRCHTACGNWNFGFCPDGKQCNCQVIPGCGCV

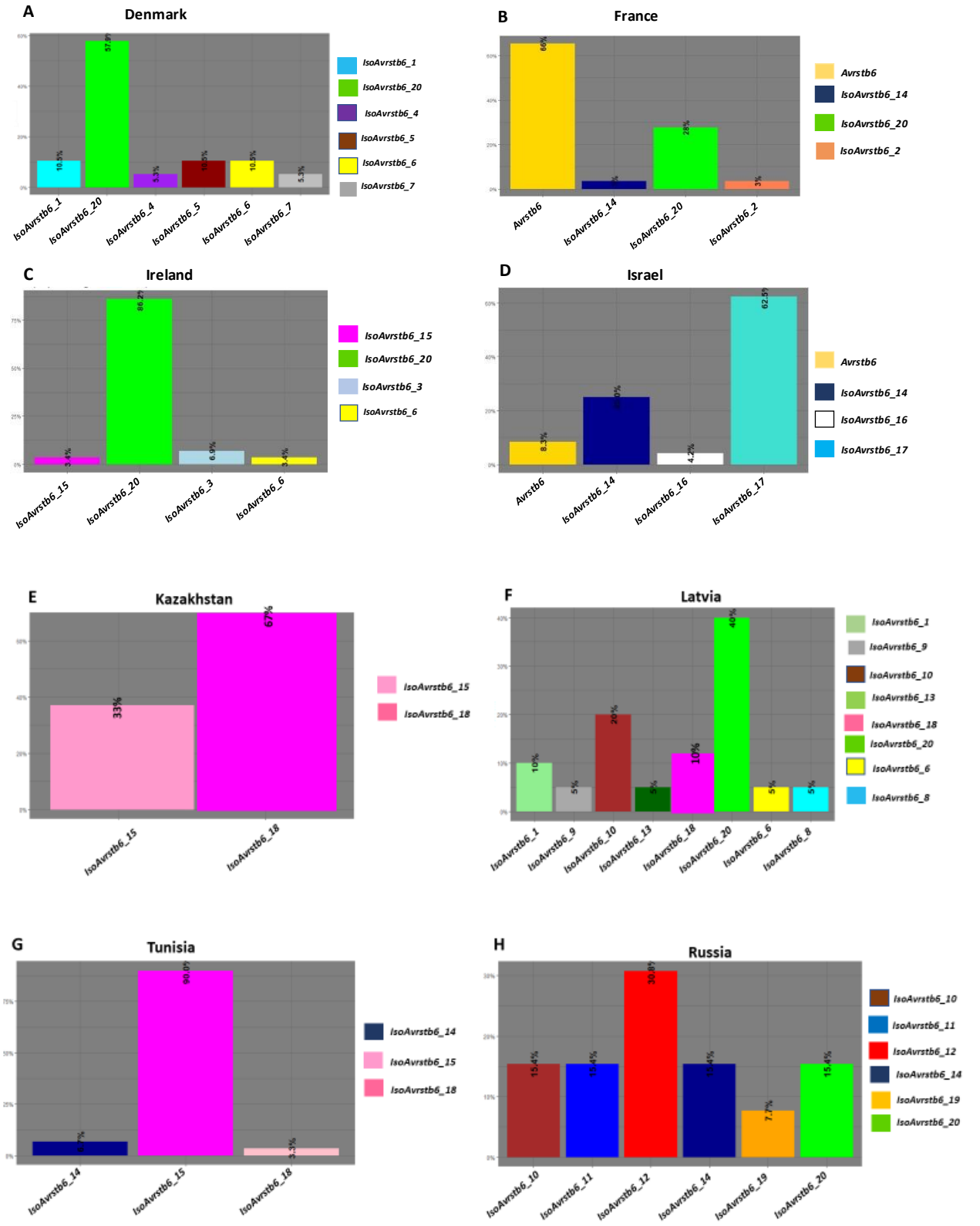

Figure 52: Frequency of the Avrstb6 isoforms within each geographic population. (A) Denmark, (B) France, (C) Ireland, (D) Israel, (E) Kazakhstan, (F) Latvia, (G) Tunisia and (H) Russia.

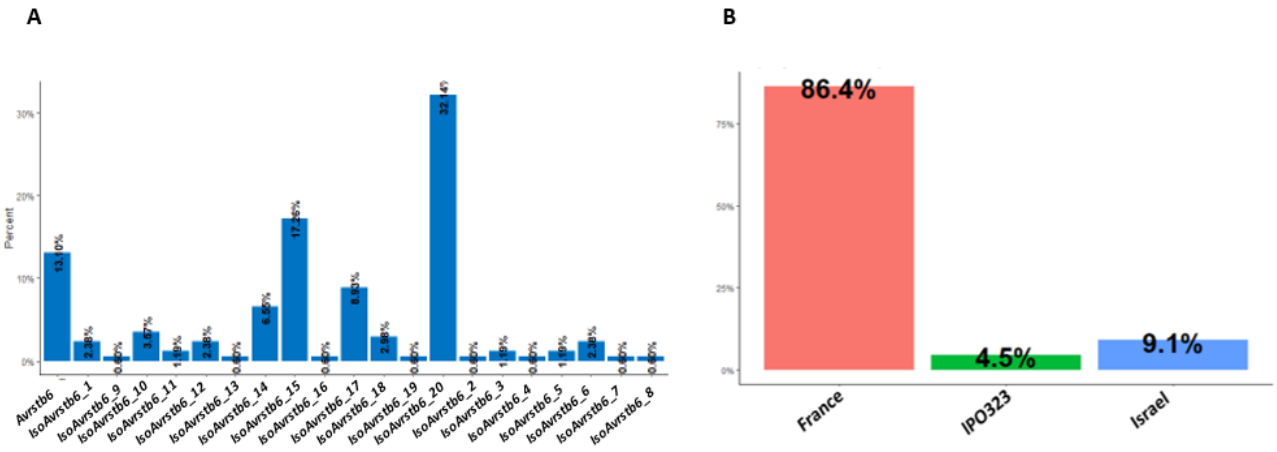

Figure 53: (A) This figure displays the frequency of each Avrstb6 isoform and WT Avrstb6 in the population overall. (B) Frequency of WT Avrstb6 isoform in the geographic populations.

4.3.5 Influence of temperature on pathogenic variability and plasticity

The influence of temperature on the two considered aggressivity traits, namely, the percentage of the leaf surface covered by lesions (PLACL) and pycnidia density (PycLes) was assessed through a pathogenicity assay at three different temperature conditions 18°C, 20°C and 22°C. For both pathogenicity traits, an independent phenotypic trait was considered at each temperature, namely, T18_PLACL, T20_PLACL, T22_PLACL, T18_PycLes, T20_PycLes, T22_PycLes. High-throughput phenotyping technique based on the analysis of images with resolution was performed to measure and assess pathogenicity symptoms through ImageJ software via a batch-processing macro described by Stewart et al., 2016 (see figure 54).

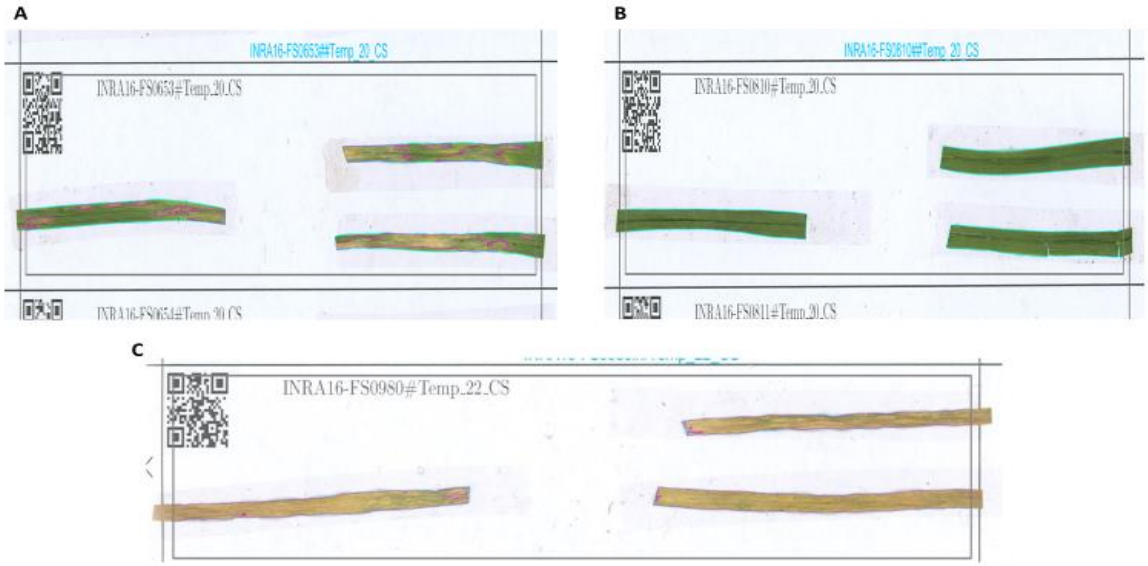

Figure 54: This figure displays the output of image analysis through Imagej software via an ad-hoc designed batch-processing macro. Blue margin refers to the total leaf area and border, purple margin refers to the identified necrotic areas with the symptoms and yellow dots identify the pycnidia across the detected necrotic area. (A) This image shows symptoms of a virulent isolate from Russia showing symptoms on the inoculated leaves. (B) This image displays an avirulent isolate from France, carrying *Avrstb6* wt isoform and therefore, showing no symptoms. (C) This image displays a highly virulent isolate from Kazakhstan showing necrotic symptoms on the inoculated leaves.

A statistically significant effect of temperature on both phenotypes was observed through ANOVA test (see table 45). Heritability and other descriptive statistic coefficients for all the 6 pathogenicity traits are displayed in table 46.

Table.45: Table displaying the results of Anova test for both aggressivity traits. ID stands for Individual, and it accounts for the total variance explained by all the isolates (df is equal to 237, total number of isolates minus 1). Temperature refers to the variance explained accounted by the temperature (df is equal to 2, since three temperature levels were considered T18, T20, T22).

	PLACL			**PycLes**		
	Sum Sq	**Df**	**Pvalue**	**Sum Sq**	**Df**	**Pvalue**
ID	4.14E+05	237	1.72E-64	2.14E+07	237	4.97E-58
Temperature	2.99E+04	2	9.20E-22	5.79E+05	2	2.48E-08
Residuals	1.31E+05	472	NA	7.52E+06	472	NA

Table.46: Table displaying the Minimum (Min), 1st Quantile, Median, Mean, 3rd Quantile, Range, Variance, Standard Deviation (std.dev), Coefficient of Variation (coef.var), Maximum (Max and broad-sense heritability (*h2*) at population level for T18_PLACL, T20_PLACL, T22_PLACL, T18_PycLes, T20_PycLes, T22_PycLes.

Traits	**Min**	**1st_Quantile**	**Median**	**Mean**	**3rd_Quantile**	**Range**	**var**	**std.dev**	**coef.var**	**Max**	***h2***
T18_PLACL	0.00	24.00	52.60	49.49	72.43	98.57	870.37	29.50	0.60	98.57	0.66
T20_PLACL	0.00	20.98	46.09	44.99	67.71	96.51	801.70	28.31	0.63	96.51	0.64
T22_PLACL	0.00	6.22	31.90	34.04	57.61	97.47	637.53	25.25	0.74	97.47	0.71
T18_PycLes	0.00	262.00	375.41	378.62	484.40	842.39	28811.15	169.74	0.45	842.39	0.62
T20_PycLes	0.00	268.20	435.46	422.83	567.60	898.04	38671.04	196.65	0.47	898.04	0.66
T22_PycLes	0.00	244.80	455.51	447.63	630.00	1302.35	55150.60	234.84	0.52	1302.35	0.65

Heritability exceeded 60% for all six temperature-related traits, indicating a strong genetic influence on the overall phenotypic variation. PLACL and PycLes displayed opposite patterns across the three temperature levels: as temperatures approached 18°C, the average population values for PLACL increased, while those for PycLes declined (see Figure 55). Symptoms were evaluated around 413 degree-days, which corresponded approximately to 20, 22 and 25 days post-inoculation for the three temperature regimes, reinforcing the hypothesis that temperature significantly influences this contrasting trend (see figure 55).

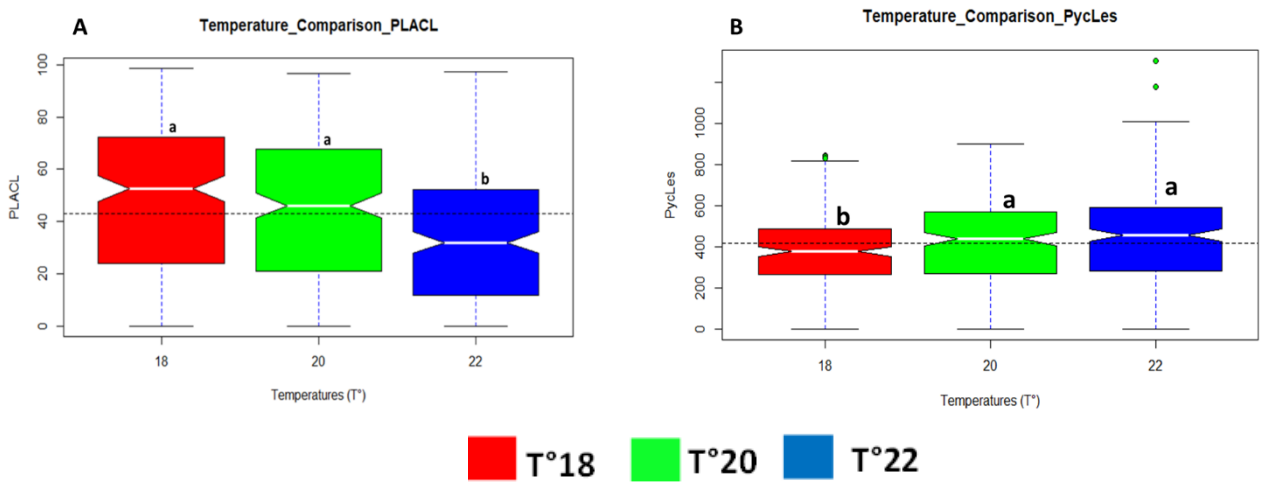

Figure 55: Image A: Boxplots showing the population performance for PLACL at the three considered temperatures (18°C, 20°C, 22°C). Dashed line is tracked in correspondence of the population average. Compact letters indicate the results of the Post-hoc Analysis with Tukey's Test. Image B: Boxplots showing the population performance for Pycnidia density (PycLes) at the three considered temperatures (18°C, 20°C, 22°C). Dashed line is tracked in correspondence of the population average. Compact letters indicate the results of the Post-hoc Analysis with Tukey's Test.

As expected, on average France and Tunisia showed the least aggressivity for both PLACL and PycLes way below the population mean across the three temperatures (see figure 56). Israel, Kazakhstan, latvia and Russia stood above the population mean for PLACL across the three temperatures, whereas Ireland and Denmark showed a progressive improvement as temperature decreases (see figure 58). As for PycLes, Israel and Kazakhstan always stood above the population mean, whereas Latvia, Ireland, Russia, and Denmark did not fall away from it (see figure 56). The comparison among subpopulations confirmed the same trend, observed within the geographic populations: Q1 and Q4 including respectively, isolates from Israel (Q1), Russia (Q4) and Kazakhstan (Q4) stood out, whereas Q2, composed of isolates from Tunisia was the least aggressive (see figure 59). Q3, the largest cluster and primarily representing Western European countries showed the longest phenotypic range, since it included both avirulent isolates from France and medium-to-high aggressive individuals from Latvia, Denmark, Kazakhstan, Russia, and Israel (see figure 57).

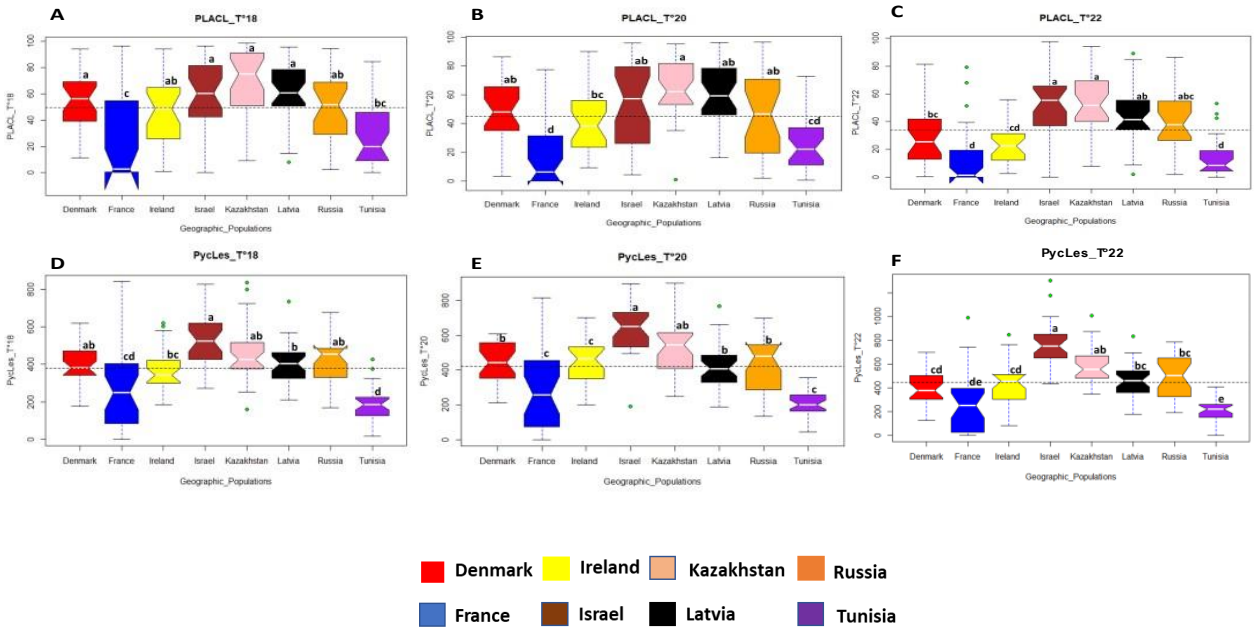

Figure 56: Phenotypic comparison among geographic populations for PLACL and PycLes at the three temperature regimes. Image A: Boxplots plotting phenotypic performance of all the isolates subdivided by geographic populations for PLACL_T°18 with compact letters indicating the results of the Post-hoc Analysis with Tukey's Test. Dashed line is tracked in correspondence of the population average. Image B: Boxplots plotting phenotypic performance of all the isolates subdivided by geographic populations for PLACL_T°20 with compact letters indicating the results of the Post-hoc Analysis with Tukey's Test. Dashed line is tracked in correspondence of the population average. Image C: Boxplots plotting phenotypic performance of all the isolates subdivided by geographic populations for PLACL_T°22 with compact letters indicating the results of the Post-hoc Analysis with Tukey's Test. Dashed line is tracked in correspondence of the population average. Image D: Boxplots plotting phenotypic performance of all the isolates subdivided by geographic populations for PycLes_T°18 with compact letters indicating the results of the Post-hoc Analysis with Tukey's Test. Dashed line is tracked in correspondence of the population average. Image E: Boxplots plotting phenotypic performance of all the isolates subdivided by geographic populations for PycLes_T°20 with compact letters indicating the results of the Post-hoc Analysis with Tukey's Test. Dashed line is tracked in correspondence of the population average. F: Boxplots plotting phenotypic performance of all the isolates subdivided by geographic populations for PycLes_T°22 with compact letters indicating the results of the Post-hoc Analysis with Tukey's Test. Dashed line is tracked in correspondence of the population average.

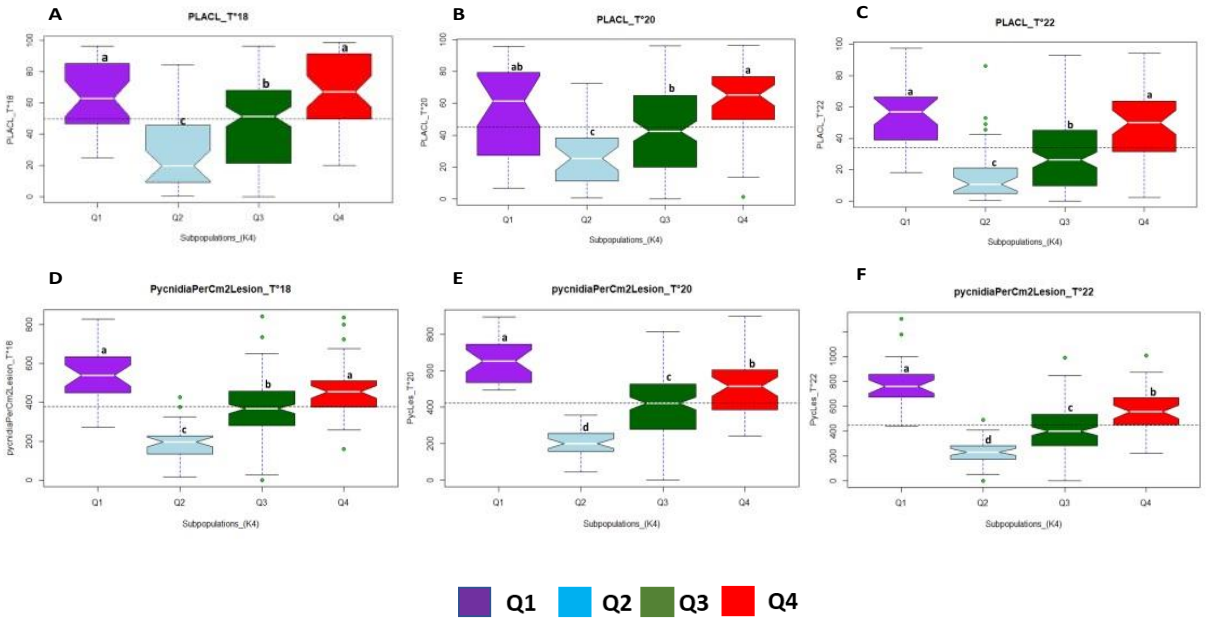

Figure 57: Phenotypic comparison among subpopulatons detected from Admixture analysis for PLACL and PycLes at the three temperature regimes. Image A: Boxplots plotting phenotypic performance of all the isolates subdivided by geographic populations for PLACL_T°18 with compact letters indicating the results of the Post-hoc Analysis with Tukey's Test. Dashed line is tracked in correspondence of the population average. Image B: Boxplots plotting phenotypic performance of all the isolates subdivided by geographic populations for PLACL_T°20 with compact letters indicating the results of the Post-hoc Analysis with Tukey's Test. Dashed line is tracked in correspondence of the population average. Image C: Boxplots plotting phenotypic performance of all the isolates subdivided by geographic populations for PLACL_T°22 with compact letters indicating the results of the Post-hoc Analysis with Tukey's Test. Dashed line is tracked in correspondence of the population average. Image D: Boxplots plotting phenotypic performance of all the isolates subdivided by geographic populations for PycLes_T°18 with compact letters indicating the results of the Post-hoc Analysis with Tukey's Test. Dashed line is tracked in correspondence of the population average. Image E: Boxplots plotting phenotypic performance of all the isolates subdivided by geographic populations for PycLes_T°20 with compact letters indicating the results of the Post-hoc Analysis with Tukey's Test. Dashed line is tracked in correspondence of the population average. F: Boxplots plotting phenotypic performance of all the isolates subdivided by geographic populations for PycLes_T°22 with compact letters indicating the results of the Post-hoc Analysis with Tukey's Test. Dashed line is tracked in correspondence of the population average.

Subsequently, the plastic phenotypic response to temperature for each individual, represented by the slope coefficient, was estimated for both aggressivity traits (PLACL_slope and PycLes_slope) across the three temperature regimes. The constrasting trend is also confirmed by a comparison between the resulting plastic response of PLACL and PycLes towards temperature (see figure 58). Individuals being avirulant or showing minimal plastic response were removed, in total 17 out of 238. As expected, most of these avirulant isolates were part of the French population and carried the *Avrstb6*, with the exception of only one carrying *IsoAvrstb6_21*. Additionally, two isolates from Tunisia and one from Ireland showed no symptoms. Notably, both isolates from Israel carrying *Avrstb6* showed minimal symptoms but plastic response and therefore, they were kept. In comparison with the other tested models, RRMM with the temperature as a fixed effect and random components, slope and intercept, for each individual accounted for 61.2 % and 63.15% of the total R2c (conditional R2), respectively for PLACL and PycLes and showed the least Akaike Information Criterion (AIC) (see table 47). As a whole, 4 coefficients were extracted from RRMM, an absolute slope coefficient for each individual, a relative slope coefficient, an absolute intercept and the corresponding relative intercept. The population-level average response (poly (ctemperature, 2, raw = T)1) estimated by the RRMM was negative for PLACL_slope and positive for PycLes_slope, therefore the most negative absolute and relative slope coefficients represent steeper reaction norm slopes and hence greater plasticity related to PLACL, conversely, more positive slope coefficients indicate a superior plastic response towards temperature for PycLes (See table 48 and figure 58). Heritability was higher than

60% for both PLACL_SLOPE and PycLes_SLOPE absolute coefficients, suggesting a strong contribution of the genetic components to the entire phenotypic variance observed (see table 48).

Table.47: Table displaying the population-level average intercept, population-level average plastic response (poly(ctemperature, 2, raw = T)1**)**, population-level average curvature (poly(ctemperature, 2, raw = T)2) and the R2m (the marginal R2 that is the fit of the fixed-effects only), and the R2c value (the conditional R2 that explains the proportion of variance accounted for by the random and fixedeffects combined).

	(Intercept)_Population Level	**poly(ctemperature, 2, raw = T)1**	**poly(ctemperature, 2, raw = T)2**	**R2m**	**R2c**
PLACL_slope	0.0866	-0.2522	-0.0868	6.75%	61.21%
PycLes_slope	0.0351	0.15	-0.0351	2.31%	63.15%

Table.48: Table displaying the Minimum (Min), 1st Quantile, Median, Mean, 3rd Quantile, Range, Variance, Standard Deviation (std.dev), Coefficient of Variation (coef.var), Maximum (Max and broad-sense heritability (*h2*) at population level for PLACL_SLOPE and PycLes_SLOPE.

	Traits	**Min**	**1st_Quantile**	**Median**	**Mean**	**3rd_Quantile**	**Range**	**var**	**std.dev**	**coef.var**	**Max**	***h2***
ENTIRE PANEL	PLACL_ SLOPE	-0.11	-0.22	-0.26	-0.25	-0.29	0.29	0.00	0.06	-0.23	-0.40	0.68
	PycLes_ SLOPE	-0.15	0.07	0.16	0.15	0.23	0.62	0.01	0.12	0.80	0.47	0.64

The relative slope coefficients for PLACL_SLOPE and PycLes_SLOPE were used to rank individuals by their slope steepness compared to the population average, which was set to zero (see Figure 59). For PLACL_SLOPE, individuals with positive relative coefficients have less steep slopes than the population average (ranking below it), while those with negative relative coefficients exhibit steeper slopes. Conversely, for PycLes_SLOPE, the population average shows a positive trend with temperature; thus, individuals with negative relative coefficients are ranked below the population average. Overall, substantial variability was observed within and among subpopulations for PLACL_SLOPE, whereas PycLes displayed a more structured phenotypic trend. Significant variability was also observed in the elevation coefficient (intercept) for PLACL_SLOPE within subpopulations, whereas a more organized pattern appeared for PycLes_SLOPE, with individuals from Israel and Tunisia consistently ranking above and below the population average, respectively, while more variability was noted in other subpopulations (Figure 58).

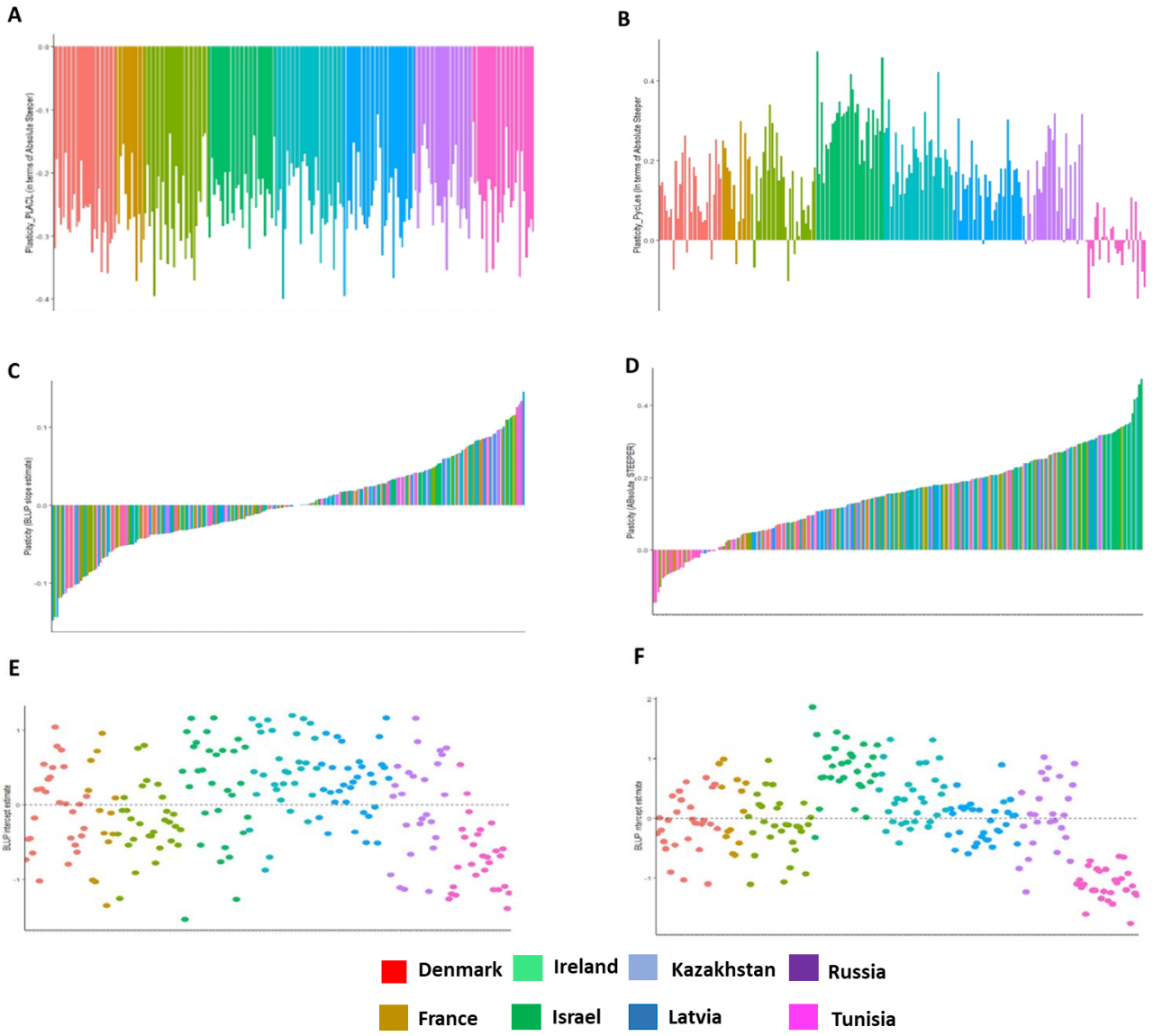

Figure 58: Comparison among subpopulations for PLACL_SLOPE and PycLes in terms of absolute coefficient, relative coefficient and relative elevation (intercept). Image A: Comparison of the absolute coefficients for PLACL_SLOPE across all individuals, organized by geographic population. Image B: Comparison of the absolute coefficients for PycLes_SLOPE across all individuals, organized by geographic population. C: Comparison among all individuals ranked based on the relative coefficient for PLACL_SLOPE. D: Comparison among all individuals ranked based on the relative coefficient for PycLes_SLOPE. E: General comparison among individuals for relative elevation coefficient (intercept) organized by geographic population for PLACL_SLOPE. F: General comparison among individuals for relative elevation coefficient (intercept) organized by geographic population for PycLes_SLOPE.

No statistically significant differences were observed for PLACL_slope in the comparison within and among geographic populations and subpopulations (figure 59, Image A). In both comparisons, all groups average plastic responses do not distance from the population mean, indicative of an unstructured nature of this trait. However, taken all groups and clusters together, all isolates carry a negative slope coefficient, which is indicative of a decreasing response as the temperature increases. Conversely, remarkable significant differences among groups were detected for PycLes_SLOPE (figure 59, image B). The general trend was consistent with the measured PycLes phenotype, with Israel standing out among all and above the population mean along with Kazakhstan. Denmark, Ireland, Latvia, Russia, and the remaining virulent isolates from France are all close to the population mean, whereas Tunisia is way below (figure 59, image B). Despite observing a positive population-level average response for PycLes_SLOPE, many isolates from Tunisia and a few from Russia,

Ireland, Latvia, Denmark and France showed a negative slope coefficient. The comparison among subpopulation confirms the same trend observed in the comparison among geographic populations with no statistically significant differences observed for PLACL_SLOPE and clear differences for PycLes_SLOPE. Q1 including only individuals from Israel stands out above the population average suggesting an increase of pycnidia production as the temperature increases. Statistically significant differences were observed between Q2 and Q3 as well. Q2 representing North-western European countries (France, Ireland and Denmark) stands at the same level of population, whereas Q3, representing East-European countries) stand slightly above due to the presence of individuals from Kazakhstan. Q4 representing individuals from Tunisia stand way below showing negative trend in most of the members for PycLes_SLOPE as temperature increases (figure 59, image D).

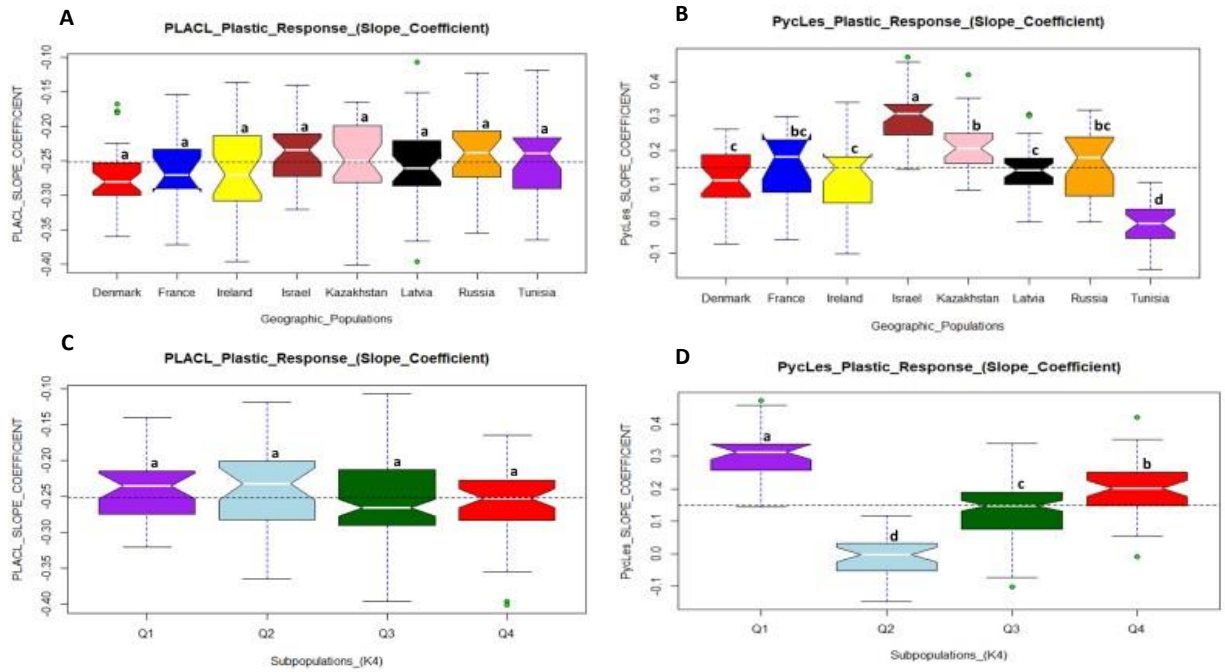

Figure 59: Image A: Boxplots plotting phenotypic performance of all the isolates subdivided by geographic populations for absolute PLACL_SLOPE with compact letters indicating the results of the Post-Hoc Analysis with Tukey's Test. Image B: Boxplots plotting phenotypic performance of all the isolates subdivided by geographic populations for absolute PycLes_ SLOPE with compact letters indicating the results of the Post-Hoc Analysis with Tukey's Test. Image C: Boxplots plotting phenotypic performance of all the isolates subdivided by the 4 admixture-derived subpopulations for absolute PLACL_ SLOPE with compact letters indicating the results of the Post-Hoc Analysis with Tukey's Test. Image D: Boxplots plotting phenotypic performance of all the isolates subdivided by the 4 admixture-derived subpopulations for absolute PycLes_SLOPE with compact letters indicating the results of the Post-Hoc Analysis with Tukey's Test.

4.3.6 GWAS and resolution increase through Local Score approach

Association analysis across the first 13 chromosomes, representing the core genome of *Z.tritici* was performed by using two models MLMM and BLINK. GWAS resolution and QTLs region confidence intervals were defined by the Lindley process through the Local score approach (see tables 49, 50, 51 and 52). GWAS results of each model, namely, the independent marker-p-values were used to detect the cumulative local association signals through LD between SNPs in a short genomic region containing a causal variant with small-to-moderate/high effect. The local score identified a region that begins on the first non-zero score of an excursion and ends at the point where the excursion comes back to 0 (figure 60, images A, B, C, D). Within every identified genomic region, the SNP showing the highest LOD for both MLMM and BLINK models was picked as peak marker of the local score segment (figures 61 and 62). The same selected peak markers were tested for downstream

analysis through Linear Model including the population structure membership score as covariate in order to estimate the phenotypic variance explained (R2) and significance though ANOVA (table 49). Despite the proximity, most of the time, the chosen most associated marker belonging to the detected Lindley region did not correspond to the peak position of the excursion (figures 61 and 62). Linear model was also performed to estimate the total phenotypic variance explained by the four Qs, both singularly and collectively, for each trait (see table 53). In total, 27 QTLs were detected for Topt (QZs_Topt) on chromosomes 1, 2 ,3, 4, 5 ,6 7, 8, 9, 11. TPB80 was the trait that revealed the largest number of associated regions, 48 QTLs (QZs_TPB80) in total, across all the chromosomes. GWAS and Local Score Approach revealed 37 QTLs for PLACL_SLOPE (QZs_PLACL_S) and 24 QTLs for PycLes_SLOPE (QZs_PycLes_S) across the entire genome. No common QTLs were detected between the four traits. In some cases, Lindley regions were detected by both tested model MLMM and BLINK but most of the time by one of them. Lindley regions peaks were extremely variable within each trait. For Topt, TPB80 and PycLes_SLOPE, the toppest peaks were medium-high respectively, at 28.74, 33.81 and 23.79 Lindley scores. Whereas, for PLACL_SLOPE, a very high peak was found on chromosome 3 with an estimated Lindley peak of 126.86. As expected, a very high collective phenotypic variance explained by the population structure was estimated for PycLes_SLOPE with R2 higher than 50% (table 50). Conversely, population structure account for no more than 8% for all the other traits with the least contribution observed for PLACL_SLOPE (R2 lower than 0.0261). The global phenotypic variance explained was estimated for all traits in an additive linear model including the the 4 Qs and all the significant most associated markers, resulted from the linear model covariated for the population structure. Overall, the global R2 was not lower than 50% for all traits with PycLes_SLOPE showing the highest value (76.4%), with a very strong population structure effect (table 53). TPB80 and PLACL_SLOPE also showed a very high global R2, respectively, 71.84% and 62.93, that in consideration of the minimal variance explained accounted by population structure, it is indicative of a high contribution of the most associated markers. Topt is the trait showing the least global R2 (58.35%) but considering the low variance explained accounted by population structure, high contribution is attributable to the detected most associated markers. Both BIC (Bayesian information criterion) and AIC (Akaike Information Criterion) selection criterions were adopted in a Stepwise regression model including the Qs as fixed predictors, in order to estimate the global R2 determined by the picked most associated markers (table 53). Interestingly, in every case global R2 estimated by the SWR performed with AIC was slightly higher than the model including all the most associated markers. Whereas, BIC was very stringent and shortlisted a restricted number of SNPs, accounting for a lower phenotypic variance explained but on the other hand, increased the confidence on the selected markers (table 53).

Table 49: GWAS and Local score results for Topt. The summary table displays the QTLs acronym, (MTA) most associated marker, Chromosome (Chr), physical position (Kbp), Major/minor alleles, LOD for MLMM and BLINK GWAS models, phenotypic variance explained (R2), markers selected by Stepwise regression model with AIC, markers selected by Stepwise regression model with BIC, start and end position of the Lindley process detected by Local Score approach in Kbp, physicial position of the Lindley process peak in Kbp and local score in correspondence of the peak.

Topt													
QTL	**MTA**	**Chr**	**Pos (Kbp)**	**Major/ minor**	**LOD_ MLMM**	**LOD_ Blink**	**R2**	**AIC**	**BIC**	**Start (Kbp)**	**End (Kbp)**	**Peak (Kbp)**	**Lindley**
QZs_Topt_1.1	rs1_5258768	1	5258.77	G/A	4.24	2.84	0.07	x		5258.64	5259.69	5259.05	17.29
QZs_Topt_1.2	rs1_5365952	1	5365.95	C/T	3.5	2.9	0.05			5365.9	5368.05	5366.7	13.13
QZs_Topt_1.3	rs1_5153214	1	5153.21	A/G	3.26	3.16	0.05	x	x	5152.82	5154.18	5153.21	6.79
QZs_Topt_1.4	rs1_1361200	1	1361.2	G/A	3.09	1.77	0.05	x	x	1361.2	1362.09	1361.37	6.51
QZs_Topt_1.5	rs1_1934831	1	1934.83	G/A	3.29	2.37	0.03	x		1934.75	1936.93	1935.38	6.28
QZs_Topt_1.6	rs1_5849228	1	5849.23	G/A	1.57	3.1	0.03			5848.8	5854.36	5853.49	9.05
QZs_Topt_2.1	rs2_1643967	2	1643.97	A/G	5.09	3.86	0.05	x	x	1643.92	1644.69	1644.24	13.03
QZs_Topt_2.2	rs2_1217579	2	1217.58	T/G	1.74	3.26	0.03	x	x	1216.66	1219.88	1217.98	7.99
QZs_Topt_3.1	rs3_1466895	3	1466.9	G/T	3.91	1.68	0.02			1466.82	1470.54	1467.31	25.33
QZs_Topt_3.2	rs3_628134	3	628.13	A/G	4.32	4.64	0.07	x	x	628.01	629.48	628.99	28.62
QZs_Topt_3.3	rs3_1796169	3	1796.17	C/T	2.91	3.93	0.05	x	x	1795.52	1798.27	1796.64	24.72
QZs_Topt_4.1	rs4_43148	4	43.15	C/T	3.52	2.44	0.05	x		42.96	46.4	45.91	13.5
QZs_Topt_4.2	rs4_998612	4	998.61	G/C	3.44	2.62	0.05	x	x	997.17	999.41	999.02	11.74
QZs_Topt_4.3	rs4_2233902	4	2233.9	C/T	2.64	3.17	0.04	x		2233.9	2234.28	2234.07	6.9
QZs_Topt_5.1	rs5_1142101	5	1142.1	A/G	4.45	3.31	0.08	x		1141.4	1144.56	1142.31	28.74
QZs_Topt_5.2	rs5_1183173	5	1183.17	C/G	3.22	0.57	0.03			1182.55	1184.34	1183.52	17.04
QZs_Topt_5.3	rs5_1582355	5	1582.36	G/A	3.78	4.37	0.07	x	x	1581.84	1582.88	1582.46	12.4
QZs_Topt_5.4	rs5_262243	5	262.24	G/A	4.42	5.41	0.07	x	x	262.17	262.54	262.24	6.12
QZs_Topt_5.5	rs5_79391	5	79.39	G/A	2.28	3.69	0.04	x		79.11	80.25	79.56	14.69
QZs_Topt_6.1	rs6_2480114	6	2480.11	G/A	2.05	3.34	0.03			2479.82	2480.29	2480.11	8.8
QZs_Topt_6.2	rs6_379404	6	379.4	G/A	4.12	1.39	0.04	x		379.13	379.85	379.46	11.87
QZs_Topt_6.3	rs6_1250399	6	1250.4	A/T	3.78	2.5	0.04	x	x	1250.37	1250.93	1250.43	6.6
QZs_Topt_7.1	rs7_1973921	7	1973.92	T/A	4.32	2.47	0.07	x	x	1973.86	1974.32	1973.95	8.92
QZs_Topt_8.1	rs8_1137289	8	1137.29	C/A	3.33	1.12	0.05			1135.83	1138.14	1137.61	15.27
QZs_Topt_9.1	rs9_687321	9	687.32	T/A	3.39	0.93	0.06			687.2	687.48	687.34	6.58
QZs_Topt_9.2	rs9_853130	9	853.13	T/C	3.62	1.62	0.05			853.12	853.75	853.39	5.58
QZs_Topt_11.1	rs11_564745	11	564.75	G/A/T	3.11	3.61	0.09	x		564.75	569.07	567.58	11.18

Table 50: GWAS and Local score results for TPB80. The summary table displays the QTLs acronym, (MTA) most associated marker, Chromosome (Chr), physical position (Kbp), Major/minor alleles, LOD for MLMM and BLINK GWAS models, phenotypic variance explained (R2), markers selected by Stepwise regression model with AIC, markers selected by Stepwise regression model with BIC, start and end position of the Lindley process detected by Local Score approach in Kbp, physicial position of the Lindley process peak in Kbp and local score in correspondence of the peak.

TPB80													
QTL	MTA	Chr	Pos (Kbp)	Major/minor	LOD_MLMM	LOD_Blink	R2	AIC	BIC	Start (Kbp)	End (Kbp)	Peak (Kbp)	Lindley
QZy_TPB80_1.1	rs1_2876095	1	2876.1	G/A	3.86	2.99	0.06	x		2875.77	2877.42	2876.25	31.61
QZy_TPB80_1.2	rs1_5777060	1	5777.06	C/G	5.27	3.92	0.06	x	x	5776.81	5780.57	5777.34	11.72
QZy_TPB80_1.3	rs1_5726925	1	5726.93	G/A	5.22	4.88	0.08	x	x	5726.66	5727.67	5727.08	11.18
QZy_TPB80_1.4	rs1_291700	1	291.7	C/A	3.61	3.35	0.05	x	x	291.62	292.26	291.9	8.73
QZy_TPB80_1.5	rs1_1671205	1	1671.21	C/A	4.74	1.82	0.06	x	x	1671.2	1672	1671.22	7.26
QZy_TPB80_1.6	rs1_2114658	1	2114.66	C/T	2.43	3.69	0.03			2114.51	2115.06	2114.9	33.81
QZy_TPB80_1.7	rs1_181158	1	181.16	A/G	2.11	3.63	0.03	x	x	180.88	181.67	181.23	6.5
QZy_TPB80_2.1	rs2_381747	2	381.75	T/C	5.5	4.53	0.07	x		381.73	382.05	381.86	10.13
QZy_TPB80_2.2	rs2_1644001	2	1644	T/C	4.68	1.48	0.05	x	x	1643.92	1644.37	1644.01	8.35
QZy_TPB80_2.3	rs2_2768524	2	2768.52	A/G	3.07	2.32	0.04			2768.35	2768.97	2768.57	5.7
QZy_TPB80_2.4	rs2_2900328	2	2900.33	C/T	1.98	3.68	0.04			2896.17	2907.19	2900.88	33.8
QZy_TPB80_2.5	rs2_1718613	2	1718.61	G/A	2.62	4.3	0.04	x	x	1718	1720.11	1718.66	16.19
QZy_TPB80_2.6	rs2_2276418	2	2276.42	C/T	2.34	3.68	0.05	x		2275.59	2277.99	2276.72	8.64
QZy_TPB80_3.1	rs3_1643411	3	1643.41	T/C	2.61	4.01	0.04	x		1642.97	1645.03	1644.4	8.08
QZy_TPB80_4.1	rs4_1304373	4	1304.37	C/A/T	3.69	3.78	0.05			1304.18	1305.41	1305.02	8.05
QZy_TPB80_5.1	rs5_2375793	5	2375.79	A/G	4.13	1.6	0.07	x		2374.59	2403.69	2375.81	18.37
QZy_TPB80_5.2	rs5_893651	5	893.65	T/C	2.75	3.23	0.05			893.11	893.92	893.65	7.57
QZy_TPB80_5.3	rs5_2459125	5	2459.13	T/C	2.66	2.95	0.04	x	x	2459.06	2459.79	2459.58	5.82
QZy_TPB80_6.1	rs6_1302311	6	1302.31	G/A	3.38	1.28	0.06			1302.25	1305.63	1303.27	9.09
QZy_TPB80_6.2	rs6_888415	6	888.42	A/C	3.68	0.52	0.03			888.12	888.8	888.5	7.14
QZy_TPB80_6.3	rs6_391426	6	391.43	T/G	3.79	1.15	0.04			390.98	392.04	391.55	5.57
QZy_TPB80_6.4	rs6_2098253	6	2098.25	C/T	2.85	0.06	0.02			2098.09	2099.08	2098.36	5.47
QZy_TPB80_6.5	rs6_1010325	6	1010.33	A/C	1.53	3.52	0.03	x	x	1009.9	1016.64	1011.08	23.16
QZy_TPB80_7.1	rs7_1494322	7	1494.32	A/C/T	4.81	5.35	0.05	x		1493.19	1502.54	1494.44	14.34
QZy_TPB80_7.2	rs7_1374526	7	1374.53	C/T	3.59	0.22	0.03	x	x	1373.25	1376.66	1374.64	9.77
QZy_TPB80_7.3	rs7_2310509	7	2310.51	A/G/T	3.05	0.71	0.06			2310.51	2316.13	2311.21	8.91
QZy_TPB80_7.4	rs7_2291876	7	2291.88	G/A	5.35	6.55	0.08	x	x	2291.85	2296.75	2291.95	8.46
QZy_TPB80_7.5	rs7_2163366	7	2163.37	C/T	2.93	0.94	0.04			2163.05	2163.78	2163.64	7.52
QZy_TPB80_7.6	rs7_1422771	7	1422.77	A/G	3.76	1.17	0.04			1422.77	1427.15	1423.53	5.9
QZy_TPB80_7.7	rs7_2132638	7	2132.64	T/C	2.56	2.79	0.02			2132.32	2143.45	2132.84	7.56
QZy_TPB80_8.1	rs8_1214205	8	1214.21	A/G	3.46	2.46	0.04	x		1213.99	1215.59	1214.6	19.41
QZy_TPB80_8.2	rs8_1147376	8	1147.38	T/G/A	5.11	7.92	0.1	x	x	1147.18	1147.89	1147.6	12
QZy_TPB80_8.3	rs8_882844	8	882.84	A/C	3.29	2.01	0.04			882.38	883.94	883.02	9.79
QZy_TPB80_8.4	rs8_2260407	8	2260.41	G/A	3.74	3.52	0.05	x		2260.41	2261.57	2260.8	8.69
QZy_TPB80_8.5	rs8_1454022	8	1454.02	G/A	3.17	2.34	0.05			1454.02	1455.55	1454.2	6.44
QZy_TPB80_8.6	rs8_1167632	8	1167.63	C/T	2.05	3.63	0.03			1167.53	1169.73	1168.8	14.65
QZy_TPB80_10.1	rs10_803281	10	803.28	A/C	4.02	3.3	0.07	x	x	802.88	804.6	804.05	16.22
QZy_TPB80_10.2	rs10_407306	10	407.31	C/T	2.74	0.89	0.05	x		406.77	407.82	407.49	9.25
QZy_TPB80_10.3	rs10_771064	10	771.06	C/T	3	0.74	0.03			770.48	771.47	771.22	7.77
QZy_TPB80_10.4	rs10_1041012	10	1041.01	A/G	3.22	1.74	0.04			1041.01	1041.25	1041.12	5.87

QZy_TPB80_11.1	rs11_936330	11	936.33	T/C	4.71	7.41	0.09	x	x	936.33	936.51	936.33	5.41
QZy_TPB80_11.2	rs11_470072	11	470.07	A/G	3.19	2.31	0.04	x		469.83	472.66	470.68	22.87
QZy_TPB80_11.3	rs11_1492046	11	1492.05	G/C/A	4.96	0.87	0.07			1491.62	1492.66	1492.36	7.42
QZy_TPB80_12.1	rs12_630996	12	631	A/G	2.62	1.02	0.03			629.66	633.28	632.21	13.45
QZy_TPB80_12.2	rs12_663750	12	663.75	C/T	3.61	2.1	0.05	x		663.38	665.04	664.01	10.56
QZy_TPB80_13.1	rs13_793429	13	793.43	G/T	4.1	2.16	0.07			793.39	793.78	793.57	8.19
QZy_TPB80_13.2	rs13_1066026	13	1066.03	G/T/A	3.27	1.1	0.07	x		1065.48	1066.7	1066.09	5.18
QZy_TPB80_13.3	rs13_561808	13	561.81	A/G	1.76	3.94	0.03	x	x	561.74	561.89	561.81	4.8

Table 51: GWAS and Local score results for PLACL_SLOPE. The summary table displays the QTLs acronym, (MTA) most associated marker, Chromosome (Chr), physical position (Kbp), Major/minor alleles, LOD for MLMM and BLINK GWAS models, phenotypic variance explained (R2), markers selected by Stepwise regression model with AIC, markers selected by Stepwise regression model with BIC, start and end position of the Lindley process detected by Local Score approach in Kbp, physicial position of the Lindley process peak in Kbp and local score in correspondence of the peak.

PLACL_SLOPE													
QTL	MTA	Chr	Pos (bps)	Major/minor	LOD_MLMM	LOD_Blink	R2	AIC	BIC	Start (Kbp)	End (Kbp)	Peak (Kbp)	Lindley
QZs_PLACL_S_1.1	rs1_314382	1	314.38	C/G	4.73	4.93	0.07	x		314.38	314.92	314.41	7.53
QZs_PLACL_S_1.2	rs1_4029069	1	4029.07	T/A	4.17	1.77	0.07	x	x	4028.76	4030.88	4029.36	10.59
QZs_PLACL_S_1.3	rs1_4785294	1	4785.29	T/C	4.24	2.65	0.07	x		4784.95	4786.24	4785.51	8.03
QZs_PLACL_S_1.4	rs1_3513480	1	3513.48	T/C	3.36	1.8	0.06			3512.61	3517.04	3513.86	19.32
QZs_PLACL_S_1.5	rs1_5725539	1	5725.54	G/C	2.85	0.89	0.05			5725.54	5726.77	5725.66	8.01
QZs_PLACL_S_1.6	rs1_5429851	1	5429.85	T/C	2.04	2.96	0.02			5429.75	5432.15	5429.95	6.69
QZs_PLACL_S_2.1	rs2_287532	2	287.53	C/G	5.68	6.32	0.09	x	x	287.41	288.05	287.85	11.84
QZs_PLACL_S_2.2	rs2_983439	2	983.44	G/A	4.26	1.62	0.06	x	x	983.41	984.27	983.5	9.14
QZs_PLACL_S_2.3	rs2_751654	2	751.65	G/A	4.13	2.18	0.07			750.53	752.4	751.74	7.25
QZs_PLACL_S_2.4	rs2_2510932	2	2510.93	A/C	3.24	1.11	0.05	x	x	2510.42	2511.73	2511.29	6.87
QZs_PLACL_S_2.5	rs2_642245	2	642.25	A/G	3.72	4.32	0.06			642.1	643.46	642.39	9.31
QZs_PLACL_S_3.1	rs3_1346601	3	1346.6	G/A	4.15	2.98	0.07	x	x	1345.84	1369.15	1347.43	42.25
QZs_PLACL_S_3.2	rs3_343684	3	343.68	G/A	4.37	0.59	0.08			343.67	343.81	343.74	6.91
QZs_PLACL_S_3.3	rs3_355877	3	355.88	C/T	3.44	4.46	0.08	x	x	353.87	358.43	357.17	126.86
QZs_PLACL_S_3.4	rs3_1551118	3	1551.12	C/T	2.73	0.6	0.03			1550.84	1551.78	1551.54	7.12
QZs_PLACL_S_3.5	rs3_3113549	3	3113.55	T/C	2.93	2.31	0.06	x		3113.19	3114.17	3113.81	6.62
QZs_PLACL_S_3.6	rs3_1414760	3	1414.76	A/G	3.87	1.73	0.08	x		1414.48	1416.05	1414.8	6.07
QZs_PLACL_S_3.7	rs3_347119	3	347.12	G/A	3.65	1.24	0.07			347.04	347.51	347.12	6.02
QZs_PLACL_S_3.8	rs3_2008227	3	2008.23	G/T	3.05	2.64	0.05	x		2008.09	2014.59	2010.6	14.71
QZs_PLACL_S_3.9	rs3_1893654	3	1893.65	T/C	2.63	3.22	0.05	x	x	1893.08	1894.16	1893.71	8.76
QZs_PLACL_S_4.1	rs4_484262	4	484.26	C/T	4.44	2.65	0.07		x	483.67	485.14	484.26	5.79
QZs_PLACL_S_4.2	rs4_2409843	4	2409.84	C/T	3.88	1.35	0.07			2408.76	2414.93	2409.9	44.39
QZs_PLACL_S_4.3	rs4_2044600	4	2044.6	C/T	2.83	1.4	0.05	x	x	2043.9	2046.61	2045.62	11.65
QZs_PLACL_S_5.1	rs5_1472179	5	1472.18	T/C	3.94	0.73	0.05	x		1471.93	1476.21	1472.19	12.01
QZs_PLACL_S_5.2	rs5_1856626	5	1856.63	A/G	2.56	1.79	0.04	x		1856.33	1857.22	1856.93	7.06
QZs_PLACL_S_5.3	rs5_1437020	5	1437.02	C/T	3.58	1.17	0.04			1436.96	1437.42	1437.26	7.16
QZs_PLACL_S_6.1	rs6_1796121	6	1796.12	A/G	5.23	4.81	0.11	x	x	1795.84	1800.7	1796.45	33.61
QZs_PLACL_S_6.2	rs6_1747583	6	1747.58	T/C	2.52	1.34	0.05			1740.19	1748.38	1747.75	7.37
QZs_PLACL_S_6.3	rs6_2299867	6	2299.87	A/G	2.32	3.23	0.04	x	x	2299.68	2300.29	2299.98	5.51
QZs_PLACL_S_8.1	rs8_893798	8	893.8	A/G	1.76	4.48	0.03			893.43	897.1	893.98	13.66
QZs_PLACL_S_8.2	rs8_772941	8	772.94	A/G	2.74	0.9	0.04	x		772.88	774.34	773.86	5.58
QZs_PLACL_S_9.1	rs9_1739518	9	1739.52	G/A	1.79	4.3	0.04	x		1739.4	1739.66	1739.52	11.61

QZs_PLACL_S_10	rs10_689415	10	689.42	G/A	2.76	2.55	0.05	x	x	689.18	690.26	689.73	10.49
QZs_PLACL_S_12.1	rs12_1096868	12	1096.87	A/T/C	4.03	2.79	0.06	x		1096.87	1097.28	1097.08	8
QZs_PLACL_S_12.2	rs12_1061508	12	1061.51	C/T	2.99	1.06	0.05	x		1061.29	1061.79	1061.63	9.31
QZs_PLACL_S_12.3	rs12_602420	12	602.42	C/T	3.21	1.53	0.04	x		602.33	602.76	602.62	8.77
QZs_PLACL_S_12.4	rs12_1389667	12	1389.67	T/G	3.75	0.75	0.05			1389.67	1389.96	1389.79	5.71

Table 52: GWAS and Local score results for PycLes_SLOPE. The summary table displays the QTLs acronym, (MTA) most associated marker, Chromosome (Chr), physical position (Kbp), Major/minor alleles, LOD for MLMM and BLINK GWAS models, phenotypic variance explained (R2), markers selected by Stepwise regression model with AIC, markers selected by Stepwise regression model with BIC, start and end position of the Lindley process detected by Local Score approach in Kbp, physicial position of the Lindley process peak in Kbp and local score in correspondence of the peak.

PycLes_slope													
QTL	**MTA**	**Chr**	**Pos (bps)**	**Major/minor**	**LOD_MLMM**	**LOD_Blink**	**R2**	**AIC**	**BIC**	**Start (Kbp)**	**End (Kbp)**	**Peak (Kbp)**	**Lindley**
QZy_PycLes_S1.1	rs1_2269909	1	2269.91	A/T	5.29	4.95	0.09	x		2269.78	2274.54	2270.86	23.79
QZy_PycLes_S1.2	rs1_4574941	1	4574.94	T/C	4.44	3.26	0.07	x	x	4574.69	4576.52	4576.21	8.82
QZy_PycLes_S1.3	rs1_5192498	1	5192.5	A/G	2.88	2.16	0.04	x	x	5192.28	5199.71	5192.59	9.43
QZy_PycLes_S1.4	rs1_4688671	1	4688.67	C/T	3.22	2.03	0.04			4688.22	4688.95	4688.67	9.3
QZy_PycLes_S1.5	rs1_5372982	1	5372.98	C/T	3.22	1.91	0.04			5372.61	5373.4	5373.04	6.86
QZy_PycLes_S1.6	rs1_2151738	1	2151.74	T/C	1.92	3.43	0.06	x		2149.29	2156.03	2151.98	13.65
QZy_PycLes_S1.7	rs1_5115834	1	5115.83	T/C	2.16	2.71	0.04	x	x	5115.62	5116.47	5116.03	8.72
QZy_PycLes_S1.8	rs1_4388571	1	4388.57	C/G	2.86	3.04	0.07			4388.32	4388.94	4388.72	6.78
QZy_PycLes_S2.1	rs2_1373477	2	1373.48	C/T	3.73	2.96	0.04	x		1373.23	1373.89	1373.57	9.21
QZy_PycLes_S2.2	rs2_2835570	2	2835.57	T/C	3.08	3.64	0.08	x	x	2835.25	2836.05	2835.81	5.95
QZy_PycLes_S3.1	rs3_27366	3	27.37	A/C	3.7	1.23	0.04	x		27.01	28.55	27.82	13
QZy_PycLes_S4.1	rs4_886139	4	886.14	A/G	2.59	2.95	0.06			886.14	886.34	886.24	6.7
QZy_PycLes_S4.2	rs4_735664	4	735.66	A/T	3.31	4.62	0.07	x	x	735.56	736.06	735.74	6.13
QZy_PycLes_S4.3	rs4_2416255	4	2416.26	A/G	3.15	2.12	0.05	x	x	2416.22	2418.19	2417.19	7.73
QZy_PycLes_S4.4	rs4_1279377	4	1279.38	G/A	2.67	2.05	0.03	x		1278.81	1281.47	1280.39	5.69
QZy_PycLes_S5	rs5_483522	5	483.52	T/C	1.34	3.51	0.04			483.42	483.86	483.53	5.61
QZy_PycLes_S6	rs6_1389446	6	1389.45	C/G	5.16	3.14	0.06	x	x	1389.08	1390.17	1389.27	8.4
QZy_PycLes_S7	rs7_1609319	7	1609.32	A/G	2.34	2.44	0.05			1608.32	1614.54	1611.81	13.44
QZy_PycLes_S8.1	rs8_197459	8	197.46	C/T	4.47	3.41	0.05	x		197.52	201.58	197.67	8.6
QZy_PycLes_S8.2	rs8_1888417	8	1888.42	G/T	1.38	3.26	0.04	x		1887.72	1888.82	1888.59	6.87
QZy_PycLes_S10.1	rs10_72761	10	72.76	C/G	2.3	2.3	0.08	x		72.71	72.93	72.76	7.22
QZy_PycLes_S10.2	rs10_217451	10	217.45	G/A	3.08	3.71	0.04	x		217.36	218.16	217.62	6.59
QZy_PycLes_S12	rs12_35333	12	35.33	G/A	1.28	3.21	0.02			35.2	37.64	36.96	8.94
QZy_PycLes_S13	rs13_177787	13	177.79	T/A	3.1	1.73	0.05	x	x	177.42	178.37	178.1	8.47

Table 53: This displays the result of linear model for the single Qs and the global adjusted R2 (%) for structure alone, all markers and Qs, BIC and AIC.

	Topt	TPB80	PLACL_SLOPE	PycLes_SLOPE
Q1	***	***	NS	****
Q2	NS	NS	NS	****
Q3	*	NS	NS	*
Q4	NS	NS	NS	***
Adjusted R2_Structure Alone (%)	6.2	4.42	2.61	51.02
Adjusted R2_Structure & All Significant Peak Markers (%)	58.4	71.84	62.93	76.4
Adjusted R2_Structure & Peak Markers_BIC (%)	48.5	63.87	53.86	71.34
Adjusted R2_Structure & Peak Markers_AIC (%)	58.2	73	64.01	76.91

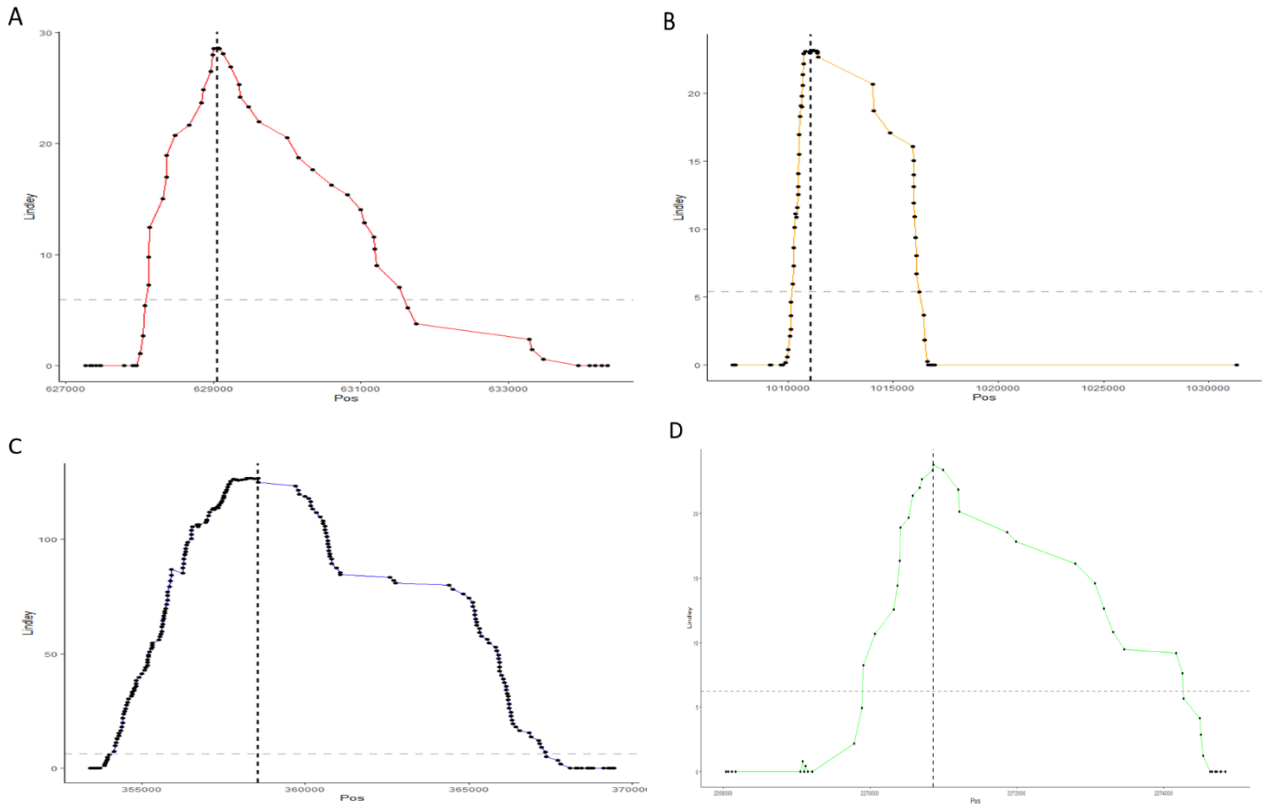

Figure 60: This figure displays the Lindley process ("the excursion") for 4 QTLs, each one related to one of the investigated traits. Figure A: This figure displays the Lindley process for QZs_Topt_3.2 detected from BLINK model on chromosome 3. xlab refers to the physical interval containing neighboring markers being part of the excursion and reported on chart as black dots. Horizontal grey dashed line refers to the local threshold for that chromosome (5.90) and vertical black dashed line refers to the excursion peak physical position. Figure B: This figure displays the Lindley process for QZy_TPB80_6.5 detected from BLINK model on chromosome 6. xlab refers to the physical interval containing neighboring markers being part of the excursion and reported on chart as black dots. Horizontal grey dashed line refers to the local threshold for that chromosome (5.40) and vertical black dashed line refers to the excursion peak physical position.
Figure C: This figure displays the Lindley process for PLACL_S_3.3 detected from BLINK model on chromosome 3. xlab refers to the physical interval containing neighboring markers being part of the excursion and reported on chart as black dots. Horizontal grey dashed line refers to the local threshold for that chromosome (6.08) and vertical black dashed line refers to the excursion peak physical position. Figure D: This figure displays the Lindley process for PycLes_S1.1 detected from MLMM model on chromosome 1. xlab refers to the physical interval containing neighboring markers being part of the excursion and reported on chart as black dots. Horizontal grey dashed line refers to the local threshold for that chromosome (6.22) and vertical black dashed line refers to the excursion peak physical position.

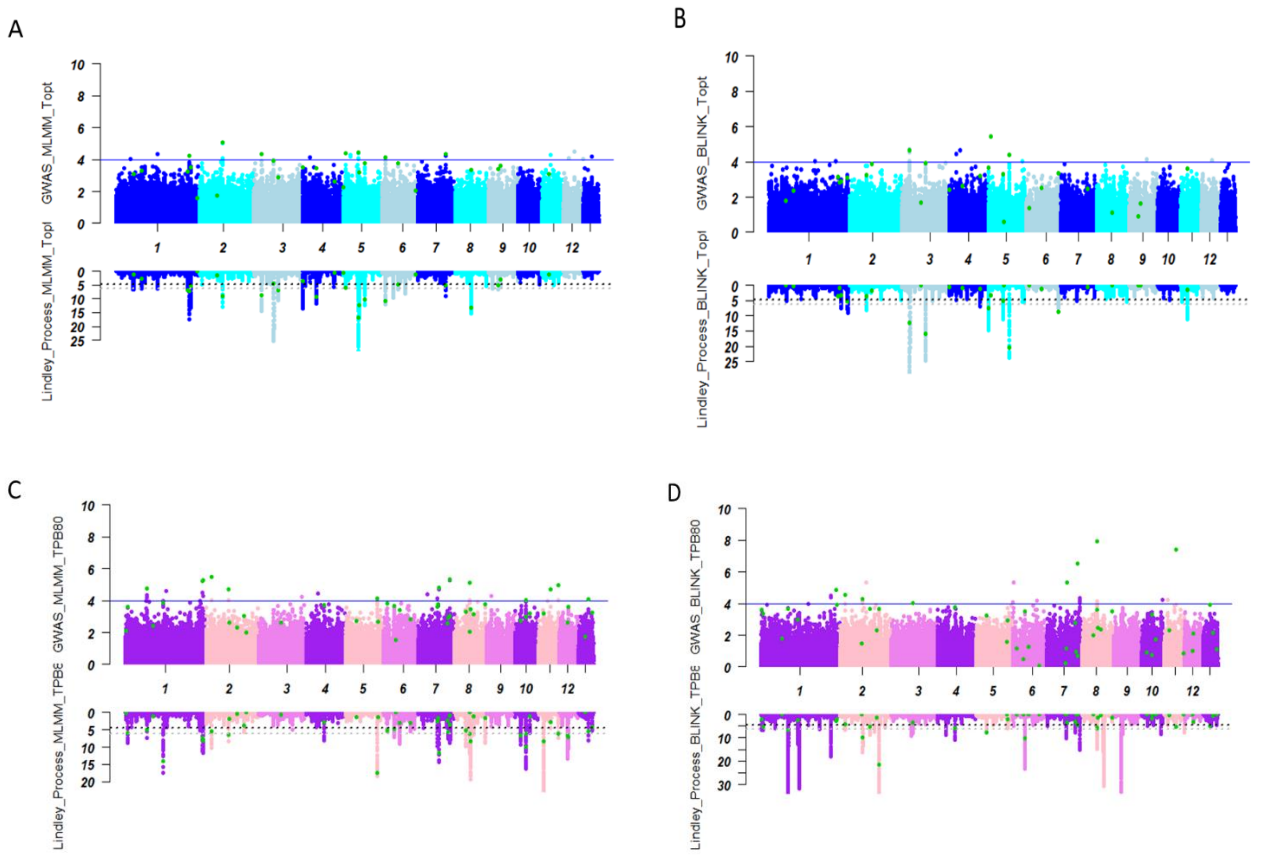

Figure 61: Mirror-shape Manatthan plots reflecting the results of GWAS and Local score for the two thermal response traits (Topt and TPB80) and GWAS model, MLMM and BLINK. Dots in green highlights the chosen MTAs for each QTL. Figure A: GWAS and Lindley process for Topt and MLMM. Horizontal blue line refers to chosen GWAS threshold equal to 4 (p-value < 0.0001). black and grey dashed line refers to highest and lowest chromosome threshold used for the Local score approach. Figure B: GWAS and Lindley process for Topt and BLINK. Horizontal blue line refers to chosen GWAS threshold equal to 4 (p-value < 0.0001). black and grey dashed line refers to highest and lowest chromosome threshold used for the Local score approach. Figure C: GWAS and Lindley process for TPB80 and MLMM. Horizontal blue line refers to chosen GWAS threshold equal to 4 (p-value < 0.0001). black and grey dashed line refers to highest and lowest chromosome threshold used for the Local score approach. Figure D:
GWAS and Lindley process for TPB80 and BLINK. Horizontal blue line refers to chosen GWAS threshold equal to 4 (p-value < 0.0001). black and grey dashed line refers to highest and lowest chromosome threshold used for the Local score approach.

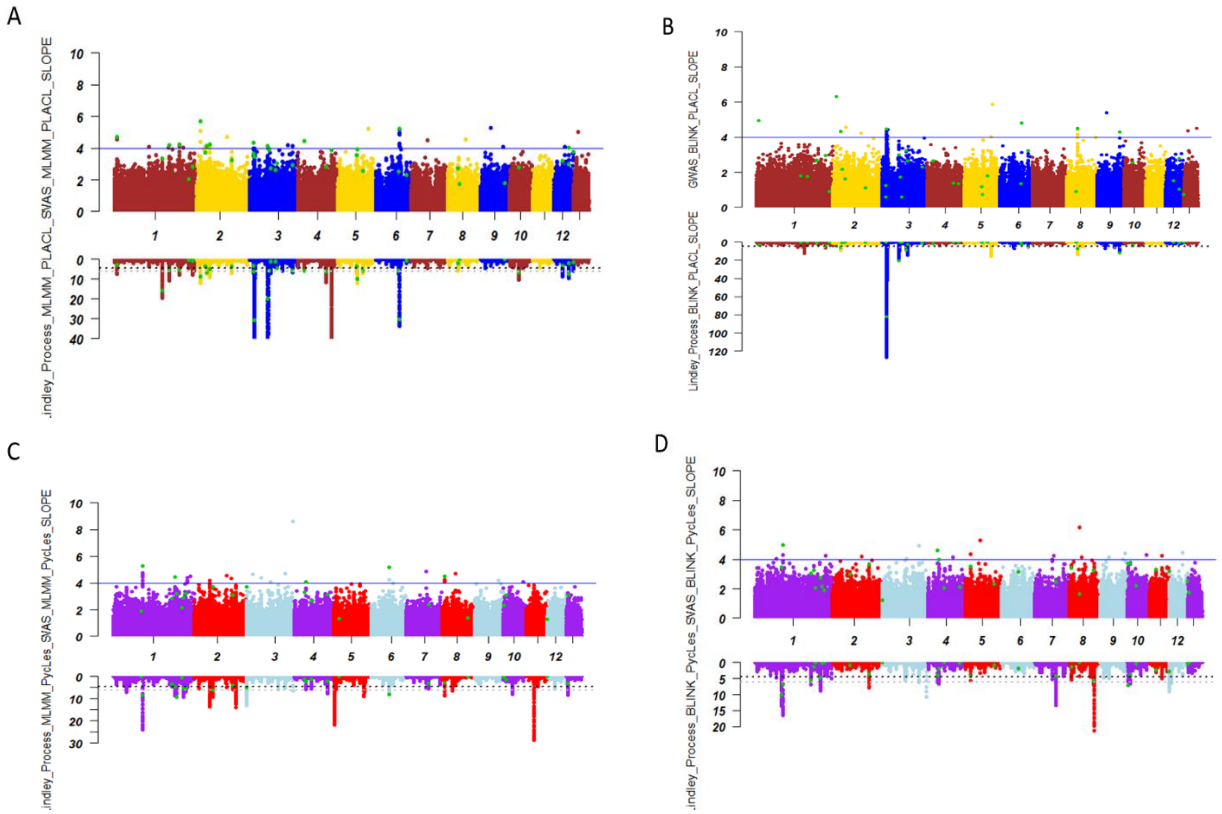

Figure 62: Mirror-shape Manatthan plots reflecting the results of GWAS and Local score for the two plastic response phenotypes (PLACL_SLOPE and PycLes_SLOPE) and GWAS model, MLMM and BLINK. Dots in green highlights the chosen MTAs for each QTL. Figure A: GWAS and Lindley process for PLACL_SLOPE and MLMM. Horizontal blue line refers to chosen GWAS threshold equal to 4 (p-value < 0.0001). black and grey dashed line refers to highest and lowest chromosome threshold used for the Local score approach. Figure B: GWAS and Lindley process for PLACL_SLOPE and BLINK. Horizontal blue line refers to chosen GWAS threshold equal to 4 (p-value < 0.0001). black and grey dashed line refers to highest and lowest chromosome threshold used for the Local score approach. Figure C: GWAS and Lindley process for PycLes_SLOPE and MLMM. Horizontal blue line refers to chosen GWAS threshold equal to 4 (p-value < 0.0001). black and grey dashed line refers to highest and lowest chromosome threshold used for the Local score approach. Figure D: GWAS and Lindley process for PycLes_SLOPE and BLINK. Horizontal blue line refers to chosen GWAS threshold equal to 4 (p-value < 0.0001). black and grey dashed line refers to highest and lowest chromosome threshold used for the Local score approach.

4.3.7 Candidate genes annotation within the QTLs Lindley region

After defining the confidence interval through the local score approach, annotated genes within the detected regions were extracted from a dedicated genome browser (https://bioinfo.bioger.inrae.fr/portal/genome140 portal/12) or on the newly created IPO323 genome web portal at JGI (https://mycocosm.jgi.doe.gov/Zymtr1/Zymtr1.home.html).
Thanks to the high density of the genotyping matrix and short LD, despite including several neighboring markers, the QTLs Lindley region were quite short. This factor was leveraged to identify a restricted number of annotated candidate genes within every single QTLs Lindley region. No common QTL among the investigated traits was found many QTLs were very proximal. For the same trait, both genes with same biological function or completely different (see tables 54, 55, 56 and 57). As for Topt, several annotated genes with diversified functions were found, such as protein binding, RNA nuclease activity, transcription factors, carbohydrate metabolism, transmembrane and sugar transporter, Oxidoreductase activity and many uncharacterized proteins (see table 54). Like Topt, diversified annotated genes were also detected for TPB80, with the addition of catalytic activity, many transcription factors (zinc ion binding), DNA and RNA binding factors as well as many other uncharacterized protein products (see table 55). As for the two plastic response phenotype traits, many transcription factors, transmembrane transporters and transcription regulators were detected (Zinc ion binding, Fungal specific transcription factor). Additionally, an

interesting heat stock protein (chaperone) was found for PycLes_SLOPE in chromosome 2 (see table 57).

Table 54: This displays the annotated candidate genes found for Topt. The QTL acronym, ZtIPO323_ID acronym extracted from Zymoseptoria tritici reference genome available browsers and gene function reported in MyGenomeBrowser and MycoCosm databases.

Topt	ZtIPO323_ID	MyGenomeBrowser	MycoCosm
QZs_Topt_1.1	ZtIPO323_020650	Homocysteine S-methyltransferase	methionine biosynthesis
QZs_Topt_1.2	ZtIPO323_021150	unnamed protein product	unnamed protein product
QZs_Topt_1.3	ZtIPO323_020290	DNA repair protein Pso2/Snm1	DNA repair metallo-beta-lactamase
QZs_Topt_1.4	ZtIPO323_004580	ABC transporter	ATP hydrolysis activity
QZs_Topt_1.5	ZtIPO323_007110	Cytochrome P450	oxidoreductase activity
QZs_Topt_1.6	ZtIPO323_023200	unnamed protein product	unnamed protein product
QZs_Topt_2.1	ZtIPO323_029590	unnamed protein product	unnamed protein product
QZs_Topt_2.2	ZtIPO323_027860	uncharacterized protein MYCGRDRAFT_107967	uncharacterized protein MYCGRDRAFT_107967
QZs_Topt_3.1	ZtIPO323_042530	NAD(P)-binding protein	NAD(P)-binding protein
QZs_Topt_3.2	ZtIPO323_039610	unnamed protein product	unnamed protein product
QZs_Topt_3.3	ZtIPO323_043740	pinin/SDK/memA domain protein	Cellular Processes And Signaling
QZs_Topt_4.1	ZtIPO323_050540	MFS1 putative major facilitator superfamily transporter	Sugar transporter
QZs_Topt_4.2	ZtIPO323_053690	hypothetical protein FE78DRAFT_42100	hypothetical protein FE78DRAFT_42100
QZs_Topt_4.3	ZtIPO323_058250	LanC-like protein GCR2	Lanthionine synthetase C-like protein
QZs_Topt_5.1	ZtIPO323_064510	uncharacterized protein MYCGRDRAFT_109465	uncharacterized protein MYCGRDRAFT_109465
QZs_Topt_5.2	ZtIPO323_064650	ribonuclease P complex subunit Pop2 like protein	RNA nuclease activity; tRNA processing
QZs_Topt_5.3	ZtIPO323_066490	IQ domain-containing protein IQM5	protein binding
QZs_Topt_5.4	ZtIPO323_061260	unnamed protein product	unnamed protein product
QZs_Topt_5.5	ZtIPO323_060710	unnamed protein product	unnamed protein product
QZs_Topt_6.1	ZtIPO323_078430	DUF453 domain protein	PrpF protein
QZs_Topt_6.2	ZtIPO323_071780	unnamed protein product	transferase activity
QZs_Topt_6.3	ZtIPO323_074330	glycoside hydrolase family 20 protein	carbohydrate metabolism
QZs_Topt_7.1	ZtIPO323_085980	uncharacterized protein MYCGRDRAFT_94685	uncharacterized protein MYCGRDRAFT_94685
QZs_Topt_8.1	ZtIPO323_092480	putative ABC transporter	Multidrug resistance-associated protein/mitoxantrone resistance protein
QZs_Topt_9.1	ZtIPO323_099080	Ca2+-modulated nonselective cation channel polycystin	PAN domain
QZs_Topt_9.2	ZtIPO323_099800	E3 ubiquitin-protein ligase	Predicted E3 ubiquitin ligase
QZs_Topt_11.1	ZtIPO323_112330	putative 26S proteasome regulatory subunit rpn9	protein binding

Table 55: This displays the annotated candidate genes found for TPB80. The QTL acronym, ZtIPO323_ID acronym extracted from Zymoseptoria tritici reference genome available browsers and gene function reported in MyGenomeBrowser and MycoCosm databases.

Topt	ZtIPO323_ID	MyGenomeBrowser	MycoCosm
QZy_TPB80_1.1	ZtIPO323_011060	unnamed protein product	unnamed protein product
QZy_TPB80_1.2	ZtIPO323_022860	uncharacterized protein MYCGRDRAFT_33514	uncharacterized protein MYCGRDRAFT_33514
QZy_TPB80_1.3	ZtIPO323_022700	Fungal specific transcription factor domain	regulation of transcription
QZy_TPB80_1.4	ZtIPO323_000710	protein FMP42-like	Major facilitator superfamily
QZy_TPB80_1.5	ZtIPO323_005840	Transcription factor atf1	DNA-binding transcription factor activity
QZy_TPB80_1.6	ZtIPO323_007870	GMC oxidoreductase	oxidoreductase activity
QZy_TPB80_1.7	ZtIPO323_000270	Protein kinase-like domain	protein kinase activity
QZy_TPB80_2.1	ZtIPO323_024810	unnamed protein product	Pre-mRNA-splicing factor Cwc2/Slt11
QZy_TPB80_2.2	ZtIPO323_029590	unnamed protein product	unnamed protein product
QZy_TPB80_2.3	ZtIPO323_033870	unnamed protein product	unnamed protein product
QZy_TPB80_2.4	ZtIPO323_034400	alpha/gamma-adaptin-binding protein p34	Alpha and gamma adaptin binding protein p34
QZy_TPB80_2.5	ZtIPO323_029840	Clavaminate synthase-like protein	Predicted phospholipase
QZy_TPB80_2.6	ZtIPO323_031920	Transcription factor IWS1	DNA binding
QZy_TPB80_3.1	ZtIPO323_043140	unnamed protein product	Domain of unknown function DUF1989
QZy_TPB80_4.1	ZtIPO323_054890	glycoside hydrolase family 64 protein	Glycoside hydrolase 64
QZy_TPB80_5.1	ZtIPO323_069170	Long-chain-fatty-acid--CoA ligase 1	Acyl-CoA synthetase
QZy_TPB80_5.2	ZtIPO323_063760	Lactation elevated protein 1	ATP binding
QZy_TPB80_5.3	ZtIPO323_069420	GPI ethanolamine phosphate transferase 1	sulfuric ester hydrolase activity
QZy_TPB80_6.1	ZtIPO323_074520	Diaminopropionate ammonia-lyase	Diaminopropionate ammonia-lyase
QZy_TPB80_6.2	ZtIPO323_072930	uncharacterized protein MYCGRDRAFT_93764	uncharacterized protein MYCGRDRAFT_93764
QZy_TPB80_6.3	ZtIPO323_071820	uncharacterized protein MYCGRDRAFT_72796	uncharacterized protein MYCGRDRAFT_72796
QZy_TPB80_6.4	ZtIPO323_007110	DNA damage-binding protein cmr1	protein binding
QZy_TPB80_6.5	ZtIPO323_073430	Baeyer-Villiger monooxygenase	Flavin-containing monooxygenase
QZy_TPB80_7.1	ZtIPO323_084250	Peroxisome biogenesis factor 10	protein turnover,chaperones
QZy_TPB80_7.2	ZtIPO323_083840	uncharacterized protein MYCGRDRAFT_110220	uncharacterized protein MYCGRDRAFT_110220
QZy_TPB80_7.3	ZtIPO323_087550	uncharacterized protein MYCGRDRAFT_94787	uncharacterized protein MYCGRDRAFT_94787
QZy_TPB80_7.4	ZtIPO323_087480	unnamed protein product	unnamed protein product
QZy_TPB80_7.5	ZtIPO323_086960	uncharacterized protein MYCGRDRAFT_94744	uncharacterized protein MYCGRDRAFT_94744
QZy_TPB80_7.6	ZtIPO323_084010	WSC domain-containing protein	WSC domain
QZy_TPB80_7.7	ZtIPO323_086780	uncharacterized protein MYCGRDRAFT_94734	uncharacterized protein MYCGRDRAFT_94734
QZy_TPB80_8.1	ZtIPO323_092880	eukaryotic translation initiation factor 4E type 2-like	translational initiation
QZy_TPB80_8.2	ZtIPO323_092550	Ribonuclease T2-like	RNA processing and modification
QZy_TPB80_8.3	ZtIPO323_091320	uncharacterized protein MYCGRDRAFT_95063	uncharacterized protein MYCGRDRAFT_95063
QZy_TPB80_8.4	ZtIPO323_096790	Protein RDR1	regulation of transcription, DNA-dependent
QZy_TPB80_8.5	ZtIPO323_094020	aromatic amino acid aminotransferase like protein	biosynthetic process
QZy_TPB80_8.6	ZtIPO323_092650	Asparagine-rich zinc finger protein AZF1	metal ion binding
QZy_TPB80_10.1	ZtIPO323_107430	glutathione s-transferase like protein	protein binding
QZy_TPB80_10.2	ZtIPO323_105720	putative P450 monooxygenase	oxidoreductase activity
QZy_TPB80_10.3	ZtIPO323_107270	signal recognition particle subunit SRP68-like	signal recognition particle
QZy_TPB80_10.4	ZtIPO323_108340	uncharacterized protein MYCGRDRAFT_96303	uncharacterized protein MYCGRDRAFT_96303
QZy_TPB80_11.1	ZtIPO323_113820	putative N-acetylglucosaminyltransferase subunit	GPI anchor biosynthesis
QZy_TPB80_11.2	ZtIPO323_111910	unnamed protein product	unnamed protein product
QZy_TPB80_11.3	ZtIPO323_115930	flavin reductase like domain-containing protein	oxidoreductase activity
QZy_TPB80_12.1	ZtIPO323_118520	R3H domain-containing protein 2-like	nucleic acid binding

QZy_TPB80_12.2	ZtIPO323_118660	Ca2+-modulated nonselective cation channel polycystin	Ca2+-modulated nonselective cation channel polycystin
QZy_TPB80_13.1	ZtIPO323_124860	uncharacterized protein MYCGRDRAFT_97455	uncharacterized protein MYCGRDRAFT_97455
QZy_TPB80_13.2	ZtIPO323_125750	probable chitin binding protein	carbohydrate metabolism
QZy_TPB80_13.3	ZtIPO323_123850	uncharacterized protein MYCGRDRAFT_97382	uncharacterized protein MYCGRDRAFT_97382

Table 56: This displays the annotated candidate genes found for PLACL_SLOPE. The QTL acronym, ZtIPO323_ID acronym extracted from Zymoseptoria tritici reference genome available browsers and gene function reported in MyGenomeBrowser and MycoCosm databases.

Topt	ZtIPO323_ID	MyGenomeBrowser	MycoCosm
QZs_PLACL_S_1.1	ZtIPO323_000800	Ca2+/calmodulin-dependent protein kinase	Ca2+/calmodulin-dependent protein kinase
QZs_PLACL_S_1.2	ZtIPO323_015720	TspO/MBR-related protein	The Mitochondrial Organic Anion Channel (MOAC) Family
QZs_PLACL_S_1.3	ZtIPO323_018880	ethanolamine kinase like protein	Ethanolamine kinase
QZs_PLACL_S_1.4	ZtIPO323_013730	plasma membrane fusion protein prm1	Plasma membrane fusion protein PRM1
QZs_PLACL_S_1.5	ZtIPO323_022700	fungal specific transcription factor domain containing protein	DNA-binding transcription factor activity
QZs_PLACL_S_1.6	ZtIPO323_021470	pumilio domain-containing protein	RNA binding
QZs_PLACL_S_2.1	ZtIPO323_024520	uncharacterized protein MYCGRDRAFT_90364	uncharacterized protein MYCGRDRAFT_90364
QZs_PLACL_S_2.2	ZtIPO323_027020	nuclear protein snf4	nuclear protein snf4
QZs_PLACL_S_2.3	ZtIPO323_026210	uncharacterized protein MYCGRDRAFT_90485	uncharacterized protein MYCGRDRAFT_90485
QZs_PLACL_S_2.4	ZtIPO323_032810	P-loop containing nucleoside triphosphate hydrolase protein	ATP binding
QZs_PLACL_S_2.5	ZtIPO323_025760	uncharacterized protein MYCGRDRAFT_90455	PPR repeat family
QZs_PLACL_S_3.1	ZtIPO323_042020	mfs transporter like protein	transmembrane transport
QZs_PLACL_S_3.2	ZtIPO323_038840	GroES-like protein	zinc ion binding
QZs_PLACL_S_3.3	ZtIPO323_038880	uncharacterized protein MYCGRDRAFT_91382	uncharacterized protein MYCGRDRAFT_91382
QZs_PLACL_S_3.4	ZtIPO323_042890	unnamed protein product	unnamed protein product
QZs_PLACL_S_3.5	ZtIPO323_048980	uncharacterized protein MYCGRDRAFT_23932	Haem-dependent oxidative N-demethylase
QZs_PLACL_S_3.6	ZtIPO323_042310	hypothetical protein TI39_contig4112g00038	hypothetical protein TI39_contig4112g00038
QZs_PLACL_S_3.7	ZtIPO323_038860	Aminopeptidase y	aminopeptidase Y
QZs_PLACL_S_3.8	ZtIPO323_044570	unnamed protein product	unnamed protein product
QZs_PLACL_S_3.9	ZtIPO323_044150	glycoside hydrolase family 13 protein	carbohydrate metabolic process
QZs_PLACL_S_4.1	ZtIPO323_051790	Ferric/cupric reductase transmembrane component 7	oxidoreductase activity
QZs_PLACL_S_4.2	ZtIPO323_058900	Pre-mRNA-splicing factor brr2	nucleic acid binding
QZs_PLACL_S_4.3	ZtIPO323_057430	YIF1-domain-containing protein	YIF1-domain-containing protein
QZs_PLACL_S_5.1	ZtIPO323_065950	triosephosphate isomerase like protein	metabolic process
QZs_PLACL_S_5.2	ZtIPO323_067340	RNA cytidine acetyltransferase	N-acetyltransferase activity
QZs_PLACL_S_5.3	ZtIPO323_065770	related to NUDIX domain protein	hydrolase activity
QZs_PLACL_S_6.1	ZtIPO323_076280	JmjC domain-containing histone demethylation protein 1	zinc ion binding
QZs_PLACL_S_6.2	ZtIPO323_076110	unnamed protein product	Choice-of-anchor B domain
QZs_PLACL_S_6.3	ZtIPO323_077680	probable E3 ubiquitin ligase	zinc ion binding
QZs_PLACL_S_8.1	ZtIPO323_091340	unnamed protein product	unnamed protein product
QZs_PLACL_S_8.2	ZtIPO323_090830	Tim10/DDP family zinc finger-domain-containing protein	Mitochondrial import inner membrane translocase
QZs_PLACL_S_9.1	ZtIPO323_102870	Phosphomevalonate kinase	ATP binding
QZs_PLACL_S_10	ZtIPO323_106910	nucleoporin NUP57-like	Nucleoporin complex subunit 54
QZs_PLACL_S_12.1	ZtIPO323_120340	general substrate transporter	transmembrane transporter activity
QZs_PLACL_S_12.2	ZtIPO323_120180	Mediator of RNA polymerase II transcription subunit 5	regulation of transcription by RNA polymerase II
QZs_PLACL_S_12.3	ZtIPO323_118490	SPX domain-containing protein	Protein involved in vacuolar polyphosphate accumulation
QZs_PLACL_S_12.4	ZtIPO323_121600	acetyl-CoA synthetase-like protein	catalytic activity

Table 57: This displays the annotated candidate genes found for PycLes_SLOPE. The QTL acronym, ZtIPO323_ID acronym extracted from Zymoseptoria tritici reference genome available browsers and gene function reported in MyGenomeBrowser and MycoCosm databases.

Topt	ZtIPO323_ID	MyGenomeBrowser	MycoCosm
QZy_PycLes_S1.1	ZtIPO323_008600	mediator of RNA polymerase II transcription subunit 15-like	mediator of RNA polymerase II transcription subunit 15-like
QZy_PycLes_S1.2	ZtIPO323_017930	DNA-directed RNA polymerase II subunit RPB3	DNA binding
QZy_PycLes_S1.3	ZtIPO323_020460	O-acetylhomoserine aminocarboxypropyltransferase	amino acid metabolic process
QZy_PycLes_S1.4	ZtIPO323_018390	Calcium-channel protein cch1	calcium ion binding
QZy_PycLes_S1.5	ZtIPO323_021190	inosine-uridine preferring nucleoside hydrolase like protein	uridine nucleosidase
QZy_PycLes_S1.6	ZtIPO323_008030	Linoleate 11-lipoxygenase	oxidoreductase activity
QZy_PycLes_S1.7	ZtIPO323_020130	DNA replication ATP-dependent helicase/nuclease dna2	DNA replication factor Dna2
QZy_PycLes_S1.8	ZtIPO323_017280	iron hydrogenase	Iron only hydrogenase large subunit
QZy_PycLes_S2.1	ZtIPO323_028480	DnaJ-domain-containing protein	heat shock protein binding
QZy_PycLes_S2.2	ZtIPO323_034130	telomere-binding alpha subunit central domain-containing protein	chromosome, telomeric region
QZy_PycLes_S3.1	ZtIPO323_037620	putative udp-glucose dehydrogenase udp-mannac protein	putative udp-glucose dehydrogenase udp-mannac protein
QZy_PycLes_S4.1	ZtIPO323_053370	regulator of gluconeogenesis Rmd5 like protein	protein binding
QZy_PycLes_S4.2	ZtIPO323_052700	uncharacterized protein MYCGRDRAFT_109000	SUR7/Pall family
QZy_PycLes_S4.3	ZtIPO323_058950	unnamed protein product	unnamed protein product
QZy_PycLes_S4.4	ZtIPO323_054780	phd finger domain-containing protein	zinc ion binding
QZy_PycLes_S5	ZtIPO323_062140	ankyrin repeat protein	metal ion transmembrane transporter activity
QZy_PycLes_S6	ZtIPO323_074900	unnamed protein product	unnamed protein product
QZy_PycLes_S7	ZtIPO323_084710	Diacylglycerol O-acyltransferase 2A	acyltransferase activity
QZy_PycLes_S8.1	ZtIPO323_089030	Striatin Pro11	protein binding
QZy_PycLes_S8.2	ZtIPO323_095440	Phenylalanyl-tRNA synthetase	RNA binding
QZy_PycLes_S10.1	ZtIPO323_104330	related to COQ2-para-hydroxybenzoate--polyprenyltransferase	Mitochondrial calcium uniporter
QZy_PycLes_S10.2	ZtIPO323_104910	GTPase-activating protein gyp7	GTPase activator activity
QZy_PycLes_S12	ZtIPO323_116360	Zn2/Cys6 DNA-binding protein	Fungal specific transcription factor domain
QZy_PycLes_S13	ZtIPO323_122330	complex i intermediate-associated protein 3	Uncharacterized conserved protein

4.4 Discussion

A panel of 238 isolates of *Zymoseptoria tritici* sampled from 8 different European countries, diversified in terms of climate and host conditions were genetically and phenotypically characterized to gain understanding about the genetic factors underlying thermal adaptation. Local score approach allowed to increase massively GWAS resolution, thereby detecting QTLs with medium-minor effect for the investigated quantitative traits. Additionally, the strong LD decay, R^2 equal to 0.2 and 0.1 were reached before 1 Kbp, was leveraged to immediately target the candidate genes within the detected QTLs Lindley region. It has to be specified that for this association study only the first 13 chromosome, being part of the core-set were considered whereas the remaining 8, being part dispensable set were discarded due to their high instability and variability among single isolates (Goodwin et al., 2011).

The thermal performance traits for each isolate, previously determined by Boixel et al. (2022), Topt and TPB80 were analyzed in order to find possible genetic determinants underlying thermal adaptation and responses. The panel was designed to house isolate from geographic extremely diversified in term of environmental conditions and regimes as previously suggested by (Boixel et al., 2018, 2022 and Feurtey et al., 2023). It has been reported in several studies that Zymoseptoria tritici pathogenicity is strongly affected and adapted to the local conditions that they encounter in their area in terms of host and climate conditions. However, following phenotyping comparison

among and within the geographic populations, large range and variability was observed more within the single geographic countries then among the single comparison. Indeed, except for the population sampled in Israel, all the other geographic population approximately stood at the same level of population average. The population structure subdivision resulted from Admixture analysis evidenced a clear subdivision of the panel into 4 subpopulations representative of geographic area clearly distant from each other, namely, East-Europe (Q4), West -Europe (Q3), North-Africa (Q2) and Mediterranean area (Q1). The phenotypic performance comparison among subpopulation clusters showed better differences among isolates for the traits. Q1, representative of Israel population entirely, showed an average phenotypic value for Topt and TPB80 above the population average and tending to the maxium, and this is in compliance with the typical regime of that area. Q3 was the largest cluster including entirely isolates from 3 subpopulations (France, Ireland and Denmark) plus a few individuals from Latvia and other geographic populations to a lesser extent. Q3 showed the largest range as expected, including individuals at both ends and stood at the population level overall. Q2 was represented entirely by isolates from Tunisia which stood above the population average for Topt in compliance with the temperature regime of that area of origin, whereas stood exactly at the population level for TPB80. Q4 represented entirely East-European countries (Russia, Kazakhstan and Latvia to some extent) and with the exception of a few isolates from Kazakhstan, stand at the same level of population average, in compliance with a cooler thermal regime characterizing those areas. The "Kazakh" population is the one showing the largest range for both Topt and TPB80. The high variability in thermal growth responses observed in individual wheat fields across different climate and temperature regimes highlights the considerable genetic diversity present within field populations of Zymoseptoria tritici (McDonald et al., 2022). This remarkable phenotypic and genotypic variability plays a crucial role in ensuring the persistence of the pathogen in wheat growing areas worldwide. (Cohen, Pfeiffer, & Francis, 2018). However, it is worth mentioning that localized temperature variations experienced during a single growing season can further influence pathogen behavior, with studies indicating that fluctuations within the wheat canopy and even among individual leaves (Chelle, 2005; Bernard et al., 2013) can significantly impact Z. tritici. Large variability and significant differences were also observed for the plastic response phenotypes (PLACL_SLOPE and PycLes_SLOPE) and temperature related aggressivity traits (T18_PLACL, T20_PLACL, T22_PLACL, T18_PycLes, T20_PycLes, T22_PycLes). The contrasting trend observed between PLACL and PycLes considering the three temperature regimes, suggest a plausible significant influence of temperature on the trade-off between necrotic area formation and pycnidia development during the hemi-biotrophic phase of *Zymoseptoria tritici*. This contrasting phenotypic pattern is also confirmed from the slope coefficient comparisons referring to the plastic response phenotypes (PLACL_SLOPE and PycLES_SLOPE). Indeed, by considering the absolute coefficients obtained from RRMM, all isolates carry a negative slope coefficient indicating a progressive decrease of PLACL symptoms as the temperature increases. However, the population structure effect is not significant at all for PLACL_SLOPE and no statistically significant differences were observed among geographic population and the 4 subpopulation clusters.

As for PycLes_SLOPE, except for some individuals from Tunisia and a few from other subpopulations, all the isolates carry a positive slope coefficient, suggesting a positive influence of temperature on Pycnidia development. Unlike PLACL_SLOPE, PycLes_Slope evidence to be a strongly structured traits, with strong differences observed among the geographic populations and subpopulations. This possible temperature-related trade-off between necrotic area formation and pycnidia development should be investigated further, as it could be potentially leveraged to design a targeted disease management strategy that incorporates the thermal adaptation of local *Zymoseptoria tritici* isolates in specific wheat-growing areas. By comprehending the genetic and phenotypic variations among isolates, it would be possible to develop localized management practices that account for the thermal profiles and adaptive traits of *Zymoseptoria tritici*, ultimately leading to improved wheat disease resistance and crop yield. Such strategies may entail the cultivation of resistant wheat varieties tailored to local thermal conditions or the timing of fungicide applications

optimized for peak disease susceptibility as suggested by studies pointing out the importance of integrating host-pathogen-environment interactions in plant disease management (Newlands, N. K., 2018).Furthermore, utilizing predictive models that take into account climatic changes can help in identifying vulnerable periods for disease outbreaks, thereby leading wheat growers to a more efficient disease management against Zymoseptoria tritici infections (Yang, L. N et al., 2023).
Limited number of association studies are document in the literature for *Zymoseptoria tritici* thermal adaptation traits and plastic response phenotypes. However, this topic has been investigated intensely lately (Minana-Posada, S et al., 2024; Stapley, J. et al., 2024; Feurtey et al., 2023. Association analys empowered with Local score approach revealed lots of significant regions underlying the investigated traits.
None of the genes annotated in this association study have been documented by Minana-Posada, S et al., 2024 and Stapley, J. et al., 2024 but many showed similar or identical function. ZtIPO323_020880, detected by Stapley, J. et al., 2024, is a gene underlying GroES-like superfamily and a gene with a similar function, ZtIPO323_038840, was identified in *QZs_PLACL_S_3.2*. A Protein kinase domain, ZtIPO323_000270, was found in *QZy_TPB80_1.7* and also detected by Stapley, J. et al., 2024, with two genes ZtIPO323_020900 and ZtIPO323_004450. Stapley, J. et al., 2024 also found A WD40/YVTN repeat-like-containing domain superfamily, ZtIPO323_005250, that was found in this study in *QZy_TPB80_6.4*, ZtIPO323_077330. Two Cytochrome P450 with oxidoreductase activity were found in ZtIPO323_007110 and ZtIPO323_105720, respectively two *QTLs*, *QZs_Topt_1.5* and *QZy_TPB80_10.2* and detected by Stapley, J. et al., 2024 in ZtIPO323_044730. Stapley, J. et al., 2024 also documented an involvement of a Zinc finger, C2H2 type, ZtIPO323_120430, in thermal response and adaptation of Zymoseptoria tritici and, a gene with the protein type was also found in this study, ZtIPO323_092650, found in *QZy_TPB80_8.6*. Furthermore, other annotated genes with a Zinc finger protein domain were found in *QZy_TPB80_8.6*, *QZy_TPB80_7.1*, *QZs_PLACL_S_8.2*, *QZy_PycLes_S4.4*. Minana-Posada, S et al., 2024 illustrated a list of candidate genes directly involved in the thermal response in *Zymoseptoria tritici* and genes with similar function were detected in this study. Like reported in Stapley, J. et al., 2024 a C2H2-type zinc-finger was found in ZtIPO323_092650. Both a nuclear protein snf4 and cAMP PKA (cAMP PKAdenosine monophosphate-protein kinase A) were found in ZtIPO323_027020, ZtIPO323_069170 and ZtIPO323_121600. Chaperone-like heat shock proteins are important proteins involved in temperature stress response by favouring morphological changes and stabilization of other proteins (Masser et al., 2019; Wu et al., 2016). A Chaperone-like heat shock protein was found in ZtIPO323_028480 and detected in *QZy_PycLes_S2.1*. Additionally, many genes have an uncharacterized protein product and should be investigated further. In conclusion, this association study was instrumental in detecting several regions and identify genes underlying thermal responses. Many genes have been compared with other genes with similar/identical functions identified by other recent association studies. A gene oncology (GO) analysis would allow to gain extensive insight into the annotated genes identified in this study.

4.5 Conclusion chapter IV

A panel of 238 Zymoseptoria tritici isolates sampled in equal number from 8 geographic countries representative of heterogenous wheat growing areas, in terms of climate and host conditions, was genetically and phenotypically characterized for thermal adaptation traits such as optimal temperature (Topt), temperature performance breadth (TPB80) and two plastic response phenotypes to temperature deriving from a pathogenicity assay at seedling stage on a selected host, slope coefficient for the percentage of the leaf surface covered by lesions (PLACL) and pycnidia per square centimeter of lesion leaf area (PycLes). Different rates of variability were observed among and within the single geographic countries and subpopulations for the four traits, suggesting a strong effect of temperature and highlighting the considerable genetic diversity present within field populations of *Zymoseptoria tritici*. Local Score approach increased GWAS resolution and revealed several regions underlying the

investigated traits. Many genes with diversified functions were found and a gene oncology analysis should be conducted to gain a better understanding of the gene function related to the four investigated traits. In conclusion, this study highlights the potential benefits of investigating variability in environmental adaptation traits in a panel of pathogenic fungi isolates. These insights could be used to outline localized management practices that incorporates the thermal adaptation of local *Zymoseptoria tritici* isolates in specific wheat-growing areas.

5 Conclusions and future perspectives

In the conclusive chapter of this thesis, the key discoveries and final assumptions from each chapter are discussed, highlighting their contribution to the understanding of disease resistance and environmental adaptation in durum wheat and *Zymoseptoria tritici*. The thesis's first chapter highlights multi-year and multi-environmental specific loci underlying resistance to Yellow Rust (*Puccinia striiformis*) in a highly diversified panel of durum wheat landraces. These loci, supported by gene projection and haplotype analysis, represent new valuable genetic resources that can be integrated into future breeding programs to obtain resistant wheat cultivars. These findings allow to trace back the origin of the resistant and susceptible haplotypes within the single subpopulations as well as obtaining information about the frequency across the panel. These resistant loci may be used to design diagnostic KASP primers to be used for Marker-Assisted-Breeding (MAB). Similarly, in the second chapter, GWAS was used to detect regions linked to *Septoria tritici blotch* (*Stb*) resistance, supported by meta-QTL analyses that revealed overlaps with previously documented and projected *Stb* resistance loci. These findings empower and outline the benefits for using landraces as a valuable gene pool for identifying resistance alleles against key fungal pathogens, thereby providing robust and valid targets for future resistance breeding efforts and disease management strategies. The third chapter shifts focus to the pathogen side and illustrates a GWAS conducted on a highly diversified panel of *Zymoseptoria tritici* isolates representative of 8 Euro-Mediterranean countries with heterogeneous climate and host conditions that revealed critical pathogenicity and thermal adaptation factors. This study underscores the adaptability of *Zymoseptoria tritici* to different thermal regimes (temperatures), highlighting the influence of environmental variability on pathogen behavioural shape and therefore, affecting crop resistance strategies. Collectively, these findings emphasize the importance of investigating genetic variability in both host and pathogen. These findings suggest an integrative approach where crop resistance and pathogen adaptation factors are addressed together, offering a more sustainable strategy for disease management that aligns with Green Deal goals by mitigating and reducing fungicides usage. Beyond the specific findings, this thesis emphasizes GWAS as an effective tool for detecting genetic regions linked to target traits, validating its broad applicability for resistance and stress adaptation studies. The GWAS results across all chapters confirm that this widely used method is applicable not only for disease resistance detection but also for targeted adaptation traits to environmental stresses. Furthermore, this thesis affirms that GWAS can not only be applied for crops but also their corresponding pathogenic fungi. Ultimately, by combining genetic insights from wheat and its pathogens, this work aims at breeding strategies that integrate local disease management based on resistance loci and thermal adaptability, contributing to more resilient, environmentally sustainable cropping systems and therefore, lessening the agricultural practices that show strong dependency on chemical disease control measures.

6 Contributions

This work involved the contribution of several UNIBO collaborators and several external partners in the research activities, both Italian and foreigners (the entire list is reported below). However, The UNIBO research team oversaw and was actively involved in all steps of the projects. However,

Thanks to involvement and support of the external partners, all the activities have been completed brilliantly:

F. de Sario[1], Chunyi Liu[1], F. Ntakirutimana[2], A.L. Boixel[2], E. Mazzucotelli[4], N. Lapalu[2], A. Prodi[1], J. Novi[1], M. Bozzoli[1], M. Campana[1], C. Forestan[1], F. Desiderio[4], S. Stefanelli[1], C. Invernizzi[3], P. Viola[3], F. Oliveri[3], M. Delanoue[2], F. Suffert[2], R. Tuberosa[1], T. Marcel[2], M. Maccaferri[1]

Conception of work and project supervision: R. Tuberosa, M. Maccaferri, T.Marcel, F. de Sario, E. Mazzucotelli.

Field management and data collection UNIBO: F.de Sario[1], Chunyi Liu[1] ,A. Prodi[1], J. Novi[1], M. Campana[1], M. Bozzoli[1], P. Viola[3], C. Invernizzi[3], F. Oliveri[3], S. Stefanelli[1], E. Mazzucotelli[4], F. Desiderio[4].

Pathogenicty assay design and characterization of *Zymoseptoria tritici* panel: F. de Sario[1], A.L. Boixel[2], F. Ntakirutimana[2], M. Delanoue[2]

Bionformatic analysis, data curation and GWAS: F.de Sario[1], Chunyi Liu[1] , N. Lapalu[2], C. Forestan[1], J. Novi[1], M. Bozzoli[1], M. Campana[1], F. De Sario[1], F. Desiderio[4].

Affiliations:

- [1]Department of Agricultural and Food Sciences, University of Bologna
- [2]Université Paris-Saclay, INRAE, UR BIOGER, Palaiseau, France
- [3]Apsovsementi S.p.A. Strada Torremenapace, 40, 27058 Voghera PV
- [4]CREA—Research Centre for Genomics and Bioinformatics, Fiorenzuola d'Arda, Italy,

7 References

Adhikari, T. B., Yang, X., Cavaletto, J. R., Hu, X., Buechley, G., Ohm, H. W., ... & Goodwin, S. B. (2004). Molecular mapping of Stb1, a potentially durable gene for resistance to septoria tritici blotch in wheat. Theoretical and Applied Genetics, 109, 944-953.

Adhikari, T. B., Cavaletto, J. R., Dubcovsky, J., Gieco, J. O., Schlatter, A. R., & Goodwin, S. B. (2004). Molecular mapping of the Stb4 gene for resistance to Septoria tritici blotch in wheat. Phytopathology, 94(11), 1198-1206.

Adhikari, T. B., Wallwork, H., & Goodwin, S. B. (2004). Microsatellite markers linked to the Stb2 and Stb3 genes for resistance to Septoria tritici blotch in wheat. Crop Science, 44(4), 1403-1411.

Alemu SK, Huluka AB, Tesfaye K,Haileselassie T, Uauy C (2021) Genome-wide association mapping identifies yellow rust resistance loci in Ethiopian durum wheat,germplasm. PLoS ONE 16(5): e0243675. https:// doi.org/10.1371/journal.pone.0243675

Allen, A.M., Winfield, M.O., Burridge, A.J., Downie, R.C., Benbow, H.R., Barker, G.L., Wilkinson, P.A. et al. (2017) Characterization of a Wheat Breeders' Array suitable for high-throughput SNP genotyping of global accessions of hexaploid bread wheat (Triticum aestivum). Plant Biotechnol. J. 15, 390–401.

Amezrou, R., Audéon, C., Compain, J., Gélisse, S., Ducasse, A., Saintenac, C., ... & Marcel, T. C. (2023). A secreted protease-like protein in Zymoseptoria tritici is responsible for avirulence on Stb9 resistance gene in wheat. *PLoS Pathogens*, *19*(5), e1011376.

Amezrou, R., Ducasse, A., Compain, J., Lapalu, N., Pitarch, A., Dupont, L., ... & Marcel, T. C. (2022). Whole-genome sequencing reveals diverse mechanisms underlying quantitative pathogenicity and host adaptation in a fungal plant pathogen. *bioRxiv*, 2022-12.

Andrew D. Yates, James Allen, Ridwan M. Amode, Andrey G. Azov, Matthieu Barba, Andrés Becerra, Jyothish Bhai, Lahcen I. Campbell, Manuel Carbajo Martinez, Marc Chakiachvili, Kapeel Chougule, Mikkel Christensen, Bruno Contreras-Moreira, Alayne Cuzick, Luca Da Rin Fioretto, Paul Davis, Nishadi H. De Silva, Stavros Diamantakis, Sarah Dyer, Justin Elser, Carla V. Filippi, Astrid Gall, Dionysios Grigoriadis, Cristina Guijarro-Clarke, Parul Gupta, Kim E. Hammond-Kosack, Kevin L. Howe, Pankaj Jaiswal, Vinay Kaikala, Vivek Kumar, Sunita Kumari, Nick Langridge, Tuan Le, Manuel Luypaert, Gareth L. Maslen, Thomas Maurel, Benjamin Moore, Matthieu Muffato, Aleena Mushtaq, Guy Naamati, Sushma Naithani, Andrew Olson, Anne Parker, Michael Paulini, Helder Pedro, Emily Perry, Justin Preece, Mark Quinton-Tulloch, Faye Rodgers, Marc Rosello, Magali Ruffier, James Seager, Vasily Sitnik, Michal Szpak, John Tate, Marcela K. Tello-Ruiz, Stephen J. Trevanion, Martin Urban, Doreen Ware, Sharon Wei, Gary Williams, Andrea Winterbottom, Magdalena Zarowiecki, Robert D. Finn and Paul Flicek. Ensembl Genomes 2022: an expanding genome resource for non-vertebrates. Nucleic Acids Research 2022 https://doi.org/10.1093/nar/gkab1007

Anilkumar, C., Sunitha, N.C., Harikrishna et al. Advances in integrated genomic selection for rapid genetic gain in crop improvement: a review. Planta 256, 87 (2022). https://doi.org/10.1007/s00425-022-03996-y

Aoun M, Rouse MN, Kolmer JA, Kumar A and Elias EM (2021) Genome-Wide Association Studies Reveal All-Stage Rust Resistance Loci in Elite Durum Wheat Genotypes.Front. Plant Sci. 12:640739.doi: 10.3389/fpls.2021.640739

Ardlie KG, Kruglyak L, Seielstad M. Patterns of linkage disequilibrium in the human genome. Nat Rev Genet. 2002 Apr;3(4):299-309. doi: 10.1038/nrg777. Erratum in: Nat Rev Genet 2002 Jul;3(7):566. PMID: 11967554.

Arnold, P. A., Kruuk, L. E., & Nicotra, A. B. (2019). How to analyse plant phenotypic plasticity in response to a changing climate. *New Phytologist*, *222*(3), 1235-1241.

Arraiano, L. S., & Brown, J. K. (2017). Sources of resistance and susceptibility to Septoria tritici blotch of wheat. Molecular Plant Pathology, 18(2), 276-292.

Arruda, M.P., Lipka, A.E., Brown, P.J., Krill, A.M., Thurber, C., Brown-Guedira, G., Dong, Y. et al. (2016) Comparing genomic selection and marker-assisted selection for Fusarium head blight resistance in wheat (Triticum aestivum L.). Mol. Breed. 36, 84.

A. Kombrink, A. Sanchez-Vallet, B.P.H.J. Thomma The role of chitin detection in plant-pathogen interactions Microbes Infect., 13 (2011), pp. 1168-1176

A Mundt, Christopher C. (2018). Pyramiding for Resistance Durability: Theory and Practice. https://apsjournals.apsnet.org/doi/abs/10.1094/PHYTO-12-17-0426-RVW

Akhunov, E.D., Akhunova, A.R. & Dvořák, J. BAC libraries of Triticum urartu, Aegilops speltoides and Ae. tauschii, the diploid ancestors of polyploid wheat. Theor Appl Genet 111, 1617–1622 (2005). https://doi.org/10.1007/s00122-005-0093-1

Ameye, M.; Allmann, S.; Verwaeren, J., et al. Green Leaf Volatile Production by Plants: A Meta-analysis. N. Phytol. 2018, 220 (3), 666683. Available from: https://doi.org/10.1111/nph.14671

Athiyannan N, Abrouk M, Boshoff WHP, Cauet S, Rodde N, Kudrna D, Mohammed N, Bettgenhaeuser J, Botha KS, Derman SS, Wing RA, Prins R, Krattinger SG. Long-read genome sequencing of bread wheat facilitates disease resistance gene cloning. Nat Genet. 2022 Mar;54(3):227-231. doi: 10.1038/s41588-022-01022-1. Epub 2022 Mar 14. PMID: 35288708; PMCID: PMC8920886.

Autrique, E., Nachit, M. M., Monneveux, P., Tanksley, S. D., and Sorrells, M. E. (1996). Genetic diversity in durum wheat based on RFLPs, morphophysiological traits, and coefficient of parentage. Crop Sci. 36, 735–742. doi: 10.2135/cropsci1996.0011183X003600030036x

Aziz, A.; Poinssot, B.; Daire, X.; Adrian, M.; Be´zier, A.; Lambert, B., et al. Laminarin Elicits Defense Responses in Grapevine and Induces Protection Against Botrytis cinerea and Plasmopara viticola. Mol. Plant-Microbe Interact. 2003, 16 (12), 11181128. Available from: https://doi.org/10.1094/MPMI.2003.16.12.1118.

Balagué-Dobón, L., Cáceres, A. and González, J.R. (2022) Fully exploiting SNP arrays: a systematic review on the tools to extract underlying genomic structure. Brief. Bioinform. 23, bbac043.

Ballini, E., Tavaud, M., Ducasse, A., Sanchez, D., Paux, E., Kitt, J., ... & Morel, J. B. (2020). Genome wide association mapping for resistance to multiple fungal pathogens in a panel issued from a broad composite cross-population of tetraploid wheat Triticum turgidum. Euphytica, 216(6), 92.

Bandillo N, Raghavan C, Muyco PA, Sevilla MAL, Lobina IT et al (2013) Multi-parent advanced generation inter-cross (MAGIC) populations in rice: progress and potential for genetics research and breeding. Rice 6:11

Bansal, U. K., Kazi, A. G., Singh, B., Hare, R. A., and Bariana, H. S. 2014a. Mapping of durable stripe rust resistance in a durum wheat cultivar Wollaroi. Mol. Breed. 33:51-59. https://doi.org/10.1007/s11032-013-9933-x Crossref

Bansal, U. K., Forrest, K. L., Hayden, M. J., Miah, H., Singh, D., & Bariana, H. S. (2011). Characterisation of a new stripe rust resistance gene Yr47 and its genetic association with the leaf rust resistance gene Lr52. Theoretical and applied genetics, 122, 1461-1466.

Bansal, U. K., Hayden, M. J., Keller, B., Wellings, C. R., Park, R. F., & Bariana, H. S. (2009). Relationship between wheat rust resistance genes Yr1 and Sr48 and a microsatellite marker. Plant Pathology, 58(6), 1039-1043.

Bao JS, Wu YR, Hu B, Wu P, Cui HR, Shu QY, 2002. QTL for rice grain quality based on a DH population derived from parents with similar apparent amylose content. Euphytica, 128: 317-324.

Bariana, H., Kant, L., Qureshi, N., Forrest, K., Miah, H., & Bansal, U. (2022). Identification and characterisation of stripe rust resistance genes Yr66 and Yr67 in wheat cultivar VL Gehun 892. Agronomy, 12(2), 318.

Bariana, H. S., Parry, N., Barclay, I. R., Loughman, R., McLean, R. J., Shankar, M., ... & Francki, M. (2006). Identification and characterization of stripe rust resistance gene Yr34 in common wheat. Theoretical and Applied Genetics, 112, 1143-1148.

Bariana, H. S., and R. A. McIntosh. "Cytogenetic studies in wheat. XV. Location of rust resistance genes in VPM1 and their genetic linkage with other disease resistance genes in chromosome 2A." Genome 36.3 (1993): 476-482.

Basnet, B. R., Singh, R. P., Herrera-Foessel, S. A., Ibrahim, A. M. H., Huerta-Espino, J., Calvo-Salazar, V., & Rudd, J. C. (2013). Genetic analysis of adult plant resistance to yellow rust and leaf rust in common spring wheat Quaiu 3. Plant Disease, 97(6), 728-736.

Bassil, N.V., Davis, T.M., Zhang, H., Ficklin, S., Mittmann, M., Webster, T., Mahoney, L. et al. (2015) Development and preliminary evaluation of a 90 K Axiom® SNP array for the allo-octoploid cultivated strawberry Fragaria × ananassa. BMC Genomics, 16, 155.

Baumgartner, I. O., Patocchi, A., Frey, J. E., Peil, A., and Kellerhals, M. (2015). Breeding elite lines of apple carrying pyramided homozygous resistance genes against apple scab and resistance against powdery mildew and fire blight. Plant Mol. Biol. Rep. 33, 1573–1583. doi: 10.1007/s11105-015-0858-x

Bebber, D. P., Ramotowski, M. A., & Gurr, S. J. (2013). Crop pests and pathogens move polewards in a warming world. *Nature climate change*, *3*(11), 985-988.

Bhaduri, A., Ringler, C., Dombrowski, I., Mohtar, R., & Scheumann, W. (2015). Sustainability in the water–energy–food nexus. Water International, 40(5-6), 723-732.

Bhatia S. 2015. Application of plant biotechnology. In: Modern applications of plant biotechnology in pharmaceutical sciences. Amsterdam: Elsevier Inc. 157-207

Blanco A, Giorgi B, Perrino R, Simeone R, 1990. Risorse genetiche e miglioramento della qualità del frumento duro. Agricoltura Ricerca, 114: 41-58.

Blasi, Barbara, Hakim Tafer, Donatella Tesei, and Katja Sterflinger. 2015. “From Glacier to Sauna: RNA-Seq of the Human Pathogen Black Fungus Exophiala dermatitidis under Varying Temperature Conditions Exhibits Common and Novel Fungal Response.” PLOS ONE 10 (6): e0127103. https://doi.org/10.1371/journal.pone.0127103.

Boixel, A. L., Chelle, M., & Suffert, F. (2022). Patterns of thermal adaptation in a globally distributed plant pathogen: local diversity and plasticity reveal two-tier dynamics. *Ecology and Evolution*, *12*(1), e8515.

Boixel, A. L., Delestre, G., Legeay, J., Chelle, M., & Suffert, F. (2019). Phenotyping thermal responses of yeasts and yeast-like microorganisms at the individual and population levels: proof-of-concept, development and application of an experimental framework to a plant pathogen. *Microbial ecology*, *78*, 42-56.

Bonhomme, M., Fariello, M. I., Navier, H., Hajri, A., Badis, Y., Miteul, H., ... & Pilet-Nayel, M. L. (2019). A local score approach improves GWAS resolution and detects minor QTL: application to

Medicago truncatula quantitative disease resistance to multiple Aphanomyces euteiches isolates. *Heredity*, *123*(4), 517-531.

Börner, A., et al. (2018). Genomic selection in wheat: an overview of potential applications. Plant Breeding, 137(1), 91-104. https://doi.org/10.1111/pbr.12577

Bozzini A. (1989). "Esperienze sul miglioramento genetico del frumento duro, il caso italiano, il grano duro e la qualità," in NOMISMA Atti Conv. Grano duro (Roma:), 46–66.

Börner, A., Röder, M. S., Unger, O., & Meinel, A. (2000). The detection and molecular mapping of a major gene for non-specific adult-plant disease resistance against stripe rust (Puccinia striiformis) in wheat. Theoretical and Applied Genetics, 100, 1095-1099.

Bourke, P.M., van Geest, G., Voorrips, R.E., Jansen, J., Kranenburg, T., Shahin, A., Visser, R.G.F. et al. (2018) polymapR -linkage analysis and genetic map construction from F1 populations of outcrossing polyploids. Bioinformatics, 34, 3496–3502.

Bradbury PJ, Zhang Z, Kroon DE, Casstevens TM, Ramdoss Y, Buckler ES. TASSEL: software for association mapping of complex traits in diverse samples. Bioinformatics. 2007 Oct 1;23(19):2633-5. doi: 10.1093/bioinformatics/btm308. Epub 2007 Jun 22. PMID: 17586829.

Breseghello, Flavio, and Mark E. Sorrells. "Association mapping of kernel size and milling quality in wheat (Triticum aestivum L.) cultivars." Genetics 172.2 (2006): 1165-1177.

Brown, J. K., Chartrain, L., Lasserre-Zuber, P., & Saintenac, C. (2015). Genetics of resistance to Zymoseptoria tritici and applications to wheat breeding. Fungal Genetics and Biology, 79, 33-41.

Brown, J. K. M. 2015. Durable resistance of crops to disease: A Darwinian perspective. Annu. Rev. Phytopathol. 53:513-539. https://doi.org/10.1146/annurev-phyto-102313-045914

B L Browning, Y Zhou, and S R Browning (2018). A one-penny imputed genome from next generation reference panels. Am J Hum Genet 103(3):338-348. doi:10.1016/j.ajhg.2018.07.015

Bruce, T. J.; Martin, J. L.; Pickett, J. A.; Pye, B. J.; Smart, L. E.; Wadhams, L. J. Cis-Jasmone Treatment Induces Resistance in Wheat Plants Against the Grain Aphid, Sitobion avenae (Fabricius) (Homoptera: Aphididae). Pest. Manage. Sci. 2003, 59 (9), 10311036. Available from: https://doi.org/10.1002/ps.730.

Burridge, A.J., Winfield, M., Przewieslik-Allen, A., Edwards, K.J., Siddique, I., Barral-Arca, R., Griffiths, S., Cheng, S., Huang, Z., Feng, C., Dreisigacker, S., Bentley, A.R., Brown-Guedira, G. and Barker, G.L. (2024), Development of a next generation SNP genotyping array for wheat. Plant Biotechnol. J, 22: 2235-2247. https://doi.org/10.1111/pbi.14341

Bouvet, L., Holdgate, S., James, L. et al. The evolving battle between yellow rust and wheat: implications for global food security. Theor Appl Genet 135, 741–753 (2022). https://doi.org/10.1007/s00122-021-03983-z

Bradshaw, A. D. (2006). Unravelling phenotypic plasticity–why should we bother?. *New Phytologist*, *170*(4), 644-648.

Cairns T, Meyer V. In silico prediction and characterization of secondary metabolite biosynthetic gene clusters in the wheat pathogen Zymoseptoria tritici. BMC Genomics. 2017 Aug 17;18(1):631. doi: 10.1186/s12864-017-3969-y. PMID: 28818040; PMCID: PMC5561558.

Calus, M. P., & Vandenplas, J. (2018). SNPrune: an efficient algorithm to prune large SNP array and sequence datasets based on high linkage disequilibrium. *Genetics Selection Evolution*, *50*(1), 1-11.

Camañes, G., Scalschi, L., Vicedo, B., González-Bosch, C. and García-Agustín, P. (2015), An untargeted global metabolomic analysis reveals the biochemical changes underlying basal resistance and priming in Solanum lycopersicum, and identifies 1-methyltryptophan as a metabolite involved in plant responses to Botrytis cinerea and Pseudomonas syringae. Plant J, 84: 125-139. https://doi.org/10.1111/tpj.12964

Cao, Q., Zhu, Z., Wu, J., Xu, X., Dong, Y., Bian, Y., ... & Hao, Y. (2024). Characterization of a 4.1 Mb inversion harboring the stripe rust resistance gene YR86 on wheat chromosome 2AL. The Crop Journal.

Casañas F, Simó J, Casals J, Prohens J. Toward an Evolved Concept of Landrace. Front Plant Sci. 2017;8:145. Published 2017 Feb 8. doi:10.3389/fpls.2017.00145

Castroagudín, V., et al. (2020). Climate change and its effect on plant pathology: An overview of current knowledge and future directions. Agricultural and Forest Meteorology, 291, 108087.

Cavanagh C, Morell M, Mackay I and Powell W, 2008. From mutations to MAGIC: resources for gene discovery, validation and delivery in crop plants. Curr. Opin. Plant Biol., 11: 215-21

Cecchini, N. M.; Steffes, K.; Schla¨ppi, M. R.; Gifford, A. N.; Greenberg, J. T. Arabidopsis AZI1 Family Proteins Mediate Signal Mobilization for Systemic Defence Priming. Nat. Commun. 2015, 6 (1), 7658. Available from: https://doi.org/10.1038/ncomms8658.

Challinor, A. J., Watson, J., Lobell, D. B., Howden, S. M., Smith, D. R., & Chhetri, N. (2014). A meta-analysis of crop yield under climate change and adaptation. Nature climate change, 4(4), 287-291.

Chandio, A. A., Ozdemir, D., & Jiang, Y. (2023). Modelling the impact of climate change and advanced agricultural technologies on grain output: Recent evidence from China. Ecological Modelling, 485, 110501.

Chang CC, Chow CC, Tellier LC, Vattikuti S, Purcell SM, Lee JJ. Second-generation PLINK: rising to the challenge of larger and richer datasets. Gigascience. 2015 Feb 25;4:7. doi: 10.1186/s13742-015-0047-8. PMID: 25722852; PMCID: PMC4342193.

Chakraborty, S., & Newton, A. C. (2011). Climate change impacts on pests and diseases in the context of food security. Food Security, 3(4), 63-70.

Chartrain, L., Sourdille, P., Bernard, M., & Brown, J. K. M. (2009). Identification and location of Stb9, a gene for resistance to septoria tritici blotch in wheat cultivars Courtot and Tonic. Plant Pathology, 58(3), 547-555.

Chartrain, L., Berry, S. T., & Brown, J. K. M. (2005). Resistance of wheat line Kavkaz-K4500 L. 6. A. 4 to Septoria tritici blotch controlled by isolate-specific resistance genes. Phytopathology, 95(6), 664-671.

Chartrain, L., Joaquim, P., Berry, S. T., Arraiano, L. S., Azanza, F., & Brown, J. K. M. (2005). Genetics of resistance to septoria tritici blotch in the Portuguese wheat breeding line TE 9111. Theoretical and Applied Genetics, 110, 1138-1144.

Chevin, L. M., & Hoffmann, A. A. (2017). Evolution of phenotypic plasticity in extreme environments. *Philosophical Transactions of the Royal Society B: Biological Sciences*, *372*(1723), 20160138.

Chevin, L. M., & Lande, R. (2011). Adaptation to marginal habitats by evolution of increased phenotypic plasticity. *Journal of evolutionary biology*, *24*(7), 1462-1476.

Chedli, R. B. H., Aouini, L., M'Barek, S. B., Bahri, B. A., Verstappen, E., Kema Gerrit, H. J., ... & Chaabane, H. (2022). Genetic diversity and population structure of Zymoseptoria tritici on bread wheat in Tunisia using SSR markers. European Journal of Plant Pathology, 163(2), 429-440.

Cheng, P., Xu, L.S., Wang, M.N. et al. Molecular mapping of genes Yr64 and Yr65 for stripe rust resistance in hexaploid derivatives of durum wheat accessions PI 331260 and PI 480016. Theor Appl Genet 127, 2267–2277 (2014). https://doi.org/10.1007/s00122-014-2378-8

Chen, X. High-temperature adult-plant resistance, key for sustainable control of stripe rust. American Journal of Plant Sciences (2013).

Chen, J. et al. Genome-wide identification of QTL conferring high-temperature adult-plant (HTAP) resistance to stripe rust (Puccinia striiformis f. sp. tritici) in wheat. Molecular Breeding 29, 791-800 (2012).

Chen, X. M. "Epidemiology and control of stripe rust [Puccinia striiformis f. sp. tritici] on wheat." Canadian Journal of Plant Pathology 27.3 (2005): 314-337.

Chen XM, Jones SS, Line RF (1995) Chromosomal location of genes for stripe rust resistance in spring wheat cultivars Compair, Fielder, Lee, and Lemhi and interactions of aneuploid wheats with races of Puccinia striiformis. Phytopathology 85:375–381

Cheng, P. E. N. G., & Chen, X. (2010). Molecular mapping of a gene for stripe rust resistance in spring wheat cultivar IDO377s. Theoretical and Applied Genetics, 121, 195-204.

Chhetri, M., Miah, H., Wong, D., Hayden, M., Bansal, U., & Bariana, H. (2023). Mapping of Stripe Rust Resistance Gene Yr72 in Two Common Wheat Landraces.

Chowdhary A, Kathuria S, Randhawa HS, Gaur SN, Klaassen CH, Meis JF. Isolation of multiple-triazole-resistant Aspergillus fumigatus strains carrying the TR/L98H mutations in the cyp51A gene in India. J Antimicrob Chemother. 2012 Feb;67(2):362-6. doi: 10.1093/jac/dkr443. Epub 2011 Oct 25. PMID: 22028200.

Cobo, N., Wanjugi, H., Lagudah, E. and Dubcovsky, J. (2019), A High-Resolution Map of Wheat QYr.ucw-1BL, an Adult Plant Stripe Rust Resistance Locus in the Same Chromosomal Region as Yr29. The Plant Genome, 12: 180055. https://doi.org/10.3835/plantgenome2018.08.0055

Cohen, J., Pfeiffer, K., & Francis, J. A. (2018). Warm Arctic episodes linked with increased frequency of extreme winter weather in the United States. *Nature communications*, *9*(1), 869.

Cohen, Y.; Vaknin, M.; Mauch-Mani, B. BABA-Induced Resistance: Milestones Along a 55-Year Journey. Phytoparasitica 2016, 44 (4), 513538. Available from: https://doi.org/10.1007/s12600-016-0546-x.

Covino, Roberto, Stephanie Ballweg, Claudius Stordeur, Jonas B. Michaelis, Kristina Puth, Florian Wernig, Amir Bahrami, Andreas M. Ernst, Gerhard Hummer, and Robert Ernst. 2016. "A Eukaryotic Sensor for Membrane Lipid Saturation." Molecular Cell 63 (1): 49–59. https://doi.org/10.1016/j.molcel.2016.05.015.

Cowling, S.G., 2006. Identification and Mapping of Host Resistance Genes to Septoria tritici Blotch of Wheat. Ph.D. thesis, University of Manitoba.

Croll, D., Zala, M., & McDonald, B. A. (2013). Breakage-fusion-bridge cycles and large insertions contribute to the rapid evolution of accessory chromosomes in a fungal pathogen. PLoS Genetics, 9(6), e1003567.

Crossa, J., et al. (2017). Genomic Selection in Plant Breeding: Methods, Models, and Applications. Nature Reviews Genetics, 18, 581–596. https://doi.org/10.1038/nrg.2017.69

Cuthbert, R. D. (2011). Molecular mapping of septoria tritici blotch resistance in hexaploid wheat (Triticum aestivum L.). University of Manitoba (Canada).

Dadkhodaie, N. A., Karaoglou, H., Wellings, C. R., & Park, R. F. (2011). Mapping genes Lr53 and Yr35 on the short arm of chromosome 6B of common wheat with microsatellite markers and studies of their association with Lr36. Theoretical and Applied Genetics, 122, 479-487.

Darvasi A, Soller M (1997) A simple method to calculate resolving power and confidence interval of QTL map location. Behav Genet 27:125–132

D.H. Alexander, J. Novembre, and K. Lange. Fast model-based estimation of ancestry in unrelated individuals. Genome Research, 19:1655–1664, 2009.

D. Couto, C. Zipfel Regulation of pattern recognition receptor signalling in plants. Nat. Rev. Immunol., 16 (2016), pp. 537-552

Darvasi A, Soller M, 1997. A simple method to calculate resolving power and confidence interval of QTL map location. Behavior Genetics, 27: 125-132.

David Guest, John Brown. 1997. Plant pathogens and plant diseases. Rockvale publications national library of Australia ISBN 1-86389-439. Page 263-260. Edited by J.F.Brown & H.J, Ogle

Desiderio F, Zarei L, Licciardello S, Cheghamirza K, Farshadfar E, Virzi N, Sciacca F, Bagnaresi P, Battaglia R, Guerra D, Palumbo M, Cattivelli L and Mazzucotelli E (2019) Genomic Regions From an Iranian Landrace Increase Kernel Size in Durum Wheat. Front. Plant Sci. 10:448. doi: 10.3389/fpls.2019.00448

de Vallavieille-Pope, C., Bahri, B., Leconte, M., Zurfluh, O., Belaid, Y., Maghrebi, E., ... & Bancal, M. O. (2018). Thermal generalist behaviour of invasive Puccinia striiformis f. sp. tritici strains under current and future climate conditions. *Plant Pathology*, *67*(6), 1307-1320.

De Vita, P., Nicosia, O. L. D., Nigro, F., Platani, C., Riefolo, C., Di Fonzo, N., et al. (2007). Breeding progress in morpho-physiological, agronomical and qualitative traits of durum wheat cultivars released in Italy during the 20th century. Europ. J. Agron. 26, 39–53. doi: 10.1016/j.eja.2006.08.009

Deutsch, C. A., Tewksbury, J. J., Tigchelaar, M., Battisti, D. S., Merrill, S. C., Huey, R. B., & Naylor, R. L. (2018). Increase in crop losses to insect pests in a warming climate. Science, 361(6405), 916-919.

Dong, Z., Hegarty, J. M., Zhang, J., Zhang, W., Chao, S., Chen, X., ... & Dubcovsky, J. (2017). Validation and characterization of a QTL for adult plant resistance to stripe rust on wheat chromosome arm 6BS (Yr78). Theoretical and Applied Genetics, 130, 2127-2137.

Dong, H.; Delaney, T. P.; Bauer, D. W.; Beer, S. V. Harpin Induces Disease Resistance in Arabidopsis Through the Systemic Acquired Resistance Pathway Mediated by Salicylic Acid and the NIM1 Gene. Plant J. 1999, 20 (2), 207215. Available from: https://doi.org/10.1046/j.1365-313x.1999.00595.x.

D'Amato (1989). The progress of Italian wheat production in the first half of the 20th century: the contribution of breeders. Agr. Med. 119 157–174.

Doerge RW, 2002. Multifactorial genetics: Mapping and analysis of quantitative trait loci in experimental populations. Nature Review Genetics, 3: 43-52.

Dostál, P., Fischer, M., & Prati, D. (2016). Phenotypic plasticity is a negative, though weak, predictor of the commonness of 105 grassland species. *Global Ecology and Biogeography*, *25*(4), 464-474.

Dracatos, P. M., Zhang, P., Park, R. F., McIntosh, R. A., & Wellings, C. R. (2016). Complementary resistance genes in wheat selection 'Avocet R'confer resistance to stripe rust. Theoretical and Applied Genetics, 129, 65-76.

Dvorak J, Akhunov ED, Akhunov AR, Deal KR, Luo MC, 2006. Molecular characterization of a diagnostic DNA marker for domesticated tetraploid wheat provides evidence for gene flow from wild tetraploid wheat to hexaploid wheat. Mol Biol Evol, 23: 1386-1396

Dormatey, Richard, Chao Sun, Kazim Ali, Jeffrey A. Coulter, Zhenzhen Bi, and Jiangping Bai. 2020. "Gene Pyramiding for Sustainable Crop Improvement against Biotic and Abiotic Stresses" Agronomy 10, no. 9: 1255. https://doi.org/10.3390/agronomy10091255

Duba, A., Goriewa-Duba, K., & Wachowska, U. (2018). A review of the interactions between wheat and wheat pathogens: Zymoseptoria tritici, Fusarium spp. and Parastagonospora nodorum. International journal of molecular sciences, 19(4), 1138.

Duncan, R. R., et al. (2018). A review of salt tolerance and waterlogging resistance in crops. The Crop Journal, 6(1), 1-10.

Eduard D. Akhunov, Andrew W. Goodyear, Shu Geng, et al. 2003. The Organization and Rate of Evolution of Wheat Genomes Are Correlated With Recombination Rates Along Chromosome Arms. Published in Advance April 14, 2003, doi:10.1101/gr.808603Genome Res. 2003. 13: 753-763

Edwards AO, Fridley BL, James KM, Sharma AK, Cunningham JM, et al. (2008) Correction: Evaluation of Clustering and Genotype Distribution for Replication in Genome Wide Association Studies: The Age-Related Eye Disease Study. PLOS ONE 3(12): 10.1371/annotation/34c41e76-e7dc-4a84-b1b7-c3f895207d9f.

El Hadrami, A.; Adam, L. R.; El Hadrami, I.; Daayf, F. Chitosan in Plant Protection. Mar. Drugs 2010, 8 (4), 968987. Available from: https://doi.org/10.3390/md8040968.

El-Orabey, W. M. (2018). Virulence of some Puccinia triticina races to the effective wheat leaf rust resistant genes Lr 9 and Lr 19 under Egyptian field conditions. Physiological and Molecular Plant Pathology, 102, 163–172. https://doi.org/10.1016/j.pmpp.2017.12.006

Ellis, J. G., Lagudah, E. S., Spielmeyer, W., and Dodds, P. N. (2014). The past, present and future of breeding rust resistant wheat. Front. Plant Sci. 5:641. doi: 10.3389/fpls.2014.00641

Eriksen, L., Afshari, F., Christiansen, M.J. et al. Yr32 for resistance to stripe (yellow) rust present in the wheat cultivar Carstens V. Theor Appl Genet 108, 567–575 (2004). https://doi.org/10.1007/s00122-003-1456-0

Eshraghi, L.; Anderson, J.; Aryamanesh, N.; Shearer, B.; McComb, J.; Hardy, G. E. S., et al. Phosphite Primed Defence Responses and Enhanced Expression of Defence Genes in Arabidopsis thaliana Infected With Phytophthora cinnamomi. Plant Pathol. 2011, 60 (6), 10861095. Available from: https://doi.org/10.1111/ j.1365-3059.2011.02471.x.

Eyal, Z. (1999). The Septoria tritici and Stagonospora nodorum blotch diseases of wheat. European journal of plant pathology, 105, 629-641.

F. Lin and X. M. Chen, "Genetics and Molecular Map-ping of Genes for Race-Specific All-Stage Resistance and Non-Race Specific High-Temperature Adult-Plant Resistance to Stripe Rust in Spring Wheat Cultivar Alpowa," Theoretical and Applied Genetics, Vol. 114, No. 7, 2007, pp. 1277-1287. doi:10.1007/s00122-007-0518-0

Fagundes, W. C., Haueisen, J., & Stukenbrock, E. H. (2020). Dissecting the biology of the fungal wheat pathogen Zymoseptoria tritici: a laboratory workflow. *Current Protocols in Microbiology*, *59*(1), e128.

Falconer DS, Mackay TFC, 1996. Introduction to quantitative genetics. 4th ed. Harlow, UK, Longman Group.

Fariello, M. I., Boitard, S., Mercier, S., Robelin, D., Faraut, T., Arnould, C., ... & SanCristobal, M. Local Score Based Method Applied On Pool-Sequenced Behavior-Divergent Lines Precisely Detected Selection Signatures Related To Autism In Quail.

Farmer, E. E.; Ryan, C. A.; Posthumus, M.; Woodcock, C. M.; Mohib, A.; Webster, B., et al. Interplant Communication: Airborne Methyl Jasmonate Induces Synthesis of Proteinase Inhibitors in Plant Leaves. Proc. Natl. Acad. Sci. U.S.A. 1990, 87 (19), 77137716. Available from: https://doi.org/10.1073/pnas.87.19.7713.

Feechan, A., Kocsis, M., Riaz, S., Zhang, W., Gadoury, D. M., Walker, M. A., et al. (2015). Strategies for RUN1 deployment using RUN2 and REN2 to manage grapevine powdery mildew informed by studies of race specificity. Phytopathology 105, 1104–1113. doi: 10.1094/phyto-09-14-0244-r

FAO. (2023). FAOSTAT Statistical Database. Food and Agriculture Organization of the United Nations. Retrieved from FAOSTAT

FAO (Food and Agriculture Organization of the United Nations). (2017). The Future of Food and Agriculture – Trends and Challenges.

Feng, J., Wang, M., See, D. R., Chao, S., Zheng, Y., & Chen, X. (2018). Characterization of novel gene Yr79 and four additional quantitative trait loci for all-stage and high-temperature adult-plant resistance to stripe rust in spring wheat PI 182103. Phytopathology, 108(6), 737-747.

Feng, J., Chen, G., Wei, Y., Liu, Y., Jiang, Q., Li, W., ... & Zheng, Y. (2014). Identification and genetic mapping of a recessive gene for resistance to stripe rust in wheat line LM168-1. Molecular breeding, 33, 601-609.

Ferguson, L. V., & Sinclair, B. J. (2020). Thermal variability and plasticity drive the outcome of a host-pathogen interaction. *The American Naturalist*, *195*(4), 603-615.

Ferjaoui, S., Aouini, L., Slimane, R. B., Ammar, K., Dreisigacker, S., Schouten, H. J., ... & Hamza, S. (2022). Deciphering resistance to Zymoseptoria tritici in the Tunisian durum wheat landrace accession 'Agili39'. BMC genomics, 23(1), 372.

Ferrari, S.; Savatin, D. V.; Sicilia, F.; Gramegna, G.; Cervone, F.; Lorenzo, G. De. Oligogalacturonides: Plant Damage-Associated Molecular Patterns and Regulators of Growth and Development. Front. Plant Sci. 2013, 4, 49. Available from: https://doi.org/10.3389/fpls.2013.00049.

Fei, W., Liu, Y. Biotrophic Fungal Pathogens: a Critical Overview. Appl Biochem Biotechnol 195, 1–16 (2023). https://doi.org/10.1007/s12010-022-04087-0

Feurtey, Alice, Cécile Lorrain, Megan C. McDonald, Andrew Milgate, Peter S. Solomon, Rachael Warren, Guido Puccetti, et al. 2023. "A Thousand-Genome Panel Retraces the Global Spread and Adaptation of a Major Fungal Crop Pathogen." Nature Communications 14 (1): 1059. https://doi.org/10.1038/s41467-023-36674-y.

Figueroa, M., Hammond-Kosack, K.E. and Solomon, P.S. (2018), A review of wheat diseases—a field perspective. Molecular Plant Pathology, 19: 1523-1536. https://doi.org/10.1111/mpp.12618

Figueroa, M., Upadhyaya, N.M., Sperschneider, J., Park, R.F., Szabo, L.J., Steffenson, B., Ellis, J.G. and Dodds, P.N. (2016) Changing the game: using integrative genomics to probe virulence mechanisms of the stem rust pathogen Puccinia graminis f. sp. tritici. Front. Plant Sci. 7, 205.

Firdissa E. Bokore , Yuefeng Ruan, Curt Mccartney, Ron E. Knox , Xiangyu Xei,Reem Aboukhaddour, Harpinder Randhawa, Karim Ammar, Brad Meyer,Richard D. Cuthbert, Samia Berraies, Ron Depauw and Pierre Fobert. High density genetic mapping of stripe rust resistance in a 'Strongfield' / 'Blackbird' durum wheat population. Firdissa E. Bokore et al., Canadian Journal of Plant Pathology. 43, S242-S255 (2021)

Foley, J.A.; Ramankutty, N.; Brauman, K.A.; Cassidy, E.S.; Gerber, J.S.; Johnston, M.; Mueller, N.D.; O'Connell, C.; Ray, D.K.; West, P.C.; et al. Solutions for a cultivated planet. Nature 2011, 478, 337–342.

Fones, H. and Gurr, S. (2015) The impact of Septoria tritici Blotch disease on wheat: an EU perspective. Fungal Genet. Biol. 79, 3–7.

Franceschetti, M., et al. Effectors of filamentous plant pathogens: commonalities amid diversity. Microbiol. Mol. Biol. Rev. 81, e00066-16 (2022). https://doi.org/10.1128/MMBR.00066-16

Friederike Bernsdorff, Anne-Christin Döring, Katrin Gruner, Stefan Schuck, Andrea Bräutigam, Jürgen Zeier, Pipecolic Acid Orchestrates Plant Systemic Acquired Resistance and Defense Priming via Salicylic Acid-Dependent and -Independent Pathways, The Plant Cell, Volume 28, Issue 1, January 2016, Pages 102–129, https://doi.org/10.1105/tpc.15.00496

Frost, C. J.; Mescher, M. C.; Carlson, J. E.; De Moraes, C. M. Plant Defense Priming Against Herbivores: Getting Ready for a Different Battle. Plant Physiol. 2008, 146 (3), 818824. Available from: https://doi.org/ 10.1104/pp.107.113027

G. Kogel, B. Beissmann, H. Reisener, K. Kogel

Single glycoprotein from Puccinia graminis f. Sp. Tritici cell-walls elicits the hypersensitive lignification response in wheat. Physiol. Mol. Biol. Plants, 33 (1988), pp. 173-185

Ganal MW, Roder MS, 2007. Microsatellite and SNP markers in wheat breeding, Vol. 2. In: Varshney RK, Tuberosa R, (Eds.), Genomic assisted crop improvement: genomics applications in crops. The Netherlands: Springer, 1- 24.

Gardiner, L. J., Bansept-Basler, P., El-Soda, M., Hall, A., & O'Sullivan, D. M. (2020). A framework for gene mapping in wheat demonstrated using the Yr7 yellow rust resistance gene. Plos one, 15(4), e0231157.

Gardiner, L. J., Bansept-Basler, P., Olohan, L., Joynson, R., Brenchley, R., Hall, N., ... & Hall, A. (2016). Mapping-by-sequencing in complex polyploid genomes using genic sequence capture: a case study to map yellow rust resistance in hexaploid wheat. The Plant Journal, 87(4), 403-419.

Gautier. Maud Recombination as a driver of genome evolution : characterisation of biased gene conversion in mice. Genetics. Université de Lyon, 2019. English. ⟨NNT : 2019LYSE1184⟩. ⟨tel-02435079⟩

Gerland, P. (2023, December). What's beneath the future: World population prospects. In Semaine Data-SHS.

Gessese, M., Bariana, H., Wong, D., Hayden, M., & Bansal, U. (2019). Molecular mapping of stripe rust resistance gene Yr81 in a common wheat landrace Aus27430. Plant disease, 103(6), 1166-1171.

Gianessi, L. P., & Reigner, N. (2007). Pesticide Use in U.S. Agriculture: Impacts on Pest Management. National Center for Food and Agricultural Policy.

Gianoli, E., & Valladares, F. (2012). Studying phenotypic plasticity: the advantages of a broad approach. *Biological Journal of the Linnean Society*, *105*(1), 1-7.

Glazebrook, J. (2005). Contrasting mechanisms of defense against biotrophic and necrotrophic pathogens. Annu. Rev. Phytopathol., 43(1), 205-227.

Glo vendal, R. A., et al. (2021). Molecular breeding for disease resistance in wheat: Opportunities and challenges. Molecular Plant Pathology, 22(7), 771-783.

Godfray, H.C.J.; Beddington, J.R.; Crute, I.R.; Haddad, L.; Lawrence, D.; Muir, J.F.; Robinson, S.; Thomas, S.M.; Toulmin, C. Food security: The challenge of feeding 9 billion people. Science 2010, 237, 812–818.

Goodwin, S. B., Cavaletto, J. R., Hale, I. L., Thompson, I., Xu, S. S., Adhikari, T. B., & Dubcovsky, J. (2015). A new map location of gene Stb3 for resistance to Septoria tritici blotch in wheat. Crop science, 55(1), 35-43.

Goodwin, S. B., Ben M'Barek, S., Dhillon, B., Wittenberg, A. H. J., Crane, C. F., Hane, J. K., ... & Faino, L. (2011). Finished genome of the fungal wheat pathogen *Mycosphaerella graminicola* reveals dispensome structure, chromosome plasticity, and stealth pathogenesis. *PLoS Genetics*, 7(6), e1002070.

Goffinet B, Gerber S. Quantitative trait loci: a meta-analysis. Genetics. 2000 May;155(1):463-73. doi: 10.1093/genetics/155.1.463. PMID: 10790417; PMCID: PMC1461053.

Gordon D, Finch SJ. Factors affecting statistical power in the detection of genetic association. J Clin Invest. 2005 Jun;115(6):1408-18. doi: 10.1172/JCI24756. PMID: 15931375; PMCID: PMC1137002.

Goswami, R. S., & Kadoo, N. Y. (2022). Climate change affects fungal pathogens and their interactions with wheat. Plant Disease, 106(8), 1743-1756

Goulson, D. (2013). An overview of the environmental risks posed by neonicotinoid pesticides. Journal of Applied Ecology, 50(4), 977-987.

Gupta, P.K., Kulwal, P.L., Mir, R.R. (2013). QTL Mapping: Methodology and Applications in Cereal Breeding. In: Gupta, P., Varshney, R. (eds) Cereal Genomics II. Springer, Dordrecht. https://doi.org/10.1007/978-94-007-6401-9_11

Gupta PK, Rustgi S, Kulwal PL, 2005. Linkage disequilibrium and association studies in higher plants: present status and future prospects. Plant Molecular Biology, 57: 461-485.

H.C. Jing, D. Lovell, R. Gutteridge, D. Jenk, D. Kornyukhin, O.P. Mitrofanova, G.H.J. Kema, K.E. Hammond-Kosack

Phenotypic and genetic analysis of the Triticum monococcum – Mycosphaerella graminicola interaction. New Phytol., 179 (2008), pp. 1121-1132

H.T. Cui, K. Tsuda, J.E. Parker. Effector-triggered immunity: from pathogen perception to robust defense. Annu. Rev. Plant Biol., 66 (2015), pp. 487-511

H.W. Choi, D.F. Klessig. DAMPs, MAMPs, and NAMPs in plant innate immunity.

BMC Plant Biol., 16 (2016), p. 232

Hana Návarová, Friederike Bernsdorff, Anne-Christin Döring, Jürgen Zeier, Pipecolic Acid, an Endogenous Mediator of Defense Amplification and Priming, Is a Critical Regulator of Inducible Plant Immunity, The Plant Cell, Volume 24, Issue 12, December 2012, Pages 5123–5141, https://doi.org/10.1105/tpc.112.103564

Hartmann, F. E., Sánchez-Vallet, A., McDonald, B. A., & Croll, D. (2017). A fungal wheat pathogen evolved host specialization by extensive chromosomal rearrangements. The ISME journal, 11(5), 1189-1204.

Heick, T. M., Justesen, A. F., & Jørgensen, L. N. (2017). Resistance of wheat pathogen Zymoseptoria tritici to DMI and QoI fungicides in the Nordic-Baltic region-a status. European Journal of Plant Pathology, 149, 669-682.

Herrera-Foessel, S. A., Singh, R. P., Lan, C. X., Huerta-Espino, J., Calvo-Salazar, V., Bansal, U. K., ... & Lagudah, E. S. (2015). Yr60, a gene conferring moderate resistance to stripe rust in wheat. Plant disease, 99(4), 508-511.

Heslot, N., Jannink, J.-L. and Sorrells, M.E. (2015), Perspectives for Genomic Selection Applications and Research in Plants. Crop Science, 55: 1-12. https://doi.org/10.2135/cropsci2014.03.0249

Hickey, J. M., et al. (2017). Genomic prediction unifies animal and plant breeding programs to form platforms for biological discovery. Nature Genetics, 49(9), 1297-1303. https://doi.org/10.1038/ng.3920

Holland JB, 2007. Genetic architecture of complex traits in plants. Current Opinion in Plant Biology, 10: 156-161.

Hou L, Jia J, Xiaojun Z, Li X, Yang Z, Ma J, Guo H, Zhan H, Qiao L, Chang Z (2016) Molecular mapping of the stripe rust resistance gene Yr69 on wheat chromosome 2AS. Plant Dis 100:1717–1724

Hou L, Chen X, Wang M, See DR, Chao S, Bulli P, et al. (2015) Mapping a Large Number of QTL for Durable Resistance to Stripe Rust in Winter Wheat Druchamp Using SSR and SNP Markers. PLoS ONE 10(5): e0126794. https://doi.org/10.1371/journal.pone.0126794

Huang, M., Liu, X., Zhou, Y., Summers, R. M. & Zhang, Z. BLINK: a package for the next level of genome-wide association studies with both individuals and markers in the millions. Gigascience 8, giy154 (2019).

Huang, W.-K.; Ji, H.-L.; Gheysen, G.; Kyndt, T. Thiamine-Induced Priming Against Root-Knot Nematode Infection in Rice Involves Lignification and Hydrogen Peroxide Generation. Mol. Plant Pathol. 2016, 17 (4), 614624. Available from: https://doi.org/10.1111/mpp.12316.

Huang BE, George AW, Forrest KL, Kilian A, Hayden MJ et al (2012) A multiparent advanced generation inter-cross population for genetic analysis in wheat. Plant Biotechnol J 10:826–839

Huerta-Espino J, Singh R,Crespo-Herrera LA, Villaseñor-Mir HE, Rodriguez-Garcia MF, Dreisigacker S,Barcenas-Santana D and Lagudah E (2020) Adult Plant Slow Rusting

Genes Confer High Levels of Resistance to Rusts in Bread Wheat Cultivars From Mexico.

Front. Plant Sci. 11:824. doi: 10.3389/fpls.2020.00824

Liu, J., Chang, Z., Zhang, X., Yang, Z., Li, X., Jia, J., ... & Wang, J. (2013). Putative Thinopyrum intermedium-derived stripe rust resistance gene Yr50 maps on wheat chromosome arm 4BL. Theoretical and Applied Genetics, 126, 265-274.

Ishii, H. In Fungicide Research in Japan An Overview, Mod. Fungic. Antifung. Compd. V. 15th Int. Reinhardsbrunn Symp. Friedrichroda, Germany, May 610, 2007, 2008; pp 1117.

Italian Ministry of Agricultural Food and Forest Policies. (2021). Exportation of Italian Food Products. Retrieved from Ministero delle Politiche Agricole Alimentari e Forestali

Kang, Y., Choi, C., Kim, J.Y., Min, K.D. and Kim, C. (2023) Optimizing genomic selection of agricultural traits using K-wheat core collection. Front. Plant Sci. 14, 1112297.

Kang, H., Sul, J., Service, S. et al. Variance component model to account for sample structure in genome-wide association studies. Nat Genet 42, 348–354 (2010). https://doi.org/10.1038/ng.548

Kanwal, M., Qureshi, N., Gessese, M., Forrest, K., Babu, P., Bariana, H., & Bansal, U. (2021). An adult plant stripe rust resistance gene maps on chromosome 7A of Australian wheat cultivar Axe. Theoretical and Applied Genetics, 134, 2213-2220.

Kaur, S., Das, A., Sheoran, S. et al. QTL Meta-Analysis: An Approach to Detect Robust and Precise QTL. Tropical Plant Biol. 16, 225–243 (2023). https://doi.org/10.1007/s12042-023-09335-z

Kearsey, M. J. The principles of QTL analysis (a minimal mathematics approach) (1998). Journal of Experimental Botany 49, 1619–1623

Kema, G. H., & van Silfhout, C. H. (1997). Genetic variation for virulence and resistance in the wheat-Mycosphaerella graminicola pathosystem III. Comparative seedling and adult plant experiments. Phytopathology, 87(3), 266-272.

Keon, J., Antoniw, J., Carzaniga, R., Deller, S., Ward, J. L., Baker, J. M., ... & Rudd, J. J. (2007). Transcriptional adaptation of Mycosphaerella graminicola to programmed cell death (PCD) of its susceptible wheat host. Molecular plant-microbe interactions, 20(2), 178-193.

Kępczyńska, E., & Król, P. (2012). The phytohormone methyl jasmonate as an activator of induced resistance against the necrotroph Alternaria porri f. sp. solani in tomato plants. Journal of Plant Interactions, 7(4), 307–315. https://doi.org/10.1080/17429145.2011.645169

Kettles, G. J., Bayon, C., Sparks, C. A., Canning, G., Kanyuka, K., & Rudd, J. J. (2018). Characterization of an antimicrobial and phytotoxic ribonuclease secreted by the fungal wheat pathogen Zymoseptoria tritici. *New Phytologist*, *217*(1), 320-331.

Kettles, G. J., Hofinger, B. J., Hu, P., et al. (2018). sRNA profiling combined with gene function analysis reveals a lack of evidence for cross-kingdom RNA interference in the wheat–Zymoseptoria tritici pathosystem. Frontiers in Plant Science, 9, 892.

Kettles, G. J., & Kanyuka, K. (2016). Dissecting the molecular interactions between wheat and the fungal pathogen Zymoseptoria tritici. Frontiers in Plant Science, 7, 508.

Keuenhof, Katharina S., Lisa Larsson Berglund, Sandra Malmgren Hill, Kara L. Schneider, Per O. Widlund, Thomas Nyström, and Johanna L. Höög. 2021. “Large Organellar Changes Occur during Mild Heat Shock in Yeast.” Journal of Cell Science 135 (5): jcs258325. https://doi.org/10.1242/jcs.258325

Khatkar, M.S., Nicholas, F.W., Collins, A.R. et al. Extent of genome-wide linkage disequilibrium in Australian Holstein-Friesian cattle based on a high-density SNP panel. BMC Genomics 9, 187 (2008). https://doi.org/10.1186/1471-2164-9-187

Kidane YG, Hailemariam BN, Mengistu DK, Fadda C, Pè ME and Dell'Acqua M (2017) Genome-Wide Association Study of Septoria tritici Blotch Resistance in Ethiopian Durum Wheat Landraces. Front. Plant Sci. 8:1586. doi: 10.3389/fpls.2017.01586

King R, Urban M, Hammond-Kosack MC, Hassani-Pak K, Hammond-Kosack KE. The completed genome sequence of the pathogenic ascomycete fungus Fusarium graminearum. BMC Genomics. 2015 Jul 22;16(1):544. doi: 10.1186/s12864-015-1756-1. PMID: 26198851; PMCID: PMC4511438.

Kitony, J.K. Nested association mapping population in crops: current status and future prospects. J. Crop Sci. Biotechnol. 26, 1–12 (2023). https://doi.org/10.1007/s12892-022-00158-0

Klymiuk, V., Chawla, H.S., Wiebe, K. et al. Discovery of stripe rust resistance with incomplete dominance in wild emmer wheat using bulked segregant analysis sequencing. Commun Biol 5, 826 (2022). https://doi.org/10.1038/s42003-022-03773-3

Klymiuk, V. et al. Cloning of the wheat Yr15 resistance gene sheds light on the plant tandem kinase-pseudokinase family. Nature communications 9, 3735 (2018).

Kollers, S., Rodemann, B., Ling, J., Korzun, V., Ebmeyer, E., Argillier, O., ... & Röder, M. S. (2013). Genetic architecture of resistance to Septoria tritici blotch (Mycosphaerella graminicola) in European winter wheat. Molecular breeding, 32, 411-423.

Krattinger, S. G. et al. A putative ABC transporter confers durable resistance to multiple fungal pathogens in wheat. science 323, 1360-1363 (2009).

Kubicek, C. P., & Druzhinina, I. S. (Eds.). (2007). *Environmental and microbial relationships*. Berlin, Heidelberg: Springer Berlin Heidelberg.

Kumar, S., Kumar, M., Mir, R.R., Kumar, R., Kumar, S. (2021). Advances in Molecular Markers and Their Use in Genetic Improvement of Wheat. In: Wani, S.H., Mohan, A., Singh, G.P. (eds) Physiological, Molecular, and Genetic Perspectives of Wheat Improvement. Springer, Cham. https://doi.org/10.1007/978-3-030-59577-7_8

Kumar, J., Sen Gupta, D., Baum, M.,Varshney, R. K., & Kumar, S. (2021). Genomics-assisted lentilbreeding: Current status and future strategies. Legume Science,3(3), e71. https://doi.org/10.1002/leg3.7120 of

Kumar, N. et al. (2021). Genomic Selection for Wheat Improvement. In: Wani, S.H., Mohan, A., Singh, G.P. (eds) Physiological, Molecular, and Genetic Perspectives of Wheat Improvement. Springer, Cham. https://doi.org/10.1007/978-3-030-59577-7_9

IPCC. (2022). Climate Change 2022: Impacts, Adaptation and Vulnerability. Cambridge University Press.

IPCC. (2014). Climate Change 2014: Impacts, Adaptation, and Vulnerability. Cambridge University Press.

Isabel M.L. Saur and Ralph Hückelhoven (2021). Recognition and defence of plant-infecting fungal pathogens. Journal of Plant Physiology. https://doi.org/10.1016/j.jplph.2020.153324

J.D. Jones, J.L. Dangl The plant immune system Nature, 444 (2006), pp. 323-329

Novi, J. B. (2023). Identification of resistance factors to the main wheat diseases in the Mediterranean area

Jagadeesh, G. S., & Sampath, P. V. (2022). A data-intensive approach for evaluating water-energy-land-food nexus at multiple scales. Authorea Preprints.

Jallet, A. J., Le Rouzic, A., & Genissel, A. (2020). Evolution and plasticity of the transcriptome under temperature fluctuations in the fungal plant pathogen Zymoseptoria tritici. *Frontiers in Microbiology*, *11*, 573829.

Jia, L. J., Tang, H. Y., Wang, W. Q., Yuan, T. L., Wei, W. Q., Pang, B., … Tang, W. H. (2019). A linear nonribosomal octapeptide from Fusarium graminearum facilitates cell-to-cell invasion of wheat. Nature Communications, 10(1). https://doi.org/10.1038/s41467-019-08726-9

Jighly, A., Alagu, M., Makdis, F., Singh, M., Singh, S., Emebiri, L. C., & Ogbonnaya, F. C. (2016). Genomic regions conferring resistance to multiple fungal pathogens in synthetic hexaploid wheat. Molecular breeding, 36, 1-19.

Jinita Sthapit, Edward E. Gbur, Gina Brown-Guedira, David S. Marshall, and Eugene A. Milus. Characterization of Resistance to Stripe Rust in Contemporary Cultivars and Lines of Winter Wheat from the Eastern United States. Plant Disease 2012 96:5, 737-745

Jones, A. D., et al. (2020). Climate change and food security: A literature review. Global Food Security, 26, 100414.

Johnson, R. 1984. A critical analysis of durable resistance. Annu. Rev. Phytopathol. 22:309-330. https://doi.org/10.1146/annurev.py.22.090184.001521

Johnson R. (1983) Genetic Background of Durable Resistance. In: Lamberti F., Waller J.M., Van der Graaff N.A. (eds) Durable Resistance in Crops. NATO Advanced Science Institutes Series (Series A: Life Sciences), vol 55. Springer, Boston, MA

Juliana, P., Singh, R.P., Singh, P.K. et al. Genome-wide association mapping for resistance to leaf rust, stripe rust and tan spot in wheat reveals potential candidate genes. Theor Appl Genet 131, 1405–1422 (2018). https://doi.org/10.1007/s00122-018-3086-6

Junyan Feng, Fangjie Yao, Meinan Wang, Deven R. See, and Xianming Chen. Molecular Mapping of Yr85 and Comparison with Other Genes for Resistance to Stripe Rust on Wheat Chromosome 1BPlant Disease 2023 107:11, 3585-3591

Langlands-Perry, C., Pitarch, A., Lapalu, N., Cuenin, M., Bergez, C., Noly, A., ... & Marcel, T. C. (2023). Quantitative and qualitative plant-pathogen interactions call upon similar pathogenicity genes with a spectrum of effects. Frontiers in Plant Science, 14, 1128546.

L.S. Arraiano, L. Chartrain, E. Bossolini, H.N. Slatter, B. Keller, J.K.M. Brown. A gene in European wheat cultivars for resistance to an African isolate of Mycosphaerella graminicola Plant. Pathol., 56 (2007), pp. 73-78

Laidò G., Mangini G., Taranto F., Gadaleta A., Blanco A., Cattivelli L., et al. (2013). Genetic diversity and population structure of tetraploid wheats (Triticum turgidum L.) estimated by SSR, DArT and pedigree data. PLoS One 8:e67280 10.1371/journal.pone.0067280

Lambers, H., et al. (2016). The role of CO2 in agriculture under climate change. Plant Physiology, 170(1), 18-28.

Lander ES, Botstein D, 1989. Mapping Mendelian factors underlying quantitative traits using RFLP linkage maps. Genetics, 121: 185-199.

Leach, Michelle D., and Leah E. Cowen. 2014. “Membrane Fluidity and Temperature Sensing Are Coupled via Circuitry Comprised of Ole1, Rsp5, and Hsf1 in Candida albicans.” Eukaryotic Cell 13 (8): 1077–84. https://doi.org/10.1128/ec.00138-14.

Lendenmann, Mark H., Daniel Croll, Javier Palma-Guerrero, Ethan L. Stewart, and Bruce A. McDonald. 2016. “QTL Mapping of Temperature Sensitivity Reveals Candidate Genes for Thermal Adaptation and Growth Morphology in the Plant Pathogenic Fungus 806 Zymoseptoria tritici.” Heredity 116 (4): 384–94. https://doi.org/10.1038/hdy.2015.111.

Li, H., Bariana, H., Singh, D., Zhang, L., Dillon, S., Whan, A., ... & Ayliffe, M. (2020). A durum wheat adult plant stripe rust resistance QTL and its relationship with the bread wheat Yr80 locus. Theoretical and Applied Genetics, 133, 3049-3066.

Li, Z., Singh, S., Singh, R.P. et al. Genetics of resistance to yellow rust in PBW343 × Kenya Kudu recombinant inbred line population and mapping of a new resistance gene YrKK . Mol Breeding 32, 821–829 (2013). https://doi.org/10.1007/s11032-013-9909-x

Li, G.Q., Li, Z.F., Yang, W.Y. et al. Molecular mapping of stripe rust resistance gene YrCH42 in Chinese wheat cultivar Chuanmai 42 and its allelism with Yr24 and Yr26 . Theor Appl Genet 112, 1434–1440 (2006). https://doi.org/10.1007/s00122-006-0245-y

Li, Z. F., Zheng, T. C., He, Z. H., Li, G. Q., Xu, S. C., Li, X. P., ... & Xia, X. C. (2006). Molecular tagging of stripe rust resistance gene YrZH84 in Chinese wheat line Zhou 8425B. Theoretical and Applied Genetics, 112, 1098-1103.

Lin X, N'Diaye A, Walkowiak S, Nilsen KT, Cory AT, Haile J, et al. (2018) Genetic analysis of resistance to stripe rust in durum wheat (Triticum turgidum L. var. durum). PLoS ONE 13(9): e0203283. https://doi.org/10.1371/journal. pone.0203283 Genetic analysis of resistance to stripe rust in durum wheat (Triticum turgidum L. var. durum). PLoS One 13, e0203283 (2018).

Lin, F., Chen, X.M. Quantitative trait loci for non-race-specific, high-temperature adult-plant resistance to stripe rust in wheat cultivar Express. Theor Appl Genet 118, 631–642 (2009). https://doi.org/10.1007/s00122-008-0894-0

Lin, F., & Chen, X. M. (2008). Molecular mapping of genes for race-specific overall resistance to stripe rust in wheat cultivar Express. Theoretical and Applied Genetics, 116, 797-806.

Lin, F., & Chen, X. M. (2007). Genetics and molecular mapping of genes for race-specific all-stage resistance and non-race-specific high-temperature adult-plant resistance to stripe rust in spring wheat cultivar Alpowa. Theoretical and Applied Genetics, 114(7), 1277-1287.

Line, R. F. & Qayoum, A. Virulence, aggressiveness, evolution and distribution of races of Puccinia striiformis (the cause of stripe rust of wheat) in North America, 1968-87. Technical bulletin (1992).

Liu W, Maccaferri M, Bulli P, Rynearson S, Tuberosa R, Chen X, Pumphrey M. Genome-wide association mapping for seedling and field resistance to Puccinia striiformis f. sp. tritici in elite durum wheat. Theor Appl Genet. 2017 Apr;130(4):649-667. doi: 10.1007/s00122-016-2841-9. Epub 2016 Dec 30. PMID: 28039515.

Liu, L. et al. Combination of all-stage and high-temperature adult-plant resistance QTL confers high-level, durable resistance to stripe rust in winter wheat cultivar Madsen. Theoretical Applied Genetics 131, 1835-1849 (2018).

Liu, W., Maccaferri, M., Chen, X. et al. Genome-wide association mapping reveals a rich genetic architecture of stripe rust resistance loci in emmer wheat (Triticum turgidum ssp. dicoccum). Theor Appl Genet 130, 2249–2270 (2017). https://doi.org/10.1007/s00122-017-2957-6

Liu W, Maccaferri M, Rynearson S, Letta T, Zegeye H, Tuberosa R, Chen X and Pumphrey M (2017) Novel Sources of Stripe Rust Resistance Identified by Genome-Wide Association Mapping in Ethiopian Durum Wheat (Triticum turgidum ssp. durum). Front. Plant Sci. 8:774. doi: 10.3389/fpls.2017.00774

Liu, X., Huang, M., Fan, B., Buckler, E. S. & Zhang, Z. Iterative usage of fixed and random effect models for powerful and efficient genome-wide association studies. PLoS genetics 12, e1005767 (2016).

Liu W, Frick M, Huel R, Nykiforuk CL, Wang X, Gaudet DA, Eudes F, Conner RL, Kuzyk A, Chen Q, Kang Z, Laroche A. The stripe rust resistance gene Yr10 encodes an evolutionary-conserved and unique CC-NBS-LRR sequence in wheat. Mol Plant. 2014 Dec;7(12):1740-55. doi: 10.1093/mp/ssu112. Epub 2014 Oct 20. PMID: 25336565.

Lobell, D. B., et al. (2011). Climate trends and global crop production since 1980. Science, 333(6042), 616-620.

Lo Presti L, Lanver D, Schweizer G, Tanaka S, Liang L, Tollot M, Zuccaro A, Reissmann S, Kahmann R. Fungal effectors and plant susceptibility. Annu Rev Plant Biol. 2015;66:513-45. doi: 10.1146/annurev-arplant-043014-114623. PMID: 25923844.

Lu, Y., Wang, M., Chen, X., See, D., Chao, S., & Jing, J. (2014). Mapping of Yr62 and a small-effect QTL for high-temperature adult-plant resistance to stripe rust in spring wheat PI 192252. Theoretical and Applied Genetics, 127, 1449-1459.

Luo PG, Hu XY, Ren ZL, Zhang HY, Shu K, Yang ZJ. Allelic analysis of stripe rust resistance genes on wheat chromosome 2BS. Genome. 2008 Nov;51(11):922-7. doi: 10.1139/G08-079. PMID: 18956025.

Lupton F. C. H. and Macer R. C. F. 1962 Inheritance of resistance to yellow rust (Puccinia glumarum Erikss. and Henn) in seven varieties of wheat. Trans. Br. Mycol. Soc. 45, 21–45.

Lynch M, Walsh B, 1998. Genetic and analysis of quantitative traits. In: Sunderland MA (Ed.), Sinauer Associates.

Lupton F. C. H. and Macer R. C. F. 1962 Inheritance of resistance to yellow rust (Puccinia glumarum Erikss. and Henn) in seven varieties of wheat. Trans. Br. Mycol. Soc. 45, 21-45.

Ma, J., Wingen, L. U., Orford, S., Fenwick, P., Wang, J., & Griffiths, S. (2015). Using the UK reference population Avalon× Cadenza as a platform to compare breeding strategies in elite Western European bread wheat. Molecular Breeding, 35, 1-18.

MA, D. F., JING, J. X., HOU, D. Y., LI, Q., ZHOU, X. L., DU, J. Y., & LU, Q. L. (2013). Genetics and Molecular Mapping of a High-Temperature Resistance Gene to Stripe Rust in Seeding-Stage in Winter Wheat Cultivar Lantian. Journal of Integrative Agriculture, 12(6), 1018-1025.

M.O. Winfield, A.M. Allen, A.J. Burridge, G.L.A. Barker, H.R. Benbow, K.J. Edwards

High-density SNP genotyping array for hexaploid wheat and its secondary and tertiary gene pool

Plant Biotechnol. J., 14 (5) (2015), pp. 1195-1206

M. S. Hovmøller, S. Walter, R. A. Bayles, A. Hubbard, K. Flath, N. Sommerfeldt, M. Leconte, P. Czembor, J. Rodriguez-Algaba, T. Thach, J. G. Hansen, P. Lassen, A. F. Justesen, S. Ali, C. Vallavieille-Pope

Maccaferri, Marco, et al. "Durum wheat genome highlights past domestication signatures and future improvement targets." Nature Genetics 51.5 (2019): 885.

Marco Maccaferri, Junli Zhang, Peter Bulli, Zewdie Abate, Shiaoman Chao, Dario Cantu, Eligio Bossolini, Xianming Chen, Michael Pumphrey, Jorge Dubcovsky, A Genome-Wide Association Study of Resistance to Stripe Rust (Puccinia striiformis f. sp. tritici) in a Worldwide Collection of Hexaploid Spring Wheat (Triticum aestivum L.), G3 Genes|Genomes|Genetics, Volume 5, Issue 3, 1 March 2015, Pages 449–465, https://doi.org/10.1534/g3.114.014563

Maccaferri, M. et al. A high-density, SNP-based consensus map of tetraploid wheat as a bridge to integrate durum and bread wheat genomics and breeding. Plant biotechnology journal 13, 648-663 (2015).

Machinandiarena, M. F.; Lobato, M. C.; Feldman, M. L.; Daleo, G. R.; Andreu, A. B. Potassium Phosphite Primes Defense Responses in Potato Against Phytophthora infestans. J. Plant Physiol. 2012, 169 (14), 14171424. Available from: https://doi.org/10.1016/J.JPLPH.2012.05.005.

Mackay IJ, Bansept-Basler P, Barber T, Bentley AR, Cockram J et al (2014) An eight-parent Multiparent Advanced Generation Inter-Cross population for winter-sown wheat: creation, properties and validation. G3 4:1603–1610

Mackay TFC, Stone EA, Ayroles JF, 2009. The genetics of quantitative traits: challenges and prospects. Nature Reviews Genetics, 10: 565-577.

Mackay I, Powell W, 2007. Methods for linkage disequilibrium mapping in crops. Trends Plant Sci, 12: 57-63.

Maclean, Calum J., Brian P. H. Metzger, Jian-Rong Yang, Wei-Chin Ho, Bryan 833 Moyers, and Jianzhi Zhang. 2017. "Deciphering the Genic Basis of Yeast Fitness 834 Variation by Simultaneous Forward and Reverse Genetics." Molecular Biology and 835 Evolution 34 (10): 2486–2502. https://doi.org/10.1093/molbev/msx151.

Mammadov, J., Chen, W., Mingus, J. et al. Development of versatile gene-based SNP assays in maize (Zea mays L.). Mol Breeding 29, 779–790 (2012). https://doi.org/10.1007/s11032-011-9589-3

Mahboubi, M., Talebi, R., Mehrabi, R., Mohammad Naji, A., Maccaferri, M., & Kema, G. H. (2022). Genetic analysis of novel resistance sources and genome-wide association mapping identified novel QTLs for resistance to Zymoseptoria tritici, the causal agent of septoria tritici blotch in wheat. Journal of Applied Genetics, 63(3), 429-445.

Mahboubi, M., Talebi, R., Mehrabi, R., Naji, A. M., Maccaferri, M., & Kema, G. (2021). Genome-wide association mapping in wheat reveals novel QTLs and potential candidate genes involved in resistance to septoria tritici blotch.

Marais, G. F., Badenhorst, P. E., Eksteen, A., & Pretorius, Z. A. (2010). Reduction of Aegilops sharonensis chromatin associated with resistance genes Lr56 and Yr38 in wheat. Euphytica, 171, 15-22.

Marais, G. F., Pretorius, Z. A., Wellings, C. R., McCallum, B., & Marais, A. S. (2005). Leaf rust and stripe rust resistance genes transferred to common wheat from Triticum dicoccoides. Euphytica, 143, 115-123.

Marchal, C., Zhang, J., Zhang, P., Fenwick, P., Steuernagel, B., Adamski, N. M., ... & Uauy, C. (2018). BED-domain-containing immune receptors confer diverse resistance spectra to yellow rust. Nature plants, 4(9), 662-668.

Marcos-Barbero, E. L., Pérez, P., Martínez-Carrasco, R., Arellano, J. B., & Morcuende, R. (2021). Genotypic variability on grain yield and grain nutritional quality characteristics of wheat grown under elevated CO2 and high temperature. *Plants*, *10*(6), 1043.

Marone D, Laidò G, Saccomanno A, Petruzzino G, Giaretta Azevedo CV, De Vita P, Mastrangelo AM, Gadaleta A, Ammar K, Bassi FM, Wang M, Chen X, Rubiales D, Matny O, Steffenson BJ and Pecchioni N (2024) Genome-wide association study of common resistance to rust species in tetraploid wheat. Front. Plant Sci. 14:1290643. doi: 10.3389/fpls.2023.1290643

Martin W Ganal, Thomas Altmann, Marion S Röder. SNP identification in crop plants. Current Opinion in Plant Biology.Volume 12, Issue 2, April 2009, Pages 211-217

Martínez-Carrasco, F., et al. (2017). Nutritional and Health Benefits of Durum Wheat. Nutrients, 9(12), 1289. doi:10.3390/nu9121289

Masser, A. E., Kang, W., Roy, J., Mohanakrishnan Kaimal, J., Quintana-Cordero, J., Friedländer, M. R., & Andréasson, C. (2019). Cytoplasmic protein misfolding titrates Hsp70 to activate nuclear Hsf1. *Elife*, *8*, e47791.

Massoud, K.; Barchietto, T.; Le Rudulier, T.; Pallandre, L.; Didierlaurent, L.; Garmier, M., et al. Dissecting Phosphite-Induced Priming in Arabidopsis Infected With Hyaloperonospora arabidopsidis. Plant Physiol. 2012, 159 (1), 286298. Available from: https://doi.org/10.1104/PP.112.194647

Mathieson, I., McVean, G. Differential confounding of rare and common variants in spatially structured populations. Nat Genet 44, 243–246 (2012). https://doi.org/10.1038/ng.1074

Mboup, M., Bahri, B., Leconte, M., De Vallavieille-Pope, C., Kaltz, O., & Enjalbert, J. (2012). Genetic structure and local adaptation of European wheat yellow rust populations: the role of temperature-specific adaptation. *Evolutionary applications*, *5*(4), 341-352.

McCaig, T. N., and Clarke, J. M. (1995). Breeding durum wheat in western Canada: historical trends in yield and related variables. Can. J. Plant Sci. 75, 55–60. doi: 10.4141/cjps95-009

McCallum, B.D., Hiebert, C.W., Cloutier, S., Bakkeren, G., Rosa, S.B., Humphreys, D.G., Marais, G.F., McCartney, C.A., Panwar, V., Rampitsch, C., Saville, B.J. and Wang, X. (2016) A review of wheat leaf rust research and the development of resistant cultivars in Canada. Can. J. Plant Pathol. 38, 1–18.

McDonald, B. A., Suffert, F., Bernasconi, A., & Mikaberidze, A. (2022). How large and diverse are field populations of fungal plant pathogens? The case of Zymoseptoria tritici. *Evolutionary Applications*, *15*(9), 1360-1373.

McDonald, B. A., & Mundt, C. C. (2016). How knowledge of pathogen population biology informs management of Septoria tritici blotch. Phytopathology, 106(9), 948-955.

McDonald, B. A., & Stukenbrock, E. H. (2016). Rapid emergence of pathogens in agro-ecosystems: global threats to agricultural sustainability and food security. *Philosophical Transactions of the Royal Society B: Biological Sciences*, *371*(1709), 20160026.

McDonald, D., McIntosh, R., Wellings, C. et al. Cytogenetical studies in wheat XIX. Location and linkage studies on gene Yr27 for resistance to stripe (yellow) rust. Euphytica 136, 239–248 (2004). https://doi.org/10.1023/B:EUPH.0000032709.59324.45

McIntosh, R. A., Dubcovsky, J., Rogers, W. J., Xia, X. C., and Raupp, W. J. 2020. Catalogue of Gene Symbols for Wheat - 2020 Supplement. Ann. Wheat Newslett. 66.

McIntosh, R., Mu, J., Han, D. & Kang, Z. Wheat stripe rust resistance gene Yr24/Yr26: A retrospective review. The Crop Journal 6, 321-329 (2018).

McIntosh, R. et al. Catalogue of gene symbols for wheat: 2010 supplement. Annual wheat newsletter 56, 273-282 (2010).

McIntosh, R. A. (1995). Wheat Rusts: an atlas of resistance genes. Csiro Publishing.

McFadden ES, Sears ER, 1946. The origin of Triticum spelta and its free-threshing hexaploid relatives. Journal of. Heredity, 37: 81-89, 107-116.

Mehrabi, A.A.; Steffenson, B.J.; Pour-Aboughadareh, A.; Matny, O.; Rahmatov, M. Genome-Wide Association Study Identifies Two Loci for Stripe Rust Resistance in a Durum Wheat Panel from Iran. Appl. Sci. 2022, 12, 4963. https://doi.org/10.3390/app12104963

Mehrotra, R.S. 1980. plant pathology. Tata McGraw-Hill, New Delhi, page 771.

Mekonnen, T., Haileselassie, T., Goodwin, S. B., & Tesfayea, K. (2020). Genetic diversity and population structure of Zymoseptoria tritici in Ethiopia as revealed by microsatellite markers. Fungal Genetics and Biology, 141, 103413.

Mesterhazy, A. Updating the Breeding Philosophy of Wheat to Fusarium Head Blight (FHB): Resistance Components, QTL Identification, and Phenotyping—A Review. Plants 2020, 9, 1702. https://doi.org/10.3390/plants9121702

Miedaner, T. (2016). Breeding Strategies for Improving Plant Resistance to Diseases. In: Al-Khayri, J., Jain, S., Johnson, D. (eds) Advances in Plant Breeding Strategies: Agronomic, Abiotic and Biotic Stress Traits. Springer, Cham. https://doi.org/10.1007/978-3-319-22518-0_15

Mikaberidze, A., McDonald, B. A., & Kronenberg, L. (2024). A genome-wide association study identifies markers and candidate genes affecting tolerance to the wheat pathogen Zymoseptoria tritici. bioRxiv, 2024-08.

Miles, C. & Wayne, M. (2008) Quantitative trait locus (QTL) analysis. Nature Education 1(1):208

Milus, E. A., Kristensen, K. & Hovmøller, M. S. Evidence for increased aggressiveness in a recent widespread strain of Puccinia striiformis f. sp. tritici causing stripe rust of wheat. Phytopathology 99, 89-94 (2009).

Minana-Posada, S., Lorrain, C., McDonald, B. A., & Feurtey, A. (2024). Thermal adaptation in worldwide collections of a major fungal pathogen. bioRxiv, 2024-09.

Möller M, Habig M, Freitag M, Stukenbrock EH. Extraordinary Genome Instability and Widespread Chromosome Rearrangements During Vegetative Growth. Genetics. 2018 Oct;210(2):517-529. doi: 10.1534/genetics.118.301050. Epub 2018 Aug 2. PMID: 30072376; PMCID: PMC6216587.

Möller M, Stukenbrock EH. Evolution and genome architecture in fungal plant pathogens. Nat Rev Microbiol. 2017 Dec;15(12):756-771. doi: 10.1038/nrmicro.2017.76. Epub 2017 Aug 7. Erratum in: Nat Rev Microbiol. 2017 Nov 10;15(12):771. doi: 10.1038/nrmicro.2017.143. PMID: 28781365.

Monneveux P, Zaharieva M, Rekika D, 2000. The utilization of Triticum and Aegilops species for the improvement of durum wheat. In: Royo C, Nachit MM, Di Fonzo N, Araus JL (Eds.), Durum Wheat Improvement in the Mediterranean Region: New Challenges. CIHEAM, Centre Udl-IRTA, ICARDA, CIMMYT, Zaragoza. Options Méditerranéennes, Series A, 40: 71-83

Moore, J. W. et al. A recently evolved hexose transporter variant confers resistance to multiple pathogens in wheat. Nature genetics 47, 1494-1498 (2015).

Morgante M, Salamini F, 2003. From plant genomics to breeding practice. Current Opinions in Biotechnology, 14: 214-219.

Motzo, R., Giunta, F., & Fois, S. (2001). Evoluzione varietale e qualità in frumento duro dalle vecchie popolazioni alle attuali cultivar. 173.

Myers, S. S., Smith, M. R., Guth, S., Golden, C. D., Vaitla, B., Mueller, N. D., ... & Huybers, P. (2017). Climate change and global food systems: potential impacts on food security and undernutrition. Annual review of public health, 38(1), 259-277.

Myers, S. S., Zanobetti, A., Kloog, I., Huybers, P., Leakey, A. D., Bloom, A. J., ... & Usui, Y. (2014). Increasing CO2 threatens human nutrition. Nature, 510(7503), 139-142.

Müller, M. E., et al. (2016). Fungal plant pathogens and climate change: The potential impact on crop diseases. Global Change Biology, 22(9), 3079-3087.

Negro, S.S., Millet, E.J., Madur, D., Bauland, C., Combes, V., Welcker, C., Tardieu, F. et al. (2019) Genotyping-by-sequencing and SNP-arrays are complementary for detecting quantitative trait loci by tagging different haplotypes in association studies. BMC Plant Biol. 19, 318.

Newlands, N. K. (2018). Model-based forecasting of agricultural crop disease risk at the regional scale, integrating airborne inoculum, environmental, and satellite-based monitoring data. Frontiers in Environmental Science, 6, 63.

Newman, M.-A.; Dow, J. M.; Molinaro, A.; Parrilli, M. Invited Review: Priming, Induction and Modulation of Plant Defence Responses by Bacterial Lipopolysaccharides. J. Endotoxin Res. 2007, 13 (2), 6984. Available from: https://doi.org/10.1177/0968051907079399.

Niks, R. E., Qi, X. Q., and Marcel, T. C. (2015). "Quantitative resistance to biotrophic filamentous plant pathogens: concepts, misconceptions and mechanisms," in Annual Review of Phytopathology, ed. N. K. VanAlfen (Palo Alto, CA: Annual Reviews), 445–470.

Nothnagel M, Ellinghaus D, Schreiber S, Krawczak M, Franke A. A comprehensive evaluation of SNP genotype imputation. Hum Genet. 2009 Mar;125(2):163-71. doi: 10.1007/s00439-008-0606-5. Epub 2008 Dec 17. PMID: 19089453.

Nsabiyera, V., Bariana, H. S., Qureshi, N., Wong, D., Hayden, M. J., & Bansal, U. K. (2018). Characterisation and mapping of adult plant stripe rust resistance in wheat accession Aus27284. Theoretical and Applied Genetics, 131, 1459-1467.

Ogawa, M.; Kadowaki, A.; Yamada, T.; Kodooka, O. Applied Development of a Novel Fungicide Isotianil (Stouts), 2011.

Oluwafemi, S.; Dewhirst, S. Y.; Veyrat, N.; Powers, S.; Bruce, T. J. A.; Caulfield, J. C., et al. Priming of Production in Maize of Volatile Organic Defence Compounds by the Natural Plant Activator Cis-Jasmone. PLoS One 2013, 8 (6), e62299. Available from: https://doi.org/10.1371/journal.pone.0062299.

Okada, K.; Abe, H.; Arimura, G. Jasmonates Induce Both Defense Responses and Communication in Monocotyledonous and Dicotyledonous Plants. Plant Cell Physiol. 2015, 56 (1), 1627. Available from: https://doi.org/10.1093/pcp/pcu158.

Onaga, G., Wydra, K., Koopmann, B., Chebotarov, D., Séré, Y., & Von Tiedemann, A. (2017). High temperature effects on Pi54 conferred resistance to Magnaporthe oryzae in two genetic backgrounds of Oryza sativa. *Journal of Plant Physiology*, *212*, 80-93.

Ordon, F., and Kühne, T. (2014). "Response to viral pathogens," in Biotechnological Approaches to Barley Improvement: Biotechnology in Agriculture and Forestry, Vol. 69, Chapter. 10, eds J. Kumlehn and N. Stein (Berlin: Springer-Verlag), 181–196. doi: 10.1007/978-3-662-44406-1_10es

Orton ES, Deller S, Brown JK. Mycosphaerella graminicola: from genomics to disease control. Mol Plant Pathol. 2011 Jun;12(5):413-24. doi: 10.1111/j.1364-3703.2010.00688.x. Epub 2011 Jan 17. PMID: 21535348; PMCID: PMC6640266.

Ouaja, M., Aouini, L., Bahri, B., Ferjaoui, S., Medini, M., Marcel, T. C., & Hamza, S. (2020). Identification of valuable sources of resistance to Zymoseptoria tritici in the Tunisian durum wheat landraces. European Journal of Plant Pathology, 156, 647-661.

Ozkan H, Levy AA, Feldman M, 2001. Allopolyploidy-induced rapid genome evolution in the wheat (Aegilops–Triticum) group. Plant Cell, 13: 1735-1747.

P. Cheng and X. M. Chen, "Molecular Mapping of a Gene for Stripe Rust Resistance in Spring Wheat Cultivar IDO377s," Theoretical and Applied Genetics, Vol. 121, No. 1, 2010, pp. 195-204. doi:10.1007/s00122-010-1302-0

Pakeerathan, K., Bariana, H., Qureshi, N., Wong, D., Hayden, M., & Bansal, U. (2019). Identification of a new source of stripe rust resistance Yr82 in wheat. Theoretical and Applied Genetics, 132, 3169-3176.

Palma-Guerrero, J., Torriani, S. F., Zala, M., Carter, D., Courbot, M., Rudd, J. J., ... & Croll, D. (2016). Comparative transcriptomic analyses of Z ymoseptoria tritici strains show complex lifestyle transitions and intraspecific variability in transcription profiles. Molecular plant pathology, 17(6), 845-859.

Panadero, J., Pallotti, C., Rodríguez-Vargas, S., Randez-Gil, F., & Prieto, J. A. (2006). A downshift in temperature activates the high osmolarity glycerol (HOG) pathway, which determines freeze tolerance in Saccharomyces cerevisiae. *Journal of Biological Chemistry*, *281*(8), 4638-4645.

Pardey, P., Beddow, J., Kriticos, D., Hurley, T., Park, R., Duveiller, E., Sutherst, R., Burdon, J. and Hodson, D. (2013) Right-sizing stem-rust research. Science, 340, 147–148.

Patial, M., Navathe, S., He, X., Kamble, U., Kumar, M., Joshi, A. K., & Singh, P. K. (2024). Novel resistance loci for quantitative resistance to Septoria tritici blotch in Asian wheat (Triticum aestivum) via genome-wide association study. BMC Plant Biology, 24(1), 846.

P.N. Dodds, J.P. Rathjen. Plant immunity: towards an integrated view of plant-pathogen interactions. Nat. Rev. Genet., 11 (2010), pp. 539-548

P.J.G.M. De Wit, P.H.M. Roseboom. Isolation, partial characterization and specificity of glycoprotein elicitors from culture filtrates, mycelium and cell walls of Cladosporium fulvum

Peter J. Bradbury, Zhiwu Zhang, Dallas E. Kroon, Terry M. Casstevens, Yogesh Ramdoss, Edward S. Buckler, TASSEL: software for association mapping of complex traits in diverse samples, Bioinformatics, Volume 23, Issue 19, October 2007, Pages 2633–2635, https://doi.org/10.1093/bioinformatics/btm308

Pilet-Nayel M-L, Moury B, Caffier V, Montarry J, Kerlan M-C, Fournet S, Durel C-E and Delourme R (2017) Quantitative Resistance to Plant Pathogens in Pyramiding Strategies for Durable Crop Protection. Front. Plant Sci. 8:1838. doi: 10.3389/fpls.2017.01838

Plissonneau, C., Hartmann, F.E. & Croll, D. Pangenome analyses of the wheat pathogen *Zymoseptoria tritici* reveal the structural basis of a highly plastic eukaryotic genome. *BMC Biol* 16, 5 (2018). https://doi.org/10.1186/s12915-017-0457-4

Poland, Jesse A., et al. "Shades of gray: the world of quantitative disease resistance." Trends in plant science 14.1 (2009): 21-29.

Pretty, J. (2018). Intensification for redesigned and sustainable agricultural systems. Science, 362(6417), eaav0294.

Pu, Z. J., Chen, G. Y., Wei, Y. M., Yang, W. Y., Yan, Z. H., & Zheng, Y. L. (2010). Identification and molecular tagging of a stripe rust resistance gene in wheat line P81. Plant breeding, 129(1), 53-57.

Pumphrey MO, Bernardo R, Anderson JA, 2007. Validating the Fhb1 QTL for Fusarium head blight resistance in near-isogenic wheat lines developed from breeding populations. Crop Science, 47: 200-206.

Quenouille, J., Paulhiac, E., Moury, B., and Palloix, A. (2014). Quantitative trait loci from the host genetic background modulate the durability of a resistance gene: a rational basis for sustainable resistance breeding in plants. Heredity 112, 579–587. doi: 10.1038/hdy.2013.138

Qureshi, N., Bariana, H., Forrest, K., Hayden, M., Keller, B., Wicker, T., ... & Bansal, U. (2017). Fine mapping of the chromosome 5B region carrying closely linked rust resistance genes Yr47 and Lr52 in wheat. Theoretical and Applied Genetics, 130, 495-504.

R Core Team (2020) R: A Language and Environment for Statistical Computing. R Foundation for Statistical Computing, Vienna, Austria. https://www.r-project.org/

Radecka-Janusik, M., Piechota, U., Piaskowska, D. et al. Haplotype-based association mapping of genomic regions associated with Zymoseptoria tritici resistance using 217 diverse wheat genotypes. BMC Plant Biol 24, 682 (2024). https://doi.org/10.1186/s12870-024-05400-1

Rafalski JA, 2010. Association genetics in crop improvement. Current Opinion in Plant Biology 13: 174-180

Rafalski A, 2002a. Applications of single nucleotide polymorphisms in crop genetics. Curr Opin Plant Biol, 5: 94-100.

Raffaele, S., & Kamoun, S. (2012). Genome evolution in filamentous plant pathogens: why bigger can be better. *Nature Reviews Microbiology*, 10(6), 417-430.

Rahman, M.Z., Hasan, M.T., Rahman, J. (2023). Kompetitive Allele-Specific PCR (KASP): An Efficient High-Throughput Genotyping Platform and Its Applications in Crop Variety Development. In: Kumar, N. (eds) Molecular Marker Techniques. Springer, Singapore. https://doi.org/10.1007/978-981-99-1612-2_2

Raman, R., Milgate, A. W., Imtiaz, M., Tan, M. K., Raman, H., Lisle, C., ... & Martin, P. (2009). Molecular mapping and physical location of major gene conferring seedling resistance to Septoria tritici blotch in wheat. Molecular Breeding, 24, 153-164.

Randhawa, M., Bansal, U., Valárik, M., Klocová, B., Doležel, J., & Bariana, H. (2014). Molecular mapping of stripe rust resistance gene Yr51 in chromosome 4AL of wheat. Theoretical and Applied genetics, 127, 317-324.

Randhawa, M.S., Bariana, H.S., Mago, R. et al. Mapping of a new stripe rust resistance locus Yr57 on chromosome 3BS of wheat. Mol Breeding 35, 65 (2015). https://doi.org/10.1007/s11032-015-0270-0

Ravichandra, N.G. 2013. Fundamentals of plant pathol., PHI Learning, New Delhi. ISBN 978-81-203-4703-8 page 43

Rebai, A. and Goffinet, B. (2000) More about quantitative trait locus mapping with diallel designs. Genet. Res. 75, 243–247.

Ren, Y., Li, S., Xia, X., Zhou, Q., He, Y., Wei, Y., ... & He, Z. (2015). Molecular mapping of a recessive stripe rust resistance gene yrMY37 in Chinese wheat cultivar Mianmai 37. Molecular Breeding, 35, 1-9.

Ren, R. S., Wang, M. N., Chen, X. M., & Zhang, Z. J. (2012). Characterization and molecular mapping of Yr52 for high-temperature adult-plant resistance to stripe rust in spring wheat germplasm PI 183527. Theoretical and Applied Genetics, 125, 847-857.

Riaz, A., KockAppelgren, P., Hehir, J. G., Kang, J., Meade, F., Cockram, J., ... & Byrne, S. (2020). Genetic analysis using a multi-parent wheat population identifies novel sources of septoria tritici blotch resistance. Genes, 11(8), 887.

Rimbert, H., Darrier, B., Navarro, J., Kitt, J., Choulet, F., Leveugle, M., Duarte, J. et al. (2018) High throughput SNP discovery and genotyping in hexaploid wheat. PLoS One, 13, e0186329.

Roelfs, A.P., Singh, R.P. and Saari, E.E. (1992) Rust Diseases of Wheat: Concepts and Methods of Disease Management. Mexico, DF: CIMMYT.

Rosa SB, Zanella CM, Hiebert CW, Brûlé-Babel AL, Randhawa HS, Shorter S, Boyd LA, McCallum BD. Genetic Characterization of Leaf and Stripe Rust Resistance in the Brazilian Wheat Cultivar Toropi. Phytopathology. 2019 Oct;109(10):1760-1768. doi: 10.1094/PHYTO-05-19-0159-R. Epub 2019 Sep 5. PMID: 31282829.

Rosewarne, G.M., Herrera-Foessel, S.A., Singh, R.P. et al. Quantitative trait loci of stripe rust resistance in wheat. Theor Appl Genet 126, 2427–2449 (2013). https://doi.org/10.1007/s00122-013-2159-9

Royo C, Ammar K, Villegas D and Soriano JM (2021) Agronomic, Physiological and Genetic Changes Associated With Evolution, Migration and Modern Breeding in Durum Wheat. Front. Plant Sci. 12:674470. doi: 10.3389/fpls.2021.674470

Royo, C., Álvaro, F., Martos, V., Ramdani, A., Isidro, J., Villegas, D., et al. (2007). Genetic changes in durum wheat yield components and associated traits in Italian and Spanish varieties during the 20th century. Euphytica 155, 259–270. doi: 10.1007/s10681-006-9327-9

Rouxel, T., Grandaubert, J., Hane, J. K., Hoede, C., van de Wouw, A. P., Couloux, A., ... & Balesdent, M. H. (2011). Effector diversification within compartments of the *Leptosphaeria maculans* genome affected by repeat-induced point mutations. *Nature Communications*, 2, 202.

Rudd JJ, Kanyuka K, Hassani-Pak K, Derbyshire M, Andongabo A, Devonshire J, Lysenko A, Saqi M, Desai NM, Powers SJ, Hooper J, Ambroso L, Bharti A, Farmer A, Hammond-Kosack KE, Dietrich RA, Courbot M. Transcriptome and metabolite profiling of the infection cycle of Zymoseptoria tritici on wheat reveals a biphasic interaction with plant immunity involving differential pathogen chromosomal contributions and a variation on the hemibiotrophic lifestyle definition. Plant Physiol. 2015 Mar;167(3):1158-85. doi: 10.1104/pp.114.255927. Epub 2015 Jan 16. PMID: 25596183; PMCID: PMC4348787.

S.M. Tabib Ghaffary, J.D. Faris, T.L. Friesen, R.G.F. Visser, T.A.J. van der Lee, O. Robert, G.H.J. Kema. New broad-spectrum resistance to Septoria tritici blotch derived from synthetic hexaploid wheat. Theor. Appl. Genet., 124 (2012), pp. 125-

S.M. Tabib Ghaffary, O. Robert, V. Laurent, P. Lonnet, E. Margale, T.A.J. van der Lee, R.G.F. Visser, G.H.J. Kema

Genetic analysis of resistance to Septoria tritici blotch in the French winter wheat cultivars Balance and Apache. Theor. Appl. Genet., 123 (2011), pp. 741-754

Salamini, F., Özkan, H., Brandolini, A., Schäfer-Pregl, R., & Martin, W. (2002). Genetics and geography of wild cereal domestication in the near east. Nature Reviews Genetics, 3(6), 429–441. https://doi.org/10.1038/nrg817

Sanchez-Vallet, A., Mesters, J. R., Thomma, B. P. H. J. (2015). The battle for chitin recognition in plant–microbe interactions. FEMS Microbiology Reviews, 39(2), 171-183.

Santure AW, Garant D. Wild GWAS—association mapping in natural populations. Mol Ecol Resour. 2018; 18: 729–738. https://doi.org/10.1111/1755-0998.12901

Sarkar P, Stebbins GL, 1956. Morphological evidence concerning the origin of the B genome in wheat. American Journal of Botany, 43: 297-304.

Sauban Musa Jibril, Bello Hassan Jakada, Ahmad Shehu Kutama and Harisu Yunusa Umar. 2016. Plant and Pathogens: Pathogen Recognision, Invasion and Plant Defense Mechanism. Int.J.Curr.Microbiol.App.Sci. 5(6): 247-257. doi: http://dx.doi.org/10.20546/ijcmas.2016.506.028

Scarascia Mugnozza G. T. (2005). "The contribution of Italian wheat geneticists: from Nazareno Strampelli to Francesco D' Amato," in Proc. Int. Congr. In Wake Double Helix From Green Revolut. to Gene Revolution, 53–75. Available online at: http://dista.unibo.it/doublehelix/proceedings/SECTION_I/HELIX%20pp%20053-075.pd

Segovia, V., Hubbard, A., Craze, M., Bowden, S., Wallington, E., Bryant, R., ... & Uauy, C. (2014). Yr36 confers partial resistance at temperatures below 18 C to UK isolates of Puccinia striiformis. Phytopathology, 104(8), 871-878.

Segura, V. et al. An efficient multi-locus mixed-model approach for genome-wide association studies in structured populations. Nature genetics 44, 825-830 (2012).

Sela, H., Ezrati, S., Ben-Yehuda, P. et al. Linkage disequilibrium and association analysis of stripe rust resistance in wild emmer wheat (Triticum turgidum ssp. dicoccoides) population in Israel. Theor Appl Genet 127, 2453–2463 (2014). https://doi.org/10.1007/s00122-014-2389-5

Shaw, M. W., & Royle, D. J. (1993). Factors determining the severity of epidemics of Septoria tritici in winter wheat in the UK. Plant Pathology, 42(6), 882-899.

Singh, R. P., Hodson, D. P., Huerta-Espino, J., Jin, Y., Njau, P., Wanyera, R., ... & Ward, R. W. (2008). Will stem rust destroy the world's wheat crop?. Advances in agronomy, 98, 271-309.

Singh, R.P., Hodson, D.P., Jin, Y., Lagudah, E.S., Ayliffe, M.A., Bhavani, S., Rouse, M.N., Pretorius, Z.A., Szabo, L.J., Huerta-Espino, J., Basnet, B.R., Lan, C. and Hovmøller, M.S. (2015) Emergence and spread of new races of wheat stem rust fungus: continued threat to food security and prospects of genetic control. Phytopathology, 105, 872–884.

Singh, R. P., Huerta-Espino, J. U. L. I. O., & WILLIAM, H. (2005). Genetics and breeding for durable resistance to leaf and stripe rusts in wheat. Turkish journal of agriculture and forestry, 29(2), 121-127.

Singh RP, William HM, Huerta-Espino J, Crosby M (2003) Identification and mapping of gene Yr31 for resistance to stripe rust in Triticum aestivum cultivar pastor, vol 1. In: Pogna NE, Romano M, Pogna EA, Galterio G (eds) Proceedings of the 10th International wheat genetics symposium. Instituto Sperimentale per la Cerealicoltura, Rome, Italy, pp 411–413

Slepecky, R. A., & Starmer, W. T. (2009). Phenotypic plasticity in fungi: a review with observations on Aureobasidium pullulans. *Mycologia*, *101*(6), 823-832.

Smith, P., et al. (2019). The impact of climate change on agriculture and food security. Nature Climate Change, 9(2), 107-112.

Soleimani, B., Lehnert, H., Keilwagen, J., Plieske, J., Ordon, F., Naseri Rad, S., Ganal, M. et al. (2020) Comparison between core set selection methods using different Illumina marker platforms: a case study of assessment of diversity in wheat. Front. Plant Sci. 11, 1040.

Soriano, J.M., Colasuonno, P., Marcotuli, I. et al. Meta-QTL analysis and identification of candidate genes for quality, abiotic and biotic stress in durum wheat. Sci Rep 11, 11877 (2021). https://doi.org/10.1038/s41598-021-91446-2

St. Clair, D. A. (2010). "Quantitative disease resistance and quantitative resistance loci in breeding," in Annual Review of Phytopathology, eds N. K. VanAlfen, G. Bruening, and J. E. Leach (Palo Alto, CA: Annual Reviews), 247–268.

Stapley, J., Zhong, Z., & McDonald, B. A. (2024). Mapping genomic regions associated with temperature stress in the wheat pathogen Zymoseptoria tritici. bioRxiv, 2024-09.

Stefansson, T. S., McDonald, B. A., & Willi, Y. (2013). Local adaptation and evolutionary potential along a temperature gradient in the fungal pathogen Rhynchosporium commune. *Evolutionary Applications*, *6*(3), 524-534.

Steinberg G. Cell biology of Zymoseptoria tritici: Pathogen cell organization and wheat infection. Fungal Genet Biol. 2015 Jun;79: 17-23. doi: 10.1016/j.fgb.2015.04.002. PMID: 26092785; PMCID: PMC4502449.

Stephens, C., Blyth, H., Olmez, F., McDonald, M., Solomon, P., Milgate, A., ... & Kanyuka, K. (2018). Dramatic changes in genetic diversity of the avirulence effector AvrStb6 in global populations of the wheat pathogen Zymoseptoria tritici. In British Society of Plant Pathology Presidential Meeting, Warwick 2018.

Stewart, E. L., Hagerty, C. H., Mikaberidze, A., Mundt, C. C., Zhong, Z., & McDonald, B. A. (2016). An improved method for measuring quantitative resistance to the wheat pathogen Zymoseptoria tritici using high-throughput automated image analysis. *Phytopathology*, *106*(7), 782-788.

Stewart, E. (2016). QTL mapping of virulence traits in Zymoseptoria tritici (Doctoral dissertation, ETH Zurich).

Stewart, E. L., & McDonald, B. A. (2014). Measuring quantitative virulence in the wheat pathogen Zymoseptoria tritici using high-throughput automated image analysis. *Phytopathology*, *104*(9), 985-992.

Stotz, G. C., Salgado-Luarte, C., Escobedo, V. M., Valladares, F., & Gianoli, E. (2021). Global trends in phenotypic plasticity of plants. *Ecology Letters*, *24*(10), 2267-2281.

Stukenbrock, E. H., & Dutheil, J. Y. (2018). Fine-scale recombination maps of fungal plant pathogens reveal dynamic recombination landscapes and intragenic hotspots. *Genetics*, 208(3), 1209-1229.

Stukenbrock, E. H., & McDonald, B. A. (2008). The origins of plant pathogens in agro-ecosystems. Annu. Rev. Phytopathol., 46(1), 75-100.

Sun, C., Dong, Z., Zhao, L., Ren, Y., Zhang, N. and Chen, F. (2020) The wheat 660K SNP array demonstrates great potential for marker-assisted selection in polyploid wheat. Plant Biotechnol. J. 18, 1354–1360.

Sun, Q., Wei, Y., Ni, Z., Xie, C., & Yang, T. (2002). Microsatellite marker for yellow rust resistance gene Yr5 in wheat introgressed from spelt wheat. Plant Breeding, 121(6), 539-541.

Taranto F, D'Agostino N, Rodriguez M, Pavan S, Minervini AP, Pecchioni N, Papa R, De Vita P. Whole Genome Scan Reveals Molecular Signatures of Divergence and Selection Related to Important

Traits in Durum Wheat Germplasm. Front Genet. 2020 Apr 21;11:217. doi: 10.3389/fgene.2020.00217. PMID: 32373150; PMCID: PMC7187681.

Tester, M.; Langridge, P. Breeding technologies to increase crop production in a changing world. Science 2010, 327, 818–822.

Thao, H. T. B.; Yamakawa, T. Phosphite (Phosphorous Acid): Fungicide, Fertilizer or Bio-Stimulator? Soil Sci. Plant Nutr. 2009, 55 (2), 228234. Available from: https://doi.org/10.1111/j.1747-0765.2009.00365.x.

Thomas Miedaner. Matthias Rapp. Kerstin Flath. C. Friedrich H. Longin , Tobias Wurschum. Genetic architecture of yellow and stem rust resistance in a durum wheat diversity panel. Euphytica (2019) 215:71 https://doi.org/10.1007/s10681-019-2394-5(0123456789().,-volV()0123456789().,-volV)

Thompson, L. U., et al. (2017). Whole Grains and Health: A Review of the Evidence. Current Developments in Nutrition, 1(9), e001335. doi:10.3945/cdn.117.001335

Thomson Michael J. (2014). High-Throughput SNP Genotyping to Accelerate Crop Improvement. Plant Breed. Biotech. 2014 (September) 2(3):195~212

Thornton, P. K., Jones, P. G., Ericksen, P. J., & Challinor, A. J. (2011). Agriculture and food systems in sub-Saharan Africa in a 4 C+ world. Philosophical Transactions of the Royal Society A: Mathematical, Physical and Engineering Sciences, 369(1934), 117-136.Tilman, D., et al. (2002). Agricultural sustainability and intensive production practices. Nature, 418(6898), 671-677.

Tilman, D., Cassman, K. G., Matson, P. A., Naylor, R., & Polasky, S. (2002). Agricultural sustainability and intensive production practices. Nature, 418(6898), 671-677.

Torriani, S. F., Melichar, J. P., Mills, C., Pain, N., Sierotzki, H., & Courbot, M. (2015). Zymoseptoria tritici: a major threat to wheat production, integrated approaches to control. Fungal Genetics and Biology, 79, 8-12.

Tralamazza, Sabina Moser, Emile Gluck-Thaler, Alice Feurtey, and Daniel Croll. 2024. “Copy Number Variation Introduced by a Massive Mobile Element Facilitates Global Thermal Adaptation in a Fungal Wheat Pathogen.” Nature Communications 15 (1): 5728. https://doi.org/10.1038/s41467-024-49913-7

Tuberosa, R., Salvi, S., Giuliani, S., Sanguineti, M. C., Frascaroli, E., Conti, S., & Landi, P. (2010). Genomics of root architecture and functions in maize. In Root genomics (pp. 179-204). Berlin, Heidelberg: Springer Berlin Heidelberg.

Tuberosa, R., Graner, A., & Frison, E. (2014). Genomics of plant genetic resources: Volume 1. Managing, sequencing and mining genetic resources. Genomics of Plant Genetic Resources: Volume 1. Managing, Sequencing and Mining Genetic Resources, 1–710. https://doi.org/10.1007/978-94-007-7572-5

United Nations. (2022). World population prospects 2022. United Nations, Department of Economic and Social Affairs.

Valladares, F., Matesanz, S., Guilhaumon, F., Araújo, M. B., Balaguer, L., Benito-Garzón, M., ... & Zavala, M. A. (2014). The effects of phenotypic plasticity and local adaptation on forecasts of species range shifts under climate change. *Ecology letters*, *17*(11), 1351-1364.

VanRaden, P. M. (2008). Efficient methods to compute genomic predictions. *Journal of dairy science*, *91*(11), 4414-4423.

Van Slageren MW, 1994. Wild wheats: a monograph of Aegilops L. and Amblyopyrum (Jaub. and Spach) Eig (Poaceae). Agricultural University, Wageningen & International Center for Agricultural Research in Dry Areas, Aleppo, Syria.

Veri, Amanda O, Nicole Robbins, and Leah E Cowen. 2018. “Regulation of the Heat Shock Transcription Factor Hsf1 in Fungi: Implications for Temperature-Dependent Virulence Traits.” FEMS Yeast Research 18 (5): foy041. 942 https://doi.org/10.1093/femsyr/foy041.

Wan, A. et al. Virulence characterization of wheat stripe rust fungus Puccinia striiformis f. sp. tritici in Ethiopia and evaluation of Ethiopian wheat germplasm for resistance to races of the pathogen from Ethiopia and the United States. Plant disease 101, 73-80 (2017).

Wang J., Zhang Z., GAPIT Version 3: Boosting Power and Accuracy for Genomic Association and Prediction, Genomics, Proteomics & Bioinformatics (2021), doi: https://doi.org/10.1016/j.gpb.2021.08.005.

Wang, X., Xiang, M., Li, H. et al. High-density mapping of durable and broad-spectrum stripe rust resistance gene Yr30 in wheat. Theor Appl Genet 137, 152 (2024). https://doi.org/10.1007/s00122-024-04654-5

Wang S, Wong D, Forrest K, Allen A, Chao S, Huang BE, Maccaferri M, Salvi S, Milner SG, Cattivelli L, Mastrangelo AM, Whan A, Stephen S, Barker G, Wieseke R, Plieske J, International Wheat Genome Sequencing Consortium, Lillemo M, Mather D, Appels R, Dolferus R, Brown-Guedira G, Korol A, Akhunova AR, Feuillet C, Salse J, Morgante M, Pozniak C, Luo M, Dvorak J, Morell M, Dubcovsky J, Ganal M, Tuberosa R, Lawley C, Mikoulitch I, Cavanagh C, Edwards KJ, Hayden M, Akhunov E (2014) haracterization of polyploid wheat genomic diversity using a high-density 90,000 single nucleotide polymorphism arrayPlant. Biotechnol J. doi:10.1111/pbi.12183

Wang, Shichen, et al. "Characterization of polyploid wheat genomic diversity using a high-density 90 000 single nucleotide polymorphism array." Plant biotechnology journal 12.6 (2014): 787-796.

Wang, Q., Tian, F., Pan, Y., Buckler, E. S. & Zhang, Z. A SUPER powerful method for genome wide association study. PloS one 9, e107684 (2014).

Weiss, Carly V., Jeremy I. Roop, Rylee K. Hackley, Julie N. Chuong, Igor V. 951 Grigoriev, Adam P. Arkin, Jeffrey M. Skerker, and Rachel B. Brem. 2018. “Genetic 952 Dissection of Interspecific Differences in Yeast Thermotolerance.” Nature Genetics 50 953 (11): 1501–4. https://doi.org/10.1038/s41588-018-0243-4

Weng DX, Xu SC, Lin RM, et al. [Microsatellite marker linked with stripe rust resistant gene Yr9 in wheat]. Yi Chuan xue bao = Acta Genetica Sinica. 2005 Sep;32(9):937-941. PMID: 16201237.

Winfield, M.O., Allen, A.M., Burridge, A.J., Barker, G.L.A., Benbow, H.R., Wilkinson, P.A., Coghill, J. et al. (2016) High-density SNP genotyping array for hexaploid wheat and its secondary and tertiary gene pool. Plant Biotechnol. J. 14, 1195–1206.

Uauy, C., Brevis, J. C., Chen, X., Khan, I., Jackson, L., Chicaiza, O., ... & Dubcovsky, J. (2005). High-temperature adult-plant (HTAP) stripe rust resistance gene Yr36 from Triticum turgidum ssp. dicoccoides is closely linked to the grain protein content locus Gpc-B1. Theoretical and Applied Genetics, 112, 97-105.

X. X. Sui, M. N. Wang, and X. M. Chen. Molecular Mapping of a Stripe Rust Resistance Gene in Spring Wheat Cultivar Zak. Phytopathology® 2009 99:10, 1209-1215

Xiang, C., Feng, J. Y., Wang, M. N., Chen, X. M., See, D. R., Wan, A. M., & Wang, T. (2016). Molecular mapping of stripe rust resistance gene Yr76 in winter club wheat cultivar Tyee. Phytopathology, 106(10), 1186-1193.

Xinli Zhou, Xiao Zhong, Jonatan Roter, Xin Li, Qiang Yao, Jiahui Yan, Suizhuang Yang, Qingyun Guo, Assaf Distelfeld, Hanan Sela, and Zhensheng Kang. Genome-Wide Mapping of Loci for Adult-Plant Resistance to Stripe Rust in Durum Wheat Svevo Using the 90K SNP Array Plant Disease 2021 105:4, 879-888

Xu, Y., Li, P., Yang, Z. and Xu, C. (2017) Genetic mapping of quantitative trait loci in crops. Crop J. 5, 175–184.

Xu, L. S., Wang, M. N., Cheng, P., Kang, Z. S., Hulbert, S. H., & Chen, X. M. (2013). Molecular mapping of Yr53, a new gene for stripe rust resistance in durum wheat accession PI 480148 and its transfer to common wheat. Theoretical and Applied Genetics, 126, 523-533.

Xu, L.S., Wang, M.N., Cheng, P. et al. Molecular mapping of Yr53, a new gene for stripe rust resistance in durum wheat accession PI 480148 and its transfer to common wheat. Theor Appl Genet 126, 523–533 (2013). https://doi.org/10.1007/s00122-012-1998-0

Xu Y, Crouch JH, 2008. Marker-assisted selection in plant breeding: from publications to practice. Crop Science, 48: 391-407

Xu S, 1995. A comment on the simple regression method for interval mapping. Genetics, 141: 1657-1659.

Yaakoub, H., Mina, S., Calenda, A., Bouchara, J. P., & Papon, N. (2022). Oxidative stress response pathways in fungi. *Cellular and Molecular Life Sciences*, *79*(6), 333.

Yang, L. N., Ren, M., & Zhan, J. (2023). Modeling plant diseases under climate change: evolutionary perspectives. Trends in Plant Science, 28(5), 519-526.

Yang, N., Ovenden, B., Baxter, B., McDonald, M. C., Solomon, P. S., & Milgate, A. (2022). Multi-stage resistance to Zymoseptoria tritici revealed by GWAS in an Australian bread wheat diversity panel. Frontiers in Plant Science, 13, 990915.

Yang, L. N., Ren, M., & Zhan, J. (2023). Modeling plant diseases under climate change: evolutionary perspectives. *Trends in Plant Science*, *28*(5), 519-526.

Yanmin Qie, Yan Liu, Meinan Wang, Xing Li, Deven R. See, Diaoguo An, and Xianming Chen. Development, Validation, and Re-selection of Wheat Lines with Pyramided Genes Yr64 and Yr15 Linked on the Short Arm of Chromosome 1B for Resistance to Stripe Rust Plant Disease 2019 103:1, 51-58

Yanjun Kou & Shiping Wang (2012), Toward an understanding of the molecular basis of quantitative disease resistance in rice, Journal of Biotechnology, Volume 159, Issue 4,

Yao E., Blake V.C, Cooper L., Wight C.P., Michel S., Cagirici H.B., Lazo G.R., Birkett C.L., Waring D.J., Jannink J.-L., Holmes, I., Waters A.J., Eickholt D.P., Sen, T.Z., "GrainGenes: A Data-Rich Repository for Small Grains Genetics and Genomics", Database, Volume 2022, 2022, baac034, https://doi.org/10.1093/database/baac034

Yin, X., et al. (2019). Climate change and wheat diseases: Impacts and management strategies. Field Crops Research, 240, 37-49.

Yuan, C., Wu, J., Yan, B. et al. Remapping of the stripe rust resistance gene Yr10 in common wheat. Theor Appl Genet 131, 1253–1262 (2018). https://doi.org/10.1007/s00122-018-3075-9

Yu, G., Cui, Y., Jiao, Y., Zhou, K., Wang, X., Yang, W., Xu, Y. et al. (2023) Comparison of sequencing-based and array-based genotyping platforms for genomic prediction of maize hybrid performance. Crop J. 11, 490–498.

Yu, J. et al. A unified mixed-model method for association mapping that accounts for multiple levels of relatedness. Nature genetics 38, 203-208 (2006).

Yufan Wang, Yanling Hu, Fangyi Gong, Yarong Jin, Yingjie Xia, Yu He, Yun Jiang, Qiang Zhou, Jingshu He, Lihua Feng, Guoyue Chen, Youliang Zheng, Dengcai Liu, Lin Huang, and Bihua Wu. Identification and Mapping of QTL for Stripe Rust Resistance in the Chinese Wheat Cultivar Shumai126 Plant Disease 2022 106:4, 1278-1285

Zadoks, J.C., Chang, T.T., & Konzak, C.F. (1974). A decimal code for the growth stages of cereals. Weed Research, 14(6), 415-421. https://doi.org/10.1111/j.1365-3180.1974.tb01084.x

Zakieh, M., Alemu, A., Henriksson, T., Pareek, N., Singh, P. K., & Chawade, A. (2023). Exploring GWAS and genomic prediction to improve Septoria tritici blotch resistance in wheat. Scientific Reports, 13(1), 15651.

Zhan, J., & McDONALD, B. A. (2011). Thermal adaptation in the fungal pathogen Mycosphaerella graminicola. *Molecular Ecology*, *20*(8), 1689-1701.

Zhang, Y., & Ye, A. (2021). Quantitatively distinguishing the impact of climate change and human activities on vegetation in mainland China with the improved residual method. GIScience & Remote Sensing, 58(2), 235-260.Zhang, C. et al. An ancestral NB-LRR with duplicated 3′ UTRs confers stripe rust resistance in wheat and barley. Nature communications 10, 4023 (2019).

Zhang, P. et al. QTL mapping of adult-plant resistance to leaf and stripe rust in wheat cross SW 8588/Thatcher using the wheat 55K SNP array. Plant disease 103, 3041-3049 (2019).

Zhang, L. B., & Feng, M. G. (2018). Antioxidant enzymes and their contributions to biological control potential of fungal insect pathogens. *Applied microbiology and biotechnology*, *102*, 4995-5004.

Zhang X, Han D, Zeng Q, Duan Y, Yuan F, et al. (2013) Fine Mapping of Wheat Stripe Rust Resistance Gene Yr26 Based on Collinearity of Wheat with Brachypodium distachyon and Rice. PLOS ONE 8(3): e57885. https://doi.org/10.1371/journal.pone.0057885

Zhang P, McIntosh RA, Hoxha S, Dong C. Wheat stripe rust resistance genes Yr5 and Yr7 are allelic. Theor Appl Genet. 2009 Dec;120(1):25-9. doi: 10.1007/s00122-009-1156-5. Epub 2009 Sep 18. PMID: 19763533.

ZHENG, J., YAN, Z., ZHAO, L. et al. Molecular mapping of a stripe rust resistance gene in wheat line C51. J Genet 93, 443–450 (2014). https://doi.org/10.1007/s12041-014-0401-0

Zhong, Z., Marcel, T. C., Hartmann, F. E., Ma, X., Plissonneau, C., Zala, M., ... & Palma-Guerrero, J. (2017). A small secreted protein in Zymoseptoria tritici is responsible for avirulence on wheat cultivars carrying the Stb6 resistance gene. *New Phytologist*, *214*(2), 619-631.

Zhou, X. L., Han, D. J., Chen, X. M., Gou, H. L., Guo, S. J., Rong, L., ... & Kang, Z. S. (2014). Characterization and molecular mapping of stripe rust resistance gene Yr61 in winter wheat cultivar Pindong 34. Theoretical and applied genetics, 127, 2349-2358.

Zhou, X.L., Wang, W.L., Wang, L.L. et al. Genetics and molecular mapping of genes for high-temperature resistance to stripe rust in wheat cultivar Xiaoyan 54. Theor Appl Genet 123, 431–438 (2011). https://doi.org/10.1007/s00122-011-1595-7

8 Supplementary Materials

Supplementary table 1 (St1): This supplementary table displays all the QTL projected from the independent mapping studies on Yr resistance in durum wheat available in the literature.

Reference	Collection size	Type of Mapping	Collection composition	Trait	Chr	Start_CI (Mbp)	Middle point (Mbp)	END_CI (Mbp)
Mehrabi et al., 2022	123	GWAS	durum landraces	YR	5B	729.86	730.56	731.26
Mehrabi et al., 2022	123	GWAS	durum landraces	YR	5B	17.94	18.64	19.34
Mehrabi et al., 2022	123	GWAS	durum landraces	YR	2B	194.98	195.68	196.38
Mehrabi et al., 2022	123	GWAS	durum landraces	YR	7A	737.61	738.31	739.01
Mehrabi et al., 2022	123	GWAS	durum landraces	YR	7B	679.48	680.18	680.88
Mehrabi et al., 2022	123	GWAS	durum landraces	YR	5B	730.16	730.86	731.56
Mehrabi et al., 2022	123	GWAS	durum landraces	YR	3B	756.65	757.35	758.05
Mehrabi et al., 2022	123	GWAS	durum landraces	YR	3B	756.65	757.35	758.05
Mehrabi et al., 2022	123	GWAS	durum landraces	YR	2A	55.07	55.77	56.47
Mehrabi et al., 2022	123	GWAS	durum landraces	YR	6A	608.77	609.47	610.17
Mehrabi et al., 2022	123	GWAS	durum landraces	YR	7B	678.53	679.23	679.93
Mehrabi et al., 2022	123	GWAS	durum landraces	YR	7B	678.53	679.23	679.93
Mehrabi et al., 2022	123	GWAS	durum landraces	YR	1B	501.97	502.67	503.37
Mehrabi et al., 2022	123	GWAS	durum landraces	YR	7B	533.02	533.72	534.42
Mehrabi et al., 2022	123	GWAS	durum landraces	YR	7B	533.02	533.72	534.42
Mehrabi et al., 2022	123	GWAS	durum landraces	YR	7B	679.48	680.18	680.88
Mehrabi et al., 2022	123	GWAS	durum landraces	YR	6B	468.58	469.28	469.98
Mehrabi et al., 2022	123	GWAS	durum landraces	YR	6B	137.00	137.70	138.40
Mehrabi et al., 2022	123	GWAS	durum landraces	YR	6B	137.00	137.70	138.40
Mehrabi et al., 2022	123	GWAS	durum landraces	YR	5A	699.91	700.61	701.31
Mehrabi et al., 2022	123	GWAS	durum landraces	YR	5B	17.94	18.64	19.34

Mehrabi et al., 2022	123	GWAS	durum landraces	YR	6B	604.64	605.34	606.04
Mehrabi et al., 2022	123	GWAS	durum landraces	YR	2A	91.31	92.01	92.71
Mehrabi et al., 2022	123	GWAS	durum landraces	YR	7B	24.20	24.90	25.60
Mehrabi et al., 2022	123	GWAS	durum landraces	YR	2A	94.57	95.27	95.97
Mehrabi et al., 2022	123	GWAS	durum landraces	YR	6A	608.77	609.47	610.17
Mehrabi et al., 2022	123	GWAS	durum landraces	YR	7B	748.21	748.91	749.61
Mehrabi et al., 2022	123	GWAS	durum landraces	YR	1A	160.27	160.97	161.67
Mehrabi et al., 2022	123	GWAS	durum landraces	YR	7A	29.94	30.64	31.34
Mehrabi et al., 2022	123	GWAS	durum landraces	YR	5B	551.86	552.56	553.26
Mehrabi et al., 2022	123	GWAS	durum landraces	YR	7B	539.86	540.56	541.26
Mehrabi et al., 2022	123	GWAS	durum landraces	YR	7B	539.86	540.56	541.26
Mehrabi et al., 2022	123	GWAS	durum landraces	YR	7B	538.03	538.73	539.43
Mehrabi et al., 2022	123	GWAS	durum landraces	YR	7B	533.35	534.05	534.75
Mehrabi et al., 2022	123	GWAS	durum landraces	YR	5A	494.04	494.74	495.44
Mehrabi et al., 2022	123	GWAS	durum landraces	YR	6A	608.77	609.47	610.17
Mehrabi et al., 2022	123	GWAS	durum landraces	YR	4B	24.05	24.75	25.45
Mehrabi et al., 2022	123	GWAS	durum landraces	YR	6A	608.77	609.47	610.17
Mehrabi et al., 2022	123	GWAS	durum landraces	YR	6B	587.82	588.52	589.22
Mehrabi et al., 2022	123	GWAS	durum landraces	YR	1B	676.30	677.00	677.70
Mehrabi et al., 2022	123	GWAS	durum landraces	YR	1B	676.30	677.00	677.70
Mehrabi et al., 2022	123	GWAS	durum landraces	YR	1B	676.31	677.01	677.71
Mehrabi et al., 2022	123	GWAS	durum landraces	YR	1B	676.50	677.20	677.90
Mehrabi et al., 2022	123	GWAS	durum landraces	YR	4A	99.54	100.24	100.94
Mehrabi et al., 2022	123	GWAS	durum landraces	YR	4A	99.54	100.24	100.94
Mehrabi et al., 2022	123	GWAS	durum landraces	YR	4A	100.38	101.08	101.78
Mehrabi et al., 2022	123	GWAS	durum landraces	YR	6A	55.97	56.67	57.37
Mehrabi et al., 2022	123	GWAS	durum landraces	YR	6A	608.77	609.47	610.17
Mehrabi et al., 2022	123	GWAS	durum landraces	YR	5A	699.91	700.61	701.31
Mehrabi et al., 2022	123	GWAS	durum landraces	YR	2A	92.85	93.55	94.25
Mehrabi et al., 2022	123	GWAS	durum landraces	YR	2A	91.31	92.01	92.71

Mehrabi et al., 2022	123	GWAS	durum landraces	YR	2A	90.78	91.48	92.18
Mehrabi et al., 2022	123	GWAS	durum landraces	YR	5B	721.14	721.84	722.54
Mehrabi et al., 2022	123	GWAS	durum landraces	YR	1B	676.30	677.00	677.70
Mehrabi et al., 2022	123	GWAS	durum landraces	YR	1B	676.30	677.00	677.70
Mehrabi et al., 2022	123	GWAS	durum landraces	YR	1B	676.31	677.01	677.71
Mehrabi et al., 2022	123	GWAS	durum landraces	YR	1B	676.50	677.20	677.90
Mehrabi et al., 2022	123	GWAS	durum landraces	YR	3B	752.71	753.41	754.11
Mehrabi et al., 2022	123	GWAS	durum landraces	YR	6B	138.24	138.94	139.64
Mehrabi et al., 2022	123	GWAS	durum landraces	YR	4A	583.30	584.00	584.70
Mehrabi et al., 2022	123	GWAS	durum landraces	YR	1A	502.53	503.23	503.93
Mehrabi et al., 2022	123	GWAS	durum landraces	YR	6A	608.77	609.47	610.17
Mehrabi et al., 2022	123	GWAS	durum landraces	YR	2B	216.41	217.11	217.81
Mehrabi et al., 2022	123	GWAS	durum landraces	YR	3B	751.37	752.07	752.77
Mehrabi et al., 2022	123	GWAS	durum landraces	YR	6B	140.48	141.18	141.88
Mehrabi et al., 2022	123	GWAS	durum landraces	YR	6B	141.72	142.42	143.12
Mehrabi et al., 2022	123	GWAS	durum landraces	YR	6B	461.22	461.92	462.62
Mehrabi et al., 2022	123	GWAS	durum landraces	YR	3B	757.59	758.29	758.99
Mehrabi et al., 2022	123	GWAS	durum landraces	YR	5A	493.79	494.49	495.19
Mehrabi et al., 2022	123	GWAS	durum landraces	YR	5A	494.04	494.74	495.44
Mehrabi et al., 2022	123	GWAS	durum landraces	YR	5A	493.79	494.49	495.19
Mehrabi et al., 2022	123	GWAS	durum landraces	YR	5A	493.79	494.49	495.19
Mehrabi et al., 2022	123	GWAS	durum landraces	YR	6B	28.96	29.66	30.36
Mehrabi et al., 2022	123	GWAS	durum landraces	YR	6A	608.77	609.47	610.17
Mehrabi et al., 2022	123	GWAS	durum landraces	YR	6A	608.77	609.47	610.17
Mehrabi et al., 2022	123	GWAS	durum landraces	YR	1A	349.92	350.62	351.32
Mehrabi et al., 2022	123	GWAS	durum landraces	YR	1A	349.36	350.06	350.76
Mehrabi et al., 2022	123	GWAS	durum landraces	YR	3B	267.98	268.68	269.38
Mehrabi et al., 2022	123	GWAS	durum landraces	YR	1A	351.53	352.23	352.93
Mehrabi et al., 2022	123	GWAS	durum landraces	YR	1A	350.85	351.55	352.25
Mehrabi et al., 2022	123	GWAS	durum landraces	YR	1A	350.16	350.86	351.56

Mehrabi et al., 2022	123	GWAS	durum landraces	YR	5A	494.04	494.74	495.44
Mehrabi et al., 2022	123	GWAS	durum landraces	YR	7B	678.53	679.23	679.93
Mehrabi et al., 2022	123	GWAS	durum landraces	YR	7B	678.53	679.23	679.93
Mehrabi et al., 2022	123	GWAS	durum landraces	YR	7B	739.87	740.57	741.27
Mehrabi et al., 2022	123	GWAS	durum landraces	YR	2B	22.96	23.66	24.36
Mehrabi et al., 2022	123	GWAS	durum landraces	YR	2B	194.98	195.68	196.38
Mehrabi et al., 2022	123	GWAS	durum landraces	YR	6B	602.63	603.33	604.03
Mehrabi et al., 2022	123	GWAS	durum landraces	YR	2A	95.32	96.02	96.72
Mehrabi et al., 2022	123	GWAS	durum landraces	YR	4A	730.27	730.97	731.67
Mehrabi et al., 2022	123	GWAS	durum landraces	YR	2B	190.71	191.41	192.11
Mehrabi et al., 2022	123	GWAS	durum landraces	YR	4A	36.49	37.19	37.89
Mehrabi et al., 2022	123	GWAS	durum landraces	YR	7B	740.12	740.82	741.52
Mehrabi et al., 2022	123	GWAS	durum landraces	YR	4B	15.90	16.60	17.30
Mehrabi et al., 2022	123	GWAS	durum landraces	YR	4B	15.90	16.60	17.30
Mehrabi et al., 2022	123	GWAS	durum landraces	YR	4B	15.90	16.60	17.30
Mehrabi et al., 2022	123	GWAS	durum landraces	YR	5A	681.53	682.23	682.93
Mehrabi et al., 2022	123	GWAS	durum landraces	YR	7B	740.14	740.84	741.54
Mehrabi et al., 2022	123	GWAS	durum landraces	YR	4A	725.51	726.21	726.91
Mehrabi et al., 2022	123	GWAS	durum landraces	YR	3B	445.67	446.37	447.07
Mehrabi et al., 2022	123	GWAS	durum landraces	YR	5B	632.35	633.05	633.75
Mehrabi et al., 2022	123	GWAS	durum landraces	YR	4A	730.27	730.97	731.67
Mehrabi et al., 2022	123	GWAS	durum landraces	YR	4A	730.27	730.97	731.67
Mehrabi et al., 2022	123	GWAS	durum landraces	YR	4A	730.27	730.97	731.67
Mehrabi et al., 2022	123	GWAS	durum landraces	YR	3B	440.04	440.74	441.44
Mehrabi et al., 2022	123	GWAS	durum landraces	YR	7A	1.51	2.21	2.91
Mehrabi et al., 2022	123	GWAS	durum landraces	YR	3B	445.33	446.03	446.73
Mehrabi et al., 2022	123	GWAS	durum landraces	YR	2A	695.94	696.64	697.34
Mehrabi et al., 2022	123	GWAS	durum landraces	YR	4A	730.27	730.97	731.67
Mehrabi et al., 2022	123	GWAS	durum landraces	YR	5B	714.95	715.65	716.35
Mehrabi et al., 2022	123	GWAS	durum landraces	YR	1A	351.53	352.23	352.93

Mehrabi et al., 2022	123	GWAS	durum landraces	YR	1A	350.85	351.55	352.25
Mehrabi et al., 2022	123	GWAS	durum landraces	YR	1A	350.16	350.86	351.56
Mehrabi et al., 2022	123	GWAS	durum landraces	YR	1A	349.92	350.62	351.32
Mehrabi et al., 2022	123	GWAS	durum landraces	YR	1A	349.36	350.06	350.76
Mehrabi et al., 2022	123	GWAS	durum landraces	YR	6B	89.70	90.40	91.10
Mehrabi et al., 2022	123	GWAS	durum landraces	YR	6B	105.32	106.02	106.72
Mehrabi et al., 2022	123	GWAS	durum landraces	YR	4A	99.54	100.24	100.94
Mehrabi et al., 2022	123	GWAS	durum landraces	YR	4A	99.54	100.24	100.94
Mehrabi et al., 2022	123	GWAS	durum landraces	YR	4A	100.38	101.08	101.78
Mehrabi et al., 2022	123	GWAS	durum landraces	YR	5B	632.35	633.05	633.75
Mehrabi et al., 2022	123	GWAS	durum landraces	YR	6B	467.75	468.45	469.15
Mehrabi et al., 2022	123	GWAS	durum landraces	YR	6B	467.68	468.38	469.08
Mehrabi et al., 2022	123	GWAS	durum landraces	YR	6B	602.63	603.33	604.03
Mehrabi et al., 2022	123	GWAS	durum landraces	YR	4A	2.66	3.36	4.06
Mehrabi et al., 2022	123	GWAS	durum landraces	YR	4A	2.67	3.37	4.07
Mehrabi et al., 2022	123	GWAS	durum landraces	YR	5B	462.22	462.92	463.62
Mehrabi et al., 2022	123	GWAS	durum landraces	YR	4A	730.27	730.97	731.67
Mehrabi et al., 2022	123	GWAS	durum landraces	YR	4B	447.25	447.95	448.65
Mehrabi et al., 2022	123	GWAS	durum landraces	YR	6B	477.33	478.03	478.73
Mehrabi et al., 2022	123	GWAS	durum landraces	YR	6B	477.25	477.95	478.65
Mehrabi et al., 2022	123	GWAS	durum landraces	YR	6B	477.19	477.89	478.59
Mehrabi et al., 2022	123	GWAS	durum landraces	YR	6B	477.27	477.97	478.67
Mehrabi et al., 2022	123	GWAS	durum landraces	YR	6B	190.05	190.75	191.45
Mehrabi et al., 2022	123	GWAS	durum landraces	YR	6B	190.05	190.75	191.45
Mehrabi et al., 2022	123	GWAS	durum landraces	YR	3B	773.06	773.76	774.46
Mehrabi et al., 2022	123	GWAS	durum landraces	YR	6B	604.64	605.34	606.04
Mehrabi et al., 2022	123	GWAS	durum landraces	YR	3B	268.68	269.38	270.08
Mehrabi et al., 2022	123	GWAS	durum landraces	YR	7B	653.83	654.53	655.23
Mehrabi et al., 2022	123	GWAS	durum landraces	YR	7B	653.83	654.53	655.23
Mehrabi et al., 2022	123	GWAS	durum landraces	YR	5B	724.83	725.53	726.23

Mehrabi et al., 2022	123	GWAS	durum landraces	YR	7A	69.86	70.56	71.26
Mehrabi et al., 2022	123	GWAS	durum landraces	YR	1B	689.79	690.49	691.19
Mehrabi et al., 2022	123	GWAS	durum landraces	YR	4A	725.50	726.20	726.90
Mehrabi et al., 2022	123	GWAS	durum landraces	YR	1A	314.62	315.32	316.02
Mehrabi et al., 2022	123	GWAS	durum landraces	YR	7B	731.09	731.79	732.49
Mehrabi et al., 2022	123	GWAS	durum landraces	YR	7B	731.08	731.78	732.48
Mehrabi et al., 2022	123	GWAS	durum landraces	YR	4A	741.15	741.85	742.55
Mehrabi et al., 2022	123	GWAS	durum landraces	YR	4A	583.30	584.00	584.70
Mehrabi et al., 2022	123	GWAS	durum landraces	YR	4A	99.50	100.20	100.90
Mehrabi et al., 2022	123	GWAS	durum landraces	YR	7B	653.83	654.53	655.23
Mehrabi et al., 2022	123	GWAS	durum landraces	YR	3B	67.27	67.97	68.67
Mehrabi et al., 2022	123	GWAS	durum landraces	YR	5B	712.90	713.60	714.30
Mehrabi et al., 2022	123	GWAS	durum landraces	YR	7B	599.04	599.74	600.44
Mehrabi et al., 2022	123	GWAS	durum landraces	YR	1B	501.97	502.67	503.37
Mehrabi et al., 2022	123	GWAS	durum landraces	YR	3B	833.02	833.72	834.42
Mehrabi et al., 2022	123	GWAS	durum landraces	YR	5B	722.80	723.50	724.20
Mehrabi et al., 2022	123	GWAS	durum landraces	YR	5B	722.80	723.50	724.20
Mehrabi et al., 2022	123	GWAS	durum landraces	YR	1A	350.85	351.55	352.25
Mehrabi et al., 2022	123	GWAS	durum landraces	YR	1A	349.36	350.06	350.76
Mehrabi et al., 2022	123	GWAS	durum landraces	YR	7A	108.65	109.35	110.05
Mehrabi et al., 2022	123	GWAS	durum landraces	YR	3B	775.03	775.73	776.43
Mehrabi et al., 2022	123	GWAS	durum landraces	YR	7B	740.12	740.82	741.52
Mehrabi et al., 2022	123	GWAS	durum landraces	YR	3B	440.04	440.74	441.44
Mehrabi et al., 2022	123	GWAS	durum landraces	YR	3B	440.04	440.74	441.44
Mehrabi et al., 2022	123	GWAS	durum landraces	YR	5B	511.75	512.45	513.15
Mehrabi et al., 2022	123	GWAS	durum landraces	YR	1B	656.44	657.14	657.84
Mehrabi et al., 2022	123	GWAS	durum landraces	YR	1A	307.45	308.15	308.85
Mehrabi et al., 2022	123	GWAS	durum landraces	YR	1A	309.78	310.48	311.18
Mehrabi et al., 2022	123	GWAS	durum landraces	YR	1A	308.33	309.03	309.73
Mehrabi et al., 2022	123	GWAS	durum landraces	YR	1A	307.53	308.23	308.93

Mehrabi et al., 2022	123	GWAS	durum landraces	YR	1A	306.85	307.55	308.25
Mehrabi et al., 2022	123	GWAS	durum landraces	YR	1A	309.59	310.29	310.99
Mehrabi et al., 2022	123	GWAS	durum landraces	YR	1A	314.89	315.59	316.29
Mehrabi et al., 2022	123	GWAS	durum landraces	YR	6B	22.81	23.51	24.21
Mehrabi et al., 2022	123	GWAS	durum landraces	YR	4B	15.90	16.60	17.30
Mehrabi et al., 2022	123	GWAS	durum landraces	YR	4B	15.90	16.60	17.30
Mehrabi et al., 2022	123	GWAS	durum landraces	YR	3B	656.01	656.71	657.41
Mehrabi et al., 2022	123	GWAS	durum landraces	YR	6B	154.86	155.56	156.26
Mehrabi et al., 2022	123	GWAS	durum landraces	YR	6B	154.86	155.56	156.26
Mehrabi et al., 2022	123	GWAS	durum landraces	YR	7B	642.81	643.51	644.21
Mehrabi et al., 2022	123	GWAS	durum landraces	YR	3B	51.77	52.47	53.17
Mehrabi et al., 2022	123	GWAS	durum landraces	YR	3B	51.78	52.48	53.18
Mehrabi et al., 2022	123	GWAS	durum landraces	YR	7B	47.15	47.85	48.55
Mehrabi et al., 2022	123	GWAS	durum landraces	YR	6B	587.82	588.52	589.22
Mehrabi et al., 2022	123	GWAS	durum landraces	YR	5A	454.20	454.90	455.60
Liu et al., 2017d	182	GWAS	Ethiopian durum wheat landraces	YR	1A	13.44	14.14	14.84
Liu et al., 2017d	182	GWAS	Ethiopian durum wheat landraces	YR	1A	16.75	17.45	18.15
Liu et al., 2017d	182	GWAS	Ethiopian durum wheat landraces	YR	1A	32.76	33.46	34.16
Liu et al., 2017d	182	GWAS	Ethiopian durum wheat landraces	YR	1A	248.17	248.87	249.57
Liu et al., 2017d	182	GWAS	Ethiopian durum wheat landraces	YR	1A	513.38	514.08	514.78
Liu et al., 2017d	182	GWAS	Ethiopian durum wheat landraces	YR	1A	524.45	525.15	525.85
Liu et al., 2017d	182	GWAS	Ethiopian durum wheat landraces	YR	1A	552.88	553.58	554.28
Liu et al., 2017d	182	GWAS	Ethiopian durum wheat landraces	YR	1A	573.87	574.57	575.27
Liu et al., 2017d	182	GWAS	Ethiopian durum wheat landraces	YR	1B	9.80	10.50	11.20
Liu et al., 2017d	182	GWAS	Ethiopian durum wheat landraces	YR	1B	335.15	335.85	336.55

Liu et al., 2017d	182	GWAS	Ethiopian durum wheat landraces	YR	1B	499.52	500.22	500.92
Liu et al., 2017d	182	GWAS	Ethiopian durum wheat landraces	YR	1B	578.18	578.88	579.58
Liu et al., 2017d	182	GWAS	Ethiopian durum wheat landraces	YR	1B	629.08	629.78	630.48
Liu et al., 2017d	182	GWAS	Ethiopian durum wheat landraces	YR	1B	629.71	630.41	631.11
Liu et al., 2017d	182	GWAS	Ethiopian durum wheat landraces	YR	1B	646.86	647.56	648.26
Liu et al., 2017d	182	GWAS	Ethiopian durum wheat landraces	YR	1B	659.00	659.70	660.40
Liu et al., 2017d	182	GWAS	Ethiopian durum wheat landraces	YR	1B	672.50	673.20	673.90
Liu et al., 2017d	182	GWAS	Ethiopian durum wheat landraces	YR	2A	515.60	516.30	517.00
Liu et al., 2017d	182	GWAS	Ethiopian durum wheat landraces	YR	2A	734.12	734.82	735.52
Liu et al., 2017d	182	GWAS	Ethiopian durum wheat landraces	YR	2A	767.85	768.55	769.25
Liu et al., 2017d	182	GWAS	Ethiopian durum wheat landraces	YR	2B	13.86	14.56	15.26
Liu et al., 2017d	182	GWAS	Ethiopian durum wheat landraces	YR	2B	22.15	22.85	23.55
Liu et al., 2017d	182	GWAS	Ethiopian durum wheat landraces	YR	2B	29.03	29.73	30.43
Liu et al., 2017d	182	GWAS	Ethiopian durum wheat landraces	YR	2B	34.06	34.76	35.46
Liu et al., 2017d	182	GWAS	Ethiopian durum wheat landraces	YR	2B	174.89	175.59	176.29
Liu et al., 2017d	182	GWAS	Ethiopian durum wheat landraces	YR	2B	193.76	194.46	195.16
Liu et al., 2017d	182	GWAS	Ethiopian durum wheat landraces	YR	2B	497.00	497.70	498.40
Liu et al., 2017d	182	GWAS	Ethiopian durum wheat landraces	YR	2B	567.02	567.72	568.42
Liu et al., 2017d	182	GWAS	Ethiopian durum wheat landraces	YR	2B	745.02	745.72	746.42
Liu et al., 2017d	182	GWAS	Ethiopian durum wheat landraces	YR	2B	778.73	779.43	780.13

Liu et al., 2017d	182	GWAS	Ethiopian durum wheat landraces	YR	2B	782.18	782.88	783.58
Liu et al., 2017d	182	GWAS	Ethiopian durum wheat landraces	YR	3A	40.55	41.25	41.95
Liu et al., 2017d	182	GWAS	Ethiopian durum wheat landraces	YR	3A	721.24	721.94	722.64
Liu et al., 2017d	182	GWAS	Ethiopian durum wheat landraces	YR	3A	730.12	730.82	731.52
Liu et al., 2017d	182	GWAS	Ethiopian durum wheat landraces	YR	3B	6.05	6.75	7.45
Liu et al., 2017d	182	GWAS	Ethiopian durum wheat landraces	YR	3B	32.94	33.64	34.34
Liu et al., 2017d	182	GWAS	Ethiopian durum wheat landraces	YR	3B	33.86	34.56	35.26
Liu et al., 2017d	182	GWAS	Ethiopian durum wheat landraces	YR	3B	658.42	659.12	659.82
Liu et al., 2017d	182	GWAS	Ethiopian durum wheat landraces	YR	3B	827.48	828.18	828.88
Liu et al., 2017d	182	GWAS	Ethiopian durum wheat landraces	YR	4A	6.40	7.10	7.80
Liu et al., 2017d	182	GWAS	Ethiopian durum wheat landraces	YR	4A	16.16	16.86	17.56
Liu et al., 2017d	182	GWAS	Ethiopian durum wheat landraces	YR	4A	39.00	39.70	40.40
Liu et al., 2017d	182	GWAS	Ethiopian durum wheat landraces	YR	4A	46.24	46.94	47.64
Liu et al., 2017d	182	GWAS	Ethiopian durum wheat landraces	YR	4A	86.38	87.08	87.78
Liu et al., 2017d	182	GWAS	Ethiopian durum wheat landraces	YR	4A	758.88	759.58	760.28
Liu et al., 2017d	182	GWAS	Ethiopian durum wheat landraces	YR	4B	0.68	1.38	2.08
Liu et al., 2017d	182	GWAS	Ethiopian durum wheat landraces	YR	4B	61.07	61.77	62.47
Liu et al., 2017d	182	GWAS	Ethiopian durum wheat landraces	YR	4B	98.29	98.99	99.69
Liu et al., 2017d	182	GWAS	Ethiopian durum wheat landraces	YR	4B	539.30	540.00	540.70
Liu et al., 2017d	182	GWAS	Ethiopian durum wheat landraces	YR	4B	554.25	554.95	555.65

Liu et al., 2017d	182	GWAS	Ethiopian durum wheat landraces	YR	4B	598.89	599.59	600.29
Liu et al., 2017d	182	GWAS	Ethiopian durum wheat landraces	YR	4B	658.18	658.88	659.58
Liu et al., 2017d	182	GWAS	Ethiopian durum wheat landraces	YR	4B	674.54	675.24	675.94
Liu et al., 2017d	182	GWAS	Ethiopian durum wheat landraces	YR	4B	683.33	684.03	684.73
Liu et al., 2017d	182	GWAS	Ethiopian durum wheat landraces	YR	4B	686.14	686.84	687.54
Liu et al., 2017d	182	GWAS	Ethiopian durum wheat landraces	YR	5A	22.98	23.68	24.38
Liu et al., 2017d	182	GWAS	Ethiopian durum wheat landraces	YR	5A	90.31	91.01	91.71
Liu et al., 2017d	182	GWAS	Ethiopian durum wheat landraces	YR	5A	479.63	480.33	481.03
Liu et al., 2017d	182	GWAS	Ethiopian durum wheat landraces	YR	5A	519.89	520.59	521.29
Liu et al., 2017d	182	GWAS	Ethiopian durum wheat landraces	YR	5A	570.92	571.62	572.32
Liu et al., 2017d	182	GWAS	Ethiopian durum wheat landraces	YR	5B	461.87	462.57	463.27
Liu et al., 2017d	182	GWAS	Ethiopian durum wheat landraces	YR	5B	517.27	517.97	518.67
Liu et al., 2017d	182	GWAS	Ethiopian durum wheat landraces	YR	5B	594.00	594.70	595.40
Liu et al., 2017d	182	GWAS	Ethiopian durum wheat landraces	YR	5B	682.48	683.18	683.88
Liu et al., 2017d	182	GWAS	Ethiopian durum wheat landraces	YR	5B	735.81	736.51	737.21
Liu et al., 2017d	182	GWAS	Ethiopian durum wheat landraces	YR	6A	15.64	16.34	17.04
Liu et al., 2017d	182	GWAS	Ethiopian durum wheat landraces	YR	6A	56.03	56.73	57.43
Liu et al., 2017d	182	GWAS	Ethiopian durum wheat landraces	YR	6B	243.71	244.41	245.11
Liu et al., 2017d	182	GWAS	Ethiopian durum wheat landraces	YR	6B	712.71	713.41	714.11
Liu et al., 2017d	182	GWAS	Ethiopian durum wheat landraces	YR	6B	736.37	737.07	737.77

Liu et al., 2017d	182	GWAS	Ethiopian durum wheat landraces	YR	7A	19.55	20.25	20.95
Liu et al., 2017d	182	GWAS	Ethiopian durum wheat landraces	YR	7A	182.07	182.77	183.47
Liu et al., 2017d	182	GWAS	Ethiopian durum wheat landraces	YR	7B	12.64	13.34	14.04
Liu et al., 2017d	182	GWAS	Ethiopian durum wheat landraces	YR	7B	24.54	25.24	25.94
Liu et al., 2017d	182	GWAS	Ethiopian durum wheat landraces	YR	7B	525.36	526.06	526.76
Liu et al., 2017d	182	GWAS	Ethiopian durum wheat landraces	YR	7B	584.10	584.80	585.50
Liu et al., 2017d	182	GWAS	Ethiopian durum wheat landraces	YR	7B	604.42	605.12	605.82
Liu et al., 2017d	182	GWAS	Ethiopian durum wheat landraces	YR	7B	633.01	633.71	634.41
Liu et al., 2017d	182	GWAS	Ethiopian durum wheat landraces	YR	7B	704.86	705.56	706.26
Liu et al., 2017d	182	GWAS	Ethiopian durum wheat landraces	YR	7B	716.18	716.88	717.58
Liu et al., 2017c	176	GWAS	Dicoccum accessions	YR	1A	245.07	245.57	246.07
Liu et al., 2017c	176	GWAS	Dicoccum accessions	YR	1A	521.61	522.11	522.61
Liu et al., 2017c	176	GWAS	Dicoccum accessions	YR	1B	326.43	326.93	327.43
Liu et al., 2017c	176	GWAS	Dicoccum accessions	YR	1B	577.66	578.16	578.66
Liu et al., 2017c	176	GWAS	Dicoccum accessions	YR	2A	734.32	734.82	735.32
Liu et al., 2017c	176	GWAS	Dicoccum accessions	YR	2B	37.91	38.41	38.91
Liu et al., 2017c	176	GWAS	Dicoccum accessions	YR	2B	707.58	708.08	708.58
Liu et al., 2017c	176	GWAS	Dicoccum accessions	YR	2B	777.61	778.11	778.61
Liu et al., 2017c	176	GWAS	Dicoccum accessions	YR	3A	644.75	645.25	645.75
Liu et al., 2017c	176	GWAS	Dicoccum accessions	YR	3B	507.76	508.26	508.76
Liu et al., 2017c	176	GWAS	Dicoccum accessions	YR	3B	582.79	583.29	583.79
Liu et al., 2017c	176	GWAS	Dicoccum accessions	YR	3B	630.21	630.71	631.21
Liu et al., 2017c	176	GWAS	Dicoccum accessions	YR	3B	827.57	828.07	828.57
Liu et al., 2017c	176	GWAS	Dicoccum accessions	YR	4A	28.12	28.62	29.12
Liu et al., 2017c	176	GWAS	Dicoccum accessions	YR	4A	751.29	751.79	752.29

Liu et al., 2017c	176	GWAS	Dicoccum accessions	YR	4B	34.98	35.48	35.98
Liu et al., 2017c	176	GWAS	Dicoccum accessions	YR	4B	587.82	588.32	588.82
Liu et al., 2017c	176	GWAS	Dicoccum accessions	YR	4B	690.90	691.40	691.90
Liu et al., 2017c	176	GWAS	Dicoccum accessions	YR	5A	447.65	448.15	448.65
Liu et al., 2017c	176	GWAS	Dicoccum accessions	YR	5A	596.32	596.82	597.32
Liu et al., 2017c	176	GWAS	Dicoccum accessions	YR	5A	675.10	675.60	676.10
Liu et al., 2017c	176	GWAS	Dicoccum accessions	YR	5B	73.20	73.70	74.20
Liu et al., 2017c	176	GWAS	Dicoccum accessions	YR	5B	357.12	357.62	358.12
Liu et al., 2017c	176	GWAS	Dicoccum accessions	YR	5B	511.04	511.54	512.04
Liu et al., 2017c	176	GWAS	Dicoccum accessions	YR	5B	609.11	609.61	610.11
Liu et al., 2017c	176	GWAS	Dicoccum accessions	YR	6A	28.73	29.23	29.73
Liu et al., 2017c	176	GWAS	Dicoccum accessions	YR	6A	585.36	585.86	586.36
Liu et al., 2017c	176	GWAS	Dicoccum accessions	YR	6A	607.79	608.29	608.79
Liu et al., 2017c	176	GWAS	Dicoccum accessions	YR	6A	618.60	619.10	619.60
Liu et al., 2017c	176	GWAS	Dicoccum accessions	YR	6B	226.93	227.43	227.93
Liu et al., 2017c	176	GWAS	Dicoccum accessions	YR	6B	477.45	477.95	478.45
Liu et al., 2017c	176	GWAS	Dicoccum accessions	YR	7A	13.96	14.46	14.96
Liu et al., 2017c	176	GWAS	Dicoccum accessions	YR	7A	526.57	527.07	527.57
Liu et al., 2017c	176	GWAS	Dicoccum accessions	YR	7A	608.38	608.88	609.38
Liu et al., 2017c	176	GWAS	Dicoccum accessions	YR	7B	47.35	47.85	48.35
Liu et al., 2017c	176	GWAS	Dicoccum accessions	YR	7B	135.99	136.49	136.99
Liu et al., 2017c	176	GWAS	Dicoccum accessions	YR	7B	504.64	505.14	505.64
Liu et al., 2017b	250	GWAS	elite durum cv	YR	1B	333.89	335.39	336.89
Liu et al., 2017b	250	GWAS	elite durum cv	YR	1B	370.47	371.97	373.47
Liu et al., 2017b	250	GWAS	elite durum cv	YR	2A	17.66	19.16	20.66
Liu et al., 2017b	250	GWAS	elite durum cv	YR	2A	396.53	398.03	399.53
Liu et al., 2017b	250	GWAS	elite durum cv	YR	2B	31.24	32.74	34.24
Liu et al., 2017b	250	GWAS	elite durum cv	YR	3B	847.68	849.18	850.68
Liu et al., 2017b	250	GWAS	elite durum cv	YR	4A	22.55	24.05	25.55
Liu et al., 2017b	250	GWAS	elite durum cv	YR	4B	111.77	113.27	114.77

Liu et al., 2017b	250	GWAS	elite durum cv	YR	5B	720.41	721.91	723.41
Liu et al., 2017b	250	GWAS	elite durum cv	YR	6B	587.89	589.39	590.89
Liu et al., 2017b	250	GWAS	elite durum cv	YR	7A	49.66	51.16	52.66
Liu et al., 2017b	250	GWAS	elite durum cv	YR	7A	67.39	68.89	70.39
Liu et al., 2017b	250	GWAS	elite durum cv	YR	7A	123.59	125.09	126.59
Liu et al., 2017b	250	GWAS	elite durum cv	YR	7A	745.92	747.42	748.92
Liu et al., 2017b	250	GWAS	elite durum cv	YR	7B	563.33	564.83	566.33
Liu et al., 2017b	250	GWAS	elite durum cv	YR	7B	715.38	716.88	718.38
Aoun et al., (2021)	248	GWAS	durum wheat cultivar	YR	5B	718.07	719.57	721.07
Aoun et al., (2021)	248	GWAS	durum wheat cultivar	YR	7B	714.75	716.25	717.75
Aoun et al., (2021)	248	GWAS	durum wheat cultivar	YR	1B	99.54	101.04	102.54
Aoun et al., (2021)	248	GWAS	durum wheat cultivar	YR	5B	729.36	730.86	732.36
Miedaner et al., (2019)	328	GWAS	durum wheat cultivar	YR	3A	4.70	6.20	7.70
Miedaner et al., (2019)	328	GWAS	durum wheat cultivar	YR	3A	21.34	22.84	24.34
Miedaner et al., (2019)	328	GWAS	durum wheat cultivar	YR	3A	736.88	738.38	739.88
Miedaner et al., (2019)	328	GWAS	durum wheat cultivar	YR	1B	2.00	3.50	5.00
Miedaner et al., (2019)	328	GWAS	durum wheat cultivar	YR	4A	769.88	771.38	772.88
Miedaner et al., (2019)	328	GWAS	durum wheat cultivar	YR	2B	567.61	569.11	570.61
Marone et al., (2024)	230	GWAS	Q2	YR	5B	562.71	564.21	565.71
Marone et al., (2024)	230	GWAS	WC	YR	5B	565.92	567.42	568.92
Marone et al., (2024)	230	GWAS	Q2	YR	7A	73.24	74.74	76.24
Alemu et al., 2021	300	GWAS	landraces, cultivars	YR	1B	336.62	338.12	339.62
Alemu et al., 2021	300	GWAS	landraces, cultivars	YR	2B	103.58	105.08	106.58
Alemu et al., 2021	300	GWAS	landraces, cultivars	YR	1A	357.75	359.25	360.75
Alemu et al., 2021	300	GWAS	landraces, cultivars	YR	5A	12.38	13.88	15.38
Array. Zhou X L et al., (2021)	137	Linkage Map	RILs	YR	1AL	518.70	531.34	561.61
Array. Zhou X L et al., (2021)	137	Linkage Map	RILs	YR	1AL	512.87	531.34	560.27
Array. Zhou X L et al., (2021)	137	Linkage Map	RILs	YR	1AL	520.69	531.34	562.26

Array. Zhou X L et al., (2021)	137	Linkage Map	RILs	YR	1AL	514.15	531.34	561.65
Array. Zhou X L et al., (2021)	137	Linkage Map	RILs	YR	1BL	660.37	662.17	666.64
Array. Zhou X L et al., (2021)	137	Linkage Map	RILs	YR	1BL	660.37	662.17	666.64
Array. Zhou X L et al., (2021)	137	Linkage Map	RILs	YR	1BL	660.37	662.17	666.40
Array. Zhou X L et al., (2021)	137	Linkage Map	RILs	YR	1BL	661.20	662.17	666.64
Array. Zhou X L et al., (2021)	137	Linkage Map	RILs	YR	1BL	661.20	662.17	666.64
Array. Zhou X L et al., (2021)	137	Linkage Map	RILs	YR	1BL	661.20	662.17	670.27
Array. Zhou X L et al., (2021)	137	Linkage Map	RILs	YR	1BL	661.20	662.17	670.27
Array. Zhou X L et al., (2021)	137	Linkage Map	RILs	YR	1BL	661.20	662.17	668.93
Array. Zhou X L et al., (2021)	137	Linkage Map	RILs	YR	1BL	661.20	662.17	668.93
Array. Zhou X L et al., (2021)	137	Linkage Map	RILs	YR	1BL	661.20	662.17	666.69
Array. Zhou X L et al., (2021)	137	Linkage Map	RILs	YR	1BL	661.20	662.17	666.69
Array. Zhou X L et al., (2021)	137	Linkage Map	RILs	YR	1BL	660.37	662.17	666.64
Array. Zhou X L et al., (2021)	137	Linkage Map	RILs	YR	1BL	661.20	662.17	666.64
Array. Zhou X L et al., (2021)	137	Linkage Map	RILs	YR	1BL	661.20	662.17	666.64
Array. Zhou X L et al., (2021)	137	Linkage Map	RILs	YR	1BL	661.20	662.17	416.34
Array. Zhou X L et al., (2021)	137	Linkage Map	RILs	YR	1BL	659.40	662.17	671.21
Array. Zhou X L et al., (2021)	137	Linkage Map	RILs	YR	1BL	661.20	662.17	666.69
Array. Zhou X L et al., (2021)	137	Linkage Map	RILs	YR	1BL	661.20	662.17	666.69
Array. Zhou X L et al., (2021)	137	Linkage Map	RILs	YR	1BL	661.20	662.17	668.99

Array. Zhou X L et al., (2021)	137	Linkage Map	RILs	YR	1BL	661.20	662.17	666.64
Array. Zhou X L et al., (2021)	137	Linkage Map	RILs	YR	1BL	661.20	662.17	666.64
Array. Zhou X L et al., (2021)	137	Linkage Map	RILs	YR	1BL	661.20	662.17	666.69
Array. Zhou X L et al., (2021)	137	Linkage Map	RILs	YR	1BL	622.81	633.14	638.55
Array. Zhou X L et al., (2021)	137	Linkage Map	RILs	YR	2AS	5.98	15.94	19.84
Array. Zhou X L et al., (2021)	137	Linkage Map	RILs	YR	2AS	175.69	15.94	19.84
Array. Zhou X L et al., (2021)	137	Linkage Map	RILs	YR	2AS	4.98	15.94	19.84
Array. Zhou X L et al., (2021)	137	Linkage Map	RILs	YR	2AS	4.98	15.94	19.84
Array. Zhou X L et al., (2021)	137	Linkage Map	RILs	YR	2BS	2.56	5.32	9.77
Array. Zhou X L et al., (2021)	137	Linkage Map	RILs	YR	3AS	18.36	21.26	22.86
Array. Zhou X L et al., (2021)	137	Linkage Map	RILs	YR	3AS	18.36	21.26	22.86
Array. Zhou X L et al., (2021)	137	Linkage Map	RILs	YR	3AS	15.84	21.26	40.65
Array. Zhou X L et al., (2021)	137	Linkage Map	RILs	YR	4AL	688.08	695.64	701.92
Array. Zhou X L et al., (2021)	137	Linkage Map	RILs	YR	4AL	569.87	695.64	701.92
Array. Zhou X L et al., (2021)	137	Linkage Map	RILs	YR	4AL	569.87	695.64	701.92
Array. Zhou X L et al., (2021)	137	Linkage Map	RILs	YR	4AL	569.87	695.64	701.92
Array. Zhou X L et al., (2021)	137	Linkage Map	RILs	YR	4AL	569.87	695.64	701.92
Array. Zhou X L et al., (2021)	137	Linkage Map	RILs	YR	4AL	569.87	695.64	701.92
Array. Zhou X L et al., (2021)	137	Linkage Map	RILs	YR	5AL	451.30	475.49	501.33
Array. Zhou X L et al., (2021)	137	Linkage Map	RILs	YR	5AL	45.63	475.49	491.23

Array. Zhou X L et al., (2021)	137	Linkage Map	RILs	YR	5AL	451.30	475.49	501.33
Array. Zhou X L et al., (2021)	137	Linkage Map	RILs	YR	5AL	622.52	629.68	636.82
Array. Zhou X L et al., (2021)	137	Linkage Map	RILs	YR	5AL	621.87	629.68	639.68
Array. Zhou X L et al., (2021)	137	Linkage Map	RILs	YR	5AL	622.52	629.68	636.82
Array. Zhou X L et al., (2021)	137	Linkage Map	RILs	YR	5AL	618.39	629.68	639.77
Firdissa E. Bokore et al.,(2021)	87	Linkage Map	DH	YR	2B	16.96	24.68	30.12
Firdissa E. Bokore et al.,(2021)	87	Linkage Map	DH	YR	2B	18.45	24.68	26.57
Firdissa E. Bokore et al.,(2021)	87	Linkage Map	DH	YR	2B	12.30	24.68	27.93
Firdissa E. Bokore et al.,(2021)	87	Linkage Map	DH	YR	3A	45.60	56.83	109.37
Firdissa E. Bokore et al.,(2021)	87	Linkage Map	DH	YR	3A	151.03	482.61	532.61
Firdissa E. Bokore et al.,(2021)	87	Linkage Map	DH	YR	3A	130.04	482.61	543.51
Firdissa E. Bokore et al.,(2021)	87	Linkage Map	DH	YR	3A	654.28	674.01	681.67
Firdissa E. Bokore et al.,(2021)	87	Linkage Map	DH	YR	3A	650.15	674.01	684.98
Firdissa E. Bokore et al.,(2021)	87	Linkage Map	DH	YR	3A	654.28	674.01	681.67
Firdissa E. Bokore et al.,(2021)	87	Linkage Map	DH	YR	3A	650.15	674.01	684.98
Firdissa E. Bokore et al.,(2021)	87	Linkage Map	DH	YR	3A	660.92	674.01	679.42
Firdissa E. Bokore et al.,(2021)	87	Linkage Map	DH	YR	3A	665.85	674.01	679.42
Firdissa E. Bokore et al.,(2021)	87	Linkage Map	DH	YR	5B	559.25	569.33	579.36
Firdissa E. Bokore et al.,(2021)	87	Linkage Map	DH	YR	5B	543.87	569.33	588.08
Lin, X., et al., (2018).	155	Linkage Map	DH	YR	5B	666.78	670.64	674.21

Lin, X., et al., (2018).	155	Linkage Map	DH	YR	5B	660.75	670.64	677.94
Lin, X., et al., (2018).	155	Linkage Map	DH	YR	7B	691.95	693.58	694.88
Lin, X., et al., (2018).	155	Linkage Map	DH	YR	7B	692.45	693.58	693.11
Lin, X., et al., (2018).	155	Linkage Map	DH	YR	7B	691.59	693.58	693.52

Supplementary table 2 (St2): This supplementary table displays all the QTL projected from the independent mapping studies on Stb resistance in durum wheat available in the literature.

Reference	Collection size	Type of Mapping	Collection composition	Trait	Chr	Start_CI (Mbp)	Middle point (Mbp)	END_CI (Mbp)
Ballini et al., 2020	189	GWAS	EPO	Stb	3A	21.83	23.33	24.83
Ballini et al., 2020	190	GWAS	EPO	Stb	5A	653.30	654.80	656.30
Ballini et al., 2020	191	GWAS	EPO	Stb	3A	18.71	20.21	21.71
Y. G. Kidane ***et al.*** **, (2017).**	318	GWAS	Ethiopian durum wheat landraces, modern varieties	Stb	1A	475.20	476.70	478.20
Y. G. Kidane ***et al.*** **, (2017).**	318	GWAS	Ethiopian durum wheat landraces, modern varieties	Stb	2B	208.91	210.41	211.91
Y. G. Kidane ***et al.*** **, (2017).**	318	GWAS	Ethiopian durum wheat landraces, modern varieties	Stb	3A	495.90	497.40	498.90
Y. G. Kidane ***et al.*** **, (2017).**	318	GWAS	Ethiopian durum wheat landraces, modern varieties	Stb	4A	756.30	757.80	759.30
Y. G. Kidane ***et al.*** **, (2017).**	318	GWAS	Ethiopian durum wheat landraces, modern varieties	Stb	5A	580.73	582.23	583.73

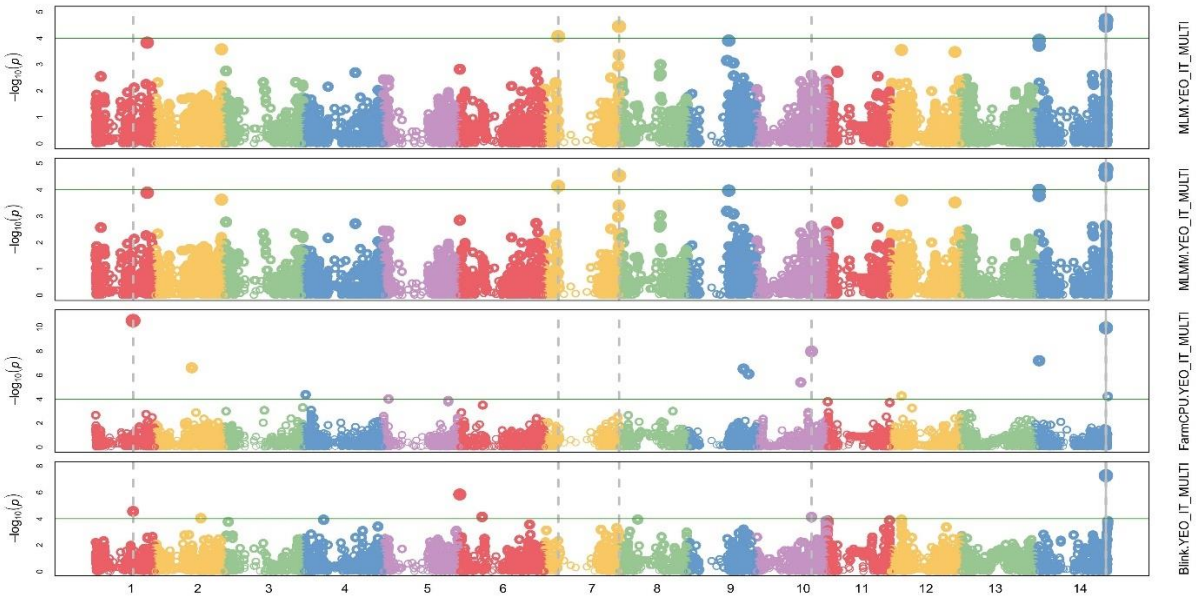

SUPPLEMENTARY FIGURE 1: Manhattan plot with all GWAS models (MLM, MLMM, FARMCPU AND BLINK) for Infection Type (IT) in the 1st cluster (Grosseto 2019, Grosseto 2021 and Izmir 2019). Numbers on the Xlab refers to the durum wheat chromosomes (1 = 1A, 2 = 1B, 3 = 2A, 4 = 2B, 5 = 3A, 6 = 3B, 7 = 4A, 8 = 4B, 9 = 5A, 10 = 5B, 11 = 6A, 12 = 6B, 13 = 7A and 14 = 7B). Ylab refers to LOD (-log10(pvalue)).

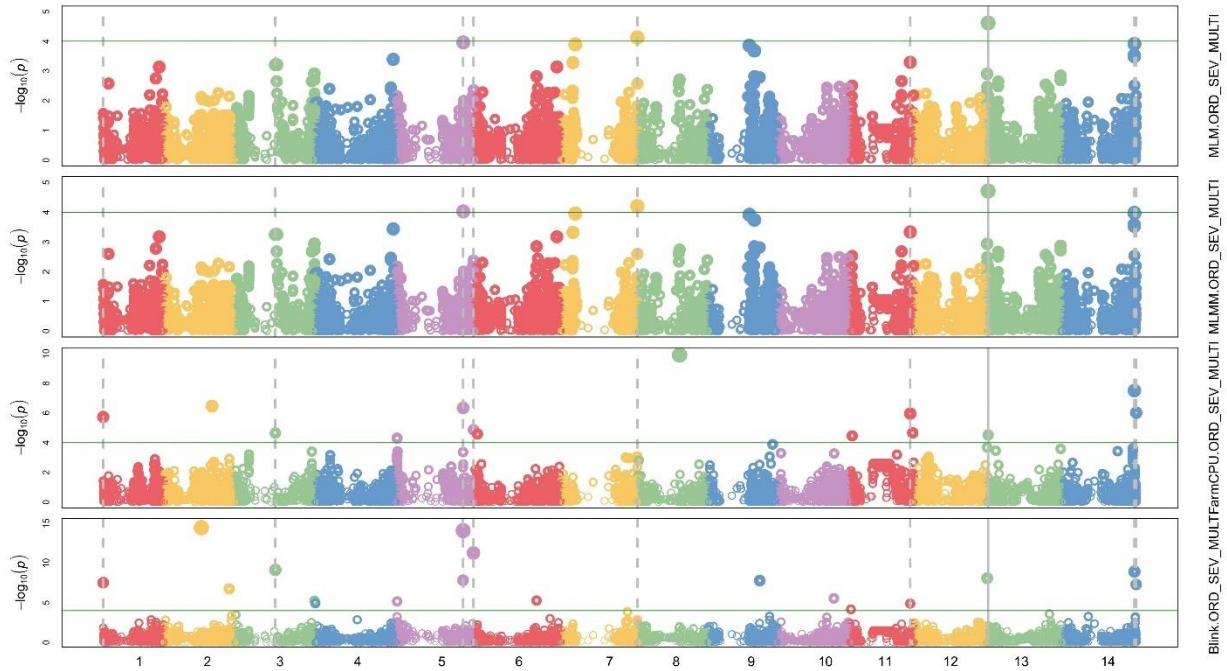

SUPPLEMENTARY FIGURE 2: Manhattan plot with all GWAS models (MLM, MLMM, FARMCPU AND BLINK) for Severity (SEV) in the 1st cluster (Grosseto 2019, Grosseto 2021 and Izmir 2019). Numbers on the Xlab refers to the durum wheat chromosomes (1 = 1A, 2 = 1B, 3 = 2A, 4 = 2B, 5 = 3A, 6 = 3B, 7 = 4A, 8 = 4B, 9 = 5A, 10 = 5B, 11 = 6A, 12 = 6B, 13 = 7A and 14 = 7B). Ylab refers to LOD ($-\log_{10}$(pvalue)).

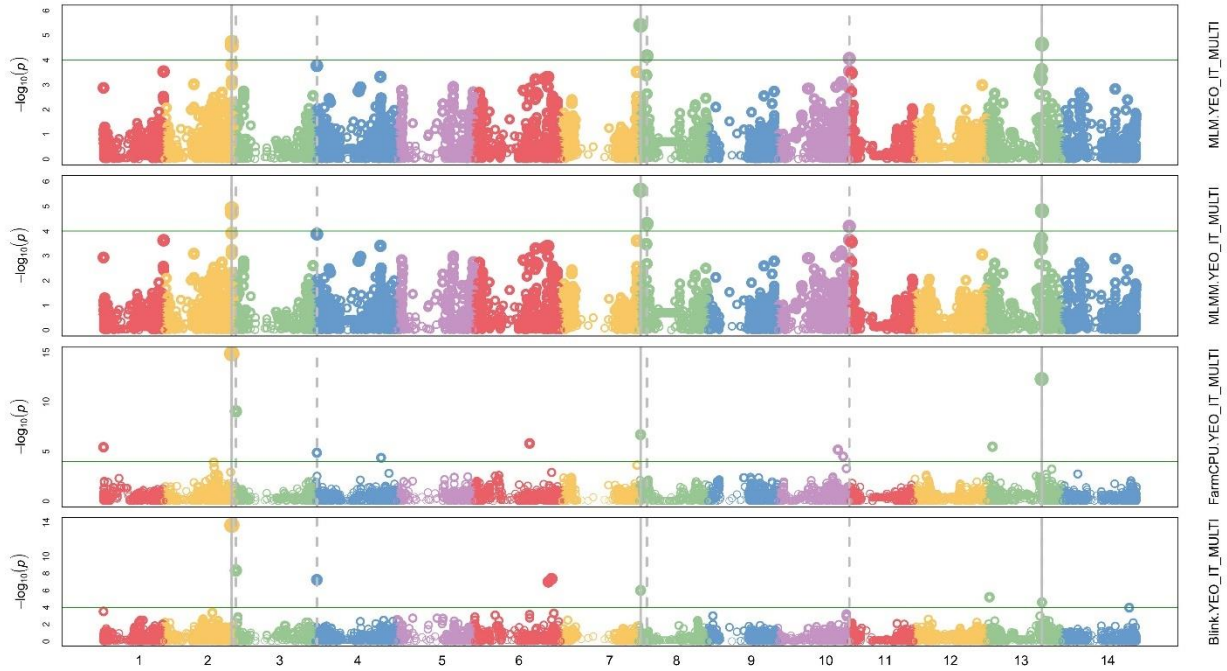

SUPPLEMENTARY FIGURE 3: Manhattan plot with all GWAS models (MLM, MLMM, FARMCPU AND BLINK) for Infection Type (IT) in the 2nd cluster (Grosseto 2018 and Lari 2019). Numbers on the Xlab refers to the durum wheat chromosomes (1 = 1A, 2 = 1B, 3 = 2A, 4 = 2B, 5 = 3A, 6 = 3B, 7 = 4A, 8 = 4B, 9 = 5A, 10 = 5B, 11 = 6A, 12 = 6B, 13 = 7A and 14 = 7B). Ylab refers to LOD ($-\log_{10}$(pvalue)).

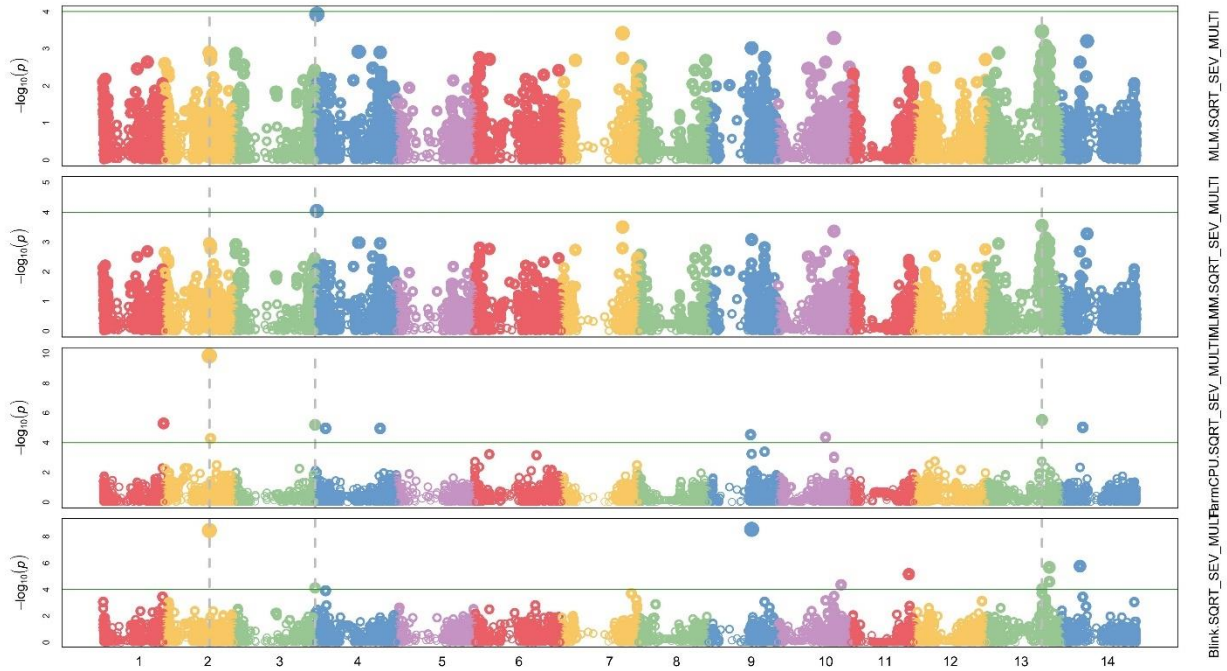

SUPPLEMENTARY FIGURE 4: Manhattan plot with all GWAS models (MLM, MLMM, FARMCPU AND BLINK) for Severity (SEV) in the 2nd cluster (Grosseto 2018 and Lari 2019). Numbers on the Xlab refers to the durum wheat chromosomes (1 = 1A, 2 = 1B, 3 = 2A, 4 = 2B, 5 = 3A, 6 = 3B, 7 = 4A, 8 = 4B, 9 = 5A, 10 = 5B, 11 = 6A, 12 = 6B, 13 = 7A and 14 = 7B). Ylab refers to LOD (-log10(pvalue)).

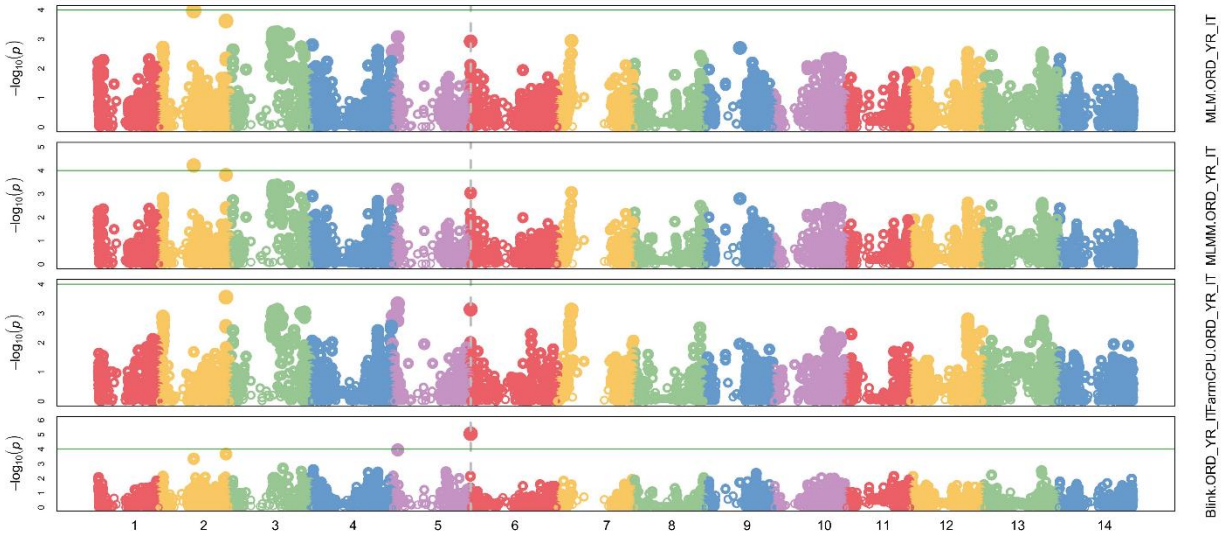

SUPPLEMENTARY FIGURE 5: Manhattan plot with all GWAS models (MLM, MLMM, FARMCPU AND BLINK) for Infection Type (IT) in Grosseto 2018. Numbers on the Xlab refers to the durum wheat chromosomes (1 = 1A, 2 = 1B, 3 = 2A, 4 = 2B, 5 = 3A, 6 = 3B, 7 = 4A, 8 = 4B, 9 = 5A, 10 = 5B, 11 = 6A, 12 = 6B, 13 = 7A and 14 = 7B). Ylab refers to LOD (-log10(pvalue)).

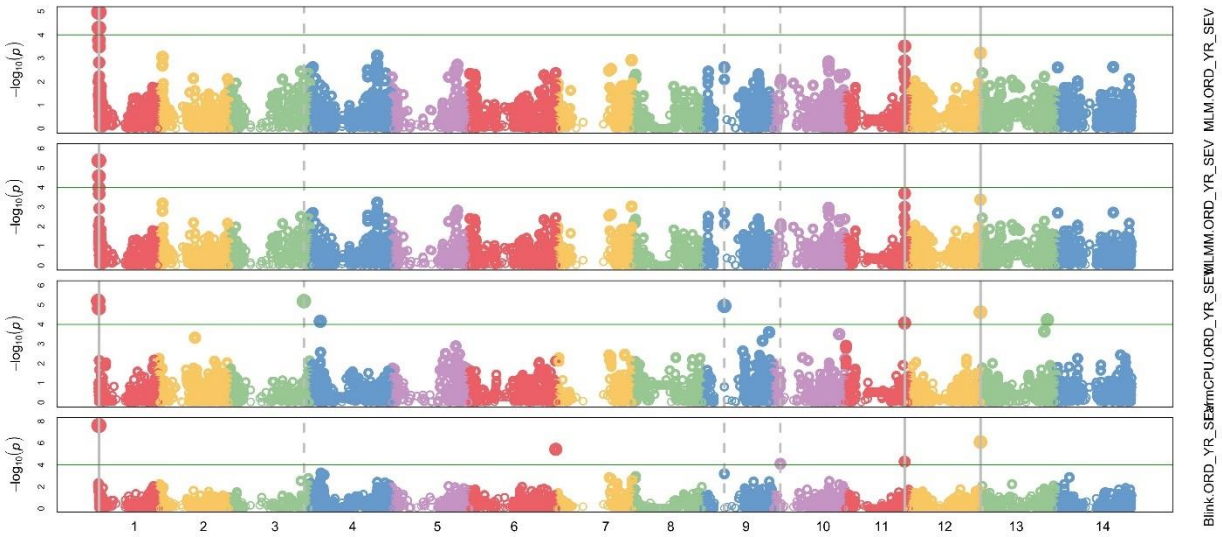

SUPPLEMENTARY FIGURE 6: Manhattan plot with all GWAS models (MLM, MLMM, FARMCPU AND BLINK) for Severity (SEV) in Grosseto 2018. Numbers on the Xlab refers to the durum wheat chromosomes (1 = 1A, 2 = 1B, 3 = 2A, 4 = 2B, 5 = 3A, 6 = 3B, 7 = 4A, 8 = 4B, 9 = 5A, 10 = 5B, 11 = 6A, 12 = 6B, 13 = 7A and 14 = 7B). Ylab refers to LOD (-log$_{10}$(pvalue)).

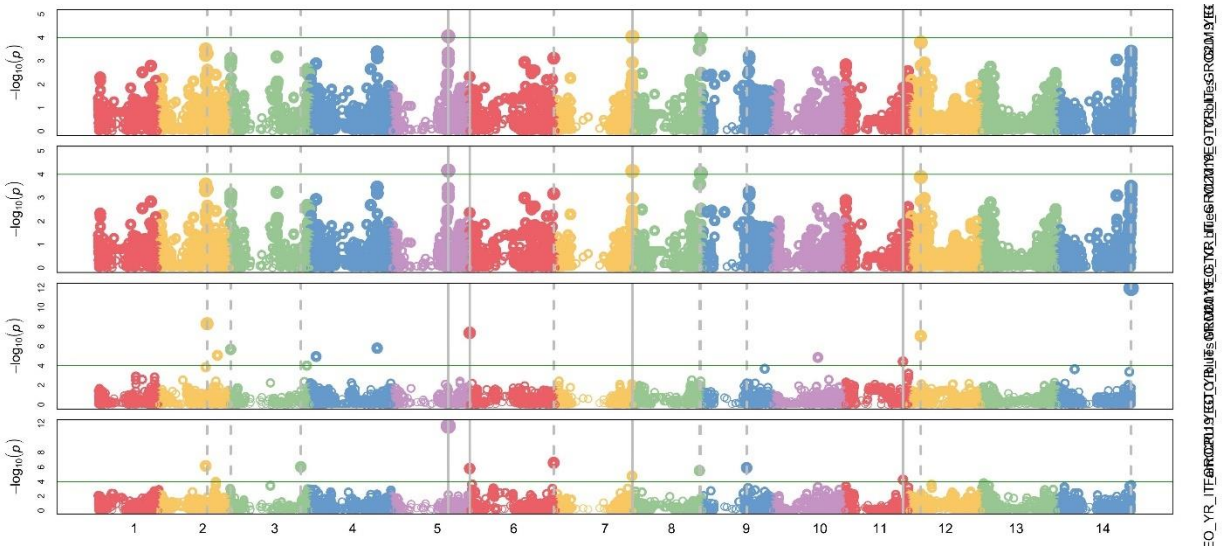

SUPPLEMENTARY FIGURE 7: Manhattan plot with all GWAS models (MLM, MLMM, FARMCPU AND BLINK) for Infection Type (IT) in Grosseto 2019. Numbers on the Xlab refers to the durum wheat chromosomes (1 = 1A, 2 = 1B, 3 = 2A, 4 = 2B, 5 = 3A, 6 = 3B, 7 = 4A, 8 = 4B, 9 = 5A, 10 = 5B, 11 = 6A, 12 = 6B, 13 = 7A and 14 = 7B). Ylab refers to LOD (-log$_{10}$(pvalue)).

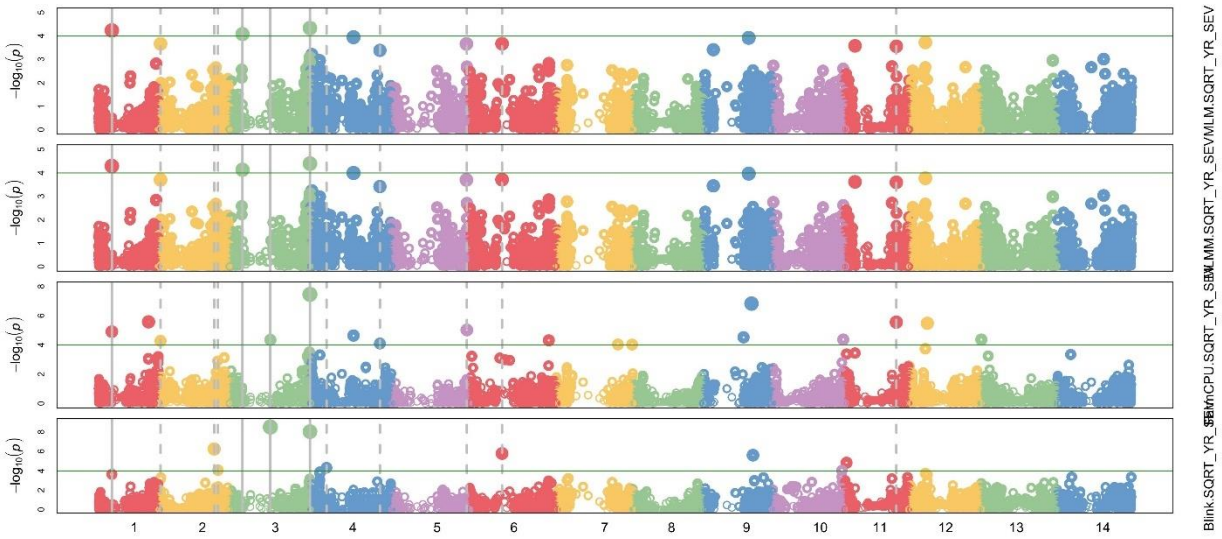

SUPPLEMENTARY FIGURE 8: Manhattan plot with all GWAS models (MLM, MLMM, FARMCPU AND BLINK) for Severity (SEV) in Grosseto 2019. Numbers on the Xlab refers to the durum wheat chromosomes (1 = 1A, 2 = 1B, 3 = 2A, 4 = 2B, 5 = 3A, 6 = 3B, 7 = 4A, 8 = 4B, 9 = 5A, 10 = 5B, 11 = 6A, 12 = 6B, 13 = 7A and 14 = 7B). Ylab refers to LOD (-log$_{10}$(pvalue)).

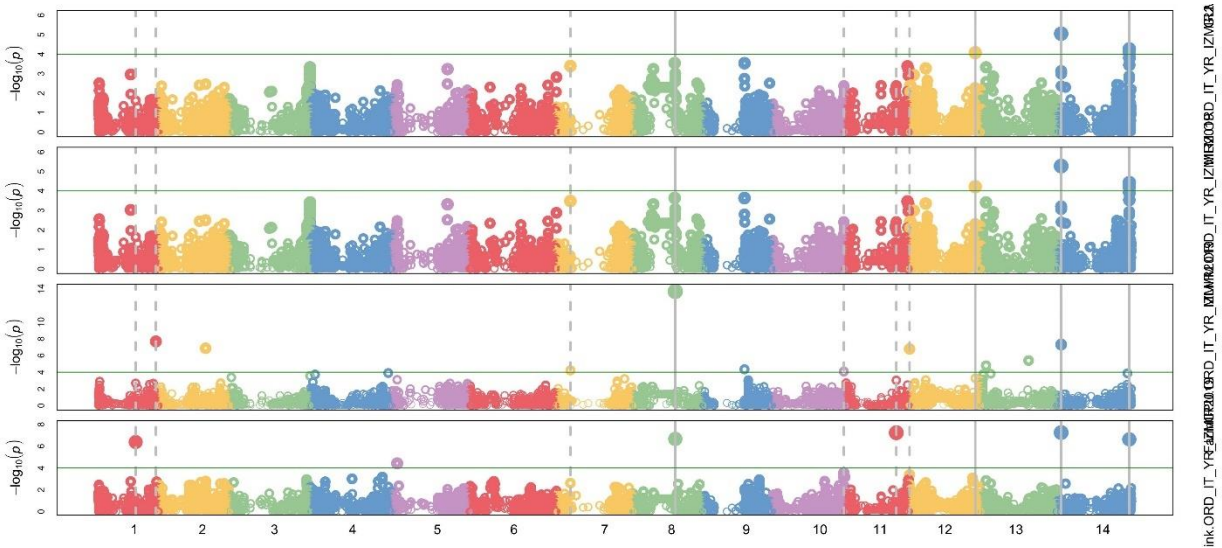

SUPPLEMENTARY FIGURE 9: Manhattan plot with all GWAS models (MLM, MLMM, FARMCPU AND BLINK) for Infection Type (IT) in Izmir 2019. Numbers on the Xlab refers to the durum wheat chromosomes (1 = 1A, 2 = 1B, 3 = 2A, 4 = 2B, 5 = 3A, 6 = 3B, 7 = 4A, 8 = 4B, 9 = 5A, 10 = 5B, 11 = 6A, 12 = 6B, 13 = 7A and 14 = 7B). Ylab refers to LOD (-log$_{10}$(pvalue)).

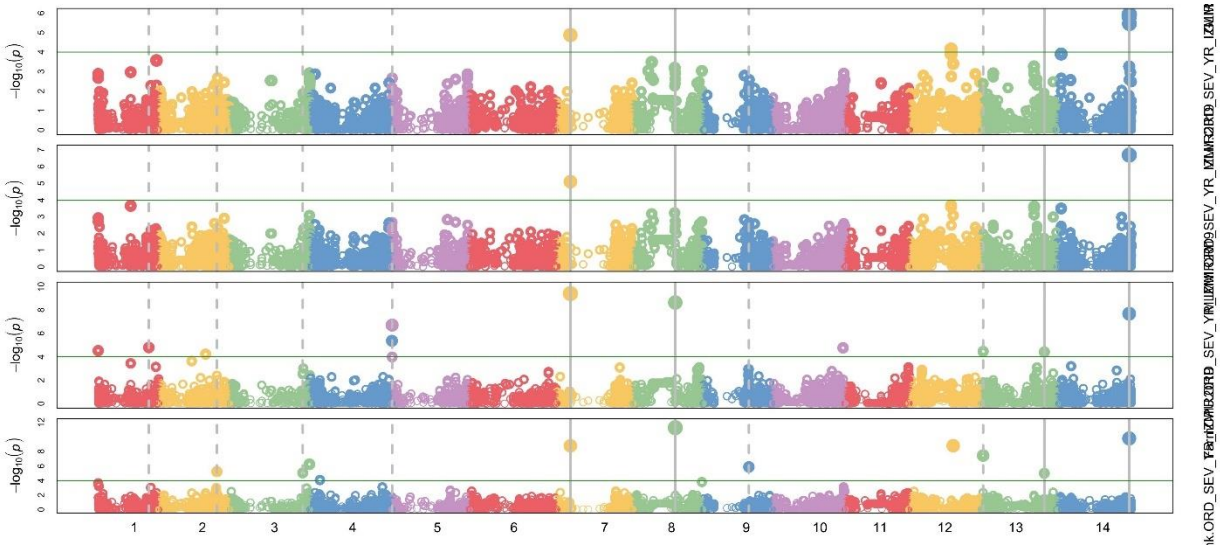

SUPPLEMENTARY FIGURE 10: Manhattan plot with all GWAS models (MLM, MLMM, FARMCPU AND BLINK) for Severity (SEV) in Izmir 2019. Numbers on the Xlab refers to the durum wheat chromosomes (1 = 1A, 2 = 1B, 3 = 2A, 4 = 2B, 5 = 3A, 6 = 3B, 7 = 4A, 8 = 4B, 9 = 5A, 10 = 5B, 11 = 6A, 12 = 6B, 13 = 7A and 14 = 7B). Ylab refers to LOD (-log$_{10}$(pvalue)).

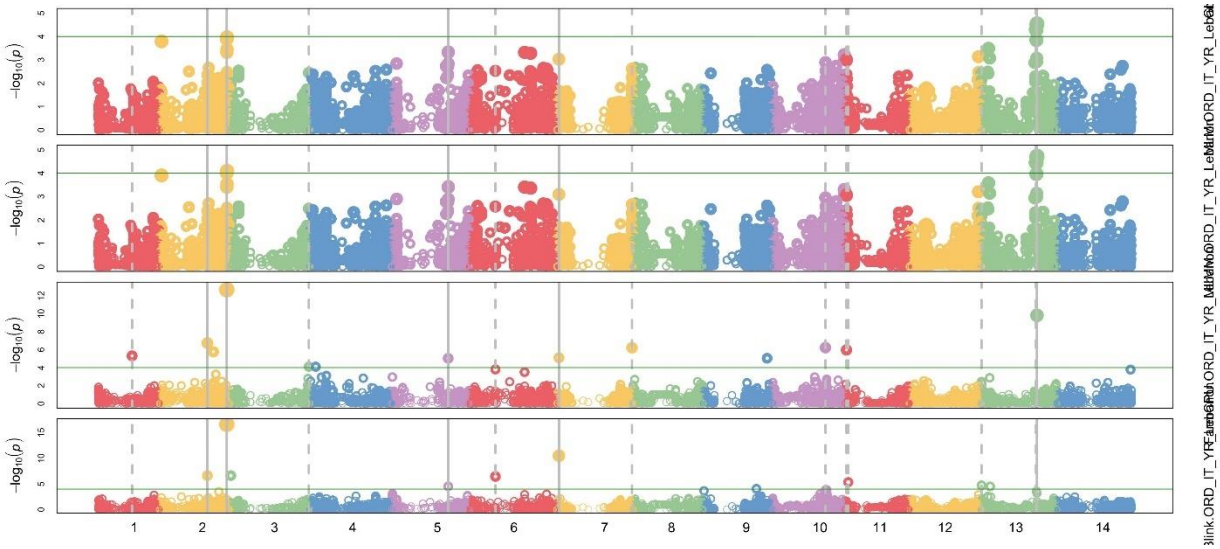

SUPPLEMENTARY FIGURE 11: Manhattan plot with all GWAS models (MLM, MLMM, FARMCPU AND BLINK) for Infection Type (IT) in Lari 2019. Numbers on the Xlab refers to the durum wheat chromosomes (1 = 1A, 2 = 1B, 3 = 2A, 4 = 2B, 5 = 3A, 6 = 3B, 7 = 4A, 8 = 4B, 9 = 5A, 10 = 5B, 11 = 6A, 12 = 6B, 13 = 7A and 14 = 7B). Ylab refers to LOD (-log$_{10}$(pvalue)).

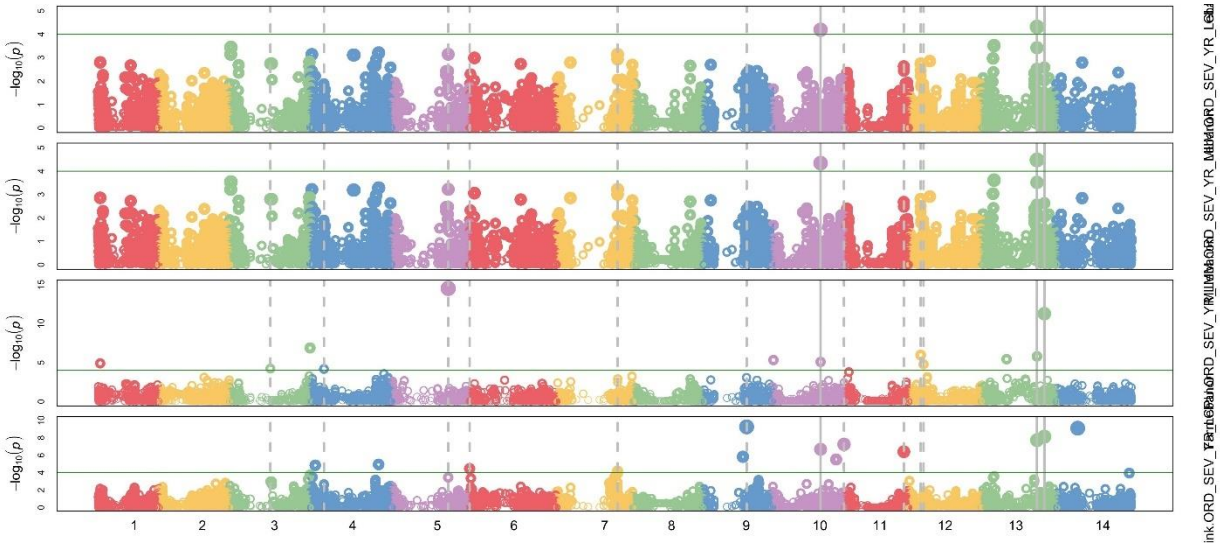

SUPPLEMENTARY FIGURE 12: Manhattan plot with all GWAS models (MLM, MLMM, FARMCPU AND BLINK) for

Severity (SEV) in Lari 2019. Numbers on the Xlab refers to the durum wheat chromosomes (1 = 1A, 2 = 1B, 3 = 2A, 4 = 2B, 5 = 3A, 6 = 3B, 7 = 4A, 8 = 4B, 9 = 5A, 10 = 5B, 11 = 6A, 12 = 6B, 13 = 7A and 14 = 7B). Ylab refers to LOD (-log$_{10}$(pvalue)).

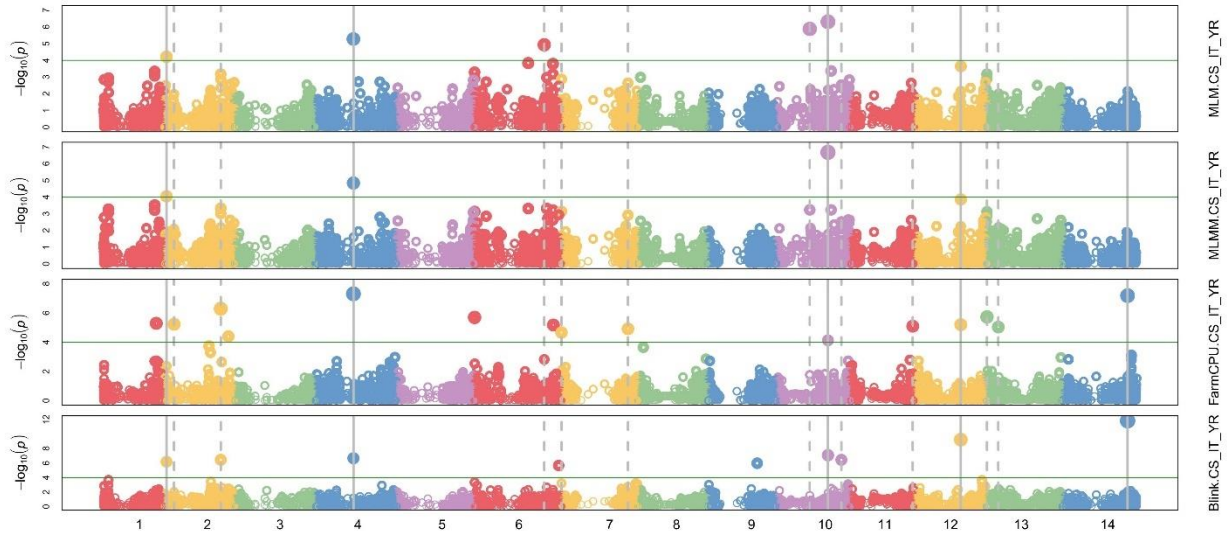

SUPPLEMENTARY FIGURE 13: Manhattan plot with all GWAS models (MLM, MLMM, FARMCPU AND BLINK) for Infection Type (IT) in Kodia 2020. Numbers on the Xlab refers to the durum wheat chromosomes (1 = 1A, 2 = 1B, 3 = 2A, 4 = 2B, 5 = 3A, 6 = 3B, 7 = 4A, 8 = 4B, 9 = 5A, 10 = 5B, 11 = 6A, 12 = 6B, 13 = 7A and 14 = 7B). Ylab refers to LOD (-log$_{10}$(pvalue)).

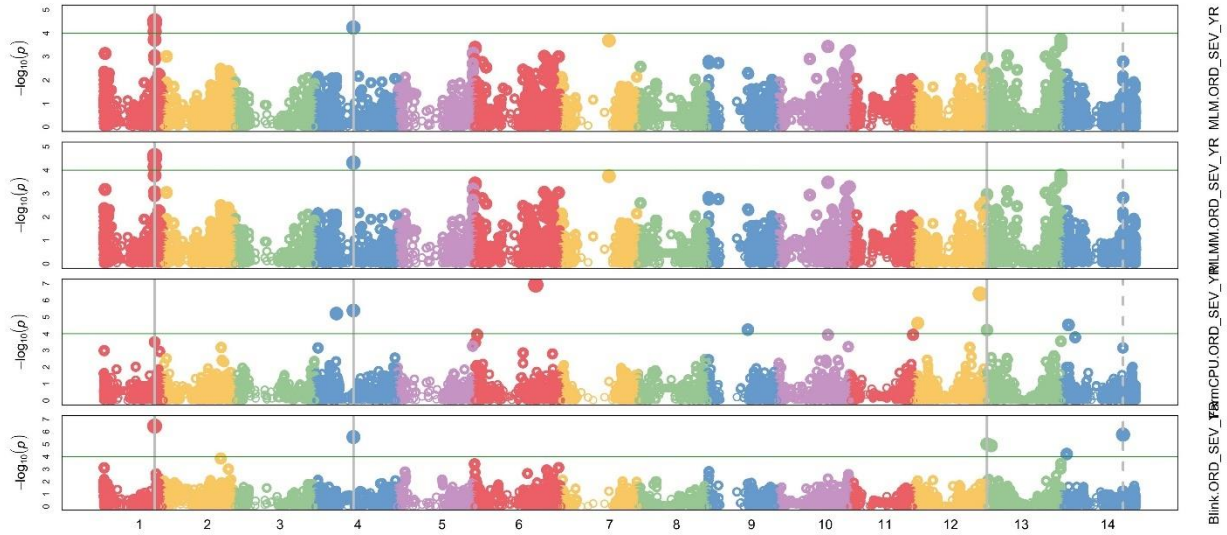

SUPPLEMENTARY FIGURE 14: Manhattan plot with all GWAS models (MLM, MLMM, FARMCPU AND BLINK) for Severity (SEV) in Kodia 2020. Numbers on the Xlab refers to the durum wheat chromosomes (1 = 1A, 2 = 1B, 3 = 2A, 4 = 2B, 5 = 3A, 6 = 3B, 7 = 4A, 8 = 4B, 9 = 5A, 10 = 5B, 11 = 6A, 12 = 6B, 13 = 7A and 14 = 7B). Ylab refers to LOD (-log$_{10}$(pvalue)).

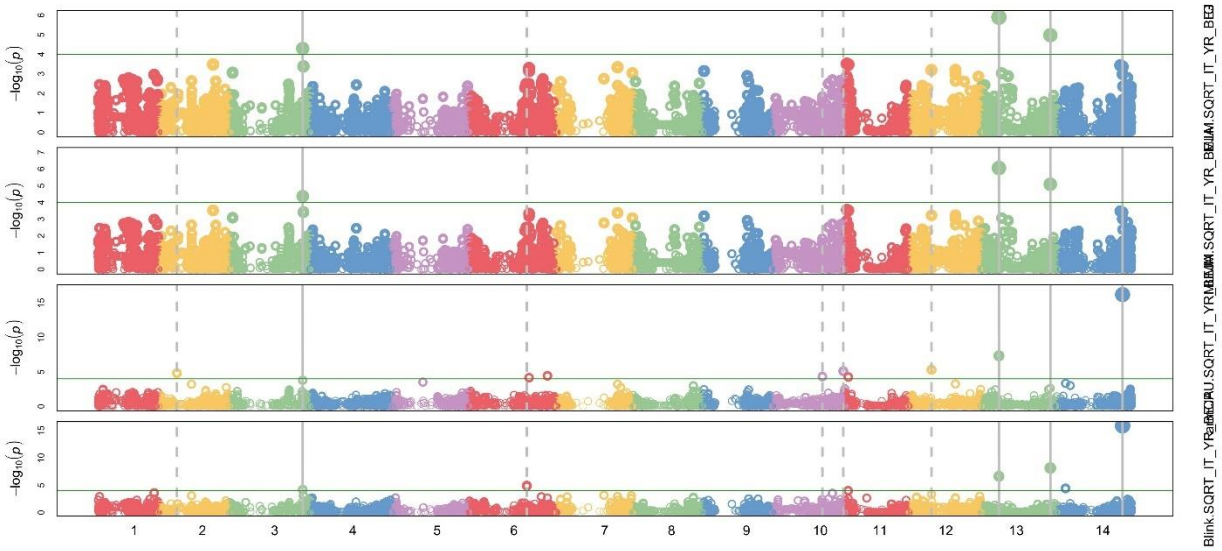

SUPPLEMENTARY FIGURE 15: Manhattan plot with all GWAS models (MLM, MLMM, FARMCPU AND BLINK) for Infection Type (IT) in Beja 2020. Numbers on the Xlab refers to the durum wheat chromosomes (1 = 1A, 2 = 1B, 3 = 2A, 4 = 2B, 5 = 3A, 6 = 3B, 7 = 4A, 8 = 4B, 9 = 5A, 10 = 5B, 11 = 6A, 12 = 6B, 13 = 7A and 14 = 7B). Ylab refers to LOD (-log$_{10}$(pvalue)).

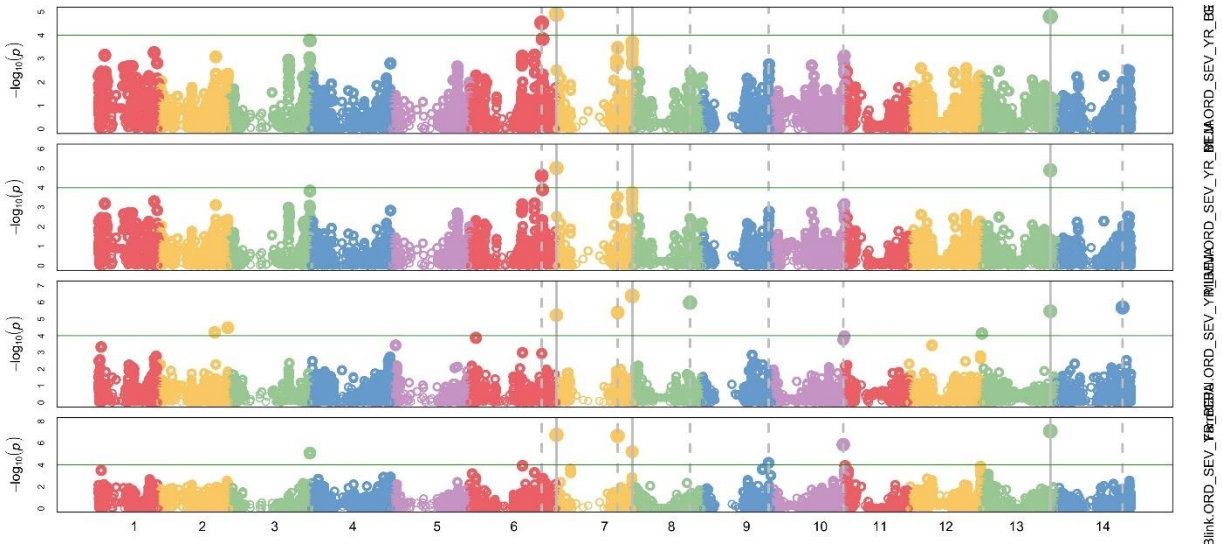

SUPPLEMENTARY FIGURE 16: Manhattan plot with all GWAS models (MLM, MLMM, FARMCPU AND BLINK) for Severity (SEV) in Beja 2020. Numbers on the Xlab refers to the durum wheat chromosomes (1 = 1A, 2 = 1B, 3 = 2A, 4 = 2B, 5 = 3A, 6 = 3B, 7 = 4A, 8 = 4B, 9 = 5A, 10 = 5B, 11 = 6A, 12 = 6B, 13 = 7A and 14 = 7B). Ylab refers to LOD (-log$_{10}$(pvalue)).

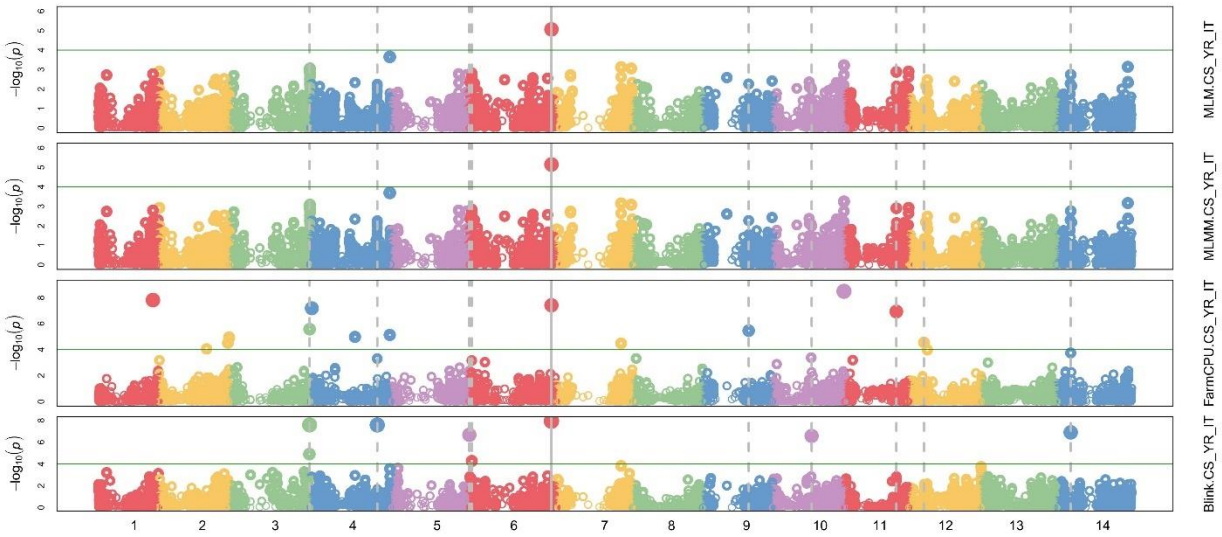

SUPPLEMENTARY FIGURE 17: Manhattan plot with all GWAS models (MLM, MLMM, FARMCPU AND BLINK) for Infection Type (IT) in Grosseto 2020. Numbers on the Xlab refers to the durum wheat chromosomes (1 = 1A, 2 = 1B, 3 = 2A, 4 = 2B, 5 = 3A, 6 = 3B, 7 = 4A, 8 = 4B, 9 = 5A, 10 = 5B, 11 = 6A, 12 = 6B, 13 = 7A and 14 = 7B). Ylab refers to LOD (-log$_{10}$(pvalue)).

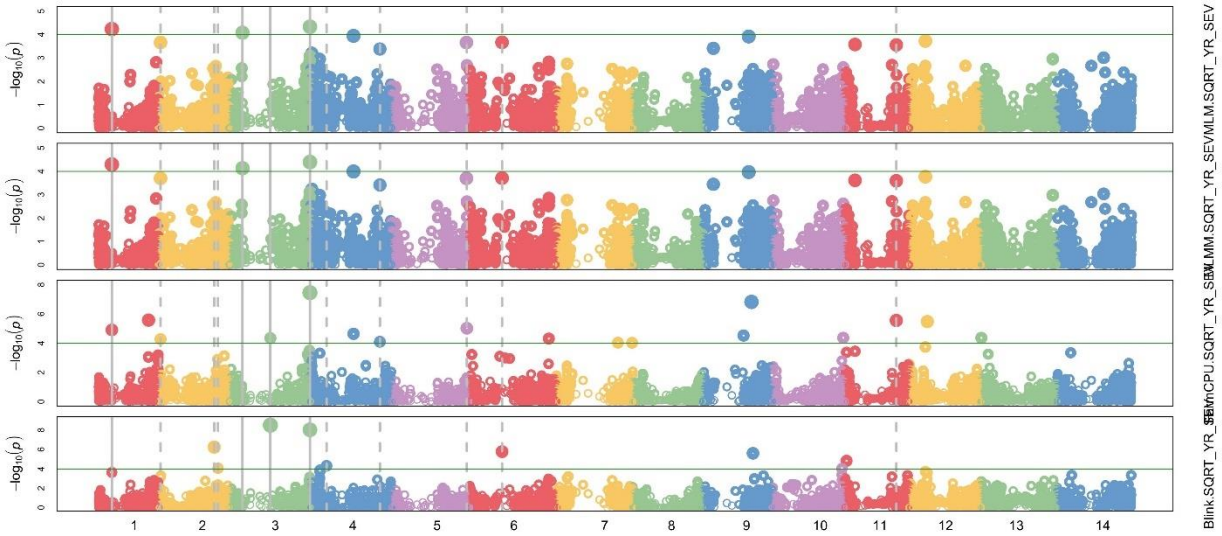

SUPPLEMENTARY FIGURE 18: Manhattan plot with all GWAS models (MLM, MLMM, FARMCPU AND BLINK) for Severity (SEV) in Grosseto 2020. Numbers on the Xlab refers to the durum wheat chromosomes (1 = 1A, 2 = 1B, 3 = 2A, 4 = 2B, 5 = 3A, 6 = 3B, 7 = 4A, 8 = 4B, 9 = 5A, 10 = 5B, 11 = 6A, 12 = 6B, 13 = 7A and 14 = 7B). Ylab refers to LOD (-log$_{10}$(pvalue)).

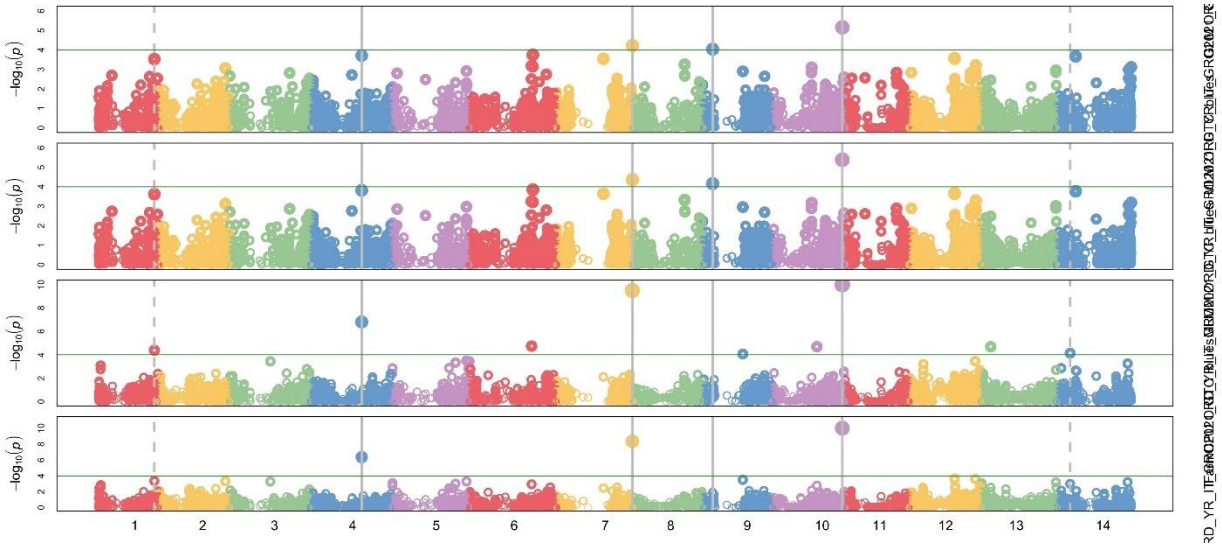

SUPPLEMENTARY FIGURE 19: Manhattan plot with all GWAS models (MLM, MLMM, FARMCPU AND BLINK) for Infection Type (IT) in Grosseto 2021. Numbers on the Xlab refers to the durum wheat chromosomes (1 = 1A, 2 = 1B, 3 = 2A, 4 = 2B, 5 = 3A, 6 = 3B, 7 = 4A, 8 = 4B, 9 = 5A, 10 = 5B, 11 = 6A, 12 = 6B, 13 = 7A and 14 = 7B). Ylab refers to LOD (-log$_{10}$(pvalue)).

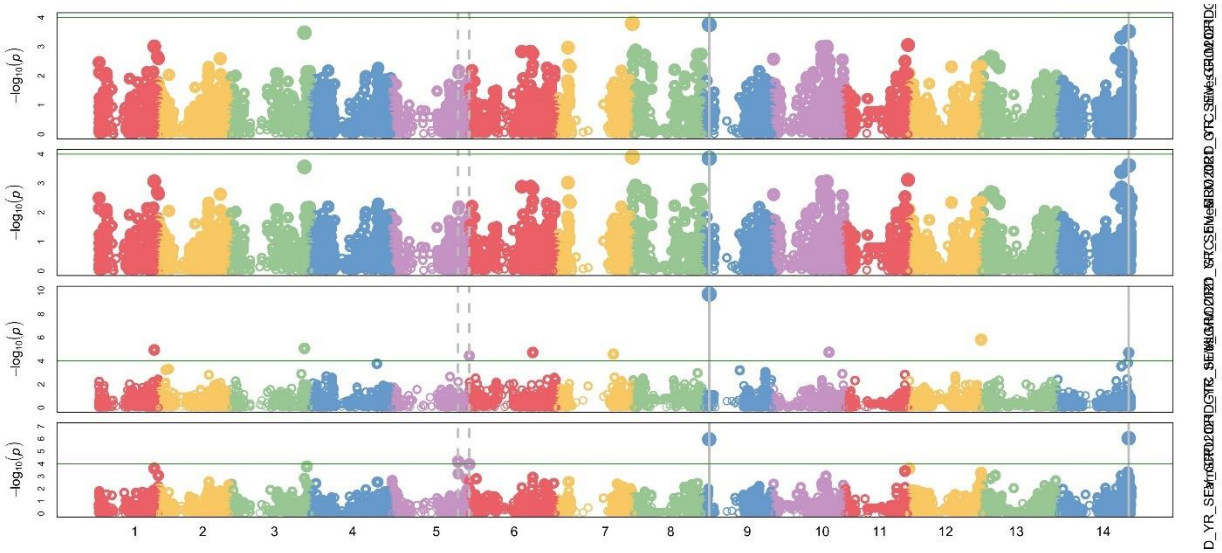

SUPPLEMENTARY FIGURE 20: Manhattan plot with all GWAS models (MLM, MLMM, FARMCPU AND BLINK) for Severity (SEV) in Grosseto 2021. Numbers on the Xlab refers to the durum wheat chromosomes (1 = 1A, 2 = 1B, 3 = 2A, 4 = 2B, 5 = 3A, 6 = 3B, 7 = 4A, 8 = 4B, 9 = 5A, 10 = 5B, 11 = 6A, 12 = 6B, 13 = 7A and 14 = 7B). Ylab refers to LOD (-log$_{10}$(pvalue)).

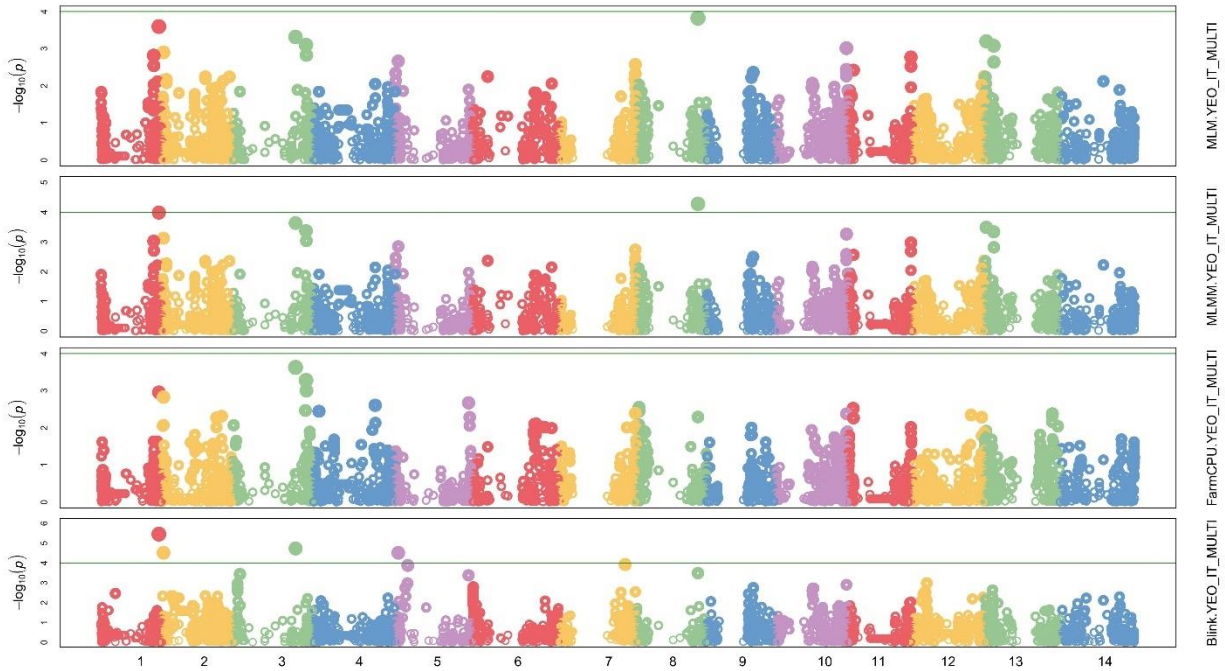

SUPPLEMENTARY FIGURE 21: Manhattan plot with all GWAS models (MLM, MLMM, FARMCPU AND BLINK) for Infection Type (IT) in the 1st cluster (Grosseto 2019, Grosseto 2021 and Izmir 2019) and Q1 (Horn_Africa_aethiopicum). Numbers on the Xlab refers to the durum wheat chromosomes (1 = 1A, 2 = 1B, 3 = 2A, 4 = 2B, 5 = 3A, 6 = 3B, 7 = 4A, 8 = 4B, 9 = 5A, 10 = 5B, 11 = 6A, 12 = 6B, 13 = 7A and 14 = 7B). Ylab refers to LOD (-log10(pvalue)).

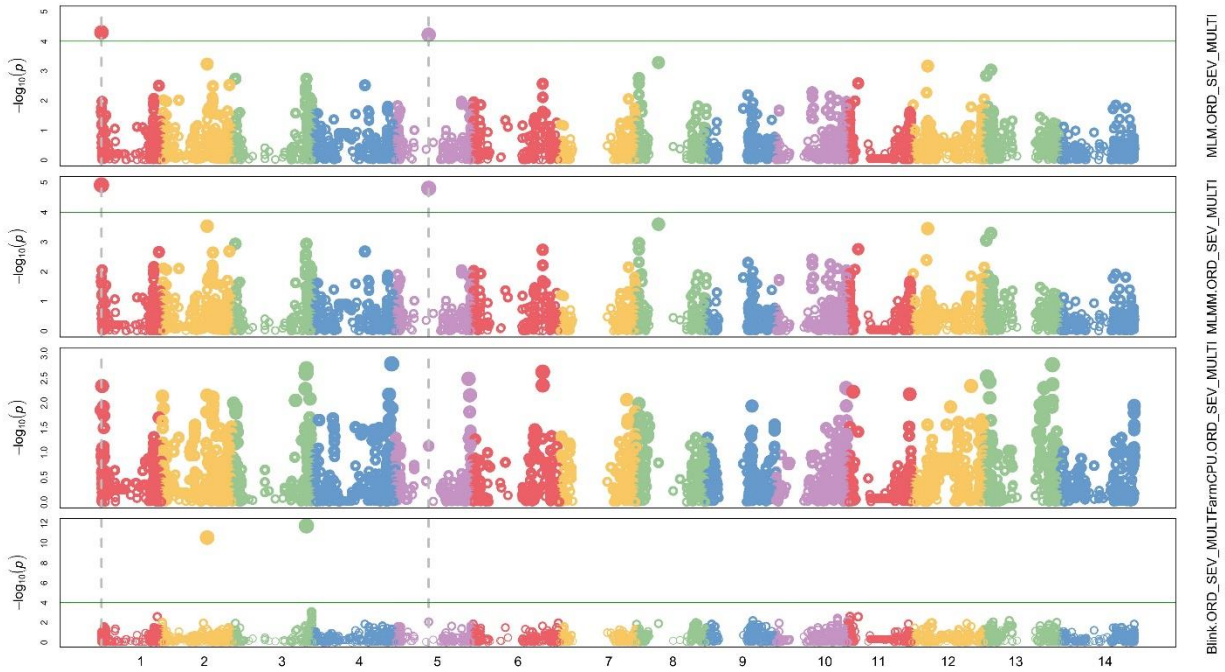

SUPPLEMENTARY FIGURE 22: Manhattan plot with all GWAS models (MLM, MLMM, FARMCPU AND BLINK) for Severity (SEV) in the 1st cluster (Grosseto 2019, Grosseto 2021 and Izmir 2019) and Q1 (Horn_Africa_aethiopicum). Numbers on the Xlab refers to the durum wheat chromosomes (1 = 1A, 2 = 1B, 3 = 2A, 4 = 2B, 5 = 3A, 6 = 3B, 7 = 4A, 8 = 4B, 9 = 5A, 10 = 5B, 11 = 6A, 12 = 6B, 13 = 7A and 14 = 7B). Ylab refers to LOD (-log10(pvalue)).

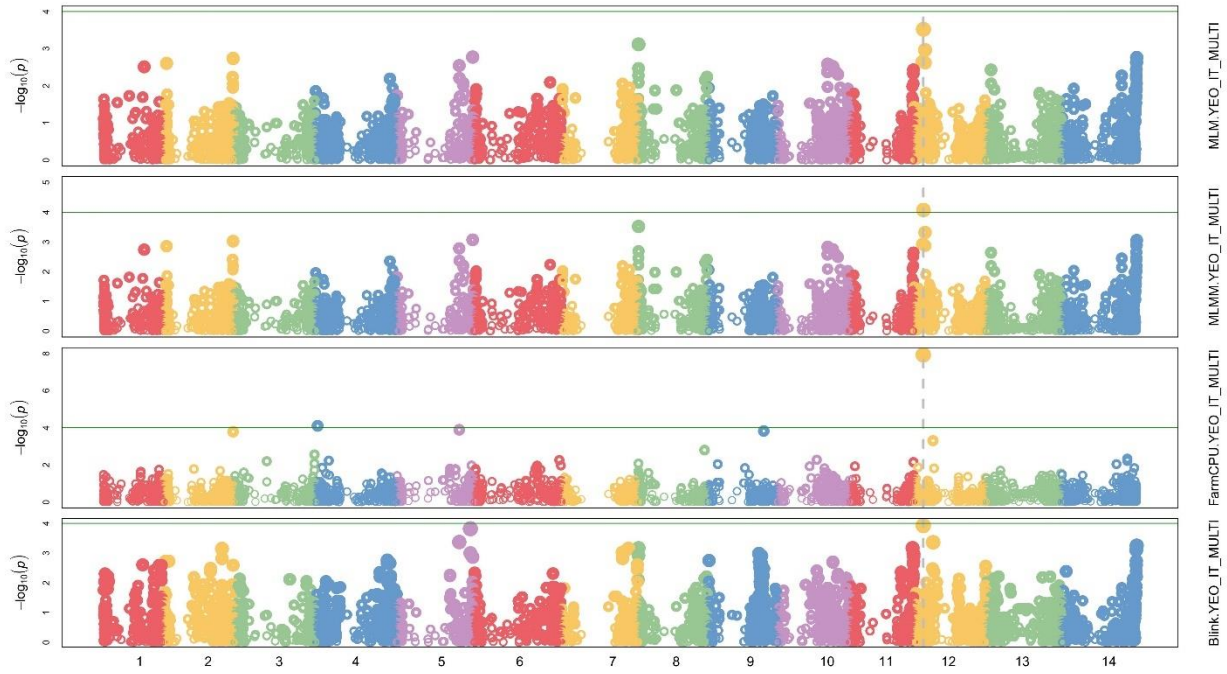

SUPPLEMENTARY FIGURE 23: Manhattan plot with all GWAS models (MLM, MLMM, FARMCPU AND BLINK) for Infection Type (IT) in 1st cluster (Grosseto 2019, Grosseto 2021 and Izmir 2019) and Q3 (Iran_Syriacum). Numbers on the Xlab refers to the durum wheat chromosomes (1 = 1A, 2 = 1B, 3 = 2A, 4 = 2B, 5 = 3A, 6 = 3B, 7 = 4A, 8 = 4B, 9 = 5A, 10 = 5B, 11 = 6A, 12 = 6B, 13 = 7A and 14 = 7B). Ylab refers to LOD (-log10(pvalue)).

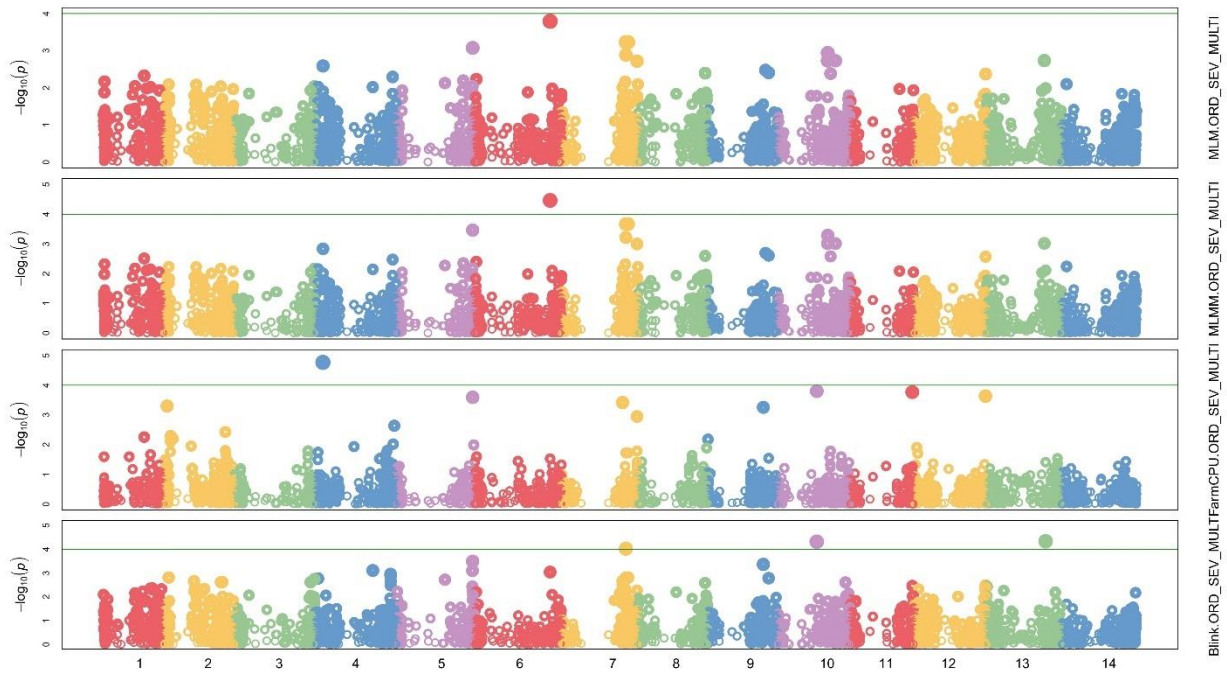

SUPPLEMENTARY FIGURE 24: Manhattan plot with all GWAS models (MLM, MLMM, FARMCPU AND BLINK) for Severity (SEV) in the 1st cluster (Grosseto 2019, Grosseto 2021 and Izmir 2019) and Q3 (Iran_Syriacum). Numbers on the Xlab refers to the durum wheat chromosomes (1 = 1A, 2 = 1B, 3 = 2A, 4 = 2B, 5 = 3A, 6 = 3B, 7 = 4A, 8 = 4B, 9 = 5A, 10 = 5B, 11 = 6A, 12 = 6B, 13 = 7A and 14 = 7B). Ylab refers to LOD (-log10(pvalue)).

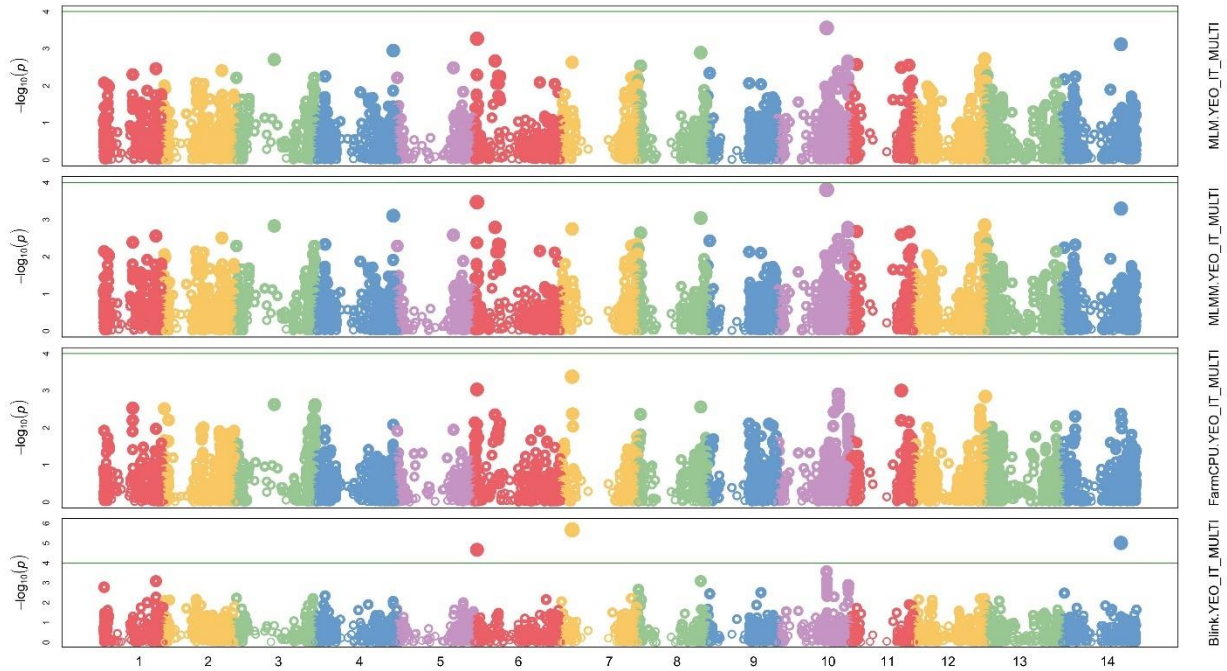

SUPPLEMENTARY FIGURE 25: Manhattan plot with all GWAS models (MLM, MLMM, FARMCPU AND BLINK) for Infection Type (IT) in the 1st cluster (Grosseto 2019, Grosseto 2021 and Izmir 2019) and Q6 (West_Caucasus). Numbers on the Xlab refers to the durum wheat chromosomes (1 = 1A, 2 = 1B, 3 = 2A, 4 = 2B, 5 = 3A, 6 = 3B, 7 = 4A, 8 = 4B, 9 = 5A, 10 = 5B, 11 = 6A, 12 = 6B, 13 = 7A and 14 = 7B). Ylab refers to LOD (-log10(pvalue)).

SUPPLEMENTARY FIGURE 26: Manhattan plot with all GWAS models (MLM, MLMM, FARMCPU AND BLINK) for Severity (SEV) in the 1st cluster (Grosseto 2019, Grosseto 2021 and Izmir 2019) and Q6 (West_Caucasus). Numbers on the Xlab refers to the durum wheat chromosomes (1 = 1A, 2 = 1B, 3 = 2A, 4 = 2B, 5 = 3A, 6 = 3B, 7 = 4A, 8 = 4B, 9 = 5A, 10 = 5B, 11 = 6A, 12 = 6B, 13 = 7A and 14 = 7B). Ylab refers to LOD (-log10(pvalue)).

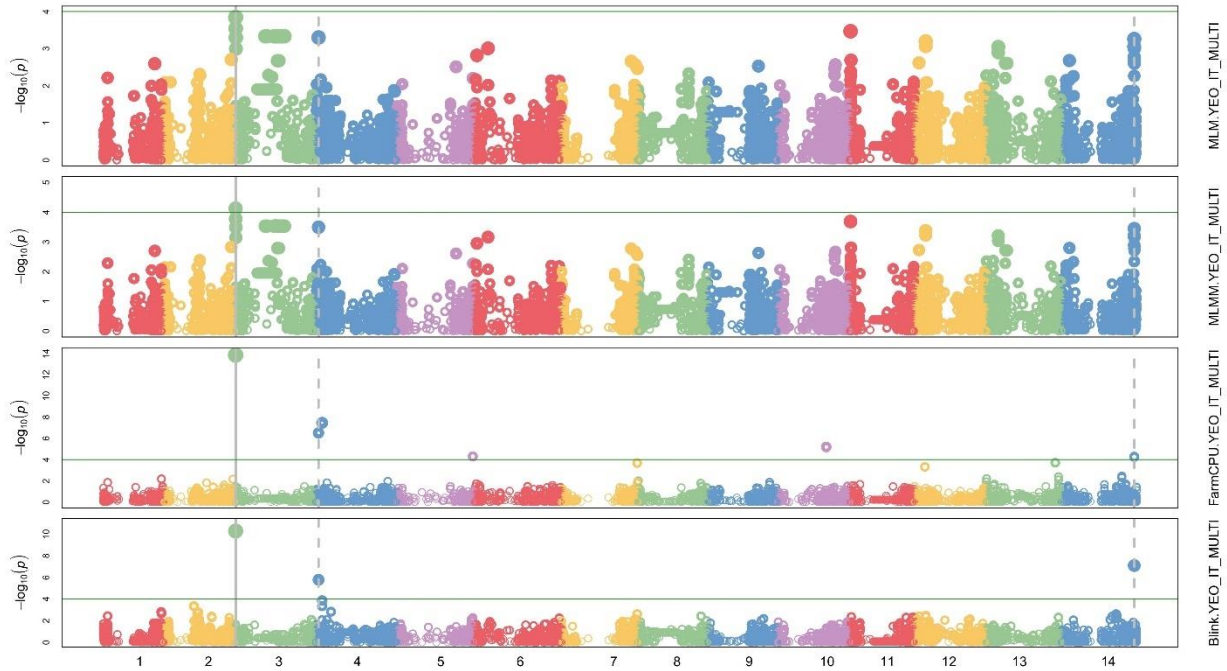

SUPPLEMENTARY FIGURE 27: Manhattan plot with all GWAS models (MLM, MLMM, FARMCPU AND BLINK) for Infection Type (IT) in the 1st cluster (Grosseto 2019, Grosseto 2021 and Izmir 2019) and Q7 (Cyprous_Iberia). Numbers on the Xlab refers to the durum wheat chromosomes (1 = 1A, 2 = 1B, 3 = 2A, 4 = 2B, 5 = 3A, 6 = 3B, 7 = 4A, 8 = 4B, 9 = 5A, 10 = 5B, 11 = 6A, 12 = 6B, 13 = 7A and 14 = 7B). Ylab refers to LOD (-log10(pvalue)).

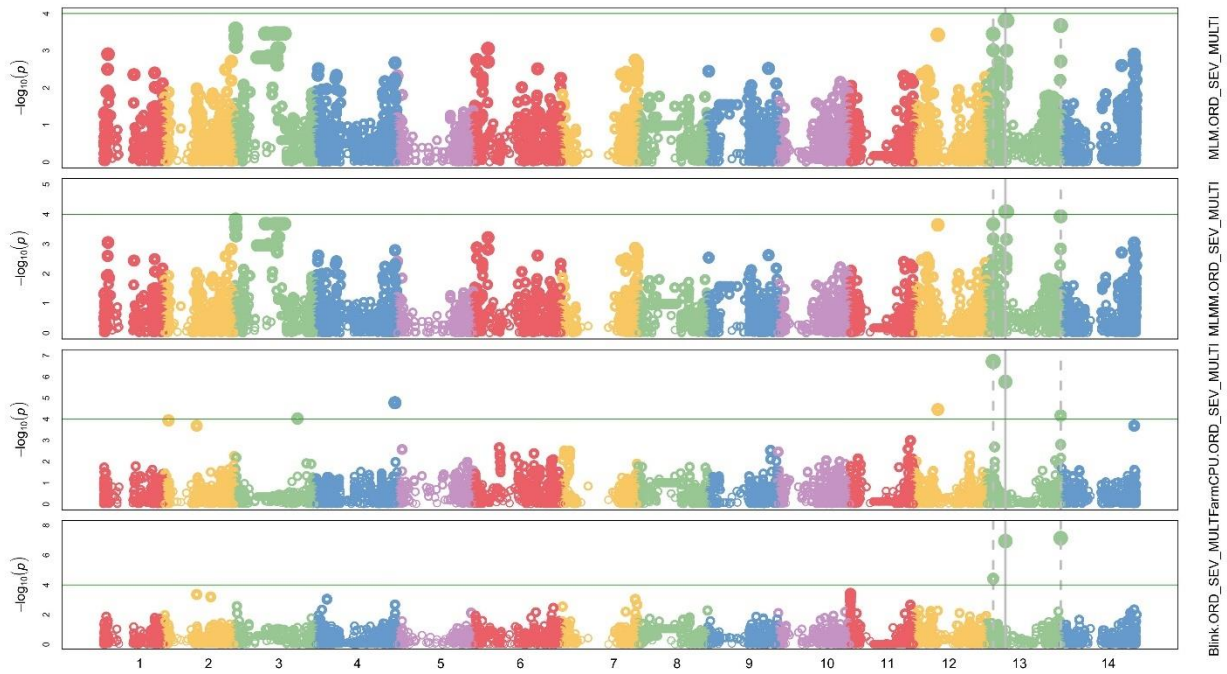

SUPPLEMENTARY FIGURE 28: Manhattan plot with all GWAS models (MLM, MLMM, FARMCPU AND BLINK) for Severity (SEV) in the 1st cluster (Grosseto 2019, Grosseto 2021 and Izmir 2019) and Q7 (Cyprous_Iberia). Numbers on the Xlab refers to the durum wheat chromosomes (1 = 1A, 2 = 1B, 3 = 2A, 4 = 2B, 5 = 3A, 6 = 3B, 7 = 4A, 8 = 4B, 9 = 5A, 10 = 5B, 11 = 6A, 12 = 6B, 13 = 7A and 14 = 7B). Ylab refers to LOD (-log10(pvalue)).

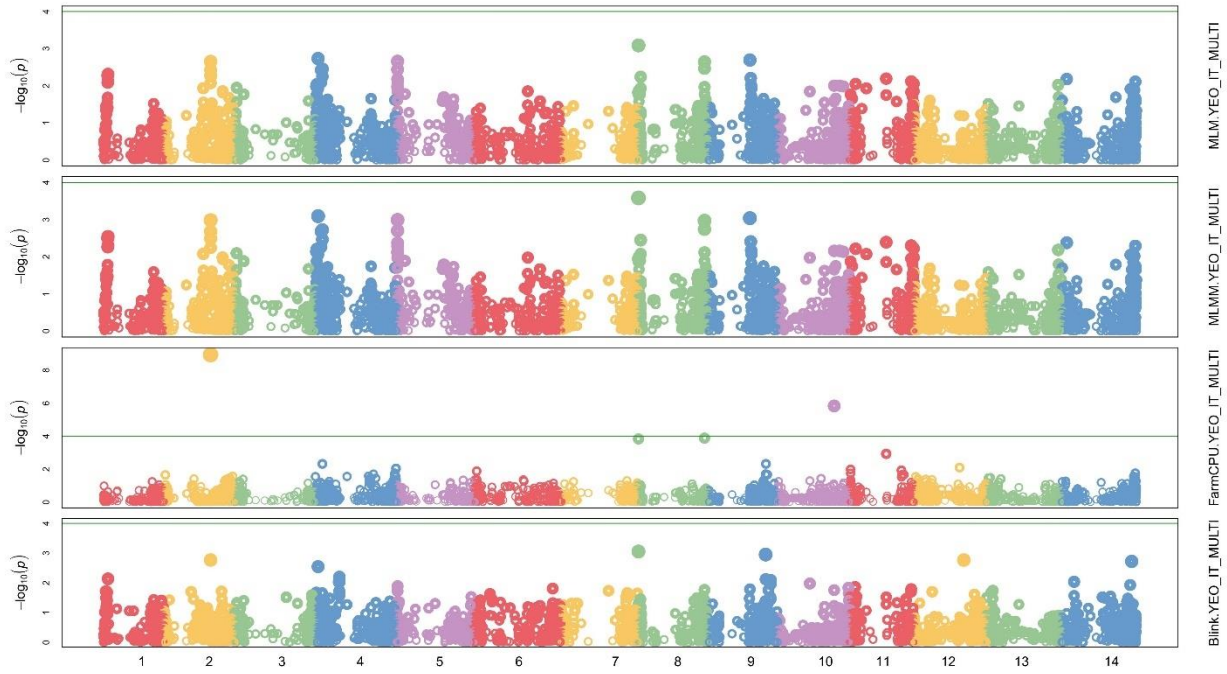

SUPPLEMENTARY FIGURE 29: Manhattan plot with all GWAS models (MLM, MLMM, FARMCPU AND BLINK) for Infection Type (IT) in the 1st cluster (Grosseto 2019, Grosseto 2021 and Izmir 2019) and Q8 (West_Asian_Founders). Numbers on the Xlab refers to the durum wheat chromosomes (1 = 1A, 2 = 1B, 3 = 2A, 4 = 2B, 5 = 3A, 6 = 3B, 7 = 4A, 8 = 4B, 9 = 5A, 10 = 5B, 11 = 6A, 12 = 6B, 13 = 7A and 14 = 7B). Ylab refers to LOD ($-\log_{10}$(pvalue)).

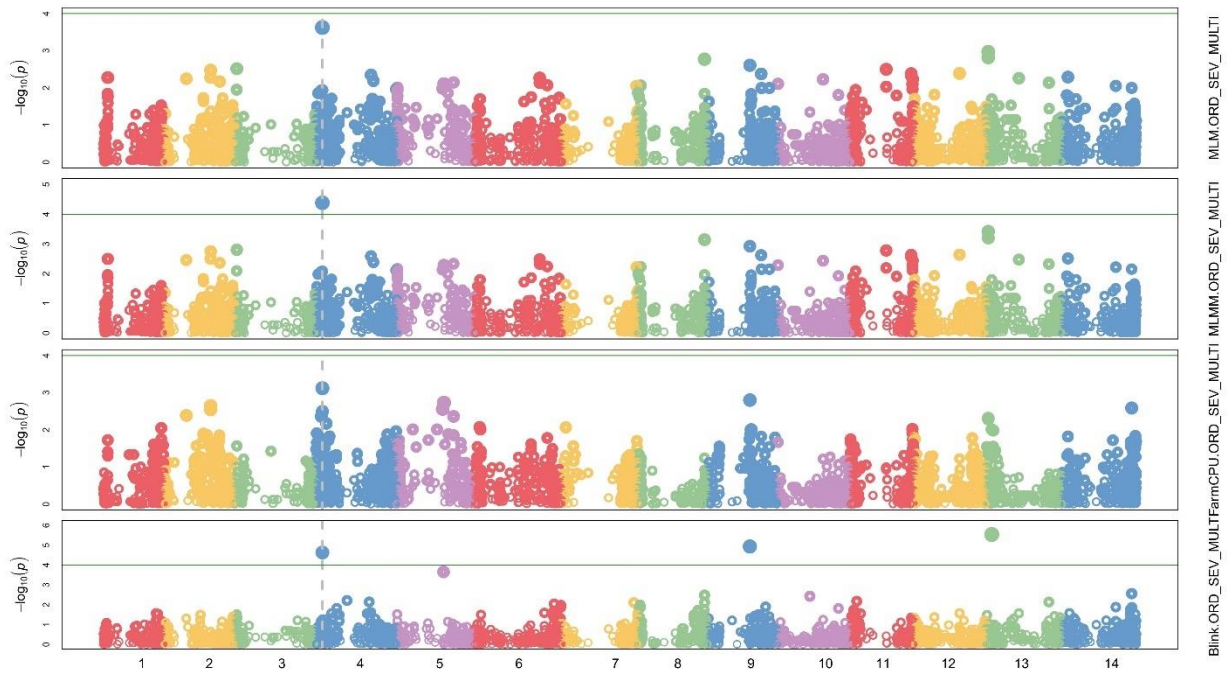

SUPPLEMENTARY FIGURE 30: Manhattan plot with all GWAS models (MLM, MLMM, FARMCPU AND BLINK) for Severity (SEV) in the 1st cluster (Grosseto 2019, Grosseto 2021 and Izmir 2019) and Q8 (West_Asian_Founders). Numbers on the Xlab refers to the durum wheat chromosomes (1 = 1A, 2 = 1B, 3 = 2A, 4 = 2B, 5 = 3A, 6 = 3B, 7 = 4A, 8 = 4B, 9 = 5A, 10 = 5B, 11 = 6A, 12 = 6B, 13 = 7A and 14 = 7B). Ylab refers to LOD ($-\log_{10}$(pvalue)).

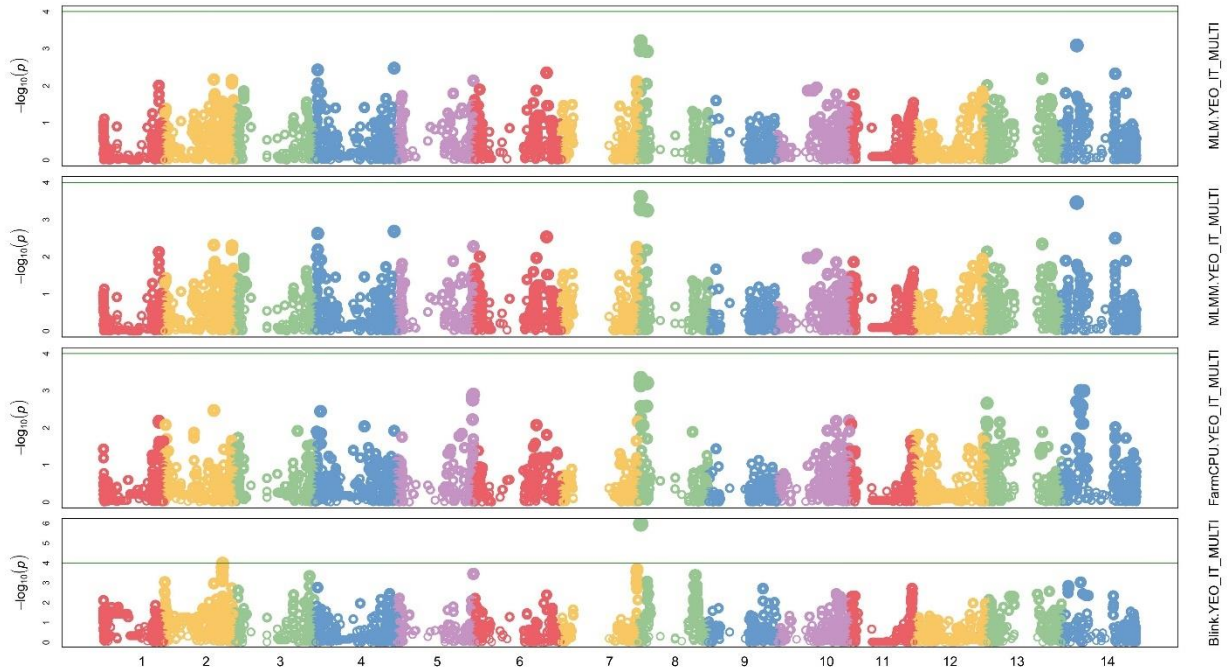

SUPPLEMENTARY FIGURE 31: Manhattan plot with all GWAS models (MLM, MLMM, FARMCPU AND BLINK) for Infection Type (IT) in the 2nd cluster (Grosseto 2018 and Lari 2019) and Q1 (Horn_Africa_aethiopicum). Numbers on the Xlab refers to the durum wheat chromosomes (1 = 1A, 2 = 1B, 3 = 2A, 4 = 2B, 5 = 3A, 6 = 3B, 7 = 4A, 8 = 4B, 9 = 5A, 10 = 5B, 11 = 6A, 12 = 6B, 13 = 7A and 14 = 7B). Ylab refers to LOD (-log10(pvalue)).

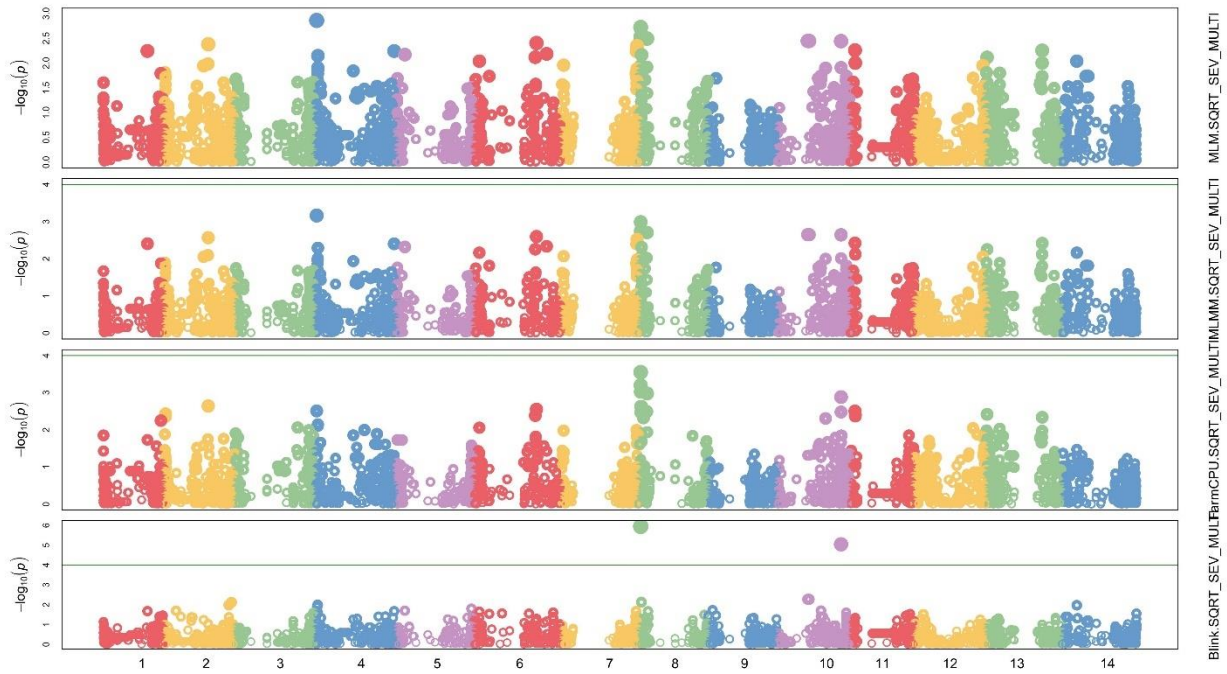

SUPPLEMENTARY FIGURE 32: Manhattan plot with all GWAS models (MLM, MLMM, FARMCPU AND BLINK) for Severity (SEV) in the 2nd cluster (Grosseto 2018 and Lari 2019) and Q1 (Horn_Africa_aethiopicum). Numbers on the Xlab refers to the durum wheat chromosomes (1 = 1A, 2 = 1B, 3 = 2A, 4 = 2B, 5 = 3A, 6 = 3B, 7 = 4A, 8 = 4B, 9 = 5A, 10 = 5B, 11 = 6A, 12 = 6B, 13 = 7A and 14 = 7B). Ylab refers to LOD (-log10(pvalue)).

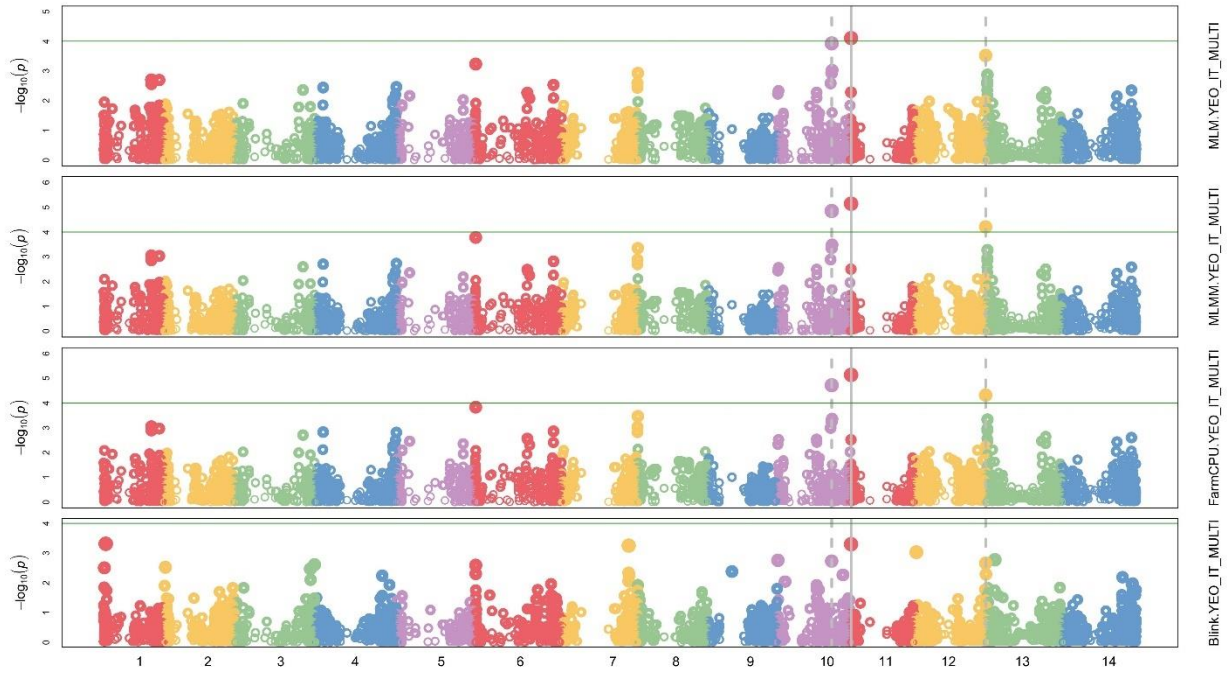

SUPPLEMENTARY FIGURE 33: Manhattan plot with all GWAS models (MLM, MLMM, FARMCPU AND BLINK) for Infection Type (IT) in the 2nd cluster (Grosseto 2018 and Lari 2019) and Q3 (Iran_syriacum). Numbers on the Xlab refers to the durum wheat chromosomes (1 = 1A, 2 = 1B, 3 = 2A, 4 = 2B, 5 = 3A, 6 = 3B, 7 = 4A, 8 = 4B, 9 = 5A, 10 = 5B, 11 = 6A, 12 = 6B, 13 = 7A and 14 = 7B). Ylab refers to LOD (-log10(pvalue)).

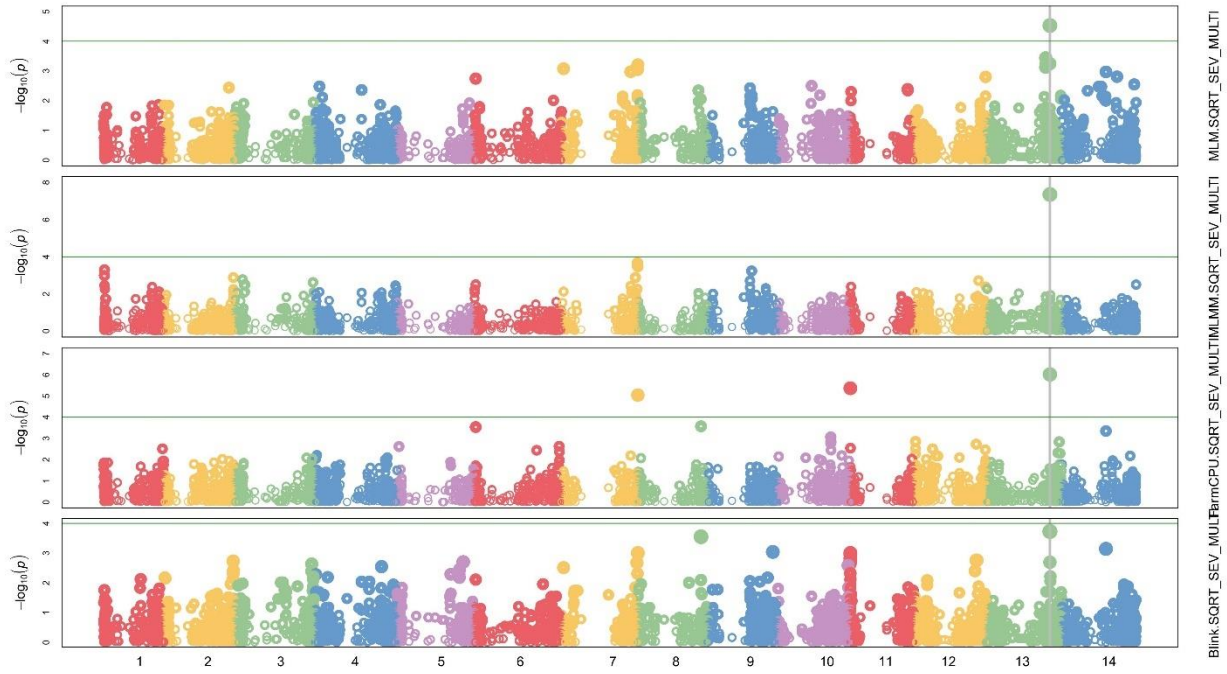

SUPPLEMENTARY FIGURE 34: Manhattan plot with all GWAS models (MLM, MLMM, FARMCPU AND BLINK) for Severity (SEV) in the 2nd cluster (Grosseto 2018 and Lari 2019) and Q3 (Iran_syriacum). Numbers on the Xlab refers to the durum wheat chromosomes (1 = 1A, 2 = 1B, 3 = 2A, 4 = 2B, 5 = 3A, 6 = 3B, 7 = 4A, 8 = 4B, 9 = 5A, 10 = 5B, 11 = 6A, 12 = 6B, 13 = 7A and 14 = 7B). Ylab refers to LOD (-log10(pvalue)).

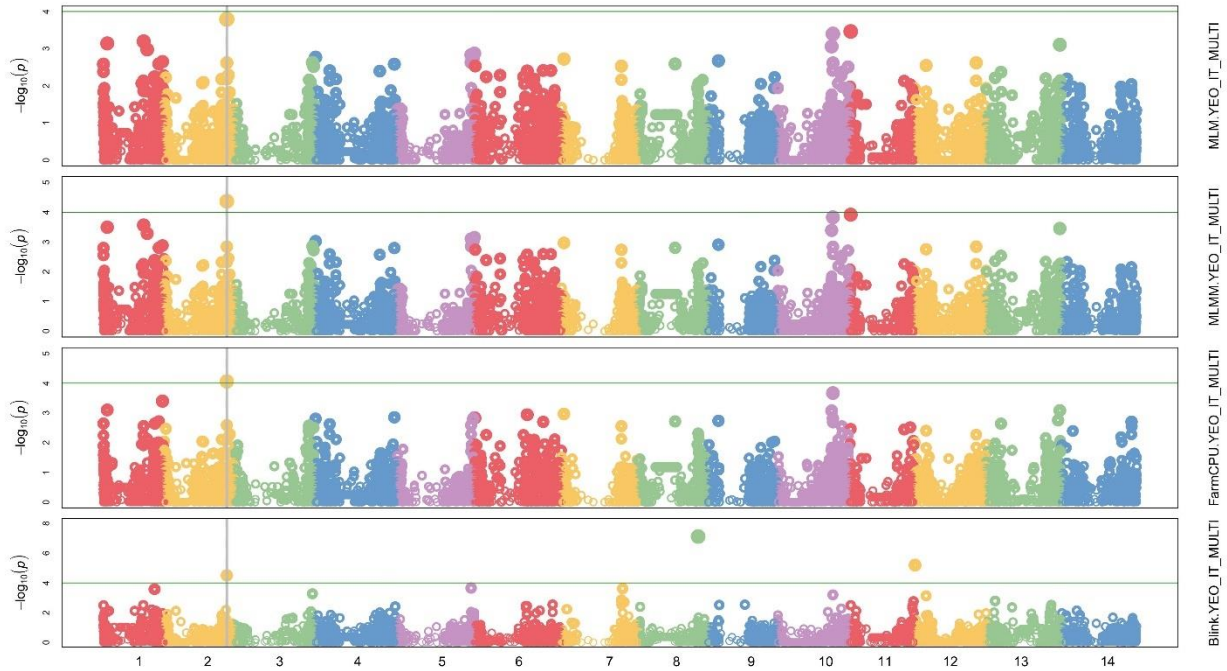

SUPPLEMENTARY FIGURE 35: Manhattan plot with all GWAS models (MLM, MLMM, FARMCPU AND BLINK) for Infection Type (IT) in the 2nd cluster (Grosseto 2018 and Lari 2019) and Q6 (WestAsia_Caucasus). Numbers on the Xlab refers to the durum wheat chromosomes (1 = 1A, 2 = 1B, 3 = 2A, 4 = 2B, 5 = 3A, 6 = 3B, 7 = 4A, 8 = 4B, 9 = 5A, 10 = 5B, 11 = 6A, 12 = 6B, 13 = 7A and 14 = 7B). Ylab refers to LOD (-log10(pvalue)).

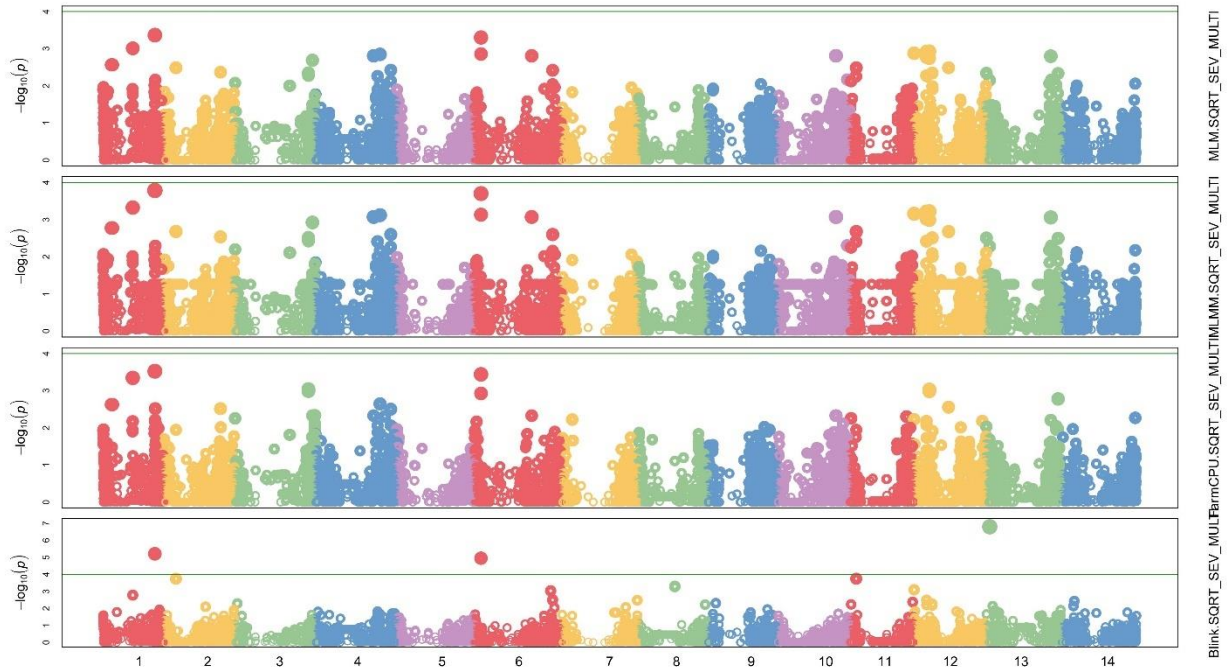

SUPPLEMENTARY FIGURE 36: Manhattan plot with all GWAS models (MLM, MLMM, FARMCPU AND BLINK) for Severity (SEV) in the 2nd cluster (Grosseto 2018 and Lari 2019) and Q6 (WestAsia_Caucasus). Numbers on the Xlab refers to the durum wheat chromosomes (1 = 1A, 2 = 1B, 3 = 2A, 4 = 2B, 5 = 3A, 6 = 3B, 7 = 4A, 8 = 4B, 9 = 5A, 10 = 5B, 11 = 6A, 12 = 6B, 13 = 7A and 14 = 7B). Ylab refers to LOD (-log10(pvalue)).

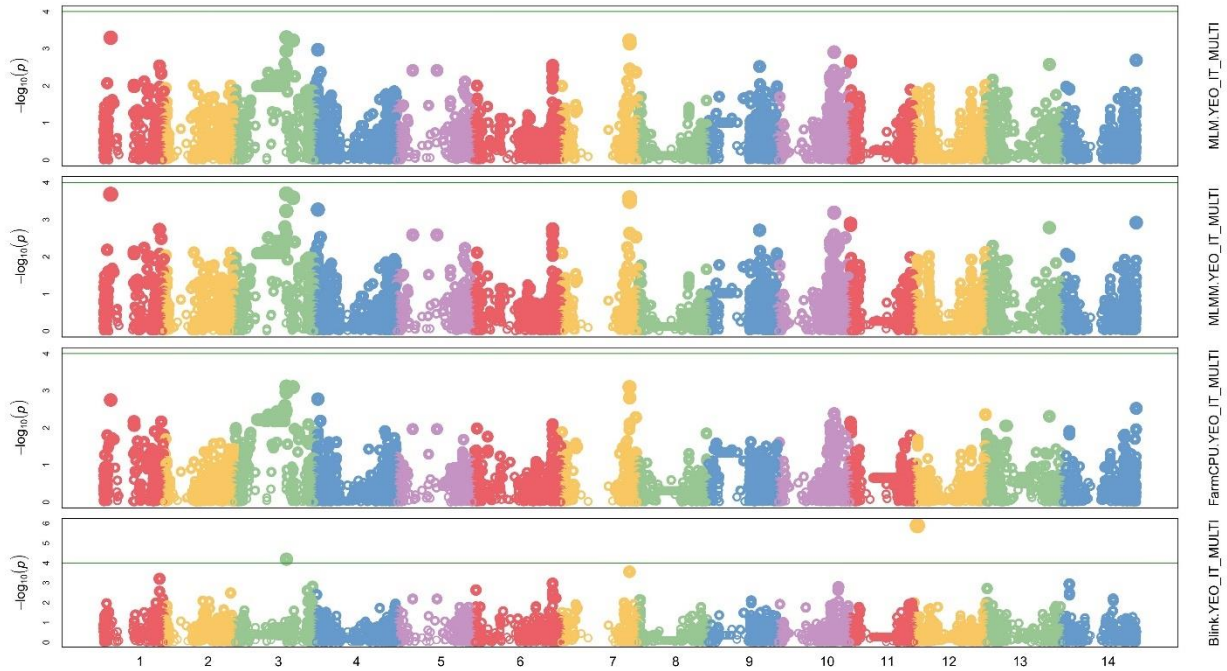

SUPPLEMENTARY FIGURE 37: Manhattan plot with all GWAS models (MLM, MLMM, FARMCPU AND BLINK) for Infection Type (IT) in the 2nd cluster (Grosseto 2018 and Lari 2019) and Q7 (Cyprous_Iberia). Numbers on the Xlab refers to the durum wheat chromosomes (1 = 1A, 2 = 1B, 3 = 2A, 4 = 2B, 5 = 3A, 6 = 3B, 7 = 4A, 8 = 4B, 9 = 5A, 10 = 5B, 11 = 6A, 12 = 6B, 13 = 7A and 14 = 7B). Ylab refers to LOD (-log10(pvalue)).

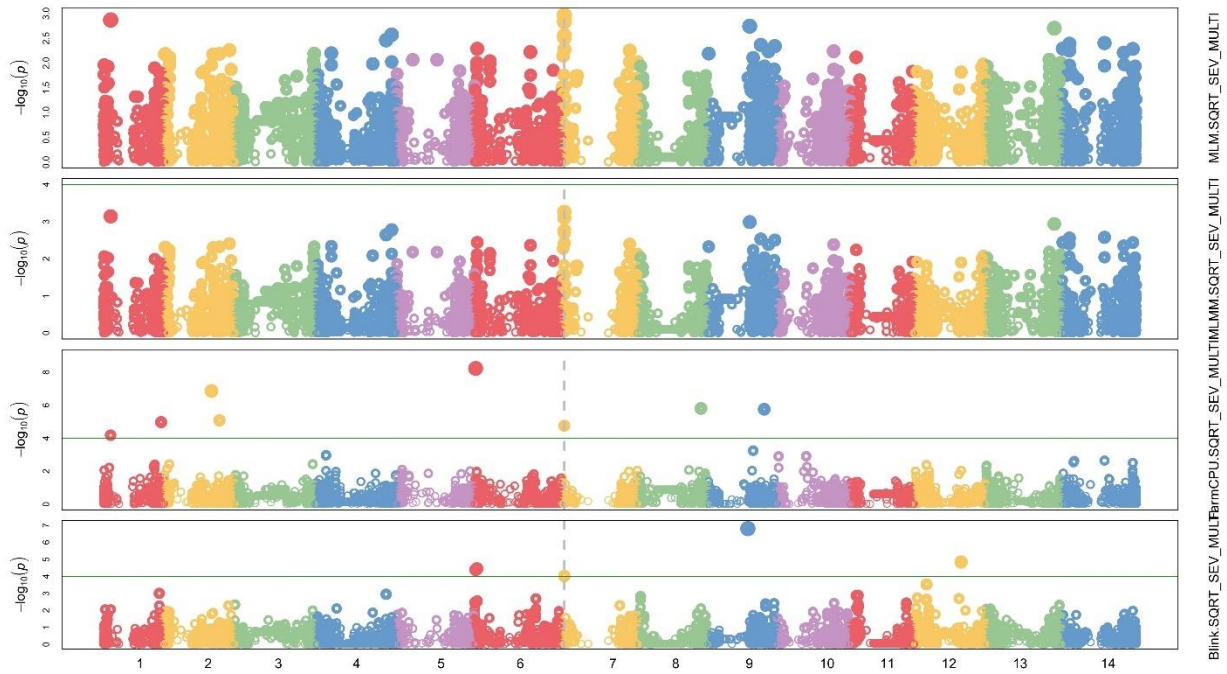

SUPPLEMENTARY FIGURE 38: Manhattan plot with all GWAS models (MLM, MLMM, FARMCPU AND BLINK) for Severity (SEV) in the 2nd cluster (Grosseto 2018 and Lari 2019) and Q7 (Cyprous_Iberia). Numbers on the Xlab refers to the durum wheat chromosomes (1 = 1A, 2 = 1B, 3 = 2A, 4 = 2B, 5 = 3A, 6 = 3B, 7 = 4A, 8 = 4B, 9 = 5A, 10 = 5B, 11 = 6A, 12 = 6B, 13 = 7A and 14 = 7B). Ylab refers to LOD (-log10(pvalue)).

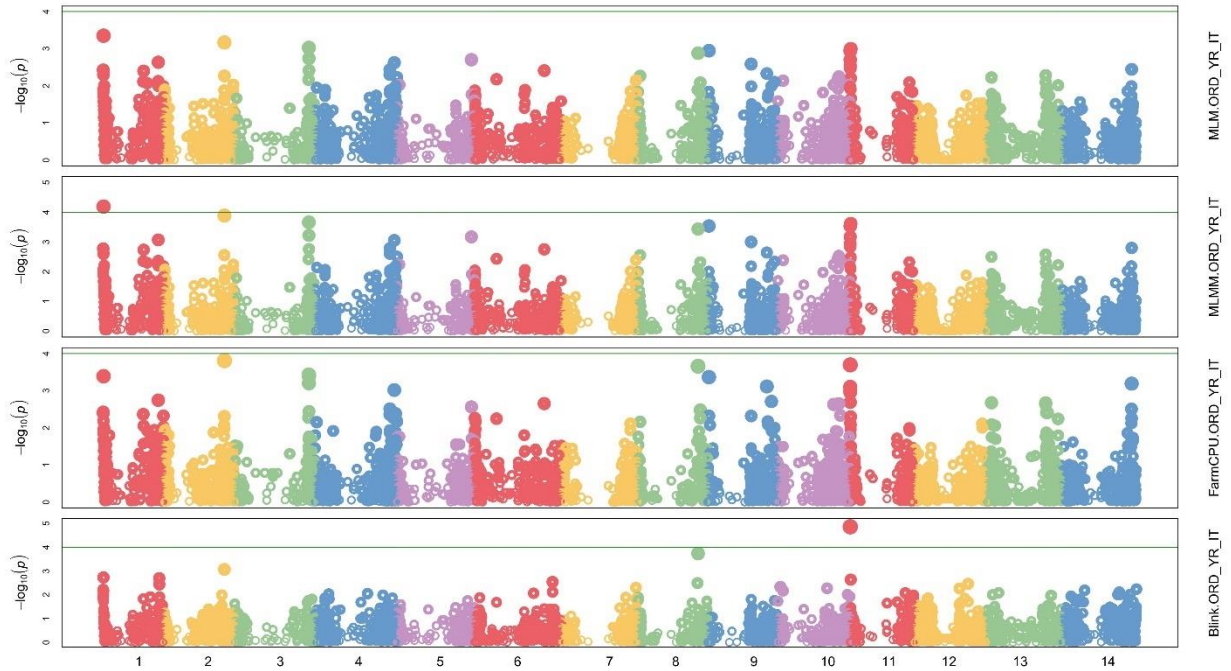

SUPPLEMENTARY FIGURE 39: Manhattan plot with all GWAS models (MLM, MLMM, FARMCPU AND BLINK) for Infection Type (IT) in Grosseto 2018 and Q6 (WestAsia_Caucasus). Numbers on the Xlab refers to the durum wheat chromosomes (1 = 1A, 2 = 1B, 3 = 2A, 4 = 2B, 5 = 3A, 6 = 3B, 7 = 4A, 8 = 4B, 9 = 5A, 10 = 5B, 11 = 6A, 12 = 6B, 13 = 7A and 14 = 7B). Ylab refers to LOD (-log$_{10}$(pvalue)).

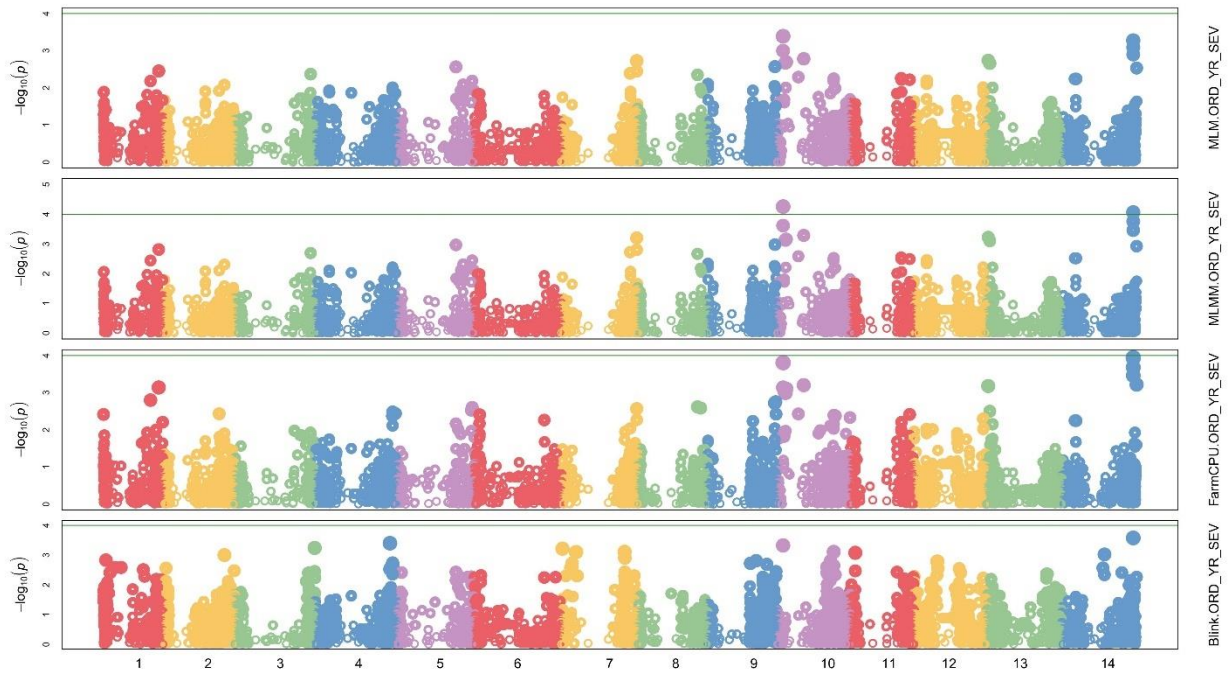

SUPPLEMENTARY FIGURE 40: Manhattan plot with all GWAS models (MLM, MLMM, FARMCPU AND BLINK) for Severity (SEV) in Grosseto 2018 and Q6 (WestAsia_Caucasus). Numbers on the Xlab refers to the durum wheat chromosomes (1 = 1A, 2 = 1B, 3 = 2A, 4 = 2B, 5 = 3A, 6 = 3B, 7 = 4A, 8 = 4B, 9 = 5A, 10 = 5B, 11 = 6A, 12 = 6B, 13 = 7A and 14 = 7B). Ylab refers to LOD (-log$_{10}$(pvalue)).

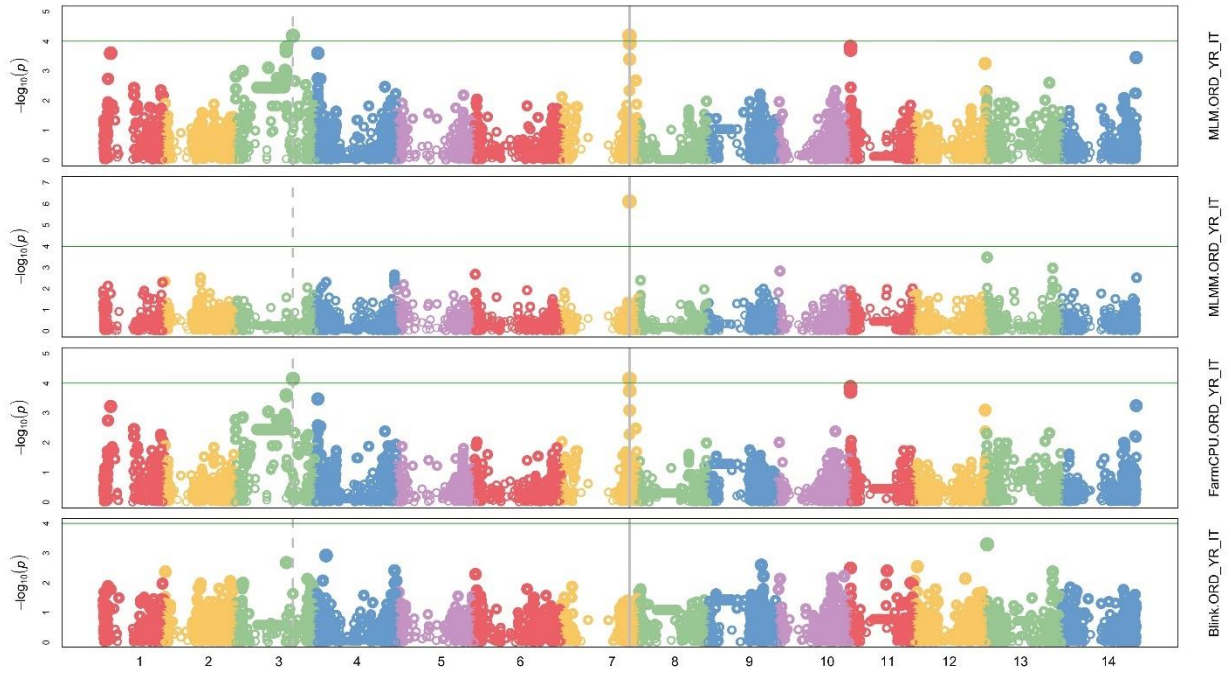

SUPPLEMENTARY FIGURE 41: Manhattan plot with all GWAS models (MLM, MLMM, FARMCPU AND BLINK) for Infection Type (IT) in Grosseto 2018 and Q7 (Cyprous_Iberia). Numbers on the Xlab refers to the durum wheat chromosomes (1 = 1A, 2 = 1B, 3 = 2A, 4 = 2B, 5 = 3A, 6 = 3B, 7 = 4A, 8 = 4B, 9 = 5A, 10 = 5B, 11 = 6A, 12 = 6B, 13 = 7A and 14 = 7B). Ylab refers to LOD (-log$_{10}$(pvalue)).

SUPPLEMENTARY FIGURE 42: Manhattan plot with all GWAS models (MLM, MLMM, FARMCPU AND BLINK) for Severity (SEV) in Grosseto 2018 and Q7 (Cyprous_Iberia). Numbers on the Xlab refers to the durum wheat chromosomes (1 = 1A, 2 = 1B, 3 = 2A, 4 = 2B, 5 = 3A, 6 = 3B, 7 = 4A, 8 = 4B, 9 = 5A, 10 = 5B, 11 = 6A, 12 = 6B, 13 = 7A and 14 = 7B). Ylab refers to LOD (-log$_{10}$(pvalue)).

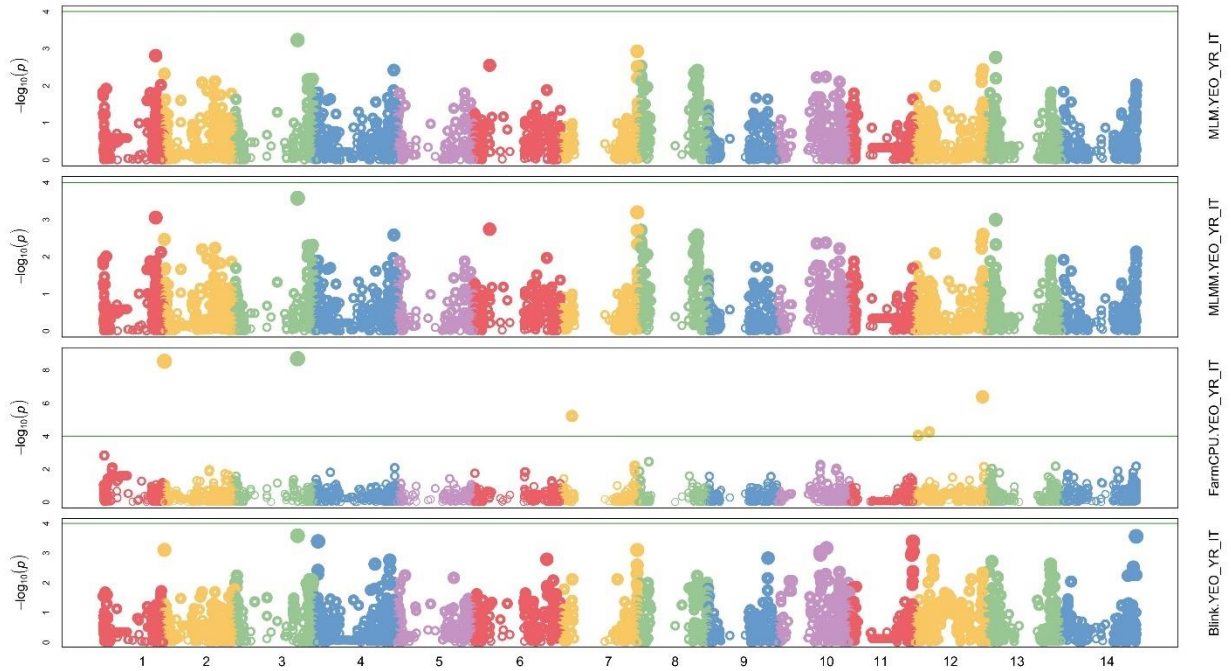

SUPPLEMENTARY FIGURE 43: Manhattan plot with all GWAS models (MLM, MLMM, FARMCPU AND BLINK) for Infection Type (IT) in Grosseto 2019 and Q1 (Horn_Africa_aethiopicum). Numbers on the Xlab refers to the durum wheat chromosomes (1 = 1A, 2 = 1B, 3 = 2A, 4 = 2B, 5 = 3A, 6 = 3B, 7 = 4A, 8 = 4B, 9 = 5A, 10 = 5B, 11 = 6A, 12 = 6B, 13 = 7A and 14 = 7B). Ylab refers to LOD (-log$_{10}$(pvalue)).

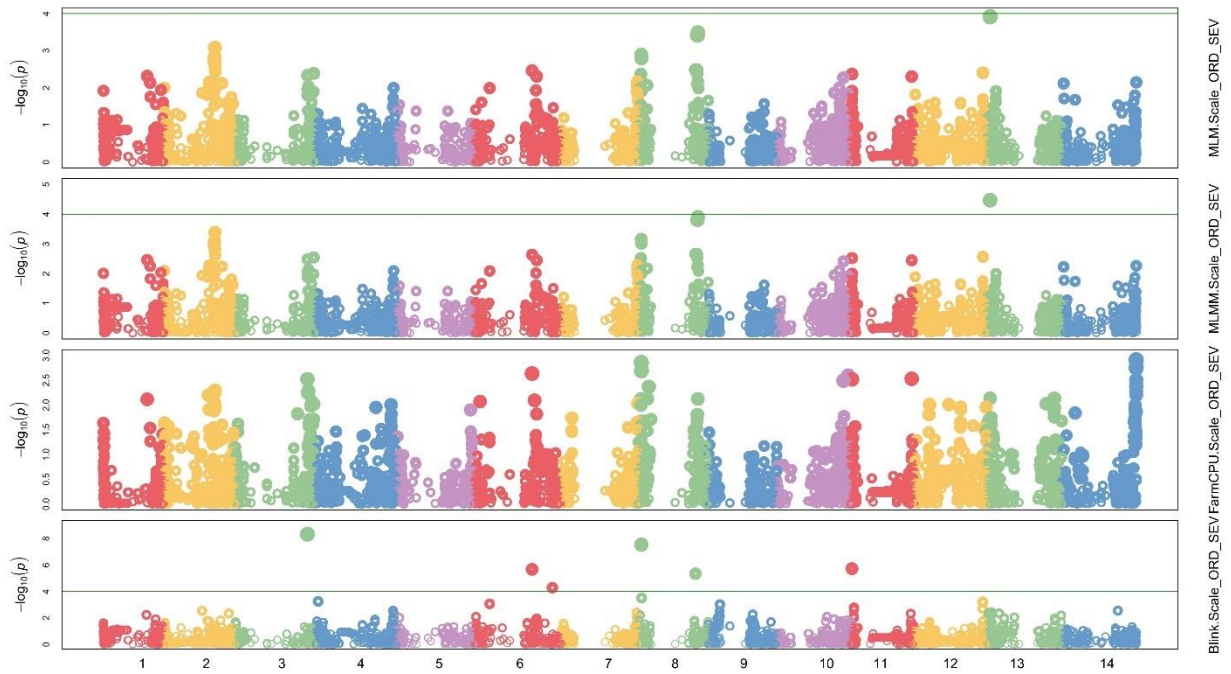

SUPPLEMENTARY FIGURE 44: Manhattan plot with all GWAS models (MLM, MLMM, FARMCPU AND BLINK) for Severity (SEV) in Grosseto 2019 and Q1 (Horn_Africa_aethiopicum). Numbers on the Xlab refers to the durum wheat chromosomes (1 = 1A, 2 = 1B, 3 = 2A, 4 = 2B, 5 = 3A, 6 = 3B, 7 = 4A, 8 = 4B, 9 = 5A, 10 = 5B, 11 = 6A, 12 = 6B, 13 = 7A and 14 = 7B). Ylab refers to LOD (-log$_{10}$(pvalue)).

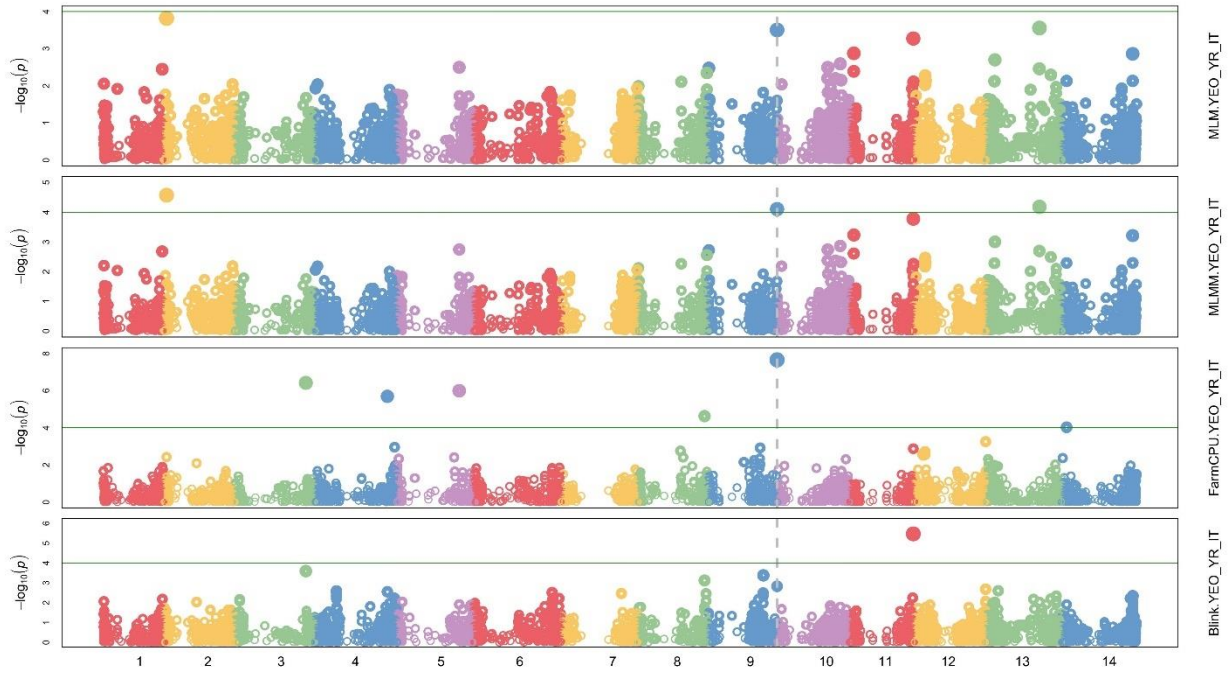

SUPPLEMENTARY FIGURE 45: Manhattan plot with all GWAS models (MLM, MLMM, FARMCPU AND BLINK) for Infection Type (IT) in Grosseto 2019 and Q3 (Iran_syriacum). Numbers on the Xlab refers to the durum wheat chromosomes (1 = 1A, 2 = 1B, 3 = 2A, 4 = 2B, 5 = 3A, 6 = 3B, 7 = 4A, 8 = 4B, 9 = 5A, 10 = 5B, 11 = 6A, 12 = 6B, 13 = 7A and 14 = 7B). Ylab refers to LOD (-log$_{10}$(pvalue)).

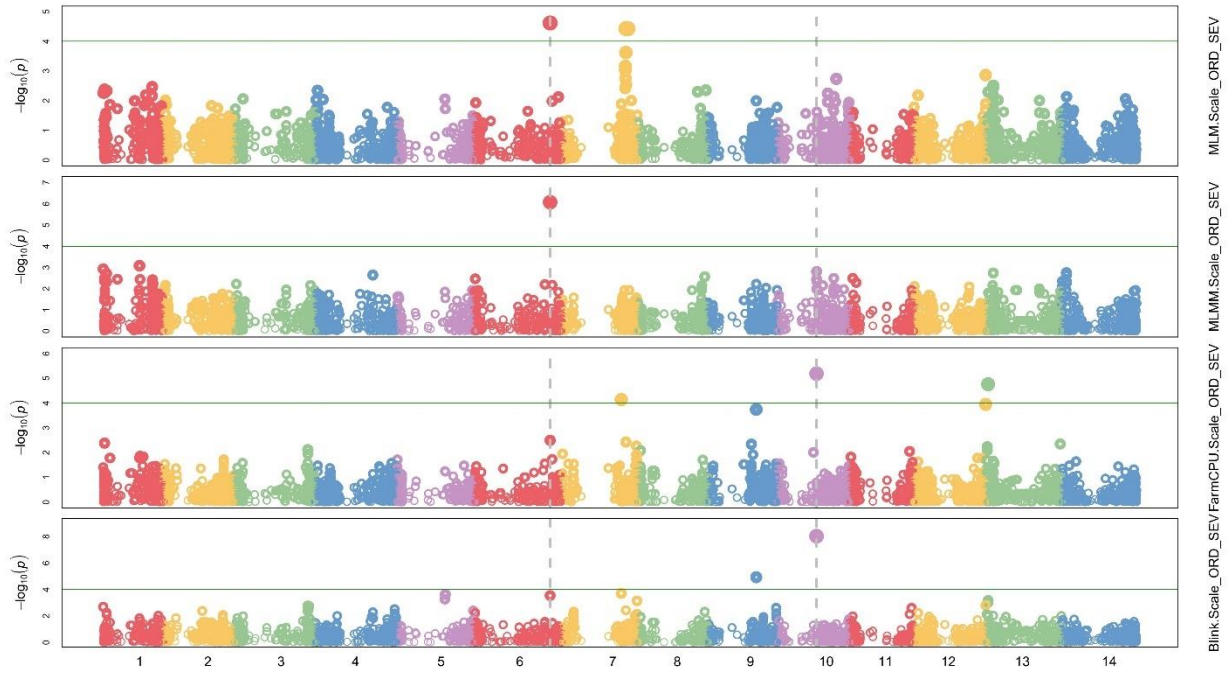

SUPPLEMENTARY FIGURE 46: Manhattan plot with all GWAS models (MLM, MLMM, FARMCPU AND BLINK) for Severity (SEV) in Grosseto 2019 and Q3 (Iran_syriacum). Numbers on the Xlab refers to the durum wheat chromosomes (1 = 1A, 2 = 1B, 3 = 2A, 4 = 2B, 5 = 3A, 6 = 3B, 7 = 4A, 8 = 4B, 9 = 5A, 10 = 5B, 11 = 6A, 12 = 6B, 13 = 7A and 14 = 7B). Ylab refers to LOD (-log$_{10}$(pvalue)).

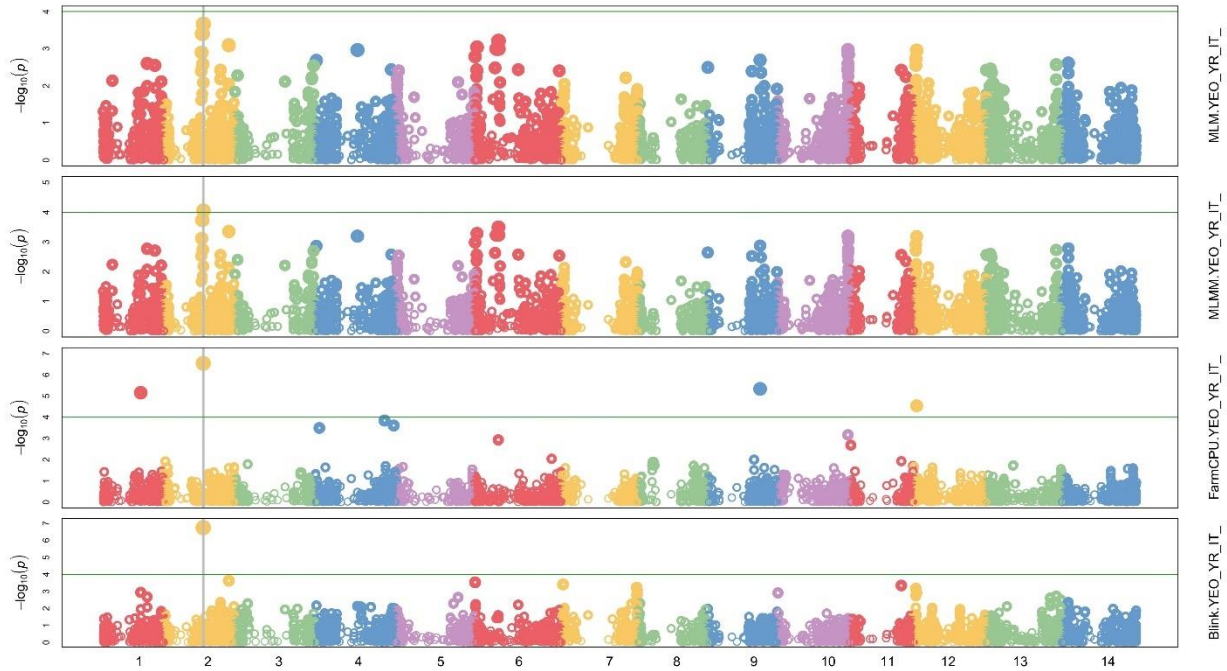

SUPPLEMENTARY FIGURE 47: Manhattan plot with all GWAS models (MLM, MLMM, FARMCPU AND BLINK) for Infection Type (IT) in Grosseto 2019 and Q6 (WestAsia_Caucasus). Numbers on the Xlab refers to the durum wheat chromosomes (1 = 1A, 2 = 1B, 3 = 2A, 4 = 2B, 5 = 3A, 6 = 3B, 7 = 4A, 8 = 4B, 9 = 5A, 10 = 5B, 11 = 6A, 12 = 6B, 13 = 7A and 14 = 7B). Ylab refers to LOD (-log$_{10}$(pvalue)).

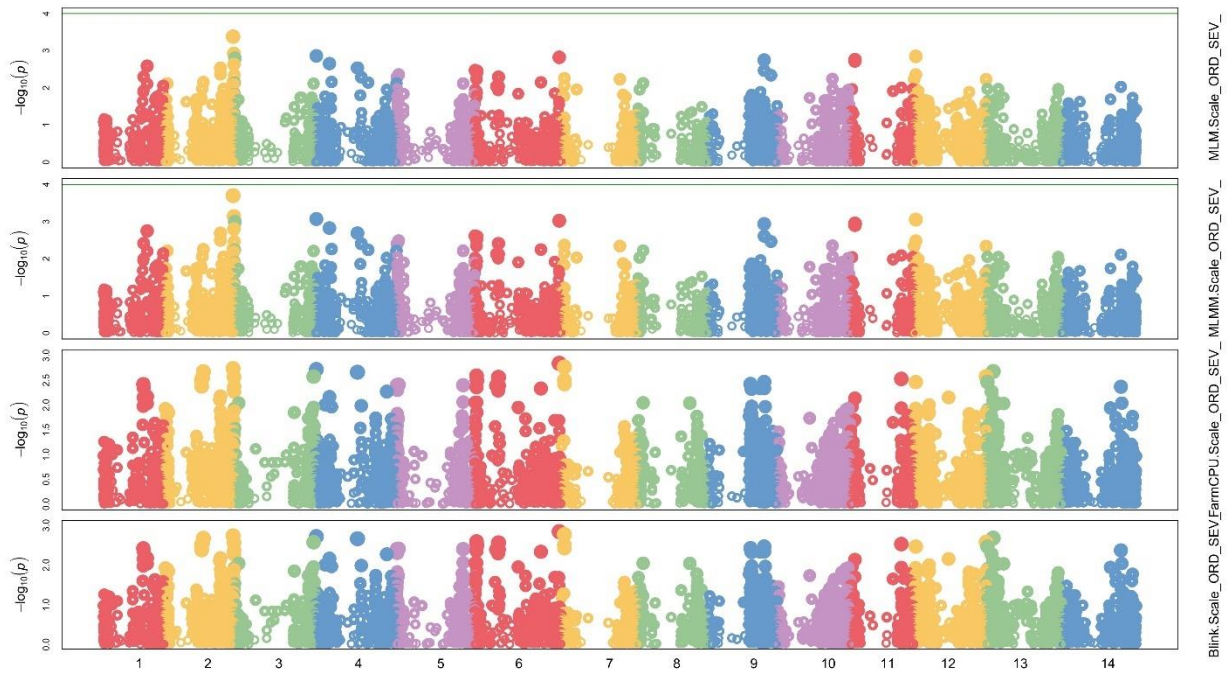

SUPPLEMENTARY FIGURE 48: Manhattan plot with all GWAS models (MLM, MLMM, FARMCPU AND BLINK) for Severity (SEV) in Grosseto 2019 and Q6 (WestAsia_Caucasus). Numbers on the Xlab refers to the durum wheat chromosomes (1 = 1A, 2 = 1B, 3 = 2A, 4 = 2B, 5 = 3A, 6 = 3B, 7 = 4A, 8 = 4B, 9 = 5A, 10 = 5B, 11 = 6A, 12 = 6B, 13 = 7A and 14 = 7B). Ylab refers to LOD (-log$_{10}$(pvalue)).

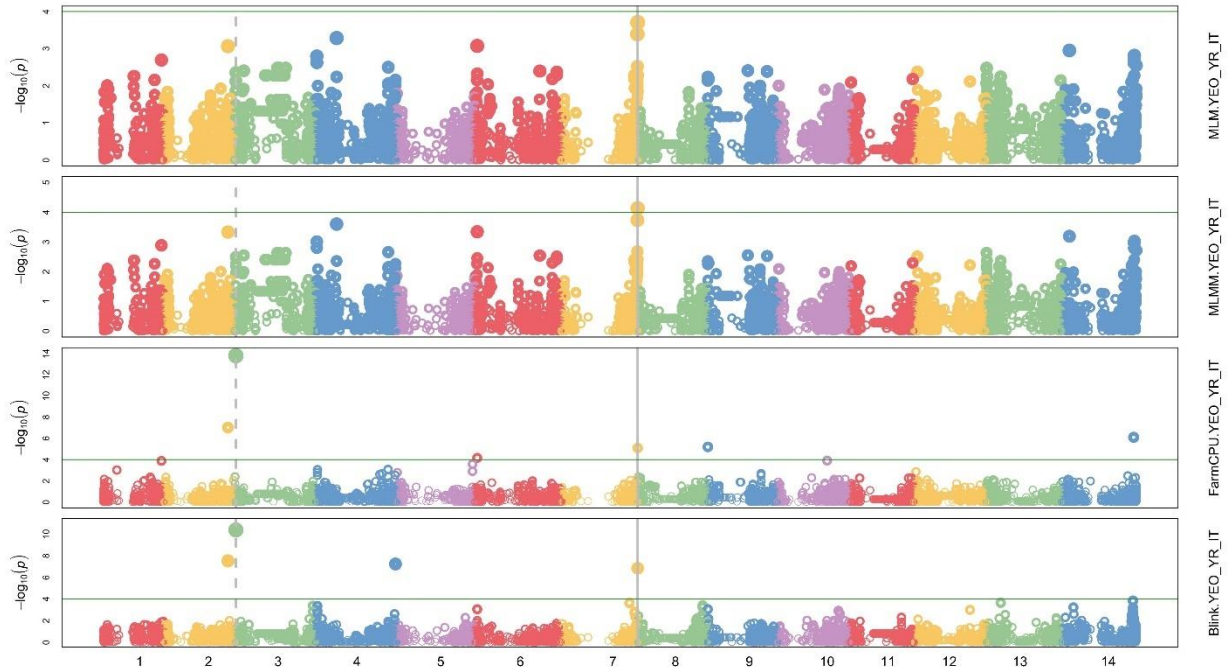

SUPPLEMENTARY FIGURE 49: Manhattan plot with all GWAS models (MLM, MLMM, FARMCPU AND BLINK) for Infection Type (IT) in Grosseto 2019 and Q7 (Cyprous_Iberia). Numbers on the Xlab refers to the durum wheat chromosomes (1 = 1A, 2 = 1B, 3 = 2A, 4 = 2B, 5 = 3A, 6 = 3B, 7 = 4A, 8 = 4B, 9 = 5A, 10 = 5B, 11 = 6A, 12 = 6B, 13 = 7A and 14 = 7B). Ylab refers to LOD (-log$_{10}$(pvalue)).

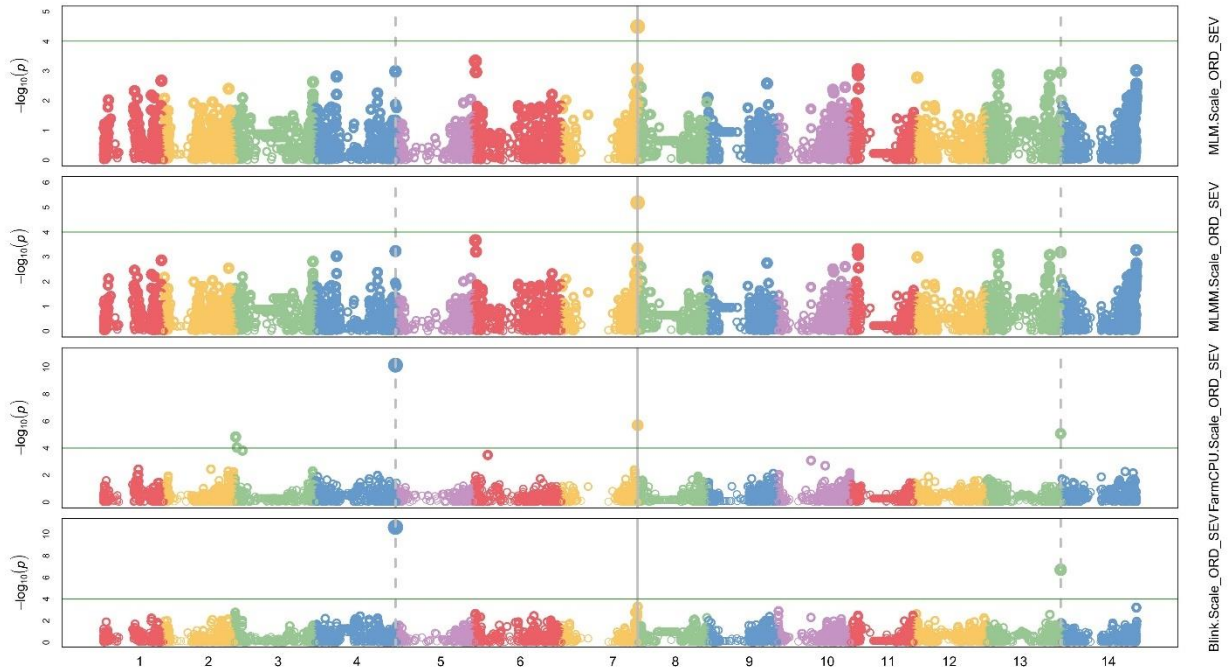

SUPPLEMENTARY FIGURE 50: Manhattan plot with all GWAS models (MLM, MLMM, FARMCPU AND BLINK) for Severity (SEV) in Grosseto 2019 and Q7 (Cyprous_Iberia). Numbers on the Xlab refers to the durum wheat chromosomes (1 = 1A, 2 = 1B, 3 = 2A, 4 = 2B, 5 = 3A, 6 = 3B, 7 = 4A, 8 = 4B, 9 = 5A, 10 = 5B, 11 = 6A, 12 = 6B, 13 = 7A and 14 = 7B). Ylab refers to LOD (-log$_{10}$(pvalue)).

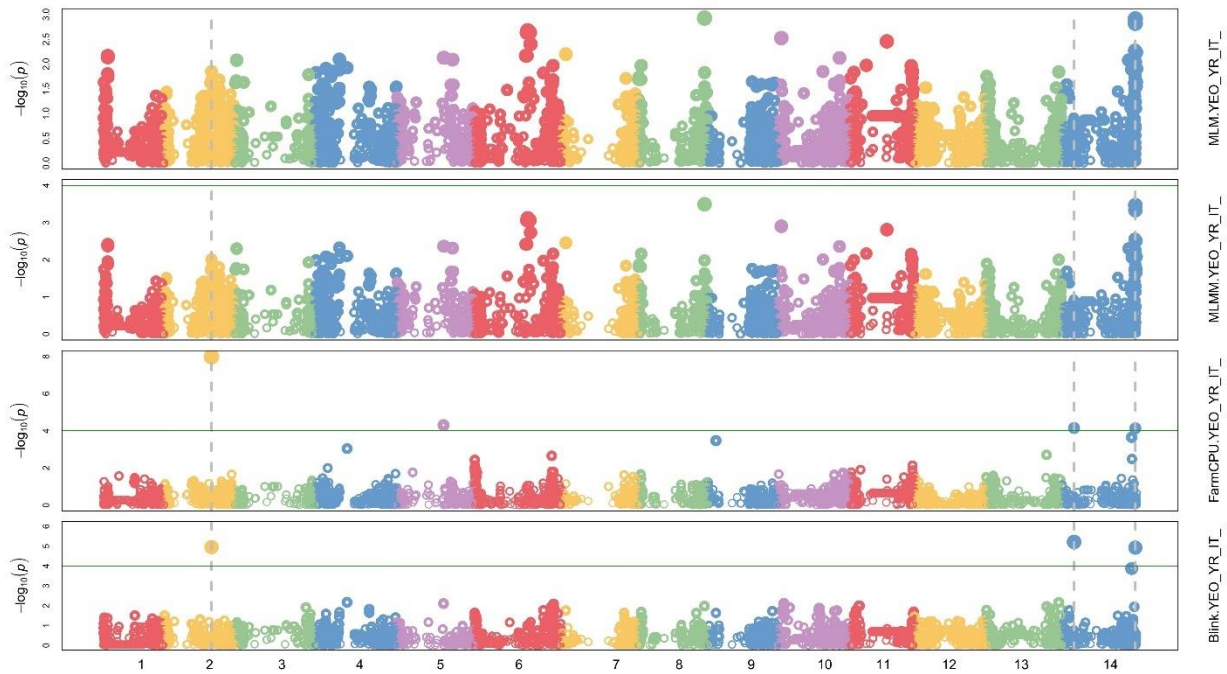

SUPPLEMENTARY FIGURE 51: Manhattan plot with all GWAS models (MLM, MLMM, FARMCPU AND BLINK) for Infection Type (IT) in Grosseto 2019 and Q8 (West_Asian_Founders). Numbers on the Xlab refers to the durum wheat chromosomes (1 = 1A, 2 = 1B, 3 = 2A, 4 = 2B, 5 = 3A, 6 = 3B, 7 = 4A, 8 = 4B, 9 = 5A, 10 = 5B, 11 = 6A, 12 = 6B, 13 = 7A and 14 = 7B). Ylab refers to LOD (-log$_{10}$(pvalue)).

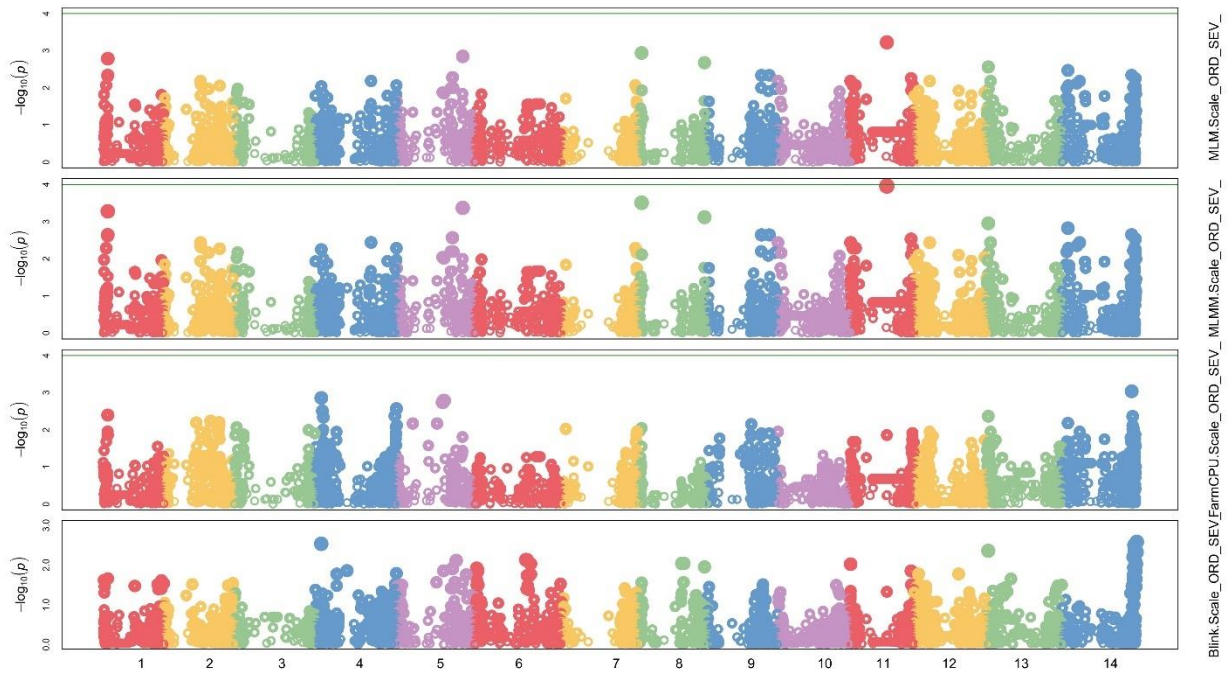

SUPPLEMENTARY FIGURE 52: Manhattan plot with all GWAS models (MLM, MLMM, FARMCPU AND BLINK) for Severity (SEV) in Grosseto 2019 and Q8 (West_Asian_Founders). Numbers on the Xlab refers to the durum wheat chromosomes (1 = 1A, 2 = 1B, 3 = 2A, 4 = 2B, 5 = 3A, 6 = 3B, 7 = 4A, 8 = 4B, 9 = 5A, 10 = 5B, 11 = 6A, 12 = 6B, 13 = 7A and 14 = 7B). Ylab refers to LOD (-log$_{10}$(pvalue)).

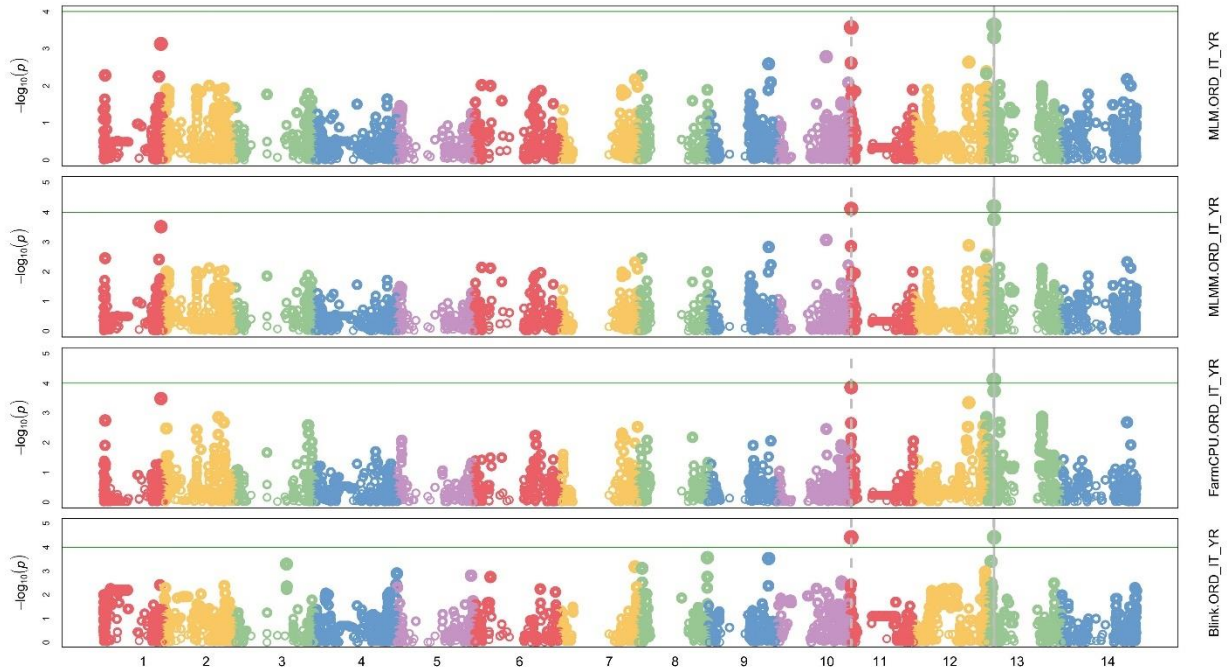

SUPPLEMENTARY FIGURE 53: Manhattan plot with all GWAS models (MLM, MLMM, FARMCPU AND BLINK) for Infection Type (IT) in Izmir 2019 and Q1 (Horn_Africa_aethiopicum). Numbers on the Xlab refers to the durum wheat chromosomes (1 = 1A, 2 = 1B, 3 = 2A, 4 = 2B, 5 = 3A, 6 = 3B, 7 = 4A, 8 = 4B, 9 = 5A, 10 = 5B, 11 = 6A, 12 = 6B, 13 = 7A and 14 = 7B). Ylab refers to LOD (-log$_{10}$(pvalue)).

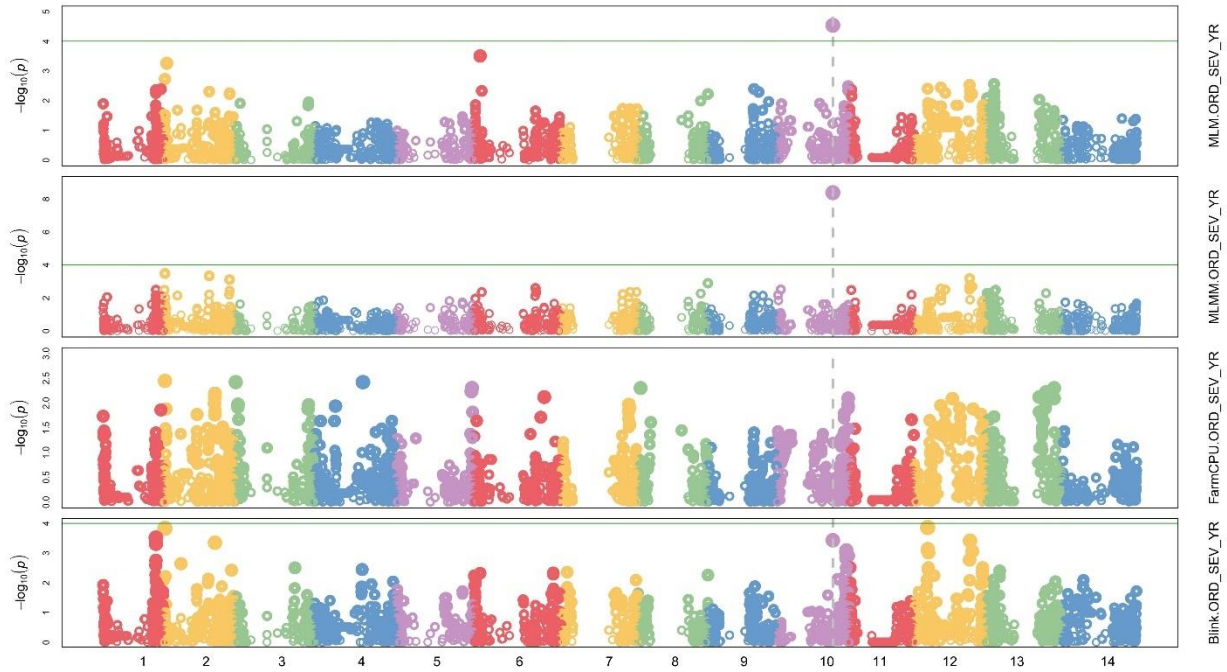

SUPPLEMENTARY FIGURE 54: Manhattan plot with all GWAS models (MLM, MLMM, FARMCPU AND BLINK) for Severity (SEV) in Izmir 2019 and Q3 (Iran_syriacum). Numbers on the Xlab refers to the durum wheat chromosomes (1 = 1A, 2 = 1B, 3 = 2A, 4 = 2B, 5 = 3A, 6 = 3B, 7 = 4A, 8 = 4B, 9 = 5A, 10 = 5B, 11 = 6A, 12 = 6B, 13 = 7A and 14 = 7B). Ylab refers to LOD (-log$_{10}$(pvalue)).

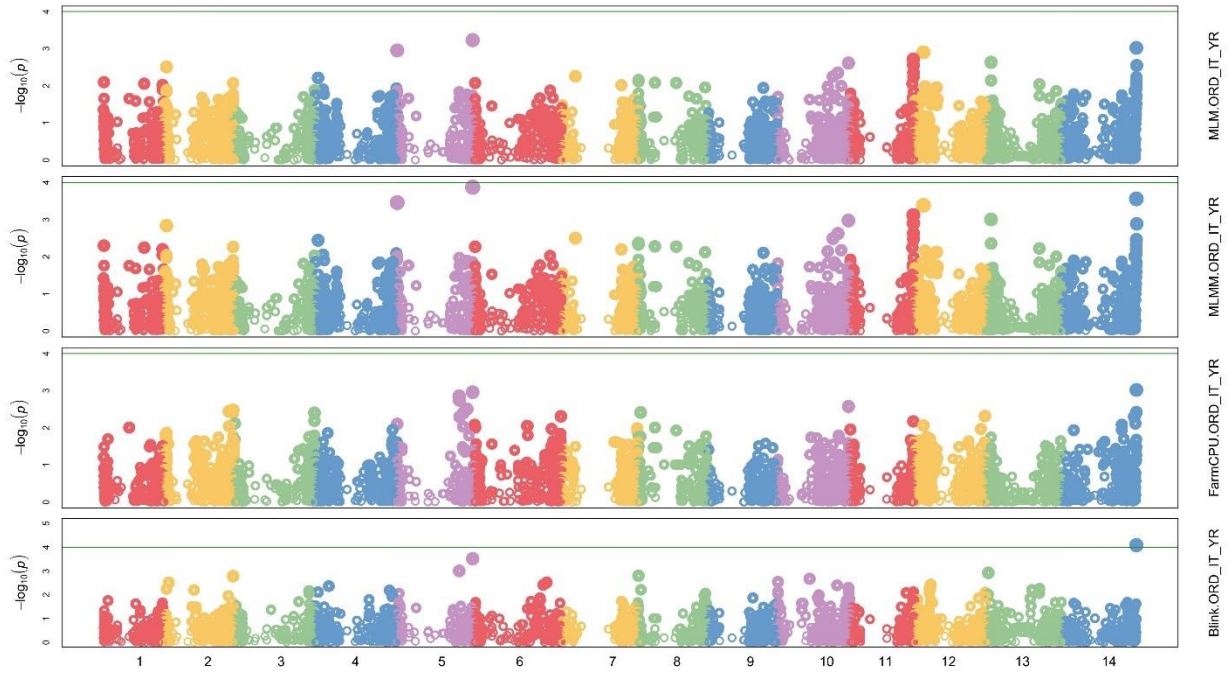

SUPPLEMENTARY FIGURE 55: Manhattan plot with all GWAS models (MLM, MLMM, FARMCPU AND BLINK) for Infection Type (IT) in Izmir 2019 and Q3 (Horn_Africa_aethiopicum). Numbers on the Xlab refers to the durum wheat chromosomes (1 = 1A, 2 = 1B, 3 = 2A, 4 = 2B, 5 = 3A, 6 = 3B, 7 = 4A, 8 = 4B, 9 = 5A, 10 = 5B, 11 = 6A, 12 = 6B, 13 = 7A and 14 = 7B). Ylab refers to LOD (-log$_{10}$(pvalue)).

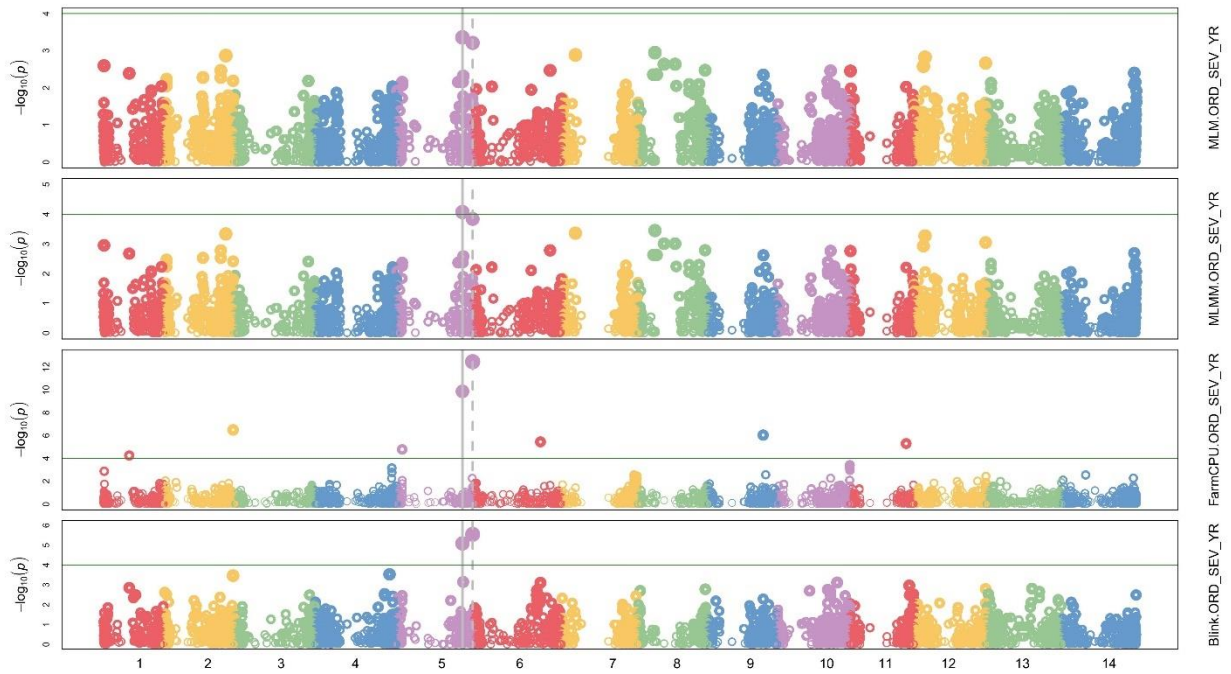

SUPPLEMENTARY FIGURE 56: Manhattan plot with all GWAS models (MLM, MLMM, FARMCPU AND BLINK) for Severity (SEV) in Izmir 2019 and Q3 (Horn_Africa_aethiopicum). Numbers on the Xlab refers to the durum wheat chromosomes (1 = 1A, 2 = 1B, 3 = 2A, 4 = 2B, 5 = 3A, 6 = 3B, 7 = 4A, 8 = 4B, 9 = 5A, 10 = 5B, 11 = 6A, 12 = 6B, 13 = 7A and 14 = 7B). Ylab refers to LOD (-log$_{10}$(pvalue)).

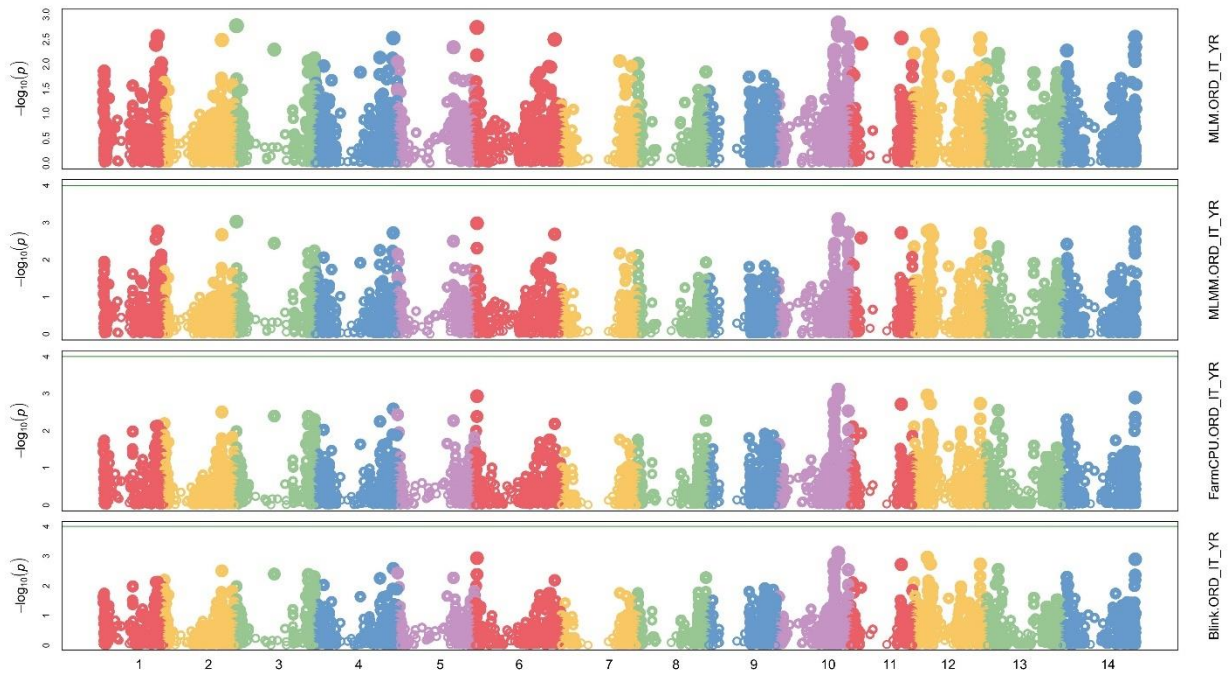

SUPPLEMENTARY FIGURE 57: Manhattan plot with all GWAS models (MLM, MLMM, FARMCPU AND BLINK) for Infection Type (IT) in Izmir 2019 and Q6 (WestAsia_Caucasus). Numbers on the Xlab refers to the durum wheat chromosomes (1 = 1A, 2 = 1B, 3 = 2A, 4 = 2B, 5 = 3A, 6 = 3B, 7 = 4A, 8 = 4B, 9 = 5A, 10 = 5B, 11 = 6A, 12 = 6B, 13 = 7A and 14 = 7B). Ylab refers to LOD (-log$_{10}$(pvalue)).

SUPPLEMENTARY FIGURE 58: Manhattan plot with all GWAS models (MLM, MLMM, FARMCPU AND BLINK) for Severity (SEV) in Izmir 2019 and Q6 (WestAsia_Caucasus). Numbers on the Xlab refers to the durum wheat chromosomes (1 = 1A, 2 = 1B, 3 = 2A, 4 = 2B, 5 = 3A, 6 = 3B, 7 = 4A, 8 = 4B, 9 = 5A, 10 = 5B, 11 = 6A, 12 = 6B, 13 = 7A and 14 = 7B). Ylab refers to LOD (-log$_{10}$(pvalue)).

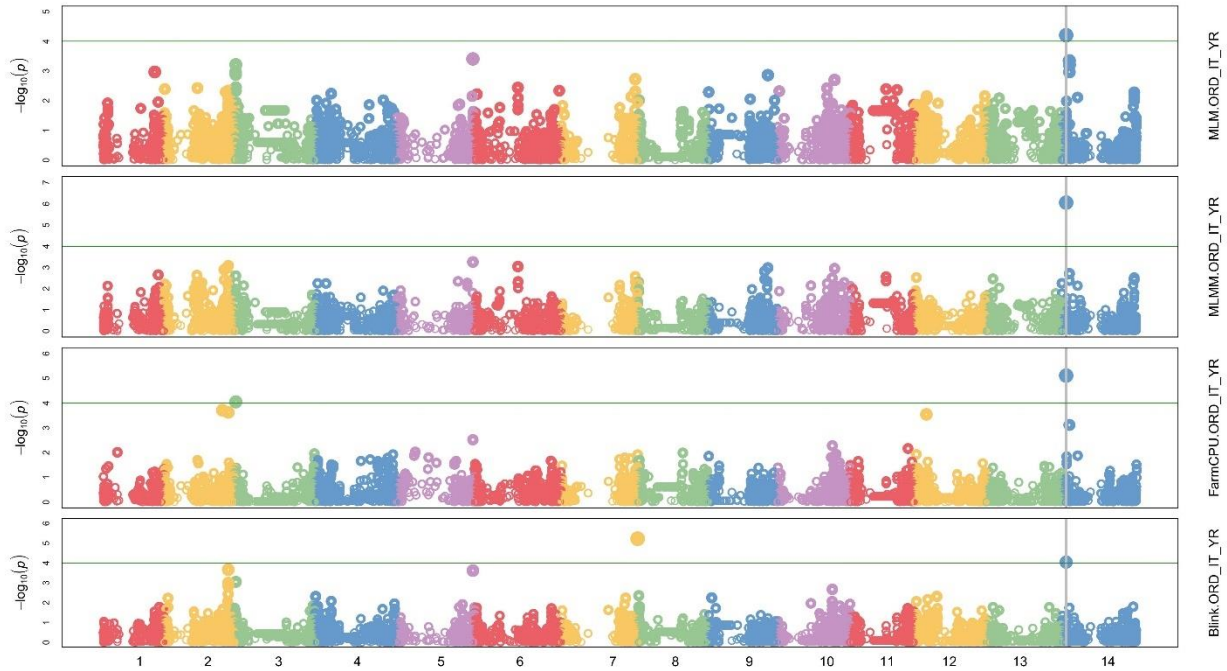

SUPPLEMENTARY FIGURE 59: Manhattan plot with all GWAS models (MLM, MLMM, FARMCPU AND BLINK) for Infection Type (IT) in Izmir 2019 and Q7 (Cyprous_Iberia). Numbers on the Xlab refers to the durum wheat chromosomes (1 = 1A, 2 = 1B, 3 = 2A, 4 = 2B, 5 = 3A, 6 = 3B, 7 = 4A, 8 = 4B, 9 = 5A, 10 = 5B, 11 = 6A, 12 = 6B, 13 = 7A and 14 = 7B). Ylab refers to LOD (-log$_{10}$(pvalue)).

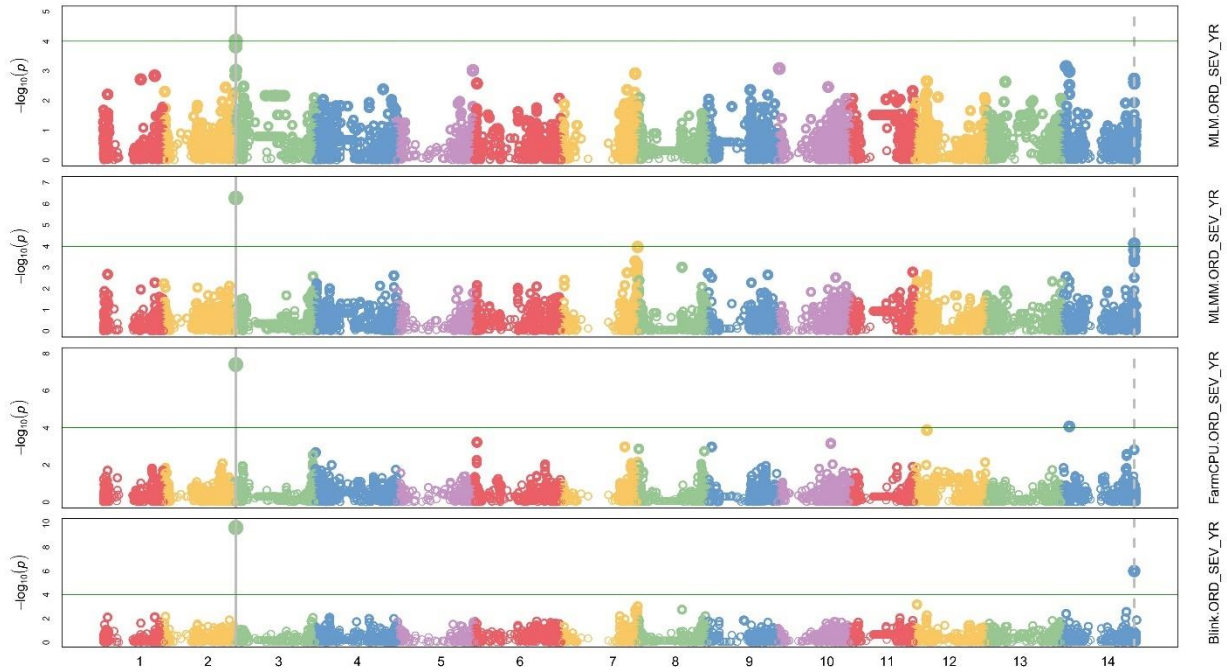

SUPPLEMENTARY FIGURE 60: Manhattan plot with all GWAS models (MLM, MLMM, FARMCPU AND BLINK) for Severity (SEV) in Izmir 2019 and Q7 (Cyprous_Iberia). Numbers on the Xlab refers to the durum wheat chromosomes (1 = 1A, 2 = 1B, 3 = 2A, 4 = 2B, 5 = 3A, 6 = 3B, 7 = 4A, 8 = 4B, 9 = 5A, 10 = 5B, 11 = 6A, 12 = 6B, 13 = 7A and 14 = 7B). Ylab refers to LOD (-log$_{10}$(pvalue)).

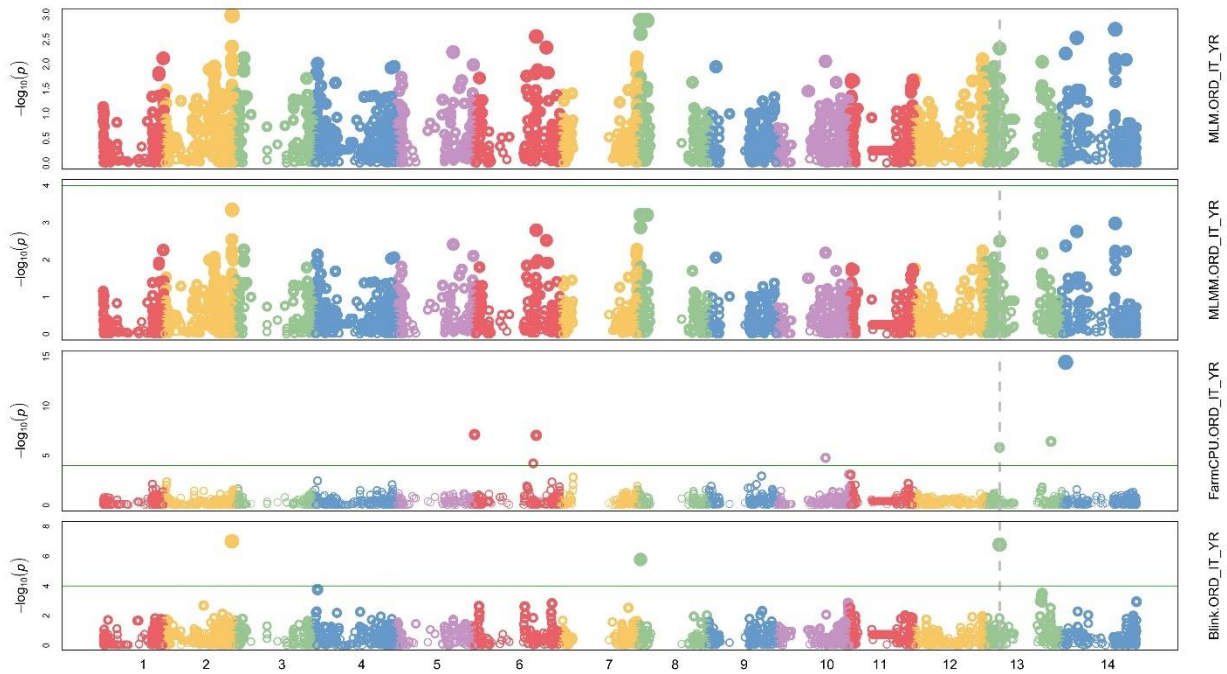

SUPPLEMENTARY FIGURE 61: Manhattan plot with all GWAS models (MLM, MLMM, FARMCPU AND BLINK) for Infection Type (IT) in Lari 2019 and Q1 (Horn_Africa_aethiopicum). Numbers on the Xlab refers to the durum wheat chromosomes (1 = 1A, 2 = 1B, 3 = 2A, 4 = 2B, 5 = 3A, 6 = 3B, 7 = 4A, 8 = 4B, 9 = 5A, 10 = 5B, 11 = 6A, 12 = 6B, 13 = 7A and 14 = 7B). Ylab refers to LOD (-log$_{10}$(pvalue)).

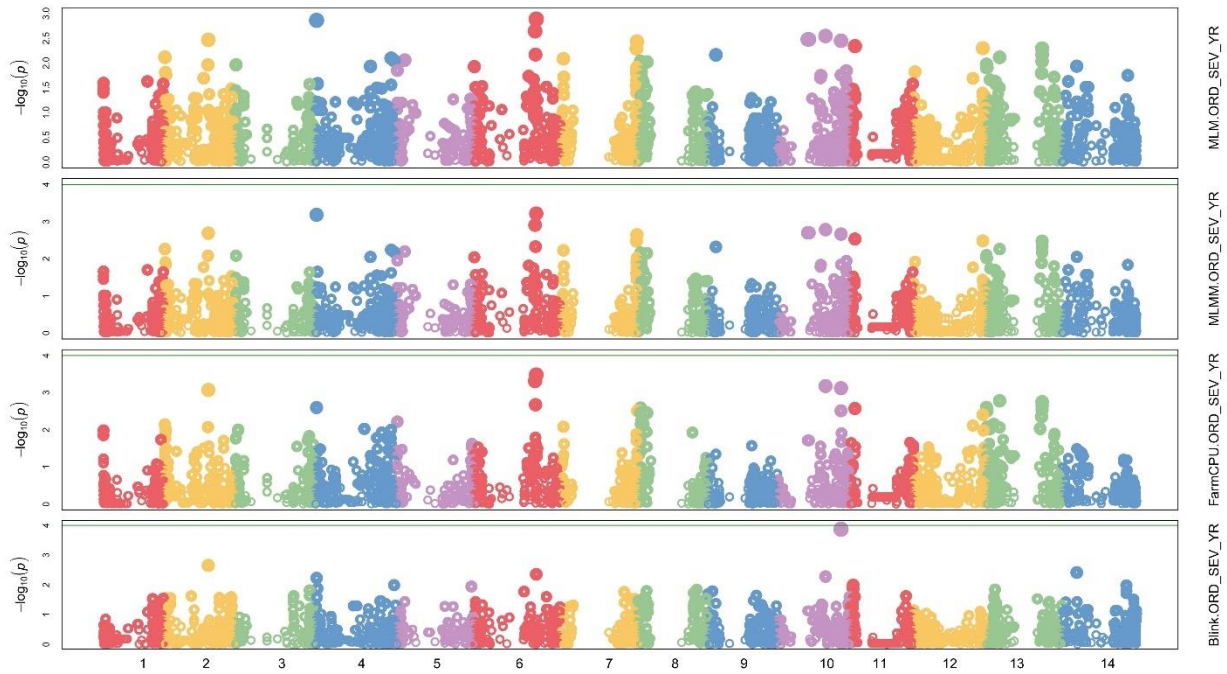

SUPPLEMENTARY FIGURE 62: Manhattan plot with all GWAS models (MLM, MLMM, FARMCPU AND BLINK) for Severity (SEV) in Lari 2019 and Q1 (Horn_Africa_aethiopicum). Numbers on the Xlab refers to the durum wheat chromosomes (1 = 1A, 2 = 1B, 3 = 2A, 4 = 2B, 5 = 3A, 6 = 3B, 7 = 4A, 8 = 4B, 9 = 5A, 10 = 5B, 11 = 6A, 12 = 6B, 13 = 7A and 14 = 7B). Ylab refers to LOD (-log$_{10}$(pvalue)).

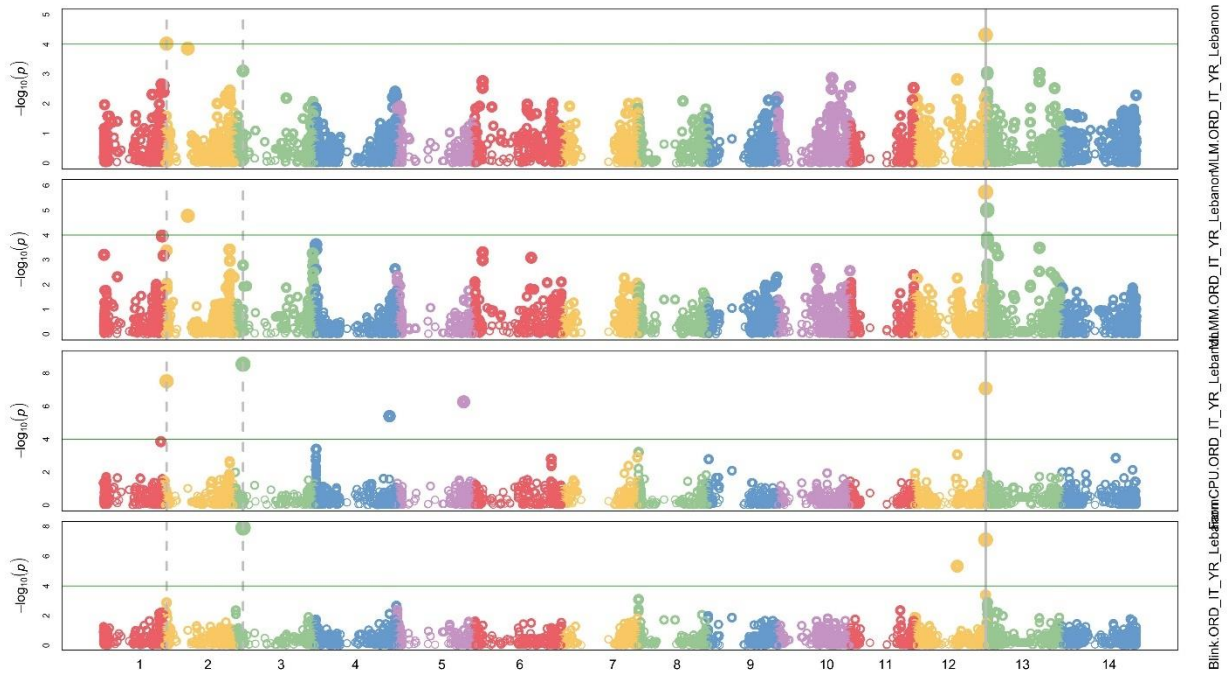

SUPPLEMENTARY FIGURE 63: Manhattan plot with all GWAS models (MLM, MLMM, FARMCPU AND BLINK) for Infection Type (IT) in Lari 2019 and Q3 (Iran_Syriacum). Numbers on the Xlab refers to the durum wheat chromosomes (1 = 1A, 2 = 1B, 3 = 2A, 4 = 2B, 5 = 3A, 6 = 3B, 7 = 4A, 8 = 4B, 9 = 5A, 10 = 5B, 11 = 6A, 12 = 6B, 13 = 7A and 14 = 7B). Ylab refers to LOD (-log$_{10}$(pvalue)).

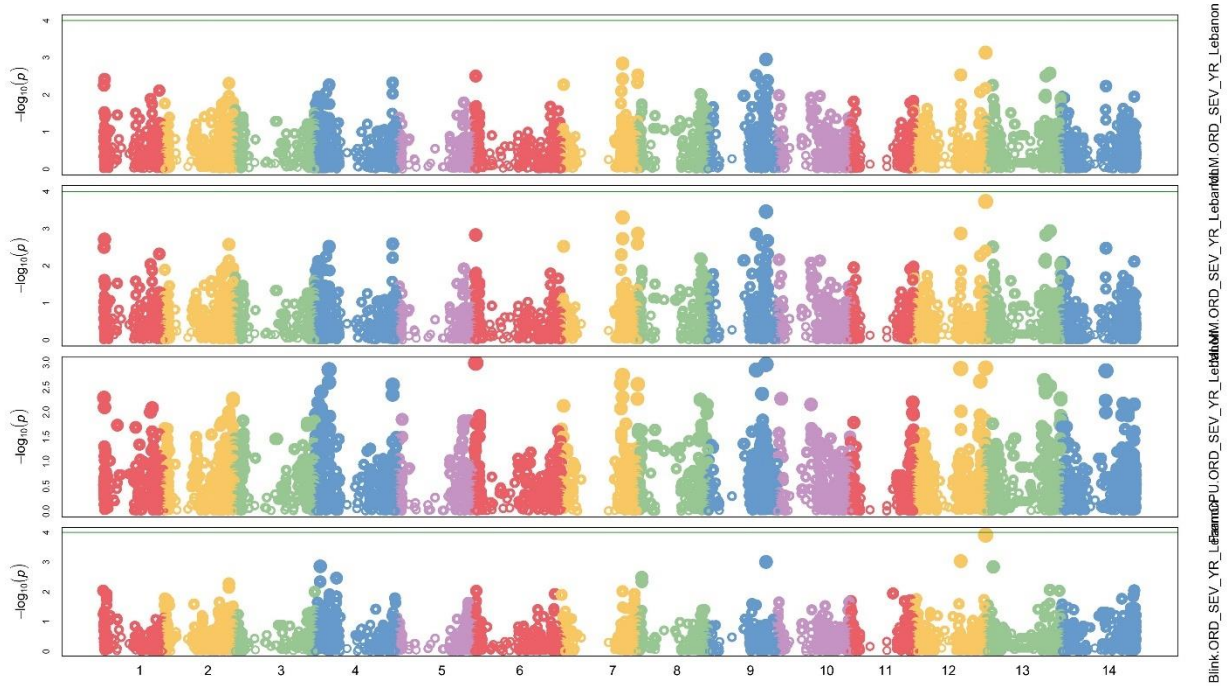

SUPPLEMENTARY FIGURE 64: Manhattan plot with all GWAS models (MLM, MLMM, FARMCPU AND BLINK) for Severity (SEV) in Lari 2019 and Q3 (Iran_Syriacum). Numbers on the Xlab refers to the durum wheat chromosomes (1 = 1A, 2 = 1B, 3 = 2A, 4 = 2B, 5 = 3A, 6 = 3B, 7 = 4A, 8 = 4B, 9 = 5A, 10 = 5B, 11 = 6A, 12 = 6B, 13 = 7A and 14 = 7B). Ylab refers to LOD (-log$_{10}$(pvalue)).

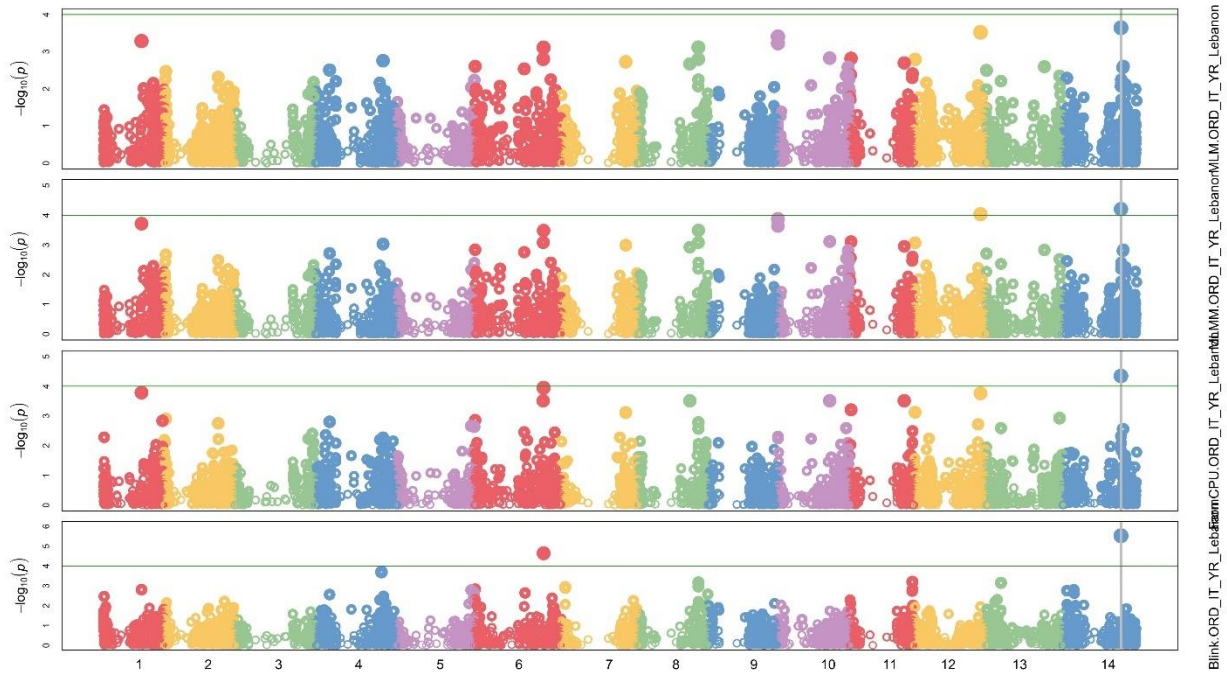

SUPPLEMENTARY FIGURE 65: Manhattan plot with all GWAS models (MLM, MLMM, FARMCPU AND BLINK) for Infection Type (IT) in Lari 2019 and Q6 (WestAsia_Caucasus). Numbers on the Xlab refers to the durum wheat chromosomes (1 = 1A, 2 = 1B, 3 = 2A, 4 = 2B, 5 = 3A, 6 = 3B, 7 = 4A, 8 = 4B, 9 = 5A, 10 = 5B, 11 = 6A, 12 = 6B, 13 = 7A and 14 = 7B). Ylab refers to LOD (-log$_{10}$(pvalue)).

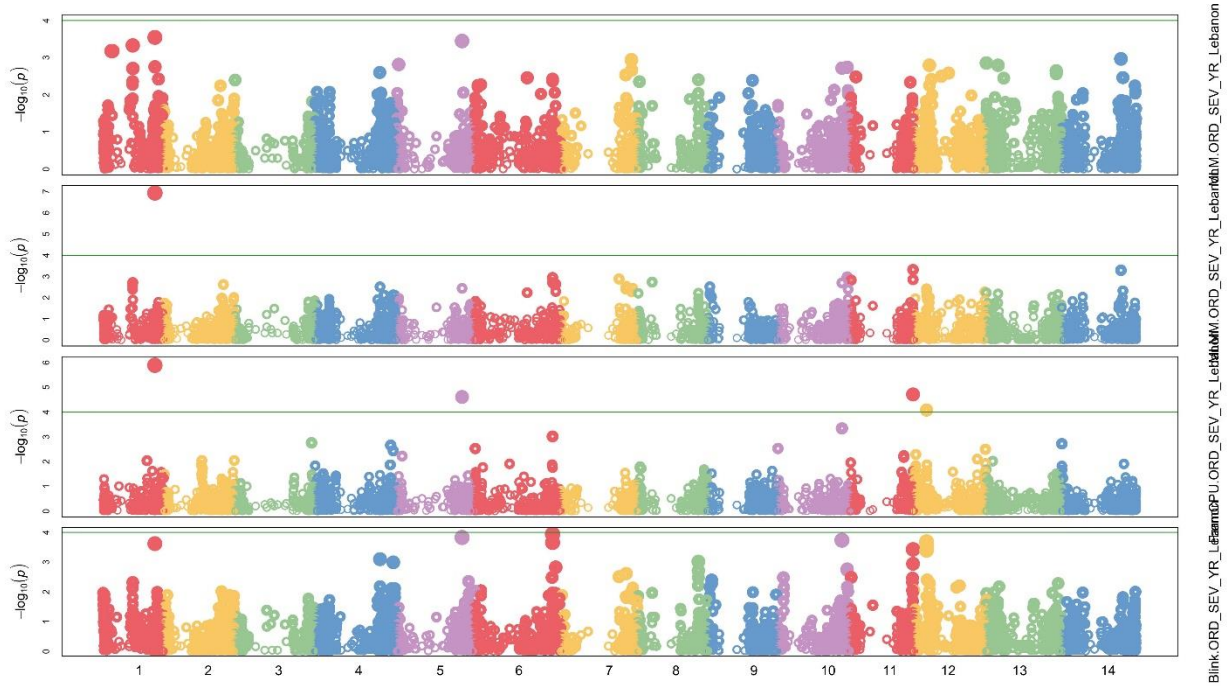

SUPPLEMENTARY FIGURE 66: Manhattan plot with all GWAS models (MLM, MLMM, FARMCPU AND BLINK) for Severity (SEV) in Lari 2019 and Q6 (WestAsia_Caucasus). Numbers on the Xlab refers to the durum wheat chromosomes (1 = 1A, 2 = 1B, 3 = 2A, 4 = 2B, 5 = 3A, 6 = 3B, 7 = 4A, 8 = 4B, 9 = 5A, 10 = 5B, 11 = 6A, 12 = 6B, 13 = 7A and 14 = 7B). Ylab refers to LOD (-log$_{10}$(pvalue)).

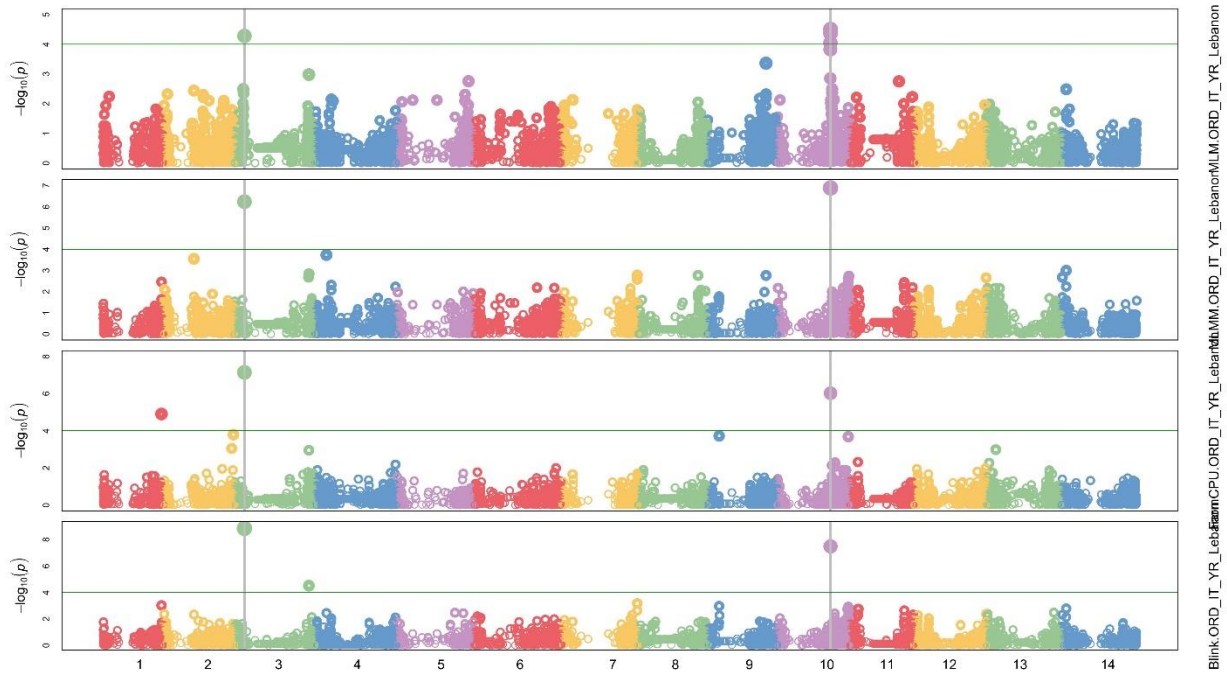

SUPPLEMENTARY FIGURE 67: Manhattan plot with all GWAS models (MLM, MLMM, FARMCPU AND BLINK) for Infection Type (IT) in Lari 2019 and Q7 (Cyprous_Iberia). Numbers on the Xlab refers to the durum wheat chromosomes (1 = 1A, 2 = 1B, 3 = 2A, 4 = 2B, 5 = 3A, 6 = 3B, 7 = 4A, 8 = 4B, 9 = 5A, 10 = 5B, 11 = 6A, 12 = 6B, 13 = 7A and 14 = 7B). Ylab refers to LOD (-log$_{10}$(pvalue)).

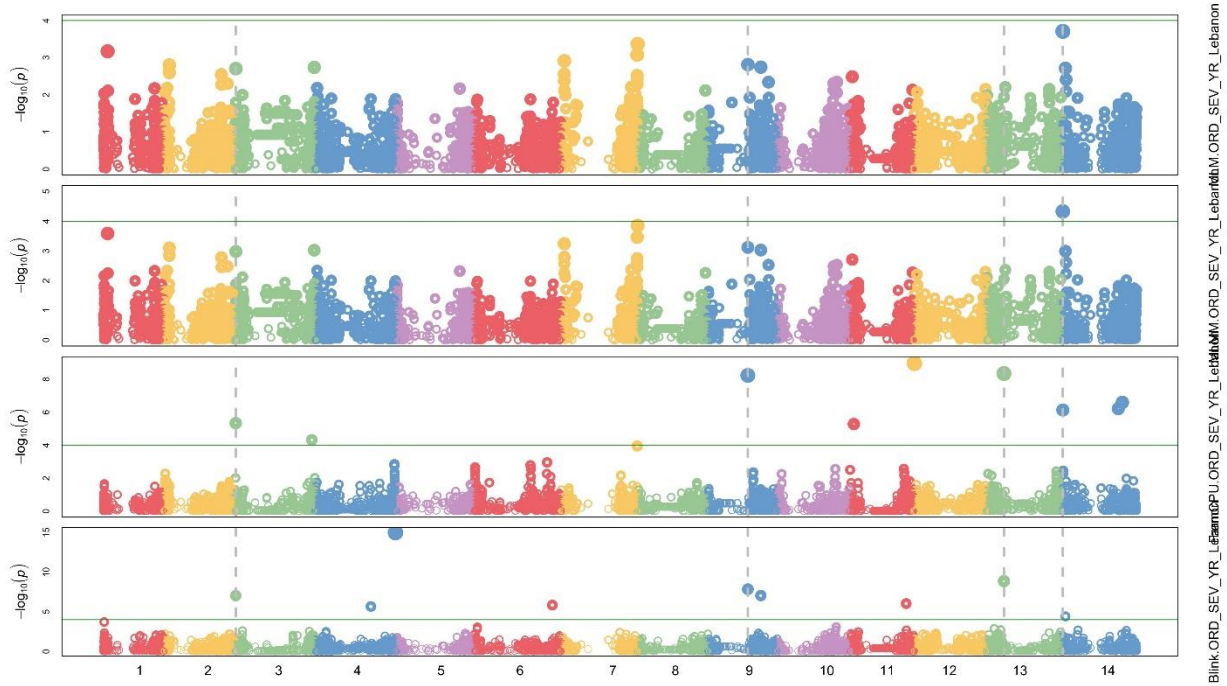

SUPPLEMENTARY FIGURE 68: Manhattan plot with all GWAS models (MLM, MLMM, FARMCPU AND BLINK) for Severity (SEV) in Lari 2019 and Q7 (Cyprous_Iberia). Numbers on the Xlab refers to the durum wheat chromosomes (1 = 1A, 2 = 1B, 3 = 2A, 4 = 2B, 5 = 3A, 6 = 3B, 7 = 4A, 8 = 4B, 9 = 5A, 10 = 5B, 11 = 6A, 12 = 6B, 13 = 7A and 14 = 7B). Ylab refers to LOD (-log$_{10}$(pvalue)).

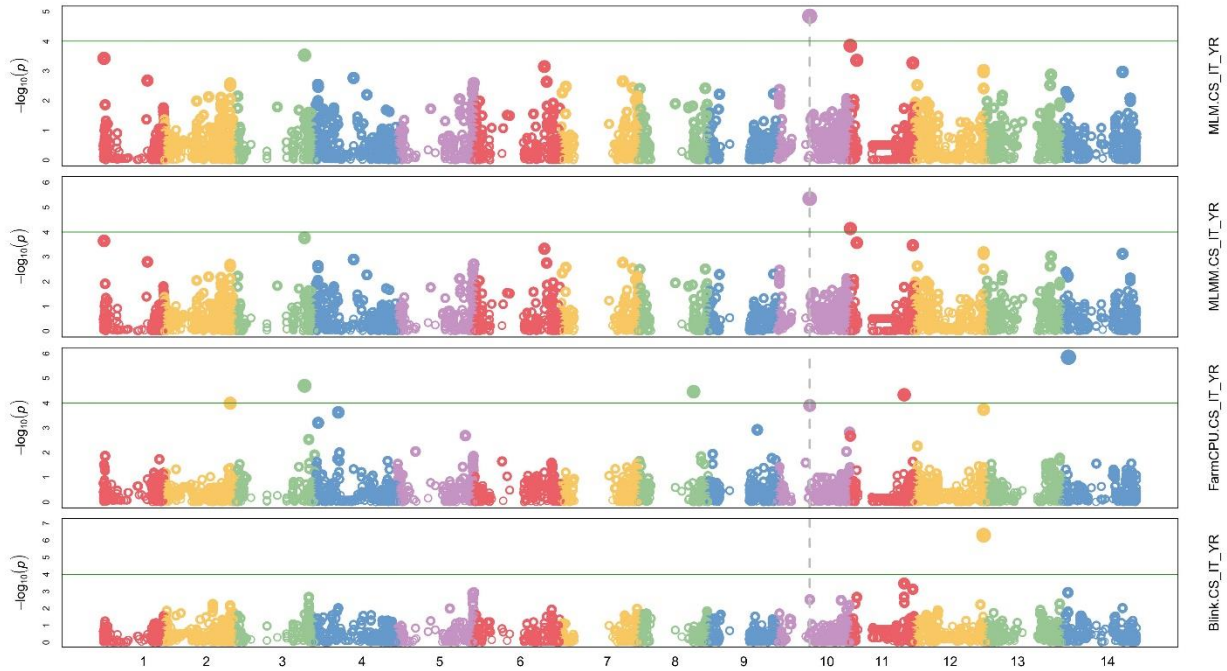

SUPPLEMENTARY FIGURE 69: Manhattan plot with all GWAS models (MLM, MLMM, FARMCPU AND BLINK) for Infection Type (IT) in Kodia 2020 and Q1 (Horn_Africa_aethiopicum). Numbers on the Xlab refers to the durum wheat chromosomes (1 = 1A, 2 = 1B, 3 = 2A, 4 = 2B, 5 = 3A, 6 = 3B, 7 = 4A, 8 = 4B, 9 = 5A, 10 = 5B, 11 = 6A, 12 = 6B, 13 = 7A and 14 = 7B). Ylab refers to LOD (-log$_{10}$(pvalue)).

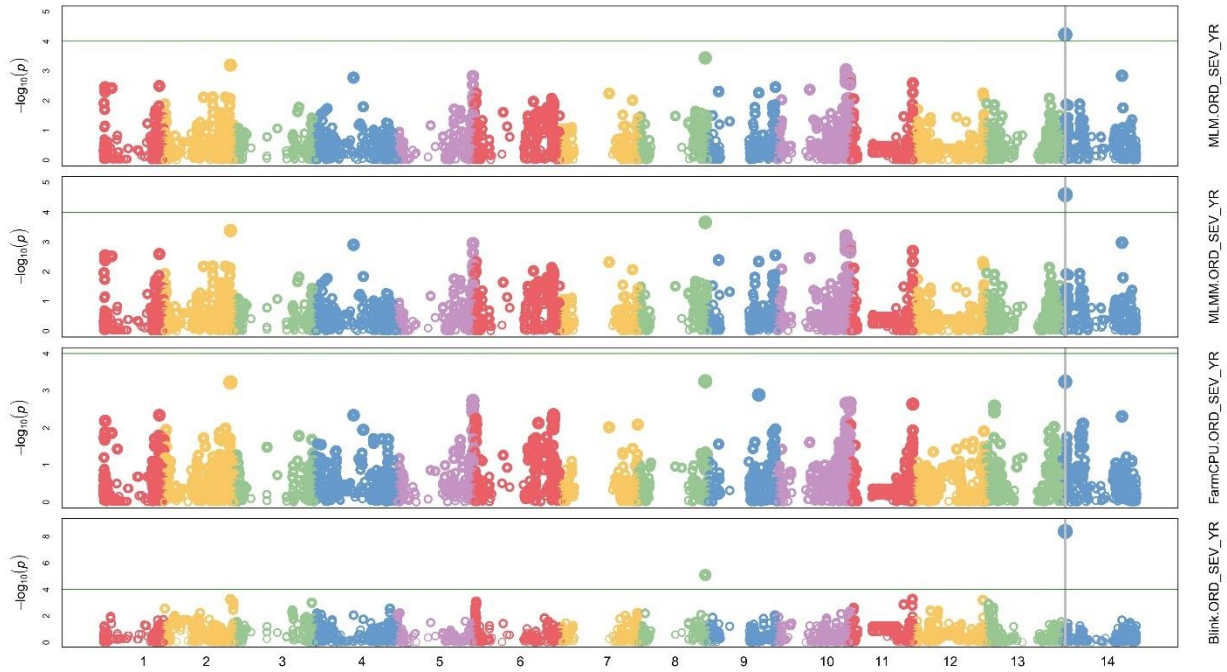

SUPPLEMENTARY FIGURE 70: Manhattan plot with all GWAS models (MLM, MLMM, FARMCPU AND BLINK) for Severity (SEV) in Kodia 2020 and Q1 (Horn_Africa_aethiopicum). Numbers on the Xlab refers to the durum wheat chromosomes (1 = 1A, 2 = 1B, 3 = 2A, 4 = 2B, 5 = 3A, 6 = 3B, 7 = 4A, 8 = 4B, 9 = 5A, 10 = 5B, 11 = 6A, 12 = 6B, 13 = 7A and 14 = 7B). Ylab refers to LOD (-log$_{10}$(pvalue)).

SUPPLEMENTARY FIGURE 71: Manhattan plot with all GWAS models (MLM, MLMM, FARMCPU AND BLINK) for Infection Type (IT) in Kodia 2020 and Q3 (Iran_Syriacum). Numbers on the Xlab refers to the durum wheat chromosomes (1 = 1A, 2 = 1B, 3 = 2A, 4 = 2B, 5 = 3A, 6 = 3B, 7 = 4A, 8 = 4B, 9 = 5A, 10 = 5B, 11 = 6A, 12 = 6B, 13 = 7A and 14 = 7B). Ylab refers to LOD (-log$_{10}$(pvalue)).

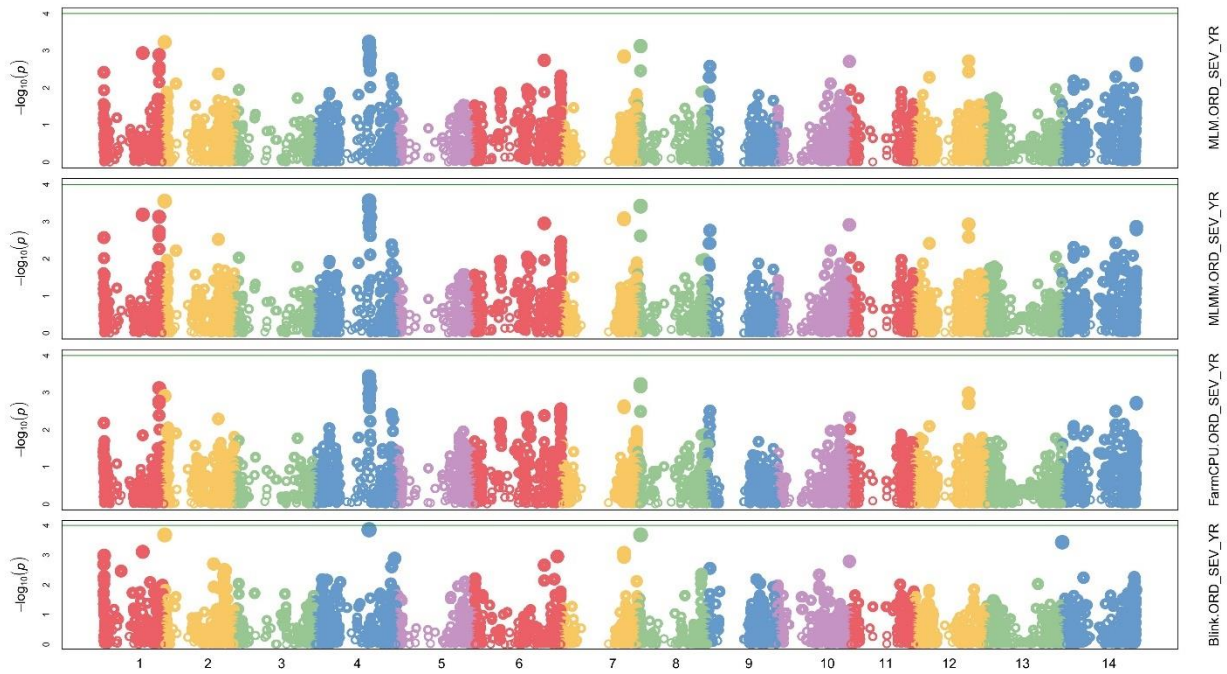

SUPPLEMENTARY FIGURE 72: Manhattan plot with all GWAS models (MLM, MLMM, FARMCPU AND BLINK) for Severity (SEV) in Kodia 2020 and Q3 (Iran_Syriacum). Numbers on the Xlab refers to the durum wheat chromosomes (1 = 1A, 2 = 1B, 3 = 2A, 4 = 2B, 5 = 3A, 6 = 3B, 7 = 4A, 8 = 4B, 9 = 5A, 10 = 5B, 11 = 6A, 12 = 6B, 13 = 7A and 14 = 7B). Ylab refers to LOD (-log$_{10}$(pvalue)).

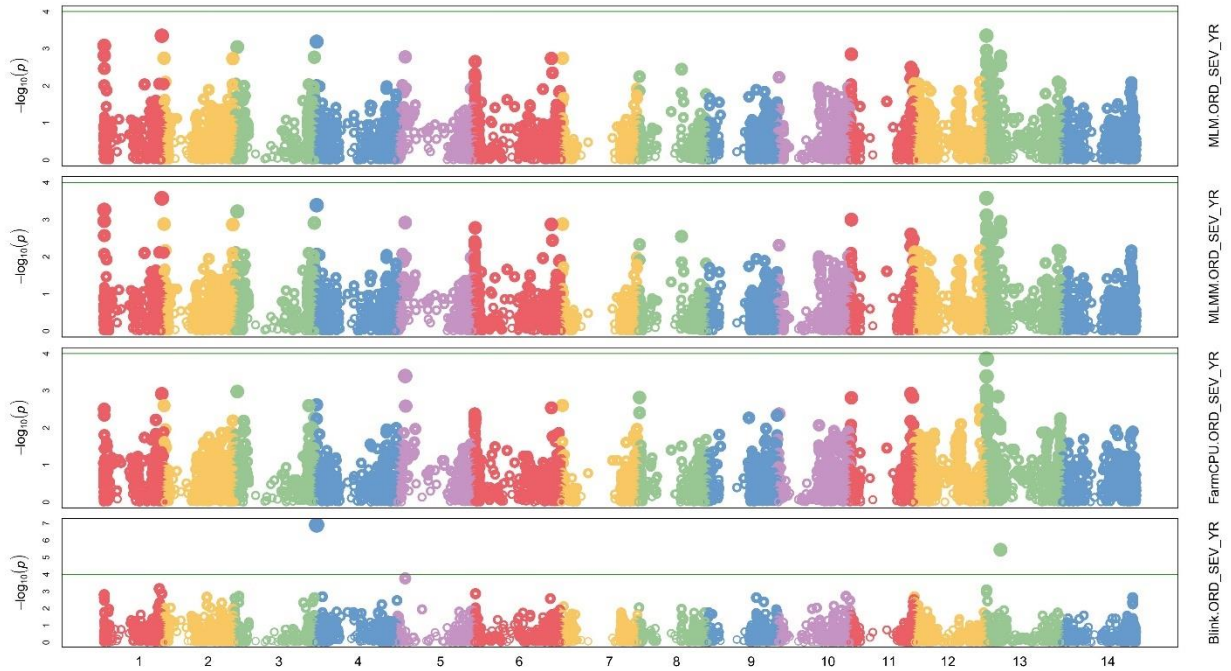

SUPPLEMENTARY FIGURE 73: Manhattan plot with all GWAS models (MLM, MLMM, FARMCPU AND BLINK) for Infection Type (IT) in Kodia 2020 and Q6 (WestAsia_Caucasus). Numbers on the Xlab refers to the durum wheat chromosomes (1 = 1A, 2 = 1B, 3 = 2A, 4 = 2B, 5 = 3A, 6 = 3B, 7 = 4A, 8 = 4B, 9 = 5A, 10 = 5B, 11 = 6A, 12 = 6B, 13 = 7A and 14 = 7B). Ylab refers to LOD (-log$_{10}$(pvalue)).

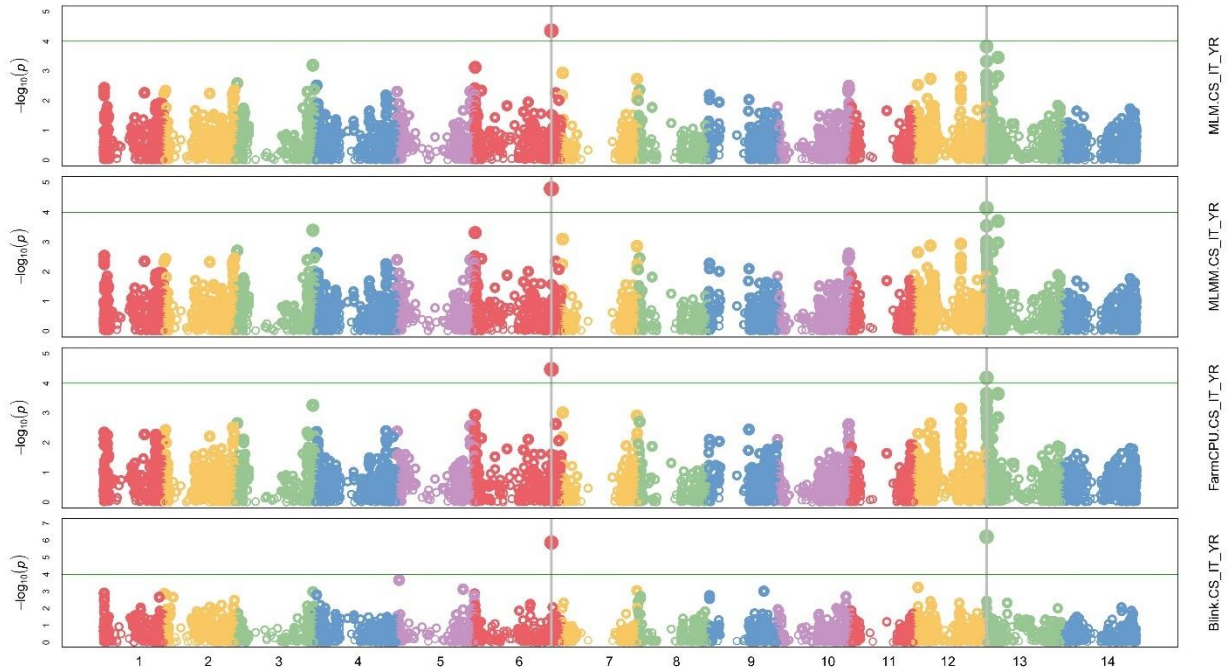

SUPPLEMENTARY FIGURE 74: Manhattan plot with all GWAS models (MLM, MLMM, FARMCPU AND BLINK) for Severity (SEV) in Kodia 2020 and Q6 (WestAsia_Caucasus). Numbers on the Xlab refers to the durum wheat chromosomes (1 = 1A, 2 = 1B, 3 = 2A, 4 = 2B, 5 = 3A, 6 = 3B, 7 = 4A, 8 = 4B, 9 = 5A, 10 = 5B, 11 = 6A, 12 = 6B, 13 = 7A and 14 = 7B). Ylab refers to LOD (-log$_{10}$(pvalue)).

SUPPLEMENTARY FIGURE 75: Manhattan plot with all GWAS models (MLM, MLMM, FARMCPU AND BLINK) for Infection Type (IT) in Kodia 2020 and Q7 (Cyprous_Iberia). Numbers on the Xlab refers to the durum wheat chromosomes (1 = 1A, 2 = 1B, 3 = 2A, 4 = 2B, 5 = 3A, 6 = 3B, 7 = 4A, 8 = 4B, 9 = 5A, 10 = 5B, 11 = 6A, 12 = 6B, 13 = 7A and 14 = 7B). Ylab refers to LOD (-log$_{10}$(pvalue)).

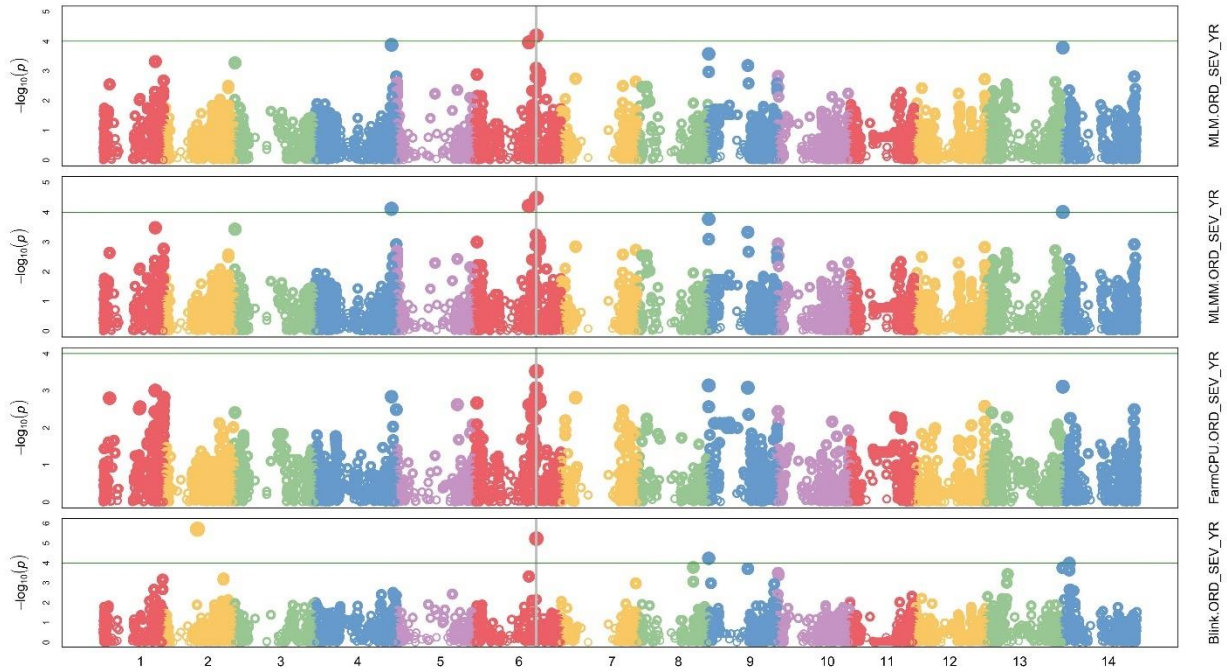

SUPPLEMENTARY FIGURE 76: Manhattan plot with all GWAS models (MLM, MLMM, FARMCPU AND BLINK) for Severity (SEV) in Kodia 2020 and Q7 (Cyprous_Iberia). Numbers on the Xlab refers to the durum wheat chromosomes (1 = 1A, 2 = 1B, 3 = 2A, 4 = 2B, 5 = 3A, 6 = 3B, 7 = 4A, 8 = 4B, 9 = 5A, 10 = 5B, 11 = 6A, 12 = 6B, 13 = 7A and 14 = 7B). Ylab refers to LOD (-log$_{10}$(pvalue)).

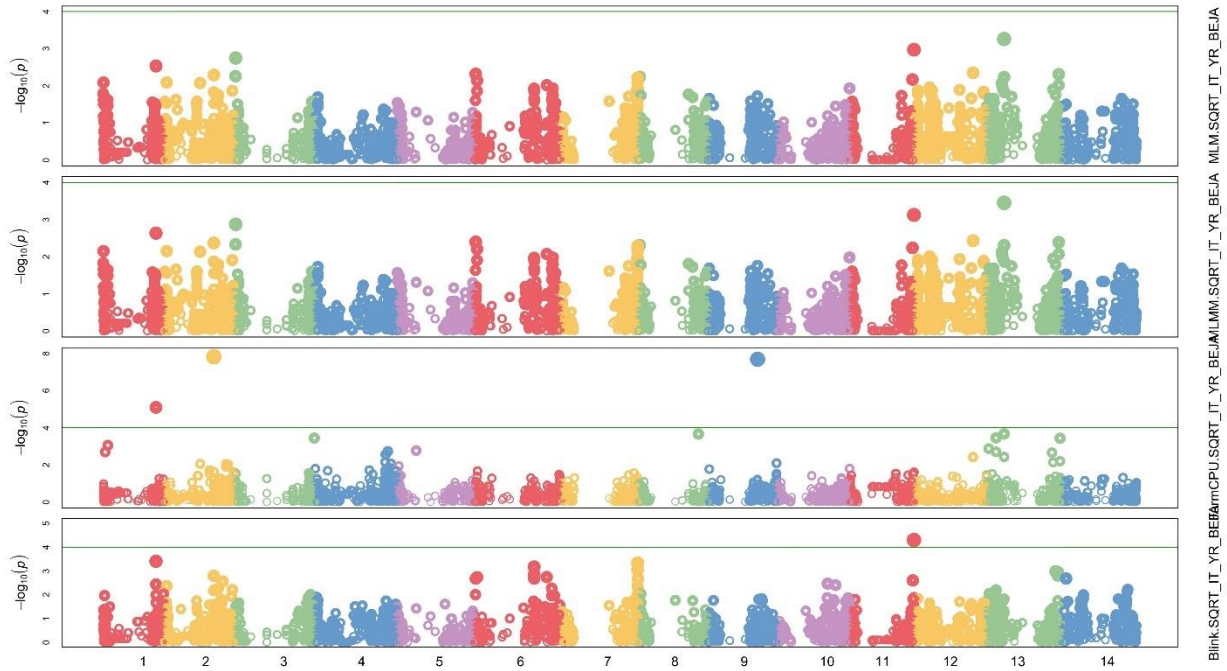

SUPPLEMENTARY FIGURE 77: Manhattan plot with all GWAS models (MLM, MLMM, FARMCPU AND BLINK) for Infection Type (IT) in Beja 2020 and Q1 (Horn_Africa_aethiopicum). Numbers on the Xlab refers to the durum wheat chromosomes (1 = 1A, 2 = 1B, 3 = 2A, 4 = 2B, 5 = 3A, 6 = 3B, 7 = 4A, 8 = 4B, 9 = 5A, 10 = 5B, 11 = 6A, 12 = 6B, 13 = 7A and 14 = 7B). Ylab refers to LOD (-log$_{10}$(pvalue)).

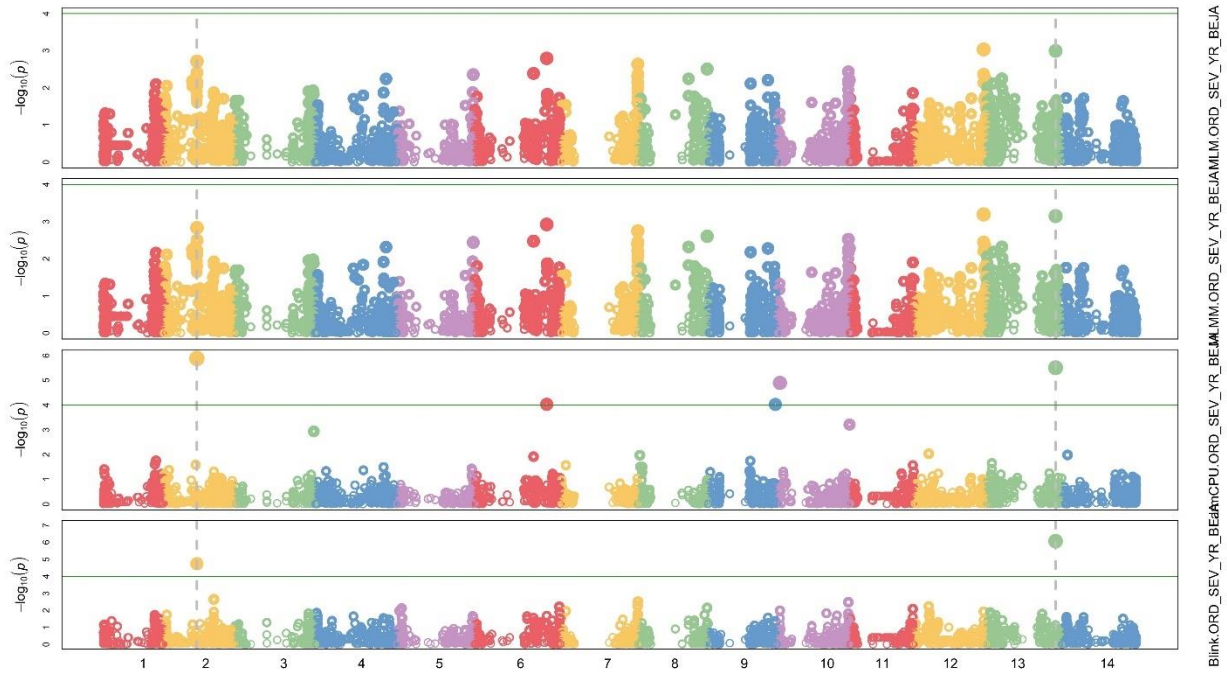

SUPPLEMENTARY FIGURE 78: Manhattan plot with all GWAS models (MLM, MLMM, FARMCPU AND BLINK) for Severity (SEV) in Beja 2020 and Q1 (Horn_Africa_aethiopicum). Numbers on the Xlab refers to the durum wheat chromosomes (1 = 1A, 2 = 1B, 3 = 2A, 4 = 2B, 5 = 3A, 6 = 3B, 7 = 4A, 8 = 4B, 9 = 5A, 10 = 5B, 11 = 6A, 12 = 6B, 13 = 7A and 14 = 7B). Ylab refers to LOD (-log$_{10}$(pvalue)).

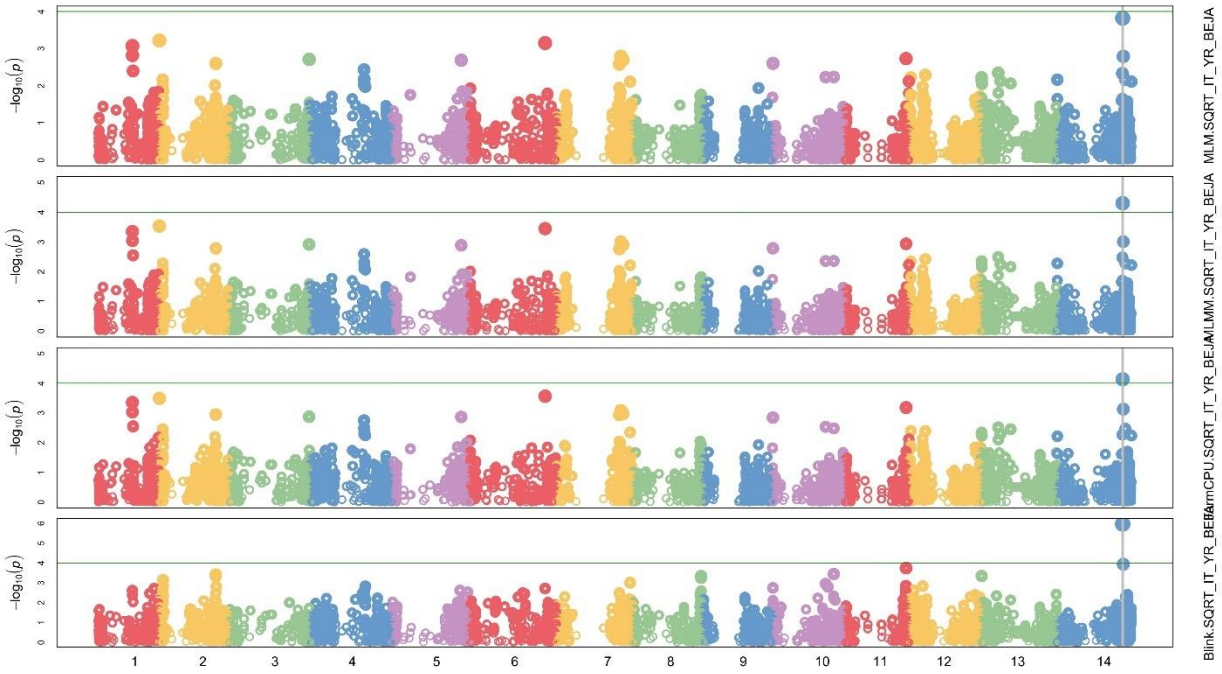

SUPPLEMENTARY FIGURE 79: Manhattan plot with all GWAS models (MLM, MLMM, FARMCPU AND BLINK) for Infection Type (IT) in Beja 2020 and Q3 (Iran_Syriacum). Numbers on the Xlab refers to the durum wheat chromosomes (1 = 1A, 2 = 1B, 3 = 2A, 4 = 2B, 5 = 3A, 6 = 3B, 7 = 4A, 8 = 4B, 9 = 5A, 10 = 5B, 11 = 6A, 12 = 6B, 13 = 7A and 14 = 7B). Ylab refers to LOD (-log$_{10}$(pvalue)).

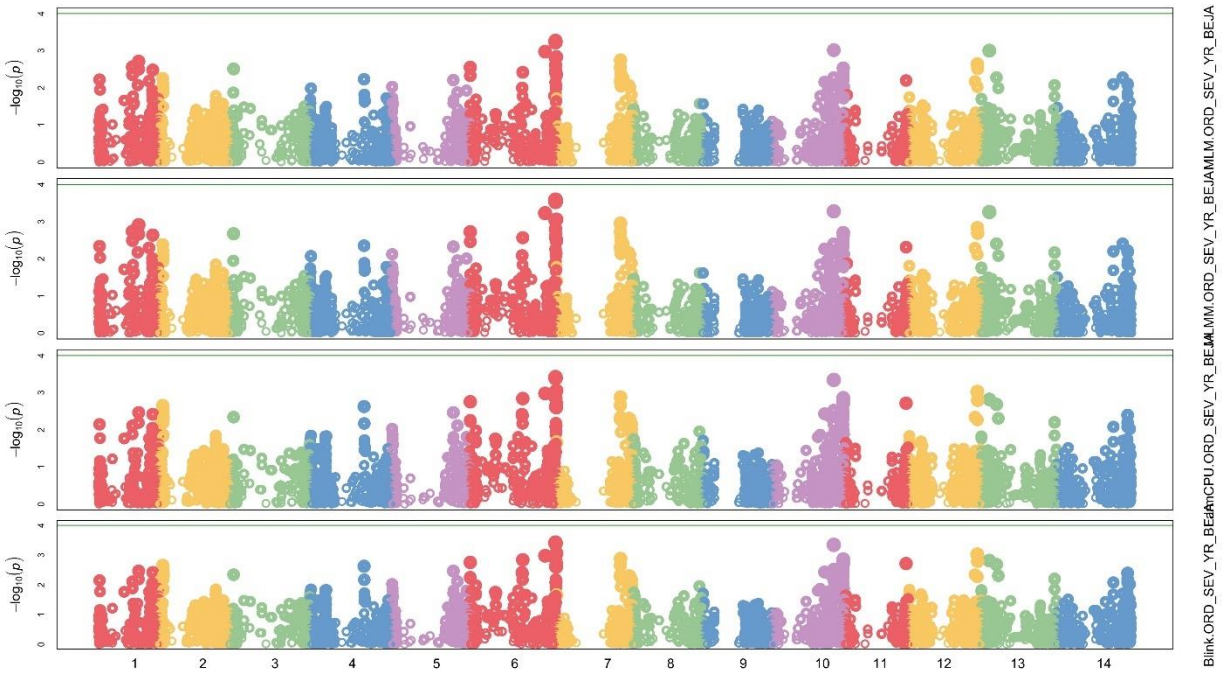

SUPPLEMENTARY FIGURE 80: Manhattan plot with all GWAS models (MLM, MLMM, FARMCPU AND BLINK) for Severity (SEV) in Beja 2020 and Q3 (Iran_Syriacum). Numbers on the Xlab refers to the durum wheat chromosomes (1 = 1A, 2 = 1B, 3 = 2A, 4 = 2B, 5 = 3A, 6 = 3B, 7 = 4A, 8 = 4B, 9 = 5A, 10 = 5B, 11 = 6A, 12 = 6B, 13 = 7A and 14 = 7B). Ylab refers to LOD (-log$_{10}$(pvalue)).

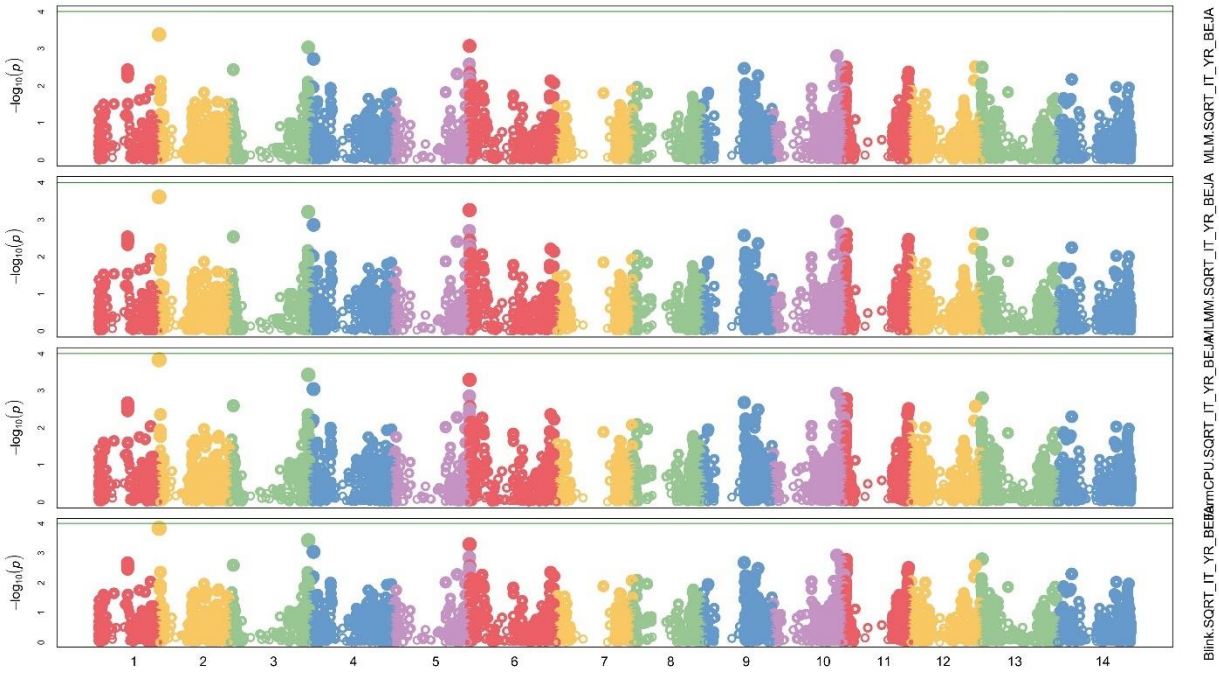

SUPPLEMENTARY FIGURE 81: Manhattan plot with all GWAS models (MLM, MLMM, FARMCPU AND BLINK) for Infection Type (IT) in Beja 2020 and Q6 (WestAsia_Caucasus). Numbers on the Xlab refers to the durum wheat chromosomes (1 = 1A, 2 = 1B, 3 = 2A, 4 = 2B, 5 = 3A, 6 = 3B, 7 = 4A, 8 = 4B, 9 = 5A, 10 = 5B, 11 = 6A, 12 = 6B, 13 = 7A and 14 = 7B). Ylab refers to LOD (-log$_{10}$(pvalue)).

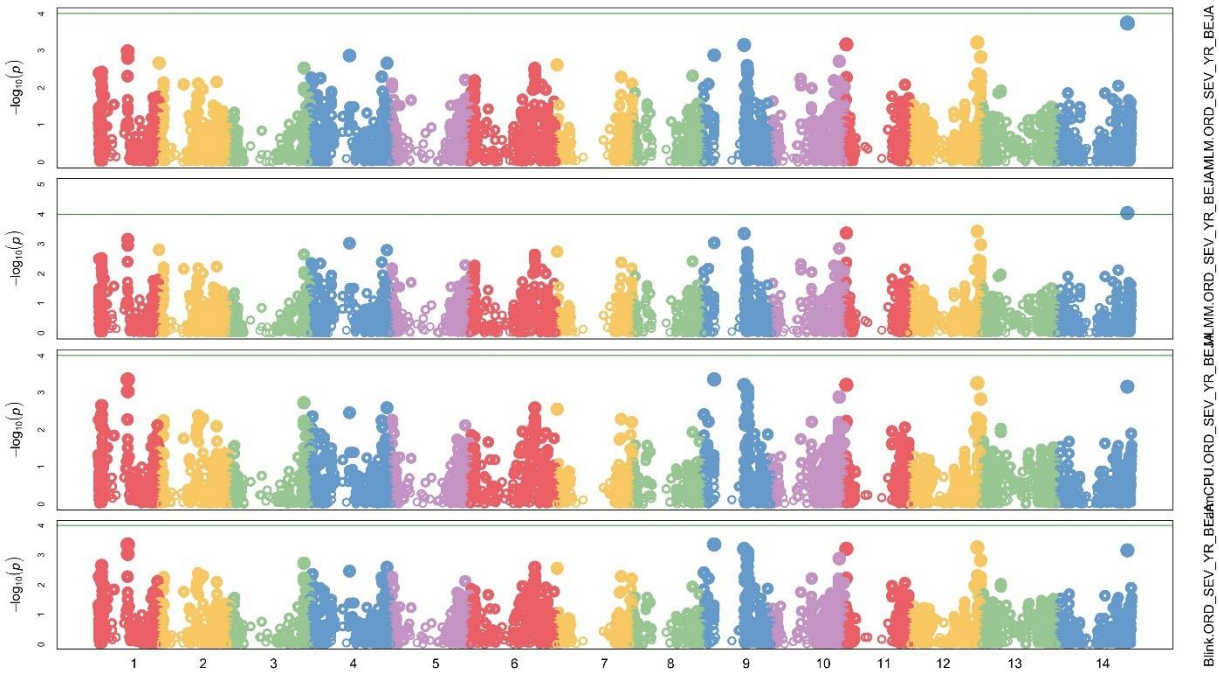

SUPPLEMENTARY FIGURE 82: Manhattan plot with all GWAS models (MLM, MLMM, FARMCPU AND BLINK) for Severity (SEV) in Beja 2020 and Q6 (WestAsia_Caucasus). Numbers on the Xlab refers to the durum wheat chromosomes (1 = 1A, 2 = 1B, 3 = 2A, 4 = 2B, 5 = 3A, 6 = 3B, 7 = 4A, 8 = 4B, 9 = 5A, 10 = 5B, 11 = 6A, 12 = 6B, 13 = 7A and 14 = 7B). Ylab refers to LOD (-log$_{10}$(pvalue)).

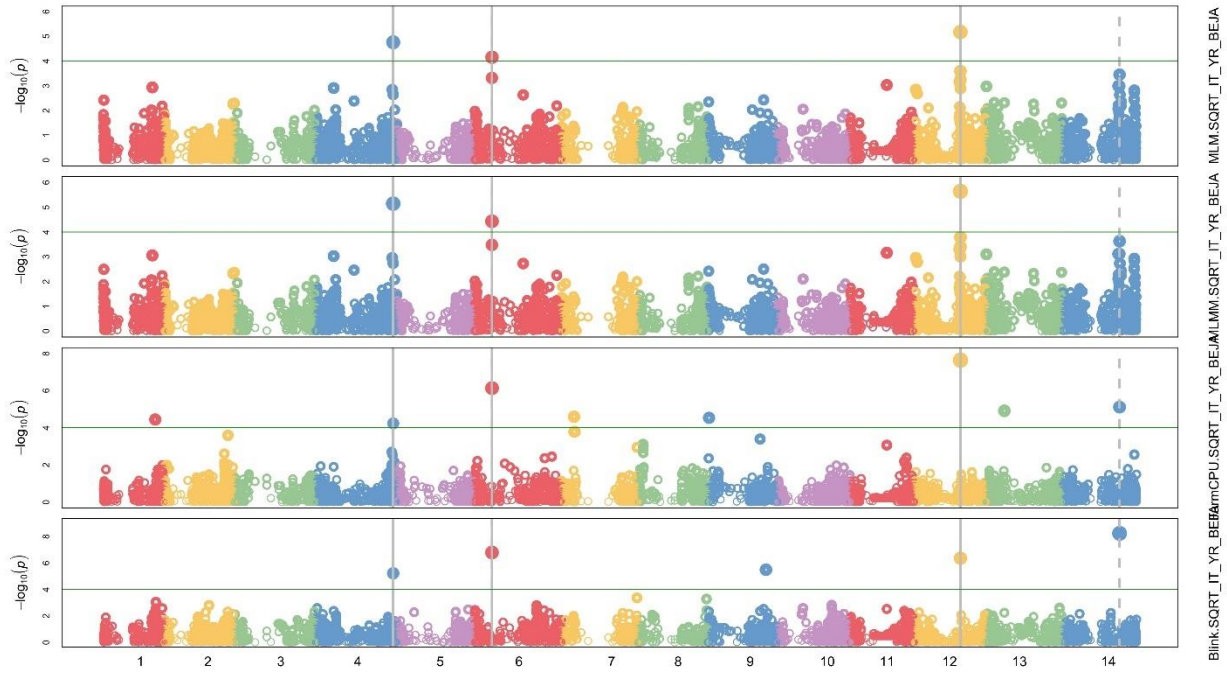

SUPPLEMENTARY FIGURE 83: Manhattan plot with all GWAS models (MLM, MLMM, FARMCPU AND BLINK) for Infection Type (IT) in Beja 2020 and Q7 (Cyprous_Iberia). Numbers on the Xlab refers to the durum wheat chromosomes (1 = 1A, 2 = 1B, 3 = 2A, 4 = 2B, 5 = 3A, 6 = 3B, 7 = 4A, 8 = 4B, 9 = 5A, 10 = 5B, 11 = 6A, 12 = 6B, 13 = 7A and 14 = 7B). Ylab refers to LOD (-log$_{10}$(pvalue)).

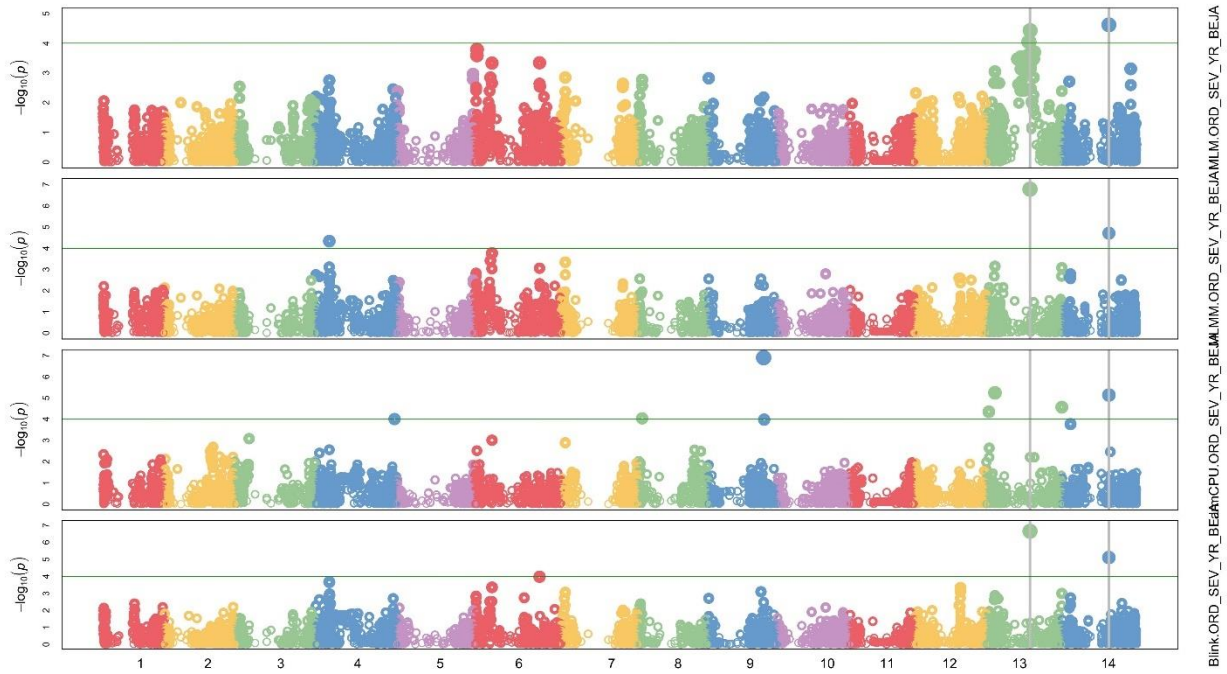

SUPPLEMENTARY FIGURE 84: Manhattan plot with all GWAS models (MLM, MLMM, FARMCPU AND BLINK) for Severity (SEV) in Beja 2020 and Q7 (Cyprous_Iberia). Numbers on the Xlab refers to the durum wheat chromosomes (1 = 1A, 2 = 1B, 3 = 2A, 4 = 2B, 5 = 3A, 6 = 3B, 7 = 4A, 8 = 4B, 9 = 5A, 10 = 5B, 11 = 6A, 12 = 6B, 13 = 7A and 14 = 7B). Ylab refers to LOD (-log$_{10}$(pvalue)).

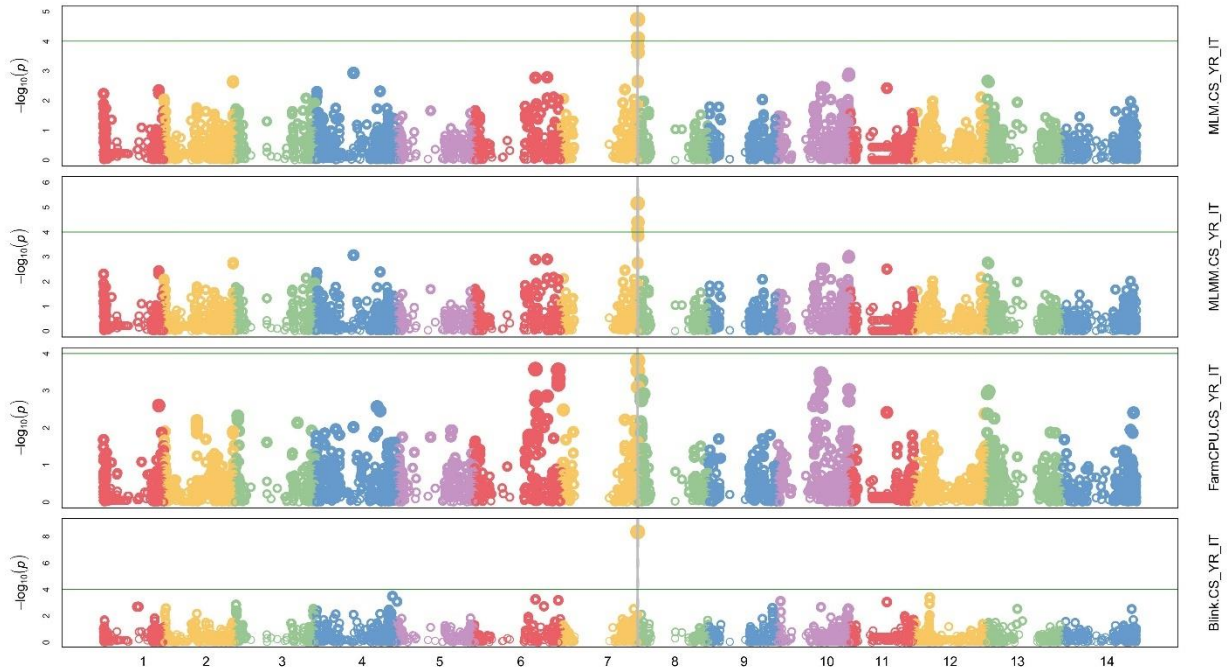

SUPPLEMENTARY FIGURE 85: Manhattan plot with all GWAS models (MLM, MLMM, FARMCPU AND BLINK) for Infection Type (IT) in Grosseto 2020 and Q1 (Horn_Africa_aethiopicum). Numbers on the Xlab refers to the durum wheat chromosomes (1 = 1A, 2 = 1B, 3 = 2A, 4 = 2B, 5 = 3A, 6 = 3B, 7 = 4A, 8 = 4B, 9 = 5A, 10 = 5B, 11 = 6A, 12 = 6B, 13 = 7A and 14 = 7B). Ylab refers to LOD (-log$_{10}$(pvalue)).

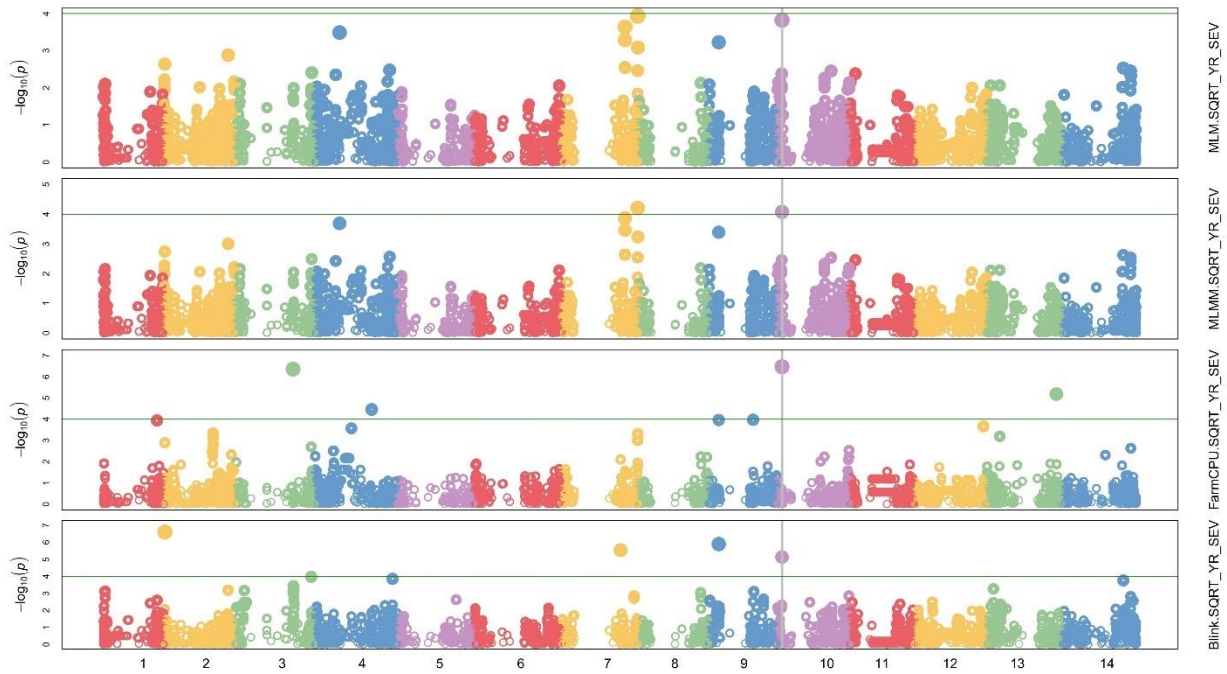

SUPPLEMENTARY FIGURE 86: Manhattan plot with all GWAS models (MLM, MLMM, FARMCPU AND BLINK) for Severity (SEV) in Grosseto 2020 and Q1 (Horn_Africa_aethiopicum). Numbers on the Xlab refers to the durum wheat chromosomes (1 = 1A, 2 = 1B, 3 = 2A, 4 = 2B, 5 = 3A, 6 = 3B, 7 = 4A, 8 = 4B, 9 = 5A, 10 = 5B, 11 = 6A, 12 = 6B, 13 = 7A and 14 = 7B). Ylab refers to LOD (-log$_{10}$(pvalue)).

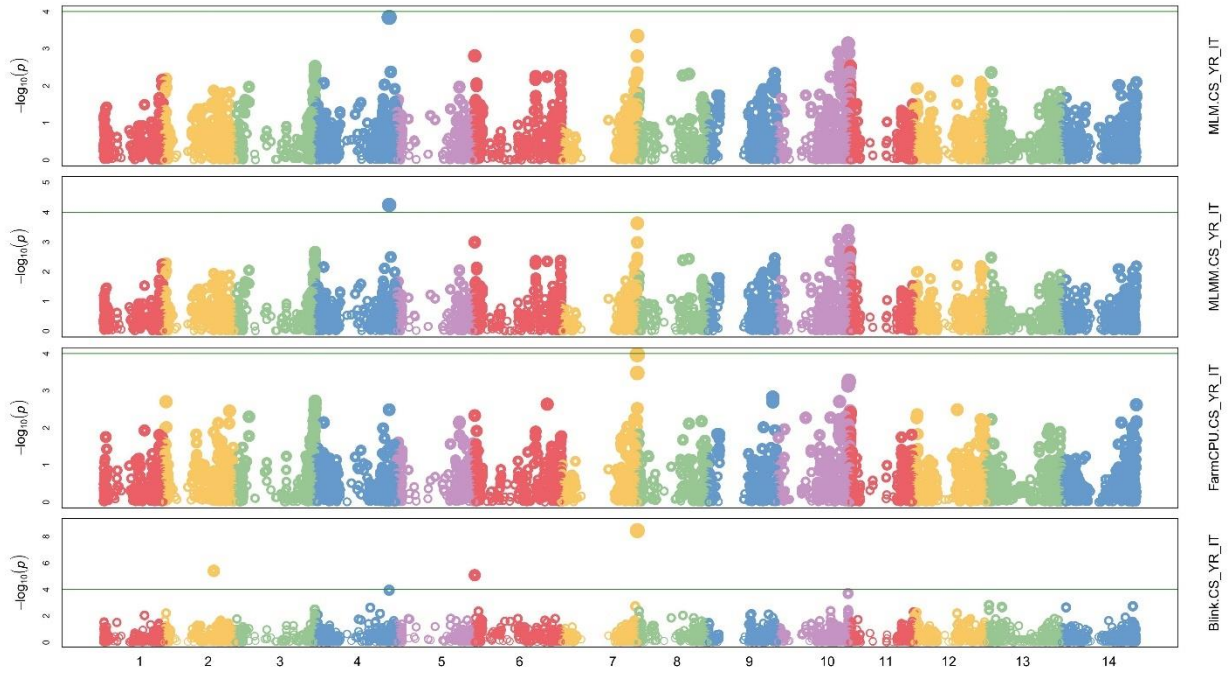

SUPPLEMENTARY FIGURE 87: Manhattan plot with all GWAS models (MLM, MLMM, FARMCPU AND BLINK) for Infection Type (IT) in Grosseto 2020 and Q3 (Iran_Syriacum). Numbers on the Xlab refers to the durum wheat chromosomes (1 = 1A, 2 = 1B, 3 = 2A, 4 = 2B, 5 = 3A, 6 = 3B, 7 = 4A, 8 = 4B, 9 = 5A, 10 = 5B, 11 = 6A, 12 = 6B, 13 = 7A and 14 = 7B). Ylab refers to LOD (-log$_{10}$(pvalue)).

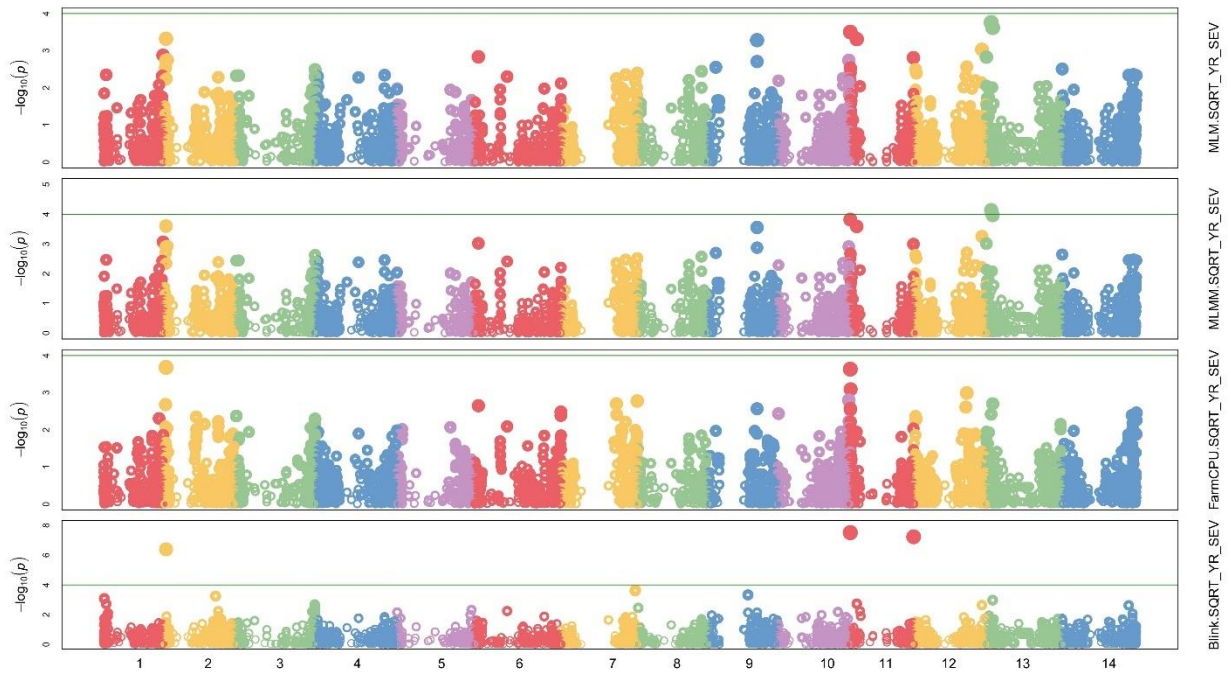

SUPPLEMENTARY FIGURE 88: Manhattan plot with all GWAS models (MLM, MLMM, FARMCPU AND BLINK) for Severity (SEV) in Grosseto 2020 and Q3 (Iran_Syriacum). Numbers on the Xlab refers to the durum wheat chromosomes (1 = 1A, 2 = 1B, 3 = 2A, 4 = 2B, 5 = 3A, 6 = 3B, 7 = 4A, 8 = 4B, 9 = 5A, 10 = 5B, 11 = 6A, 12 = 6B, 13 = 7A and 14 = 7B). Ylab refers to LOD (-log$_{10}$(pvalue)).

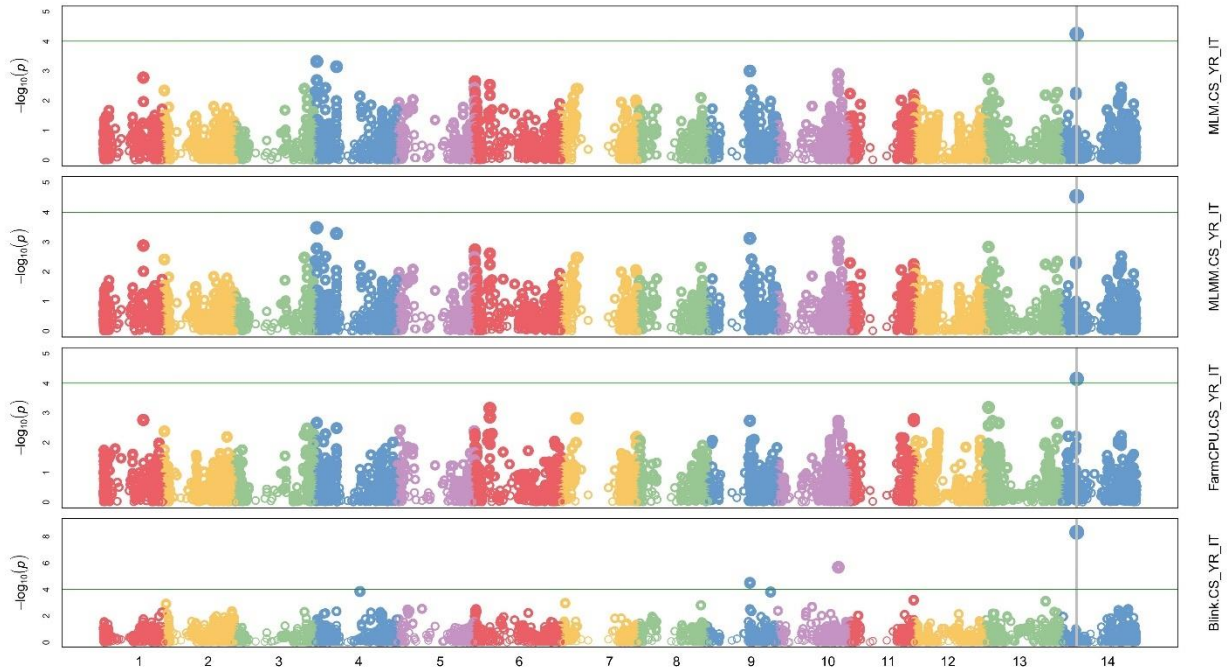

SUPPLEMENTARY FIGURE 89: Manhattan plot with all GWAS models (MLM, MLMM, FARMCPU AND BLINK) for Infection Type (IT) in Grosseto 2020 and Q6 (WestAsia_Caucasus). Numbers on the Xlab refers to the durum wheat chromosomes (1 = 1A, 2 = 1B, 3 = 2A, 4 = 2B, 5 = 3A, 6 = 3B, 7 = 4A, 8 = 4B, 9 = 5A, 10 = 5B, 11 = 6A, 12 = 6B, 13 = 7A and 14 = 7B). Ylab refers to LOD (-log$_{10}$(pvalue)).

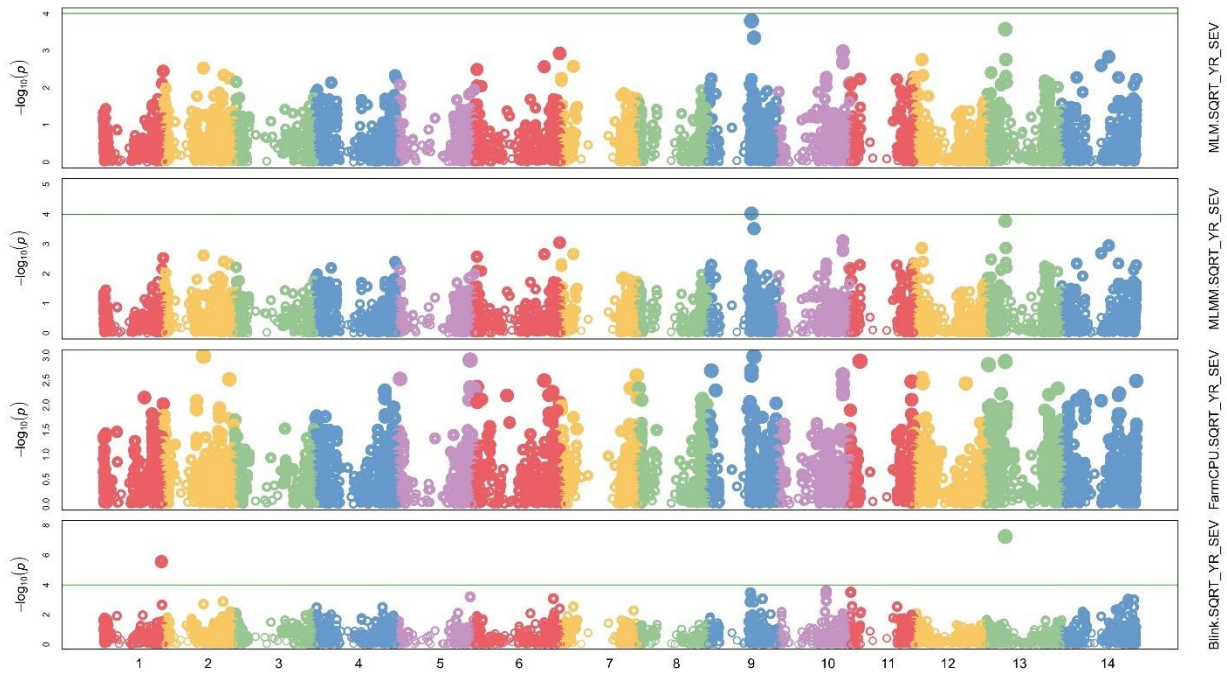

SUPPLEMENTARY FIGURE 90: Manhattan plot with all GWAS models (MLM, MLMM, FARMCPU AND BLINK) for Severity (SEV) in Grosseto 2020 and Q6 (WestAsia_Caucasus). Numbers on the Xlab refers to the durum wheat chromosomes (1 = 1A, 2 = 1B, 3 = 2A, 4 = 2B, 5 = 3A, 6 = 3B, 7 = 4A, 8 = 4B, 9 = 5A, 10 = 5B, 11 = 6A, 12 = 6B, 13 = 7A and 14 = 7B). Ylab refers to LOD (-log$_{10}$(pvalue)).

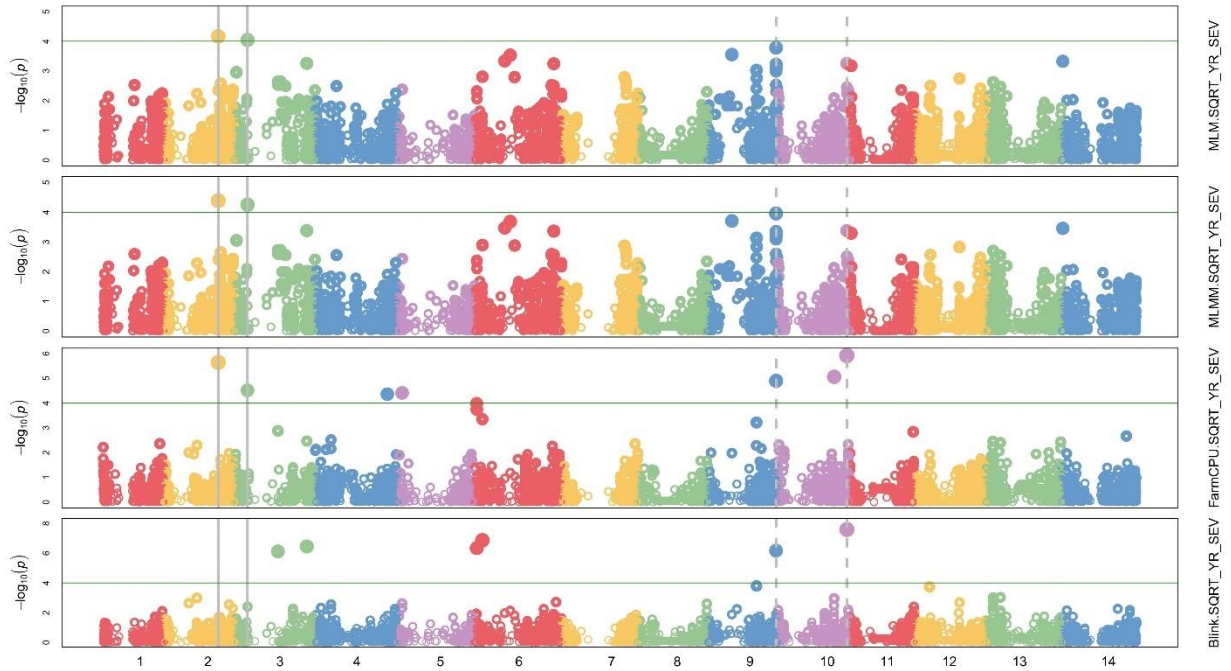

SUPPLEMENTARY FIGURE 91: Manhattan plot with all GWAS models (MLM, MLMM, FARMCPU AND BLINK) for Infection Type (IT) in Grosseto 2020 and Q7 (WestAsia_Caucasus). Numbers on the Xlab refers to the durum wheat chromosomes (1 = 1A, 2 = 1B, 3 = 2A, 4 = 2B, 5 = 3A, 6 = 3B, 7 = 4A, 8 = 4B, 9 = 5A, 10 = 5B, 11 = 6A, 12 = 6B, 13 = 7A and 14 = 7B). Ylab refers to LOD (-log$_{10}$(pvalue)).

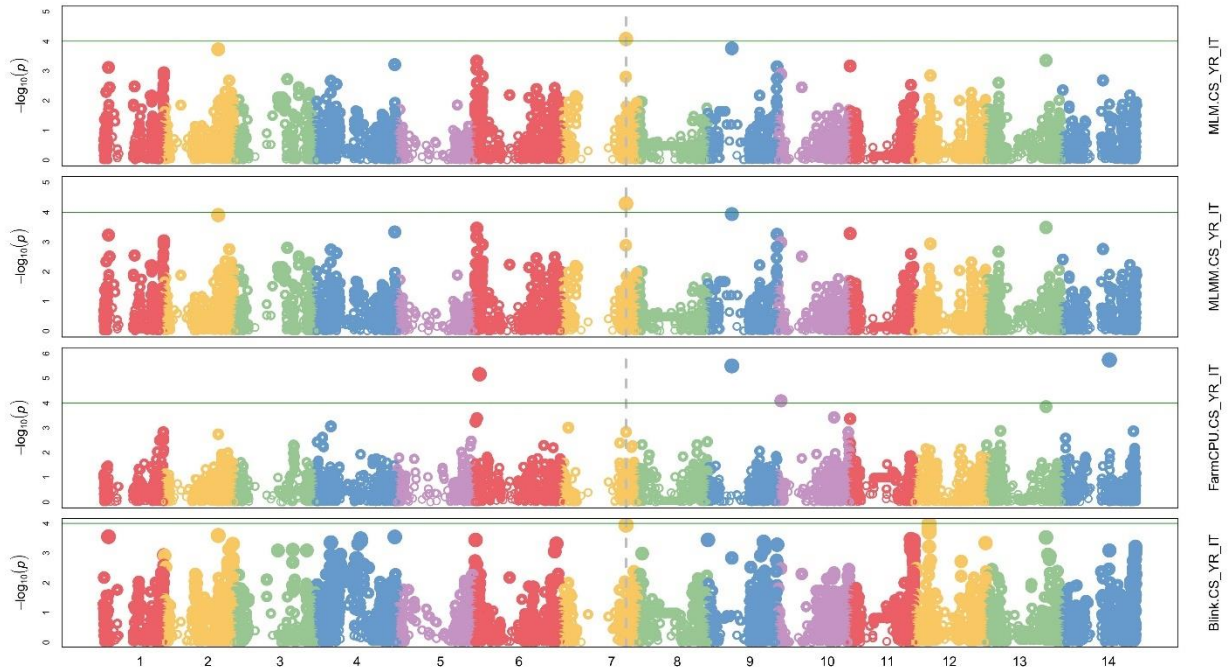

SUPPLEMENTARY FIGURE 92: Manhattan plot with all GWAS models (MLM, MLMM, FARMCPU AND BLINK) for Severity (SEV) in Grosseto 2020 and Q7 (Cyprous_Iberia). Numbers on the Xlab refers to the durum wheat chromosomes (1 = 1A, 2 = 1B, 3 = 2A, 4 = 2B, 5 = 3A, 6 = 3B, 7 = 4A, 8 = 4B, 9 = 5A, 10 = 5B, 11 = 6A, 12 = 6B, 13 = 7A and 14 = 7B). Ylab refers to LOD (-log$_{10}$(pvalue)).

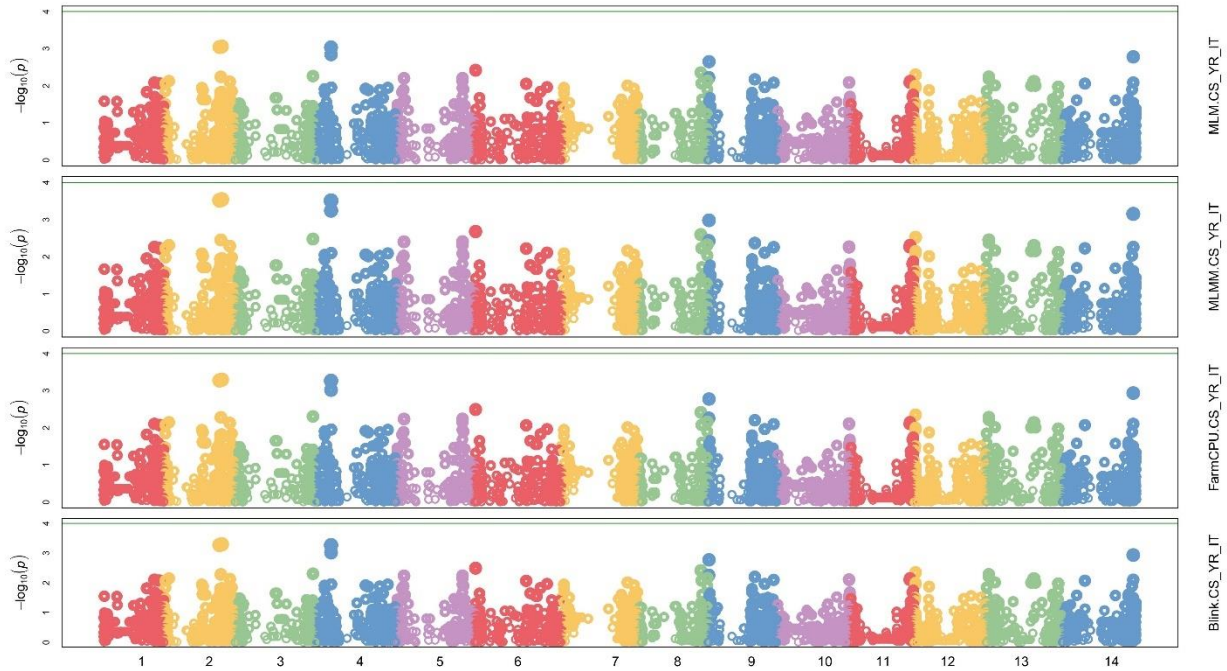

SUPPLEMENTARY FIGURE 93: Manhattan plot with all GWAS models (MLM, MLMM, FARMCPU AND BLINK) for Infection Type (IT) in Grosseto 2020 and Q8 (West_Asian_Founders). Numbers on the Xlab refers to the durum wheat chromosomes (1 = 1A, 2 = 1B, 3 = 2A, 4 = 2B, 5 = 3A, 6 = 3B, 7 = 4A, 8 = 4B, 9 = 5A, 10 = 5B, 11 = 6A, 12 = 6B, 13 = 7A and 14 = 7B). Ylab refers to LOD (-log$_{10}$(pvalue)).

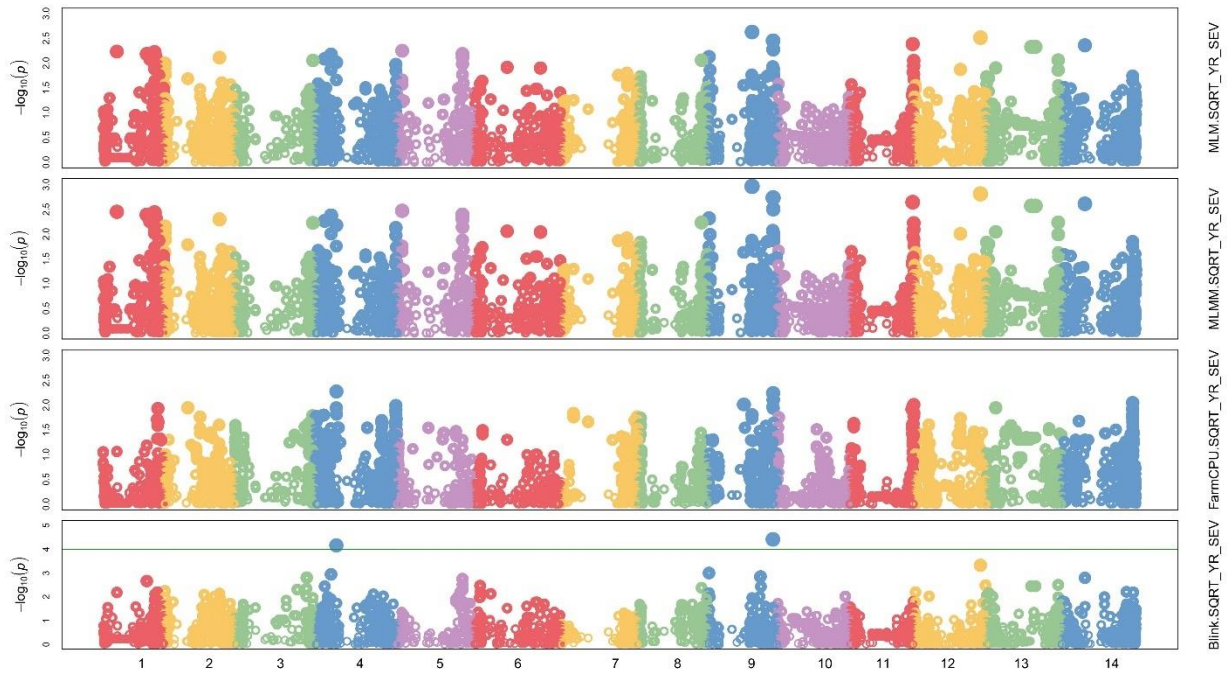

SUPPLEMENTARY FIGURE 94: Manhattan plot with all GWAS models (MLM, MLMM, FARMCPU AND BLINK) for Severity (SEV) in Grosseto 2020 and Q8 (West_Asian_Founders). Numbers on the Xlab refers to the durum wheat chromosomes (1 = 1A, 2 = 1B, 3 = 2A, 4 = 2B, 5 = 3A, 6 = 3B, 7 = 4A, 8 = 4B, 9 = 5A, 10 = 5B, 11 = 6A, 12 = 6B, 13 = 7A and 14 = 7B). Ylab refers to LOD (-log$_{10}$(pvalue)).

SUPPLEMENTARY FIGURE 95: Manhattan plot with all GWAS models (MLM, MLMM, FARMCPU AND BLINK) for Infection Type (IT) in Grosseto 2021 and Q6 (Horn_Africa_aethiopicum). Numbers on the Xlab refers to the durum wheat chromosomes (1 = 1A, 2 = 1B, 3 = 2A, 4 = 2B, 5 = 3A, 6 = 3B, 7 = 4A, 8 = 4B, 9 = 5A, 10 = 5B, 11 = 6A, 12 = 6B, 13 = 7A and 14 = 7B). Ylab refers to LOD (-log$_{10}$(pvalue)).

SUPPLEMENTARY FIGURE 96: Manhattan plot with all GWAS models (MLM, MLMM, FARMCPU AND BLINK) for Severity (SEV) in Grosseto 2021 and Q6 (Horn_Africa_aethiopicum). Numbers on the Xlab refers to the durum wheat chromosomes (1 = 1A, 2 = 1B, 3 = 2A, 4 = 2B, 5 = 3A, 6 = 3B, 7 = 4A, 8 = 4B, 9 = 5A, 10 = 5B, 11 = 6A, 12 = 6B, 13 = 7A and 14 = 7B). Ylab refers to LOD (-log$_{10}$(pvalue)).

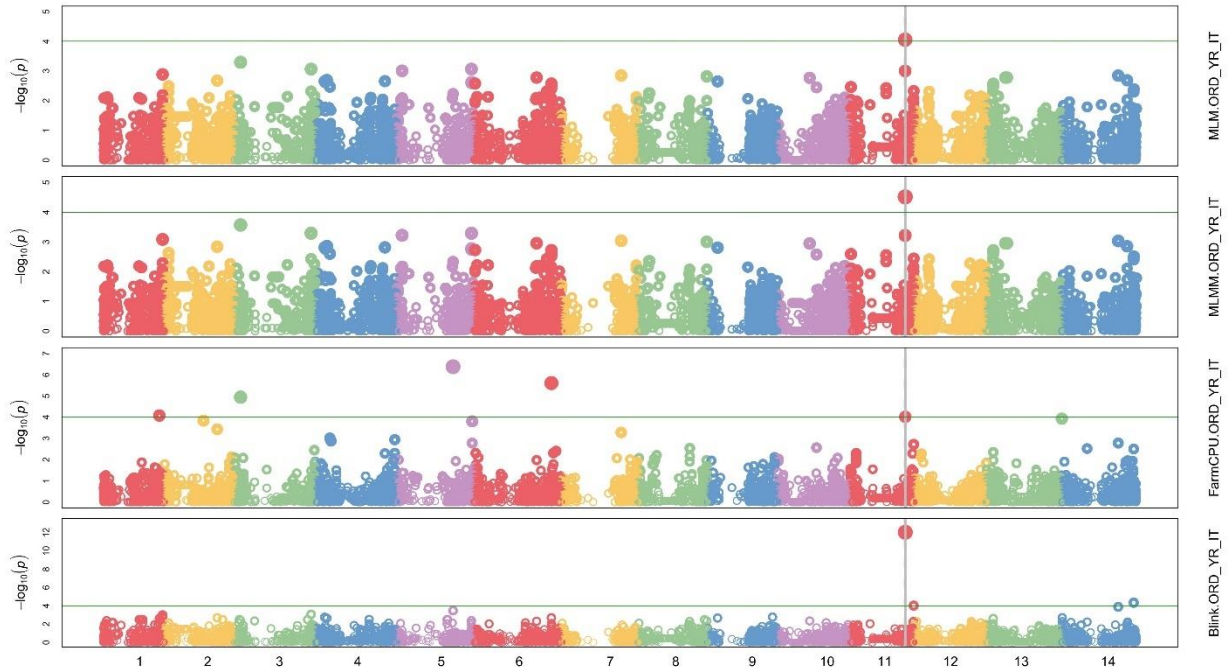

SUPPLEMENTARY FIGURE 97: Manhattan plot with all GWAS models (MLM, MLMM, FARMCPU AND BLINK) for Infection Type (IT) in Grosseto 2021 and Q7 (Cyprous_Iberia). Numbers on the Xlab refers to the durum wheat chromosomes (1 = 1A, 2 = 1B, 3 = 2A, 4 = 2B, 5 = 3A, 6 = 3B, 7 = 4A, 8 = 4B, 9 = 5A, 10 = 5B, 11 = 6A, 12 = 6B, 13 = 7A and 14 = 7B). Ylab refers to LOD (-log$_{10}$(pvalue)).

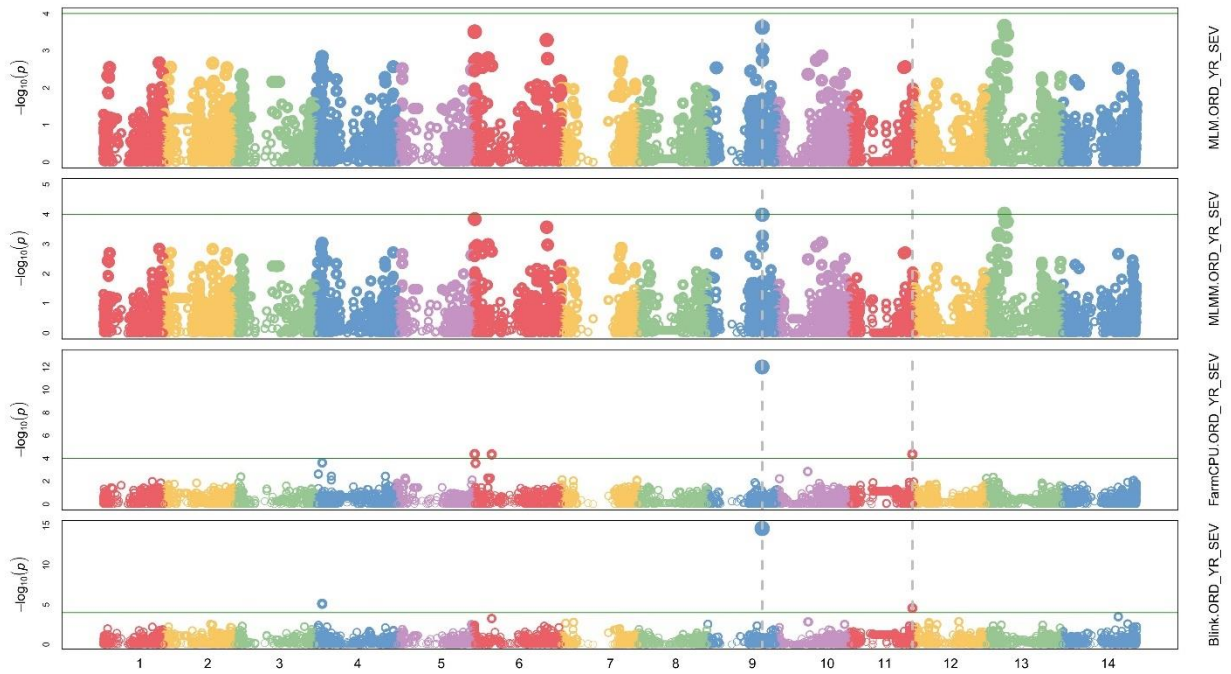

SUPPLEMENTARY FIGURE 98: Manhattan plot with all GWAS models (MLM, MLMM, FARMCPU AND BLINK) for Severity (SEV) in Grosseto 2021 and Q7 (Cyprous_Iberia). Numbers on the Xlab refers to the durum wheat chromosomes (1 = 1A, 2 = 1B, 3 = 2A, 4 = 2B, 5 = 3A, 6 = 3B, 7 = 4A, 8 = 4B, 9 = 5A, 10 = 5B, 11 = 6A, 12 = 6B, 13 = 7A and 14 = 7B). Ylab refers to LOD (-log$_{10}$(pvalue)).

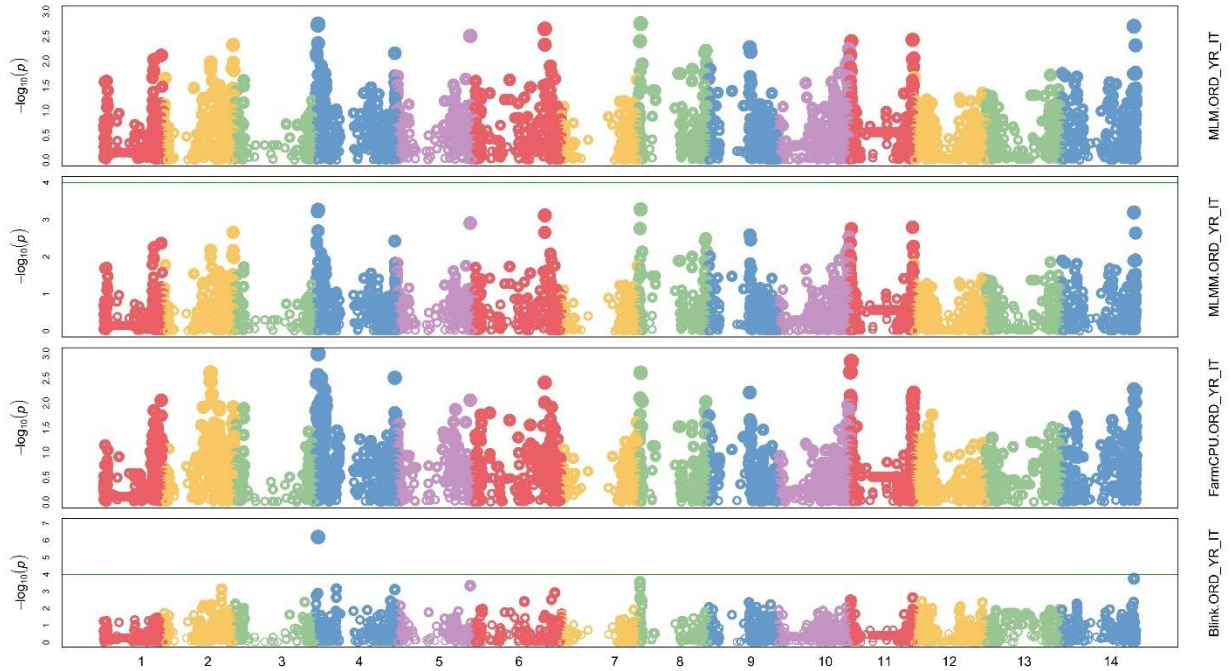

SUPPLEMENTARY FIGURE 99: Manhattan plot with all GWAS models (MLM, MLMM, FARMCPU AND BLINK) for Infection Type (IT) in Grosseto 2021 and Q8 (West_Asian_Founders). Numbers on the Xlab refers to the durum wheat chromosomes (1 = 1A, 2 = 1B, 3 = 2A, 4 = 2B, 5 = 3A, 6 = 3B, 7 = 4A, 8 = 4B, 9 = 5A, 10 = 5B, 11 = 6A, 12 = 6B, 13 = 7A and 14 = 7B). Ylab refers to LOD (-log$_{10}$(pvalue)).

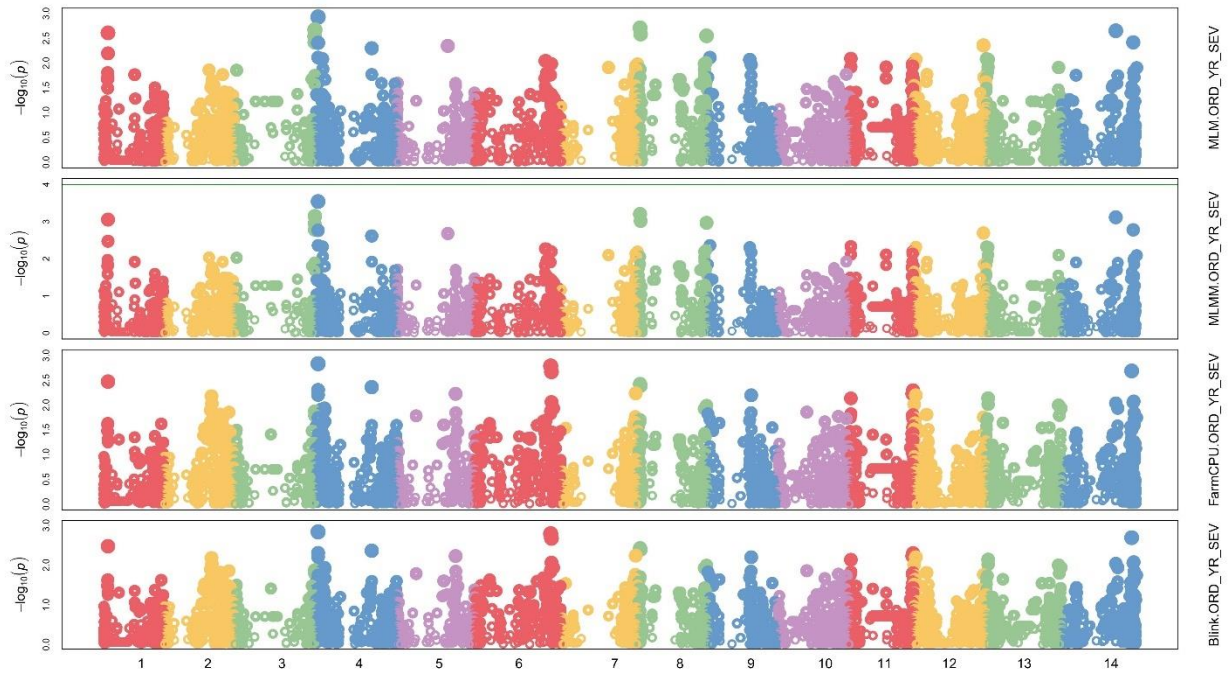

SUPPLEMENTARY FIGURE 100: Manhattan plot with all GWAS models (MLM, MLMM, FARMCPU AND BLINK) for Severity (SEV) in Grosseto 2021 and Q8 (West_Asian_Founders). Numbers on the Xlab refers to the durum wheat chromosomes (1 = 1A, 2 = 1B, 3 = 2A, 4 = 2B, 5 = 3A, 6 = 3B, 7 = 4A, 8 = 4B, 9 = 5A, 10 = 5B, 11 = 6A, 12 = 6B, 13 = 7A and 14 = 7B). Ylab refers to LOD (-log$_{10}$(pvalue)).

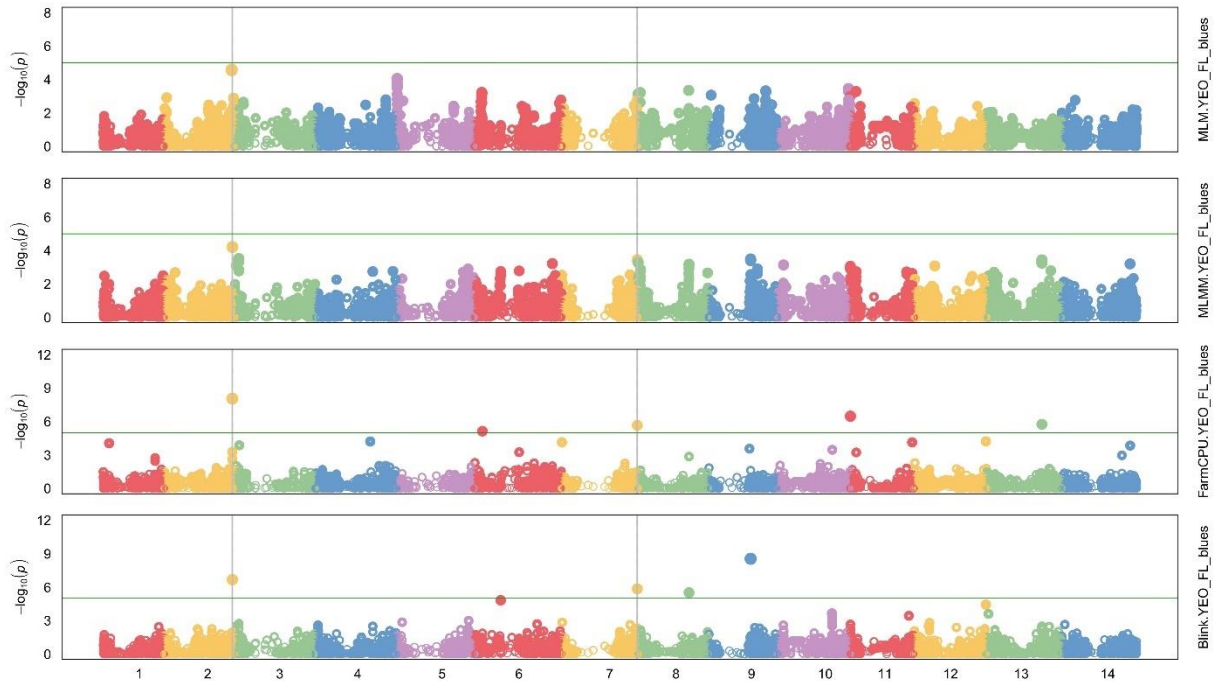

SUPPLEMENTARY FIGURE 101: Manhattan plot with all GWAS models (MLM, MLMM, FARMCPU AND BLINK) for Infection Type in the Flag Leaf (IT_Fl) in Grosseto 2022. Numbers on the Xlab refers to the durum wheat chromosomes (1 = 1A, 2 = 1B, 3 = 2A, 4 = 2B, 5 = 3A, 6 = 3B, 7 = 4A, 8 = 4B, 9 = 5A, 10 = 5B, 11 = 6A, 12 = 6B, 13 = 7A and 14 = 7B). Ylab refers to LOD (-log$_{10}$(pvalue)).

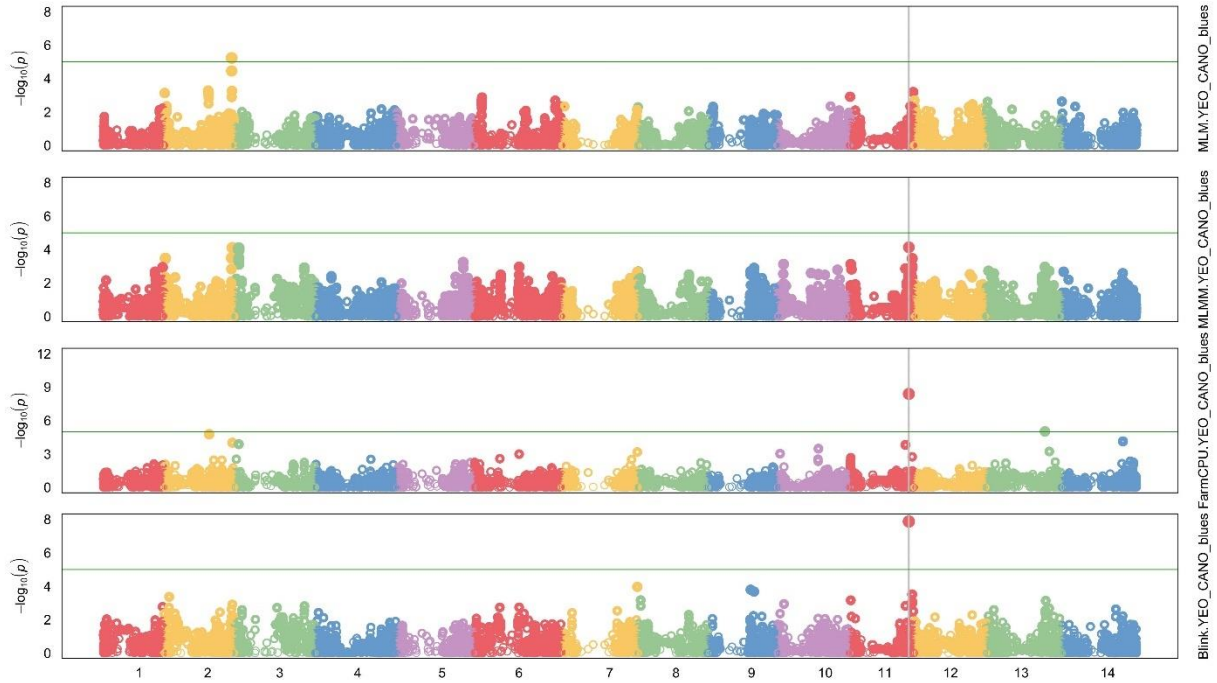

SUPPLEMENTARY FIGURE 102: Manhattan plot with all GWAS models (MLM, MLMM, FARMCPU AND BLINK) for Infection Type in the Canopy (IT_CANOPY) in Grosseto 2022. Numbers on the Xlab refers to the durum wheat chromosomes (1 = 1A, 2 = 1B, 3 = 2A, 4 = 2B, 5 = 3A, 6 = 3B, 7 = 4A, 8 = 4B, 9 = 5A, 10 = 5B, 11 = 6A, 12 = 6B, 13 = 7A and 14 = 7B). Ylab refers to LOD (-log$_{10}$(pvalue)).

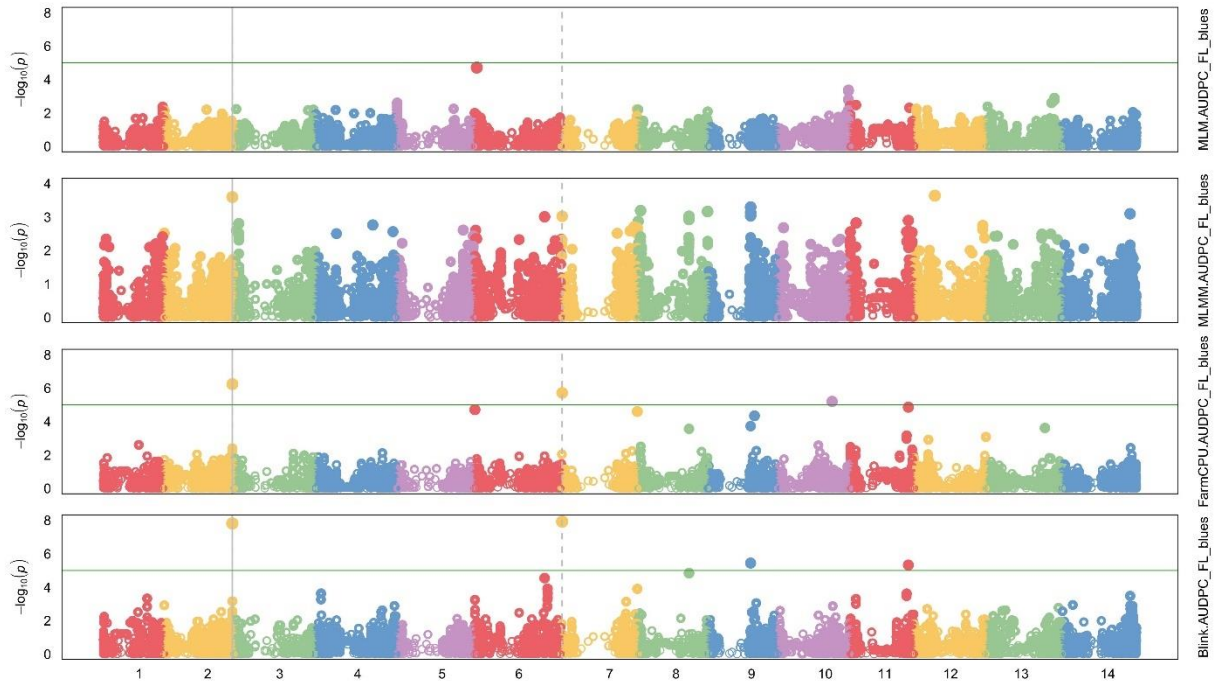

SUPPLEMENTARY FIGURE 103: Manhattan plot with all GWAS models (MLM, MLMM, FARMCPU AND BLINK) for AUDPC_Infection Type in the flag leaf (AUDPC_FL) in Grosseto 2022. Numbers on the Xlab refers to the durum wheat chromosomes (1 = 1A, 2 = 1B, 3 = 2A, 4 = 2B, 5 = 3A, 6 = 3B, 7 = 4A, 8 = 4B, 9 = 5A, 10 = 5B, 11 = 6A, 12 = 6B, 13 = 7A and 14 = 7B). Ylab refers to LOD (-log$_{10}$(pvalue)).

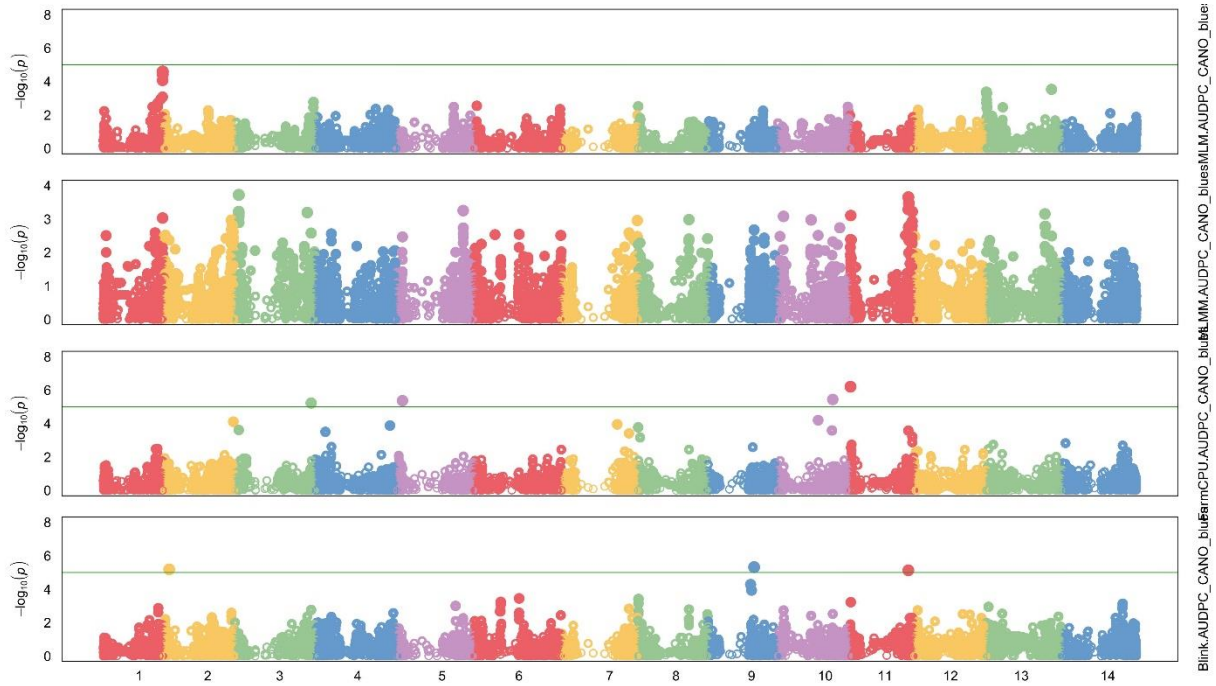

SUPPLEMENTARY FIGURE 104: Manhattan plot with all GWAS models (MLM, MLMM, FARMCPU AND BLINK) for AUDPC_Infection Type in the Canopy (AUDPC_CANOPY) in Grosseto 2022. Numbers on the Xlab refers to the durum wheat chromosomes (1 = 1A, 2 = 1B, 3 = 2A, 4 = 2B, 5 = 3A, 6 = 3B, 7 = 4A, 8 = 4B, 9 = 5A, 10 = 5B, 11 = 6A, 12 = 6B, 13 = 7A and 14 = 7B). Ylab refers to LOD (-log$_{10}$(pvalue)).

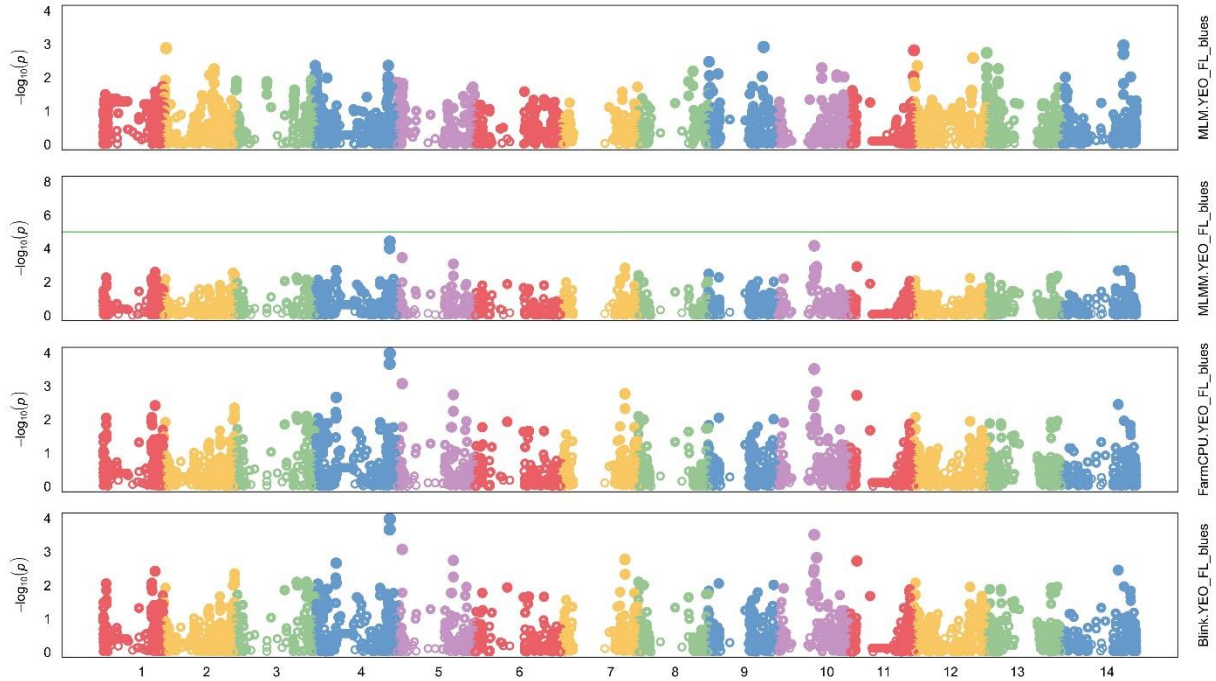

SUPPLEMENTARY FIGURE 105: Manhattan plot with all GWAS models (MLM, MLMM, FARMCPU AND BLINK) for Infection Type in the Flag Leaf (IT_Fl) in Grosseto 2022 and Q1 (Horn_Africa_aethiopicum). Numbers on the Xlab refers to the durum wheat chromosomes (1 = 1A, 2 = 1B, 3 = 2A, 4 = 2B, 5 = 3A, 6 = 3B, 7 = 4A, 8 = 4B, 9 = 5A, 10 = 5B, 11 = 6A, 12 = 6B, 13 = 7A and 14 = 7B). Ylab refers to LOD (-log$_{10}$(pvalue)).

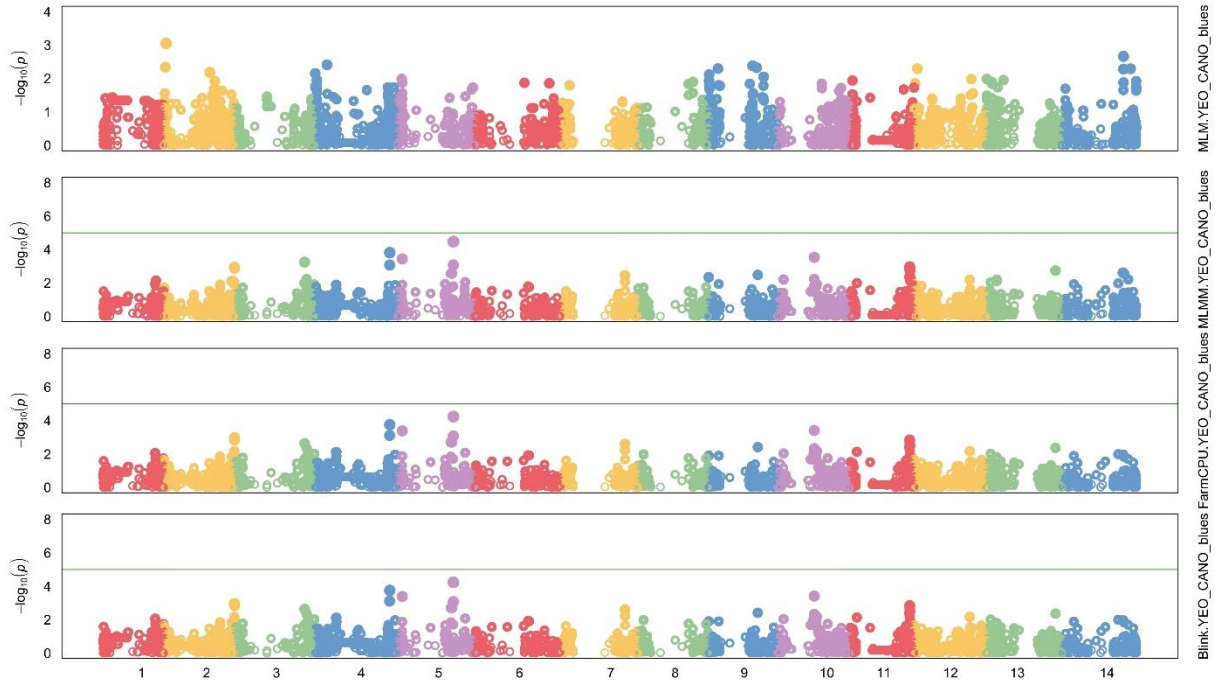

SUPPLEMENTARY FIGURE 106: Manhattan plot with all GWAS models (MLM, MLMM, FARMCPU AND BLINK) for Infection Type in Canopy (IT_CANOPY) in Grosseto 2022 and Q1 (Horn_Africa_aethiopicum). Numbers on the Xlab refers to the durum wheat chromosomes (1 = 1A, 2 = 1B, 3 = 2A, 4 = 2B, 5 = 3A, 6 = 3B, 7 = 4A, 8 = 4B, 9 = 5A, 10 = 5B, 11 = 6A, 12 = 6B, 13 = 7A and 14 = 7B). Ylab refers to LOD (-log$_{10}$(pvalue)).

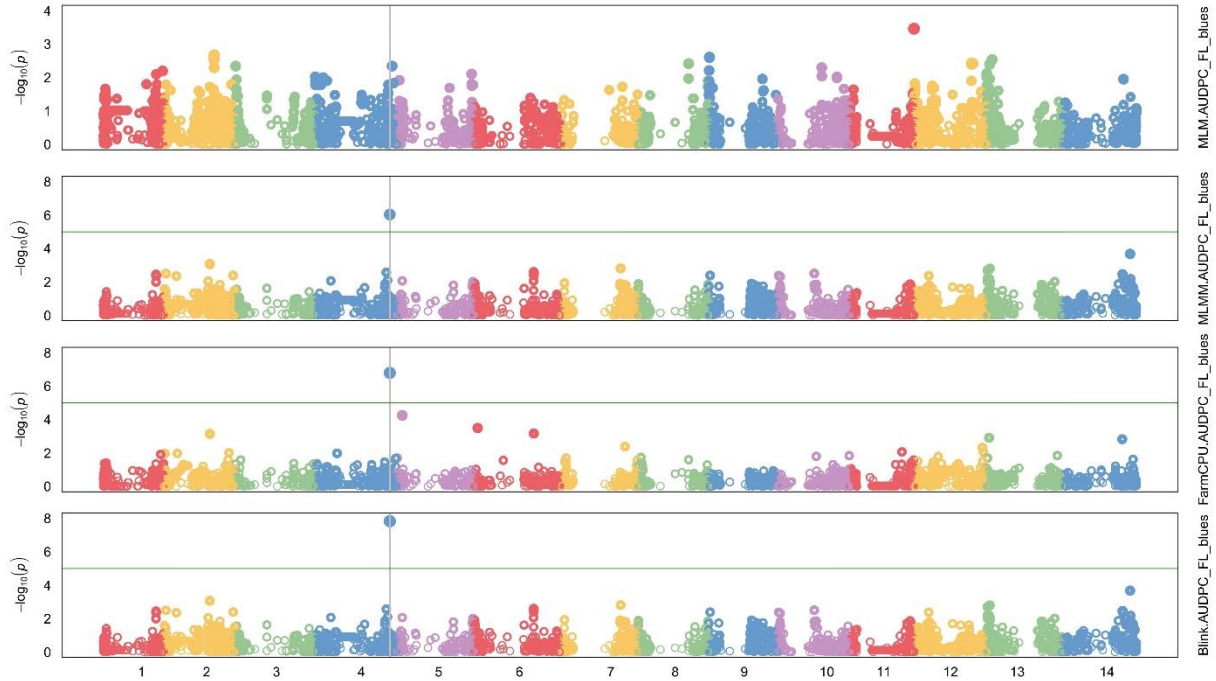

SUPPLEMENTARY FIGURE 107: Manhattan plot with all GWAS models (MLM, MLMM, FARMCPU AND BLINK) for AUDPC_Infection Type in the flag leaf (AUDPC_Fl) in Grosseto 2022 and Q1 (Horn_Africa_aethiopicum). Numbers on the Xlab refers to the durum wheat chromosomes (1 = 1A, 2 = 1B, 3 = 2A, 4 = 2B, 5 = 3A, 6 = 3B, 7 = 4A, 8 = 4B, 9 = 5A, 10 = 5B, 11 = 6A, 12 = 6B, 13 = 7A and 14 = 7B). Ylab refers to LOD (-log$_{10}$(pvalue)).

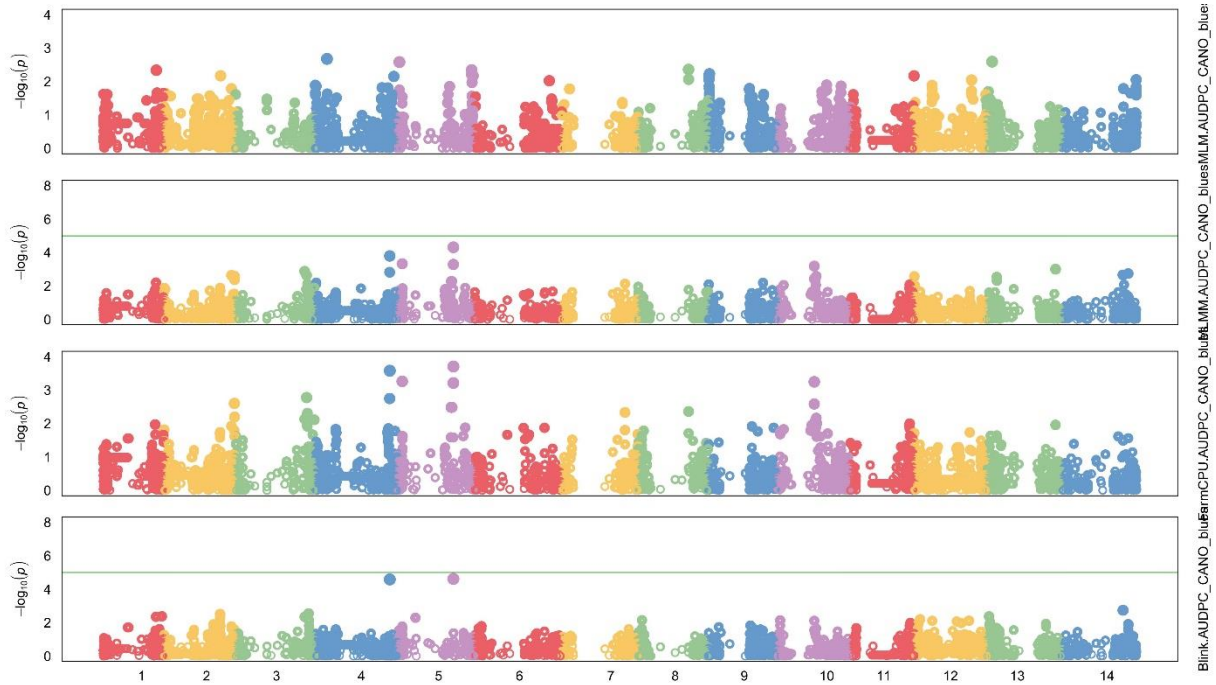

SUPPLEMENTARY FIGURE 108: Manhattan plot with all GWAS models (MLM, MLMM, FARMCPU AND BLINK) for AUDPC_Infection Type in the CANOPY (AUDPC_CANOPY) in Grosseto 2022 and Q1 (Horn_Africa_aethiopicum). Numbers on the Xlab refers to the durum wheat chromosomes (1 = 1A, 2 = 1B, 3 = 2A, 4 = 2B, 5 = 3A, 6 = 3B, 7 = 4A, 8 = 4B, 9 = 5A, 10 = 5B, 11 = 6A, 12 = 6B, 13 = 7A and 14 = 7B). Ylab refers to LOD (-log$_{10}$(pvalue)).

SUPPLEMENTARY FIGURE 109: Manhattan plot with all GWAS models (MLM, MLMM, FARMCPU AND BLINK) for Infection Type in the Flag Leaf (IT_Fl) in Grosseto 2022 and Q3 (Iran_syriacum). Numbers on the Xlab refers to the durum wheat chromosomes (1 = 1A, 2 = 1B, 3 = 2A, 4 = 2B, 5 = 3A, 6 = 3B, 7 = 4A, 8 = 4B, 9 = 5A, 10 = 5B, 11 = 6A, 12 = 6B, 13 = 7A and 14 = 7B). Ylab refers to LOD (-log$_{10}$(pvalue)).

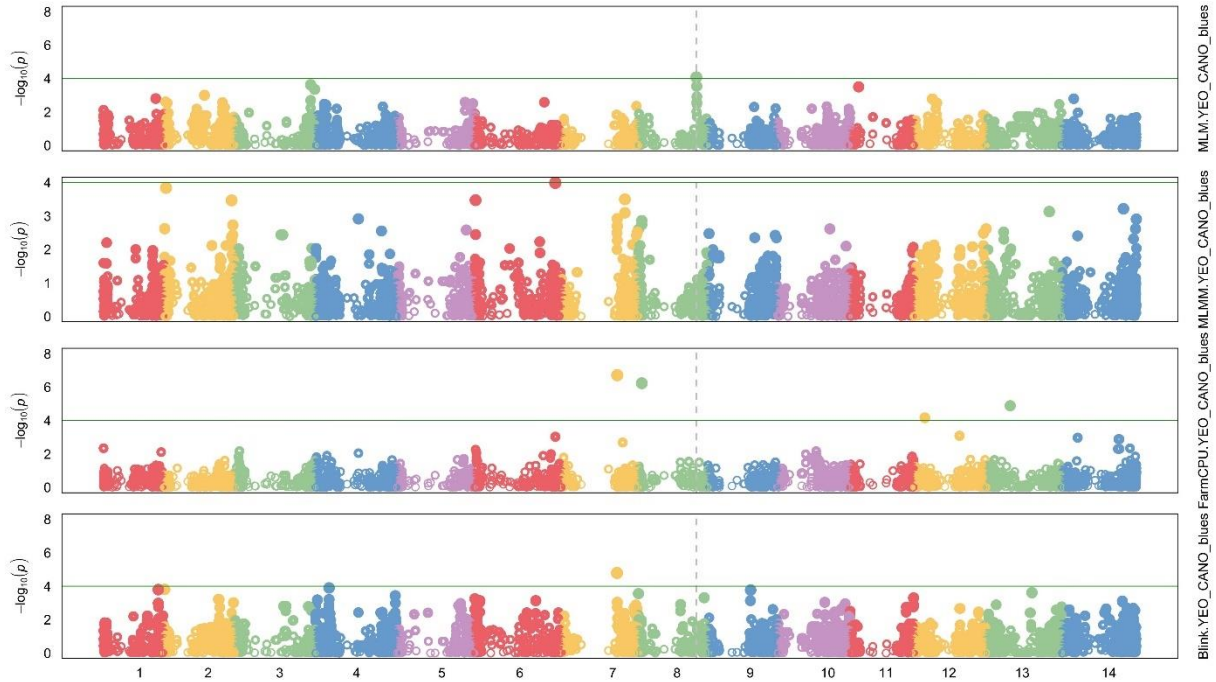

SUPPLEMENTARY FIGURE 110: Manhattan plot with all GWAS models (MLM, MLMM, FARMCPU AND BLINK) for Infection Type in the Canopy (IT_CANOPY) in Grosseto 2022 and Q3 (Iran_Syriacum). Numbers on the Xlab refers to the durum wheat chromosomes (1 = 1A, 2 = 1B, 3 = 2A, 4 = 2B, 5 = 3A, 6 = 3B, 7 = 4A, 8 = 4B, 9 = 5A, 10 = 5B, 11 = 6A, 12 = 6B, 13 = 7A and 14 = 7B). Ylab refers to LOD (-log$_{10}$(pvalue)).

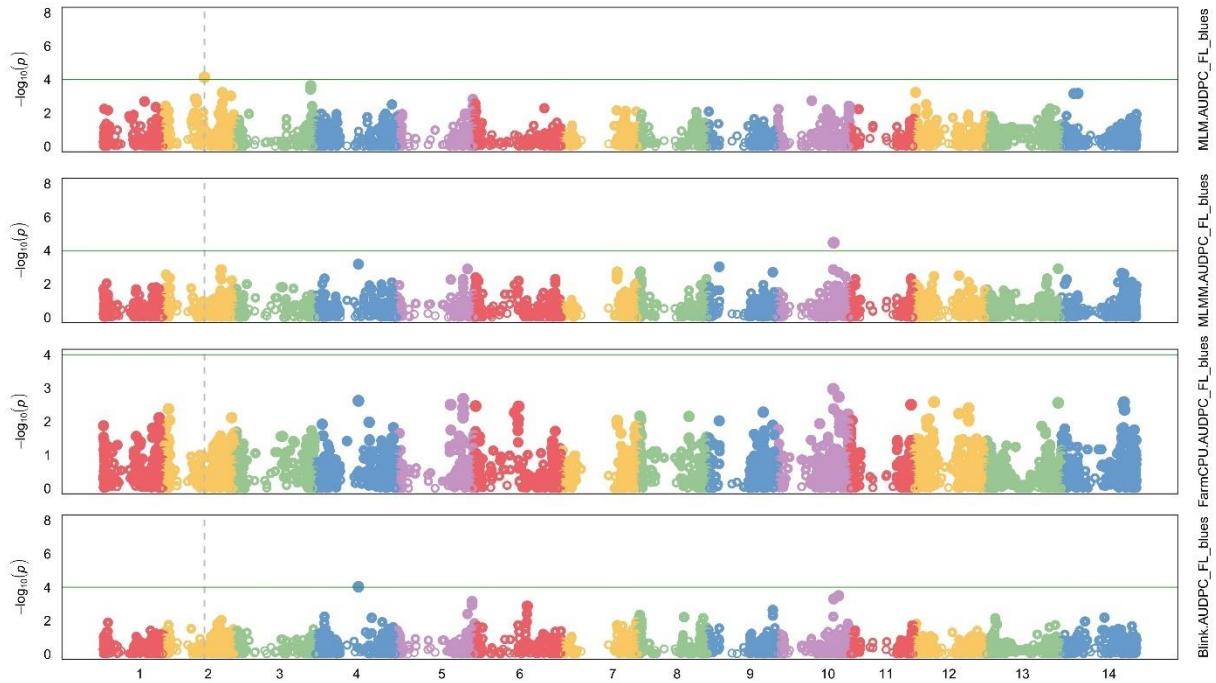

SUPPLEMENTARY FIGURE 111: Manhattan plot with all GWAS models (MLM, MLMM, FARMCPU AND BLINK) for AUDPC_Infection Type in the flag leaf (AUDPC_FL_IT) in Grosseto 2022 and Q3 (Iran_Syriacum). Numbers on the Xlab refers to the durum wheat chromosomes (1 = 1A, 2 = 1B, 3 = 2A, 4 = 2B, 5 = 3A, 6 = 3B, 7 = 4A, 8 = 4B, 9 = 5A, 10 = 5B, 11 = 6A, 12 = 6B, 13 = 7A and 14 = 7B). Ylab refers to LOD (-log$_{10}$(pvalue)).

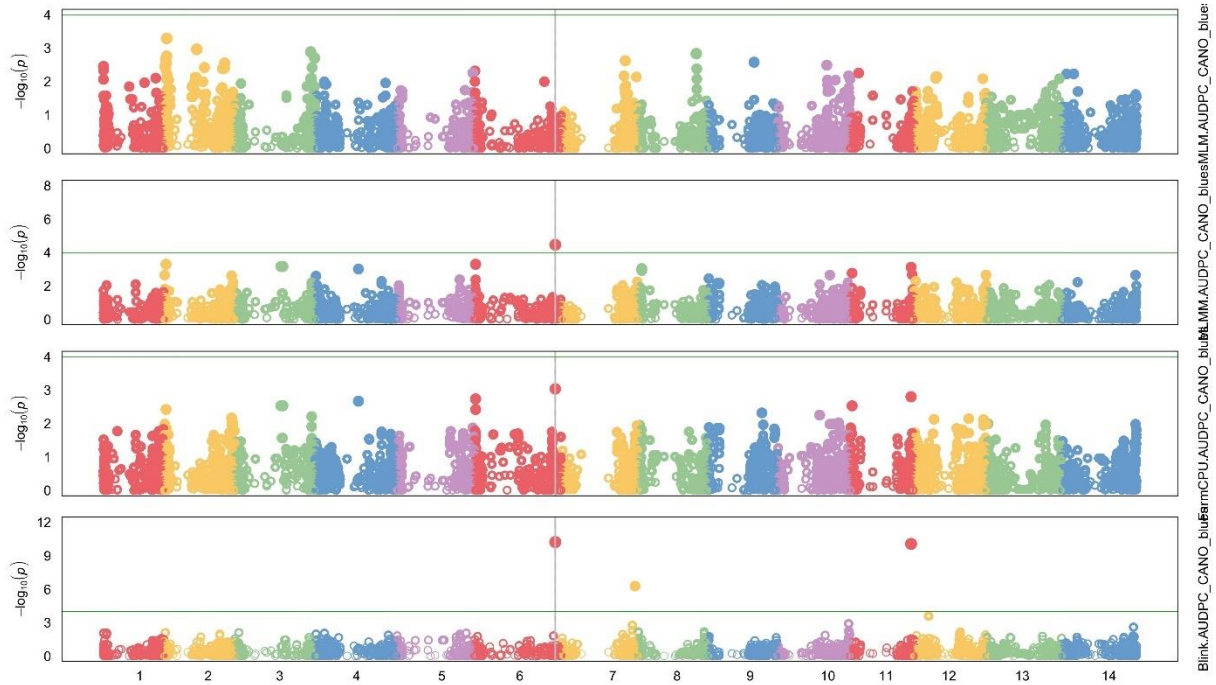

SUPPLEMENTARY FIGURE 112: Manhattan plot with all GWAS models (MLM, MLMM, FARMCPU AND BLINK) for AUDPC_Infection Type in the CANOPY (AUDPC_CANOPY) in Grosseto 2022 and Q3 (Iran_Syriacum). Numbers on the Xlab refers to the durum wheat chromosomes (1 = 1A, 2 = 1B, 3 = 2A, 4 = 2B, 5 = 3A, 6 = 3B, 7 = 4A, 8 = 4B, 9 = 5A, 10 = 5B, 11 = 6A, 12 = 6B, 13 = 7A and 14 = 7B). Ylab refers to LOD (-log$_{10}$(pvalue)).

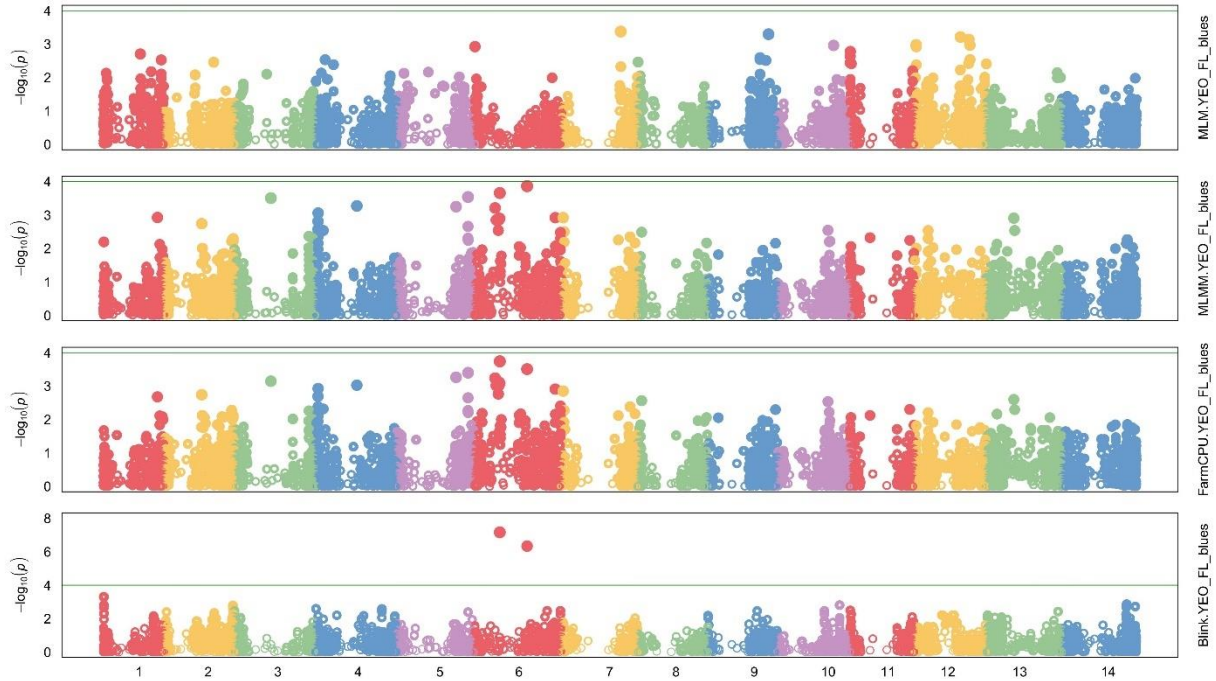

SUPPLEMENTARY FIGURE 113: Manhattan plot with all GWAS models (MLM, MLMM, FARMCPU AND BLINK) for Infection Type in the Flag Leaf (IT_Fl) in Grosseto 2022 and Q6 (WestAsia_Caucasus). Numbers on the Xlab refers to the durum wheat chromosomes (1 = 1A, 2 = 1B, 3 = 2A, 4 = 2B, 5 = 3A, 6 = 3B, 7 = 4A, 8 = 4B, 9 = 5A, 10 = 5B, 11 = 6A, 12 = 6B, 13 = 7A and 14 = 7B). Ylab refers to LOD (-log$_{10}$(pvalue)).

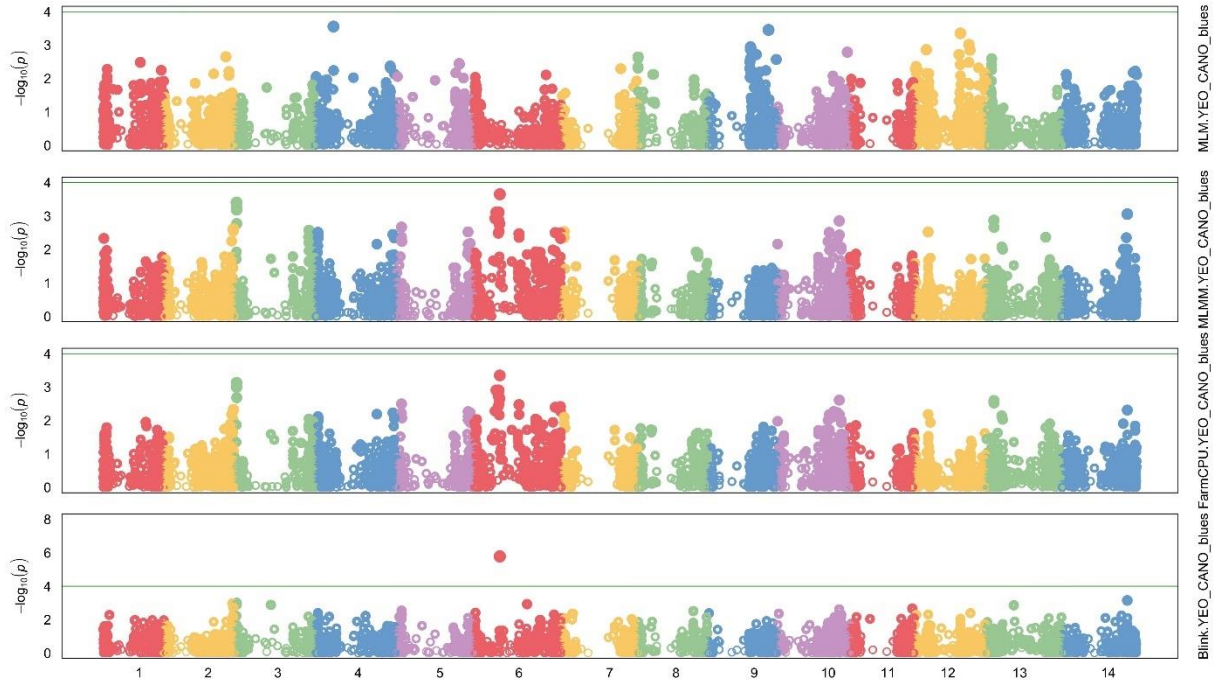

SUPPLEMENTARY FIGURE 114: Manhattan plot with all GWAS models (MLM, MLMM, FARMCPU AND BLINK) for Infection Type in the Canopy (IT_CANOPY) in Grosseto 2022 and Q6 (WestAsia_Caucasus). Numbers on the Xlab refers to the durum wheat chromosomes (1 = 1A, 2 = 1B, 3 = 2A, 4 = 2B, 5 = 3A, 6 = 3B, 7 = 4A, 8 = 4B, 9 = 5A, 10 = 5B, 11 = 6A, 12 = 6B, 13 = 7A and 14 = 7B). Ylab refers to LOD (-log$_{10}$(pvalue)).

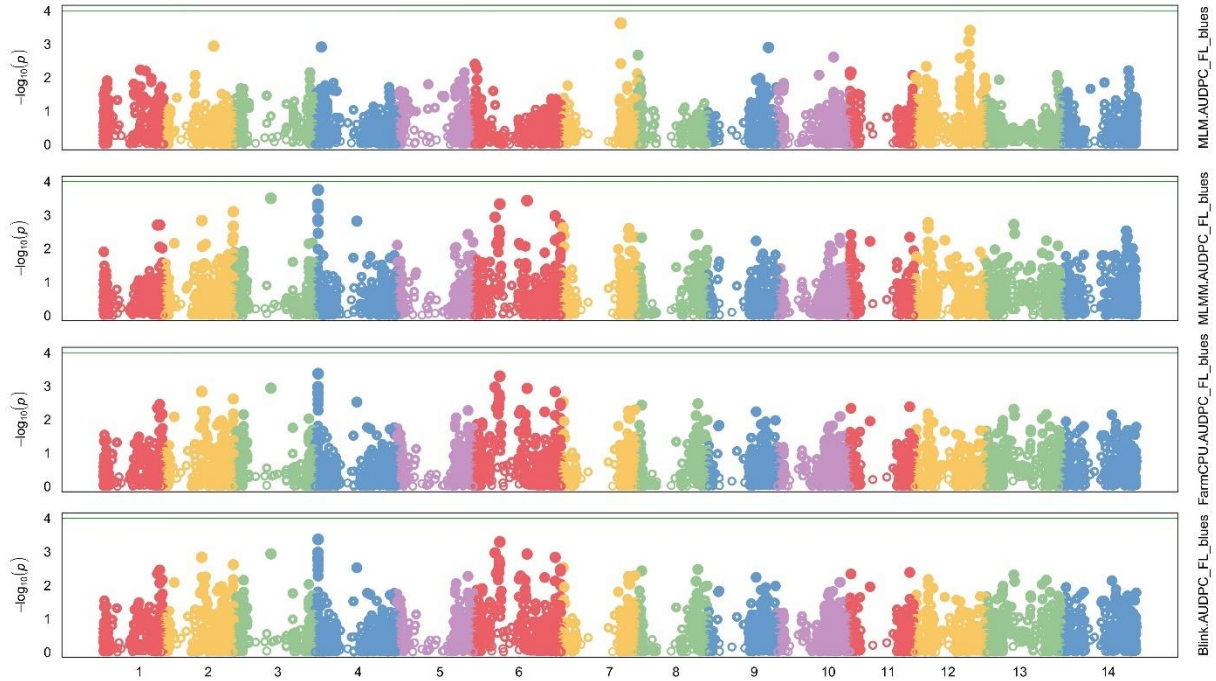

SUPPLEMENTARY FIGURE 115: Manhattan plot with all GWAS models (MLM, MLMM, FARMCPU AND BLINK) for AUDPC_Infection Type in the Flag leaf (AUDPC_FL) in Grosseto 2022 and Q6 (WestAsia_Caucasus). Numbers on the Xlab refers to the durum wheat chromosomes (1 = 1A, 2 = 1B, 3 = 2A, 4 = 2B, 5 = 3A, 6 = 3B, 7 = 4A, 8 = 4B, 9 = 5A, 10 = 5B, 11 = 6A, 12 = 6B, 13 = 7A and 14 = 7B). Ylab refers to LOD (-log$_{10}$(pvalue)).

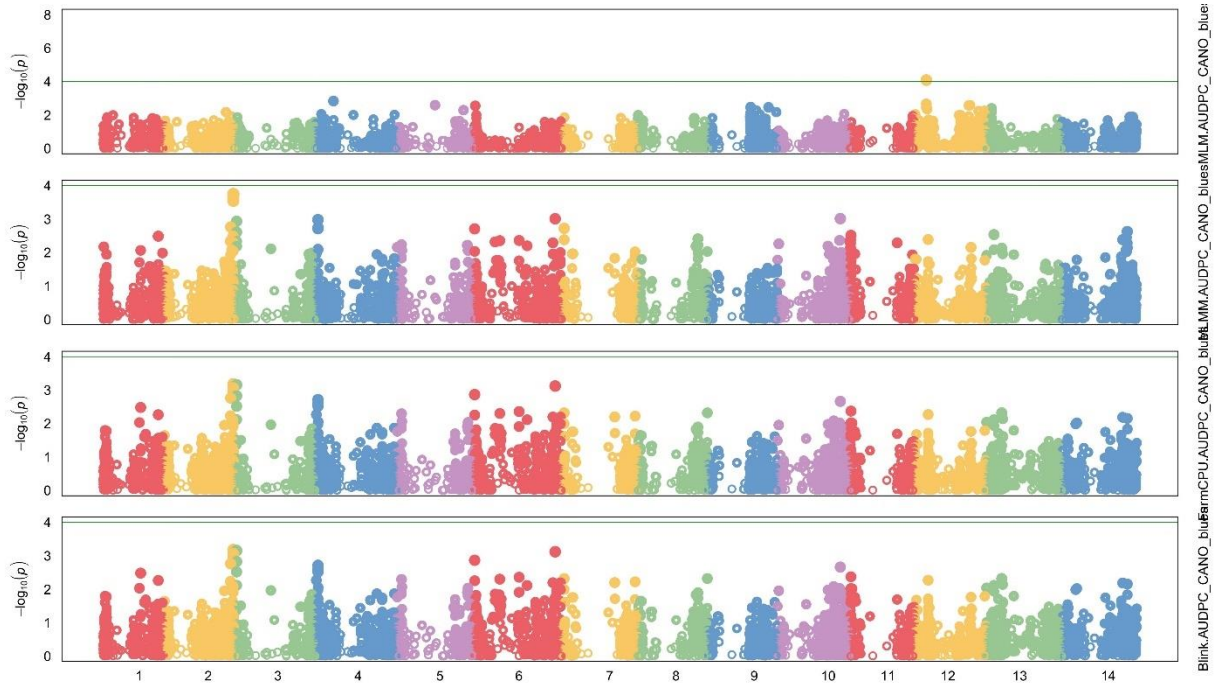

SUPPLEMENTARY FIGURE 116: Manhattan plot with all GWAS models (MLM, MLMM, FARMCPU AND BLINK) for AUDPC_Infection Type in the CANOPY (AUDPC_CANOPY) in Grosseto 2022 and Q6 (WestAsia_Caucasus). Numbers on the Xlab refers to the durum wheat chromosomes (1 = 1A, 2 = 1B, 3 = 2A, 4 = 2B, 5 = 3A, 6 = 3B, 7 = 4A, 8 = 4B, 9 = 5A, 10 = 5B, 11 = 6A, 12 = 6B, 13 = 7A and 14 = 7B). Ylab refers to LOD (-log$_{10}$(pvalue)).

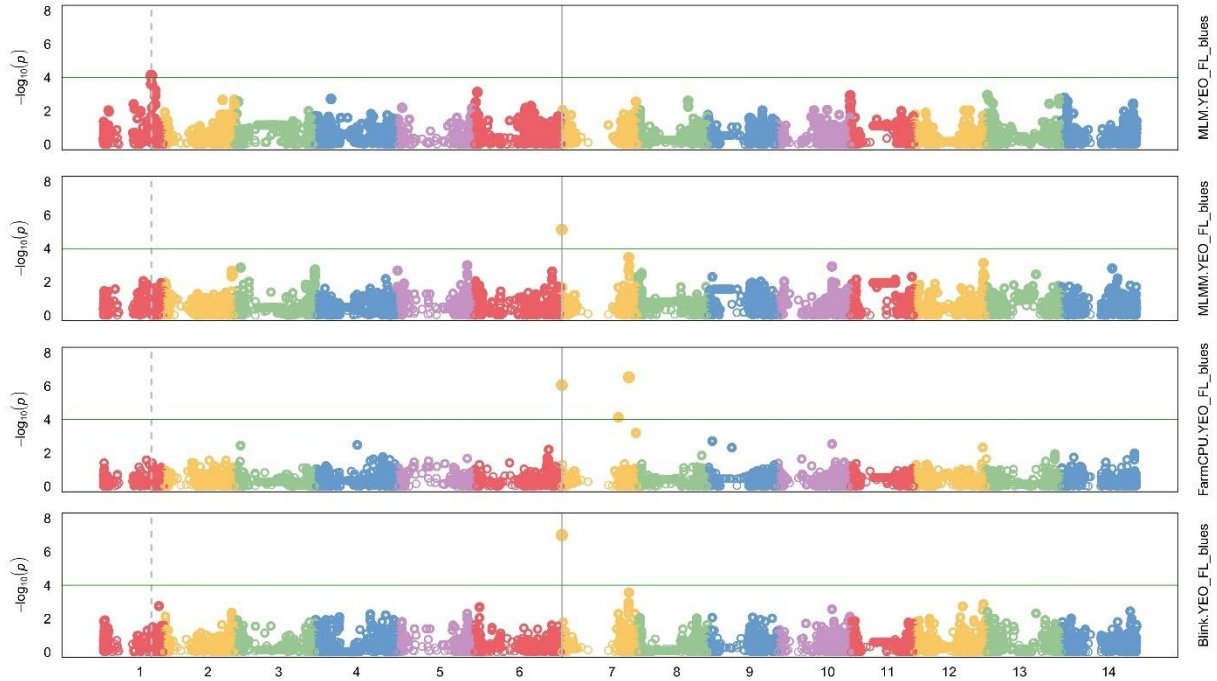

SUPPLEMENTARY FIGURE 117: Manhattan plot with all GWAS models (MLM, MLMM, FARMCPU AND BLINK) for Infection Type in the Flag Leaf (IT_Fl) in Grosseto 2022 and Q7 (Cyprous_Iberia). Numbers on the Xlab refers to the durum wheat chromosomes (1 = 1A, 2 = 1B, 3 = 2A, 4 = 2B, 5 = 3A, 6 = 3B, 7 = 4A, 8 = 4B, 9 = 5A, 10 = 5B, 11 = 6A, 12 = 6B, 13 = 7A and 14 = 7B). Ylab refers to LOD ($-\log_{10}$(pvalue)).

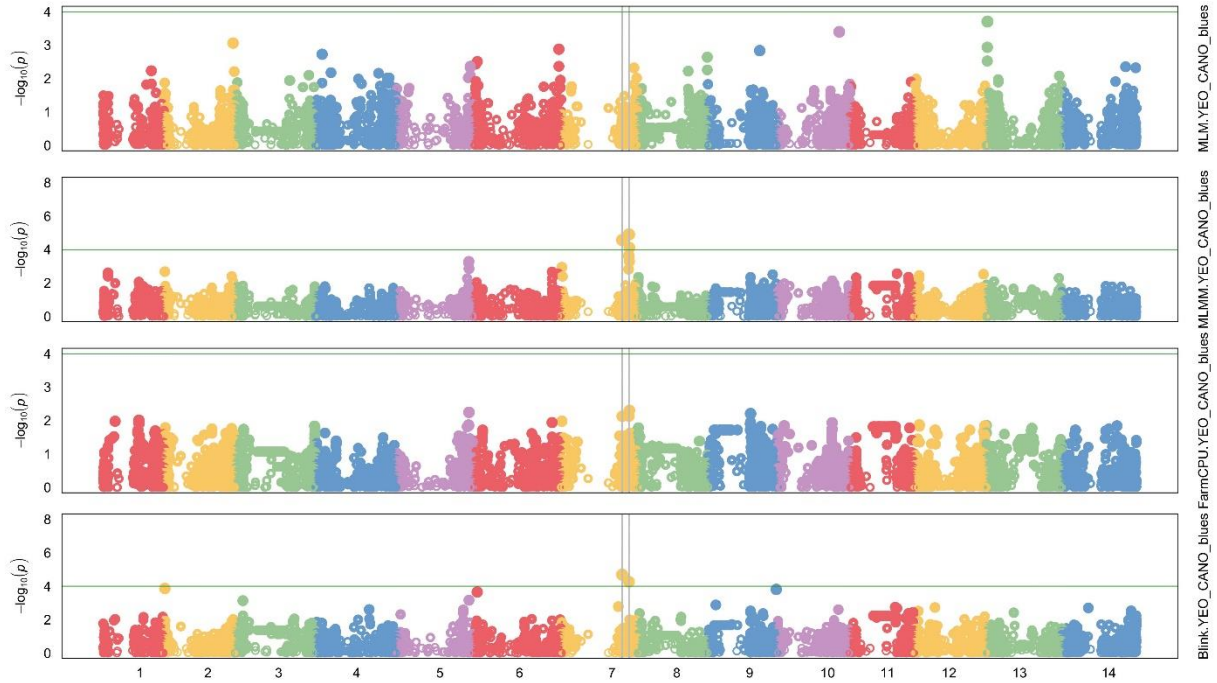

SUPPLEMENTARY FIGURE 118: Manhattan plot with all GWAS models (MLM, MLMM, FARMCPU AND BLINK) for Infection Type in the Canopy (IT_CANOPY) in Grosseto 2022 and Q7 (Cyprous_Iberia). Numbers on the Xlab refers to the durum wheat chromosomes (1 = 1A, 2 = 1B, 3 = 2A, 4 = 2B, 5 = 3A, 6 = 3B, 7 = 4A, 8 = 4B, 9 = 5A, 10 = 5B, 11 = 6A, 12 = 6B, 13 = 7A and 14 = 7B). Ylab refers to LOD ($-\log_{10}$(pvalue)).

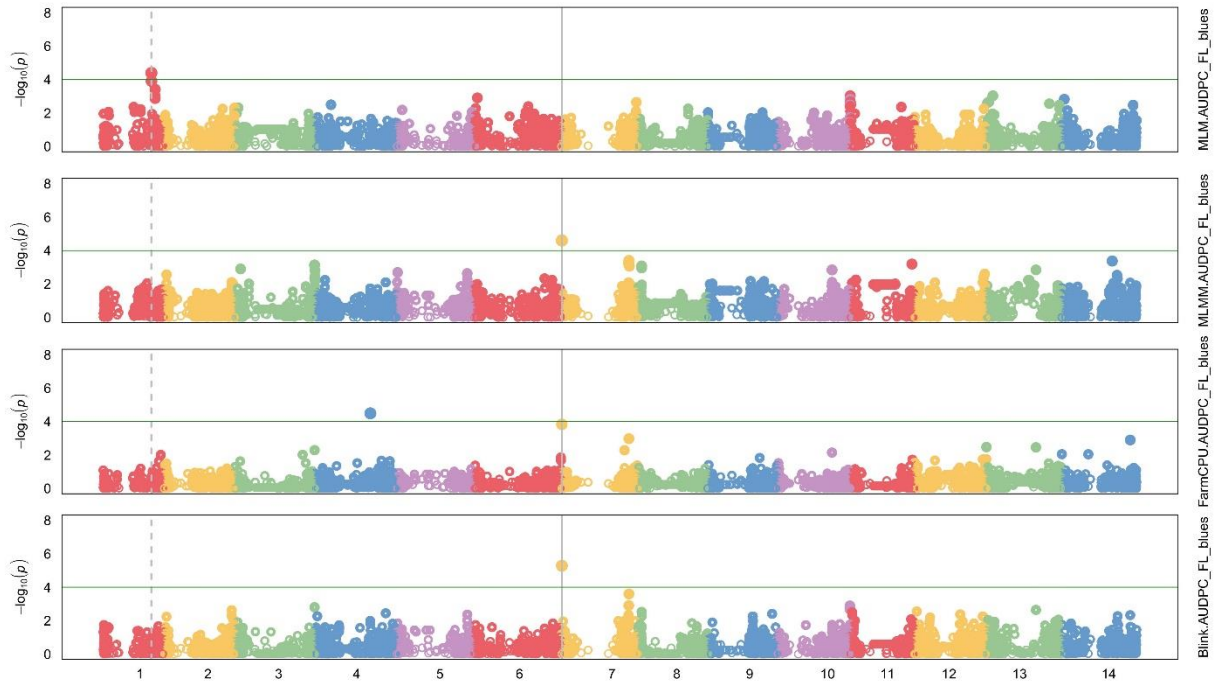

SUPPLEMENTARY FIGURE 119: Manhattan plot with all GWAS models (MLM, MLMM, FARMCPU AND BLINK) for AUDPC_Infection Type in the Flag leaf (AUDPC_Fl) in Grosseto 2022 and Q7 (Cyprous_Iberia). Numbers on the Xlab refers to the durum wheat chromosomes (1 = 1A, 2 = 1B, 3 = 2A, 4 = 2B, 5 = 3A, 6 = 3B, 7 = 4A, 8 = 4B, 9 = 5A, 10 = 5B, 11 = 6A, 12 = 6B, 13 = 7A and 14 = 7B). Ylab refers to LOD (-log$_{10}$(pvalue)).

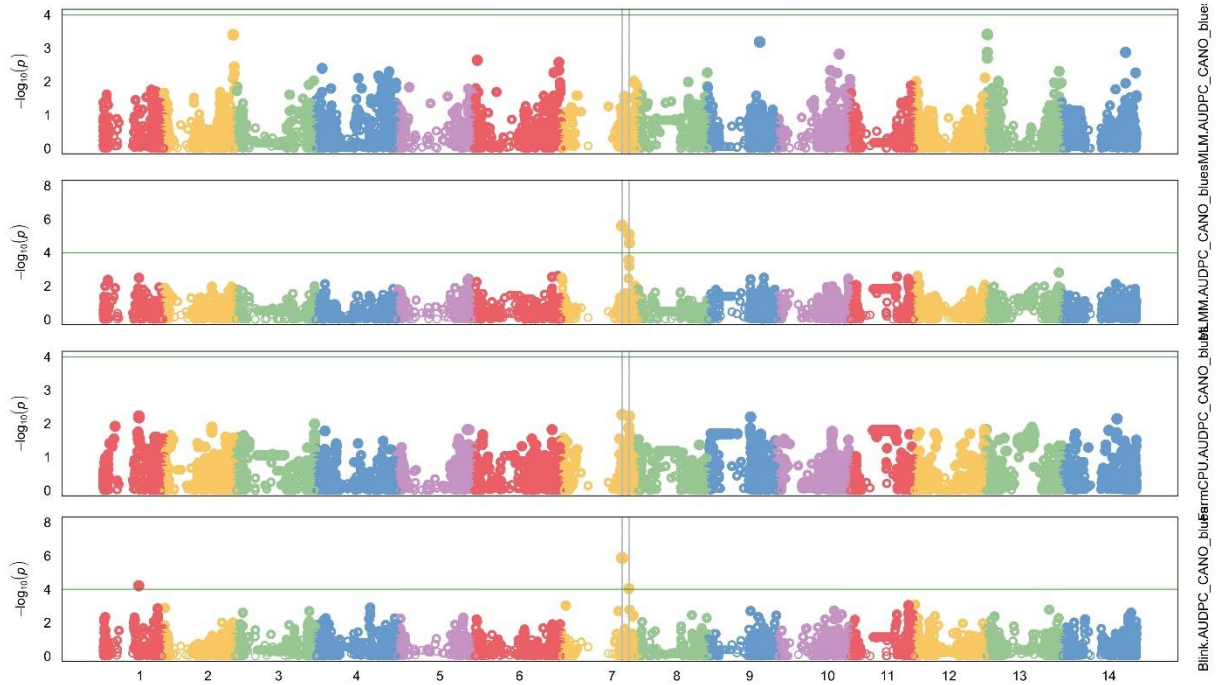

SUPPLEMENTARY FIGURE 120: Manhattan plot with all GWAS models (MLM, MLMM, FARMCPU AND BLINK) for AUDPC_Infection Type in the CANOPY (AUDPC_CANOPY) in Grosseto 2022 and Q7 (Cyprous_Iberia). Numbers on the Xlab refers to the durum wheat chromosomes (1 = 1A, 2 = 1B, 3 = 2A, 4 = 2B, 5 = 3A, 6 = 3B, 7 = 4A, 8 = 4B, 9 = 5A, 10 = 5B, 11 = 6A, 12 = 6B, 13 = 7A and 14 = 7B). Ylab refers to LOD (-log$_{10}$(pvalue)).

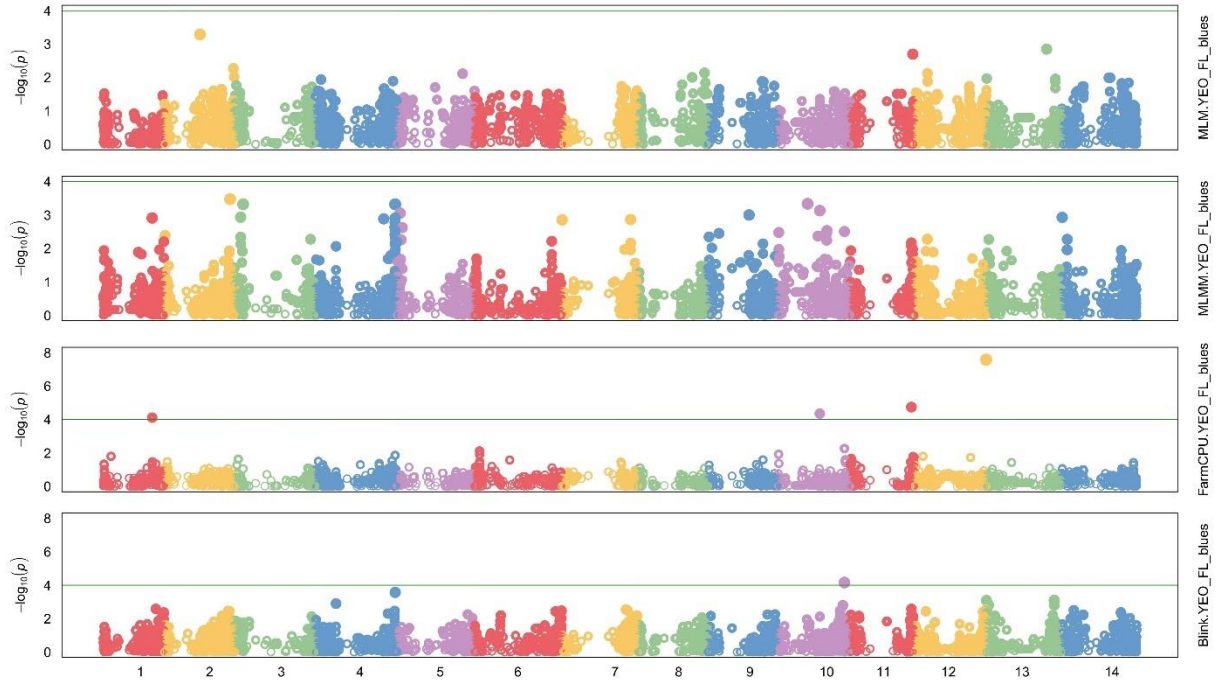

SUPPLEMENTARY FIGURE 121: Manhattan plot with all GWAS models (MLM, MLMM, FARMCPU AND BLINK) for Infection Type in the Flag Leaf (IT_Fl) in Grosseto 2022 and Q8 (West_Asian_Founders). Numbers on the Xlab refers to the durum wheat chromosomes (1 = 1A, 2 = 1B, 3 = 2A, 4 = 2B, 5 = 3A, 6 = 3B, 7 = 4A, 8 = 4B, 9 = 5A, 10 = 5B, 11 = 6A, 12 = 6B, 13 = 7A and 14 = 7B). Ylab refers to LOD (-log$_{10}$(pvalue)).

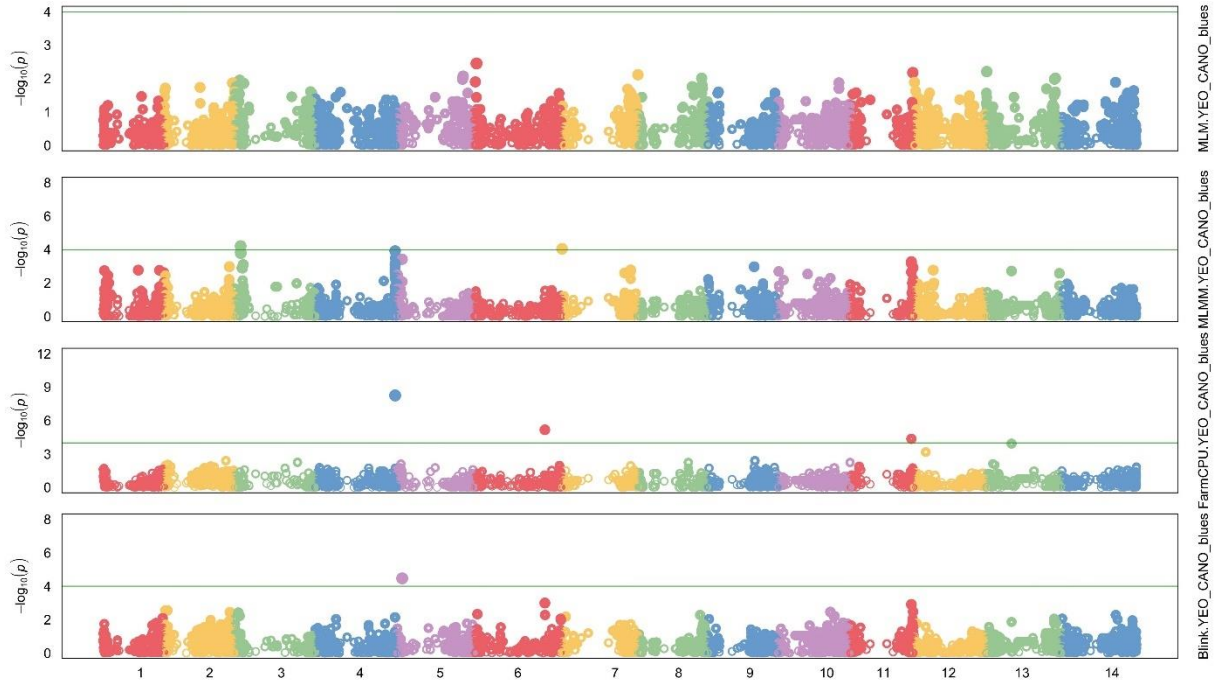

SUPPLEMENTARY FIGURE 122: Manhattan plot with all GWAS models (MLM, MLMM, FARMCPU AND BLINK) for Infection Type in the CANOPY (IT_CANOPY) in Grosseto 2022 and Q8 (West_Asian_Founders). Numbers on the Xlab refers to the durum wheat chromosomes (1 = 1A, 2 = 1B, 3 = 2A, 4 = 2B, 5 = 3A, 6 = 3B, 7 = 4A, 8 = 4B, 9 = 5A, 10 = 5B, 11 = 6A, 12 = 6B, 13 = 7A and 14 = 7B). Ylab refers to LOD (-log$_{10}$(pvalue)).

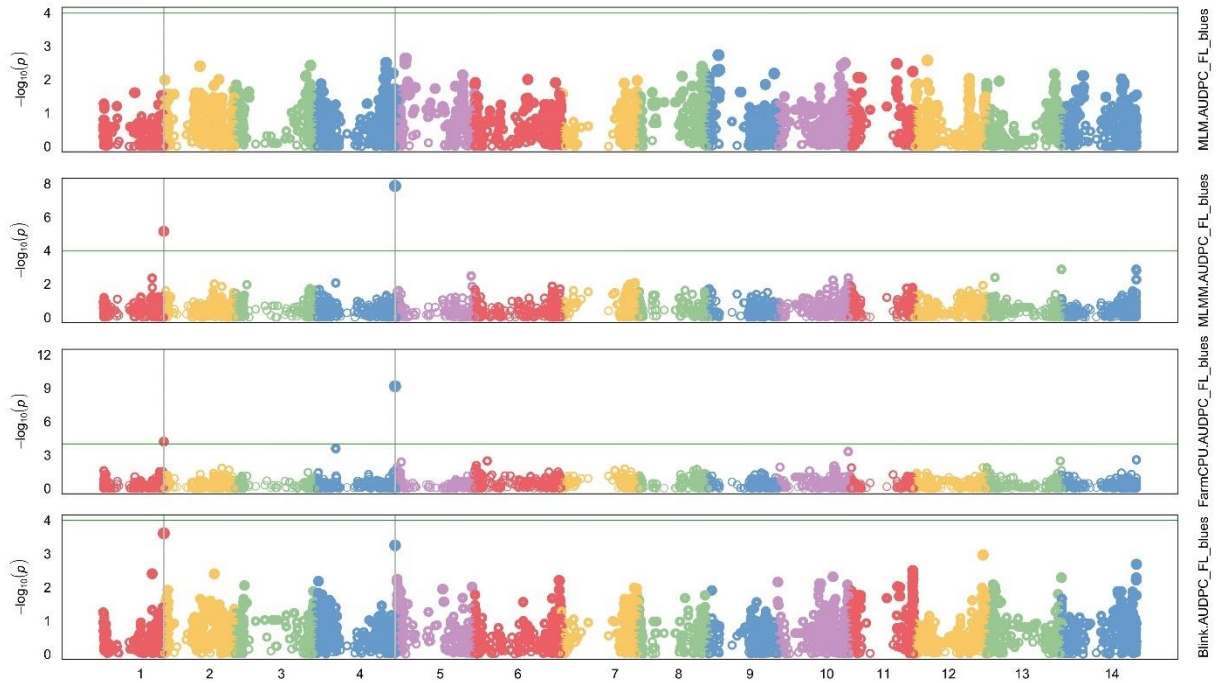

SUPPLEMENTARY FIGURE 123: Manhattan plot with all GWAS models (MLM, MLMM, FARMCPU AND BLINK) for AUDPC_Infection Type in the Flag leaf (AUDPC_Fl) in Grosseto 2022 and Q8 (West_Asian_Founders). Numbers on the Xlab refers to the durum wheat chromosomes (1 = 1A, 2 = 1B, 3 = 2A, 4 = 2B, 5 = 3A, 6 = 3B, 7 = 4A, 8 = 4B, 9 = 5A, 10 = 5B, 11 = 6A, 12 = 6B, 13 = 7A and 14 = 7B). Ylab refers to LOD (-log$_{10}$(pvalue)).

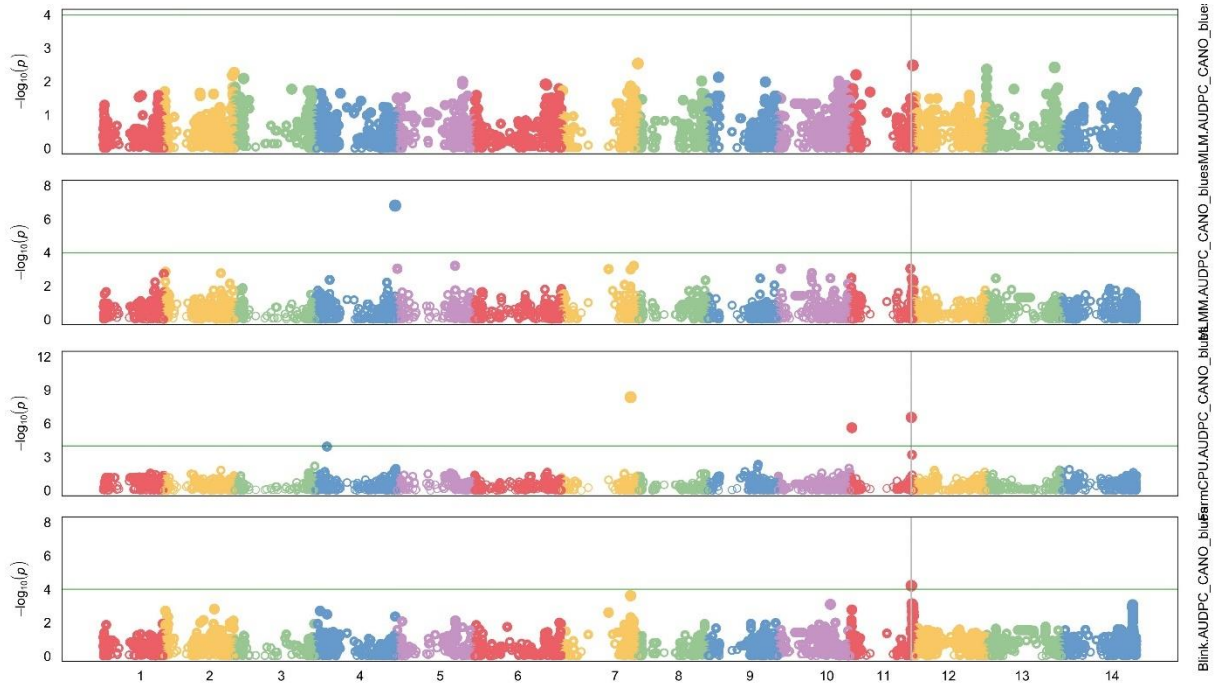

SUPPLEMENTARY FIGURE 124: Manhattan plot with all GWAS models (MLM, MLMM, FARMCPU AND BLINK) for AUDPC_Infection Type in the CANOPY (AUDPC_CANOPY) in Grosseto 2022 and Q8 (West_Asian_Founders). Numbers on the Xlab refers to the durum wheat chromosomes (1 = 1A, 2 = 1B, 3 = 2A, 4 = 2B, 5 = 3A, 6 = 3B, 7 = 4A, 8 = 4B, 9 = 5A, 10 = 5B, 11 = 6A, 12 = 6B, 13 = 7A and 14 = 7B). Ylab refers to LOD (-log$_{10}$(pvalue)).